



**HAL**  
open science

# Elabotation and characterization of oriented and nanostructured hybrid materials of interest for organic electronics

Lucia Hartmann

► **To cite this version:**

Lucia Hartmann. Elabotation and characterization of oriented and nanostructured hybrid materials of interest for organic electronics. Other. Université de Strasbourg, 2012. English. NNT : 2012STRAE028 . tel-00819804

**HAL Id: tel-00819804**

**<https://theses.hal.science/tel-00819804>**

Submitted on 2 May 2013

**HAL** is a multi-disciplinary open access archive for the deposit and dissemination of scientific research documents, whether they are published or not. The documents may come from teaching and research institutions in France or abroad, or from public or private research centers.

L'archive ouverte pluridisciplinaire **HAL**, est destinée au dépôt et à la diffusion de documents scientifiques de niveau recherche, publiés ou non, émanant des établissements d'enseignement et de recherche français ou étrangers, des laboratoires publics ou privés.



# UNIVERSITÉ DE STRASBOURG

*ÉCOLE DOCTORALE de Physique et Chimie Physique (ED 182)*

Institut Charles Sadron (CNRS UPR 122) et

INAC/SPrAM (UMR 5819 CEA-CNRS-UJF)

## THÈSE

présentée par :

**Lucia Hartmann**

soutenue le : **04 Avril 2012**

pour obtenir le grade de : **Docteur de l'université de Strasbourg**

Discipline/ Spécialité : Physique

**Elaboration et étude de matériaux hybrides  
orientés et nanostructurés d'intérêt pour  
l'électronique organique**

**Elabotation and characterization of oriented and  
nanostructured hybrid materials of interest for organic  
electronics**

**THÈSE dirigée par :**

**Monsieur Martin Brinkmann**  
**Monsieur Frédéric Chandezon**

Chargé de recherche, Institut Charles Sadron, Strasbourg  
Chercheur CEA, CEA Grenoble

**RAPPORTEURS :**

**Monsieur Yves Henri Geerts**  
**Monsieur Thierry Toupance**

Professeur, Université Libre de Bruxelles  
Professeur, Université Bordeaux 1

---

**AUTRES MEMBRES DU JURY :**

**Monsieur Johann Bouclé**  
**Monsieur Thomas Heiser**  
**Madame Marie Louise Saboungi**

Maître de Conférences, Université de Limoges  
Professeur, Université de Strasbourg  
Professeur, Université d'Orléans



# *Remerciements*

Cette thèse a été réalisée en co-direction à l'Institut Charles Sadron (UPR CNRS, Strasbourg) dans l'équipe Systèmes Complexes Moléculaires et Macromoléculaires Organisés (SYCOMMOR) sous la direction de Martin Brinkmann d'une part, et au Laboratoire de Structure et Propriétés d'Architectures Moléculaires (SPrAM, UMR 519 CEA-CNRS-UJF) au CEA Grenoble sous la direction de Frédéric Chandezon. Ce travail de recherche pluridisciplinaire m'a amenée à interagir avec de nombreuses personnes, qui m'ont permis de bénéficier de leur expérience tout au long de mon doctorat.

Tout d'abord un grand merci à Thomas Heiser pour m'avoir fait l'honneur de présider le jury. Un grand merci à Yves Geerts et Thierry Toupance pour leur travail en tant que rapporteurs de ce travail de thèse. Merci également à Johann Bouclé et Marie-Louise Saboungi pour avoir accepté de faire partie de mon jury de thèse. Merci à tous les membres du jury pour le grand intérêt qu'ils ont accordé à mes travaux, pour les questions constructives et pour s'être déplacé jusqu'à Strasbourg le jour de la soutenance.

Je tiens également à remercier Jean François Legrand et Jean Pierre Travers de m'avoir accueillie dans leurs laboratoires respectifs.

Je remercie la région Alsace ainsi que le CEA pour le soutien financier apporté à la réalisation de ce travail de thèse. Je remercie également à ce titre l'Agence Nationale pour la Recherche (ANR) qui a également contribué au succès de ce travail à travers le projet MYOSOTIS (projet n°ANR-08-NANO-012-01).

Je remercie du fond du cœur Frédéric et Martin pour m'avoir confié ce sujet intéressant et pluridisciplinaire et pour m'avoir encadré tout au long de cette thèse. En allemand, les directeurs de thèse sont communément appelés «*Doktorvater*», et je regrette qu'en français ce ne soit pas le cas. De mon côté je trouve que ce mot traduit très bien les relations que nous avons eues durant ces trois années. Vous m'avez guidé à travers cette thèse chacun à sa manière et ce fut très complémentaire. Vous avez su m'encadrer tout en me laissant la liberté de proposer mes propres idées et de prendre des initiatives. Nous avons eu des discussions parfois longues lorsque l'on n'était pas d'accord sur un point de vue. Vous

avez pris le temps de me laisser me rendre compte moi-même que souvent je n'avais pas raison. Vous m'avez poussé toujours un peu plus loin et dans les moments difficiles vous m'avez aidée à relever la tête. J'ai pu venir frapper à votre porte à n'importe quel moment et vous avez toujours trouvé le temps pour répondre à mes questions. Merci pour votre gentillesse, votre disponibilité, votre ouverture d'esprit, la liberté et la confiance que vous m'avez accordées. Merci aussi pour tout le reste! Merci de m'avoir donné l'occasion de participer à des conférences pour présenter mes travaux. Ce fut une expérience très riche !

David, un grand merci à toi pour ton amitié, pour avoir toujours été là pour moi, pour avoir écrit les *proposals* pour les mesures synchrotron et surtout pour avoir passé les nuits à ANKA et à l'ESRF. Je n'oublierai jamais les expériences de synchrotron qui sont tellement épuisantes et exceptionnelles à la fois. Un grand merci d'être venu me soutenir le jour de la soutenance ! Sans toi, cette thèse ne serait pas ce qu'elle est.

Merci à Peter Reiss et à Paul Baxter pour m'avoir permis de travailler dans vos laboratoires respectifs et pour m'avoir expliqué beaucoup de choses sur la chimie lors de nombreuses discussions très intéressantes. Vielen Dank Peter für die Hilfe Bei der « Synthèse grande échelle » das war immer sehr aufregend und ein Erlebnis für sich ! Un grand merci également à Angela pour la synthèse des nanobâtonnets et pour m'avoir toujours aidée quand j'étais perdue en chimie, ce qui arrivait assez souvent. Merci aussi à Nicolas Nerambourg pour avoir fait la première synthèse grande échelle avec moi. Merci à Matthias Welker pour avoir pris la suite sur le travail des échanges de ligands et pour sa collaboration!

Un grand merci également à Marina Gromova, Michel Bardet et à Pierre-Alain Bayle pour votre collaboration et votre grande expertise en RMN. Merci Marina d'avoir relu la partie sur la RMN de ma thèse.

Un grand merci à Lucian Roiban et à Ovidiu Ersen pour leur collaboration sur la tomographie qui a permis de découvrir la structure en bi-couche.

Merci également à Carine Julien-Rabant et Robert Pansu pour m'avoir accueilli à plusieurs reprises à Cachan et pour m'avoir initié aux mesures de photophysique et pour m'avoir donné l'opportunité de travailler dans leur laboratoire.

Jérôme et Nicolas, je vous remercie de m'avoir initiée à la physique des transistors et aux mesures de transport et au travail en salle blanche. Egalement merci à Kim Tremel et à Sabine Ludwigs pour leur collaboration sur les mesures de transport.

Merci à Jean François Legrand et Stéphanie Pouget pour nous avoir soutenu avec leur expertise lors des manips de synchrotron. Merci également à Steven Doyle, contact local à ANKA, pour les croissants du samedi matin et pour son enthousiasme et sa disponibilité. Merci également à Alexei Vorobiev, local contact à l'ESRF, pour sa disponibilité.

Navaphun, ขอขอบคุณสำหรับมิตรภาพและความช่วยเหลือ thank you for everything! Un grand merci à Sureeporn Uttiya pour avoir initié les travaux sur le brossage mécanique et pour sa collaboration.

Merci à Bernard Lotz et à Annette Thierry pour être toujours là pour répondre aux nombreuses questions des jeunes du labo et pour partager leur expérience et expertise. Merci Bernard pour les nombreux conseils concernant l'art de faire de faire de bonnes présentations !

Merci à Jean Michel Guneut, Marc Schmutz, Christian Blanc, Eric Gonthier, Patrycia, Tatjana Thomasso, Johanna, Alexandru et tous les autres pour les bons moments passés ensemble.

Je remercie également Christophe Lambour et Laurent Hermann qui m'ont aidée pour tout besoin de construction mécanique et électronique.

Chiara et Elsa merci pour les nombreuses discussions scientifiques ou non autour d'un café. Merci également à Antoine, Sudarsan Aurélie, Axel, Cécile, Dmitry, Evan, Zaireen, Mathieu, Manue, Anastasia, Saïd, Ben, Renaud, Yann, Christian. Patrice merci pour les nombreux articles. Majhoub, merci de m'avoir partagé ton bureau avec moi ! Je remercie également tous les autres membres du LEMOH !

De manière générale, je garderai un excellent souvenir de toutes les personnes de l'ICS et du LEMOH qui m'ont permis d'avancer dans ce projet scientifique mais également toutes les personnes qui ont contribué à faire que ces trois années se passent dans une atmosphère agréable. Merci entre autre aux équipes administratives des deux laboratoires.

Merci à Virginie et Florian pour votre amitié et pour m'avoir hébergé tellement souvent en me disant que je pouvais rester autant de temps que je voulais. Merci à tous mes amis Christelle et Siva, Béatrice, Audrey, Maxime, Hélène, Pauline, Rosanna, Christian, Astrid, Max, Janine, Doro, les parents Vergnats, Justine merci pour notre superbe coloc, Ousmane, merci pour m'avoir soutenu dans cette aventure, et il y a tant d'autres que je devrais citer.

Je ne pourrai pas m'arrêter là sans remercier ma famille proche ou plus lointaine qui m'a toujours soutenu et encouragée de près ou de loin durant toutes ces années et sans qui je ne serais pas là.



# Résumé de la thèse en Français

## 1. Contexte de la thèse :

Le but de cette thèse était d'élaborer et d'étudier des films minces hybrides orientés et nanostructurés composés d'un polymère semiconducteur, le poly(3-hexylthiophène) regiorégulier (P3HT) et de nanocristaux colloïdaux semiconducteurs de CdSe. Pour cela, principalement deux méthodes ont été mises en œuvre: la technique de croissance épitaxiale directionnelle initialement développée par M. Brinkmann et coll. (1), et l'orientation par broissage mécanique.

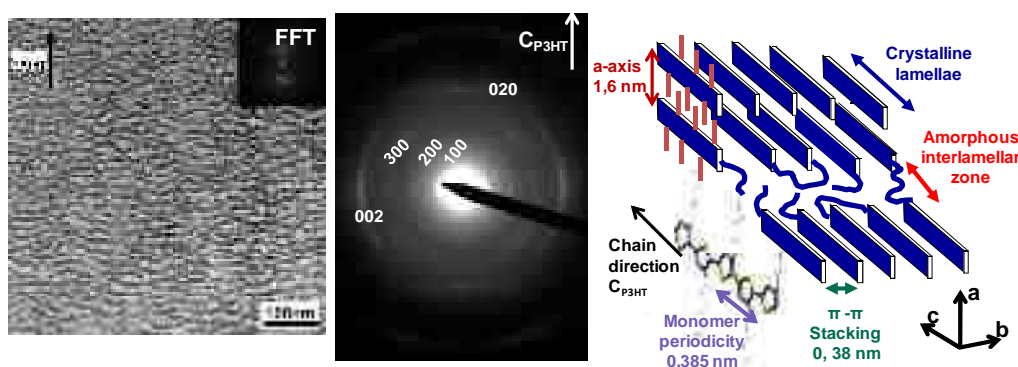


**Figure 1-1 :** *Gauche et milieu:* image TEM en champ clair et cliché de diffraction électronique correspondant d'un film de P3HT fabriqué par croissance épitaxiale directionnelle. L'image en champ clair indique une structure lamellaire formée par l'alternance de domaines cristallins (zones sombres) et de zones interlamellaires amorphes (claires). Le cliché de diffraction électronique correspond à celui d'un matériau fibrillaire semicristallin. **Droite:** Représentation schématique de la structure lamellaire du P3HT semicristallin ainsi que des directions cristallographiques du P3HT dans la phase cristallisée (1).

L'intérêt de l'orientation et de la nanostructuration de composés de P3HT et de nanoparticules (NPs) de CdSe se trouve surtout dans l'importance de la morphologie des films pour des applications dans le domaine du photovoltaïque ou de l'électronique plastique où de tels hybrides P3HT/CdSe peuvent être utilisés comme couche active (2–4). Dans le cas de cellules solaires, le P3HT (NPs de CdSe) joue le rôle de matériau donneur (accepteur) d'électrons et de transporteur de trous (électrons). L'absorption d'un photon par l'hybride génère un exciton qui peut se dissocier aux interfaces entre P3HT et NPs en une paire d'électron et trou libres, ceci du fait de la différence des affinités électroniques entre les

matériaux. La percolation des charges libres jusqu'aux électrodes induit ainsi un courant photovoltaïque. Un point majeur dans de tels matériaux est que la morphologie et les propriétés électroniques sont intimement corrélées. En effet, la longueur de diffusion d'un exciton dans le P3HT étant d'environ 10 nm, une séparation de phases entre P3HT et NPs à l'échelle de la dizaine de nm est essentielle pour optimiser la dissociation des excitons (5, 6). Par ailleurs, le transport des charges dans des polymères  $\pi$ -conjugués est généralement anisotrope, avec dans le cas du P3HT une mobilité meilleure le long de l'axe des chaînes de polymères (axe  $\mathbf{c}_{\text{P3HT}}$ ) et dans la direction du  $\pi$ -stacking (axe  $\mathbf{b}_{\text{P3HT}}$ ) comparé à l'axe des chaînes alkyles latérales du P3HT (axe  $\mathbf{a}_{\text{P3HT}}$ ) (7–10). C'est dans ce sens qu'il est intéressant de pouvoir contrôler l'orientation du polymère et l'échelle de nanostructuration de matériaux hybrides dérivés suivant l'application envisagée en électronique plastique.

M. Brinkmann et coll. ont obtenu des films de P3HT orientés et nanostructurés présentant une structure lamellaire avec alternance de zones cristallines et amorphes par croissance épitaxiale. Ils ont observé qu'avec le même procédé, en rajoutant des NPs sphériques de CdSe, ces dernières se localisent dans les zones amorphes du P3HT (11, 12). Des films hybrides orientés et nanostructurés ont ainsi été obtenus avec une échelle de nanostructuration d'environ 10-20 nm, ce qui correspond environ à la longueur de diffusion d'un exciton dans le P3HT. Cependant, la méthode utilisée pour ces travaux repose sur un procédé contrôlé manuellement et ne permettant pas une bonne reproductibilité en termes d'épaisseur et de superficie des films orientés. Les surfaces de zones homogènes étaient ainsi trop faibles pour certaines caractérisations fondamentales des films telles la diffraction des rayons X ou la mesure de propriétés optiques ainsi que pour l'utilisation de ces films dans des dispositifs type cellules solaires et transistors.

Sur la base de ces études, ce travail de thèse a consisté notamment en un développement du procédé de la croissance épitaxiale afin de l'améliorer pour obtenir des films de meilleure qualité en termes d'homogénéité de surface et d'épaisseur des films. Un deuxième aspect a consisté à appliquer le procédé développé pour le polymère seul à des mélanges polymères-nanoparticules de CdSe et d'étudier les propriétés morphologiques et structurales ainsi que la dispersion des nanoparticules dans le volume des films par tomographie électronique. Enfin, le travail a porté sur l'élaboration de films hybrides orientés de P3HT seul puis de films hybrides par un autre procédé basé sur un brossage mécanique. Dans tous les cas, la structure et les propriétés des films obtenus ont été étudiés et caractérisés par diverses techniques (microscopie électronique à transmission, diffraction électronique, diffraction de RX en incidence rasante, spectroscopie d'absorption UV-vis). Ceci a permis d'établir un modèle de la structure des films et de connaître l'importance des paramètres du procédé (vitesse de croissance, nature des substrats, poids moléculaire du polymère, proportion de NC dans le mélange, etc.) sur la structure des films.

## **2. Amélioration de la méthode de croissance épitaxiale**

Un aspect important de ce travail de thèse a consisté à améliorer la méthode de croissance épitaxiale directionnelle de films de P3HT et de matériaux hybrides P3HT/nanocristaux de CdSe. Ce travail a permis d'augmenter la surface des zones orientées à des valeurs de

l'ordre du  $\text{cm}^2$  et ce de manière reproductible. Cette amélioration a été rendue possible grâce (i) à une croissance à vitesse contrôlée (entre  $200 \mu\text{m/s}$  et  $4 \mu\text{m/s}$ ) du front de cristallisation du TCB et du P3HT à l'aide d'un système de translation motorisé, (ii) l'utilisation d'un dispositif de fusion de zone pour éviter l'évaporation du TCB lors de la croissance, (iii) l'utilisation d'un substrat guidant le PTFE et des revêtements de surface adéquats des lames de verres pour améliorer l'homogénéité des films. La *Figure 2-1* montre un schéma très simplifié de la méthode. Sur la base de ces développements, l'influence des différents paramètres expérimentaux sur la qualité des films obtenus (épaisseur, homogénéité, degré d'orientation, superficie des zones orientés, microstructure) a été étudiée. La *Figure 2-1* illustre l'effet de la vitesse de croissance sur le degré d'orientation des films.

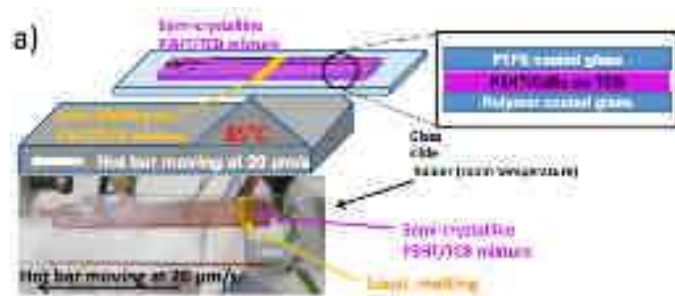


*Figure 2-1 : Schéma simplifié du procédé de croissance épitaxiale à vitesse contrôlée.*

La microscopie optique à polariseurs croisés montre qu'un film orienté de P3HT préparé à  $200 \mu\text{m/s}$  présente encore des zones claires contrairement au film préparé à  $4 \mu\text{m/s}$  pour lequel l'extinction est presque totale à l'exception d'une zone en bas de l'image (voir *Figure 2-2*). Une faible vitesse de croissance ( $4 \mu\text{m/s}$ ) permet ainsi d'obtenir des films plus homogènes sur des zones plus grandes. La structure vibronique d'absorption des films de P3HT fabriqué par cette nouvelle méthode est particulièrement bien définie et des rapports dichroïques atteignant 10 ont pu être obtenus ce qui à notre connaissance est la valeur la plus élevée mesurée pour un film de P3HT. Une analyse plus poussée de la structure vibronique d'absorption de ces films en fonction du poids moléculaire du P3HT a relevé que l'intensité relative de la contribution 0-0 augmente avec poids moléculaire. Les études de nanomorphologie par MET en haute résolution montrent que la taille des segments conjugués dans les zones cristallines tend à augmenter avec  $M_w$ . Ainsi nous montrons une corrélation très nette entre la longueur de conjugaison des zones cristallines et le poids relatif de la raie 0-0 en absorption.

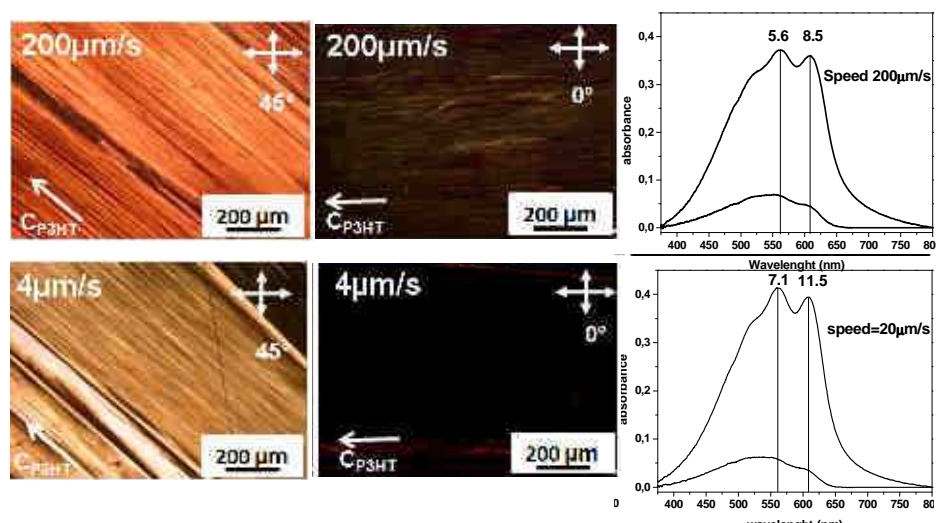


Figure 2-2 : Images de microscope optique à polariseurs croisés et spectre d'absorption UV-vis d'un film de P3HT (Haut) : préparé à une vitesse de translation du front de croissance du TCB de 200  $\mu\text{m/s}$  (bas) : préparé à 4  $\mu\text{m/s}$  (20  $\mu\text{m/s}$  pour le spectre d'absorption UV-vis).

### 3. Structure et morphologie des films épitaxiés

Des mesures de diffraction de rayons X au synchrotron ESRF ont permis de mettre en évidence d'importantes différences structurales des films en fonction de  $M_w$ . Alors que les échantillons de P3HT de masse élevée et moyenne ( $M_w \sim 50$  kDa et  $M_w \sim 20$  kDa) présentent clairement une symétrie de fibre avec comme axe de fibre l'axe des chaînes  $\text{CP}_{3\text{HT}}$ , les échantillons de P3HT de faible masse  $M_w < 10$  kDa se comportent différemment. En effet, au lieu d'une symétrie de fibre, ces échantillons présentent des domaines cristallins avec principalement trois plans de contacts préférentiels. Ainsi, nous avons pu identifier des domaines avec l'axe des chaînes perpendiculaire au substrat, des domaines avec l'axe des chaînes tiltées de  $45^\circ$  par rapport au substrat et des domaines ayant une orientation « flat-on ». Ces différences structurales se reflètent directement dans la morphologie des films observés par MET.

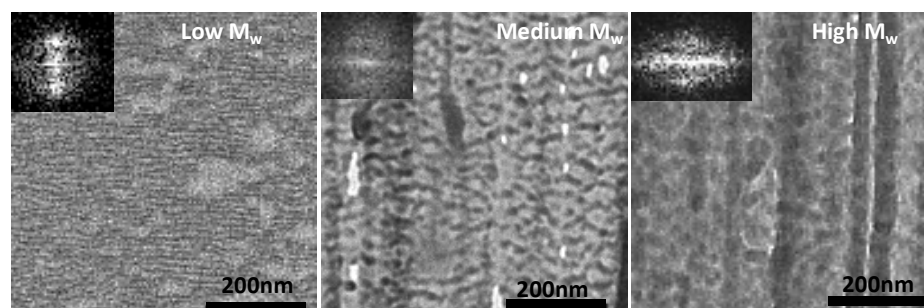


Figure 3-1 : Image de microscopie en transmission en mode champ clair pour des films avec des masses molaires des P3HT différents.

La masse moléculaire  $M_w$  du P3HT influence aussi fortement la structure lamellaire semi-cristalline (13). Pour les films préparés par la méthode à croissance lente, de grandes

périodicités lamellaires ont pu être observées (voire *Figure 3-1*). En effet pour un P3HT de masse molaire  $M_w = 50$  kDa, les périodicités  $L$  mesurées sont d'environ 40 à 45 nm. Dans la littérature, les périodicités lamellaires observées généralement sont plutôt l'ordre de  $\sim 30$  nm (*13, 14*). Nous attribuons cette augmentation de la périodicité lamellaire pour des basses vitesses de croissance à une croissance préférentielle selon l'axe des chaînes d'autant plus favorisée que la cinétique de croissance du TCB est faible.

#### 4. Orientation de Films de P3HT par broissage mécanique

En parallèle de la croissance par épitaxie, des films de P3HT et hybrides ont été orientés par la technique de broissage. Contrairement à la croissance épitaxiale, cette technique n'est pas basée sur l'utilisation d'un substrat orientant mais sur celle de forces de cisaillement permettant d'orienter les chaînes polymères. Techniquement, le principe est assez simple : un film de P3HT (ou d'un mélange hybride P3HT : CdSe) est préalablement déposé sur un substrat (par dépôt à la tournette par exemple). Puis ce film est broissé par un tissu à microfibrilles à l'aide d'un cylindre en rotation appliqué sur le film avec une pression contrôlée. Nous avons étudié le degré d'orientation et d'ordre cristallin du P3HT dans ces films broissés par spectroscopie UV-vis, TEM en haute résolution et par diffraction électronique. Des mesures de diffraction de rayons X nous ont permis de mieux comprendre le processus d'orientation des films en fonction du nombre de cycles de broissage. Le broissage mécanique de films de P3HT induit les effets suivants: (i) une orientation des chaînes de P3HT parallèlement à la direction du broissage ; (ii) l'orientation des domaines cristallins change d'une orientation préférentielle « *edge-on* » avant le broissage à une orientation « *flat-on* » après le broissage (voir sur la *Figure 4-1*).

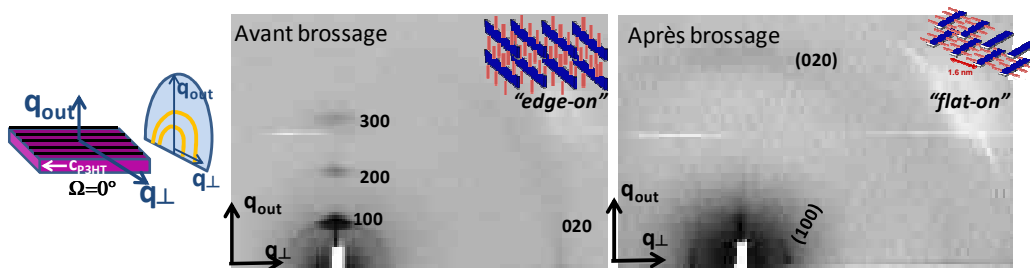


*Figure 4-1* : Clichés de diffraction de rayons X d'un échantillon avant et après broissage. Le schéma à gauche illustre la configuration des mesures. Ces mesures ont été réalisées à L'ESRF.

A l'aide de mesures de diffraction en fonction de l'angle d'incidence, nous avons pu montrer que l'orientation des films se propage de l'interface film-air à travers l'épaisseur des films avec un nombre croissant des cycles de broissage. Un impact important de la masse moléculaire du polymère a été mis en évidence. L'orientation dans le plan des films est facilement induite par broissage mécanique pour des échantillons de faible masse alors que l'orientation d'échantillons de masse élevée s'est avérée plus difficile. Ceci est attribué aux repliements et aux enchevêtrements des chaînes qui empêchent une réorientation des plans de chaînes de P3HT liés aux plans voisins du fait du  $\pi$ -stacking.

## 5. Comparaison de films brossés et épitaxiés

La comparaison de la morphologie et de la structure des films épitaxiés et brossés du P3HT a révélé des différences notables. La *Figure 5-1* montre les images de haute résolution de TEM ainsi que les clichés de diffraction électroniques. Pour les films épitaxiés, il est possible de distinguer clairement des zones cristallines séparées par des zones amorphes. Cette distinction entre amorphe et cristallin est beaucoup plus ambiguë pour des films brossés où on ne peut pas réellement mettre en évidence de limite entre les zones amorphes et zones cristallines. Les clichés de diffraction montrent aussi des différences significatives. En particulier l'absence de la réflexion (002) correspondant à la répétition des monomères le long des chaînes de P3HT est significative. Ceci peut être expliqué par différents niveaux d'ordre dans les films brossés et épitaxiés. En effet l'observation de cette réflexion suggère un ordre transrationalnel dans la direction de l'axe des chaînes impliquant un ordre cristallin 3D dans les films épitaxiés.

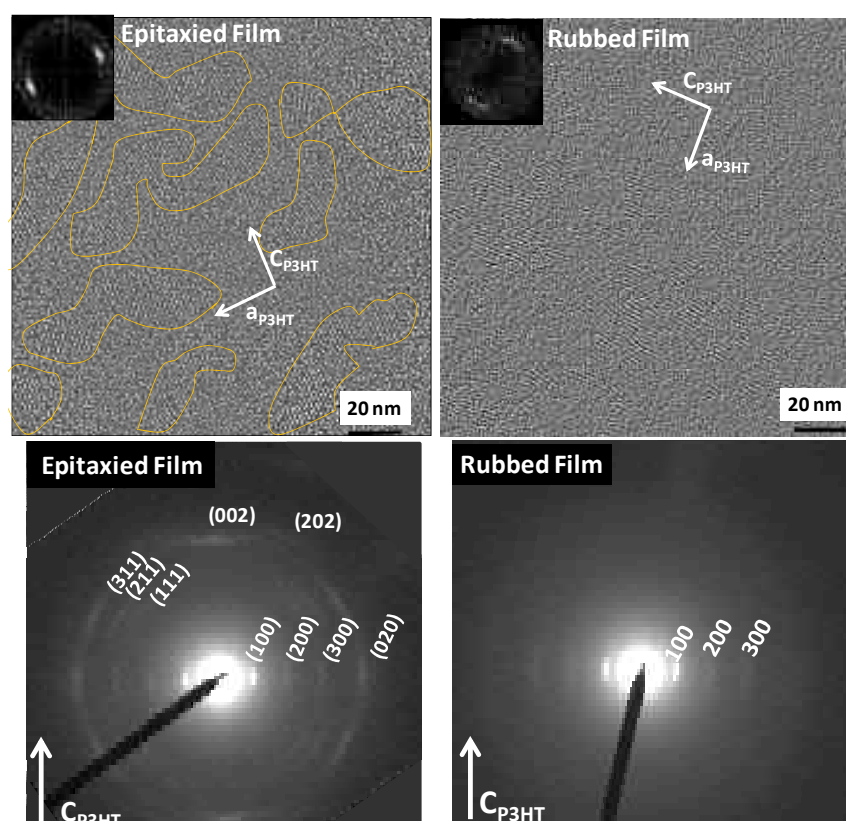


*Figure 5-1 : Images de haute résolution TEM et clichés de diffraction électroniques pour un film de P3HT ( $M_w=17,6kDa$ ) épitaxié et brossé.*

Pour les films brossés, il y a ainsi un désordre transrationalnel statistique selon l'axe des chaînes  $c_{P3HT}$ . Ceci empêche un ordre cristallin 3D et explique l'absence de la réflexion (002) dans les films brossés. Les importantes différences d'ordre et de structure entre les films épitaxiés et brossés se reflètent directement dans les spectres d'absorption UV-vis. Comme le montre la *Figure 5-2*, les films épitaxiés montrent une structure nettement plus claire que les

films brossés. En particulier, la contribution vibronique 0-0 est particulièrement intense et bien définie dans les films épitaxiés. Ceci confirme l'ordre cristallin élevé dans ces films épitaxiés.

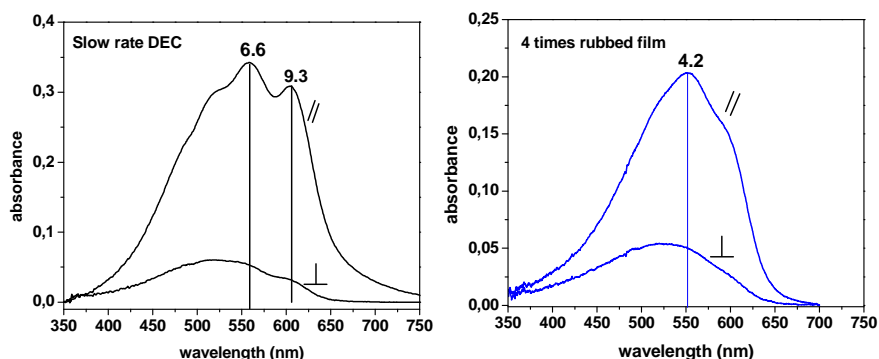


Figure 5-2: Comparaison des spectres d'absorption UV-vis de films de P3HT ( $M_w=17.2kD$ ) épitaxiés (gauche) et brossés (droite). La lumière incidente est polarisée parallèlement (//) ou perpendiculairement ( $\perp$ ) à l'axe des chaînes  $c_{P3HT}$ . Les valeurs numériques indiquent les rapports dichroïques.

## 6. Morphologie et structure de Films hybrides épitaxiés

Le procédé de croissance épitaxiale amélioré pour la croissance de films de P3HT a été également appliqué à des mélanges polymères (P3HT) et NPs colloïdales (CdSe) au cours de ce travail de thèse. Les NPs de CdSe sont composés d'un cœur inorganique recouvert d'une couche de molécules organiques, les ligands. Ces derniers assurant la stabilité colloïdale des NPs en solution (15–18). Cependant, la couche de ligands issue de la synthèse forme une barrière isolante défavorable au transfert de charge polymère  $\leftrightarrow$  NPs. Il est donc nécessaire d'échanger les ligands de synthèse par d'autres plus adaptés pour faciliter ce transfert de charge pour des applications dans dispositifs électronique ou optoélectroniques (par exemple transistors ou cellules solaires). Durant la thèse, trois points ont plus spécialement été étudiés: (i) l'influence de la taille et de la morphologie des NPs ainsi que l'effet de la proportion P3HT:NPs sur la nanostructuration ; (ii) l'étude de la distribution des NPs dans le volume des films par tomographie électronique ; (iii) l'étude de l'influence des ligands de surface sur la morphologie des films obtenus. Pour cela des protocoles d'échanges de ligands ont été spécialement développés. Toutes ces analyses ont impliqué de synthétiser des lots importants de NPs sphériques et de nano-bâtonnets (*nanorods*) de rapport d'aspect variables.

### 6.1. Distribution des NP dans le volume des films

L'étude de films hybrides par des méthodes de TEM standard ne permet pas de conclure quant à la distribution des nanoparticules dans le volume. En effet, le TEM standard donne uniquement une projection 2D du volume sondé de l'échantillon. Ainsi, pour avoir une information sur la distribution des NPs dans le volume des films, des techniques plus avancées comme la tomographie électronique sont nécessaires. En collaboration avec Ovidiu

Ersen et Lucian Roiban de l'Institut de Physique et de Chimie des Matériaux de Strasbourg (IPCMS), de telles mesures de tomographie ont pu être réalisées sur des films hybrides fabriqués par croissance épitaxiale. Des films ayant différentes charges en NPs (P3HT:NP 1:1, 1:2 et 1:3) ont été ainsi analysés. La *Figure 6-1* montre les résultats de cette analyse. Contrairement à toute attente, les NPs ne sont pas distribués dans l'ensemble du volume comme cela a souvent été observé pour des films hybrides similaires préparés par dépôt à la tournette (2, 19–21).

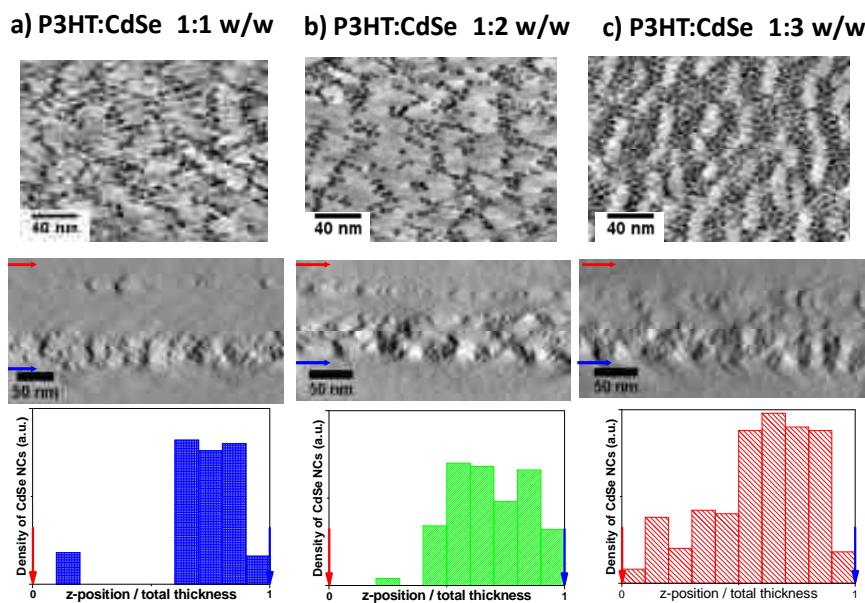


*Figure 6-1 : Etude par tomographie de films hybrides composés de P3HT:CdSe avec des proportions (w/w) a) 1:1, b) 1:2 and c) 1:3. **haut**: Coupes longitudinales extraites des volumes reconstitués. **Milieu**: Coupes observés à partir des reconstructions tomographiques **Bas**: Histogrammes normalisés montrant la variation de la densité de NPs à travers la section des films. Les flèches rouges et bleues indiquent le côté TCB ou P3HT respectivement.*

En effet, dans les films hybrides préparés par épitaxie, on observe clairement une structure en bicouche. Une couche de polymère seule avec une décoration de quelques nanoparticules puis une couche hybride nanostructurée composée d'un mélange de polymère et de nanoparticules. Plus la proportion des NPs dans le film est élevée, plus la couche hybride devient épaisse. Des analyses statistiques ont permis de conclure que pour la proportion 1:1 la couche hybride occupe environ 40% de l'épaisseur totale du film alors que pour la proportion 1:3, cette couche hybride occupe plus de 70% de l'épaisseur totale du film. Afin d'expliquer cette structure originale en bicouche, nous proposons un mécanisme de croissance faisant intervenir une concentration seuil à partir de laquelle les nanoparticules s'agrègent dans les zones amorphes du polymère.

## 6.2. Effet des ligands de surface sur la morphologie

Dans ce travail, nous avons choisi d'étudier la fonctionnalisation des NPs de CdSe par des ligands polypyridines comme la 3-*n*-hexylpyridine (HexPy), la 1-10 phénanthroline (Phen), et la 4,4',4''-tri-*tert*-butyl-2,2':6',2''-terpyridine (TerPy). Dans un premier temps, des protocoles d'échanges adaptés à ces ligands ont été mis au point. La caractérisation des réactions d'échanges de ligands a été réalisée par des techniques photophysiques (PL, UV-vis) et par RMN. Les NPs fonctionnalisées ont ensuite été insérées dans les films de P3HT afin d'étudier l'influence des ligands sur la morphologie des films. Un exemple des résultats obtenus est présenté en *Figure 6-2*. Une bonne nanostructuration est obtenue dans le cas des ligands de TerPy et de Hex Py (ayant tous les 2 des groupements solubilisants) alors que le ligand entièrement conjugué Phen conduit à une agrégation des NCs.

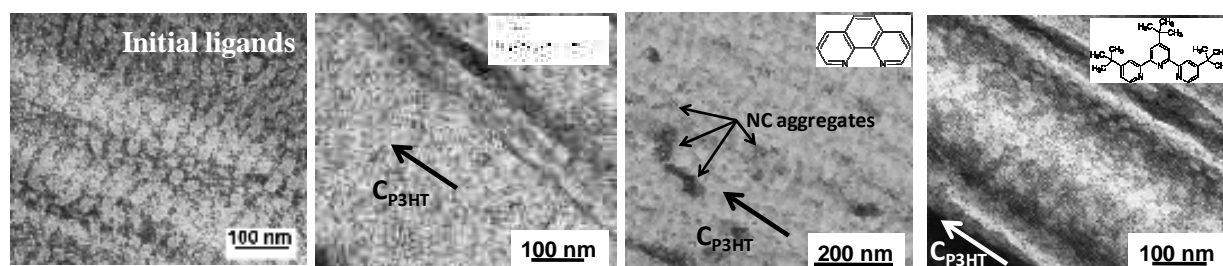


*Figure 6-2: Influence de la nature des ligands de surface des NPs de CdSe sur la morphologie des films hybrides préparés par croissance épitaxiale.*

## 7. Orientation par brossage mécanique de films hybrides

La méthode d'orientation par brossage mécanique a également été appliquée à des films hybrides. La *Figure 7-1* montre une image de TEM en haute résolution et le cliché de diffraction électronique correspondant d'un film hybride brossé. La distribution angulaire azimuthale des réflexions  $(100)_{\text{P3HT}}$  et  $(002)_{\text{CdSe}}$  mesurées à partir du cliché de diffraction est également représentée. Sur l'image de haute résolution ainsi que sur le cliché de diffraction, on voit clairement que les nanobâtonnets et les chaînes de P3HT s'orientent parallèlement à la direction de brossage. Nous avons ainsi pu montrer par des analyses supplémentaires que c'est l'orientation de la matrice polymère qui entraîne l'orientation des nanobâtonnets.

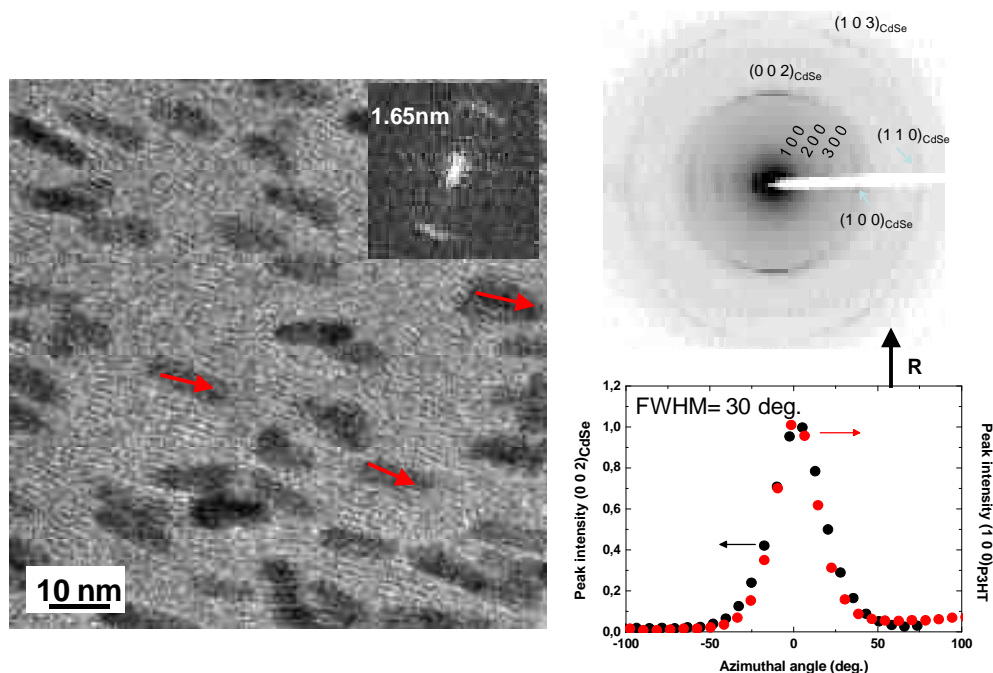


Figure 7-1 : **Gauche**: image de TEM haute résolution, l'orientation des nanorods suit l'orientation des chaînes polymères. **Droite**: cliché de diffraction électronique d'un film hybride orienté par brossage. La distribution angulaire des chaînes de polymère est identique à celle des nanorods .

La comparaison de films hybrides composés de P3HT et de nanobâtonnets de CdSe préparés par brossage mécanique et par croissance épitaxiale s'avère intéressante. La *Figure 7-2* montre des clichés de diffraction et des images en champ clair correspondantes d'un film hybride préparé par brossage mécanique et d'un second préparé par épitaxie. La comparaison de ces films montre des différences notables. Tout d'abord, l'orientation dans le plan des nanobâtonnets est clairement définie dans les films brossés alors que dans les films épitaxiés cette orientation est peu marquée. De plus, dans les films brossés, les nanobâtonnets sont clairement orientés avec leur axe  $c_{CdSe}$  (grand axe) parallèle à la surface du film alors que l'image en champ clair du film épitaxié ainsi que la faible intensité de la réflexion  $(002)_{CdSe}$  suggèrent la présence de nanobâtonnets inclinés. Par ailleurs, la nanostructuration clairement visible dans les films épitaxiés est absente dans les films brossés. Ceci est lié à l'absence d'une structure lamellaire semi-cristalline bien définie dans le cas des films brossés.

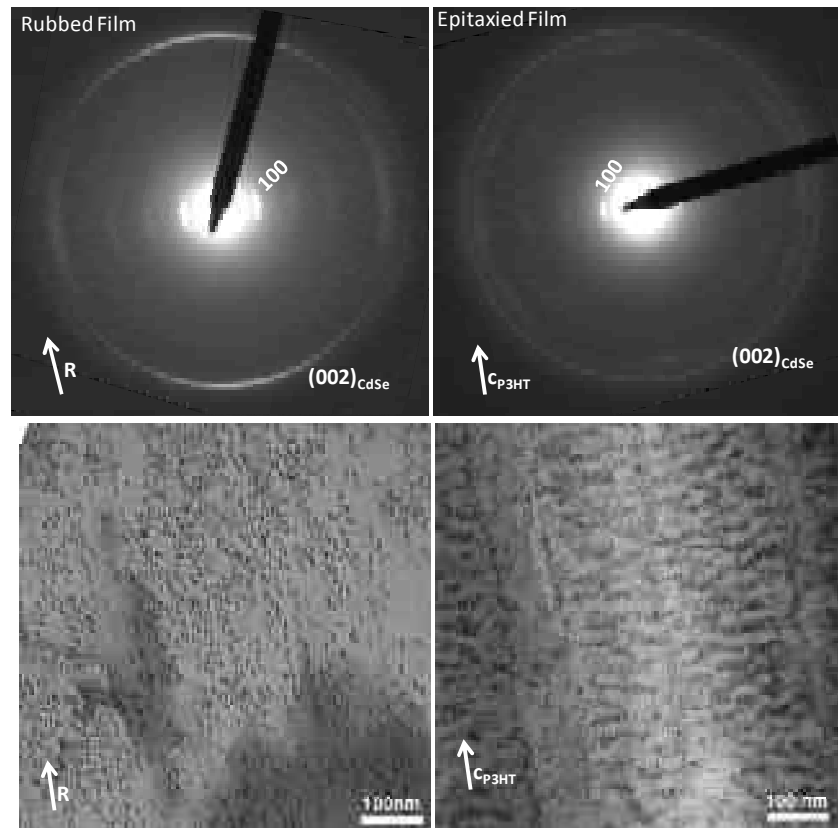


Figure 7-2 : Clichés de diffraction électronique et images TEM en champs clair d'un film hybride orienté par brossage mécanique et d'un film préparé par croissance épitaxiale directionnelle. La masse moléculaire du P3HT est de  $M_w = 17,6$  kDa et les dimensions nanobâtonnets sont  $20 \text{ nm} \times 5 \text{ nm}$ .

## 8. Conclusion

Ce travail de thèse avait pour but d'élaborer des films orientés et nanostructurés de matériaux hybrides polymères conjugués : NPs colloïdales présentant un intérêt pour l'électronique plastique. Deux méthodes ont principalement été mises en œuvre pour l'élaboration de ces films : la croissance épitaxiale directionnelle et le brossage mécanique. Pour la méthode de croissance épitaxiale directionnelle, des développements instrumentaux en vue d'améliorer la qualité des films orientés en termes d'homogénéité sur de grandes surfaces ont été réalisés. L'influence des différents paramètres (vitesse de croissance, substrats, etc.) sur la qualité des films obtenus a été étudiée. En parallèle, l'influence du poids moléculaire sur la morphologie et la structure des films épitaxiés et brossés a été mis en évidence. D'importantes différences d'orientation, de structure et de morphologie sont observées aussi bien en fonction du poids moléculaire du P3HT qu'en fonction de la méthode de préparation des films. Concernant les films hybrides épitaxiés, des mesures de tomographie électronique ont mis en évidence une structure en bi-couche jamais observée jusqu'alors pour de tels films. Ces observations ont permis de proposer un scénario de croissance des films. Ce travail présente une caractérisation en termes de morphologie, structure et orientation assez complète des systèmes de P3HT seul ainsi que des films hybrides épitaxiés et brossés. Dans le

futur, des caractérisations électriques (transport de charge) et des applications de ces systèmes dans des dispositifs sont envisagés. Les procédés et méthodes développés au cours de ce travail peuvent être appliqués à d'autres systèmes (autres polymères et NCs). Des études préliminaires effectuées au laboratoire ont également permis de montrer que des polymères à faible gap d'énergie peuvent être orientés à l'aide de la croissance épitaxiale directionnelle à vitesse contrôlée. Ceci ouvre de nouvelles perspectives par exemple dans le domaine de la détermination de la structure cristalline de ces polymères afin de mieux comprendre les corrélations entre la structure et les propriétés de ces polymères.

- (1) Brinkmann, M.; Wittmann, J.-C. Orientation of regioregular poly(3-hexylthiophene) by directional solidification: a simple method to reveal the semicrystalline structure of a conjugated polymer. *Advanced Materials* **2006**, *18*, 860-863.
- (2) Huynh, W. U.; Dittmer, J. J.; Alivisatos, A. P. Hybrid nanorod-polymer solar cells. *Science* **2002**, *295*, 2425-7.
- (3) Xu, T.; Qiao, Q. Conjugated polymer-inorganic semiconductor hybrid solar cells. *Energy & Environmental Science* **2011**, *4*, 2700.
- (4) Borchert, H. Elementary processes and limiting factors in hybrid polymer/nanoparticle solar cells. *Energy & Environmental Science* **2010**, *3*, 1682.
- (5) Günes, S.; Neugebauer, H.; Sariciftci, N. S. Conjugated polymer-based organic solar cells. *Chemical reviews* **2007**, *107*, 1324-38.
- (6) Yang, X.; Loos, J. Toward high-performance polymer solar cells: the importance of morphology control. *Macromolecules* **2007**, *40*, 1353-1362.
- (7) Jimison, L. H.; Toney, M. F.; McCulloch, I.; Heeney, M.; Salleo, A. Charge-transport anisotropy due to grain boundaries in directionally crystallized thin films of regioregular poly(3-hexylthiophene). *Advanced Materials* **2009**, *21*, 1568-1572.
- (8) O'Connor, B.; Kline, R. J.; Conrad, B. R.; Richter, L. J.; Gundlach, D.; Toney, M. F.; DeLongchamp, D. M. Anisotropic structure and charge transport in highly strain-aligned regioregular poly(3-hexylthiophene). *Advanced Functional Materials* **2011**, *21*, 3697-3705.
- (9) Sirringhaus, H.; Brown, P. J.; Friend, R. H.; Nielsen, M. M.; Bechgaard, K.; Laneveld-Voss, B. M. W.; Spiering, A. J. H.; Janssen, R. . J.; Meijer, E. W.; Herwig, P.; Leeuw, D. M. Two-dimensional charge transport in self-organized, high-mobility conjugated polymers. *Nature* **1999**, *401*, 685-688.
- (10) Sirringhaus, H.; Bird, M.; Richards, T.; Zhao, N. Charge transport physics of conjugated polymer field-effect transistors. *Advanced Materials* **2010**, *4307*, n/a-n/a.
- (11) Brinkmann, M.; Wittmann, J.-C. Orientation of regioregular poly(3-hexylthiophene) by directional solidification: a simple method to reveal the semicrystalline structure of a conjugated polymer. *Advanced Materials* **2006**, *18*, 860-863.
- (12) Brinkmann, M.; Aldakov, D.; Chandezon, F. Fabrication of oriented and periodic hybrid nanostructures of regioregular poly(3-hexylthiophene) and CdSe nanocrystals by directional epitaxial solidification. *Advanced Materials* **2007**, *19*, 3819-3823.
- (13) Brinkmann, M.; Rannou, P. Effect of molecular weight on the structure and morphology of oriented thin films of regioregular poly(3-hexylthiophene) grown by directional epitaxial solidification. *Advanced Functional Materials* **2007**, *17*, 101-108.
- (14) Zhang, R.; Li, B.; Iovu, M. C.; Jeffries-El, M.; Sauv e, G.; Cooper, J.; Jia, S.; Tristram-Nagle, S.; Smilgies, D. M.; Lambeth, D. N.; McCullough, R. D.; Kowalewski, T. Nanostructure dependence of field-effect mobility in regioregular poly(3-hexylthiophene) thin film field effect transistors. *Journal of the American Chemical Society* **2006**, *128*, 3480-1.
- (15) Park, J.; Joo, J.; Kwon, S. G.; Jang, Y.; Hyeon, T. Synthesis of monodisperse spherical nanocrystals. *Angewandte Chemie (International ed. in English)* **2007**, *46*, 4630-60.

- (16) Murray, C. B.; Kagan, C. R.; Bawendi, M. G. Synthesis and characterization of monodisperse nanocrystals and close-packed nanocrystal assemblies. *Annual Review of Materials Science* **2000**, *30*, 545-610.
- (17) Talapin, D. V.; Lee, J.-S.; Kovalenko, M. V.; Shevchenko, E. V. Prospects of colloidal nanocrystals for electronic and optoelectronic applications. *Chemical reviews* **2010**, *110*, 389-458.
- (18) Green, M. The nature of quantum dot capping ligands. *Journal of Materials Chemistry* **2010**, *10*, 5797-5809.
- (19) Li, S.-S.; Chang, C.-P.; Lin, C.-C.; Lin, Y.-Y.; Chang, C.-H.; Yang, J.-R.; Chu, M.-W.; Chen, C.-W. Interplay of three-dimensional morphologies and photocarrier dynamics of polymer/TiO<sub>2</sub> bulk heterojunction solar cells. *Journal of the American Chemical Society* **2011**, *133*, 11614-20.
- (20) Oosterhout, S. D.; Wienk, M. M.; van Bavel, S. S.; Thiedmann, R.; Koster, L. J. A.; Gilot, J.; Loos, J.; Schmidt, V.; Janssen, R. a J. The effect of three-dimensional morphology on the efficiency of hybrid polymer solar cells. *Nature materials* **2009**, *8*, 818-24.
- (21) Van-Bavel, S. S.; Sourty, E.; de With, G.; Loos, J. Three-dimensional nanoscale organization of bulk heterojunction polymer solar cells. *Nano letters* **2009**, *9*, 507-13.





# Table of Contents

RESUME DE LA THESE EN FRANÇAIS.....	V
TABLE OF CONTENTS.....	XXI
ABBREVIATIONS USED IN THE TEXT .....	XXIX
INTRODUCTION .....	1
CHAPTER 1. FUNDAMENTAL CONCEPTS AND STATE OF THE ART .....	7
1. CONJUGATED POLYMERS .....	9
2. SEMI-CRYSTALLINE POLYMERS: THE CASE OF REGIOREGULAR POLY(3-HEXYLTIOPHENE) .....	11
2.1. CRYSTAL STRUCTURE OF P3HT .....	12
2.2. CHAIN FOLDING AND LAMELLAR STRUCTURE .....	13
2.3. VARIOUS MORPHOLOGIES AND ORIENTATION OF P3HT THIN FILMS .....	15
2.3.1. <i>Effect of the molecular weight</i> .....	16
2.3.2. <i>Specific processing methods and specific morphologies</i> .....	16
3. CONTROLLED ORIENTATION OF POLYMERS.....	18
3.1. ORIENTATION BY USING MECHANICAL SHEARING FORCES .....	19
3.2. ORIENTATION BY USING AN ORIENTING SUBSTRATE.....	21
3.3. DIRECTIONAL CRYSTALLIZATION AND ZONE CASTING.....	22
3.4. INTEREST OF THE ORIENTATION OF CONJUGATED POLYMERS: EXAMPLES .....	23
3.4.1. <i>Anisotropy of charge transport</i> .....	23
3.4.2. <i>Anisotropy of optical properties</i> .....	24
4. COLLOIDAL SEMICONDUCTING NANOCRYSTALS.....	25
4.1. BASIC PHYSICAL PROPERTIES.....	25
4.2. CRYSTAL STRUCTURE OF THE NANOCRYSTALS .....	27
4.3. SYNTHESIS.....	28
4.4. LIGAND EXCHANGE AND SURFACE TREATMENT .....	29
4.4.1. <i>Necessity for ligand exchange</i> .....	29
4.4.2. <i>Different approaches for ligand exchange/surface treatment</i> .....	29
5. HYBRID MATERIALS .....	31
5.1. HYBRID VERSUS ALL ORGANIC MATERIALS .....	31

## Table of Contents

---

5.2.	CHARGE GENERATION AND TRANSPORT IN HYBRID MATERIALS .....	32
5.3.	THE CONCEPT OF BULK HETEROJUNCTION AND IMPORTANCE OF THE MORPHOLOGY CONTROL .....	33
5.4.	FABRICATION OF HYBRID MATERIALS.....	34
5.4.1.	<i>Simple blends of the components</i> .....	34
5.4.2.	<i>Hybrids via capping the NCs with the conjugated polymer</i> .....	35
5.4.3.	<i>Hybrids via molecular recognition</i> .....	36
5.4.4.	<i>In situ growth</i> .....	36
5.5.	ORIENTED AND NANOSTRUCTURED HYBRIDS.....	37
<b>6.</b>	<b>SCOPE OF THIS WORK.....</b>	<b>37</b>
 <b>CHAPTER 2. CDSE NANOCRYSTALS: SYNTHESIS AND SURFACE FUNCTIONALIZATION.....</b>		<b>49</b>
<b>1.</b>	<b>GENERALITIES ON THE SYNTHESIS OF CDSE NANOCRYSTALS.....</b>	<b>51</b>
<b>2.</b>	<b>SYNTHESIS OF SPHERICAL NANOCRYSTALS.....</b>	<b>52</b>
2.1.	SYNTHESIS ON THE LAB SCALE .....	53
2.2.	LARGE SCALE SYNTHESIS .....	54
2.2.1.	<i>Synthesis</i> .....	54
2.2.2.	<i>Purification of the nanocrystals</i> .....	55
2.3.	CHARACTERIZATION OF THE OBTAINED CDSE NANOCRYSTALS.....	56
2.3.1.	<i>Particle size determination</i> .....	57
2.3.2.	<i>Crystallinity</i> .....	60
<b>3.</b>	<b>SYNTHESIS OF ROD SHAPED CDSE NANOCRYSTALS .....</b>	<b>61</b>
<b>4.</b>	<b>STUDY OF THE LIGAND CAPPING OF AS PREPARED CDSE NANOCRYSTALS.....</b>	<b>62</b>
<b>5.</b>	<b>SURFACE CHEMISTRY OF THE NANOCRYSTALS: LIGAND EXCHANGE WITH POLYPYRIDINES.....</b>	<b>69</b>
5.1.	PRINCIPLE AND CHARACTERIZATION OF LIGAND EXCHANGE .....	72
5.2.	INFLUENCE OF THE CAPPING LIGANDS ON THE OPTICAL PROPERTIES OF NCS .....	74
5.2.1.	<i>Influence on the static absorption and photoluminescence spectra</i> .....	74
5.3.	ADSORPTION-DESORPTION KINETICS OF THE LIGANDS ON THE NCS SURFACES.....	78
5.3.1.	<i>Fast adsorption-desorption kinetics: Py, HexPy and Phen</i> .....	78
5.3.2.	<i>Slow adsorption-desorption kinetics: TerPy</i> .....	82
<b>6.</b>	<b>CONCLUSION .....</b>	<b>86</b>

---

<b>CHAPTER 3. ORIENTATION OF P3HT BY DIRECTIONAL EPITAXIAL CRYSTALLIZATION: PROCESS AND PROCESS IMPROVEMENT.....</b>	<b>95</b>
<b>1. DESCRIPTION OF THE ORIENTATION METHOD AND THE STRUCTURE .....</b>	<b>97</b>
1.1. PRINCIPLE .....	97
1.2. MORPHOLOGY AND STRUCTURE OF THE ORIENTED P3HT FILMS.....	98
1.3. CRYSTALLINE STRUCTURE OF P3HT .....	99
<b>2. THE INITIAL DEC PROCESS USING A KOEFFLER BENCH .....</b>	<b>101</b>
<b>3. IMPROVEMENT OF THE METHOD: TOWARDS A PERFECT TCB SUBSTRATE .....</b>	<b>104</b>
3.1. REDUCTION OF THE GRAIN BOUNDARIES: CONTROL OF THE GROWTH KINETICS AND LOCAL MELTING .....	104
3.2. IMPROVEMENT OF THE IN-PLANE ORIENTATION: INTRODUCTION OF A GUIDING SUBSTRATE OF PTFE.....	106
<b>4. APPLICATION TO P3HT .....</b>	<b>108</b>
<b>5. IDEAL SUBSTRATES FOR UNIFORM AND EXTENDED P3HT FILMS .....</b>	<b>111</b>
5.1.1. <i>Attempts on silicon substrates</i> .....	111
5.1.2. <i>Growth on polymeric substrates</i> .....	112
5.1.3. <i>Recapitulation:</i> .....	113
<b>6. THE FINAL SLOW-DEC PROCESS .....</b>	<b>114</b>
<b>7. DEC VERSUS SLOW-DEC: IN-PLANE ORIENTATION AND LAMELLAR STRUCTURE .....</b>	<b>115</b>
<b>8. CONCLUSION .....</b>	<b>117</b>
<b>CHAPTER 4. ORIENTED P3HT FILMS BY SLOW DIRECTIONAL EPITAXIAL CRYSTALLIZATION .....</b>	<b>121</b>
<b>1. MORPHOLOGY, STRUCTURE, CRYSTALLINITY: EXAMPLE OF A MEDIUM-<math>M_w</math> SAMPLE.....</b>	<b>123</b>
1.1. MACROSCOPIC MORPHOLOGY.....	123
1.2. STRUCTURAL ANALYSIS BY GIXD : PREFERENTIAL CONTACT PLANE VERSUS FIBER SYMMETRY .....	125
1.2.1. <i>Scattering geometries</i> .....	125
1.2.2. <i>1D and 2D GIXD measurements</i> .....	127
1.3. SHAPE AND SIZE OF THE CRYSTALLINE DOMAINS .....	131
<b>2. THE EFFECT OF THE MOLECULAR WEIGHT .....</b>	<b>135</b>
2.1. EFFECT OF $M_w$ ON THE STRUCTURE AND ORIENTATION .....	136
2.1.1. <i>Low-<math>M_w</math> P3HT (<math>M_w = 6.1</math> kDa)</i> .....	136
2.1.2. <i>High-<math>M_w</math> sample (<math>M_w = 50.1</math> kDa)</i> .....	139
2.1.3. <i>Effect of <math>M_w</math> on the degree of in-plane orientation</i> .....	141
2.2. EFFECT OF $M_w$ ON THE LAMELLAR STRUCTURE AND PERIODICITY .....	142
2.2.1. <i>TEM observations</i> .....	142

2.2.2.	Discussion.....	144
2.3.	EFFECT OF $M_w$ ON THE NANOMORPHOLOGY AND CRYSTALLITE SHAPE .....	145
2.4.	CORRELATION BETWEEN THIN FILM STRUCTURE AND OPTICAL PROPERTIES.....	148
2.4.1.	Anisotropy and vibronic structure of the absorption .....	149
2.4.2.	Evolution of the absorption spectrum with $M_w$ .....	150
2.4.3.	Discussion on the origin of the vibronic structure of the absorption spectra.....	151
<b>3.</b>	<b>CONCLUSION .....</b>	<b>155</b>
<b>CHAPTER 5.</b>	<b>ORIENTED THIN P3HT FILMS VIA MECHANICAL RUBBING .....</b>	<b>161</b>
<b>1.</b>	<b>INTRODUCTION AND PRINCIPLE OF THE TECHNIQUE.....</b>	<b>163</b>
<b>2.</b>	<b>EPERIMENTAL CONDITIONS.....</b>	<b>164</b>
2.1.	MECHANICAL RUBBING.....	164
2.2.	GIXD MEASUREMENTS .....	164
<b>3.</b>	<b>EFFECT OF MECHANICAL RUBBING ON THE STRUCTURE AND ORIENTATION OF MEDIUM <math>M_w</math> (17.6 KDA) P3HT FILM .....</b>	<b>165</b>
3.1.	MORPHOLOGY OF THE RUBBED P3HT FILMS .....	165
3.2.	IN-PLANE ORIENTATION OF THE RUBBED FILMS.....	166
3.3.	EVOLUTION OF THE STRUCTURE WITH INCREASING RUBBING LENGTH.....	168
3.3.1.	Thin Film structure and orientation before rubbing.....	168
3.3.2.	After one rubbing cycle R1 .....	169
3.3.3.	After two rubbing cycles (R2):.....	171
3.4.	PROPAGATION OF THE ORIENTATION TROUGH THE FILM THICKNESS .....	172
3.4.1.	Case of the 1R sample.....	172
3.4.2.	Case of the 2R sample.....	175
3.5.	POSSIBLE SCENARIO AND INTERPRETATION OF THE ORIENTATION OF P3HT UPON RUBBING: .....	176
<b>4.</b>	<b>EFFECT OF <math>M_w</math> ON P3HT FILM ORIENTED BY MECHANICAL RUBBING .....</b>	<b>179</b>
4.1.	IN-PLANE ORIENTATION VS $M_w$ .....	179
4.2.	STRUCTURE AND ORIENTATION OF LOW- $M_w$ SAMPLES.....	181
4.2.1.	Effect of $M_w$ on the crystallinity and crystal structure of rubbed films .....	182
4.2.2.	Orientation of the crystalline domains of a low- $M_w$ sample.....	184
A)	DESCRIPTION OF THE $Q_L$ AND THE $Q_{\parallel}$ 2D GIXD PATTERN: .....	184
B)	EVOLUTION OF THE STRUCTURE WITH $P(\alpha)$ : .....	186
4.3.	MORPHOLOGY AND NANOMORPHOLOGY: MEDIUM- VERSUS LOW- $M_w$ .....	186
4.4.	VIBRONIC STRUCTURE OF ABSORBANCE .....	188
4.4.1.	Effect of rubbing on the vibronic structure of absorbance.....	188

4.4.2.	<i>Effect of <math>M_w</math> on the vibronic structure of absorbance</i> .....	189
4.5.	IMPACT OF RUBBING AND $M_w$ ON THE FIELD EFFECT CHARGE MOBILITY .....	191
4.5.1.	<i>Transistor fabrication and experimental protocol</i> .....	191
4.5.2.	<i>Charge transport anisotropy</i> .....	192
<b>5.</b>	<b>RUBBING VERSUS SLOW-DEC: A COMPARATIVE STUDY</b> .....	<b>194</b>
5.1.	STRUCTURE: FIBER SYMMETRY VERSUS PREFERENTIAL CONTACT PLANE .....	194
5.2.	IN-PANE ORIENTATION NANOMORPHOLOGY AND CRYSTALLINE ORDER .....	195
5.3.	UV-VIS ABSORBANCE SPECTROSCOPY .....	200
<b>6.</b>	<b>CONCLUSION</b> .....	<b>201</b>
<b>CHAPTER 6.</b>	<b>ORIENTED AND NANOSTRUCTURED HYBRID THIN FILMS PREPARED BY</b> .....	<b>207</b>
	<b>SLOW DIRECTIONAL EPITAXIAL CRYSTALLIZATION</b> .....	<b>207</b>
<b>1.</b>	<b>INTRODUCTION TO NANOSTRUCTURED HYBRID MATERIALS</b> .....	<b>209</b>
<b>2.</b>	<b>HYBRID THIN FILMS PREPARED WITH AS SYNTHESIZED CDSE NCS</b> .....	<b>211</b>
2.1.	CASE OF SPHERICAL NCS .....	211
2.1.1.	<i>In-plane orientation of the hybrid thin films</i> .....	211
2.1.2.	<i>Crystallinity of the hybrid films</i> .....	212
2.1.3.	<i>3D distribution of CdSe nanospheres within the hybrid films</i> .....	213
2.1.4.	<i>Proposal for a growth scenario of the oriented hybrid films</i> .....	219
2.2.	CASE OF ROD SHAPED NCS .....	222
2.2.1.	<i>Effect of the shape of the NCs on the morphology of the hybrid films</i> .....	222
2.2.2.	<i>In-plane of the hybrids: effect of the weight ratio of the nanorods</i> .....	223
2.2.3.	<i>Orientation of CdSe nanorods</i> .....	224
2.2.4.	<i>In-plane orientation of the P3HT</i> .....	226
2.2.5.	<i>Tomographic analysis of samples with CdSe nanorods</i> .....	227
<b>3.</b>	<b>EFFECT OF THE SURFACE FUNCTIONALIZATION OF THE CDSE NCS ON THE MORPHOLOGY OF THE ORIENTED HYBRID FILMS</b> .....	<b>228</b>
<b>4.</b>	<b>CONCLUSION</b> .....	<b>231</b>
<b>CHAPTER 7.</b>	<b>ORIENTED HYBRID THIN FILMS BY MECHANICAL RUBBING</b> .....	<b>239</b>
<b>1.</b>	<b>ORIENTATION OF NANORODS AND HYBRIDS: STATE OF THE ART</b> .....	<b>241</b>
<b>2.</b>	<b>EFFECT OF RUBBING ON THIN FILMS OF NRS</b> .....	<b>242</b>
<b>3.</b>	<b>RUBBED HYBRID THIN FILMS: MORPHOLOGY, STRUCTURE, ORIENTATION</b> .....	<b>244</b>

3.1.	CASE OF THE AS DEPOSITED FILM (NOT RUBBED R0).....	244
3.2.	STUCTURE AND MORPHOLOGY OF HYBRID THIN FILMS AFTER RUBBING .....	246
3.2.1.	<i>Comparison of the in-plane and out-of plane distribution of the NRs</i> .....	248
3.2.2.	<i>Effect of the wt% of NR on the in-plane orientation</i> .....	251
<b>4.</b>	<b>ANISOTROPY OF THE UV-VIS ABSORBANCE</b> .....	<b>256</b>
<b>5.</b>	<b>RUBBING VS EPITAXY: A COMPARATIVE STUDY</b> .....	<b>258</b>
<b>6.</b>	<b>CONCLUSION</b> .....	<b>260</b>
	<b>CONCLUSIONS AND PERSPECTIVES</b> .....	<b>267</b>
	<b>ANNEXES AND EXPERIMENTAL PROTOCOLS</b> .....	<b>275</b>
<b>1.</b>	<b>STEP BY STEP INSTRUCTION FOR SLOW RATE DEC</b> .....	<b>277</b>
1.1.	THE POWDER PREPARATION .....	277
1.2.	THE FILM PREPARATION .....	277
<b>2.</b>	<b>PTFE MACHINES IMPROVEMENT AND USERS' GUIDE</b> .....	<b>279</b>
<b>3.</b>	<b>DETAILED EXPERIMENTAL DESCRIPTION OF MECHANICAL RUBBING</b> .....	<b>280</b>
3.1.	PREPARATION OF THE THIN FILMS BY THE DOCTOR BLADE METHOD .....	282
3.1.1.	<i>Pure P3HT films</i> .....	282
3.2.	HYBRID FILMS (P3HT + NANORODS).....	282
<b>4.</b>	<b>PREPARATION OF THE SUBSTRATES</b> .....	<b>283</b>
<b>5.</b>	<b>OPTICAL CHARACTERIZATIONS</b> .....	<b>284</b>
5.1.	UV-VISIBLE ABSORPTION SPECTROSCOPY .....	284
5.1.1.	<i>UV-vis spectroscopy of colloidal solutions of CdSe</i> .....	284
5.1.2.	<i>Polarized UV-vis of P3HT or hybrid thin films</i> .....	284
5.2.	PHOTOLUMINESCENCE .....	285
5.2.1.	<i>PL spectroscopy of colloidal solutions of CdSe</i> .....	285
5.3.	OPTICAL POLARIZED MICROSCOPY.....	285
<b>6.</b>	<b>X-RAY DIFFRACTION</b> .....	<b>285</b>
6.1.	XRD ON P3HT AND HYBRID THIN FILMS.....	285
6.2.	XRD ON CdSe NCS AFTER SYNTHESIS .....	285
	<b>XRD SPECTRA OF THE AS-SYNTHESISED NANOCRYSTALS</b> .....	<b>285</b>
<b>7.</b>	<b>TRANSMISSION ELECTRON MICROSCOPY (TEM) MEASUREMENTS</b> .....	<b>286</b>

7.1.	TEM ON AS-SYNTHESIZED CdSe NANOCRYSTALS .....	286
7.2.	STANDARD TEM AND TEM TOMOGRAPHY ON P3HT AND HYBRID THIN FILMS .....	286
7.2.1.	<i>TEM sample preparation</i> .....	286
7.2.2.	<i>Standard TEM</i> .....	286
7.2.3.	<i>Electron tomography experiments</i> .....	287
<b>8.</b>	<b>NMR</b> .....	<b>287</b>
<b>9.</b>	<b>THERMOGRAVIMETRIC ANALYSIS ON NCS</b> .....	<b>288</b>
<b>10.</b>	<b>TRANSISTOR FABRICATION</b> .....	<b>288</b>



## *Abbreviations used in the text*

<b>AIZ</b>	Amorphous interlamellar zone
<b>BF</b>	Bright Field
<b>CdSt<sub>2</sub></b>	Cadmium stearate
<b>CL</b>	Contour length of the polymer (length of the extended chain)
<b>DEC</b>	Directional Epitaxial Crystallization
<b>DR</b>	Dichroic ratio
<b>ED</b>	Electron diffraction
<b>E-P coupling</b>	Electron-phonon coupling
<b>FET</b>	Field-effect transistor
<b>FFT</b>	Fast Fourier Transform
<b>FWHM</b>	Full Width at Half Maximum
<b>GIXD</b>	Grazing Incidence X-ray Diffraction
<b>HexPy</b>	3,n-hexylpyridine
<b>HOMO</b>	Highest Occupied Molecular Orbital
<b>HR-TEM</b>	High resolution Transmission Electron Microscopy
<b>ITO</b>	Indium Tin oxide
<b>JCPDS</b>	Joint Committee on Powder Diffraction Standards
<b>L</b>	Total lamellar periodicity (crystalline + amorphous)
<b>L<sub>a</sub></b>	Extension of the crystalline domains in the <b>a<sub>P3HT</sub></b> direction
<b>L<sub>b</sub></b>	Extension of the crystalline domains in the <b>b<sub>P3HT</sub></b> direction
<b>L<sub>stem</sub></b>	Length of a stem within a crystalline domain
<b>LUMO</b>	Lowest Unoccupied Molecular Orbital
<b>M<sub>w</sub></b>	Molecular weight
<b>NC</b>	Nanocrystal
<b>NMR</b>	Nuclear magnetic resonance
<b>NP</b>	Nanoparticle
<b>NR</b>	Nanorod
<b>OA</b>	Oleylamine

<b>ODE</b>	Octadecene
<b>OFET</b>	Organic Field Effect Transistor
<b>OTS</b>	Octadecyltrichlorosilane
<b>PCBM</b>	1-[3-(méthoxycarbonyl)propyl]-1-phényl-[6,6]C <sub>61</sub>
<b>PCE</b>	Power conversion efficiency
<b>PDI</b>	Polydispersity Index
<b>PEDOT:PSS</b>	Poly(3,4-ethylenedioxythiophene):poly(styrenesulfonate)
<b>PET</b>	Polyethylene
<b>Phen</b>	1-10, phenanthroline
<b>PL</b>	Photoluminescence
<b>POM</b>	Polarized Optical Microscope
<b>PTFE</b>	Polytetrafluoroethylene (or teflon)
<b>P3HT</b>	Poly(3-hexylthiophene)
<b>PVP</b>	Poly(4-vinyl-phenol)
<b>Py</b>	Pyridine
<b>R0, R1....R4</b>	Rubbed 0,1....4 times
<b>rr-P3HT</b>	regioregular poly(3-hexylthiophene)
<b>SA</b>	Stearic acid
<b>SEM</b>	Scanning electron microscope
<b>Slow-DEC</b>	Directional Epitaxial Crystallization at slow rate (improved method)
<b>TCB</b>	1,3,5 trichlorobenzene
<b>TEM</b>	Transmission Electron Microscopy
<b>TEM-BF</b>	Transmission Electron Microscopy in the Bright Field mode
<b>TOPO</b>	Trioctylphosphine oxide
<b>TOPSe</b>	Selenium Trioctylphosphine
<b>TerPy</b>	4,4',4''-Tri- <i>tert</i> -Butyl-2,2':6',2''-terpyridine
<b>UV-vis</b>	Ultraviolet-visible spectroscopy
<b>XRD</b>	X-ray diffraction





# *Introduction*

Inorganic materials based electronic devices have become ubiquitous in our society and in our everyday life. During the last fifty years, many efforts were put into the miniaturization of inorganic based electronic devices and the reduction of their cost to make them accessible to a broader public. The field of organic electronics *i.e.* devices based on carbon materials seeks for an additional reduction of the production costs using processing techniques of the electro-active materials from inks using *e.g.* roll-to-roll printing techniques. In addition, organic electronic devices are lighter and flexible as compared to their inorganic counterparts. Indeed, organic solar cells produced by roll-to-roll printing techniques on flexible substrates or flexible displays are among the goals in the field of organic electronics and some products have already appeared on the market.

The recent tremendous developments in the field can mainly be ascribed to the discovery in the 1970<sup>ies</sup> of  $\pi$ -conjugated polymers that are conducting in their doped state, *i.e.* that behave as synthetic metals (1). This breakthrough was awarded in 2000 by the Nobel Prize of Chemistry with Alan J. Heeger, Alan MacDiarmid and Hideki Shirakawa as the recipients. Few years after their discovery, it was shown that  $\pi$ -conjugated polymers exhibit semiconducting properties in their undoped state. This was probably one of the most meaningful progresses made in the field of organic electronics. Indeed the solution processability in combination with their semi conducting properties made of conjugated polymers the main actors in organic electronics. Nowadays these materials are already widely used for example in organic solar cells (2), organic light emitting diodes (3, 4) or organic field effect transistors (5).

Other solution processable semiconductors are inorganic semiconductor colloidal nanocrystals. Although the synthesis of such nanoparticles was known for years, novel and highly successful methods of synthesis in terms of the size control and size polydispersity appeared in the 1990<sup>ies</sup> raised a lot of attention of the scientific community on these nano-objects in view of their numerous potential applications. Inorganic semiconductor

nanocrystals are of main interest due to their size-dependent energy bandgap and thus their tunable photoluminescence and absorption properties. To cite only one example, such nanocrystals have already been successfully used for light emitting diodes (6, 7).

Both colloidal NCs as well as semiconducting conjugated polymers possess the main advantage of cost-efficient solution processability. The association of inorganic NCs and conjugated polymers to form hybrid electro-active materials gave rise to the field of hybrid electronics although this terminology is not frequently used. These hybrid materials aim at combining the advantages of both the organic and inorganic components in order to achieve better devices performances as compared to all-organic ones. Hybrid materials were first successfully used for the fabrication of light emitting diodes (8) and later in solar cells at the beginning of the 2000<sup>ies</sup> (9, 10). Since then, hybrid materials have raised increasing interest in relation with the development of the so-called Organic and Large Area Electronics.

For a successful application of conjugated polymers, nanocrystals and hybrid materials in electronic devices, a deep understanding of their physical properties is essential. A key role is played by the macromolecular organization, the crystallinity, the structure and the orientation of the polymers. In the case of hybrids, the orientation but also the morphology and the dispersion of the NCs within the polymer matrix are of major importance. This opens the door to a large field of fundamental research on the controlled orientation and the controlled structuration of conjugated polymers as well as of hybrid materials.

In the scope of this work, we were mainly interested in the controlled orientation and the structural and morphological characterization of thin films of regioregular poly(3-hexylthiophene) (rr-P3HT). Therefore, we used mainly two preocssing methods: **directional epitaxial crystallization** and **mechanical rubbing**. Of main interest in this work was also the elaboration and the full characterization of hybrid thin films composed of P3HT and CdSe nanocrystals prepared by these two methods. Another point of focus was to understand the processes allowing for the orientation and the nanostructuration of such hybrid materials.

The first part of this thesis (**chapter 1**) introduces the current state of the art and the main fundamental properties of the materials used in the scope of this work. It also emphasizes the main principles in view of the successful applications of such hybrid materials in organic electronic devices such as solar cells. Semi-crystalline polymers as well as main approaches for the controlled orientation of polymers will be introduced. The concept of excitonic bulk heterojunction and the required materials architectures will be described. Finally main approaches described in the literature for the controlled fabrication of hybrid materials will be presented.

In **Chapter 2**, we focus on the synthesis and the surface chemistry of CdSe nanocrystals. Main attention will be paid to the surface functionalization of CdSe nanocrystals using various polypyridine ligands. The number of anchoring groups of the ligands to the NCs was varied and the influence of the latter on the adsorption-desorption kinetics of the ligands

on the nanocrystals as studied by advanced  $^1\text{H}$  nuclear magnetic resonance methods will be studied.

**Chapter 3** is devoted to the preparation of highly oriented P3HT thin films by directional epitaxial crystallization (DEC) (11). The method will be presented and the main improvements of the method realized in the frame of this PhD work will be described. The improved method will be called slow-DEC.

In **Chapter 4**, thin P3HT films prepared by the improved slow-DEC method will be fully characterized in terms of orientation, morphology, structure and UV-vis absorption spectra. The impact of the slow growth kinetics as well as of the molecular weight  $M_w$  of the P3HT on the structure and shape of the crystalline domains will be studied.

**Chapter 5** is devoted to an alternative orientation method for P3HT thin films, namely mechanical rubbing. The thin P3HT films will be fully characterized in terms of the morphology, the degree of orientation, the structure and the influence of the UV-vis absorption spectra. A comparative study of P3HT films grown using directional epitaxial crystallization or mechanical rubbing will also be presented in this Chapter.

**Chapters 6 and 7** are devoted to the elaboration of highly oriented thin hybrid films composed of P3HT and CdSe nanocrystals. **Chapter 6** treats about hybrid thin films grown by slow-DEC. A main focus of this Chapter is to unravel the 3D distribution of the nanocrystals within the hybrid thin films using the electron tomography technique. The impact of the chemical nature of the capping ligands of the NCs on their integration into the P3TH matrix is also explored. In **Chapter 7**, the elaboration and the characterization of hybrid thin films by mechanical rubbing is discussed. A comparative study of oriented hybrid thin films prepared by slow-DEC and by mechanical rubbing in terms of morphology and orientation will also be presented

- (1) Shirakawa, H.; Louis, E.; Macdiarmid, A.; Chiang, C.; Heeger, A. Synthesis of electrically conducting organic polymers: halogen derivatives of polyacetylene, (CH)<sub>x</sub>. *Journal of the Chemical Society, Chemical Communications* **1977**, *16*, 578-580.
- (2) Günes, S.; Neugebauer, H.; Sariciftci, N. S. Conjugated polymer-based organic solar cells. *Chemical reviews* **2007**, *107*, 1324-38.
- (3) Friend, R. H.; Gymer, R. W.; Holmes, A. B.; Burroughes, J. H.; Marks, R. N.; Taliani, C.; Bradley, D. D. C.; Lo, M.; Salaneck, W. R.; Santos, D. A. D.; Bre, J. L. Electroluminescence in conjugated polymers. *Nature* **1999**, 121-128.
- (4) Burroughes, J. .; Bradley, D. D. C.; Brown, A. R.; Marks, R. N.; Mackay, K.; Friend, R. H.; Bruns, P. L.; Holmes, A. B. Light-emitting diodes based on conjugated polymers. *Nature* **1990**, *347*, 539-541.
- (5) Sirringhaus, H.; Kawase, T.; Friend, R. H.; Shimoda, T.; Inbasekaran, M.; Wu, W.; Woo, E. P. High-resolution inkjet printing of all-polymer transistor circuits. *Science* **2000**, *290*, 2123-2126.
- (6) Hikmet, R. A. M.; Chin, P. T. K.; Talapin, D. V.; Weller, H. Polarized-light-emitting quantum-rod diodes. *Advanced Materials* **2005**, *17*, 1436-1439.
- (7) Rizzo, A.; Nobile, C.; Mazzeo, M.; De Giorgi, M.; Fiore, A.; Carbone, L.; Cingolani, R.; Manna, L.; Gigli, G. Polarized light emitting diode by long-range nanorod self-assembling on a water surface. *ACS nano* **2009**, *3*, 1506-12.
- (8) Colvin, V. L.; Schlamp, M. C.; Alivisatos, A. P. Light-emitting diodes made from CdSe nanocrystals and a semi-conducting polymer. *Nature* **1995**, *370*, 354.
- (9) Huynh, W. U.; Peng, X.; Alivisatos, A. P. CdSe nanocrystal rods/poly (3-hexylthiophene) composite photovoltaic devices. *Advanced materials* **1999**, *11*, 923-927.
- (10) Huynh, W. U.; Dittmer, J. J.; Alivisatos, A. P. Hybrid nanorod-polymer solar cells. *Science* **2002**, *295*, 2425-7.
- (11) Brinkmann, M.; Wittmann, J.-C. Orientation of regioregular poly(3-hexylthiophene) by directional solidification: a simple method to reveal the semicrystalline structure of a conjugated polymer. *Advanced Materials* **2006**, *18*, 860-863.





# ***Chapter 1. Fundamental concepts and state of the art***

*This chapter is dedicated to the introduction of techniques and concepts relevant to this PhD work. In a first part,  $\pi$ -conjugated and semi-crystalline polymers will be briefly introduced. Several techniques for the controlled orientation of polymers will thereafter be presented. Basic physical and chemical properties of semiconducting nanocrystals will be in the focus of an ensuing part. Finally, the last part of this chapter focuses on hybrid materials. We will mainly introduce hybrid materials of interest for organic and large area electronics. Some basic concepts about the application of such hybrids will be presented. The main strategies for the fabrication of hybrids materials will be introduced and discussed.*



## 1. Conjugated polymers

$\pi$ -conjugated polymers (hereafter referred to as conjugated polymers) are macromolecules presenting delocalized  $\pi$  orbitals and electrons in their backbone (1–4). On a chemical point of view, conjugated polymers are composed of  $sp_2$  hybridized carbon atoms in their backbone (Figure 1-1). This means that two neighbouring  $sp_2$  carbon atoms are bound via double bonds composed of one  $\sigma$ -bond and one  $\pi$ -bond, each carbon providing one electron of each type (1–4). The  $2s$  orbital of each carbon atom hybridizes with the  $2p_x$  and  $2p_y$  to form the  $sp_2$  orbital. On the other hand, the  $\pi$  orbitals form via the hybridization of the  $2p_z$  orbitals. This is illustrated in Figure 1-1 in the case of the  $C_2H_4$  ethylene molecule (represented as  $H_2C=CH_2$ ), the simplest and model molecule for  $sp_2$  hybridization. A conjugated polymer will be composed of alternating double and single bonds which allows to have delocalized  $\pi$ -orbitals along the backbone of the polymer (1, 2). The length scale of this delocalization is the so-called conjugation length. The conjugation length is generally not equivalent to the total length of the polymer chain as small chemical defects, twisting or chain folding of the polymer chain can interrupt the conjugation.

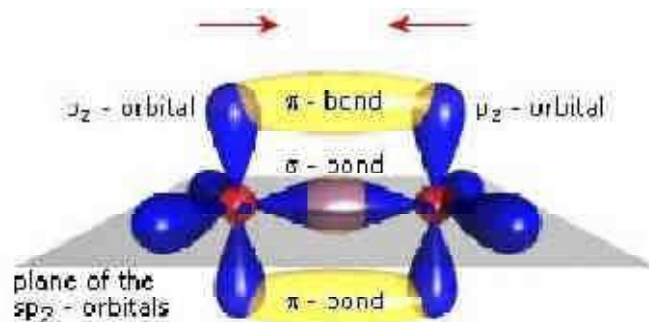


Figure 1-1: Schematic illustration of the formation of double bond in ethylene ( $C_2H_4$ ). Reproduced from (4).

The existence of free  $\pi$  electrons in conjugated polymers gives them specific optical and electronic properties as compared to saturated organic macromolecules. In particular, the delocalization of  $\pi$  electrons makes the propagation of electric excitation along the entire macromolecule possible. The deformation of the  $\pi$ -orbitals induced by external electric fields renders polarization effects important (2). The delocalization and conjugation of the  $\pi$ -orbitals in one plane also induces a stiffness of the polymer backbone which tends to planarize the macromolecule. A lack of planarity of the conjugated backbone therefore goes along with the loss of conjugation (2). This stiffness of conjugated polymers has also a strong influence on its organisation in the solid phase.

To a certain extent, energy bands in conjugated polymers are formed in a similar way as in inorganic crystals (Figure 1-2). For a single atom, discrete energy values are available. If several atoms associate to form a molecule, the energy levels of each atom are degenerated and slightly shifted as compared to the levels of a single atom. In the case of the ethylene

molecule, a bonding ( $\pi$ ) and antibonding ( $\pi^*$ ) orbitals are formed due to the  $sp_2$  hybridization. The  $\pi$  orbital is frequently called highest occupied molecular orbital (HOMO) and the  $\pi^*$  orbital lowest unoccupied molecular orbital (LUMO). In the case of a macromolecule such as polyacetylene containing an infinite amount of  $sp_2$  carbon atoms, these energy levels form the valence ( $\pi$ ) and the conduction ( $\pi^*$ ) energy bands which are separated by the bandgap (Figure 1-2). The bandgap of the conjugated polymer depends on the chemical structure of the polymer and on its conjugation length: the longer the conjugation length, the smaller the bandgap. In their undoped form, conjugated polymers are intrinsically semiconductors. It is possible to transform them into conductors via doping. Due to the position of their HOMO-LUMO levels, most conjugated polymers are p-type conductors. In order to have n-type semiconducting conjugated polymers, the LUMO level should be lower to approx. -4 eV with respect to the vacuum level (3). By analogy, p-type semiconducting conjugated polymers should have a high HOMO level(3).

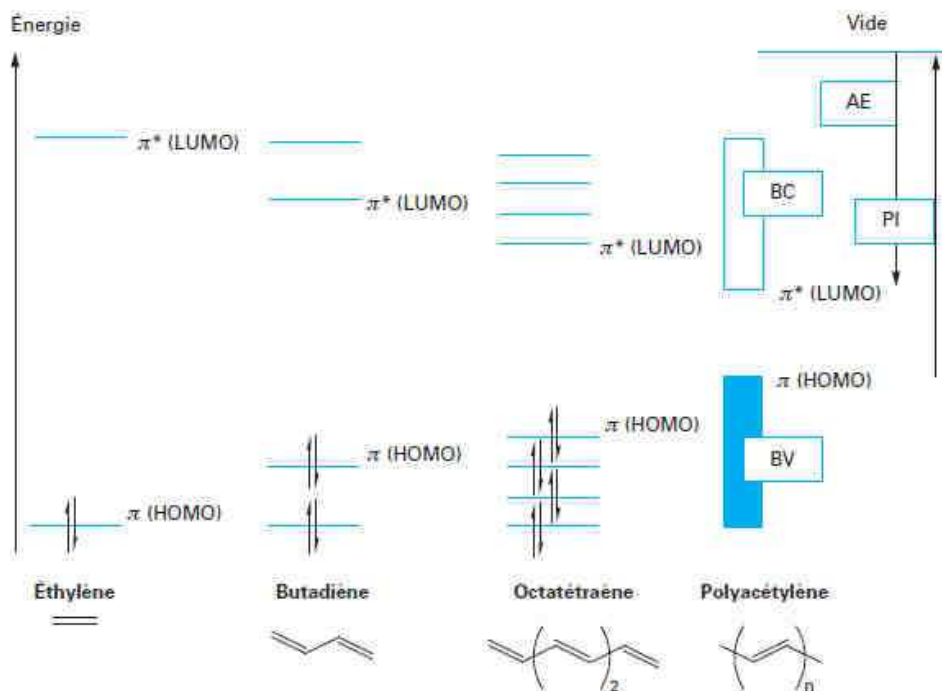
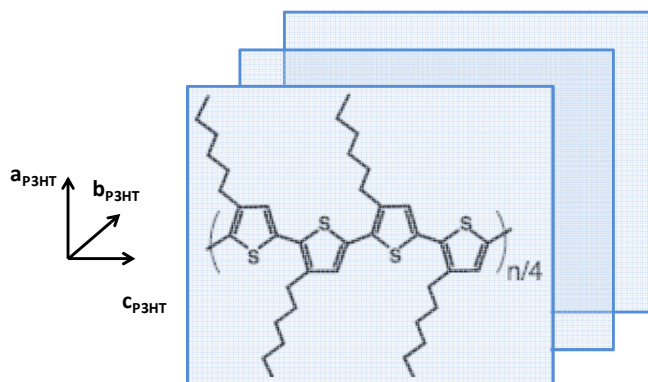


Figure 1-2 : Illustration of the formation of the conduction band (BC) and the valence band (BV) in polyacetylene  $CH_3(C_2H_2)_nCH_3$ . Reproduced from (2).

One of the most successful and most used conjugated polymer is nowadays regioregular poly(3-hexylthiophene) (rr-P3HT). Figure 1-3 shows the chemical structure of rr-P3HT. P3HT is composed of a conjugated backbone of thiophene rings and lateral hexyl side chains that provide solubility and allow to prepare semiconducting inks in common solvents (5). Regioregularity refers to the control of the configuration of the lateral side chains. Regioregular P3HT is mostly defined as the head-tail head-tail (*i.e.* the monomers bind between the position 2 of the first one and the position 5' of the second one) configuration. Although widely used, P3HT is not an ideal system. The HOMO level of P3HT lies quite high and this impedes a long term operating stability because of oxygen doping.

Also, the bandgap of P3HT (2.0-2.1 eV, depending on the molecular weight) is such that the absorption spectrum of P3HT only covers the visible portion of the solar spectrum (3).

In the solid state, P3HT chains can stack via the  $\pi$ -stacking interactions to form molecular crystals. *Figure 1-3* illustrates the formation of  $\pi$ -stacked planes of P3HT. The convention used for the different crystallographic axis in P3HT crystallites is also illustrated in *Figure 1-3*.



*Figure 1-3: Chemical structure of rr-P3HT and definition of the crystallographic directions  $\pi$ -stacked P3HT layers (scales not respected in this representation).*

Conjugated polymer crystals differ in an important point from inorganic crystals. In fact, the forces in the three crystallographic directions in a crystal or a solid of conjugated polymer crystals are strongly anisotropic. For regioregular poly(3-hexylthiophene) or P3HT for example, these interactions are strong along the  $\pi$ -stacking direction whereas in the direction of the alkyl-side chains the interactions are dominated by weak van der Waals forces. This anisotropy of interaction within the solid strongly influences the mechanical and electrical properties of the polymer. In the following, we will introduce in more detail the properties of P3HT in its solid and crystallized phase.

## **2. Semi-crystalline polymers: the case of regioregular poly(3-hexylthiophene)**

The crystallization of polymers is known since the first half of the 20<sup>th</sup> century (5–8). To be able to crystallize, a polymer must have a completely regular chain conformation such as linear polymers (polyethylene, polyamine, *etc.*) or a stereoregular polymers (having lateral side chains) as for example polystyrene or poly(alkyl-thiophenes) (8). B. Lotz showed that in order to understand the crystallization of polymers, three scales of organization can be distinguished (8):

- The crystal structure of the polymer which treats about the conformation of the chains within the unit cell (on a scale of a few Å up to ~20 Å).

- The lamellar structure, which results from the chain folding which is characteristic of the polymer chemical structure (on a scale of  $\sim 50\text{-}500 \text{ \AA}$ ).
- The organization of these lamellae into more complex structures such as spherulites, fibres, etc. These structures define the final morphology of the polymer in the solid phase, for example in a thin film (from the  $\mu\text{m}^2$  to the  $\text{cm}^2$  scale).

In the following we will treat these different aspects on the basis of published works for the case of rr-P3HT.

### 2.1. Crystal structure of P3HT

P3HT is known to crystallize easily and it is almost impossible to generate thin films of purely amorphous P3HT. Therefore the crystal structure of P3HT got a lot of attention (5, 6). However, to date the exact structural model of P3HT is still not determined. The lack of knowledge about the exact structure is mainly due to the difficulty to grow large areas of P3HT single crystals (5,6). One of the first proposed crystal structures for poly(alkylthiophene)s is based on well organized lamellar packing of planar backbones that are uniformly spaced by the alkyl side chains. It was proposed by Prosa and coworkers in 1992 (9). Since then, several crystal structures for poly(alkylthiophene)s have been published. Among those, some were proposed by Tashiro *et al.* (10). These authors combined molecular modelling and X-ray diffraction measurements on stretch aligned P3HT. Their proposed structures vary mainly in number of polymer chains in the unit cell (10). More recently, Dag *et al.* proposed a structure based on molecular dynamics simulations (11). One of the most recent refinements of the P3HT crystal structure, based on electron diffraction measurements, is that published by Kayunkid *et al.*(12). The authors performed selected area electron diffraction on highly oriented P3HT films obtained by directional epitaxial crystallization (12). *Figure 2-1* shows the crystal structure of P3HT as determined by Kayunikd *et al.* The authors propose a monoclinic unit cell containing two chains shifted relatively to each other ( $\mathbf{a}_{\text{P3HT}}=1.60 \text{ nm}$ ,  $\mathbf{b}_{\text{P3HT}}=0.78 \text{ nm}$ ,  $\mathbf{c}_{\text{P3HT}}=0.78 \text{ nm}$  and  $\gamma=86.5^\circ$ ). The definition of the crystallographic directions in the structure of P3HT is the following: the  **$\mathbf{c}_{\text{P3HT}}$ -axis** refers always to the P3HT backbone direction. The  **$\mathbf{b}_{\text{P3HT}}$ -axis** refers to the  $\pi$ - $\pi$  stacking direction and the  **$\mathbf{a}_{\text{P3HT}}$ -axis** corresponds to the *n*-hexyl side-chain direction. The observed shift of the two neighbouring polymer chains is enforced by the hexyl-side chains that crystallize into an orthogonal sub-cell (12). To date, the main difficulty for the determination of the exact crystal structure of P3HT lies in the determination of the exact configuration and orientation of the hexyl-side chains. In the scope of this thesis, we used the P3HT crystal structure proposed by Kayunkid *et al.* (12).

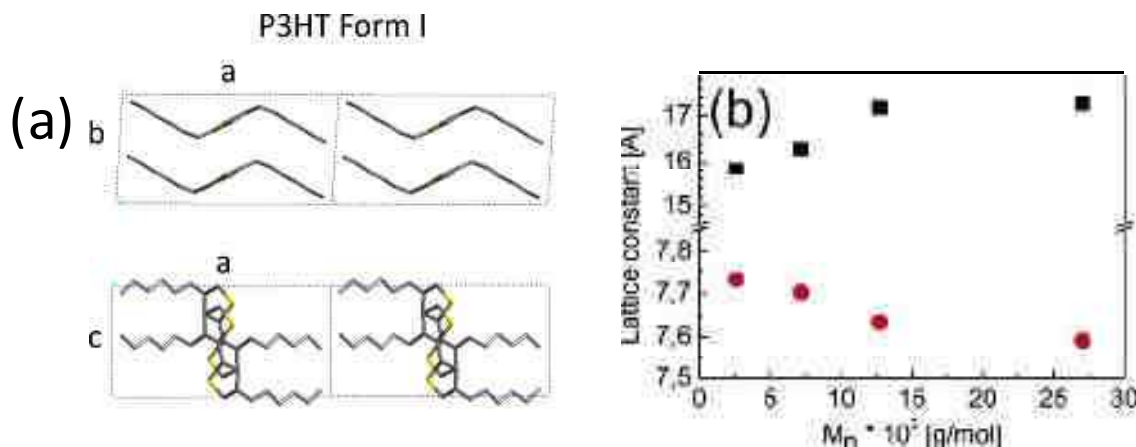


Figure 2-1 : (a) Crystal structures of P3HT as determined by Kayunkid *et al.* viewed along two different crystallographic directions (hydrogen atoms have been omitted for the sake of clarity). Reproduced from (5). (b) Evolution of the lattice parameter  $a_{P3HT}$  in black and the lattice parameter  $b_{P3HT}$  in red with increasing molecular weight. Reproduced from (13).

Several authors reported polymorphisms in poly(alkylthiophene)s (14–16). Two crystal phases of P3HT, phase I and II, have been proposed with a transition from phase I to phase II at a temperature of about 60°C (14). The main difference between phase I and phase II is the order within the hexyl side chains. Wu *et al.*, evidence recently side-chain disorder by using  $^{13}\text{C}$  MAS NMR and X-ray diffraction (14). Phase I is described as a well organized 3D crystalline phase whereas phase II is a 2D crystalline phase in which the side chains are less ordered *i.e.* a smectic-like structure.

Another kind of polymorphism evidenced for P3HT is the change of the  $a_{P3HT}$  and  $b_{P3HT}$  lattice parameters with increasing molecular weight. Indeed, Zen *et al.* evidenced an increase of the lattice parameter  $a_{P3HT}$  and a decrease of  $b_{P3HT}$  with increasing molecular weight (13). Figure 2-1 (b) shows this evolution of the lattice parameters  $a_{P3HT}$  and  $b_{P3HT}$  with  $M_w$ .

## 2.2. Chain folding and lamellar structure

One of the most important concepts for the understanding of semi-crystalline polymers is chain folding (7, 8). Figure 2-2 represents schematically a lamellar crystal of polyethylene. The concept is the similar for other semi-crystalline polymers in particular poly(alkylthiophene)s (5, 17).

The polymer chains are well crystallized within the crystalline lamellae of size  $L$ . The polymer chains are however generally longer than the crystalline phase and thus, these chains tend to fold. Chain folds and chain ends cannot be introduced into the crystalline lattice and form thus a much less ordered phase which is generally referred to as the amorphous phase within the semi-crystalline polymer (7, 8).

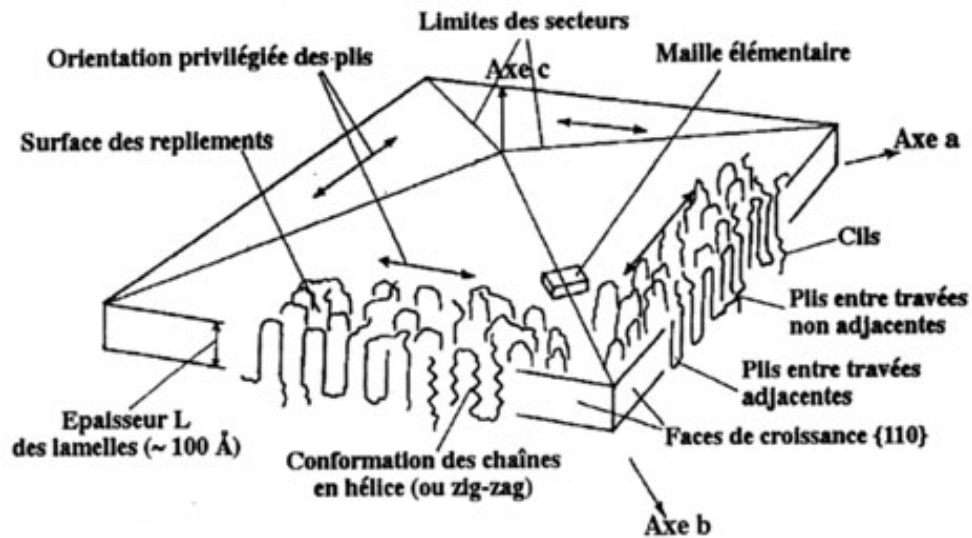


Figure 2-2 : Schematic representation of a lamellar polyethylene crystal. Reproduced from reference (8).

In the case of P3HT, chain folding could be directly evidenced and imaged using scanning tunnelling microscopy (STM). The first works in this sense were performed by Mena-Osteritz *et al.* and Grévin *et al.* (18–22). Such works are of great interest as they allow the direct visualization of the chain folding of semi-crystalline P3HT and other poly(alkylthiophene)s. Figure 2-3 represents the visualization of chain folding using STM and the corresponding model of the chain conformation determined by semi-empirical calculations.

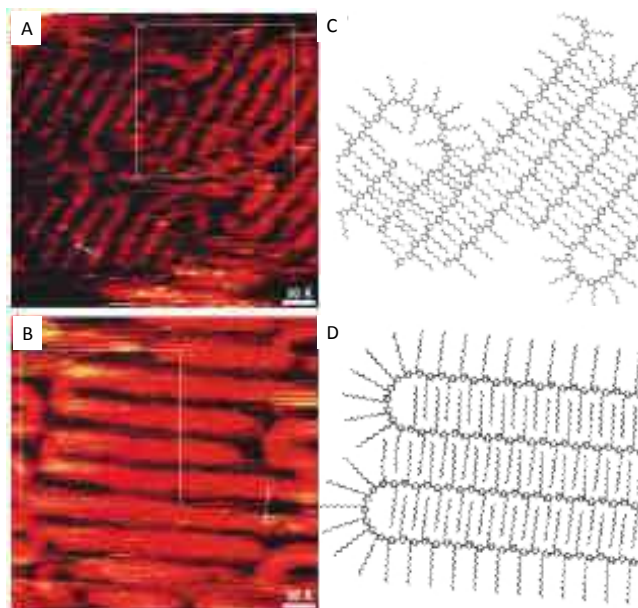


Figure 2-3 : (a and b) STM image showing the short-range ordering of regioregular P3AT. (c and d) 2D crystalline packing as modeled by semi-empirical calculations. The “hairpin” intramolecular folds are composed of several 3-alkylthiophene monomers in all-cis conformation, whereas folds of larger radius may include both cis and trans conformations. Reproduced from (18).

The ratio of crystalline/amorphous *i.e.* the extension of the crystalline lamellae  $L$  depends on many factors. In the case of P3HT,  $L$  depends strongly on the chain length (*i.e.* the molecular weight) and the processing conditions. For very short P3HT chains, chain folding does almost not occur, and the system is in majority composed of the crystalline phase (23). The threshold molecular weight for which chain folding sets in is reported to be around  $M_w=10$  kDa for rr-P3HT (24, 25). In fact, the evolution of the lamellar period as a function of the molecular weight was found to show two phases. For molecular weights up to  $M_w=10$  kDa, the lamellar periodicity increases and then reaches a plateau value of  $L \sim 30$ nm (24–26). Another, indirect indication for chain folding is the evolution of the lattice parameter  $a_{P3HT}$  with increasing molecular weight (*see Figure 2-1*). In fact, the higher amount of re-entrant chains into the lattice (after folding) exert a stress on the close packing of the molecules and induces an increase of the lattice parameter with increasing amount of folds and re-entrant chains (*e.g.* with increasing molecular weight) (5, 13).

A part from the molecular weight, the processing conditions are of great importance regarding the lamellar period. The crystallization kinetics plays a specific role. In this sense Crossland *et al.* evidenced an increase of the lamellar period by strongly slowing down the crystallization kinetics (27). A similar observation was made in the scope of this work and will be treated in Chapter 4.

The molecular weight, the solvents, the temperature and the processing conditions strongly influence the morphology and thus the lamellar periodicity of P3HT thin films (28–31). In the following, some of the most characteristic morphologies obtained for P3HT thin films will be presented.

### **2.3. Various morphologies and orientation of P3HT thin films**

Properties of conjugated polymers such as charge mobility depend on the chemical structure of the polymer backbone. But they depend also very strongly on the morphology and the crystallinity of the polymer in the solid phase (24, 32). In particular, as polymer chains are intrinsically 1D objects, orientation of the chains plays an important role. The macroscopic properties can therefore be highly anisotropic for highly oriented samples (33, 34). As mentioned above, the morphology as well as the degree of crystallinity in a polymer depend strongly on the processing conditions. Indeed in solution-processed thin films of polymers, the solvent evaporation rate rules the crystallization kinetics. Therefore, films deposited from high boiling point solvents exhibit in general a higher degree of crystallinity as compared to the films deposited from low boiling point solvents (35, 36). The latter is also influenced by the deposition technique which can be more or less fast. For example, spin coating is fast as compared to drop casting (36). Most P3HT thin films deposited by these methods give rise to a fibrillar morphology (24, 28, 36, 37). In the following we will present some examples on how the molecular weight and the processing can influence the thin film morphology of such spin coated or drop casted thin films. In a second step other processing methods used for P3HT and their influence on the obtained nanomorphology will be presented.

### 2.3.1. Effect of the molecular weight

The effect of the molecular weight of P3HT has been extensively studied (25, 28, 36–38). Herein, we will present one example out of numerous published works (36). *Figure 2-4* shows the AFM phase images of thin layers obtained from rr-P3HT fractions of different  $M_n$  deposited by (i) dip coating from a chloroform solution, (ii) drop casting from a chloroform:tetrahydrofuran mixed solvent (14:3, v/v) and (iii) spin coating from chloroform. All these films show the typically observed fibrillar morphology frequently observed for P3HT. The two slowest deposition techniques (dip coating and drop casting) show well defined nanorod-type morphology independently of  $M_n$ , whereas the fast deposition (spin coating) shows such a morphology only for the lower molecular weight samples. The formation of anisotropic fiber structures is favored by low molecular weights, except for very slow deposition for which high molecular weights lead to fibril formation as well.

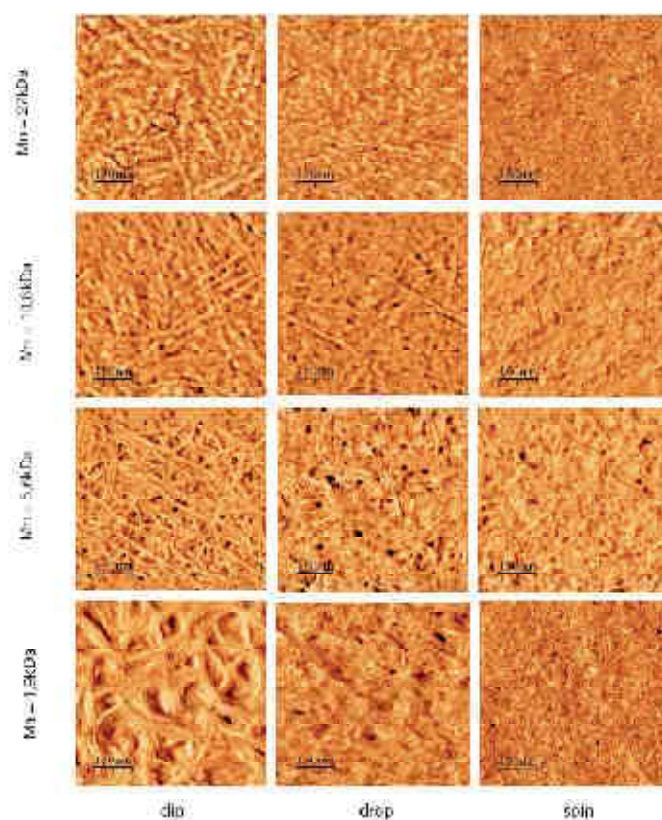


*Figure 2-4 : Atomic force microscopy phase images of thin layers obtained from RR-P3HT fractions of different  $M_n$  and using different processing techniques. Reproduced from (36).*

### 2.3.2. Specific processing methods and specific morphologies

As seen previously, P3HT films deposited by spin coating or drop casting present a fibrillar morphology (24, 36, 37, 39). The solvent plays an important role on the crystallinity of these nanofibers. However, under special crystallization and processing conditions, the P3HT morphology can be tuned. For example, Crossland *et al*, generated P3HT spherulites

under controlled crystallization conditions (27). These spherulites were generated by swelling and deswelling the films in  $\text{CS}_2$  vapours under controlled vapour pressure. The spherulite morphology of the films by Crossland *et al.* is shown in *Figure 2-5*. Besides the spherulitic morphology of the P3HT, the work of Crossland *et al.* is particularly interesting in the sense that they can control the nucleation density within the films. They have developed a simple methodology to control homogeneous nucleation in thin films by using a controlled swelling/deswelling of the films. For P3HT, spherulitic domains of 10–100 nm diameter were obtained reproducibly by controlling the saturated vapor pressure of  $\text{CS}_2$  which determines the nucleation density of P3HT spherulites in a thin film. *Figure 2-5* shows the nucleation density as a function of the vapor pressure.

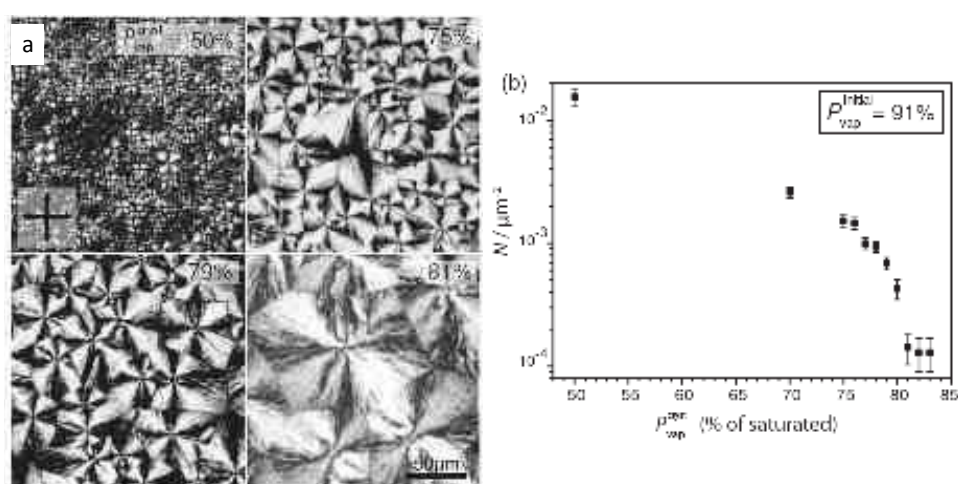


*Figure 2-5* : POM images ( $200 \mu\text{m} \times 200 \mu\text{m}$ ) of a 40 nm thick P3HT film grown from  $\text{CS}_2$  solvent after an initial swelling at 91.0 %  $P_{\text{vap}}^{\text{init}}$  for 600 s. The sequence of polarized optical microscope images shows the dependence of the nucleation density of spherulites versus  $P_{\text{vap}}^{\text{cryst}}$ . (b) Graph showing the variation of homogeneous nucleation density of spherulites versus  $P_{\text{vap}}^{\text{cryst}}$ . Reproduced from (27).

Another example of original morphology of P3HT was reported by Brinkmann *et al.* (40). In this work, the authors prepared so-called Shish-Kebab fibers of P3HT (40). Such Shish-Kebab fibers are composed of an oriented core (the shish) onto which lateral crystalline fibrils made of folded polymer chains (the ‘‘kebabs’’) are connected with a periodicity in the 18–30 nm range (see *Figure 2-6*). The P3HT chain axis is oriented parallel to the fiber axis, whereas the  $\pi$ -stacking direction is perpendicular to it. Such Shish-Kebab fibers can be generated by epitaxial crystallization of 1,3,5 trichlorobenzene in the presence of a bad solvent of P3HT such as for example pyridine or cyclohexanone. Such fibers present highly anisotropic optical properties.

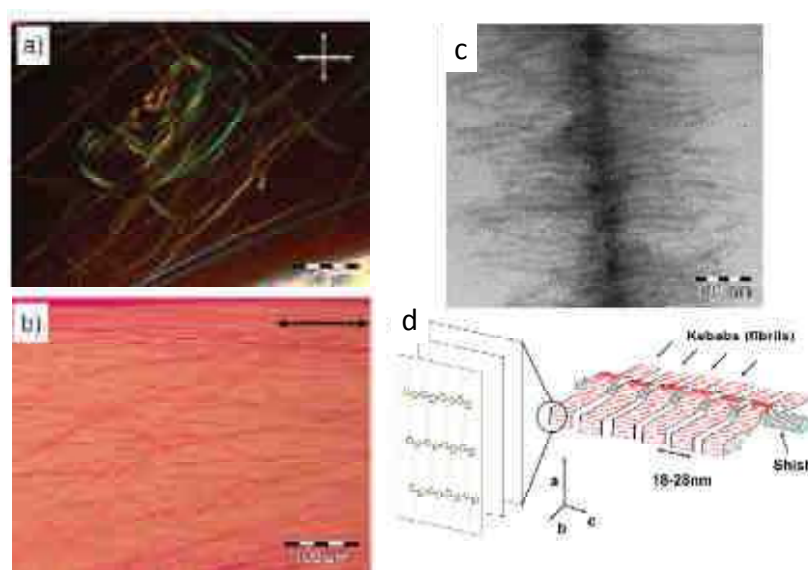


Figure 2-6 : a) Optical micrograph of a Shish-Kebab fiber taken with crossed polarizers, showing highly birefringent TCB needles decorated with highly oriented P3HT fibers (the orientation of the polarizer and analyzer are depicted by two arrows). b) Highly oriented P3HT fibers decorating the TCB needles as observed under the polarized light microscope. The polarization of the incident light is given by the arrow. c) Enlarged TEM-bright-field image of a shish-kebab fiber of P3HT showing the tight packing of nanofibrils (kebabs) along the backbone of the fiber (shish). d) Schematic structure of a shish-kebab fiber. The axis directions for the unit cell are depicted by arrows. Reproduced from (40).

### 3. Controlled orientation of polymers

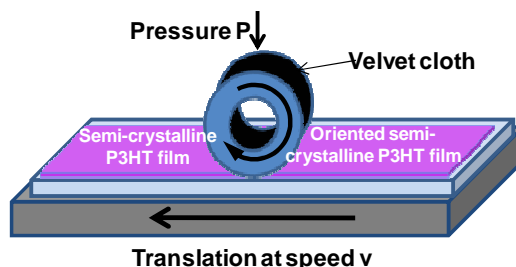
Besides the control of the nucleation and crystallization of the polymer, the control of the orientation of the latter in the solid phase is of high interest as it can induce a strong anisotropy of the macroscopic properties. The interest of orientation of conjugated molecules is twofold. In particular, two properties relevant to the field of organic electronics that can be tuned by the orientation are: (i) the charge transport properties (33, 34) (ii) the optical properties (41).

Presently there exist several approaches for the orientation. Some methods make use of an orienting substrate onto which the polymer grows by molecular self-assembly (31, 42, 43). Other methods make use of the application of mechanical shearing forces: these methods are mainly based on the anisotropy of the strength of the forces in the polymer along the chain direction and between two neighbouring polymer chains (44–46). These methods are quite general for all kind of polymers. Herein we will present a selection of those which are of particular interest for this work and those which were successfully applied to  $\pi$ -conjugated polymers and in particular to P3HT.

### 3.1. Orientation by using mechanical shearing forces

- **Mechanical rubbing** consists in applying a cylinder covered with a velvet cloth and rotating it at a controlled velocity onto a thin film of polymer undergoing a translational motion. *Figure 3-1* shows a schematical representation of the process.

*Figure 3-1: Schematical representation of the mechanical rubbing of a thin P3HT film.*



Mechanical rubbing is extensively used for the orientation of polymers such as of polyimides and polycarbonates (44, 47–50) as well as for the orientation of small organic molecules such as  $\alpha$ -sexithiophenes (51, 52). Orientation of P3HT by mechanical rubbing with the  $\mathbf{c}_{\text{P3HT}}$  direction parallel to the rubbing direction is also frequently reported in the literature although a deep understanding of the orientation process is lacking (41, 53–56). In the scope of this thesis, an explanation of the orientation process of P3HT upon mechanical rubbing will be presented and discussed (see Chapter 5). The advantage of mechanical rubbing is the possibility to generate large surfaces of oriented films on any type of substrate in a relatively easy and cost-efficient way. The main drawback of the technique is the difficulty to control accurately the final film thickness and the appearance of scratches in the films.

- **Friction transfer** is of importance for this work as it was used for the preparation for the substrates of PTFE. Friction transfer for PTFE was originally developed by Smith and Wittmann (45). The rather simple principle is illustrated in *Figure 3-2 b*. A block of the polymer to be oriented is applied with controlled pressure onto a translating substrate at a given temperature. By this way, polymer chains are deposited onto the substrate with an average orientation corresponding to the direction of translation of the substrate. Nagamatsu *et al.* successfully applied the friction transfer method for the fabrication of oriented films of poly(2,5-dioctyloxy-1,4-Phenylenevinylene) and rr-poly(3-alkylthiophene)s. *Figure 3-2* shows a SEM image of a P3HT thin film prepared by this method. The distribution of the in-plane orientation of the P3HT chain axis ( $\mathbf{c}_{\text{P3HT}}$ ) is of around  $10^\circ$  as measured from GIXD rocking curves. This corresponds to a high degree of orientation. The authors reported preferential “flat-on” orientation of the crystalline domains in P3HT thin films prepared by friction transfer.

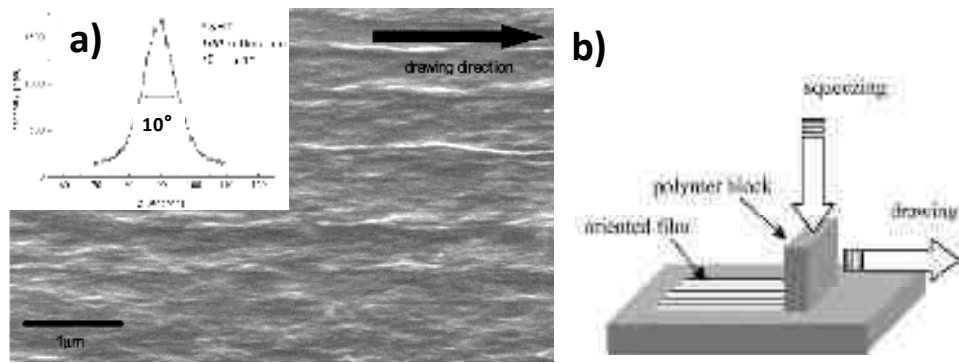


Figure 3-2 : a) SEM image of the friction-transferred P3HT film. The drawing direction of friction transfer is indicated by the arrow; **inset** GIXD rocking curve around the 100 reflection. Reproduced from (57). b) Schematic representation of the friction-transfer technique. Reproduced from (58).

▪ **Strain alignment** was introduced in the late 1970<sup>ies</sup> by Petermann and Gohil for the fabrication of highly oriented polyethylene (59). The method consists in stretching a molten polymer film followed by a crystallization step that takes place at a temperature below the melting temperature of the polymer. This avoids the relaxation of the molecules and allows the “freezing” of the oriented state. A schematic description of the method can be found in Figure 3-3. O’Connor and coworkers prepared highly oriented P3HT films using a modified version of the Petermann’s process (34). They deposited a film of P3HT onto PDMS. Afterwards the PDMS was strained up to a desired percentage. This method yielded highly oriented P3HT films with the  $c_{P3HT}$  direction parallel to the stretching direction. O’Connor *et al.* reported an in-plane orientation of the strain aligned P3HT characterized by a FWHM~20°.

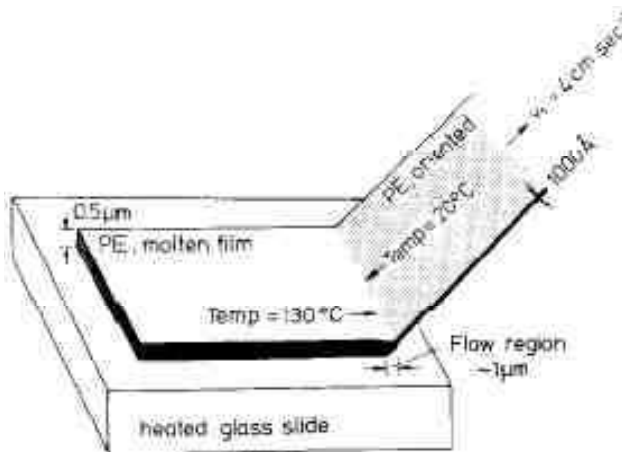


Figure 3-3 : Schematic diagram for the method of preparing polyethylene oriented films by strain alignment as proposed by Peterman *et al.* Reproduced from (59).

### 3.2. Orientation by using an orienting substrate

▪ **Epitaxy** consists in the oriented growth of a crystal (guest crystal) on top of the surface of another crystal (host crystal) in one or more crystallographic axes (42). Generally one can distinguish between homo-epitaxy where the host and the guest crystals have the same chemical nature and hetero-epitaxy where the guest and the host crystals have a different chemical nature. For a successful epitaxial growth, both crystals must have some symmetry relations. In particular, the lattice parameters of both crystals have to match in at least one crystallographic direction. A mismatch of the lattice parameters of guest and host of 10-15% is considered as an upper limit for a successful epitaxial orientation (42). Epitaxy was first described for inorganic crystals and epitaxy of polymers on organic or polymeric crystals made many progresses since the seminal works in the 1950<sup>ies</sup> (42, 60). Wittmann and Lotz mentioned that: “As a general rule, the guest polymer chains lie with their chain axis parallel to the substrate surface” (42).

Several authors describe epitaxial orientation of P3HT on organic substrates (17, 23, 25, 40, 43, 61). Since the work of Brinkmann *et al.* on the epitaxial crystallization of P3HT on a aromatic substrate of 1,3,5 trichlorobenzene (TCB), the guest/host couple P3HT/TCB was for some years the only reported work on epitaxial crystallization of P3HT. In the case the oriented growth of P3HT on TCB, the method is successful due to the good agreement of the parameters  $c_{P3HT}$  and  $c_{TCB}$  with  $c_{P3HT} \approx 2c_{TCB}$  (54). In 2009, Brinkmann *et al.* reported epitaxial orientation of P3HT on an aromatic salt of BrKz (61). And recently, epitaxial orientation of P3HT on an oriented polyethylene (oriented by the Peterman and Gohil method) substrate was reported (43). In this work the P3HT backbone aligns parallel to the polyethylene chains.

Epitaxial growth of P3HT plays a major role in this work as this method was improved and extensively used for the growth of highly oriented thin films of P3HT or hybrid materials (P3HT and nanoparticles) on an aromatic substrate of TCB. The method will be described in detail in Chapter 3.

▪ **Grapho-epitaxy** is also called “artificial epitaxy” because it is not based on the matching of the crystalline lattice of host and guest but rather relies on the matching of “artificial lattices” such as for example a symmetric micro-relief of the substrate onto which the guest fits (62). In contrast to epitaxy, in the case of grapho-epitaxy, the substrate is not necessarily crystalline. In some cases it is difficult to distinguish between a pure grapho-epitaxial and a pure epitaxial effect. Lieser *et al.* reported orientation by grapho-epitaxy of a polyfluorene derivative on an oriented substrate of polyimide (63). Tanaka *et al.* reported the alignment of linear dye molecules into the grooves of a friction transferred PTFE film and a grapho-epitaxial effect was suggested to explain the results (64). Oriented films of P3HT were obtained by drop casting a P3HT solution on friction transferred PTFE (65). Although the authors did not conclude about the orientation process, a grapho-epitaxial effect due to the topography of the PTFE is possible. In the scope of this work a grapho-epitaxial effect was observed for the oriented growth of TCB crystals on substrate of PTFE prepared by friction transfer.

### 3.3. Directional crystallization and zone casting

▪ **Directional crystallization using a thermal gradient** is well developed in the field of inorganic semiconductors (66, 67). It consists in crystallizing from the melt the molecules/polymers by moving the sample at very slow speeds (from a few  $\mu\text{m/s}$  to a few  $\mu\text{m/min}$ ) in a temperature gradient. Directional solidification (crystallization) is a relatively old technique that was used for example in the 1970<sup>ies</sup> by Lovinger *et al.* for the crystallization of poly(ethylene oxide) spherulites and polyamides (68–70). It seems that directional crystallization fell into oblivion for several years and is being rediscovered nowadays. Schweicher *et al.* showed recently that it can be used for the growth of single crystals of sexithiophenes (67). Recently Toda *et al.* used directional crystallization in a temperature gradient for the crystallization of poly(butane-1), poly(vinylidene fluoride) and polyethylene (71). Directional crystallization in a temperature gradient is one method used in the present work for the growth of oriented TCB crystals that will serve as substrate for the epitaxial orientation of P3HT (see Chapter 3).

**Zone casting** (72–75) consists in depositing a molecule/polymer from solution (kept at a temperature  $T_1$ ) onto a moving substrate (temperature  $T_2$ ) where the solvent evaporates therefore leaving a thin film of the solute only. The solution is continuously supplied to the substrate by a flat nozzle. The supply rate, the substrate velocity and the temperature  $T_2$ , as well as the solutions concentrations are the main parameters to control for the crystallization and orientation process and they should be carefully chosen. *Figure 3-4* illustrates the principle of the technique. This method is widely used for the oriented deposition of small molecules such as pentacene (73). Recently Lee *et al.* obtained well oriented nanoribbons of the conjugated polymer poly(2,5-bis(3-alkylthiophen-2-yl)thieno[3,2-b]thiophene) (PBTTT) (74).

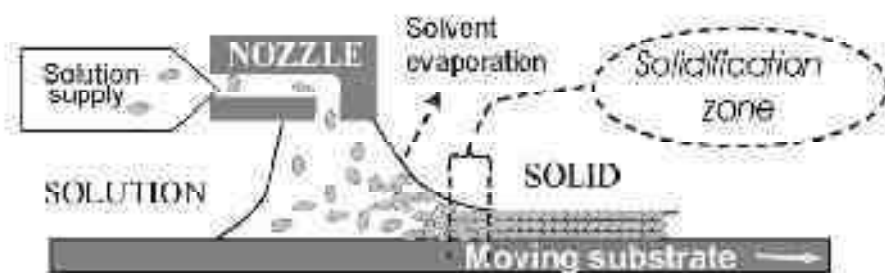


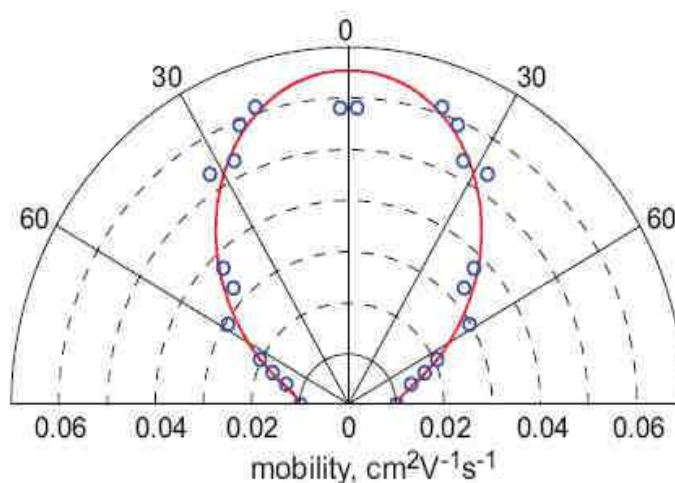
*Figure 3-4 : Schematic representation of the zone casting technique. Reproduced from (72).*

### 3.4. Interest of the orientation of conjugated polymers: Examples

#### 3.4.1. Anisotropy of charge transport

Dimitrakopoulos *et al.* showed that for small molecules such as pentacene, the charge carrier mobility is correlated to the degree of order in the thin films. They showed that disordered pentacene molecules behave as insulators with a mobility of  $10^{-9} \text{ cm}^2 \cdot \text{V}^{-1} \cdot \text{s}^{-1}$  while well ordered and  $\pi$ -stacked pentacene act as conductors having mobilities in the range of  $10^{-3}$  (76, 77).

*Figure 3-5 : Mobility versus angle for strain aligned P3HT films. The films were strained by 100 %. The data is from six strained films applied to orthogonal transistors. The mobility data is reported from  $0^\circ$  to  $90^\circ$  and reflected to show the expected behavior of the mobility anisotropy over a  $180^\circ$  range. The semicrystalline nature of the film along with the crystalline distribution around the strain direction allows for this expectation. Reproduced from (34).*



For conjugated polymers such as P3HT, many studies evidenced that the charge transport properties are closely related to the intrinsic properties of the polymer such as the molecular weight (28, 36). But it was also widely reported that orientation and morphology play a key role (37). The charge mobility in the direction perpendicular to the chain strongly depends on the orientation of the crystalline domains of P3HT. Along the  $\pi$ -stacking direction this mobility is higher than along the  $\mathbf{a}_{\text{P3HT}}$  direction. Jimison *et al.* showed that in the case of P3HT oriented by directional epitaxial crystallization, the charge mobility is one order of magnitude larger along the polymer chain direction ( $\mathbf{c}_{\text{P3HT}}$ ) than in the direction of the alkyl side-chains ( $\mathbf{a}_{\text{P3HT}}$ ) (33). Recently O'Connor *et al.* measured the charge transport in strain aligned P3HT as a function of the angle relative to the  $\mathbf{c}_{\text{P3HT}}$  direction (34). The results are displayed in *Figure 3-5*. They reported a maximum anisotropy of 9 for the charge carrier mobility. High anisotropy of the charge transport is not only desired to maximize the charge carrier mobility within devices by appropriately placing the electrode in the directions of the fast transport direction. It also allows for example to have less cross talks between adjacent transistors in arrays of OFETs (78).

3.4.2. Anisotropy of optical properties

The anisotropy of optical properties of conjugated polymers is a very interesting feature for their use as polarizing films. An example for the use of an oriented P3HT-PCBM<sup>1</sup> photovoltaic device as an electricity generating polarizer in Liquid Crystal Displays (LCD) was recently presented (41). The idea is to use P3HT oriented by mechanical rubbing as polarizer. On the oriented P3HT, PCBM was deposited by evaporation for the fabrication of a polarizing organic photovoltaic device. Such a device could thus play the role of electricity generating polarizer allowing to use the back scattered light to generate power. *Figure 3-6* shows a schematic illustration of such a setup and of a rubbed P3HT film with anisotropic optical properties.

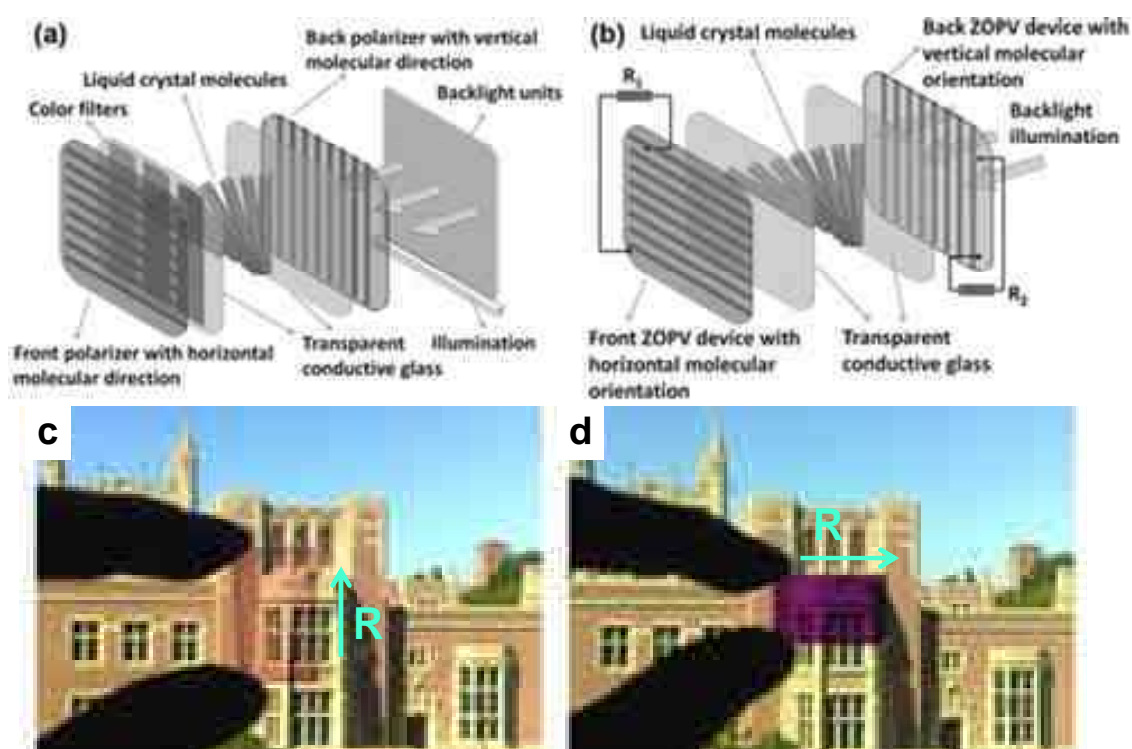


*Figure 3-6 : (a) Schematic constructions of LCD and (b) the potential LCD system integrated with an oriented organic photovoltaic device (c) oriented-P3HT film with the rubbing direction parallel or (d) perpendicular to the molecular orientation in the analyzer. Reproduced from (41).*

<sup>1</sup> PCBM is a fullerene derivative frequently used as electron acceptor in organic solar cells.

## 4. Colloidal semiconducting nanocrystals

### 4.1. Basic physical properties

Nanocrystals (NCs) are colloids formed of an inorganic core which is stabilized by a layer of organic molecules, the ligands (*Figure 4-1*). For nanocrystals having a diameter of 1-10 nm, the inorganic core is composed of a few tens to a few thousands of atoms (79). The small size of the NCs makes them objects where quantum mechanical phenomena influence their physical properties. For this reason, they are also referred to as “quantum dots”.

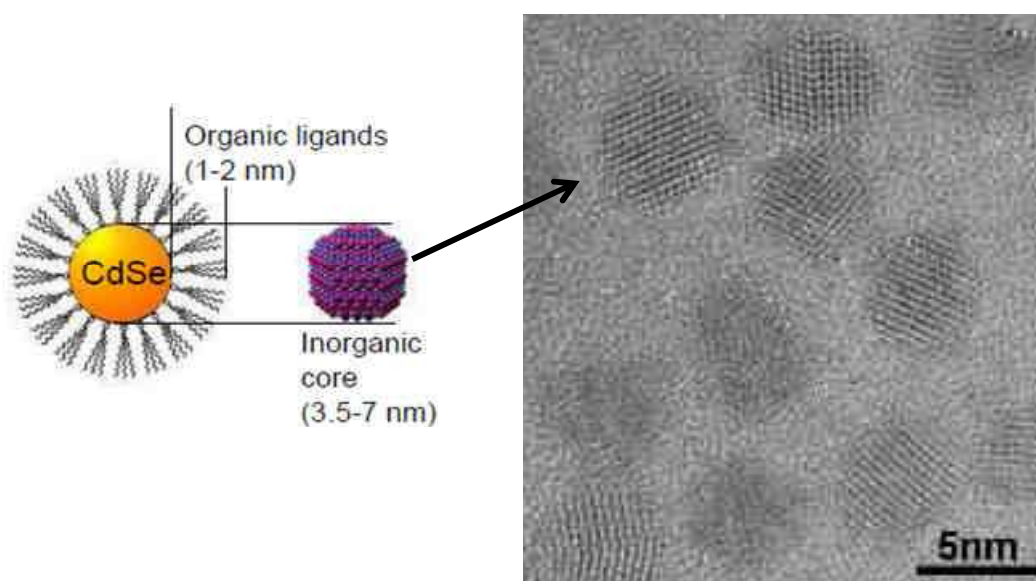


*Figure 4-1 : Schematic illustration of the architecture of colloidal NCs and high resolution image of CdSe NCs.*

In bulk crystalline semiconductors, the energy bands are formed by the delocalization of the charge carriers over a large amount of unit cells. The electronic structure of bulk semiconductors is thus described by two bands: the conduction and the valence band that are separated by a forbidden band of energies whose width is called the bandgap. If this bandgap is too large, the conduction band is empty at room temperature. With an external excitation (*e.g.* illumination), it is possible to excite charge carriers from the valence band to the conduction band. If the photon energy is close to the bandgap, rather than having a free electron and hole pair one can have the formation of a coulombically bound electron-hole pair called exciton. By analogy with a hydrogen atom, an exciton can be described by its effective Bohr radius  $a_0$  which is usually a few nm. In the case of bulk CdSe, it is about 5 nm (80). As NCs have sizes in the same order of magnitude as the Bohr radius, the excitons are confined in such nanoparticles. The quantum confinement in the quantum dot tends to change the energy levels of the exciton in the way that the stronger the confinement (*i.e.* the smaller the quantum dot), the larger the bandgap is. Therefore, the bandgap energy in the case of semiconducting NCs is strongly size dependent. The evolution of the bandgap energy of NCs can be expressed by the following way (81, 82):

$$E_g^{nanocrystal}(r) = E_g^{bulk} + \frac{\hbar^2 \pi^2}{2r^2} \left( \frac{1}{m_e} + \frac{1}{m_h} \right) - \frac{1,8e^2}{4\pi\epsilon\epsilon_0 r}$$

where  $E_g^{bulk}$  is the bulk value of the energy gap;  $m_e$  and  $m_h$  are respectively the electron and hole effective masses relative to the electron and hole masses,  $r$  is the radius of the NC and  $\epsilon$  is the dielectric constant of the bulk semiconductor relative to the dielectric constant of vacuum. Roughly speaking, the second term in the formula corresponds to the quantum confinement effect whereas the last term is related to the coulombic interaction of the electron and hole. To summarize, when the radius  $r$  of the quantum dots is very large, the energy gap tends towards the bulk value  $E_g^{bulk}$ . This is schematically illustrated in *Figure 4-2*.

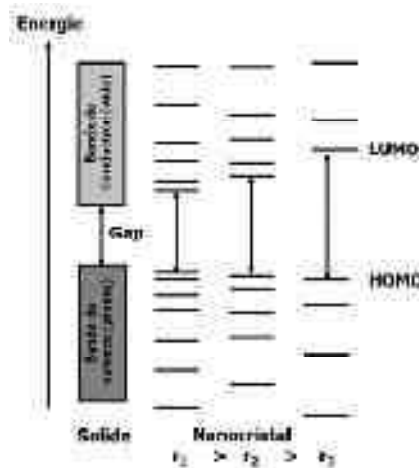


*Figure 4-2* : Schematic illustration of the energy band gap of the NCs as a function of their size. Reproduced from (79).

This size dependence of the band gap of the NCs translates directly into size depended optical properties. The photoluminescence as well as the UV-vis absorbance are strongly size dependent. *Figure 4-3* shows the size dependent emission under UV excitation of spherical CdSe NCs with diameters ranging from 2 to 7 nm.



*Figure 4-3* : Emission of colloidal dispersions of CdSe spherical nanocrystals with diameters varying between 2 nm (left) to 7 nm (right). Due to the quantum confinement effect, the increase in the size of nanocrystals leads to a red-shift of the photoluminescence from approx. 480 nm to 650 nm.

## 4.2. Crystal structure of the nanocrystals

Depending on the reaction temperature and the kinetics of the growth, two competing crystal structures can occur for CdSe nanocrystals: the zinc blende (cubic) and the wurtzite (hexagonal) crystal structure (83). *Figure 4-4* illustrates these two crystal structures on the model system of ZnS.

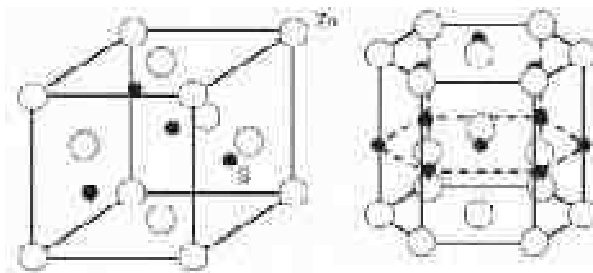
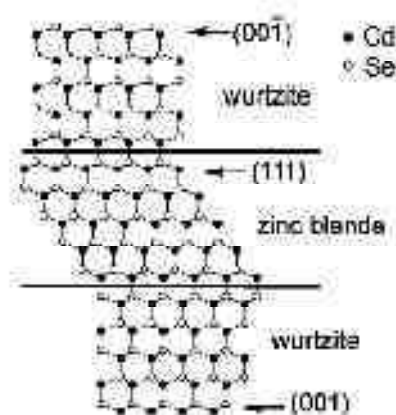


*Figure 4-4: Zinc-blende (cubic) and wurtzite (hexagonal) crystal structures of ZnS nanocrystals. Reproduced from reference (84).*

The lattice parameters of CdSe in the zinc-blende phase are:  $a_{\text{CdSe}} = b_{\text{CdSe}} = c_{\text{CdSe}} = 6.077 \text{ \AA}$ , and in the wurtzite phase:  $a_{\text{CdSe}} = b_{\text{CdSe}} = 4.299 \text{ \AA}$ , and  $c_{\text{CdSe}} = 7.010 \text{ \AA}$  (from JCPDS<sup>2</sup>). It was reported that the zinc-blende form is more stable at lower temperatures whereas the wurtzite form is more stable at high temperatures (83). Therefore, the zinc-blende form is preferentially formed at lower synthesis temperature (200-240°C), as compared to the wurtzite structure which forms preferentially at higher temperatures (about 300°C) (83). Although the wurtzite form is the most widely reported, there is a strong competition between the formation of both phases and a coexistence of both polymorphs occurs frequently. Indeed, the transition of one phase to another is possible via a simple stacking fault as illustrated in *Figure 4-5*. Indeed, the wurtzite form has an ABAB stacking while the zinc blende structure shows a ABCABC stacking. The (111) face of zinc blende and the (11 $\bar{1}$ ) face of wurtzite have both planes alternately composed of Cd and Se atoms (85).

*Figure 4-5: Two dimensional representation showing the relationship between the wurtzite and the zinc blende structures. Wurtzite has ABAB stacking while zinc blende has an ABCABC stacking. The (111) face of zinc blende and the (11 $\bar{1}$ ) face of wurtzite both have planes alternately composed of Cd and Se atoms. One nanoparticle can switch between the two structures with a stacking fault. Reproduced from (85).*



### 4.3. Synthesis

For the wet chemical synthesis of semiconducting nanocrystals, there exist several approaches. Among these, two of them can be distinguished: (i) the synthesis in organic solvents at high temperature and (ii) the synthesis at room temperature in aqueous solutions or in oil water mixtures and (3, 84). In the monophasic synthesis in aqueous solutions, the nanocrystals are formed in aqueous solutions containing stabilizers which can be either ligands or polymers. These stabilizers bind to the NCs surface and avoid aggregation of the latter via steric hindrance or by electrostatic repulsion (3). In the bi-phase (oil water mixture) method, the particles are formed in the water droplets dispersed in the oil phase thanks to surfactants. This allows for the stabilization of the NCs (3). The advantages of these techniques are their simplicity and the fact that synthesis is realized at room temperature. However, these methods give rise to strongly polydisperse populations of NCs having a low crystalline quality.

Nowadays, NCs are thus generally synthesized at high temperature in organic solvents. The main advantages of the high temperature methods are the high crystalline quality of the NCs, their low polydispersity and the possibility to control their shape. In the scope of this work, NCs were synthesized by the latter methods which will be described in detail in Chapter 2. The first efficient synthesis of CdSe spherical nanocrystals following this method was published in 1993 by Murray and coworkers (86). Furthermore, since the seminal works of Alivisatos *et al.* on the control of the shape of CdSe NCs, many progresses were made in this sense (87, 88). Nowadays the synthesis of soluble and well dispersed CdSe NCs of various shapes is well mastered. *Figure 4-6* shows some examples of CdSe NCs with different shapes.

In the present work, we synthesized spherically-shaped and nanorods-shaped CdSe nanocrystals with the high temperature synthesis in organic solvents. This will be detailed in Chapter 2.

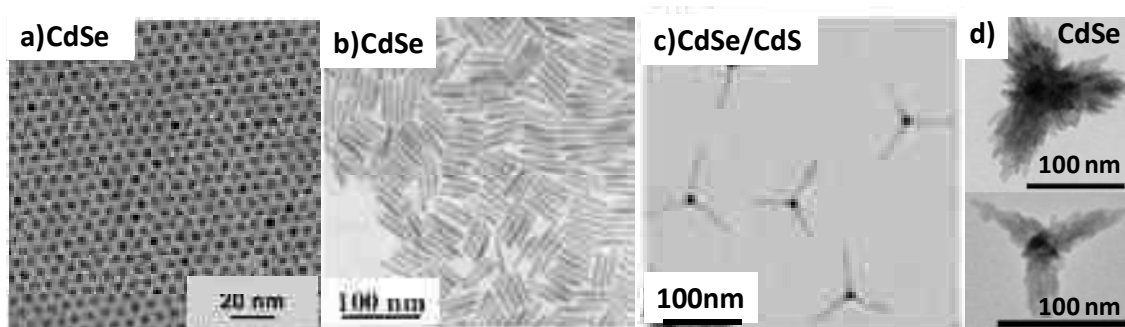


*Figure 4-6: Transmission electron microscope images of CdSe nanocrystals of different shapes. a) spherical CdSe NCs (89) b) rod-shaped CdSe (nanorods or NRs in short) (90); c) tetrapods with a CdS core and CdSe arms (89); d) hyperbranched CdSe nanostructures (91).*

#### 4.4. Ligand exchange and surface treatment

##### 4.4.1. Necessity for ligand exchange

The synthesis in organic solvents at high temperature yields nanocrystals composed of an inorganic core and an organic capping layer of ligands (see *Figure 4-1*).

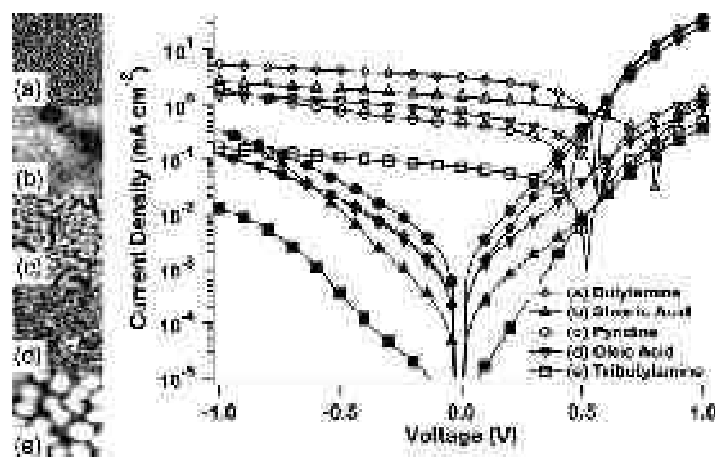


*Figure 4-7* : **left**: AFM images and *J/V* characteristics of solar cells based on CdSe/P3HT films as active layers using NCs capped with different ligands: butylamine (a), stearic acid (b), oleic acid (c), pyridine (d), and tributylamine (e). Each AFM image is  $15 \mu\text{m}^2$ . **Right**: *J/V* characteristics of the corresponding devices. The characteristics under illumination (hollow symbols) were recorded under a simulated AM1.5D spectrum at  $100 \text{ mW}=\text{cm}^2$ . Full symbols correspond to measurements in the dark. Reproduced from (93).

These ligands are necessary for the stabilization of the nanocrystals as a colloidal solution as well as for a good dispersion of the NCs in the polymer matrix in the case of hybrid materials. Nevertheless, the synthesis ligands are generally formed of long alkyl chains which behaves as an insulating layer regarding charge transfer. It has thus been shown that the charge transport properties as well as the morphology of hybrid thin films composed of CdSe NCs and P3HT are strongly dependent on the capping ligands of the NCs (92, 93). *Figure 4-7* illustrates the effect of the capping ligands on both the morphology of spin coated P3HT/CdSe nanocrystals used as active layers in solar cells. The most efficient devices and the smallest morphology features were observed for the shortest ligand examined, namely butylamine.

##### 4.4.2. Different approaches for ligand exchange/surface treatment

Surface treatment of the nanocrystals via ligand exchange is an important step for all device applications comprising CdSe nanocrystals. Different approaches were developed for the ligand exchange process. Two main approaches can be distinguished: (i) the post synthesis ligand exchange/surface treatment in solution and (ii) the post deposition ligand exchange/surface treatment of the NCs after the film deposition.

#### 4.4.2.1. Post synthesis ligand exchange/surface treatment

The ligand exchange with short molecules such as pyridine in solution after the synthesis and before the introduction of the NCs into the polymer matrix is probably the most common approach for the fabrication of hybrid devices such as solar cells (92, 94–96). However in most reports, the efficiency of the exchange reaction is poorly characterized. In the scope of this thesis, we used this approach to perform ligand exchange reactions of CdSe nanocrystals using various polypyridine ligands. This approach with its advantages and drawbacks will be extensively described in Chapter 2.

An alternative and interesting ligand exchange method was recently proposed via the acid surface treatment of the NCs (97, 98). In this case, the NCs are subjected after synthesis, to a washing procedure with hexanoic acid. The improvement of the solar cell efficiency was attributed to an efficient removal of the synthesis ligands. Surprisingly the authors report that the NCs stay soluble after the surface treatment which makes their integration into solar cell devices possible.

#### 4.4.2.2. Post deposition ligand exchange/surface treatment

Ligand exchange after the deposition of the thin film constitutes another approach for the surface treatment of the NCs (99–102). This post film processing ligand exchange involves mainly two steps: (i) the as prepared thin film is immersed during a given time in a solution containing the new ligand; (ii) the ligand-exchanged film is afterwards rinsed in a suitable solvent to remove the initial ligands. Another similar post-deposition surface treatment of the NCs is to subject the film to washing procedures with hydrazine. This allows to remove the initial ligands and to efficiently passivate at the same time the created trap states (103). The main advantage of the post-deposition ligand exchange is that the solution processability of the NCs is not influenced by the aggregation of the NCs as is often observed for ligand exchange reactions in solution. It makes possible to use for example small molecules having two anchoring sites (diamines, dithiols, etc.) which allow to crosslink two adjacent nanocrystals. Post deposition surface treatment and ligand exchange is an approach that seems well suited for thin films of NCs alone. Indeed, if it is performed in the presence of a polymer, it has to be ensured that immersion of the entire film into a solution of new ligand as well as the washing procedures and eventually annealing will not dissolve or affect the polymer fraction of the film.

The most adequate method strongly depends on the system. For the present work, we applied the ligand exchange method in solution before integrating the NCs in the films of interest. Further details on this aspect of the work will be given in Chapter 2.

## 5. Hybrid materials

The terminology of hybrid materials is widely used and concerns almost all materials in which organic and inorganic components are associated. Hybrid materials are reputed for their particular properties which result not only in the combination the properties of both the organic and the inorganic phases but often provide novel properties. In particular, hybrid materials can present interesting mechanical properties. For example, some hydrogels are of main interest for biomedical applications but at high water uptakes, their mechanical properties are strongly impeded. Adding silica nanoparticles to such hydrogels allows to provide also better mechanical stability and to strongly limit the swelling of the hydrogel at high water contents (104, 105). An improvement of the stiffness and the tensile strength of one order of magnitude was also reported for hybrid materials associating clay nanosheets and polymer (poly(vinyl alcohol)) processed by a layer by layer deposition method (106).

Due to the very wide field of hybrid materials, we will restrict in the following mainly to hybrids associating conjugated polymers and semiconducting nanocrystals of interest for organic electronics applications and in particular solar cells. First we will present the main advantages and the drawbacks of hybrid materials for the fabrication of organic electronic devices in comparison with all organic materials. In a second part, we will discuss the charge transport properties of the hybrids and the concept of bulk heterojunctions relevant for organic and flexible solar cells. Finally, we will review some approaches for the fabrication of such hybrid materials.

### 5.1. Hybrid versus all organic materials

Herein we will introduce the main differences between an “all-organic” solar cell and a hybrid solar cell. One of the keys for organic/hybrid solar cells is the creation of a p-n heterojunction. A p-n heterojunction is based on the association of one electron donating material with one electron accepting material. This means that the two materials have their HOMO-LUMO levels positioned in a way as to allow for an efficient charge transfer (see *Figure 5-1*), the electron being transferred to the acceptor and the hole to the donor. Usually, conjugated polymer plays the role of the electron donor. In an all-organic solar cells the electron acceptor is in most cases a soluble fullerene derivative PCBM (107). In hybrid polymer-nanoparticle materials, the frequently used small molecule PCBM is replaced by inorganic semiconducting nanocrystals such as CdSe NCs (96, 98). Some advantage of NCs as alternative solutions to PCBM are (i) the contribution of the nanocrystals to the absorbance of the materials regarding the solar spectrum; (ii) the tunability of the NCs bandgap with its size and morphology which allows to adjust the bandgap according to that of the polymer and to tune to some extent the absorption spectrum; (iii) the shape control of the NCs which makes it possible to use long nanorods or tetrapods for an improved charge transport (96, 98). Despite these advantages, to date the efficiencies of hybrid polymer-nanoparticle solar cells remain below those of all organic cells. Some reasons for this the issue of ligand exchange and the lack of fundamental understanding of the role of the ligands in the device, a limited

control of the morphology of the nanocomposite, the rather inefficient charge transport in the nanocrystal phase via hopping, etc (3, 96, 98).

## **5.2. Charge generation and transport in hybrid materials**

Electronic processes in hybrid materials are rather complex (3, 96, 98). A charge generation can occur either by doping or by external excitation (*e.g.* illumination with solar or UV light) of the hybrid. Herein we will focus on the charge generation by the absorption of a photon and illustrate the electronic processes as they occur in hybrid solar cells (3, 96, 98).

**Formation of excitons:** After the absorption of a photon by the hybrid material, an exciton can be formed either in the NCs phase or in the polymer phase.

**Diffusion of the exciton or recombination:** the photogenerated exciton can undergo one of the different phenomena: (i) the diffusion close to a donor- acceptor interface where under given conditions it can be separated in a free electron-hole pair, the electron remaining in the nanoparticle acceptor phase and the hole in the donor polymer phase; (ii) a radiative or non radiative recombination if the exciton does not reach the interface during its lifetime. Indeed, as excitons are neutral, their motion is not influenced by any internal electrical field and they are thus subject to random diffusion. The diffusion length of the excitons in P3HT is generally reported to  $\sim 10\text{nm}$  (108).

**Dissociation of the exciton into free charges:** in the case where within its lifetime the exciton could reach a donor-acceptor interface, it can dissociate into a free charge carriers. This process is fundamental for efficient photovoltaic conversion and many conditions have to be fulfilled for a successful charge generation. At this point, the question of the ligand becomes fundamental. Indeed, the chemical structure and the size of the ligands determine the electron transfer between the donor and the acceptor phase. The ligand shell can either favor or impede the charge transfer. In addition, the energy levels of the NCs and the polymer must be adequately adjusted in order to allow this charge transfer (see *Figure 4-7*). However, little is known on the effect of the binding of ligands on the energy levels of the NCs (3, 109). Depending on the energy levels of the NCs and the polymer, the exciton can be either confined in the phase where it was formed or it can dissociate at the p-n junction formed by the donor and acceptor.

**Charge carrier transport:** After the charge separation, the free electron and hole have to travel through the material in order to be collected at the electrodes in a solar cell device. As the  $e^-$  and  $h^+$  are bound via weak coulomb forces, a spatial separation is thus necessary to avoid recombination. The charge carriers will therefore travel through the respective phases towards the electrodes, provided that there are percolation pathways that lead towards the respective electrodes. The charge transport is partly assisted by an internal electrical field originating from the work function difference between the anode (generally ITO) and the cathode (a low work function metal such as Al).

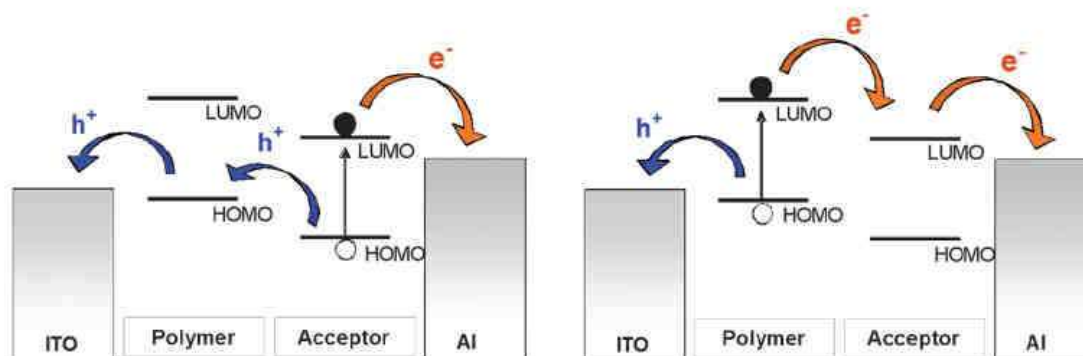


Figure 5-1 : Energy levels alignment in a conjugated polymer/semiconductor nanocrystals hybrid allowing the dissociation of the excitons into a free electron and hole pair. **Left panel:** case where the excitons are photogenerated in the nanocrystal phase; **right panel:** case where the excitons are formed in the polymer phase. The electron ( $e^-$ ) and hole ( $h^+$ ) transfer processes are indicated with arrow. The electrodes are made from ITO and Aluminum. Reproduced from (3)

### 5.3. The concept of bulk heterojunction and importance of the morphology control

A bulk heterojunction is an interpenetrated network of the electron donor (polymer) and the electron acceptor (nanocrystals) phases. Figure 5-2 shows a schematical representation of a bulk heterojunction. An efficient bulk heterojunction must fulfill essentially two points: (i) donor and acceptor phases interpenetrated on a length scale in the same range as the length of diffusion of the excitons in order to allow most excitons to reach the interface so as to be separated into free charge carriers; (ii) the donor and acceptor phases must provide percolation pathways for the charge carriers towards the respective electrodes.

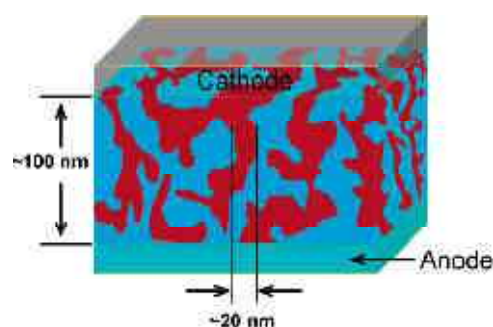


Figure 5-2: Schematical representation of a bulk heterojunction like solar cell. Reproduced from (108).

As mentioned above, the diffusion length of exciton in P3HT is reported to be around 10 nm (108). Therefore, the control of the nanomorphology of the hybrids composed of P3HT and NCs must be controlled on this length scale. The concept of bulk heterojunction was first introduced in the middle of the 1990<sup>ies</sup> by Yu *et al.* for polymer solar cells composed of MEH-PPV and fullerenes (110, 111). This was a breakthrough in the field of organic photovoltaics as it allowed to obtain much more efficient devices. Few years afterwards, the first hybrid bulk heterojunction composed of nanocrystals and polymer for the fabrication of light emitting diodes was presented (112). The first example of a hybrid bulk heterojunction for

photovoltaic applications was presented in 1996 by the group of Alivisatos (University of Berkeley) first with a mixture of MEH-PPV and CdSe nanocrystals but the solar cells had quite low power conversion efficiencies (PCE) (113). It was a few years later in 2002 that the same group published a seminal work where they presented solar cell devices with PCEs up to 1,7 % based on blends of P3HT and CdSe nanorod-shaped nanocrystals (114). Since then, research has steadily progressed in the field and state-of-the-art devices provide PCEs of 4,1% based on P3HT nanofibrils and CdS spherical nanocrystals (3, 115)

#### **5.4. Fabrication of hybrid materials**

The elaboration of hybrid materials composed of nanocrystals and conjugated polymers requires specific methods due to the limited compatibility of the components (3). Many approaches were developed for the fabrication of such materials. In some cases the polymer and the NCs are simply blended. In other approaches, chemical bonds are formed between the organic and the inorganic materials. Herein some selected and representative examples will be presented and discussed (3).

##### **5.4.1. Simple blends of the components**

In most cases, the organic and inorganic components of the hybrid are first synthesized separately and in a second step are blended in a common solvent (or mixture of solvents) before solution processing the hybrid as a thin film. Although this approach seems rather simple, it bears limitations. In fact, the dispersion of the nanocrystals in the polymer matrix is not guaranteed and there is limited control of the dispersion/aggregation of the nanocrystals in the polymer matrix. Whereas for NCs with their initial capping ligands (long alkyl chains) the process is rather simple, after ligand exchange the situation is more complicated often implying to use solvent mixtures. Indeed, after ligand exchange it is often difficult to find common solvents for both the NCs and the polymer. Thus solvent mixtures must be used and the choice of the solvent as well as the volume ratio of each solvents are essential factors that will influence the nanomorphology of the hybrid thin film. Other parameters such as the concentration, the relative amount of the organic (polymer) to the inorganic phase (nanocrystals), the deposition technique used to process the film (spin coating, dip coating, drop casting, etc) also strongly influence the nanomorphology of the hybrid.

Huynh *et al.* processed the active layer of the hybrid solar cells by spin coating a mixture a P3HT and pyridine exchanged NRs from a solvent mixture chloroforme/pyridine by using 5-15% of Py in the mixture (116, 117). Jui *et al.* showed recently that the choice of solvent mixture influences the efficiency of the hybrid solar cells (118). They used various solvent mixtures: Chlorofomre/Pyridine, orthodichlorobenzen/ Pyridine and chlorobenzene/pyridine in a ratio (95/5 vol%). They reported PCEs of respectively 0,2%, 1,44% and 1,54%. The improvement of the efficiancy for high boiling point solvents was attributed to slower crystallization kinetics of the P3HT forming films with higher crystalline order.

As mentioned previously, simple blending of the two components to fabricate hybrid materials brings some limitations and problems. To overcome the latter, other strategies allowing a better control and if possible allowing to avoid the ligand exchange reaction have been developed.

#### 5.4.2. Hybrids via capping the NCs with the conjugated polymer

Another approach for the fabrication of hybrids is to functionalize the conjugated polymers with anchoring groups allowing the chemical adsorption of the organic compound onto the surface of the nanocrystals.

Following this strategy, Liu and co-workers prepared hybrids from functionalized CdSe nanorods and a P3HT end-functionalized with amino groups (119). The amino-terminated P3HT were attached to the NCs just after the ligand exchange reaction with the labile pyridine ligand. This approach allowed to have a good control of the morphology with a nice dispersion of the nanocrystals into the polymer matrix. These hybrids were incorporated as active layers in solar cells and allowed to improve the photovoltaic efficiencies compared to simple blends of pyridine exchanged nanorods and standards rr-P3HT. Figure 5-3(a) shows the TEM images of the hybrid thin films prepared with standard P3HT whereas Figure 5-3 (b) shows the corresponding image prepared from the functional P3HT (119).

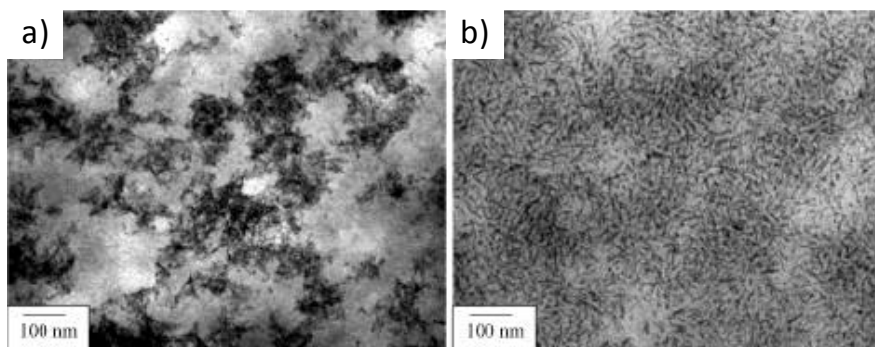
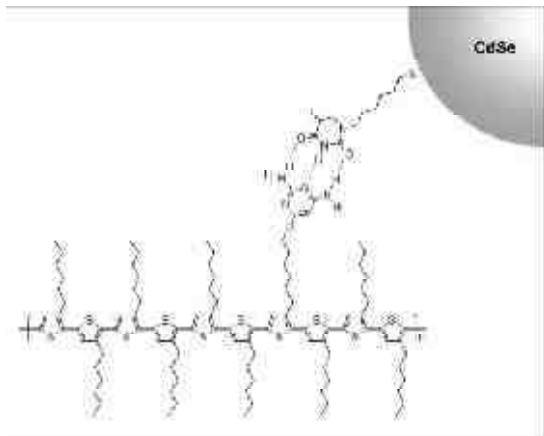


Figure 5-3: TEM images corresponding to two hybrid films containing 40 wt% of nanorods. (A) Use of normal P3HT. In this case, the P3HT and the NRs do not have any specific interactions. (b) Use of end-functionalized P3HT that can attach to the NCs surface. Reproduced from (119).

A similar approach was used by Zhang *et al.* to prepare hybrids from CdSe NRs and vinyl terminated P3HT (120). The developed process involves several steps. First the as-synthesized nanocrystals are ligand exchanged with pyridine. In a second step, pyridine is replaced by an arylbromide which thus yields arylbromide capped nanocrystals. In a second step, vinyl-terminated P3HT is coupled to the arylbromide capped NCs giving rise to a hybrid of P3HT grafted on the surface of CdSe NCs. Another example of capping the NCs directly with a functional group was proposed by Aldakov *et al.* who prepared oligothiophene having a aniline anchoring group capped 4-formyldithiobenzoate functionalized nanocrystals (121). More recently, the same group developed polythiophene copolymers side-functionalized with carboxylic groups in order to graft them onto the surface of CdSe nanorods. A nice dispersion of the nanoparticles could be obtained again in solution-processed hybrids (122).

### 5.4.3. Hybrids via molecular recognition

Besides the capping of the NCs, another approach is the molecular recognition strategy. Molecular recognition does not involve a direct capping of the polymer on the NCs, but it allows to control the dispersion of the NCs in the polymer matrix by introducing chemical groups onto the nanocrystals that recognize complementary ones on the polymer. Following this idea, De Girolamo *et al.* prepared a solution processable P3HT derivative containing diaminopyrimidine side groups, namely poly(3-hexylthiophene-co-3-(6-oxy-2,4-diaminopyrimidine)hexylthiophene) (P3HT-co-P3(ODAP)HT). On the other hand the authors functionalized CdSe nanocrystals with 1-(6-mercaptohexyl)thymine (MHT). Both, the functionalized polymer and NCs could recognize each other via the three hydrogen bonds as shown in *Figure 5-4* (123). This molecular recognition process forces a uniform distribution of individual nanocrystals within the polymer matrix (123, 124). The advantage of the use of hydrogen bonds lies in the possibility to modulate the strength of the interaction by the polarity of the used solvent or the temperature but in all case the hydrogen bonds allow for a better cohesion of the hybrid thin films in the solid state (123, 124).



*Figure 5-4 : Interactions between Poly(3-hexylthiophene-co-3-(6-oxy-2,4-diaminopyrimidine) hexyl-thiophene)(P2) and 1-(6-mercaptohexyl)thymine Capped CdSe (CdSe-4) via Hydrogen Bonding.*

### 5.4.4. In situ growth

A rather different method from the ones previously described for the fabrication of hybrid materials is the in-situ growth of the NCs directly into the polymer matrix. The principle of this approach is based on the dissolution of chemical precursors of the nanocrystals in a solution of the polymer, and the growth of the nanocrystals directly in the polymer template (125, 126). Beek *et al.* prepared in this way a hybrid bulk heterojunction composed of ZnO and MDMO-PPV (125). They started from diethylzinc as precursor for the ZnO formation. The conversion of diethyl zinc into ZnO involves two steps which are hydrolysis and condensation, both of them occur if diethylzinc is exposed to air (125). Therefore, the authors obtained a crystalline ZnO network by spin coating a mixture of MDMO-PPV and diethyl zinc (125). For a better control of the reaction, the temperature and solvent mixtures were carefully chosen.

More recently a similar approach was used by Yuan *et al.* who showed the possibility to grow ZnO nanorods by hydrolysis directly in a block copolymer of poly(3-

hexylthiophene)-b-poly(zinc methacrylate acetate) matrix (126). The block-copolymer plays a twofold role in this work. It is at the same time a precursor for the ZnO particles and a template for the organization of the nanorods. As the poly(zinc methacrylate acetate) block of the blockcopolymer serves as precursor for the ZnO nanorod formation, the authors obtained a P3HT/ ZnO hybrid. They reported a strong fluorescence quenching which they attributed to a heterojunction composed of P3HT and ZnO nanorods.

Liao *et al* reported in situ synthesis of another kind of NCs, namely CdS nanorods of various aspect ratios directly in a P3HT matrix (127). They incorporated the obtained hybrid materials in solar cells and reported power conversion efficiencies up to 2.9 % under AM1.5 simulated solar illumination (100 mW.cm<sup>2</sup>).

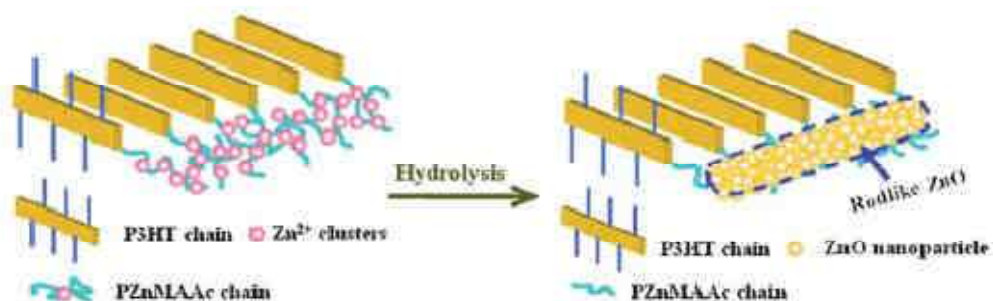


Figure 5-5 : Schematic representation of proposed mechanism for the growth of rodlike ZnO nanocrystals. Reproduced from (126).

### 5.5. Oriented and nanostructured hybrids

Other interesting strategies and approaches regarding the controlled processing of hybrid materials have been described in the literature. Particular interest was paid to the controlled nanostructuring of hybrid materials using for example templates or block copolymers (128, 129). Another point that was addressed much is the orientation of rod-shaped nanocrystals in a polymer matrix (130, 131). The nanostructuring and the controlled fabrication of oriented hybrid materials composed of P3HT and CdSe NCs was one of the aims of this thesis. More particularly we were interested in the fabrication of materials where both, the P3HT as well as the rod shaped nanocrystals have a well defined in-plane orientation. The state of the arts regarding the nanostructuring and orientation of hybrid materials will be presented in more details the corresponding chapters (see Chapter 6 and Chapter 7).

## 6. Scope of this work

In this chapter, we have presented a literature survey about the main properties and applications of materials that we were interested in the scope of this work. The main

properties of P3HT as a conjugated semi-crystalline and semiconducting polymer were introduced. Furthermore, main strategies for the controlled orientation of polymers in general and P3HT in particular were discussed. We also introduced the basic properties of colloidal semiconducting nanocrystals and their application in devices such as solar cells. Some strategies for the controlled fabrication of hybrid materials were presented.

The scope of this work was to develop and study highly oriented and nanostructured hybrid polymer-nanoparticle materials. Following this general aim, three main points were addressed: (i) the controlled elaboration of highly oriented thin films of pure P3HT by applying some of the orientation methods described here above; (ii) the controlled fabrication of oriented and nanostructured hybrid materials composed of P3HT and CdSe nanocrystals; (iii) in addition, we were interested in the surface functionalization of CdSe with various polypyridine ligands and the influence of these ligands on the thin films morphology of the resulting hybrids. We will now present in the following the methods and techniques developed and the results obtained in the frame of this work.

- (1) Pron, A.; Rannou, P. Processible conjugated polymers: from organic semiconductors to organic metals and superconductors. *Progress in Polymer Science* **2002**, *27*, 135-190.
- (2) Attias, A. J. Polymères conjugués et polymères conducteurs électroniques. *Techniques de l'ingénieur E1862*, 1-20.
- (3) Reiss, P.; Couderc, E.; De Girolamo, J.; Pron, A. Conjugated polymers/semiconductor nanocrystals hybrid materials-preparation, electrical transport properties and applications. *Nanoscale* **2010**.
- (4) Verilhac, J.-M. Transistors organiques à base de dérivés du polythiophène effets de la structure moléculaire et supramoléculaire, PhD dissertation, INP Grenoble, 2006.
- (5) Brinkmann, M. Structure and morphology control in thin films of regioregular poly(3-hexylthiophene). *Journal of Polymer Science Part B: Polymer Physics* **2011**, *49*, 1218-1233.
- (6) Lim, J. A.; Liu, F.; Ferdous, S.; Muthukumar, M.; Briseno, A. L. Polymer semiconductor crystals. *Materials Today* **2010**, *13*, 14-24.
- (7) Ungar, G.; Zeng, X. B. Learning polymer crystallization with the aid of linear, branched and cyclic model compounds. *Chemical reviews* **2001**, *101*, 4157-88.
- (8) Lotz, B. Structure et morphologie des polymères à l'état condensé. *Bulletin de L'union des Physiciens* **1981**, *639*, 337.
- (9) Prosa, T. J.; Winokur, M. J.; Moulton, J.; Smith, P.; Heeger, a. J. X-ray structural studies of poly(3-alkylthiophenes): an example of an inverse comb. *Macromolecules* **1992**, *25*, 4364-4372.
- (10) Tashiro, K.; Kobayashi, M.; Kawai, T.; Yoshino, K. Crystal structural change in poly(3-alkyl thiophene)s induced by iodine doping as studied by an organized combination of X-ray diffraction, infrared/Raman spectroscopy and computer simulation techniques. *Polymer* **1997**, *38*, 2867-2879.
- (11) Dag, S.; Wang, L.-W. Packing structure of poly(3-hexylthiophene) crystal: ab initio and molecular dynamics studies. *The journal of physical chemistry. B* **2010**, *114*, 5997-6000.
- (12) Kayunkid, N.; Uttiya, S.; Brinkmann, M. Structural model of regioregular poly(3-hexylthiophene) obtained by electron diffraction analysis. *Macromolecules* **2010**, *43*, 4961-4967.
- (13) Zen, A.; Saphiannikova, M.; Neher, D.; Grenzer, J.; Grigorian, S.; Pietsch, U.; Asawapirom, U.; Janietz, S.; Scherf, U.; Lieberwirth, I.; Wegner, G. Effect of molecular weight on the structure and crystallinity of poly(3-hexylthiophene). *Macromolecules* **2006**, *39*, 2162-2171.
- (14) Wu, Z.; Petzold, A.; Henze, T.; Thurn-Albrecht, T.; Lohwasser, R. H.; Sommer, M.; Thelakkat, M. Temperature and molecular weight dependent hierarchical equilibrium structures in semiconducting poly(3-hexylthiophene). *Macromolecules* **2010**, *43*, 4646-4653.
- (15) Pascui, O. F.; Lohwasser, R.; Sommer, M.; Thelakkat, M.; Thurn-Albrecht, T.; Saalwächter, K. High Crystallinity and Nature of Crystal-Crystal Phase Transformations in Regioregular Poly(3-hexylthiophene). *Macromolecules* **2010**, *43*, 9401-9410.

- (16) Yuan, Y.; Zhang, J.; Sun, J.; Hu, J.; Zhang, T.; Duan, Y. Polymorphism and structural transition around 54 ° C in regioregular poly ( 3-hexylthiophene ) with high crystallinity as revealed by infrared spectroscopy. *Macromolecules* **2011**, *in press*.
- (17) Brinkmann, M.; Wittmann, J.-C. Orientation of regioregular poly(3-hexylthiophene) by directional solidification: a simple method to reveal the semicrystalline structure of a conjugated polymer. *Advanced Materials* **2006**, *18*, 860-863.
- (18) Mena-Osteritz, E.; Meyer, A.; Langeveld-voss, B. M. W.; Janssen, R. A. J.; Meijer, E. W.; Bäuerle, P. Two-dimensional crystals of poly(3-alkyl-thiophen)s: direct visualization of polymer folds in submolecular resolution. *Angewandte Chemie (International ed. in English)* **2000**, *39*, 2679-2684.
- (19) Mena-Osteritz, E. Superstructures of self-organizing thiophenes. *Advanced Materials* **2002**, *14*, 609.
- (20) Grévin, B.; Rannou, P.; Payerne, R.; Pron, A.; Travers, J.-P. Scanning tunneling microscopy investigations of self-organized poly(3-hexylthiophene) two-dimensional polycrystals. *Advanced Materials* **2003**, *15*, 881-884.
- (21) Grévin, B.; Rannou, P.; Payerne, R.; Pron, A.; Travers, J. P. Multi-scale scanning tunneling microscopy imaging of self-organized regioregular poly(3-hexylthiophene) films. *The Journal of Chemical Physics* **2003**, *118*, 7097.
- (22) Payerne, R.; Brun, M.; Rannou, P.; Baptist, R.; Grévin, B. STM studies of poly ( 3-alkylthiophene)s□: model systems for plastic electronics. *Synthetic Metals* **2004**, *146*, 311-315.
- (23) Brinkmann, M.; Rannou, P. Molecular weight dependence of chain packing and semicrystalline structure in oriented films of regioregular poly(3-hexylthiophene) revealed by high-resolution transmission electron microscopy. *Macromolecules* **2009**, *42*, 1125-1130.
- (24) Zhang, R.; Li, B.; Iovu, M. C.; Jeffries-El, M.; Sauv e, G.; Cooper, J.; Jia, S.; Tristram-Nagle, S.; Smilgies, D. M.; Lambeth, D. N.; McCullough, R. D.; Kowalewski, T. Nanostructure dependence of field-effect mobility in regioregular poly(3-hexylthiophene) thin film field effect transistors. *Journal of the American Chemical Society* **2006**, *128*, 3480-1.
- (25) Brinkmann, M.; Rannou, P. Effect of molecular weight on the structure and morphology of oriented thin films of regioregular poly(3-hexylthiophene) grown by directional epitaxial solidification. *Advanced Functional Materials* **2007**, *17*, 101-108.
- (26) M uller, C.; Zhigadlo, N. D.; Kumar, A.; Baklar, M. A.; Karpinski, J.; Smith, P.; Kreouzis, T.; Stingelin, N. Enhanced charge-carrier mobility in high-pressure-crystallized poly (3-hexylthiophene). *Macromolecules* **2011**, *44*, 1221-1225.
- (27) Crossland, E. J. W.; Rahimi, K.; Reiter, G.; Steiner, U.; Ludwigs, S. Systematic control of nucleation density in poly (3-hexylthiophene) thin films. *Advanced Functional Materials* **2010**, *21*, 518-524.
- (28) Kline, R. J.; McGehee, M. D.; Kadnikova, E. N.; Liu, J.; Fr echet, J. M. J. Controlling the Ffield-effect mobility of regioregular polythiophene by changing the molecular weight. *Advanced Materials* **2003**, *15*, 1519-1522.
- (29) Joseph Kline, R.; McGehee, M. D.; Toney, M. F. Highly oriented crystals at the buried interface in polythiophene thin-film transistors. *Nature Materials* **2006**, *5*, 222-228.

- (30) Yang, H.; LeFevre, S. W.; Ryu, C. Y.; Bao, Z. Solubility-driven thin film structures of regioregular poly ( 3-hexyl thiophene ) using volatile solvents. *Applied Physics Letters* **2007**, *90*, 172116.
- (31) Brinkmann, M.; Wittmann, J.-C. Orientation of regioregular poly(3-hexylthiophene) by directional solidification: a simple method to reveal the semicrystalline structure of a conjugated polymer. *Advanced Materials* **2006**, *18*, 860-863.
- (32) Sirringhaus, H.; Bird, M.; Richards, T.; Zhao, N. Charge transport physics of conjugated polymer field-effect transistors. *Advanced Materials* **2010**, *4307*, n/a-n/a.
- (33) Jimison, L. H.; Toney, M. F.; McCulloch, I.; Heeney, M.; Salleo, A. Charge-transport anisotropy due to grain boundaries in directionally crystallized thin films of regioregular poly(3-hexylthiophene). *Advanced Materials* **2009**, *21*, 1568-1572.
- (34) O'Connor, B.; Kline, R. J.; Conrad, B. R.; Richter, L. J.; Gundlach, D.; Toney, M. F.; DeLongchamp, D. M. Anisotropic structure and charge transport in highly strain-aligned regioregular poly(3-hexylthiophene). *Advanced Functional Materials* **2011**, *21*, 3697-3705.
- (35) Clark, J.; Chang, J.-F.; Spano, F. C.; Friend, R. H.; Silva, C. Determining exciton bandwidth and film microstructure in polythiophene films using linear absorption spectroscopy. *Applied Physics Letters* **2009**, *94*, 163306.
- (36) Verilhac, J.-M.; LeBlevenec, G.; Djurado, D.; Rieutord, F.; Chouiki, M.; Travers, J.-P.; Pron, A. Effect of macromolecular parameters and processing conditions on supramolecular organisation, morphology and electrical transport properties in thin layers of regioregular poly(3-hexylthiophene). *Synthetic Metals* **2006**, *156*, 815-823.
- (37) Kline, R. J.; McGehee, M. D.; Kadnikova, E. N.; Liu, J.; Fréchet, J. M. J.; Toney, M. F. Dependence of regioregular poly(3-hexylthiophene) film morphology and field-effect mobility on molecular weight. *Macromolecules* **2005**, *38*, 3312-3319.
- (38) Zen, A.; Pflaum, J.; Hirschmann, S.; Zhuang, W.; Jaiser, F.; Asawapirom, U.; Rabe, J. P.; Scherf, U.; Neher, D. Effect of molecular weight and annealing of Poly(3-hexylthiophene)s on the performance of organic field-effect transistors. *Advanced Functional Materials* **2004**, *14*, 757-764.
- (39) Berson, S.; De Bettignies, R.; Bailly, S.; Guillerez, S. Poly(3-hexylthiophene) Fibers for Photovoltaic Applications. *Advanced Functional Materials* **2007**, *17*, 1377-1384.
- (40) Brinkmann, M.; Chandezon, F.; Pansu, R. B.; Julien-Rabant, C. Epitaxial growth of highly oriented fibers of semiconducting polymers with a Shish-Kebab-like superstructure. *Advanced Functional Materials* **2009**, *19*, 2759-2766.
- (41) Zhu, R.; Kumar, A.; Yang, Y. Polarizing organic photovoltaics. *Advanced Materials* **2011**, *23*, 4193-4198.
- (42) Wittmann, J. C.; Lotz, B. Epitaxial crystallization of polymers on organic and polymeric substrates. *Progress in Polymer Science* **1990**, *15*, 909.
- (43) Zhou, H.; Jiang, S.; Yan, S. Epitaxial crystallization of poly(3-hexylthiophene) on a highly oriented polyethylene thin film from solution. *The journal of physical chemistry. B* **2011**, *115*, 13449-54.
- (44) Van Aerle, N. A. J. M.; Barmantlo, M.; Hollering, R. W. J. Effect of rubbing on the molecular orientation within polyimide orienting layers of liquid-crystal displays. *Journal of Applied Physics* **1993**, *74*, 3111-3120.

- (45) Wittmann, J. C.; Smith, P. Highly oriented thin films of poly(tetrafluoroethylene) as a substrate for oriented growth of materials. *Nature* **1991**, *352*, 414-417.
- (46) Nagamatsu, S.; Takashima, W.; Kaneto, K.; Yoshida, Y.; Tanigaki, N.; Yase, K.; Omote, K. Backbone arrangement in “friction-transferred” regioregular poly(3-alkylthiophene)s. *Macromolecules* **2003**, *36*, 5252-5257.
- (47) Kim, Y. B.; Olin, H.; Park, S. Y.; Choi, J. W.; Komitov, L.; Matuszczyk, M.; Lagerwall, S. T. Rubbed polyimide films studied by scanning force microscopy. *Applied Physics Letters* **1995**, *66*, 2218.
- (48) Brinkmann, M.; Pratontep, S.; Chaumont, C.; Wittmann, J.-C. Oriented and nanostructured polycarbonate substrates for the orientation of conjugated molecular materials and gold nanoparticles. *Macromolecules* **2007**, *40*, 9420-9426.
- (49) Vergnat, C.; Uttiya, S.; Pratontep, S.; Kerdcharoen, T.; Legrand, J.-F.; Brinkmann, M. Oriented growth of zinc(II) phthalocyanines on polycarbonate alignment substrates: Effect of substrate temperature on in-plane orientation. *Synthetic Metals* **2011**, *161*, 251.
- (50) Vergnat, C.; Landais, V.; Legrand, J.-F.; Brinkmann, M. Orienting semiconducting nanocrystals on nanostructured polycarbonate substrates: impact of substrate temperature on polymorphism and in-plane orientation. *Macromolecules* **2011**, *44*, 3817-3827.
- (51) Matsushima, T.; Murata, H. Enhanced charge-carrier injection caused by molecular orientation. *Applied Physics Letters* **2011**, *98*, 253307.
- (52) Chen, X. L.; Lovinger, A. J.; Bao, Z.; Sapjeta, J. Morphological and transistor studies of organic molecular semiconductors with anisotropic electrical characteristics. *Chemistry of Materials* **2001**, *13*, 1341-1348.
- (53) Abbas, M.; D’Amico, F.; Ali, M.; Mencarelli, I.; Setti, L.; Bontempi, E.; Gunnella, R. Rubbing effects on the structural and optical properties of poly(3-hexylthiophene) films. *Journal of Physics D: Applied Physics* **2010**, *43*, 035103.
- (54) Heil, H.; Finnberg, T.; von Malm, N.; Schmechel, R.; von Seggern, H. The influence of mechanical rubbing on the field-effect mobility in polyhexylthiophene. *Journal of Applied Physics* **2003**, *93*, 1636.
- (55) Bolognesi, A.; Botta, C.; Mercogliano, C.; Porzio, W.; Jukes, P. C.; Geoghegan, M.; Grell, M.; Durell, M.; Trolley, D.; Das, A.; Macdonald, J. E. Structural features in aligned poly(3-alkylthiophene) films revealed by grazing incidence X-ray diffraction. *Polymer* **2004**, *45*, 4133-4138.
- (56) Derue, G.; Coppée, S.; Gabriele, S.; Surin, M.; Geskin, V.; Monteverde, F.; Leclère, P.; Lazzaroni, R.; Damman, P. Nanorubbing of polythiophene surfaces. *Journal of the American Chemical Society* **2005**, *127*, 8018-9.
- (57) Nagamatsu, S.; Takashima, W.; Kaneto, K.; Yoshida, Y.; Tanigaki, N.; Yase, K.; Omote, K. Backbone arrangement in “friction-transferred” regioregular poly(3-alkylthiophene)s. *Macromolecules* **2003**, *36*, 5252-5257.
- (58) Nagamatsu, S.; Misaki, M.; Chikamatsu, M.; Kimura, T.; Yoshida, Y.; Azumi, R.; Tanigaki, N.; Yase, K. Crystal structure of friction-transferred poly(2,5-dioctyloxy-1,4-phenylenevinylene). *The journal of physical chemistry. B* **2007**, *111*, 4349-54.

- (59) Petermann, J.; Gohil, R. M. A new method for the preparation of high modulus thermoplastic films. *Journal of Materials Science* **1976**, *14*, 2260-2264.
- (60) Li, H.; Yan, S. Surface-induced polymer crystallization and the resultant structures and morphologies. *Macromolecules* **2011**, *44*, 417-428.
- (61) Brinkmann, M.; Contal, C.; Kayunkid, N.; Djuric, T.; Resel, R. Highly oriented and nanotextured films of regioregular poly(3-hexylthiophene) grown by epitaxy on the nanostructured surface of an aromatic substrate. *Macromolecules* **2010**, *43*, 7604-7610.
- (62) Givargizov, E. Graphoepitaxy as an approach to oriented crystallization on amorphous substrates. *Journal of Crystal Growth* **2008**, *310*, 1686-1690.
- (63) Lieser, G.; Oda, M.; Miteva, T.; Meisel, A.; Nothofer, H.-G.; Scherf, U. Ordering , graphoepitaxial orientation , and conformation of a polyfluorene derivative of the “ hairy-rod ” type on an oriented substrate of polyimide. *Macromolecules* **2000**, *33*, 4490-4495.
- (64) Tanaka, T.; Ishitobi, M. Atomic groove effect of aligned poly(tetrafluoroethylene) surfaces upon oriented growth of linear dye molecules. *The Journal of Physical Chemistry B* **2002**, *106*, 564-569.
- (65) Amundson, K. R.; Sapjeta, B. J.; Lovinger, A. J.; Bao, Z. An in-plane anisotropic organic semiconductor based upon poly (3-hexyl thiophene). *Thin Solid Films* **2002**, *414*, 143-149.
- (66) Müller, G. The Czochralski Method - where we are 90 years after Jan Czochralski's invention. *Crystal Research and Technology* **2007**, *42*, 1150-1161.
- (67) Schweicher, G.; Paquay, N.; Amato, C.; Resel, R.; Koini, M.; Talvy, S.; Lemaur, V.; Cornil, J.; Geerts, Y.; Gbabode, G. Toward single crystal thin films of terthiophene by directional crystallization using a thermal gradient. *Crystal Growth and Design* **2011**, *11*, 3663-3672.
- (68) Lovinger, A. J.; Gryte, C. C. The morphology of directionally solidified poly( ethylene oxide) spherulites. *Macromolecules* **1976**, *9*, 247-253.
- (69) Lovinger, A. J. Crystallographic factors affecting the structure of polymeric spherulites. II. X-ray diffraction analysis of directionally solidified polyamides and general conclusions. *Journal of Applied Physics* **1978**, *49*, 5014.
- (70) Lovinger, A. J. Model for the shape of polymer spherulites formed in a temperature gradient. *Journal of Applied Physics* **1976**, *47*, 1999.
- (71) Toda, A.; Taguchi, K.; Kajioka, H. Structure evolution in directional crystallization of polymers under temperature gradient. *Macromolecules* **2011**, in-press.
- (72) Tracz, A.; Pakula, T.; Jeszka, J. Zone casting—a universal method of preparing oriented anisotropic layers of organic materials. *Materials science-Poland* **2004**, *22*.
- (73) Duffy, C. M.; Andreasen, J. W.; Breiby, D. W.; Nielsen, M. M.; Ando, M.; Minakata, T.; Sirringhaus, H. High-mobility aligned pentacene films grown by zone-casting. *Chemistry of Materials* **2008**, *20*, 7252-7259.
- (74) Lee, M. J.; Gupta, D.; Zhao, N.; Heeney, M.; McCulloch, I.; Sirringhaus, H. Anisotropy of charge transport in a uniaxially aligned and chain-extended, high-mobility, conjugated polymer semiconductor. *Advanced Functional Materials* **2011**, *21*, 932-940.

- (75) Breiby, D. W.; Bunk, O.; Pisula, W.; Sølling, T. I.; Tracz, A.; Pakula, T.; Müllen, K.; Nielsen, M. M. Structure of zone-cast HBC-C12H25 films. *Journal of the American Chemical Society* **2005**, *127*, 11288-11293.
- (76) Dimitrakopoulos, C. D.; Brown, a. R.; Pomp, a. Molecular beam deposited thin films of pentacene for organic field effect transistor applications. *Journal of Applied Physics* **1996**, *80*, 2501.
- (77) Dimitrakopoulos, C. D.; Malenfant, P. R. L. Organic Thin Film Transistors for Large Area Electronics. *Advanced Materials* **2002**, *14*, 99-117.
- (78) Liu, S.; Wang, W. M.; Briseno, A. L.; Mannsfeld, S. C. B.; Bao, Z. Controlled deposition of crystalline organic semiconductors for field-effect-transistor applications. *Advanced Materials* **2009**, *21*, 1217-1232.
- (79) Chandezon, F.; Reiss, P. Nanocristaux semi-conducteurs fluorescents. *Techniques de l'ingenieur* **2004**, *22*, 1-15.
- (80) Couderc, E. Transport de charge dans des matériaux hybrides composés de polymères pi-conjugués et de nanocristaux de semi-conducteurs, PhD dissertation, Université Joseph Fourier de Grenoble, 2011.
- (81) Brus, L. Electronic wave functions in semiconductor clusters: experiment and theory. *Journal of Physical Chemistry* **1986**, *90*, 2555-2560.
- (82) Brus, L. E. Electron–electron and electron-hole interactions in small semiconductor crystallites: The size dependence of the lowest excited electronic state. *The Journal of Chemical Physics* **1984**, *80*, 4403.
- (83) Deng, Z.; Cao, L.; Tang, F.; Zou, B. A new route to zinc-blende CdSe nanocrystals: mechanism and synthesis. *The journal of physical chemistry. B* **2005**, *109*, 16671-5.
- (84) Protière, M. Synthèse de nanocristaux fluorescents de semi-conducteurs II-VI et III-V augmentation de l'échelle de synthèse, PhD dissertation, Université Joseph Fourier de Grenoble, 2007.
- (85) Manna, L.; Scher, E. C.; Alivisatos, A. P. Synthesis of soluble and processable rod-, arrow-, teardrop-, and tetrapod-shaped CdSe nanocrystals. *Journal of the American Chemical Society* **2000**, *122*, 12700-12706.
- (86) Murray, C. B.; Norris, D. J.; Bawendi, M. G. Synthesis and characterization of nearly monodisperse CdE (E = S, Se, Te) semiconductor nanocrystallites. *Journal of the American Chemical Society* **1993**, *115*, 8706-8715.
- (87) Alivisatos, A. P. Perspectives on the physical chemistry of semiconductor nanocrystals. *The Journal of Physical Chemistry* **1996**, *100*, 13226-13239.
- (88) Peng, X.; Manna, L.; Yang, W.; Wickham, J.; Scher, E.; Kadavanich, A.; Alivisatos, A. P. Shape control of CdSe nanocrystals. *Nature* **2000**, *404*, 59-61.
- (89) Talapin, D. V.; Lee, J.-S.; Kovalenko, M. V.; Shevchenko, E. V. Prospects of colloidal nanocrystals for electronic and optoelectronic applications. *Chemical reviews* **2010**, *110*, 389-458.
- (90) Peng, X. Mechanisms for the shape-control and shape-evolution of colloidal semiconductor nanocrystals. *Advanced Materials* **2003**, *15*, 459-463.

- (91) Kanaras, A. G.; Sönnichsen, C.; Liu, H.; Alivisatos, a P. Controlled synthesis of hyperbranched inorganic nanocrystals with rich three-dimensional structures. *Nano letters* **2005**, *5*, 2164-7.
- (92) Aldakov, D.; Chandezon, F.; Bettignies, R. D.; Firon, M.; Reiss, P.; Pron, A. Hybrid organic-inorganic nanomaterials□: ligand effects. *The European physical journal Applied Physics* **2007**, *36*, 261-265.
- (93) Olson, J. D.; Gray, G. P.; Carter, S. a. Optimizing hybrid photovoltaics through annealing and ligand choice. *Solar Energy Materials and Solar Cells* **2009**, *93*, 519-523.
- (94) Lokteva, I.; Radychev, N.; Witt, F.; Borchert, H.; Parisi, J.; Kolny-Olesiak, J. Surface treatment of CdSe nanoparticles for application in hybrid solar cells: the effect of multiple ligand exchange with pyridine. *The Journal of Physical Chemistry C* **2010**, *114*, 12784-12791.
- (95) Radychev, N.; Lokteva, I.; Witt, F.; Kolny-Olesiak, J.; Borchert, H.; Parisi, J. Physical origin of the impact of different nanocrystal surface modifications on the performance of CdSe / P3HT hybrid solar cells. *Journal of Physical Chemistry C* **2011**, *115*, 14111-14122.
- (96) Borchert, H. Elementary processes and limiting factors in hybrid polymer/nanoparticle solar cells. *Energy & Environmental Science* **2010**, *3*, 1682.
- (97) Zhou, Y.; Riehle, F. S.; Yuan, Y.; Schleiermacher, H.-F.; Niggemann, M.; Urban, G. A.; Kru□ger, M. Improved efficiency of hybrid solar cells based on non-ligand-exchanged CdSe quantum dots and poly(3-hexylthiophene). *Applied Physics Letters* **2010**, *96*, 013304.
- (98) Zhou, Y.; Eck, M.; Krüger, M. Bulk-heterojunction hybrid solar cells based on colloidal nanocrystals and conjugated polymers. *Energy & Environmental Science* **2010**, *3*, 1851.
- (99) Lefrançois, A.; Couderc, E.; Faure-Vincent, J.; Sadki, S.; Pron, A.; Reiss, P. Effect of the treatment with (di-)amines and dithiols on the spectroscopic, electrochemical and electrical properties of CdSe nanocrystals' thin films. *Journal of Materials Chemistry* **2011**, *21*, 11524.
- (100) Law, M.; Luther, J. M.; Song, Q.; Hughes, B. K.; Perkins, C. L.; Nozik, A. J. Structural, optical, and electrical properties of PbSe nanocrystal solids treated thermally or with simple amines. *Journal of the American Chemical Society* **2008**, *130*, 5974-5985.
- (101) Luther, J. M.; Law, M.; Song, Q.; Perkins, C. L.; Beard, M. C.; Nozik, A. J. Structural, optical , and electrical properties of self-assembled films of PbSe nanocrystals treated with 1,2-ethanedithiol. *ACS NANO* **2008**, *2*, 271-280.
- (102) Seo, J.; Kim, S. J.; Kim, W. J.; Singh, R.; Samoc, M.; Cartwright, A. N.; Prasad, P. N. Enhancement of the photovoltaic performance in PbS nanocrystal:P3HT hybrid composite devices by post-treatment-driven ligand exchange. *Nanotechnology* **2009**, *20*, 095202.
- (103) Talapin, D. V.; Murray, C. B. PbSe nanocrystal solids for n- and p-channel thin film field-effect transistors. *Science* **2005**, *310*, 86-9.

- (104) Kyritsis, A.; Spanoudaki, A.; Pandis, C.; Hartmann, L.; Pelster, R.; Shinyashiki, N.; Rodríguez Hernández, J. C.; Gómez Ribelles, J. L.; Monleón Pradas, M.; Pissis, P. Thermal transitions and dynamics in nanocomposite hydrogels. *Journal of Thermal Analysis and Calorimetry* **2011**.
- (105) Stathopoulos, A.; Klonos, P.; Kyritsis, A.; Pissis, P.; Christodoulides, C.; Rodriguez Hernández, J. C.; Monleón Pradas, M.; Gómez Ribelles, J. L. Water sorption and polymer dynamics in hybrid poly(2-hydroxyethyl-co-ethyl acrylate)/silica hydrogels. *European Polymer Journal* **2010**, *46*, 101-111.
- (106) Podsiadlo, P.; Kaushik, A. K.; Arruda, E. M.; Waas, A. M.; Shim, B. S.; Xu, J.; Nandivada, H.; Pumphlin, B. G.; Lahann, J.; Ramamoorthy, A.; Kotov, N. a Ultrastrong and stiff layered polymer nanocomposites. *Science* **2007**, *318*, 80-3.
- (107) Günes, S.; Neugebauer, H.; Sariciftci, N. S. Conjugated polymer-based organic solar cells. *Chemical reviews* **2007**, *107*, 1324-38.
- (108) Yang, X.; Loos, J. Toward high-performance polymer solar cells: the importance of morphology control. *Macromolecules* **2007**, *40*, 1353-1362.
- (109) Green, M. The nature of quantum dot capping ligands. *Journal of Materials Chemistry* **2010**, *10*, 5797-5809.
- (110) Yu, G.; Heeger, a. J. Charge separation and photovoltaic conversion in polymer composites with internal donor/acceptor heterojunctions. *Journal of Applied Physics* **1995**, *78*, 4510.
- (111) Yu, G.; Gao, J.; Hummelen, J. C.; Wudl, F.; Heeger, A. J. Polymer Photovoltaic Cells: Enhanced Efficiencies via a Network of Internal Donor-Acceptor Heterojunctions. *Science* **1995**, *270*, 1789-1791.
- (112) Colvin, V. L.; Schlamp, M. C.; Alivisatos, A. P. Light-emitting diodes made from CdSe nanocrystals and a semi-conducting polymer. *Nature* **1995**, *370*, 354.
- (113) Greenham, N.; Peng, X.; Alivisatos, A. Charge separation and transport in conjugated-polymer/semiconductor-nanocrystal composites studied by photoluminescence quenching and photoconductivity. *Physical review. B, Condensed matter* **1996**, *54*, 17628-17637.
- (114) Huynh, W. U.; Peng, X.; Alivisatos, A. P. CdSe nanocrystal rods/poly (3-hexylthiophene) composite photovoltaic devices. *Advanced materials* **1999**, *11*, 923-927.
- (115) Ren, S.; Chang, L.-Y.; Lim, S.-K.; Zhao, J.; Smith, M.; Zhao, N.; Bulović, V.; Bawendi, M.; Gradecak, S. Inorganic-organic hybrid solar cell: bridging quantum dots to conjugated polymer nanowires. *Nano letters* **2011**, *11*, 3998-4002.
- (116) Huynh, W. U.; Dittmer, J. J.; Alivisatos, A. P. Hybrid nanorod-polymer solar cells. *Science* **2002**, *295*, 2425-7.
- (117) Huynh, W. U.; Dittmer, J. J.; Libby, W. C.; Whiting, G. L.; Alivisatos, A. P. Controlling the morphology of nanocrystal-polymer composites for solar cells. *Advanced Functional Materials* **2003**, *13*, 73-79.
- (118) Jiu, T.; Reiss, P.; Guillerez, S.; de Bettiigies, R.; Bailly, S.; Chandezon, F. Hybrid solar cells based on blends of CdSe. *IEEE J. Sel. Top. in Quantum Electronics* **2010**, *16*, 1619-1626.

- (119) Liu, J.; Tanaka, T.; Sivula, K.; Alivisatos, A. P.; Fréchet, J. M. J. Employing end-functional polythiophene to control the morphology of nanocrystal-polymer composites in hybrid solar cells. *Journal of the American Chemical Society* **2004**, *126*, 6550-1.
- (120) Zhang, Q.; Russell, T. P.; Emrick, T. Synthesis and characterization of CdSe nanorods functionalized with regioregular Poly(3-hexylthiophene). *Chemistry of Materials* **2007**, *19*, 3712-3716.
- (121) Aldakov, D.; Querner, C.; Kervella, Y.; Joussetme, B.; Demadrille, R.; Rossitto, E.; Reiss, P.; Pron, A. Oligothiophene-functionalized CdSe nanocrystals: preparation and electrochemical properties. *Microchimica Acta* **2007**, *160*, 335-344.
- (122) Aldakov, D.; Jiu, T.; Zagorska, M.; de Bettignies, R.; Jouneau, P.-H.; Pron, A.; Chandezon, F. Hybrid nanocomposites of CdSe nanocrystals distributed in complexing thiophene-based copolymers. *Physical chemistry chemical physics* **2010**, *12*, 7497-505.
- (123) De Girolamo, J.; Reiss, P.; Pron, A. Supramolecularly assembled hybrid materials via molecular recognition between diaminopyrimidine-functionalized poly(hexylthiophene) and thymine-capped CdSe nanocrystals. *Journal of Physical Chemistry C* **2007**, *111*, 14681-14688.
- (124) De Girolamo, J. Architectures hybrides auto-assemblées a base de systèmes polyconjugués et de nanocristaux de semi-conducteurs pour le photovoltaïque plastique, PhD dissertation, Université Joseph Fourier de Grenoble, 2007.
- (125) Beek, W. J. E.; Slooff, L. H.; Wienk, M. M.; Kroon, J. M.; Janssen, R. a. J. Hybrid solar cells using a zinc oxide precursor and a conjugated polymer. *Advanced Functional Materials* **2005**, *15*, 1703-1707.
- (126) Yuan, K.; Li, F.; Chen, Y.; Wang, X.; Chen, L. In situ growth nanocomposites composed of rodlike ZnO nanocrystals arranged by nanoparticles in a self-assembling diblock copolymer for heterojunction optoelectronics. *Journal of Materials Chemistry* **2011**, *21*, 11886.
- (127) Liao, H.-C.; Chen, S.-Y.; Liu, D.-M. In-situ growing CdS single-crystal nanorods via P3HT polymer as a soft template for enhancing photovoltaic performance. *Macromolecules* **2009**, *42*, 6558-6563.
- (128) Schweikart, A.; Pazos-Pérez, N.; Alvarez-Puebla, R. a.; Fery, A. Controlling inter-nanoparticle coupling by wrinkle-assisted assembly. *Soft Matter* **2011**, *7*, 4093.
- (129) Zhang, Q.; Gupta, S.; Emrick, T.; Russell, T. P. Surface-functionalized CdSe nanorods for assembly in diblock copolymer templates. *Journal of the American Chemical Society* **2006**, *128*, 3898-9.
- (130) Van der Zande, B. M. I.; Pagès, L.; Hikmet, R. A. M.; Van Blaaderen, A. Optical properties of aligned rod-shaped gold particles dispersed in poly ( vinyl alcohol ) films. *Journal of Physical Chemistry B* **1999**, *103*, 5761-5767.
- (131) Gupta, S.; Zhang, Q.; Emrick, T.; Russell, T. P. "Self-corralling" nanorods under an applied electric field. *Nano letters* **2006**, *6*, 2066-9.



## ***Chapter 2. CdSe Nanocrystals: synthesis and surface functionalization***

*This part is dedicated to CdSe colloidal nanocrystals, more precisely to their synthesis using the so-called “hot-injection” method, to their properties and to their surface functionalization. CdSe is one of the best known systems in the field of semiconducting colloidal nanoparticles and thus constitutes a model system (1–4). The synthesis of such nanocrystals is well known and developed. Presently, very reproducible protocols leading to narrow size distributions do exist for different nanocrystal shapes (nanodots, nanorods, nanotetrapods, etc...). For the present work, the synthesis of CdSe nanocrystals was performed by following a protocol previously developed in the laboratory (5, 6). Mainly two types of CdSe nanocrystals were used and studied: spherical and rod-shaped nanocrystals, the latter having various aspect ratios. For the spherical particles, the used protocol is particular in the sense that it allows to obtain large quantities (~2 g) per synthesis with a low polydispersity. In the following, the synthesis of CdSe nanocrystals will be described and the characteristics of the obtained nanocrystals will be presented and discussed. A second part will deal with the surface functionalization of spherical CdSe nanocrystals with various polypyridine molecules. The functionalization protocol as well as the characterization of the functionalized nanocrystals with various physico-chemical techniques will be discussed. Depending on the chemical nature of the ligands, two adsorption-desorption kinetics on the NMR timescale of the ligand on the NCs surfaces could be evidenced and will be discussed.*



## 1. Generalities on the synthesis of CdSe nanocrystals

The colloidal nanocrystals (NCs) used in this work were synthesized using the so-called hot-injection method. More details about the synthesis of CdSe colloidal NCs can be found in references (1–5). Briefly, in the hot-injection method, the formation of nanocrystals such as CdSe involves three main steps (Figure 1-1) (1–5, 7, 8). The first step is the fast nucleation of nuclei after injecting the reagents into the reaction vessel. This is followed by a much slower growth of the NCs from these seeds. Finally, Ostwald ripening takes place which leads to a “dissolution” of the smaller nanocrystals at the benefit of the larger ones.

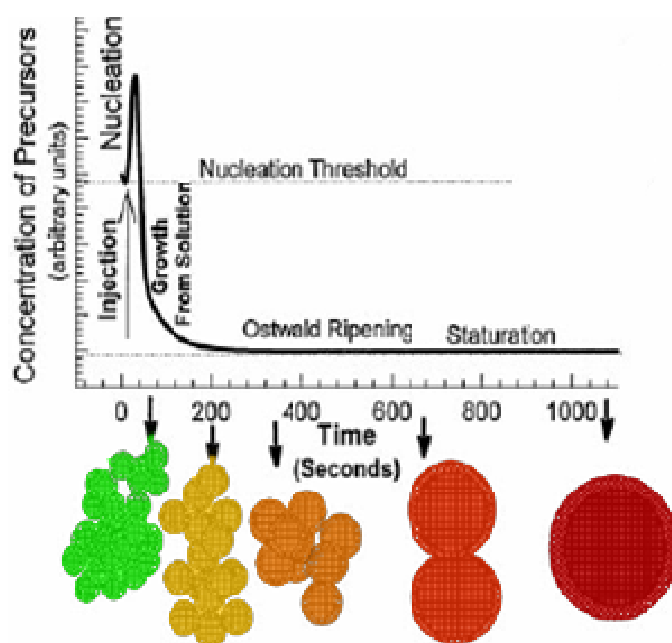


Figure 1-1 : Schematic representation of the different stages involved during a typical synthesis of CdSe nanocrystals. It takes place in three steps which are: the homogenous nucleation of seeds induced by the fast injection of a precursor, the much slower nanocrystal growth where the “free precursors” in the solution are consumed to form the nanocrystals. Once all precursors reacted the Ostwald ripening regime sets in. During Ostwald ripening, small nanocrystals with a high free energy disappear at the benefit of the larger ones. Reproduced from ref (1).

As it was pointed out in the seminal work of LaMer and Dinegar in the early 1950<sup>ies</sup>, it is essential to temporally separate the nucleation step from the crystal growth in order to obtain population of NCs with a low polydispersity. The former should take place on a much shorter timescale than the latter (1–5, 7, 8). If all the nuclei are generated at exactly the same time, the nanocrystals will start growing simultaneously and a population with a low polydispersity will finally be obtained (1–5, 7, 8). The polydispersity of a sample can be quantified by calculating the relative standard deviation  $\sigma$  (in %) which is the standard deviation of the size distribution of the nanocrystals normalized by the average size. Such size distributions are usually obtained from transmission electron microscopy analysis (*vide infra*). A sample is generally considered monodisperse if the relative standard deviation  $\sigma$  is below 5% (1). If  $\sigma < 10\%$ , the sample is considered having a low polydispersity (1, 9).

In *Figure 1-1*, the nucleation step can be described as a consequence of a supersaturation of precursors in the solution induced by the rapid injection of precursor reagents to the solution (1–5, 7, 8). A nucleation burst of stable crystal seeds instantly decreases the concentration and the nucleation stops as soon as the solution is out of the supersaturated regime (*Figure 1-1*) (1–5, 7, 8). The homogenous growth of the NCs then takes place as long as there are available precursors in the solution. Once all the precursors in the solution are consumed, the so-called “Ostwald ripening” regime sets in. In this regime, small NCs having a higher surface energy will be dissolved at the benefit of the larger ones until an equilibrium state occurs which involves a much longer time scale than the two previous steps. In the Ostwald regime, the number of nanoparticles is thus continuously decreasing to the benefit of fewer and larger NCs. In some specific cases, Ostwald ripening is used to get a very monodisperse population of NCs but for the present work, the reaction was stopped before the Ostwald ripening regime could set in as it would lead to the degradation of the polydispersity of the NCs’ population (5, 6). In fact, if the system does not reach equilibrium, Ostwald ripening tends to increase the width of the size distribution as some particles are shrinking in size whilst others are growing. As the aim is usually to obtain NCs of a few nanometers in diameter, the system cannot be left until an equilibrium state is reached because the obtained nanoparticles would be too large and it would involve far too long times to reach the final equilibrium state. As mentioned above, for the present work, in order to obtain NCs with a low polydispersity, we stopped the reaction before the Ostwald ripening regime was reached by cooling the reaction vessel.

Experimentally, the decoupling of the nucleation and the nanocrystal growth steps is obtained by a very fast injection of a precursor reagent into the reaction vessel. This injection has to be very fast in order to limit the nucleation step in time and to avoid any further nucleation whilst the nanocrystal growth step has set-in. Therefore the initial concentrations of reagents have to be carefully chosen.

## **2. Synthesis of spherical nanocrystals**

Within the differently shaped CdSe nanocrystals, the easiest to handle are the nanospheres because (i) they can be synthesized in large quantities and (ii) they present a higher stability in solution whereas nanorods and tetrapods present sometimes problems of solubility (10, 11). The longer the nanorods, the lower their solubility in common solvents due to higher interparticle interactions that cannot be shielded by the surface ligands.

For the present work, two batches of spherical NCs were synthesized using a large scale synthesis protocol developed by Myriam Protière during her PhD thesis (5, 6). The advantage of this large scale protocol is the possibility to obtain gram scale batches of spherical NCs presenting a low polydispersity. These NCs are all from the same batch and thus their properties and surface chemistry are identical. As comparison, a standard laboratory-scale synthesis of CdSe NCs yields approximately 100-200 mg of nanocrystals.

The following sections will be devoted to describing the gram-scale synthesis based on the work of Myriam Protière (5, 6). For our work two large-scale batches were synthesized. Each of those allowed to obtain approximately 1.5 g of spherical CdSe NCs. Before discussing the gram-scale synthesis protocol and the characteristics of the obtained NCs, the laboratory-scale synthesis of CdSe spherical NCs as used in the laboratory will be presented.

### 2.1. Synthesis on the lab scale

In the laboratory-scale synthesis protocol of CdSe spherical NCs, a Cd precursor (*e.g.* Cd stearate CdSt<sub>2</sub>) is dissolved in a high boiling point non coordinating solvent such as octadecene (5–7, 12, 13). Stearic acid (SA) and oleylamine (OA) are also added to the solution to serve as stabilizing ligands of the nanoparticles after the synthesis. trioctylphosphine (TOP) serves also as ligand but will be injected afterwards with the selenium precursor. The ligands are composed of an anchoring group that can coordinate to the metal cation at the NC surface and of solubilising alkyl chains allowing to keep the NCs as a colloidal dispersion in hydrophobic solvents. During a synthesis, the ligands ensure a double role depending on the temperature. At high temperatures, the ligands can easily desorb from the NC surface so as not to impede further growth of the NCs. At room temperature, the stabilizing ligands will be coordinated to the NCs' surface to prevent their aggregation. Without these stabilizing ligands, the solution would be metastable and the NCs would tend to aggregate due to the large attractive Van der Waals forces between the NCs (7). Metastable and aggregated NCs are useless for solution processing. *Figure 2-1* shows schematically the experimental setup, the reagents and solvents used for the synthesis.

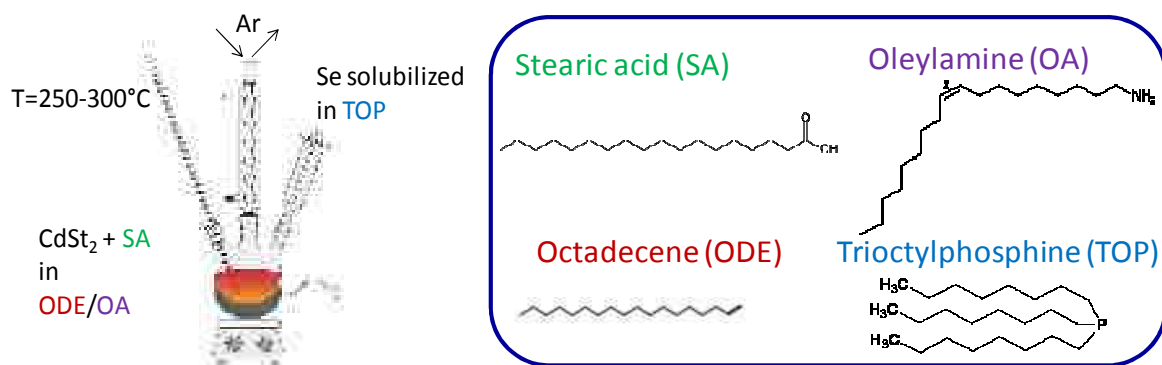


*Figure 2-1: Schematic representation of the synthesis of spherical CdSe nanocrystals at the laboratory-scale with the chemical structures of the solvents and ligands used.*

In practice, the solution of the Cd precursor is heated up to 250°C under constant stirring and under an argon atmosphere. The initially yellow solution then turns colourless after the complexation of the Cd by oleylamine and stearic acid. Besides, a solution of selenium in TOP (TOPSe) is prepared in a glove box. Once the Cd solution is colorless and the right injection temperature is reached, the TOPSe solution is quickly injected into the reaction flask leading to the formation of seeds followed by nanocrystal growth, as explained

above. Once the desired NCs size is reached the flask is taken out of the oil bath to allow a temperature drop which stops further growth of the NCs. After the synthesis, the NCs are separated from the non reacted reagents by a procedure of precipitation of the NCs by adding a non solvent for the NCs and a solvent for the reagents to the solution. A centrifugation procedure allows to precipitate out the NCs which can be redispersed in common hydrophobic solvents such as hexane or chloroform for example. This washing procedure is essential because it allows to eliminate all the excess ligands and other products of the synthesis such as for example the ODE. In some cases the washing procedure is repeated 3-4 times.

## 2.2. Large scale synthesis

### 2.2.1. Synthesis

The gram-scale synthesis of spherical CdSe NCs was carried out in a 2-L reactor by multiplying the quantities of all reagents by a factor of 20 compared to the lab-scale synthesis. Myriam Protière developed during her PhD an experimental protocol that allows to synthesize gram-scale batches of spherical CdSe nanocrystals with diameters of approximately 4 nm, 5 nm or 6.7 nm (5, 6). For the present work, we applied the protocol to obtain two batches of NCs with a diameter of 5 nm. More details about the synthesis protocol can be found in references (5, 6). For the fast injection of the selenium precursor, a specific peristaltic pump is used. This pump is able to inject up to 0.5 L in 3.5s (6). The TOPSe solution for injection is placed in a 0.5 L bottle and connected to the reactor via the injection pump. A photography of the experimental setup is displayed in *Figure 2-2*. The stirring of the solution in the reactor is ensured by a mechanical stirrer moved electrically. Efficient stirring and a fast injection are crucial points for a successful synthesis of monodisperse NCs of CdSe.

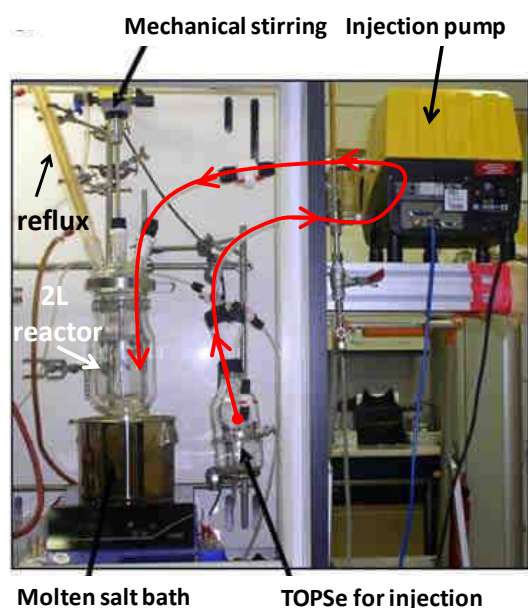


*Figure 2-2: Photography of the 2L reactor for the large scale synthesis of nanocrystals with the injection pump. The selenium precursor (Se dissolved in TOP) is localized in the small bottle at the right. The injection pump is activated by a foot pedal. The equipment is the same than the one used in references (5, 6).*

Figure 2-3 shows the reaction medium at different steps of the synthesis. In the left picture, one can see the reactor with the CdSt<sub>2</sub> precursor in octadecene, stearic acid and oleylamine before the system has been heated up to the injection temperature. The middle picture corresponds to the hot solution after the injection of the TOPSe solution and at the final stage of nanocrystal growth. At the right of Figure 2-3 is a picture of the reaction medium at the end of the reaction with the solution of non purified nanocrystals.

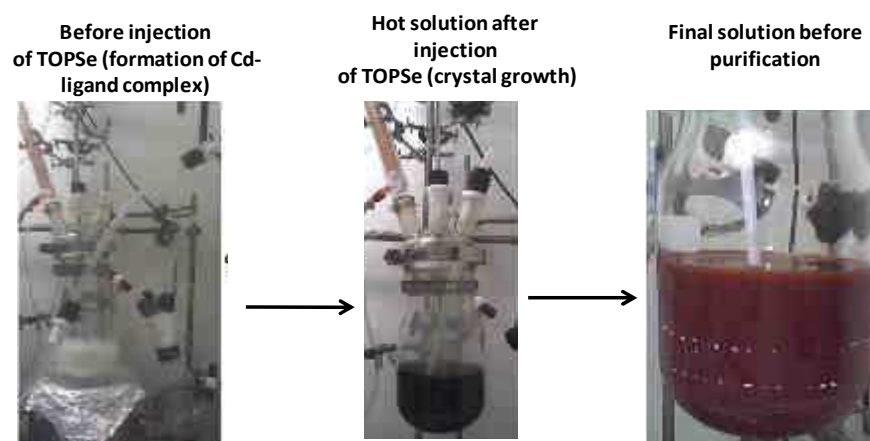


Figure 2-3: Photography of the different steps during the large scale synthesis of the CdSe nanocrystals. **Left:** Initial solution of Cd complexed in a solution of oleylamine and stearic acid with octadecene. **Middle:** After the injection of the TOPSe solution, after nucleation and during the growth of the nanocrystals. **Right:** final solution of CdSe nanocrystals with a diameter of around 5 nm at the end of the reaction before purification. Reproduced from reference (5).

## 2.2.2. Purification of the nanocrystals

### 2.2.2.1. Purification of the nanocrystals of batch 1

Following the synthesis, the purification of the nanocrystals is an essential step. This allows removing most of the ligands (stearic acid, oleylamine, TOPO) in excess, *i.e.* not attached on the surface of NCs. This purification step allows also to transfer the nanoparticles from the octadecene to more common hydrophobic solvents such as hexane. The main difficulty for the purification in the present case is the presence of stearic acid which has a melting temperature of 70°C and is thus solid at room temperature. The total volume of solution after the synthesis is about 1.5 L. The classical purification procedure by precipitation followed by centrifugation as used at the laboratory scale would be very time consuming as in the laboratory, it is possible to centrifugate a maximum of four flasks each containing 60 mL.

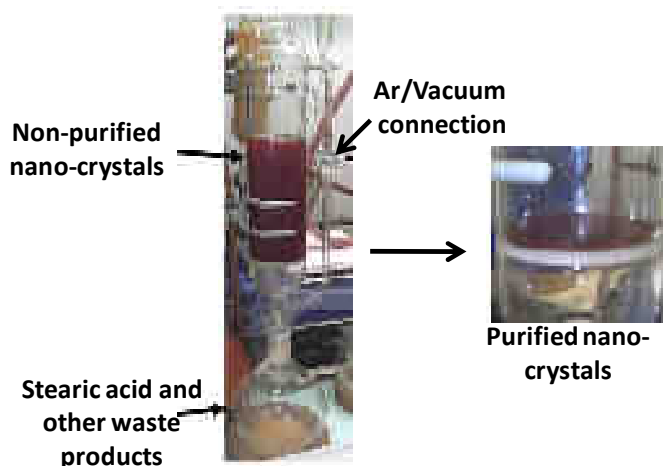


Figure 2-4: Apparatus for the purification of the nanocrystals by using a column with a glass filter. The purification allows to eliminate the excess of ligand molecules and other waste products from the synthesis and to transfer the nanocrystals in common solvents such as hexane. Reproduced from reference (5).

An alternative purification method developed by Myriam Protière during her PhD and described in references (5, 6) was therefore used. In this approach, the NCs are purified using a funnel with a glass filter column connected to a vacuum line in order to facilitate the passage of the excess stearic acid and other side products through the glass filter. The solution of the non purified nanocrystals has to be kept at a temperature  $T > 70^{\circ}\text{C}$  in order to avoid the solidification of the stearic acid. This is realized by the use of a heat gun. The purified precipitated nanocrystals can be recovered from the glass filter and are redissolved in hexane. At the end of the purification procedure, approximately 1.5 g of nanocrystals were recovered.

#### 2.2.2.2. Simplification of the purification: batch 2

For the second large scale synthesis (batch 2), the purification procedure has been simplified compared to the one described above for batch 1. After the addition of methanol and acetone for the precipitation of the NCs, the reactor was placed overnight in an oven heated at around  $70^{\circ}\text{C}$ . This allows to keep the stearic acid in its liquid phase and the nanocrystals precipitate at the bottom of the reactor. The supernatant can then be easily removed and the nanocrystals remaining at the bottom of the reactor are recovered. The volume is now significantly reduced and most of the stearic acid has been eliminated. Thus the purification can be performed by precipitating and centrifuging the nanocrystals as done for the laboratory-scale synthesis. This precipitation and centrifugation was performed twice before the purified nanocrystals were redispersed in hexane. For this batch 2, approximately 1.5 g of nanocrystals were obtained after the purification.

### 2.3. Characterization of the obtained CdSe nanocrystals

As mentioned above, two gram-scale synthesis of spherical CdSe nanocrystals were performed giving two batches: batch 1 and batch 2. In the following, the characteristics of the obtained nanoparticles in terms of size, polydispersity, crystal structure and surface chemistry are presented.

### 2.3.1. Particle size determination

The average nanocrystal diameter  $D$  can be directly determined by two methods: one direct and the other indirect. The first direct method relies on measuring the NC size for a selection of NCs using Transmission Electron Microscopy (TEM) operated in bright field mode. This yields a histogram of sizes for a sample of NCs (typically 100 nanoparticles are considered for such an analysis) from which an average diameter is determined. The polydispersity  $\sigma$  of each batch is the ratio of the standard deviation of the population normalized by the average value of the particle diameter and it is expressed as a percentage. An alternative indirect method to obtain the particle size is obtained via the position of the first absorption maximum in the UV-Vis absorption spectrum of a colloidal dispersion of NCs which is directly correlated to the average size of the NCs. In fact, by correlating the absorption spectra with size measurements by TEM, Jasieniak *et al.* established that spherical CdSe NCs with a diameter  $D$  is in the range of 2-8 nm obey to the following empirical law (14):

$$D \text{ (nm)} = 59.60816 - 0.54736 \cdot \lambda + 1.8873 \cdot 10^{-3} \cdot \lambda^2 - 2.85743 \cdot 10^{-6} \cdot \lambda^3 + 1.62974 \cdot 10^{-9} \cdot \lambda^4 \quad (\text{Eq.1})$$

where  $\lambda$  is the wavelength corresponding to the first absorption maximum (excitonic peak) in the absorption the NCs.

The polydispersity  $\sigma$  of the size distribution can also be determined indirectly from the shape of the PL emission peak for spherical CdSe NCs. Qu and Peng determined a relation between the FWHMs of the PL emission and the size distribution assuming that each single NCs size has a  $\delta$  function emission (15). The relative FWHM of the size distribution can be calculated using the empirical formula:

$$\frac{\Delta D}{D} = e^{B\Delta\lambda/2} - e^{-B\Delta\lambda/2} \quad (\text{Eq. 2})$$

where  $\Delta D$  is the FWHM of the size distribution,  $D$  is the average diameter of the NCs,  $A$  and  $B$  are two parameters respectively equal to 0.0566 and 0.0071 for spherical CdSe NCs and  $\Delta\lambda$  is the FWHM of the PL peak of the sample. As expected, the larger the FWHM of the PL spectrum, the larger the polydispersity of the sample.

The average diameter  $D$  as well the polydispersity  $\sigma$  (%) of batch 1 and batch 2 were determined using the three above cited methods. The results are summarized in *Table 2-1*.

Both methods give very similar results in what concerns the particle average size  $D$ . The polydispersities  $\sigma$  extracted from TEM and from the shape of the PL peak show somewhat larger differences. This can be explained by the relatively poor statistics provided by TEM measurements. In fact, 100 nanoparticles out of a batch of 1.5 g is a very little minority out of the total population. Therefore the indirect method via PL and UV-vis measurements might be more accurate due to the better statistics provided by these methods. However TEM analysis of the NCs after the synthesis is essential to control the shape of the obtained NCs as the latter cannot be accessed via any other type of characterization. *Figure*

2-5 shows TEM-BF images of the two batches and the corresponding histograms with the size distributions. These images confirm that the synthesis provided spherical particles as expected. Batch 1 is composed of slightly bigger particles compared to batch 2 but remain nevertheless close to the expected value 5 nm (5, 6).

	Average size D from TEM (nm)	$\sigma$ from TEM (%)	Excitonic peak maximum (nm)	Average size from UV-vis (nm)	PL peak maximum (nm)	FWHM PL (nm)	$\sigma$ from PL FWHM (%)
<b>Batch 1</b>	<b>5.3</b>	16.5	620	<b>5.5</b>	635	31	11
<b>Batch 2</b>	<b>4.8</b>	13.3	602	<b>4.8</b>	620	36	12.5

Table 2-1 : Average CdSe nanocrystal sizes and corresponding size distributions for batches 1 and 2 as determined from TEM and from the position of the excitonic peak in the UV-Vis absorption spectrum.

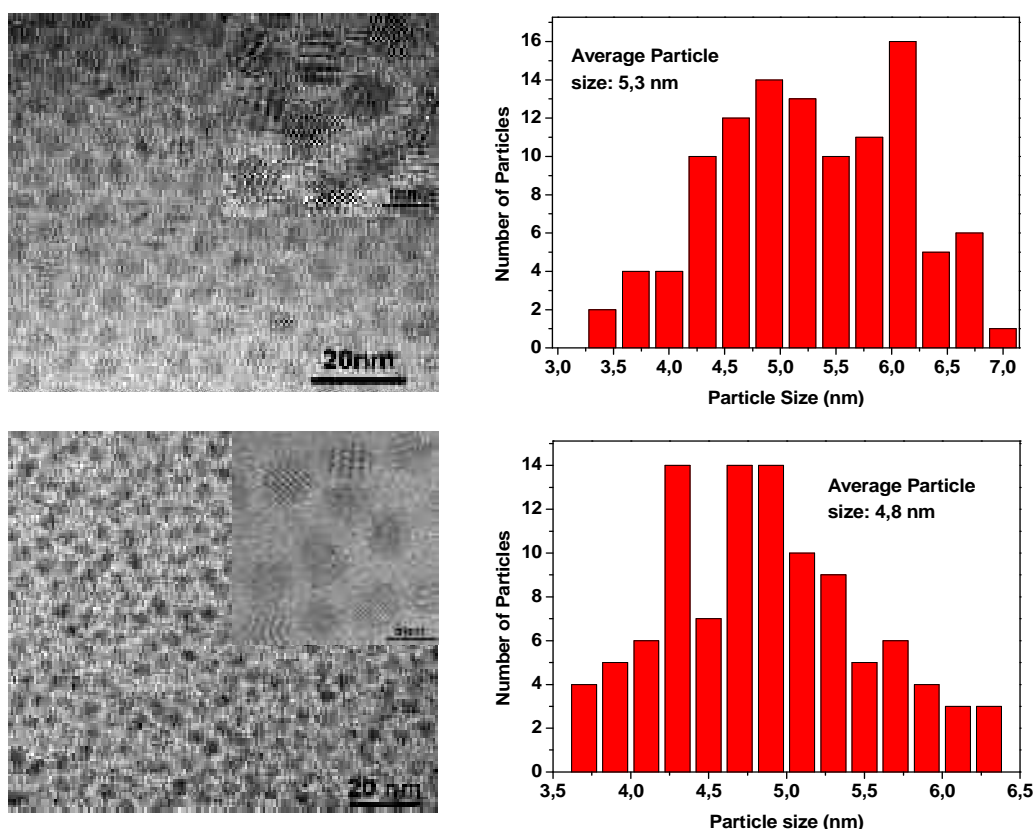


Figure 2-5: TEM-BF images and derived size distributions for the nanocrystals of batch 1 (top pictures and histogram) and batch 2 (down). The average nanoparticle diameter measured on approximately 100 particles is approximately 5.3 nm for batch 1 and of 4.8 nm for batch 2.

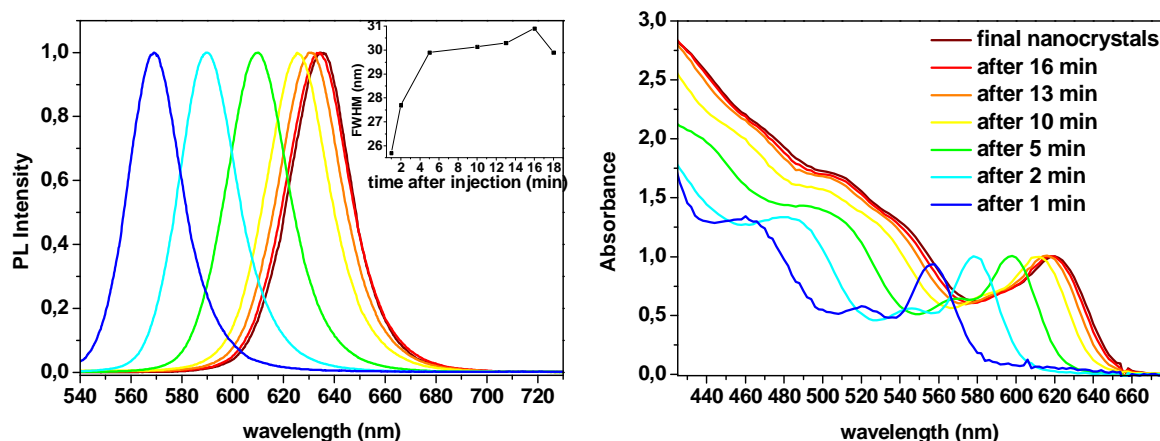


Figure 2-6: Evolution of the PL and UV-Vis absorption spectra with reaction time during the synthesis of batch 1. The inset shows the evolution of the FWHM of the PL spectrum. The FWHM is about 31 nm indicating a low polydispersity of the NCs, in agreement with what was previously reported by M. Protière using the same synthesis method (5, 6).

During the synthesis of batch 1, the growth of the NCs was followed by extracting some aliquots from the reactor at different reaction times during the NCs growth phase. These samples were characterized by photoluminescence and absorbance spectroscopy. Figure 2-6 shows the evolution of the PL and absorbance spectra with the reaction time. As expected, the PL peak and the excitonic peak in the UV-Vis absorption spectrum are red-shifted with increasing reaction time indicating the growth of the NCs. The FWHM of the PL peak which as mentioned above is connected to the polydispersity of the NCs, increases strongly during the first 4 minutes after the injection and finally stabilizes at a value of ~31 nm (see inset of Figure 2-6). M. Protière *et al.* reported similar FWHM values. The obtained FWHM and polydispersity are slightly larger than what can be achieved using a classical laboratory-scale synthesis (5, 6). However, the size distributions are still very satisfying and a large amount of NCs is more important than a very low polydispersity in our case as we want to make comparative studies with the same batch of NCs.

For batch 2 the PL and the UV-Vis absorption spectra of the nanocrystals at the end of the reaction are displayed and are compared to the PL and UV-vis absorption of the NCs of batch 1 (see Figure 2-7). With a final FWHM of 36 nm, the PL peak is slightly larger than in the case of batch 1, indicating a slightly larger size distribution and polydispersity for this batch, as already mentioned. This can be explained by some slight differences in the synthesis of batch 2 compared to batch 1. In fact, during the synthesis of batch 2, some small problems during the injection occurred and possibly the time window of the injection was slightly larger than expected. Accordingly, the temporal separation of the nucleation and the NCs growth were not optimal therefore leading to a slight degradation of the polydispersity. However, the NCs of batch 2 are still of good quality and can be used for our studies. As already observed by TEM, the particles of batch 2 have an average size of 4.8 nm, slightly smaller than the ones of batch 1 (5.3 nm from TEM).

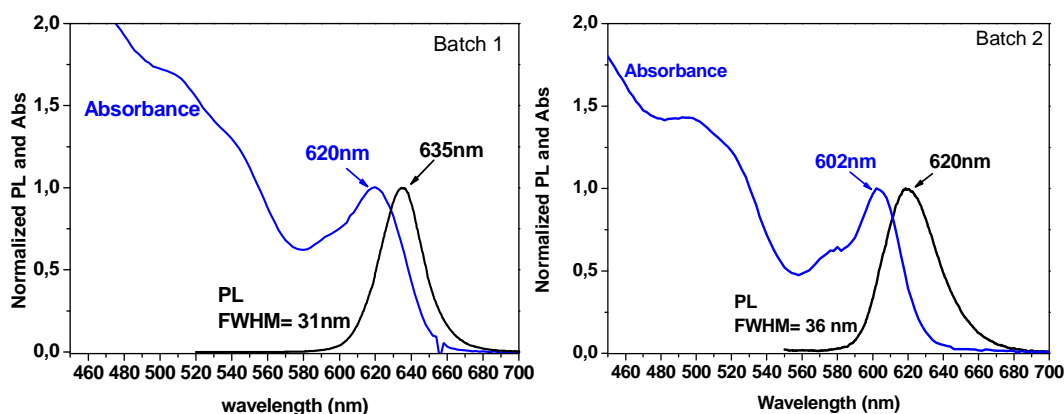


Figure 2-7: Normalized photoluminescence and UV-Visible absorption spectrum of batch 1 and batch 2 of CdSe NCs. The FWHM of the PL is higher than for batch 1 indicating a slightly higher polydispersity of the nanocrystals. The position of the excitonic peak of absorbance indicates smaller particles than the ones of batch 1 as already observed by TEM.

### 2.3.2. Crystallinity

X-ray powder diffraction measurements are a standard technique to analyze the crystal structure and crystallinity of NCs after the synthesis. Such measurements were performed on both batches. Below only the results for batch 1 are presented as the two diffractograms are identical. The obtained powder X-ray diffractogram (Figure 2-8) is very similar to the one reported by M. Protière *et al.* for CdSe nanoparticles synthesized using the same method (5, 6). As in her case, we find a predominant wurtzite-like (hexagonal) crystal structure for the NCs by comparing the obtained diffractograms to the reference spectrum for bulk wurtzite CdSe from the Joint Committee on Powder Diffraction Standards (JCPDS). This is in agreement with what is generally reported in the literature for CdSe spherical NCs (1, 4, 13). However, a closer look at the diffractograms shows clearly that the intensities of some reflections, in particular those corresponding to the (102) and (103) reflections, are very low compared to the expected JCPDS values (see Figure 2-8). An excessive attenuation of the (102) and the (103) reflections has previously been attributed by Murray *et al.* to the presence of stacking defects along the [002] axis (1). Such stacking defects were frequently observed in the high resolution TEM (HR-TEM) images and an example is displayed in Figure 2-8. These defects originate from a strong competition between the hexagonal (wurtzite) and the cubic (zinc blende) phase during the synthesis of CdSe NCs. It is indeed known that both phases can occur in such systems depending on the exact conditions of the synthesis and the size of the NCs. The small nanoparticle size (~5 nm) as well as the polycrystallinity of some of them accounts for the broadening of the X-ray diffraction peaks which makes the resolution of the triplet of reflections (100), (002) and (101) as well as the triplet (200), (112) and (201) reflections impossible (1,4).

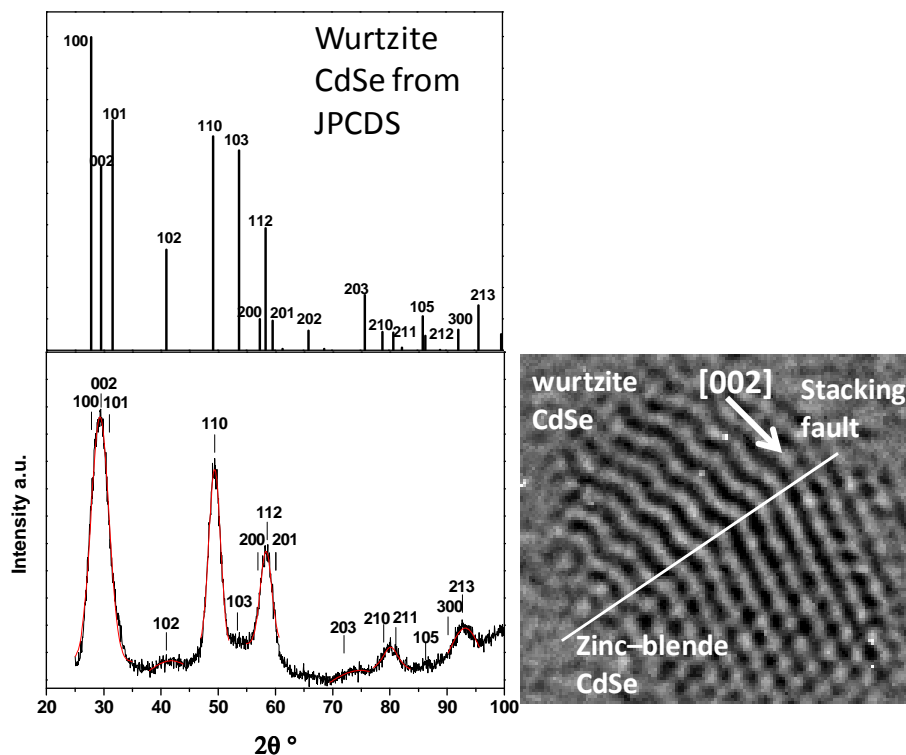


Figure 2-8: (left) Powder X-ray diffractogram of CdSe nanocrystals from batch 1 and peak position for wurtzite CdSe from the Joint Committee on Powder Diffraction Standards (JCPDS). The diffractogram is very similar to the one obtained by Protière who concluded that the crystal structure of the NCs was wurtzite-like (2). (right) high resolution TEM image showing a NC with a stacking fault corresponding to the transition between a wurtzite (hexagonal) and a zinc blende (cubic) crystal structure.

### 3. Synthesis of rod shaped CdSe nanocrystals

Rod shaped nanocrystals were also used in the frame of the present work. These nanorods (NR) were synthesized by Dr. Angela Fiore, post doctoral fellow at the “Laboratoire d’Electronique Moléculaire Organique et Hybride” (LEMOH) in Grenoble.

As for nanorods, no large scale synthesis protocol is available several batches of 50-100 mg were synthesized using laboratory scale protocols. The synthesis of these nanorods follows the so-called seeded-growth approach which was originally developed to obtain rod-shaped nano-heterostructures (17, 18). In brief, pre-formed seeds of CdSe are first prepared and purified, then they are co-injected with Se-TOP solution to the reaction mixture that contains solvent, surfactants and the cadmium precursor. The aspect ratio (*i.e.* rod length/rod diameter) of the nanorods is controlled by varying the seed size or their concentration. Lowering the concentration of the injected seeds results in longer nanorods. Using this method, nanorods with low polydispersity and aspect ratio (*i.e.* length over diameter ratio) between approximately 1 and 10 can be obtained. Figure 3-1 displays the PL and UV-Vis absorption spectra for CdSe nanorods with a size  $5 \text{ nm} \times 17 \text{ nm}$  synthesized in the frame of

the present work as well as a typical scanning transmission electron microscopy (STEM) image of these nanoparticles.

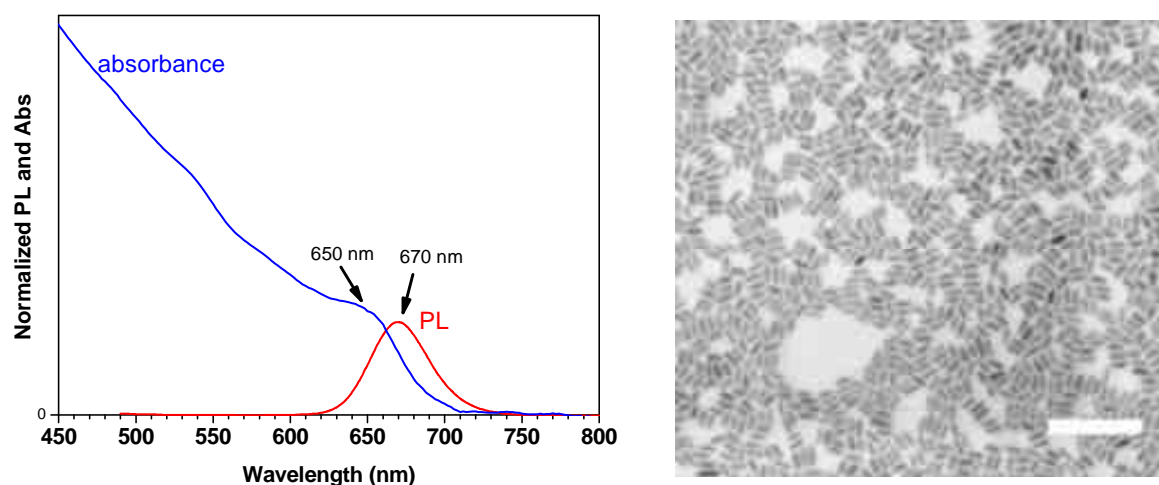


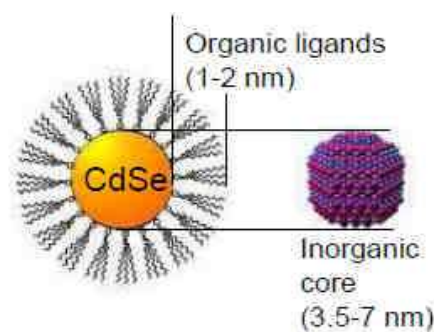
Figure 3-1: (left) PL and UV-Vis absorption spectra for CdSe nanorods  $5 \text{ nm} \times 17 \text{ nm}$  synthesized according to the seeded growth approach. (right) STEM image of the nanorods (the scalebar corresponds to 100 nm).

The latter shows the low polydispersity of the sample. One can also note that the photoluminescence peak is significantly red-shifted compared to nanospheres of similar diameter: the PL peak maximum is located at 670 nm for the  $5 \text{ nm} \times 17 \text{ nm}$  to be compared to 620 nm for the nanospheres of batch 2 with 4.8 nm in diameter (see Figure 2-7). This is due to the fact that for nanorods, quantum confinement of the electrons and the holes takes place along two directions: along the NR long axis and across the diameter, the latter providing a stronger confinement as compared to the former. In overall, this will lead to the fact that the UV-Vis and PL spectra of the nanorods will be intermediate between those of nanospheres 5 nm in diameter and 17 nm in diameter.

#### 4. Study of the ligand capping of as prepared CdSe nanocrystals

As mentioned above, NCs are capped by a layer of organic molecules called surfactants or ligands which stabilize the colloidal dispersion (19). This is the case for spherical as well as for rod shaped NCs. Figure 4-1 illustrates the architecture of a spherical CdSe NC after synthesis. The ligands form the surface layer of the NCs which, in the case of assemblies of nanoparticles, will constitute the interface between two adjacent NCs. In hybrid materials associating nanocrystals with polymers, the ligand shell forms the interface between the nanocrystals and the polymer. Therefore the control of the ligand capping is essential for all applications involving semiconducting nanocrystals.

Figure 4-1: Schematic representation of a CdSe nanocrystal. The inorganic CdSe core is covered by a shell of ligands, which allow the stabilization of the colloidal dispersion of NCs.



More precisely, there are two main reasons to properly tailor the capping layer of the NCs. The first one is that it has a huge influence on the solubility of nanocrystals in a given solvent and plays thus a key role for the solution processing of nanoparticles-containing nanomaterials (1, 5). The solubility of the NCs in a given solvent is determined by the chemical nature of the ligands (hydrophobic or hydrophilic) and therefore, independently of the inorganic core, NCs can be either dissolved in hydrophilic or hydrophobic solvents (20). The second reason is that in solution-processed hybrid materials associating colloidal nanocrystals and  $\pi$ -conjugated polymers, the resulting morphology depends strongly on the ligand layer: this can lead to either a good dispersion of the nanoparticles in the polymer matrix or to an aggregation and a macrophase separation between the polymer and the nanocrystals (10, 13, 21–23). Intrinsic properties of the hybrid materials also depend very strongly on the chemical structure of the ligands. For example charge transfer between the NCs and the polymer as well as charge transport by the NCs phase are strongly influenced by the ligand layer. In fact, charge transfer/transport can be either hindered or favored by the ligands depending if the latter allow a transit of the charges or if they behave as an insulating layer (21). The optical properties of a colloidal dispersion of NCs *e.g.* the photoluminescence and UV-vis absorption are also strongly influenced by the surface chemistry of the NCs. Enhanced PL quantum yields are obtained by passivating the surface trap states present at the NCs surface by some organic ligands or polymers (24, 25). Alternatively, strong PL quenching is observed by treating the NCs with ligands such as ethylenedioxythiophene (EDOT) or pyridine, for example (22). The enhancement or quenching of PL quantum yields depends on many factors, the chemical structure of the capping ligands being an essential one (22, 24). For all these reasons, the quantitative characterization as well as the controlled modification of the ligand shell of nanocrystals are essential aspects in view of the perspective of their applications in nanomaterials for photodetectors, LEDs, solar cells or biological imaging (19, 26).

Although the importance of the ligand shell of colloidal NCs was recognized very early in the field (1, 3), the details of the interactions involved in the binding of the ligands onto the surface of the NCs is not yet fully understood and is still under investigation (19, 27). Schematically, one can say that a ligand is constituted of two parts: (i) an anchoring group (*e.g.* a phosphine oxide, an amine or a carboxylic acid group for quantum dots) which binds onto the surface of the NC and (ii) a chain which will constitute the interface of the nanoparticle and its surroundings, *i.e.* the solvent molecules for a colloidal solution or other nanoparticles or polymer chains in a hybrid material. It is generally assumed that ligands bind

to the surface of a NC by forming dative bonds thanks to the lone electron pairs on the anchoring group of the ligand (19, 28). The ligands of as synthesized NCs can be removed and replaced by other ligands as a function of the desired application. This process is generally referred to as *surface functionalization, ligand exchange or surface treatment*.

The strength of the bond between the ligands and the surface of the NCs depends on many factors including the crystallographic facets onto which the ligand binds (19, 27). In fact, some facets present a higher binding energy than others for a given anchoring group (19, 27). The affinity of the latter one regarding the surface of a NC therefore influences strongly the strength of the bond. The most frequently used anchoring groups for semiconductor nanocrystals are phosphines oxides, phosphines, amines, thiols as well as carboxylic acids (7, 13, 29–31). In most of the above cited anchoring groups, the ligands generally bind to the Cd surface atoms of the NCs. It is therefore important to know the number of surface Cd sites to be able to evaluate the maximum number of ligands per NC (28, 32). Following this, Taylor *et al.* showed that different CdSe nanocrystals have different ratios of Cd:Se at the nanocrystal surface (33). In most cases an excess of Cd atoms at the surface is reported in the literature (33–35). However, *ab initio* calculations showed that in the case of amines, the ligands could bind both to Cd and Se surface atoms (27, 28). In the literature regarding the capping ligands and surface functionalization, it is also frequently mentioned that the ligands bind to the surface of the nanoparticles in a reversible equilibrium state (34–41). The position of this equilibrium depends on different factors such as the binding energy of the ligand, the concentration of “free” ligands in the solution, the temperature, etc (39). This equilibrium can therefore be displaced by varying one of these parameters and this is the basic principle of the ligand exchange process.

In the following sections of this chapter, we will show that this adsorption-desorption equilibrium can follow different dynamics depending on the chemical nature of the ligands. In the frame of this work we essentially focussed on polypyridine ligands as these molecules should be more suitable for charge transport than the native ligands covering the NCs (42, 43). But before proceeding to the ligand exchange of the NCs, it is essential to know the detailed composition of the ligand shell of the as-synthesised NCs.

**Composition of the NCs surface:** In the frame of this work, we more precisely focussed on the spherical CdSe NCs and used  $^1\text{H}$  nuclear magnetic resonance (NMR) to study the composition of the capping layer of the as-synthesised NCs. In the gram scale synthesis protocol used for this batch, the nanoparticles are stabilized by a mixture of three ligands, which are trioctylphosphine (TOP), oleylamine (OA) and stearic acid (SA), see *Figure 2-1*. The *Figure 4-2* shows the  $^1\text{H}$  NMR spectra of the as-synthesised NCs for batch 1 in deuterated chloroform ( $\text{CDCl}_3$ ). To ease the peak identification, the  $^1\text{H}$  NMR spectra of the free ligand molecules (OA, SA, TOPO) recorded in the same solvent are also displayed. The attribution of the NMR signals of the as-synthesised NCs to the three different ligands is however difficult. In fact, the NMR signal of a molecule complexed to a metal is not identical to the NMR signal of the free molecule. Therefore significant changes are expected in the NMR signals corresponding to ligands that are grafted onto a “nanoscopic” object such a NC.

The peaks are expected to be shifted and broadened due to different effects (24, 35–39, 44). These include: the reduced mobility of the ligands attached to the surface of NCs compared to free ligands, the diversity of chemical shifts due to factors such as different orientations of the molecules attached to different NCs facets and the corresponding difference of binding strength depending on the facet, etc. Therefore it is possible to attribute with certitude only the isolated NMR signals at chemical shifts of 5.3 and 2 ppm corresponding respectively to the protons of OA indexed (G) and (C) (see Figure 4-2).

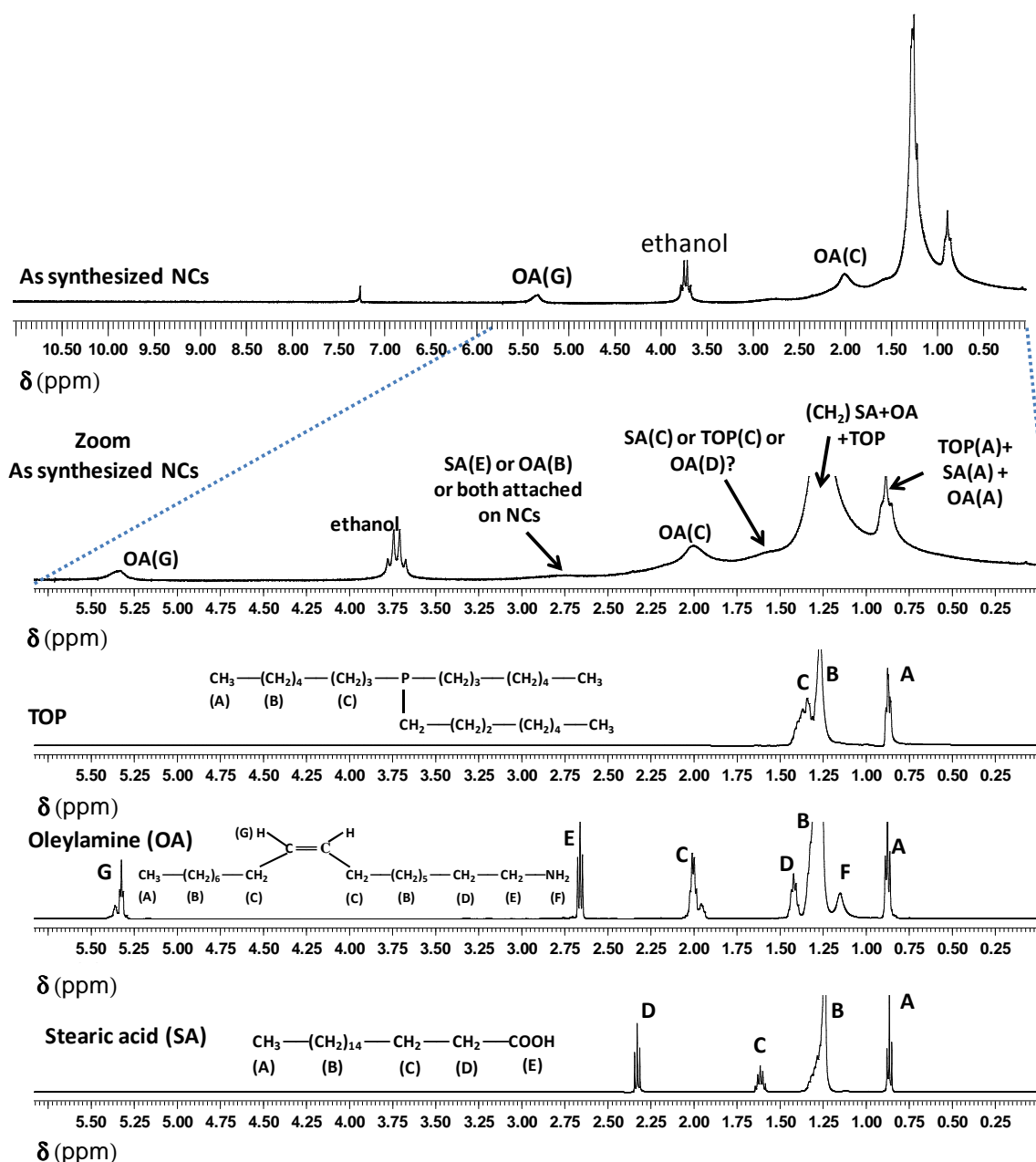


Figure 4-2: Aliphatic region of the  $^1\text{H}$  NMR of the as-synthesized CdSe NCs (batch 1) and of the free ligand molecule in deuterated chloroform. The proton attribution for the free ligand molecules was made with help of the Spectral Database for Organic Compounds (SDBS database) (45). The letters above the peaks indicate the corresponding protons. Traces of chloroform and ethanol can be observed in the NMR spectrum of the as-synthesized NCs, the latter coming from the purification procedure.

The broad signal at 2.75 ppm can correspond either to signals of protons SA(D) or OA(E) or both of them attached to the NCs. The broad and intense signal at  $\delta \sim 1.5$  ppm and  $\delta \sim 1$  ppm can be attributed respectively to the protons of the methylene (-CH<sub>2</sub>-) and methyl (-CH<sub>3</sub>) groups of the three ligands TOP, OA and SA. The presence of peaks related to ethanol in the NMR spectrum of the as-synthesized NCs can be explained by the use of this solvent in the washing procedure of the NCs. Traces of chloroform can also be observed and were used as reference

Our system is quite complex as after synthesis the surface of the NCs is passivated by a mixture of three molecules having long alkyl chains. Initially this study was meant to quantify the proportions of the initial ligands coordinated to the surface of the NCs. We were furthermore interested in determining an exchange ratio of the ligands after exchange with polypyridines and therefore a quantification of the initially coordinated ligands is necessary. It would also be interesting to know which of the three ligands is replaced preferentially during functionalization with polypyridines. However, performing an accurate quantification of the ligands with standard <sup>1</sup>H-NMR in CDCl<sub>3</sub> as presented in *Figure 4-2* remains difficult as only OA presents a distinct NMR signal in the spectra. Also, there are always some remaining free ligands in the solution. Therefore for some ligands, it can be difficult to distinguish the signal related to free ligands and those grafted onto the surface of the NCs. The contribution of those free ligands would therefore add uncertainties when performing the quantification.

In order to perform an accurate quantification of the surface composition, a collaboration with Marina Gramova, Michel Bardet and co-workers from the Laboratoire Résonances Magnétiques (LRM) at the Institute for Nanosciences and Cryogeny (INAC) of the CEA Grenoble was initiated. The measurement and quantification procedure will be detailed in an article in preparation and only the main ideas and results will be discussed here. In a first step, we use the so-called diffusion <sup>1</sup>H NMR based on pulsed field gradients (PFG-NMR in short) (40, 44, 46, 47). The main idea of this technique is to differentiate the NMR signals of free and grafted ligands using the fact that grafted ligands have a diffusion coefficient *D* approx. one order of magnitude lower than the free ligands, according to Stokes-Einstein law (44):

$$d_h = \frac{k_B T}{3\pi\eta D} \quad (Eq. 3)$$

where *d<sub>h</sub>* is the hydrodynamic diameter of the species (ligand bound to a NC or free ligand) in solution, *k<sub>B</sub>* is the Boltzmann constant,  $\eta$  the dynamic viscosity of the liquid and *T* the temperature of the solution. In the case of a hard-sphere particle *d<sub>h</sub>* is equal to the true diameter of the particle (44).

Therefore, these species will give different contributions to the spectra when pulsed field gradients are applied and the contribution of free ligands can eventually be totally eliminated. This technique allows thus an unambiguous identification of ligands bound to the surface of NCs. The absolute quantification is then performed on standard <sup>1</sup>H NMR relaxed spectra using a recycling time of 45 s. A controlled amount of the compound CH<sub>2</sub>Br<sub>2</sub> is added to a solution of NCs of known concentration (determined from the absorbance at the excitonic

peak (14) ) to serve as a quantitative reference for the organic compounds. These measurements were mostly performed on CdSe NCs of batch 1 in deuterated toluene as convection effects in  $\text{CDCl}_3$  perturb the measurements in diffusion NMR. The results are expected to be similar for NCs of batch 2. From the isolated OA peak, the number of OA molecules can be determined and their contribution can be subtracted from the methyl and methylene NMR related peaks. As the proportion of methyl and methylene protons in SA and TOP are different, the integration of the peaks related to those protons provides two equations from which the number of SA and TOP can subsequently be derived. Such calculations yielded the results summarized in *Table 4-1*.

	<b>Trioctylphosphine (TOP)</b>	<b>Oleylamine (OA)</b>	<b>Stearic acid (SA)</b>
<b>Average number of ligands per NC</b>	13	160	74
<b>Average number of ligands per NC surface area (<math>\text{nm}^{-2}</math>)</b>	0.18	2.22	1.03

*Table 4-1: Quantification of the ligands present in the as-synthesised CdSe NCs of batch 2 by  $^1\text{H}$ -NMR in deuterated toluene (collaboration with M. Gromova, M. Bardet and coll., CEA Grenoble/INAC/SCIB/LRM).*

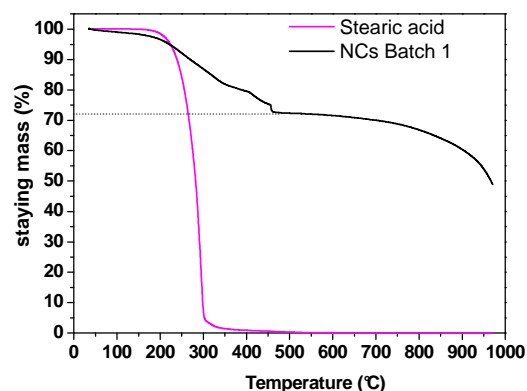
The results indicate that the predominant ligands are oleylamines (160 ligands on average per NC) followed by stearic acid (74 ligands/NC) and finally trioctylphosphine (TOP with 13 ligands/NC). Taking into account that CdSe NCs of batch 2 are nanospheres with an inorganic core 4.8 nm in diameter, the surface area of NC is approx.  $72 \text{ nm}^2$ . One can therefore calculate the average number of each ligand per unit area of surface of the NCs. The corresponding numbers are given in the second line of *Table 4-1*. It turns out that in total there are approx. 3.4 ligands per  $\text{nm}^2$  of surface. This is close to the results obtained for CdSe NCs by the group of Z. Hens and collaborators although the ligand shells have slightly different compositions (40, 46). From the results in *Table 4-1*, one can also extract the average weight proportion of ligands  $m_{\text{ligands}}$  compared to CdSe inorganic core  $m_{\text{CdSe}}$ , the total average mass of a NC being  $m_{\text{NC}} = m_{\text{ligands}} + m_{\text{CdSe}}$ . The average mass of the inorganic core can be approximated from the density of bulk CdSe, *i.e.*  $5.81 \text{ g/cm}^3$ . The spherical CdSe NCs of batch 2 with a diameter 4.8 nm have a volume of  $58 \text{ nm}^3$  and therefore  $m_{\text{CdSe}} = 337 \cdot 10^{-21} \text{ g}$ . As for the mass of the ligand shell per NC, it can be calculated from the values of *Table 4-1* and the molar mass of each ligand, *i.e.*  $M_{\text{TOP}} = 370.64 \text{ g/mol}$ ,  $M_{\text{OA}} = 267.49 \text{ g/mol}$  and  $M_{\text{SA}} = 284.48 \text{ g/mol}$ : this gives  $m_{\text{ligands}} = 114 \cdot 10^{-21} \text{ g}$ . The total average mass of CdSe NCs of batch 2 ( $\varnothing = 4.8 \text{ nm}$ ) is therefore  $m_{\text{NC}} = 451 \cdot 10^{-21} \text{ g}$  out of which approx. 25% correspond to the ligand shell and the rest to the CdSe inorganic core. One could also calculate the molar mass of CdSe NCs by simply multiplying the above number  $m_{\text{NC}}$  by the constant of Avogadro  $N_A =$

$6.02214 \times 10^{23} \text{ mol}^{-1}$  which gives  $M_{\text{NC}} = m_{\text{NC}} \times N_{\text{A}} = 2.72 \times 10^5 \text{ g}$ . From this result, one straightforward conclusion is that the mass of the ligand shell represents a significant fraction of the total mass of such colloidal CdSe NCs and cannot be neglected.

Although we did not measure the ratio Cd/Se at the surface of our NCs, the number of surface Cd sites on the NCs was estimated based on previous works (13, 33). The number of surface atoms is calculated by estimating first the total number of CdSe units in a NC of radius R and by subtracting afterwards the number of the CdSe units in the core of the NC, *i.e.* in a sphere of radius  $R - 0.263 \text{ nm}$  (0.263 nm being the closest neighbour distance in CdSe). The number of Cd surface atoms can then be estimated by taking into account that there is usually an excess of Cd atoms on the surface of the NC (13). Usually this excess corresponds to approx. 1.2 times more Cd atoms than Se (33). For NCs with a diameter of 4.8 nm ( $R = 2.4 \text{ nm}$ ), we therefore estimate a total number of surface Cd atoms of approximately 340. As the Cd atoms are generally the binding sites of the ligands, the number of surface Cd atoms corresponds to the maximum number of ligands that can be bound to the surface of NCs without considering the steric hindrance between neighbouring ligand molecules. The total number of ligands per NC (247 ligands /NC) as determined by NMR (Table 4-1) therefore corresponds to a surface coverage of approximately 73 % of the available binding sites which shows that the ligand shell is quite dense. This surface coverage is similar to the values measured by Rutherford Backscattering spectroscopy by Taylor *et al.* although in that case, the CdSe NCs studied were covered only with TOPO molecules (33). One could expect that with more bulkier ligands (*i.e.* only branched ligands), the surface coverage would be lower.

The ratio of organic to inorganic material can also be determined by thermogravimetry. Figure 4-3 shows the results of the thermogravimetric measurements performed on the NCs of batch 1. For means of comparison the same measurements were performed on stearic acid. Unfortunately the other synthesis ligands could not be measured as they are liquid at room temperature. For the as synthesized NCs, three phases can be distinguished in the thermogram of the CdSe NCs. First a loss of mass can be observed up to a temperature of  $\sim 500^\circ\text{C}$  and for temperature  $500^\circ\text{C} < T < 800^\circ\text{C}$  no significant loss in mass can be observed. For  $T > 800^\circ\text{C}$  a significant loss of mass can be observed. We believe that the first decrease of mass for  $T < 500^\circ\text{C}$  corresponds to the loss of organic materials *i.e.* the ligand shell and that for  $T > 800^\circ\text{C}$ , the inorganic CdSe cores of the NCs start to be damaged. Considering this, we get approx. 27% of organic material in the sample. This is in very good agreement with the results obtained from the NMR measurements mentioned above.

Figure 4-3 : Thermogram of the NCs of batch 1 after synthesis. For means of comparison the thermogram of stearic acid is displayed. Oleylamine and TOP could not be measured as they are liquid at room temperature



## 5. Surface chemistry of the nanocrystals: ligand exchange with polypyridines

As mentioned above, the synthesis ligands can be replaced by other ligands which are more suited for the desired application. Since the works of Huynh *et al.*, pyridine is one of the most frequently used ligands in hybrid photovoltaics at least for CdSe-P3HT mixtures (10, 21, 23, 26, 48–52). The improvement of the efficiency of hybrid solar cells with pyridine-exchanged nanocrystals compared to as-synthesized NCs was attributed to a strong reduction of the inter-particle space due to the very small size of the pyridine molecule (49). Still, pyridine exchanged nanocrystals are far from being an ideal system for hybrid photovoltaics, one important reason being that pyridine exchanged nanocrystals are not soluble in usual solvents such as chloroform. Thus, for processing CdSe NCs-P3HT based hybrid solar cells, a solvent mixture containing a small amount pyridine is generally used (10, 53). As pyridine is a bad solvent for P3HT, this can induces some changes in the morphology making the control of the latter difficult (54).

Similarly to the details of the interactions between ligands and NCs surface, ligand exchange of CdSe NCs is not sufficiently understood although it remains a key point for the fabrication of working hybrid materials for electronic applications. Many experimental methods do exist to get a qualitative indication that the surface chemistry of the NCs has been changed upon ligand exchange (quenching of the PL, changes in the solubility, NMR, etc.) but a quantitative evaluation of the exchange rate or the number of ligands per NC remains a difficult task (22, 24). Thus the comparison and the establishment of international standards concerning hybrid materials devices remain difficult.

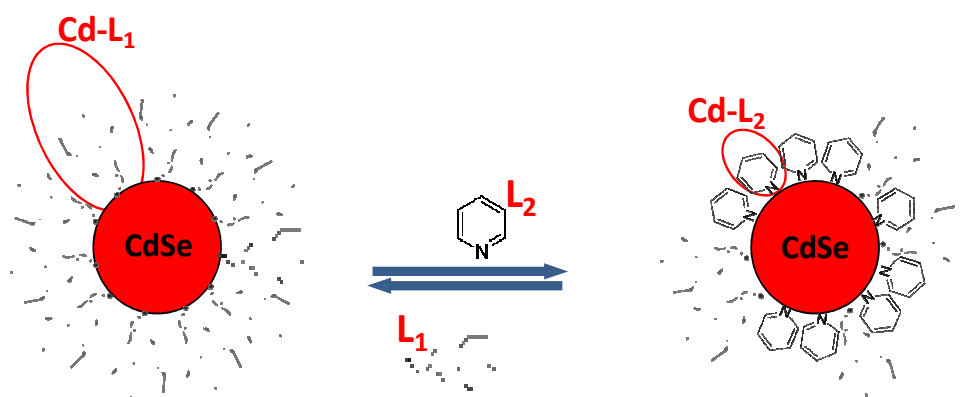


Figure 5-1: Schematical illustration of ligand exchange with pyridine.

For example, the efficiency of hybrid solar cells composed of P3HT and CdSe capped with butylamine led to device performances of 1.8% (55), but as far as the exchange ratio of the pyridine and butylamine coated nanocrystals is not comparable, the origin of this improvement cannot be attributed with certitude to the chemical nature of the ligand. In a following chapter (see Chapter 6), an example of phenanthroline exchanged NCs, shows that the morphology of hybrid thin films (CdSe NCs+P3HT) seems to depend more on the rate of exchange than on the chemical nature of the ligand.

Various authors studied the surface chemistry and ligand exchange of nanoparticles in more detail using various ligands. Some of these works were fundamental studies of the surface chemistry and the influence of the ligands on the properties of NCs (30, 36–38, 44, 56, 57), whereas other ones were focused on the influence of the capping ligands on the transport properties of the resulting materials and on the performances of derived devices (29, 58, 59). In this work, we studied the surface chemistry of the CdSe nanocrystals after ligand exchange with several polypyridine molecules: Pyridine (Py), 3-n-hexylpyridine (HexPy), 1,10-Phenanthroline (Phen) and 4,4',4''-Tri-*tert*-Butyl-2,2':6',2''-terpyridine (TerPy) (see Figure 5-2). The influence of the chemical nature of the ligand on the resulting morphology of hybrid materials grown by slow-DEC<sup>3</sup> was also studied and will be discussed in Chapter 6.

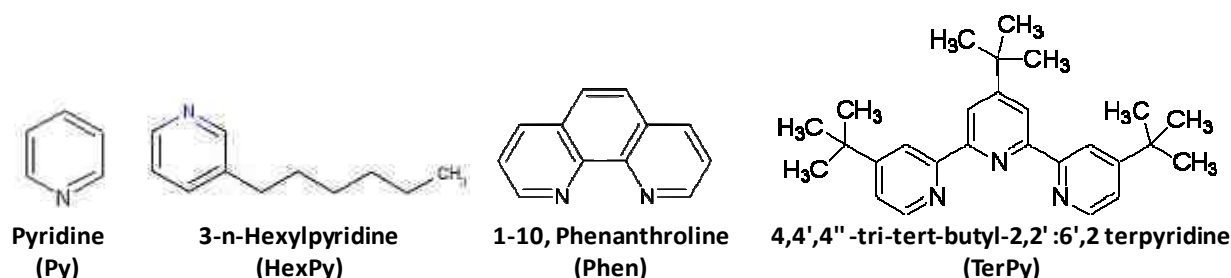


Figure 5-2 : Chemical structure of the polypyridine ligands studied in this work.

<sup>3</sup>

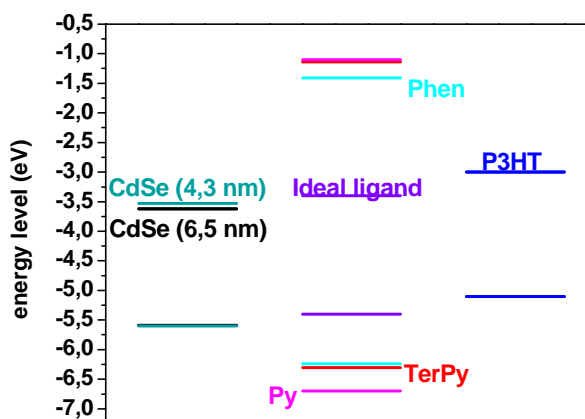
Directional epitaxial crystallization at slow growth rate.

For the fabrication of efficient hybrid devices, the new ligands have to play two key roles which are: (i) the stabilization of the NCs in such a way as to allow the homogeneous dispersion of the NCs in the  $\pi$ -conjugated polymer matrix and therefore avoid a macro phase separation and (ii) to improve the mobility of the charge carriers (electrons) in the NCs network. In this sense, the ideal ligand should have its HOMO-LUMO electronic levels positioned relatively to those of the NCs and the P3HT so as to ease the electron transfer between the NCs and the polymer. In other words, the HOMO-LUMO energy levels for the three components should present a type II staggering.

Figure 5-3 shows the HOMO-LUMO levels of the used ligands in comparison of the HOMO-LUMO level of P3HT and CdSe NCs. The values were taken from literature for the CdSe NCs and P3HT (60, 61) and calculated by Christophe Morell and André Grand (CEA Grenoble/INAC/SCIB/LAN) for Phen and TerPy.

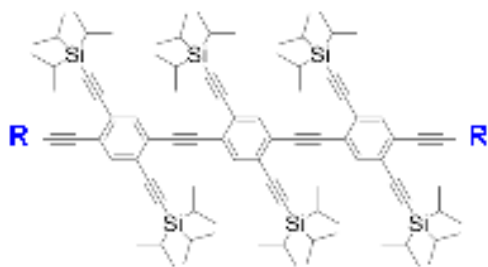
From this diagram, it follows that the polypyridine ligands do not present the level scheme expected for an ideal ligand. The main reason for that is that the polypyridine ligands are too compact and that larger ligands with a more extended  $\pi$  electron system would be needed in order to decrease the HOMO-LUMO gap. One should however note that the levels indicated in Figure 5-3 correspond to those of the free molecules and could be modified by the complexation to the surface of the NCs. The reason why pyridine-treated NCs based hybrids give significant power conversion efficiencies is that although pyridine behaves as an energy barrier towards charge transfer, it is significantly smaller compared to the original ligands such as TOP, OA, etc. so as to allow tunnelling of electrons between NCs and P3HT. In addition, pyridine is very weakly bound to the NCs and can therefore be easily removed by post-deposition treatment (such as thermal annealing) (10).

Figure 5-3 : HOMO-LUMO levels of the used ligands compared to the HOMO-LUMO levels of CdSe NCs and P3HT. The values for the HOMO-LUMO levels were taken from literature for Py (22), CdSe NCs (60), and P3HT (61) and calculated by Christophe Morell and André Grand (CEA Grenoble/INAC/SCIB/LAN) for Phen and TerPy.



In this sense, the work presented here was performed with a twofold goal. One was to understand the influence of the capping ligands on the morphology of the resulting hybrid thin films grown by slow-DEC (see Chapter 6) and to get a full control of the ligand exchange

process in order to develop a reproducible protocol. Another longer term aim of this work was related to the fact that this PhD work entered in the scope of an ANR-funded project which had as one objective to develop crosslinking ligands able to interconnect adjacent NCs. The aim of such a crosslinking ligand is to facilitate an efficient charge transport between neighbouring NCs. A schematic design of such a bifunctional ligand designed by Paul Baxter, Matthias Welker (Charles Sadron Institute, CNRS, Strasbourg) is presented in *Figure 5-4*. An adequate anchoring group **R** allows the binding of the ligand onto the surface of CdSe NCs.



*Figure 5-4: Schematic design of a crosslinking ligand for the nanoparticles. R represents an anchoring group that allows the binding onto the surface of CdSe NCs.*

Our choice of ligands is thus motivated by two aspects. First, to know what are the conditions that ligands have to respect in order to generate nanocrystals staying soluble after ligand exchange and what is the influence of the capping ligand on the resulting morphology of the thin hybrid films. Here the choice was to compare fully  $\pi$ -conjugated molecules, with molecules having a solubilizing group. The second goal was to study the influence of an increasing number of anchoring sites of the ligands on the strength of binding of the latter to the surface of the nanocrystals with the aim to choose the most tightly bound ligand as the anchoring group **R** for the crosslinking ligand. Therefore different ligands were studied: two monodentate ligands which are pyridine (Py) and 3-n-hexylpyridine (HexPy), one fully conjugated bidentate ligand which is 1,10-penanthroline (Phen) and a tri-dentate ligand having solubilising groups which is 4,4',4''-Tri-tert-Butyl-2,2':6',2''-terpyridine (TerPy). The chemical nature of these ligands is presented in *Figure 5-2*.

### 5.1. Principle and characterization of ligand exchange

The protocols to perform ligand exchange reactions with pyridine (Py) described in the literature are numerous and generally involve the dispersion under reflux of the nanoparticles in neat Py. After ligand exchange, the Py-exchanged NCs are recovered by precipitation with a non solvent and are redispersed in a good solvent. There are nevertheless huge variations in terms of the duration and the temperature of the process : some authors leave the NCs for 48 h in pure Py at room temperature whilst others describe the ligand exchange process for 10 min at 110°C (10, 44, 48, 49, 51, 52).

But independently of the ligands, the general principle of surface functionalization of NCs is the following: the exchange is performed by adding a large excess of the “new” ligand to a colloidal dispersion of as-synthesized nanocrystals (*i.e.* covered by the initial ligands). If

some of the initial ligands desorb from the surface of NCs, they are replaced by the new ligands as these are present in large excess: thus the probability that a “new” ligand is fixed on the nanoparticle surface is much higher than the probability that the initial ligand gets back to its initial position. To accelerate the desorption process, heating of the sample can be used. Once the ligand exchange reaction is finished (the process usually lasts for several hours and can be accelerated by heating the solution), the unbound initial ligands and the large excess of “new” ligands must be removed from the solution. This washing procedure is performed by adding a bad solvent for the exchanged nanocrystals and a good solvent for the excess “new” ligands and the initial ones. Thus a centrifugation of the solution allows recovering the exchanged nanoparticles. This washing procedure is essential in ligand exchange reactions with CdSe NCs and nanoparticles in general. At the same time, this washing procedure is a critical step for the elaboration of a reproducible ligand exchange protocol as many ligands such as pyridine are only loosely bound to the nanocrystal surface and thus, with each washing or only diluting the solution, some pyridine ligands are removed from the surface and the equilibrium is strongly disturbed (see section 5.2).

Qualitative methods giving an indication that a surface modification of the CdSe NCs took place are the quenching of the photoluminescence (PL) intensity (22, 24, 30, 41). This quenching is attributed to the creation of trap states at the surface of the nanocrystals due to the modification of their surface chemistry. Munro *et al.* however showed that the adsorption of one single molecule of octadecanethiol onto the surface of a single CdSe NC can induce a quenching of the PL of 50% (30). Nevertheless, even if changes in the PL intensity of nanocrystals after surface treatment is often used to characterize ligand exchange reactions (22, 34, 62–64), it should be handled with care as it is a very sensitive technique and no clear direct quantitative relation between PL quenching and the efficiency could be demonstrated to date. Another indication of ligand exchange is the change of the solubility properties of the NCs after the process.

At last, NMR measurements are powerful techniques to study ligand exchange reactions. Proton NMR of ligands bound to the surface of NCs generally show shifted and broadened peaks compared to the spectra of free ligands. Depending on the adsorption-desorption dynamics of the ligands and on their binding strength regarding the surface of NCs, these effects can be more or less marked. Standard  $^1\text{H}$ -NMR measurements can be sometimes insufficient to get a full understanding of the ligand exchange reactions because this is a dynamic process: there is a continuous exchange between bound and unbound ligands. In fact, the NMR signals of the bound and unbound ligands cannot be distinguished in the case of a fast or medium kinetics on the timescale of NMR measurements. Therefore, more specific NMR techniques such as diffusion  $^1\text{H}$  NMR based on pulsed field gradients (PFG-NMR) have to be employed (38, 44).

In the following, we will discuss the results obtained using a combination of techniques with the previously presented polypyridine ligands (*Figure 5-2*). We will first focus on the influence of ligand exchange on the optical properties of the ligand-exchanged NCs. We will thereafter address the quantification results obtained by  $^1\text{H}$ -NMR using similar techniques as discussed in Section 4. In particular, we will show that depending on the

chemical nature of the polypyridine ligand, different adsorption-desorption kinetics can be evidenced by NMR.

## 5.2. Influence of the Capping ligands on the optical properties of NCs

### 5.2.1. Influence on the static absorption and photoluminescence spectra

In the following, all surface treatments were performed on the spherical CdSe nanocrystals of batch 1. In a first step, ligand exchange with pyridine (Py) was studied by photoluminescence (PL) quenching. Despite the problems of solubility that occur upon Py ligand exchange reactions, Py was chosen as it is one of the most frequently used and described ligands in the literature (10, 23, 49–52, 65–68). When doing this study, our aim was to understand the influence of the concentration of the ligand and to determine the duration necessary to obtain a good rate of ligand exchange and therefore a strong PL quenching, as is usually observed for Py-exchanged CdSe NCs (22, 49, 51, 52). Another point we wished to address was the reproducibility of ligand exchange reactions. We chose to use a temperature around 90-100°C to perform the ligand exchange reactions, similar to what has been described in references (51, 52). All ligand exchange reactions were performed under an inert argon atmosphere and with reflux. All results presented are recorded without post-exchange washing procedure in order to keep the system as close as possible to its equilibrium state.

To perform the study of the evolution of the PL quenching with time, 2 different procedures were developed and repeated each one two times in order to check their reproducibility. The details of the two ligand-exchange procedures that were used are described hereafter.

**Procedure 1:** Ligand exchange is performed under high concentration conditions with the NCs dispersed in almost pure pyridine: 1 mL of Pyridine and 0.1 mL of NCs dispersed in hexane with an initial concentration of 61.1 mg/mL. At different exchange times aliquots are removed from the solution. The extracted NCs are placed into a PL quartz cuvette and chloroform is added in order to have an adequate concentration for PL. *i.e.* **solvent is added to the exchanged nanocrystals before recording the PL and UV-vis spectra.**

**Procedure 2:** Ligand exchange is performed under very dilute conditions in chloroform. Before starting the exchange, chloroform is added to the pyridine-nanocrystal solution in order to get a dilute solution adequate for PL measurements (98% ClCH<sub>3</sub>, 1.96% Py, 0.4% Hex and 0.1 mL of a solution of NCs dispersed in hexane with a concentration of 61.1 mg/mL) and to this solution, we added 1mL of pyridine. **PL spectra and UV-vis are recorded without adding or removing anything to the extracted aliquots.**

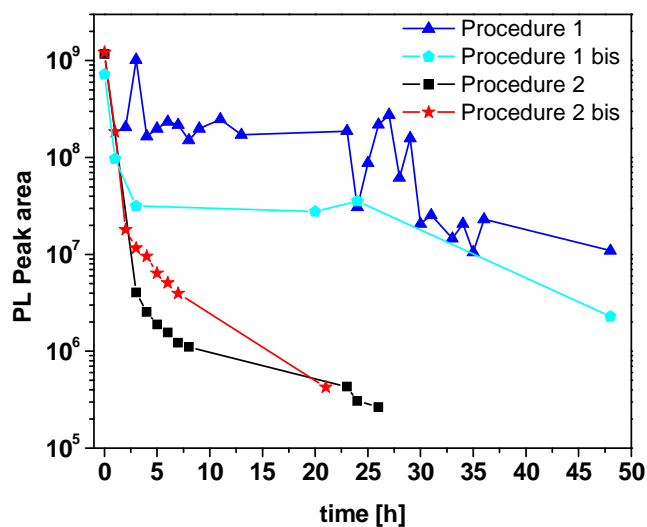


Figure 5-5: Compared evolution of the PL quenching of two different procedures of ligand exchange with pyridine. The curves show the evolution of the PL peak area with the duration of the ligand exchange.

Figure 5-5 shows the evolution with ligand exchange time of the PL integrated peak area for the 4 ligand exchange reactions performed (two for each procedure). The results show clearly that Py is very loosely attached to the surface of the NCs as already mentioned in literature (32, 49). In fact, a simple dilution of the system by adding chloroform to the solution (**procedure 1**) changes the PL quenching of the sample quite strongly. This results in a very wavy evolution of the PL quenching using this procedure. The PL quenching of Procedure 1bis shows a smoother evolution but this can also come from the fact that much less points were measured in this case. Still, one should note that as the figure is presented with a log scale, the variation of PL intensity after 25 hours of ligand exchange is important (>10).

In contrast to Procedure 1, the evolution of the PL for Procedure 2 is more monotonous. We attribute this to the fact that the only factor that can disturb the system equilibrium is the temperature drop (from 90° to room temperature) when taking an aliquot. The comparison of the results obtained with both protocols shows that Procedure 2 is more reproducible and results in a much stronger PL quenching. This point can be explained by a good solubility of the initial ligands (SA, OA, TOP) in chloroform and thus they are more easily removed from the surface of NCs and replaced by pyridine molecules. The better reproducibility of Procedure 2 lies in the fact that the equilibrium of the system is not disturbed by adding some additional solvent after taking an aliquot for the PL analysis. This makes the control and reproducibility of ligand exchange reactions with loosely bound ligands such as pyridine very difficult as the equilibrium will be disturbed by any perturbation, in particular washing steps when purifying the NCs.

To conclude, this study allowed us to determine that the ligand exchange reactions should be performed during at least 20 hours at a temperature of 90°C, after which the PL

quenching seems to reach more or less a constant value. This is valid for Procedure 1 as well as for Procedure 2. This study also pointed to the fact that performing ligand exchange under dilute conditions in chloroform seems to have a positive effect as the initial ligands have a very good solubility in chloroform and thus, they can be more easily removed from the surface of the NCs. A recently published study on the effect of the concentration on the ligand exchange reactions showed similar results (69).

For the ligand exchange reactions performed with the other polypyridine ligands HexPy, Phen and TerPy, (see Figure 5-2), we developed protocols based on some of the results obtained with Py. Nevertheless, it was not possible to apply procedure 2 to these ligand exchange reactions as the latter were performed to integrate the surface treated NCs, into a matrix of P3HT and to study the influence of the chemical nature of the ligand on the hybrid thin film morphology. Indeed in this case a washing-purification step is always compulsory. Also we assumed that ligand exchange conditions appropriate for pyridine are also appropriate for the other polypyridine ligands. We used CdSe NCs of batch 1 to make the ligand exchanges with HexPy, Phen and TerPy (see details below). All ligand exchange reactions were performed in argon atmosphere and under reflux at 90-100°C. The reactions were done in deuterated chloroform ( $\text{CDCl}_3$ ) in order to study by NMR the influence of the washing step (see section 5.3).

- **HexPy:** 200  $\mu\text{L}$  of NCs dispersed in hexane (61.1 mg/ml) blended with 200  $\mu\text{L}$  of HexPy and 5 mL of  $\text{CDCl}_3$ . Duration of the ligand exchange: 24h
- **Phen:** 330  $\mu\text{L}$  of NCs dispersed in hexane (61.1 mg/ml) blended with 61 mg Phen and 4mL of  $\text{CDCl}_3$ . Duration of the ligand exchange: 31h.
- **TerPy:** 333  $\mu\text{L}$  of NCs dispersed in hexane (61.1 mg/ml) blended with 66 mg of TerPy and 4mL of  $\text{CDCl}_3$ . Duration of the ligand exchange: 32h

Figure 5-6 shows the PL spectra of these samples before and after ligand exchange. The maximum of the PL peak before exchange was normalized to 1. As the concentration of NCs after the exchange reaction is difficult to know due to the washing step which induces always some loss of material, the PL before and after ligand exchange was normalised by the absorbance of the solution at the maximum of the first excitonic peak.

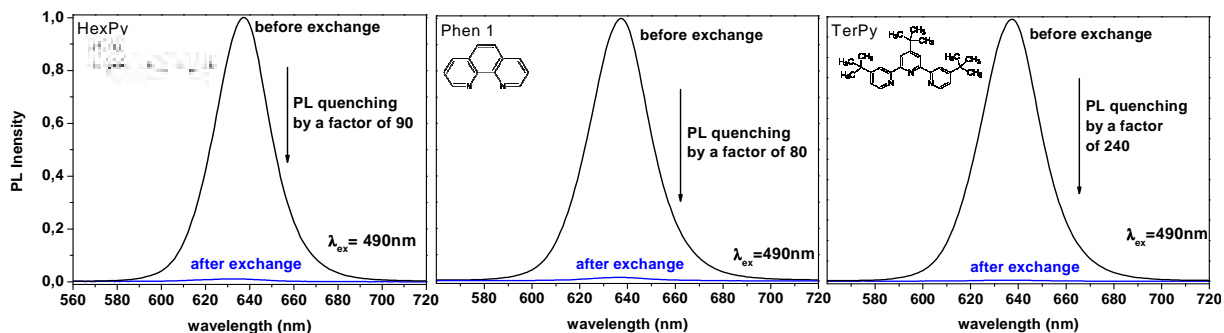
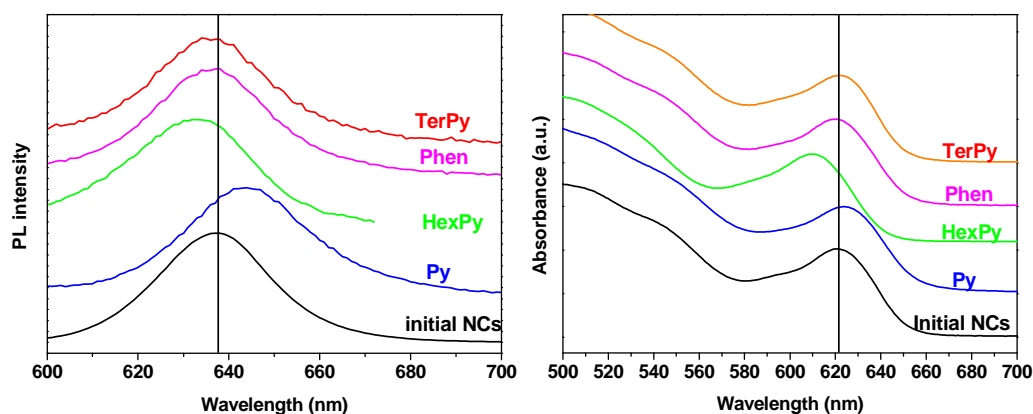


Figure 5-6: PL quenching of CdSe Nanocrystals after ligand exchange with HexPy, Phen and TerPy (see Figure 5-2). The indicated quenching factor corresponds to the ratio of the PL peak area before and after ligand exchange.

HexPy and Phen showed a similar PL quenching by a factor of respectively 90 and 80 whereas the PL quenching observed for TerPy was much stronger, with a quenching factor of approx. 240. This is by far the highest PL quenching that we observed by surface treatment of NCs with polypyridine ligands and we interpret it as a strong indication that the surface composition of NCs has dramatically changed. This comparative PL quenching experiment can be considered as a first indication that the case of TerPy is different from HexPy and Phen.

The  $^1\text{H}$  NMR results discussed in the following section will further confirm this observation (see section 5.3). In addition to the PL quenching, the position of the PL maximum emission and of the maximum of the UV-vis first excitonic peak can provide further information about the ligand exchange. The normalized PL and UV-Vis spectra for the as-synthesized NCs are represented in *Figure 5-7*. The position of the maxima of the PL and the first excitonic peak in the UV-Vis absorption spectra are summarized in *Table 5-1*. Compared to the spectra recorded for the as-synthesized NCs, no significant changes in the peak positions were observed for Phen and TerPy treated NCs. In contrast to this, a noticeable blue-shift (12 nm) was observed for HexPy-treated NCs. A slight red-shift was furthermore observed for the Py treated NCs. Such shifts of the position of the first excitonic peak are frequently observed after surface treatment of NCs (29, 62, 70–72). There exist several explanations in the literature to explain these shifts. Bullen and Mulvaney attribute such shifts to electronic effects of the ligands due to enhanced delocalization of the exciton in the ligand shell (red shift) (62). Talapin *et al.* showed that a blue shift can be explained with a slight decrease of the particle size by loss of surface Cd and Se atoms which would effectively lead to a reduction of the bandgap of the NCs (70). Finally, red shifts in densely packed PbSe NCs thin films have also been attributed to polarization effects due to a change of the dielectric environment of the NCs (71). It is difficult in the present work to conclude about the exact origin of the shifts observed and to correlate it to the chemical structure of the polypyridine ligand used. These shifts are nevertheless another indication of the effect of surface treatment on the optical properties of NCs.



*Figure 5-7: UV-vis Absorbance before and after ligand exchange with polypyridine ligands. The spectra are vertically shifted for clarity.*

	PL Peak position (nm)	Excitonic peak position (nm)
<b>Initial NCs</b>	635	620
<b>Py</b>	644	625
<b>HexPy</b>	632	609
<b>Phen</b>	635	620
<b>TerPy</b>	636	622

Table 5-1 : Positions of the maxima of the PL and the first excitonic peak in the UV-Vis absorption spectra

### 5.3. Adsorption-Desorption kinetics of the ligands on the NCs surfaces

As mentioned earlier, the binding of most ligands onto the surface of nanocrystals is a dynamic process: there is a continuous exchange between bound and free molecules in the solution and the ratio of bound and unbound ligands depends in particular on the binding strength of the ligand towards the surface of NCs. In the following, we study the adsorption-desorption kinetics of the polypyridines ligands from the surface of NCs. This study was mainly performed by  $^1\text{H}$  NMR spectroscopy and thus, the qualification of the dynamics as fast or slow always refers to the NMR timescale. Two different adsorption-desorption kinetics could be distinguished depending on the number of binding sites on the polypyridine ligands. At the same time, the importance of the washing procedure described for the ligand exchange experimental protocol was evidenced.

#### 5.3.1. Fast adsorption-desorption kinetics: Py, HexPy and Phen

As we are interested in the behaviour of polypyridine ligands bound to the surface of NCs, we will focus in the following only on the aromatic region in terms of chemical shifts of the  $^1\text{H}$  NMR spectra. *Figure 5-8* and *Figure 5-9* show the spectra in deuterated chloroform  $\text{CDCl}_3$  for CdSe NCs exchanged with Phen and HexPy, respectively, before and after several washing steps. For means of comparison, a proton NMR of the free ligand molecule and the NMR spectrum of the initial NCs are displayed. For both HexPy and Phen exchanged NCs, the  $^1\text{H}$  NMR spectra in the aromatic region of the exchanged but unwashed NCs are almost identical with the NMR spectrum of the pure ligand. Only a slight shift towards lower chemical shifts  $\delta$  can be noticed. The origin of this shift remains unclear. It could originate from the presence of the NCs and some additional solvents, leading to slight changes in the environment of the system that are reflected in the chemical shifts of the peaks. The similarity of the NMR spectrum of the unwashed NCs with that of the free ligands can be explained by the large excess of free ligands in the system added according to the ligand exchange protocol.

After one washing step, significant changes in the NMR spectra occur: the NMR signals of the polypyridines are significantly enlarged and shifted towards higher chemical

shifts  $\delta$ . This is the case for both Phen and HexPy treated NCs. For Phen (*Figure 5-8*), a second washing step led to a further broadening and to a shift to higher  $\delta$  of the Phen related NMR peaks. A second washing step can however be critical and is not always possible. In fact if the exchange rate is too high, a second washing step can lead to an irreversible aggregation of the nanoparticles as each washing step goes along with a loss of initial ligands (22, 24). Nevertheless, these results clearly show that a washing step is essential to remove excess ligands.

The effect of washing steps was indeed previously studied by NMR and optical spectroscopies by Kalyuzhny and Murray on as-synthesized CdSe NCs stabilized with TOPO as the ligand (24). In accordance with our results, they observed an increasing broadening of the  $^1\text{H}$  NMR peaks related to TOPO with each washing step. They attributed this broadening to the loss of ligands which are loosely bound to the NCs surface, therefore leaving only the ligands which are more tightly bound. InP nanocrystals exchanged with pyridine showed also such a broadening of the Py NMR peaks (44). It was interpreted as a fast adsorption-desorption kinetics from the surface of NCs. The authors claimed that the majority of the Py molecules are unbound ones (44). Schmelz *et al.* also observed very similar effects to ours (broadening of the peaks and shift towards higher chemical shifts  $\delta$ ) for CdSe NCs exchanged with diazaperylene, another polypyridine ligand attached onto the surface of NCs by two nitrogen atoms, similarly to 1,10-phenanthroline (39). The authors interpreted the enlargement of the NMR signals by a multitude of chemical shifts due to reduced mobility of the ligands and to different micro-environments and orientations of the ligands onto the surface of NCs. 1-10, phenanthroline was also successfully attached to the surface of gold NCs, but no NMR measurements were presented in this case (73).

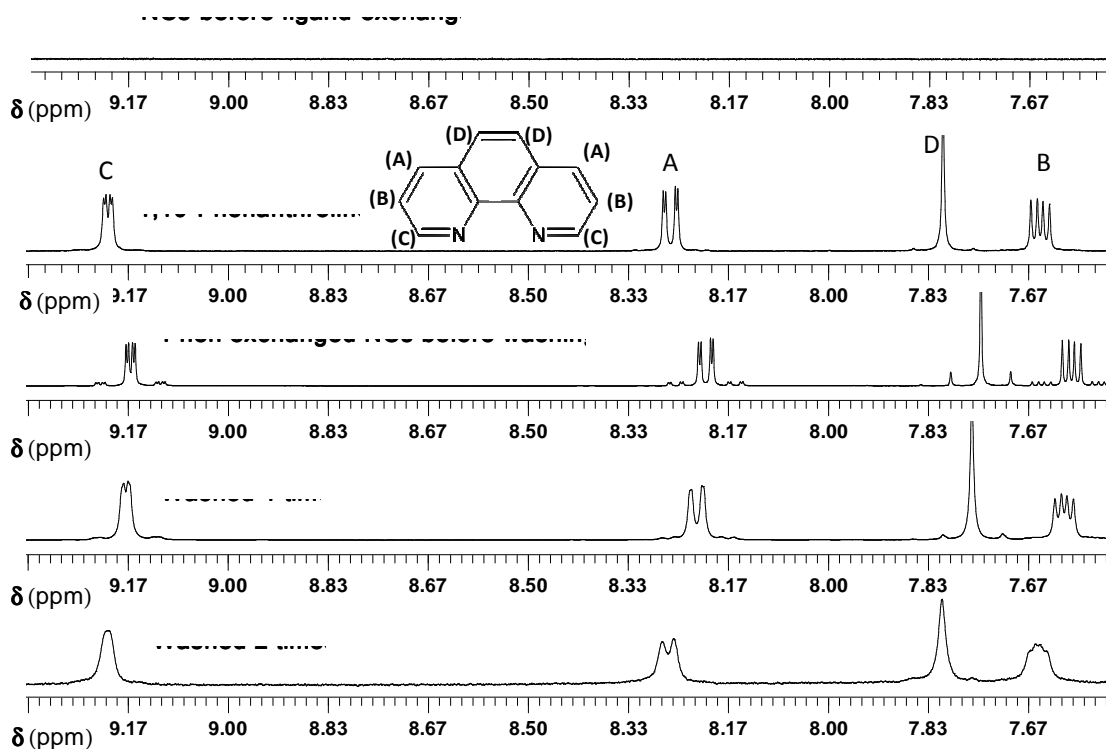


Figure 5-8: Aromatic region of  $^1\text{H}$  NMR spectra for Phenanthroline (Phen) exchanged NCs and for pure Phen in deuterated chloroform ( $\text{CDCl}_3$ ). The spectra of Phen-NCs show the evolution of the characteristic peaks of phenanthroline with an increasing number of washing steps. Before washing, the spectrum is identical to that of pure Phen. After 1 washing step, the peaks are broadened indicating that an important fraction of the excess Phen has been removed. More than 2 washing steps lead to irreversible aggregation of the NCs.

Our results are in accordance with those different works. The washing procedure allows to remove partially the excess of unbound ligands left in solution. Nevertheless, as mentioned above, the binding of ligands is a dynamic process with a continuous exchange between bound and unbound ligands. Therefore a washing step of the NCs will lead to a desorption of some ligands to establish a new equilibrium thus leading to a decrease of the total number of ligands attached to the NCs. The time kinetics of the ligand binding compared to the NMR timescale can also influence the NMR spectra. If the adsorption-desorption kinetics is fast compared to the NMR time scale, as a consequence only enlarged NMR signals will be observed. We believe this is the case for Phen and HexPy surface treated NCs. In fact, we observe a weighted average of the signals of the bound and unbound ligands. The NMR signals get larger with each washing step as more and more ligands which are free in solution are removed and the relative weight of the attached ligands in the spectrum increases.

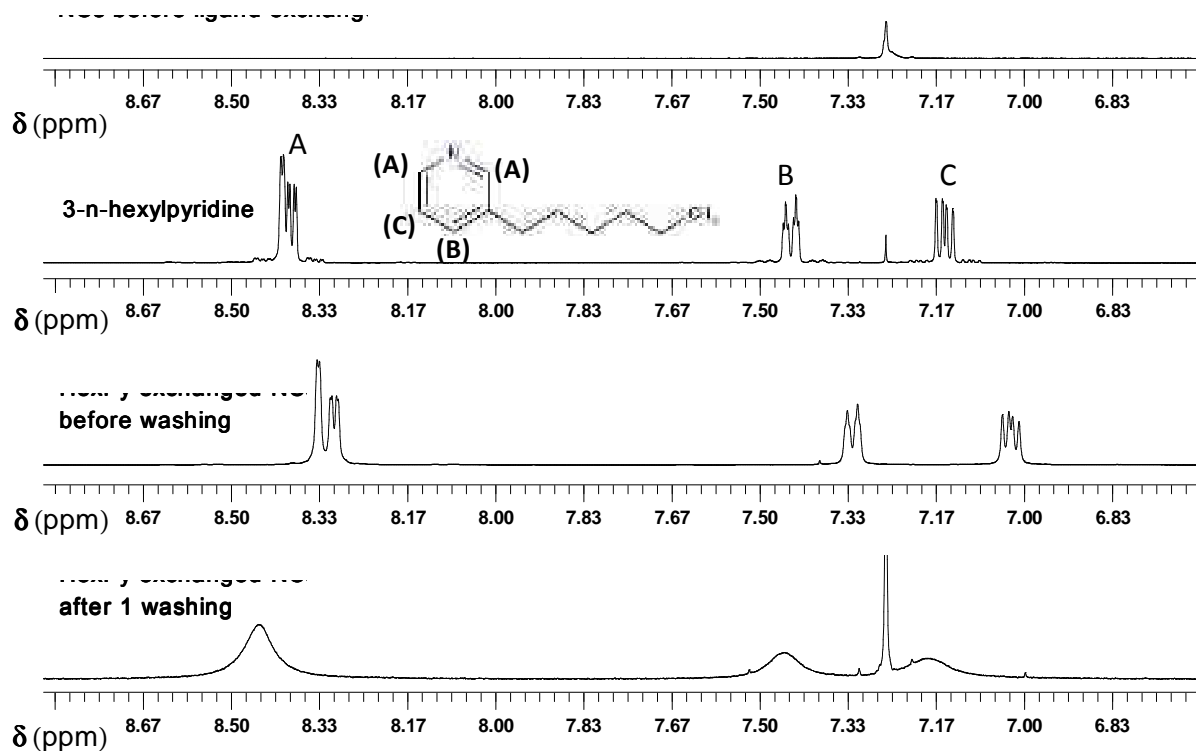


Figure 5-9: Aromatic region of  $^1\text{H}$  NMR spectra for 3n-hexylpyridine (HexPy) exchanged NCs and for pure Phen in deuterated chloroform ( $\text{CDCl}_3$ ). The spectrum for the NCs before ligand exchange is also displayed as a reference (top). The spectra show the evolution of the characteristic peaks of HexPy with an increasing number of washing steps. Before washing, the spectrum is identical to that of pure HexPy.

This interpretation is also corroborated by results obtained using PL spectroscopy. Figure 5-10 shows the PL of Phen after one and two washing steps. The spectra were normalised by the intensities of the PL of the NCs and the relative intensities of the PL of Phen could be compared. It appears clearly that the amount of free Phen compared to the NCs was reduced significantly after the second washing step. The PL of the Phen attached to the NCs surface is probably quenched and thus here the PL of free Phen in solution is measured. The effects observed for the HexPy exchanged NCs (shift and broadening of the NMR signals) are slightly more pronounced than for Phen after one washing step. There are several interpretations to that effect. In contrast to Phen which is solid at room temperature, HexPy is liquid in the same conditions. Thus a washing step is more efficient in removing most of the free excess HexPy. In contrast, the Phen exchanged NCs are washed with hexane, and Phen is soluble in hexane only at low concentrations. Therefore, in the case of HexPy, the contribution of bound ligands in the NMR peaks is larger in contrast to Phen. It is also possible that HexPy is more strongly bound to the NCs surface compared to Phen which would influence the kinetics of binding therefore leading to the observed changes in the NMR signals.

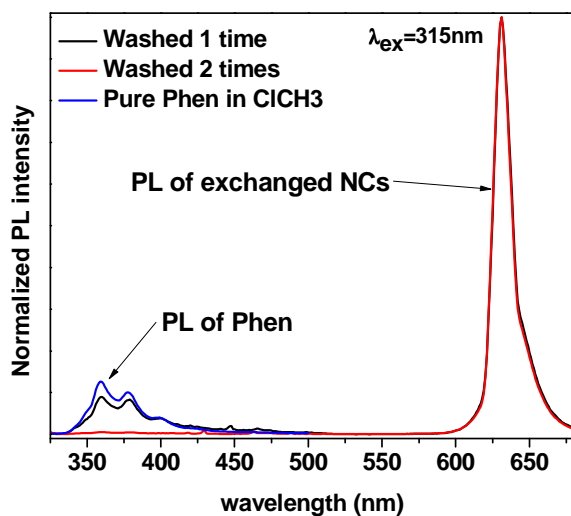


Figure 5-10: The relative intensity of the PL peak of Phen compared to that of the NCs decreases with each washing step.

For both Phen and HexPy, a quantification of the ligands attached on the NCs and the determination of the rate of ligand exchange is rather difficult due to the above mentioned dynamic aspect of the system which makes the separation of the contribution of bound and unbound ligands difficult. This lack of quantification and also the lack of reproducibility of ligand exchange reactions due to the washing procedure which can strongly perturb the equilibrium between bound and unbound ligands is a general problem in the field of colloidal NCs. In particular, it can be difficult to get comparable hybrid materials involving ligands loosely bound to the NCs surface. This will be illustrated with the example of Phen capped NCs integrated into a hybrid thin film in Chapter 6.

### 5.3.2. Slow adsorption-desorption kinetics: TerPy

In contrast to the mono and bidentate ligands Hexpy and Phen which showed a fast exchange kinetics on the NMR time scale, the tridentate ligand 4,4',4''-Tri-*tert*-Butyl-2,2':6',2''-terpyridine (TerPy) seems to obey to a slower exchange kinetics. Figure 5-12 compares the  $^1\text{H-NMR}$  of TerPY exchanged NCs after a single washing step with that of the free TerPy ligand and of NCs before exchange.

Contrarily to what was observed with HexPy and Phen, the NMR signals provided by the TerPy ligand are not simply broadened and slightly shifted to lower fields. There appears a superposition of two groups of peaks easily distinguishable. The sharp and non shifted peaks can be attributed to free TerPy molecules remaining in the solvent (deuterated chloroform  $\text{CDCl}_3$ ). A second group of peaks is significantly broadened and shifted to higher chemical shifts  $\delta$ . Following previous published works, such broadened and shifted peaks are the fingerprints of ligands bound to NCs (37, 44). These observations indicate clearly that the adsorption-desorption kinetics of TerPy ligands from the surface of NCs must be slow compared to the NMR timescale. This can be attributed to a higher affinity of the tridentate Terpy ligands regarding the surface of the CdSe NCs compared to Hexpy and Phen. It is

important to mention that whatever the vertical zooming of the  $^1\text{H}$  NMR spectra for Hexpy and Phen-exchanged NCs, no trace of broad peaks as observed for Terpy-NCs could be observed. The appearance of such broad peaks is reproducible and was observed for different ligand exchange experiments that were performed with TerPy.

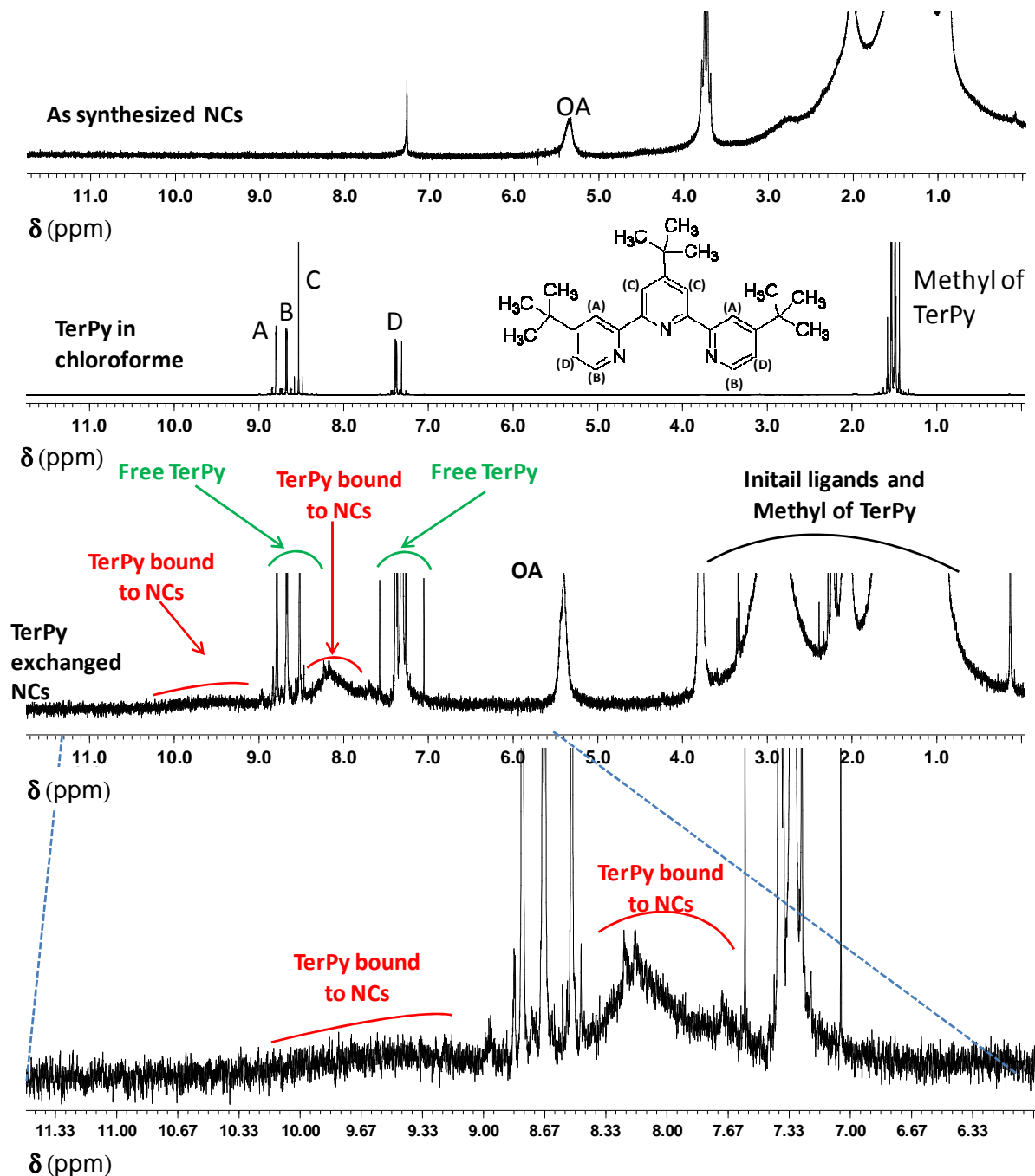


Figure 5-12:  $^1\text{H}$  NMR spectrum of as synthesized NCs, TerPy in  $\text{CDCl}_3$  and TerPy exchanged NCs after 1 washing step. For more clarity, a zoom on the aromatic region of the  $^1\text{H}$  NMR spectrum of TerPy-exchanged NCs is also displayed.

Further support about this interpretation and a quantitative characterization of the ligand exchange rate was obtained from complementary NMR measurements performed by Marina Gromova, M. Bardet and co-workers (CEA Grenoble/INAC/SCIB/LRM) on ligand exchanged CdSe NCs of batch 2 in deuterated toluene. In particular diffusion  $^1\text{H}$  NMR measurements based on pulsed field gradients (PFG-NMR) and spectral hole burning measurements were performed. According to Stokes-Einstein law (see Section 4), the diffusion coefficient of a free TerPy ligand should be significantly higher than for a TerPy molecule attached on the surface of a NC.

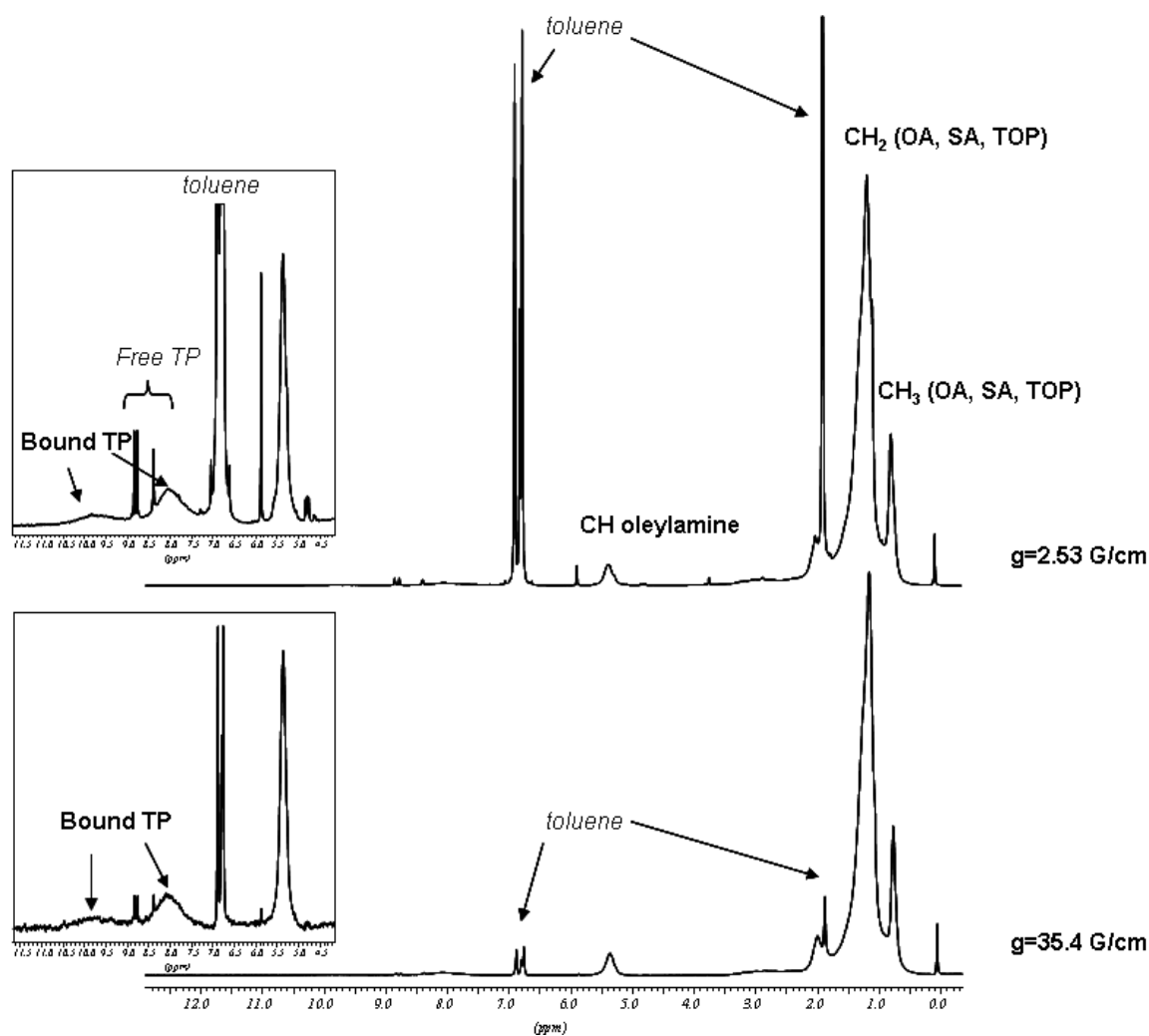


Figure 5-132: Diffusion-filtered  $^1\text{H}$ -NMR spectra of TerPy-exchanged CdSe NCs in deuterated toluene. **Top:** Spectra obtained with a low gradient amplitude ( $g = 2.53 \text{ G/cm}$ ). The inset shows an enlargement of the aromatic region of the spectrum. Signals corresponding to ligands (un)bound to NCs are present giving a superimposition of sharp (unbound ligands) and broad (bound ligands) peaks. **Bottom:** Spectra obtained with a high gradient amplitude ( $g = 35.4 \text{ G/cm}$ ). Mainly broad peaks are present corresponding to ligands bound to the surface of NCs. The signals corresponding to free ligands and the solvent (which have a higher diffusion coefficient) are almost entirely filtered out. These measurements were performed in collaboration with Marina Gromova and Michel Bardet (CEA Grenoble/INAC/SCIB/LRM).

Thus diffusion NMR measurements allow to discriminate between bound and unbound species identified by a peak in the  $^1\text{H}$  NMR spectrum via the variation of their diffusion coefficient. This is performed by applying a series of increasing field gradients. The faster a species diffuses, the more quickly the intensity of its signal is attenuated. Therefore, with increasing field gradients, the strength of the signals attributed to the fast species (unbound) are reduced more strongly compared to the signals of the bound species. The PFG-NMR measurements allow thus to filter out the contribution of the unbound fast diffusion ligands.

*Figure 1-12* illustrates this on the example of bound and unbound TerPy. It can be clearly seen that for a field gradient of  $g=35.4\text{G/cm}$ , the relative intensity of the signal of the bound TerPy is much stronger compared to a field gradient of  $g= 2.53\text{G/cm}$ . From the attenuation of the signals as a function of the applied field gradient, the diffusion coefficient of the species can be extracted. And afterwards, from the diffusion coefficient, one can derive the hydrodynamic radius. We performed such measurements on the broad shifted peaks and on the sharp peaks respectively attributed to bound and unbound TePy (*Figure 5-11*). Whereas for the sharp peaks the extracted diffusion coefficient is in the  $10^{-9} \text{ m}^2 \cdot \text{s}^{-1}$  range, as expected for free terpy ligands, it is one order of magnitude lower with  $D \approx 1.5 \times 10^{-10} \text{ m}^2 \cdot \text{s}^{-1}$  for the broad shifted peaks. For these large shifted signals, a diffusion coefficient of  $D \approx 1.5 \times 10^{-10} \text{ m}^2 \cdot \text{s}^{-1}$  was extracted. This corresponds to an hydrodynamic diameter of approx. 5,4 nm. These results are in very good accordance with the diameter of the NCs determined by TEM or UV-vis spectroscopy. Therefore the diffusion NMR measurements confirm the interpretation of the  $^1\text{H}$  NMR spectra of *Figure 5-11* attributing the sharp peaks to free TerPy and the broadened signals to attached TerPy ligands.

As for this sample free and adsorbed ligands can well be distinguished, the quantification of the composition of the ligand shell can be performed using the same procedure as explained in Section 4 of the present chapter. The results of the quantification are summarized in *Table 5-2* and compared to the results before ligand exchange. The results before ligand exchange were the ones already discussed in Section 4. It has to be mentioned that the main source of error for these measurements is a mis-estimation of the NMR peak areas for the bound ligands due essentially to unbound ones. We estimate an error of approximately 20 % for these NMR quantification measurements.

From *Table 4-1*, it can be clearly seen that the ligand exchange reaction with TerPy goes along with a loss of ligands. In fact, before the exchange reaction, the average number of ligands per NC is of 247 whereas after the ligand exchange reaction this number decreases to 148. This means that the substitution of initial ligands by TerPy is not a 1:1 process. Regarding the relative amount of the synthesis ligands, after ligand exchange mainly the OA is removed from the system. In fact the amount of OA/NC was diminished by ~50% whereas the amount of SA was diminished only by 30% and the number of TOP ligands did almost not change before and after ligand exchange with TerPy. With  $M_{\text{TerPy}}=401.59\text{g/mol}$  one finds for the total mass of ligands after the ligand exchange with TerPy  $m_{\text{ligand}}=75.10 \cdot 10^{-21}\text{g}$ . At this point, it is reasonable to assume that the mass of the inorganic core did not change upon

ligand exchange and is as determined before *i.e.*  $m_{\text{CdSe}} = 337 \cdot 10^{-21}$  g. After the ligand exchange reaction with TerPy, the total mass of a single NC is thus  $m_{\text{NC}} = 412 \cdot 10^{-21}$  g. After the ligand exchange the mass of the NCs is thus composed of 18% of ligands and 82% of inorganic core.

It can be anticipated that the ligand exchange ratio should depend both on the binding strength and on the size of the ligand as well as on the volume it occupies on the surface of NCs. It should therefore be different for Phen and HexPy compared to TerPy. But these are mere assumptions as we could not derive the exact surface composition of Phen and Hexpy exchanged NCs from the NMR data.

		TOP	OA	SA	Terpy	Total
As synthesized	Average number of ligands per NC	13	160	74	0	247
	Average number of ligands per NC surface area (nm <sup>-2</sup> )	0.18	2.22	1.03	0	3.43
After exchange with Terpy	Average number of ligands per NC	11	58	52	27	148
	Average number of ligands per NC surface area (nm <sup>-2</sup> )	0.15	0.80	0.72	0.38	2.05

Table 5-2: Quantification of the ligands present of Terpy exchanged CdSe NCs of batch1 ( $\varnothing = 4.8$  nm) by <sup>1</sup>H-NMR in deuterated toluene (collaboration with M. Gromova, M. Bardet and coll., CEA Grenoble/INAC/SCIB/LRM). The composition before ligand exchange is also given in the first two rows as a reminder (data of Table 4-1).

## 6. Conclusion

Two batches of 1.5 g each of CdSe NCs (size approx. 5 nm) with a low polydispersity were synthesised following an already developed and published synthesis protocol. The obtained NCs were characterized by TEM, PL, UV-vis and X-ray diffraction. The obtained NCs are of similar quality in terms of size, polydispersity and crystallinity than those obtained in the literature (5, 6). A study of the composition of the ligand shell for these as-synthesised NCs was performed by <sup>1</sup>H NMR measurements. It shows that the total mass of a single NC is composed by 25% of ligands on average.

Following this extensive characterization of the as-synthesized NCs, ligand exchange reactions with various polypyridine ligands were performed and the functionalized NCs were characterized. Qualitative indications that the surface chemistry of the NCs is strongly modified during ligand exchange reactions is obtained for example by the observation of a strong quenching of the PL after exchange. However, a more quantitative analysis and the extraction of an exchange rate after ligand exchange was more difficult and could not be performed for all polypyridine ligands investigated herein. Depending on the chemical nature of the polypyridine, two different adsorption-desorption kinetics could be distinguished from the NMR spectra. A fast exchange adsorption-desorption kinetics on the NMR timescale was observed for the mono- and bidentate ligands HexPy and Phen respectively whereas a slow exchange kinetics could be evidenced for the tridentate ligand TerPy (see Figure 5-2 for the chemical structures of these ligands). This is attributed to a stronger binding of the TerPy ligands on the NCs surface probably due to the presence of 3 binding sites on this molecule.

For the TerPy-exchanged NCs, more advanced NMR studies were performed in collaboration with Marina Gromova *et al.* and allowed a quantitative analysis of the sample and in particular to derive the average amount of each type of ligands on the surface of NCs. The results show that following the ligand exchange, there is globally a loss of amount and weight of ligands compared to the inorganic CdSe cores. Furthermore, out of the four polypyridine ligands studied, TerPy is the only one that clearly shows peaks related to TerPy ligands bound to NCs. This motivated the choice to use TerPy as group **R** for the crosslinking ligand designed and synthesized by Paul Baxter and Mathias Welker, organic chemists with whom I collaborated in the frame of this PhD work (see *Figure 5-4*). The challenge for the future will thus be to crosslink NCs with crosslinking ligands by avoiding the aggregation of the NCs to keep their main advantage which is the solution processability. A better control of the ligand exchange reactions is in our opinion a key for the efficient fabrication of devices containing colloidal NCs.

The NCs functionalized with the different polypyridine ligands were integrated into hybrid thin films prepared by directional epitaxial crystallization with the aim of understanding the influence of the capping ligands of the NCs on the morphology of such hybrid thin films. These results will be presented in Chapter 6.

- (1) Murray, C. B.; Kagan, C. R.; Bawendi, M. G. Synthesis and characterization of monodisperse nanocrystals and close-packed nanocrystal assemblies. *Annual Review of Materials Science* **2000**, *30*, 545-610.
- (2) Park, J.; Joo, J.; Kwon, S. G.; Jang, Y.; Hyeon, T. Synthesis of monodisperse spherical nanocrystals. *Angewandte Chemie (International ed. in English)* **2007**, *46*, 4630-60.
- (3) Murray, C. B.; Norris, D. J.; Bawendi, M. G. Synthesis and characterization of nearly monodisperse CdE (E = S, Se, Te) semiconductor nanocrystallites. *Journal of the American Chemical Society* **1993**, *115*, 8706-8715.
- (4) de Mello Donegá, C.; Liljeroth, P.; Vanmaekelbergh, D. Physicochemical evaluation of the hot-injection method, a synthesis route for monodisperse nanocrystals. *Small* **2005**, *1*, 1152-62.
- (5) Protière, M. Synthèse de nanocristaux fluorescents de semi-conducteurs II-VI et III-V augmentation de l'échelle de synthèse, PhD dissertation, Université Joseph Fourier de Grenoble, 2007.
- (6) Protière, M.; Nerambourg, N.; Renard, O.; Reiss, P. Rational design of the gram-scale synthesis of nearly monodisperse semiconductor nanocrystals. *Nanoscale research letters* **2011**, *6*, 472.
- (7) Querner, C. Synthèse et caractérisation de matériaux hybrides organiques-inorganiques à base d'architectures  $\pi$ -conjuguées et de nanocristaux de semi-conducteurs II-VI, PhD dissertation, Université Joseph Fourier de Grenoble, 2005.
- (8) LaMer, V. K.; Dinegar, R. H. Theory, production and mechanism of formation of monodisperse Hydrosols. *Journal of the American Chemical Society* **1950**, *72*, 4847-4854.
- (9) Reiss, P.; Carayon, S.; Bleuse, J.; Pron, A. Low polydispersity core / shell nanocrystals of CdSe / ZnSe and CdSe / ZnSe / ZnS type  $\square$ : preparation and optical studies. *Synthetic Metals* **2003**, *139*, 649-652.
- (10) Huynh, W. U.; Dittmer, J. J.; Libby, W. C.; Whiting, G. L.; Alivisatos, A. P. Controlling the morphology of nanocrystal-polymer composites for solar cells. *Advanced Functional Materials* **2003**, *13*, 73-79.
- (11) Gur, I.; Fromer, N. a; Chen, C.-P.; Kanaras, A. G.; Alivisatos, A. P. Hybrid solar cells with prescribed nanoscale morphologies based on hyperbranched semiconductor nanocrystals. *Nano letters* **2007**, *7*, 409-14.
- (12) Yu, W. W.; Peng, X. Formation of high-quality CdS and other II  $\pm$ VI semiconductor nanocrystals in noncoordinating solvents:tunable reactivity of monomers. *Angewandte Chemie* **2002**, *114*, 2474-2477.
- (13) De Girolamo, J. Architectures hybrides auto-assemblées a base de systèmes polyconjugués et de nanocristaux de semi-conducteurs pour le photovoltaïque plastique, PhD dissertation, Université Joseph Fourier de Grenoble, 2007.
- (14) Jasieniak, J.; Smith, L.; Embden, J. V.; Mulvaney, P. Re-examination of the size-dependent absorption properties of CdSe quantum dots. *Journal of Physical Chemistry C* **2009**, *113*, 19468-19474.
- (15) Qu, L.; Peng, X. Control of photoluminescence properties of CdSe nanocrystals in growth. *Journal of the American Chemical Society* **2002**, *124*, 2016-2018.

- (16) Reiss, P.; Protière, M.; Li, L. Core/Shell semiconductor nanocrystals. *Small* **2009**, *5*, 154-68.
- (17) Talapin, D. V.; Nelson, J. H.; Shevchenko, E. V.; Aloni, S.; Sadtler, B.; Alivisatos, A. P. Seeded growth of highly luminescent CdSe/CdS nanoheterostructures with rod and tetrapod morphologies. *Nano letters* **2007**, *7*, 2951-9.
- (18) Carbone, L.; Nobile, C.; De Giorgi, M.; Sala, F. D.; Morello, G.; Pompa, P.; Hytch, M.; Snoeck, E.; Fiore, A.; Franchini, I. R.; Nadasan, M.; Silvestre, A. F.; Chiodo, L.; Kudera, S.; Cingolani, R.; Krahn, R.; Manna, L. Synthesis and micrometer-scale assembly of colloidal CdSe/CdS nanorods prepared by a seeded growth approach. *Nano letters* **2007**, *7*, 2942-50.
- (19) Green, M. The nature of quantum dot capping ligands. *Journal of Materials Chemistry* **2010**, *10*, 5797-5809.
- (20) Lin, W.; Fritz, K.; Guerin, G.; Bardajee, G. R.; Hinds, S.; Sukhovatkin, V.; Sargent, E. H.; Scholes, G. D.; Winnik, M. A. Highly luminescent lead sulfide nanocrystals in organic solvents and water through ligand exchange with poly ( acrylic acid ). *Langmuir* **2008**, *24*, 8215-8219.
- (21) Reiss, P.; Couderc, E.; De Girolamo, J.; Pron, A. Conjugated polymers/semiconductor nanocrystals hybrid materials-preparation, electrical transport properties and applications. *Nanoscale* **2010**.
- (22) Aldakov, D.; Chandezon, F.; Bettignies, R. D.; Firon, M.; Reiss, P.; Pron, A. Hybrid organic-inorganic nanomaterials: ligand effects. *The European physical journal Applied Physics* **2007**, *36*, 261-265.
- (23) Borchert, H. Elementary processes and limiting factors in hybrid polymer/nanoparticle solar cells. *Energy & Environmental Science* **2010**, *3*, 1682.
- (24) Kalyuzhny, G.; Murray, R. W. Ligand effects on optical properties of CdSe nanocrystals. *The journal of physical chemistry. B* **2005**, *109*, 7012-21.
- (25) Wang, M.; Oh, J. K.; Dykstra, T. E.; Lou, X.; Scholes, G. D.; Winnik, M. a. Surface Modification of CdSe and CdSe/ZnS Semiconductor Nanocrystals with Poly( N , N - dimethylaminoethyl methacrylate). *Macromolecules* **2006**, *39*, 3664-3672.
- (26) Talapin, D. V.; Lee, J.-S.; Kovalenko, M. V.; Shevchenko, E. V. Prospects of colloidal nanocrystals for electronic and optoelectronic applications. *Chemical reviews* **2010**, *110*, 389-458.
- (27) Puzder, A.; Williamson, A. J.; Zaitseva, N.; Galli, G.; Manna, L.; Alivisatos, A. P. The effect of organic ligand binding on the growth of CdSe nanoparticles probed by ab initio calculations. *Nano Letters* **2004**, *4*, 2361-2365.
- (28) Owen, J. S.; Park, J.; Trudeau, P.-E.; Alivisatos, A. P. Reaction chemistry and ligand exchange at cadmium-selenide nanocrystal surfaces. *Journal of the American Chemical Society* **2008**, *130*, 12279-81.
- (29) Lefrançois, A.; Couderc, E.; Faure-Vincent, J.; Sadki, S.; Pron, A.; Reiss, P. Effect of the treatment with (di-)amines and dithiols on the spectroscopic, electrochemical and electrical properties of CdSe nanocrystals' thin films. *Journal of Materials Chemistry* **2011**, *21*, 11524.
- (30) Munro, A. M.; Ginger, D. S. Photoluminescence quenching of single CdSe nanocrystals by ligand adsorption. *Nano letters* **2008**, *8*, 2585-90.

- (31) Milliron, D. J.; Alivisatos, A. P.; Pitois, C.; Edder, C.; Fréchet, J. M. J. Electroactive surfactant designed to mediate. *Advanced Materials* **2003**, *15*, 58-61.
- (32) Alivisatos, A. P. Perspectives on the physical chemistry of semiconductor nanocrystals. *The Journal of Physical Chemistry* **1996**, *100*, 13226-13239.
- (33) Taylor, J.; Kippeny, T.; Rosenthal, S. J. Surface stoichiometry of CdSe nanocrystals determined by rutherford backscattering spectroscopy. *Journal of Cluster Science* **2001**, *12*.
- (34) Munro, A. M.; Jen-La Plante, I.; Ng, M. S.; Ginger, D. S. Quantitative study of the effects of surface ligand concentration on CdSe nanocrystal photoluminescence. *Journal of Physical Chemistry C* **2007**, *111*, 6220-6227.
- (35) Fritzinger, B.; Capek, R. K.; Lambert, K.; Martins, J. C.; Hens, Z. Utilizing self-exchange to address the binding of carboxylic acid ligands to CdSe quantum dots. *Journal of the American Chemical Society* **2010**, *132*, 10195-201.
- (36) Fritzinger, B.; Moreels, I.; Lommens, P.; Koole, R.; Hens, Z.; Martins, J. C. In situ observation of rapid ligand exchange in colloidal nanocrystal suspensions using transfer NOE nuclear magnetic resonance spectroscopy. *Journal of the American Chemical Society* **2009**, *131*, 3024-32.
- (37) Moreels, I.; Martins, J. C.; Hens, Z. Ligand adsorption/desorption on sterically stabilized InP colloidal nanocrystals: observation and thermodynamic analysis. *Chemical Physics and Physical Chemistry* **2006**, *7*, 1028-31.
- (38) Moreels, I.; Fritzinger, B.; Martins, J. C.; Hens, Z. Surface chemistry of colloidal PbSe nanocrystals. *Journal of the American Chemical Society* **2008**, *130*, 15081-6.
- (39) Schmelz, O.; Mews, A.; Basché, T.; Herrmann, A.; Müllen, K. Supramolecular Complexes from CdSe Nanocrystals and Organic Fluorophors. *Langmuir* **2001**, 2861-2865.
- (40) Hassinen, A.; Moreels, I.; de Mello Donegá, C.; Martins, J. C.; Hens, Z. Nuclear magnetic resonance spectroscopy demonstrating dynamic stabilization of CdSe quantum dots by alkylamines. *The Journal of Physical Chemistry Letters* **2010**, *1*, 2577-2581.
- (41) Ji, X.; Copenhaver, D.; Sichmeller, C.; Peng, X. Ligand bonding and dynamics on colloidal nanocrystals at room temperature: the case of alkylamines on CdSe nanocrystals. *Journal of the American Chemical Society* **2008**, *130*, 5726-35.
- (42) Kuposov, A. Y.; Szymanski, P.; Cardolaccia, T.; Meyer, T. J.; Klimov, V. I.; Sykora, M. Electronic properties and structure of assemblies of CdSe nanocrystal quantum dots and Ru-polypyridine complexes probed by steady state and time-resolved photoluminescence. *Advanced Functional Materials* **2011**, *21*, 3159-3168.
- (43) Winter, A.; Hager, M. D.; Newkome, G. R.; Schubert, U. S. The marriage of terpyridines and inorganic nanoparticles: synthetic aspects, characterization techniques, and potential applications. *Advanced materials* **2011**, *in press*, 5728-5748.
- (44) Hens, Z.; Moreels, I.; Martins, J. C. In situ <sup>1</sup>H NMR study of the trioctylphosphine oxide capping of colloidal InP nanocrystals. *Chemical Physics and Physical Chemistry* **2005**, *6*, 2578.
- (45) Spectral Database for Organic Compounds, S. [http://riodb01.ibase.aist.go.jp/sdbs/cgi-bin/cre\\_index.cgi](http://riodb01.ibase.aist.go.jp/sdbs/cgi-bin/cre_index.cgi).

- (46) Gomes, R.; Hassinen, A.; Szczygiel, A.; Zhao, Q.; Vantomme, A.; Martins, J. C.; Hens, Z. Binding of phosphonic acids to CdSe quantum dots: a solution NMR study. *The Journal of Physical Chemistry Letters* **2011**, *2*, 145-152.
- (47) Shen, L.; Soong, R.; Wang, M.; Lee, A.; Wu, C.; Scholes, G. D.; Macdonald, P. M.; Winnik, M. a Pulsed field gradient NMR studies of polymer adsorption on colloidal CdSe quantum dots. *The journal of physical chemistry. B* **2008**, *112*, 1626-33.
- (48) Huynh, W. U.; Dittmer, J. J.; Alivisatos, A. P. Hybrid nanorod-polymer solar cells. *Science* **2002**, *295*, 2425-7.
- (49) Lokteva, I.; Radychev, N.; Witt, F.; Borchert, H.; Parisi, J.; Kolny-Olesiak, J. Surface treatment of CdSe nanoparticles for application in hybrid solar cells: the effect of multiple ligand exchange with pyridine. *The Journal of Physical Chemistry C* **2010**, *114*, 12784-12791.
- (50) Sun, B.; Greenham, N. C. Improved efficiency of photovoltaics based on CdSe nanorods and poly(3-hexylthiophene) nanofibers. *Physical chemistry chemical physics* □: *PCCP* **2006**, *8*, 3557-60.
- (51) Aldakov, D.; Jiu, T.; Zagorska, M.; de Bettignies, R.; Jouneau, P.-H.; Pron, A.; Chandezon, F. Hybrid nanocomposites of CdSe nanocrystals distributed in complexing thiophene-based copolymers. *Physical chemistry chemical physics* **2010**, *12*, 7497-505.
- (52) Radychev, N.; Lokteva, I.; Witt, F.; Kolny-Olesiak, J.; Borchert, H.; Parisi, J. Physical origin of the impact of different nanocrystal surface modifications on the performance of CdSe / P3HT hybrid solar cells. *Journal of Physical Chemistry C* **2011**, *115*, 14111-14122.
- (53) Jiu, T.; Reiss, P.; Guillerez, S.; De Bettignies, R.; Bailly, S.; Chandezon, F. Hybrid solar cells based on blends of CdSe nanorods and poly(3-alkylthiophene) nanofibers. *IEEE J. Sel. Top. Quantum Electron* **2010**, *16*, 1619-1626.
- (54) Brinkmann, M.; Chandezon, F.; Pansu, R. B.; Julien-Rabant, C. Epitaxial growth of highly oriented fibers of semiconducting polymers with a Shish-Kebab-like superstructure. *Advanced Functional Materials* **2009**, *19*, 2759-2766.
- (55) Olson, J. D.; Gray, G. P.; Carter, S. a. Optimizing hybrid photovoltaics through annealing and ligand choice. *Solar Energy Materials and Solar Cells* **2009**, *93*, 519-523.
- (56) Kovalenko, M. V.; Scheele, M.; Talapin, D. V. Colloidal nanocrystals with molecular metal chalcogenide surface ligands. *Science* **2009**, *324*, 1417-1420.
- (57) Hanrath, T.; Veldman, D.; Choi, J. J.; Christova, C. G.; Wienk, M. M.; Janssen, R. A. J. PbSe nanocrystal network formation during pyridine ligand displacement. *Applied Materials and Interfaces* **2009**, *1*, 244-250.
- (58) Chen, J.; Song, J. L.; Sun, X. W.; Deng, W. Q.; Jiang, C. Y.; Lei, W.; Huang, J. H.; Liu, R. S. An oleic acid-capped CdSe quantum-dot sensitized solar cell. *Applied Physics Letters* **2009**, *94*, 153115.
- (59) Zhou, Y.; Eck, M.; Krüger, M. Bulk-heterojunction hybrid solar cells based on colloidal nanocrystals and conjugated polymers. *Energy & Environmental Science* **2010**, *3*, 1851.

- (60) Querner, C.; Reiss, P.; Sadki, S.; Zagorska, M.; Pron, A. Size and ligand effects on the electrochemical and spectroelectrochemical responses of CdSe nanocrystals. *Physical chemistry chemical physics* **2005**, *7*, 3204-9.
- (61) Saunders, B. R.; Turner, M. L. Nanoparticle-polymer photovoltaic cells. *Advances in colloid and interface science* **2008**, *138*, 1-23.
- (62) Bullen, C.; Mulvaney, P. The effects of chemisorption on the luminescence of CdSe quantum dots. *Langmuir* **2006**, *22*, 3007-13.
- (63) Aldana, J.; Wang, Y. A.; Peng, X. Photochemical instability of CdSe nanocrystals coated by hydrophilic thiols. *Journal of the American Chemical Society* **2001**, *123*, 8844-8850.
- (64) Knowles, K. E.; Tice, D. B.; McArthur, E. a; Solomon, G. C.; Weiss, E. a Chemical control of the photoluminescence of CdSe quantum dot-organic complexes with a series of para-substituted aniline ligands. *Journal of the American Chemical Society* **2010**, *132*, 1041-50.
- (65) Lek, J. Y.; Xi, L.; Kardynal, B. E.; Wong, L. H.; Lam, Y. M. Understanding the effect of surface chemistry on charge generation and transport in poly (3-hexylthiophene)/CdSe hybrid solar cells. *ACS applied materials & interfaces* **2011**, *3*, 287-92.
- (66) Li, S.-S.; Chang, C.-P.; Lin, C.-C.; Lin, Y.-Y.; Chang, C.-H.; Yang, J.-R.; Chu, M.-W.; Chen, C.-W. Interplay of three-dimensional morphologies and photocarrier dynamics of polymer/TiO<sub>2</sub> bulk heterojunction solar cells. *Journal of the American Chemical Society* **2011**, *133*, 11614-20.
- (67) Webber, D. H.; Brutchey, R. L. Ligand exchange on colloidal CdSe nanocrystals using thermally labile tert-butylthiol for improved photocurrent in nanocrystal films. *Journal of the American Chemical Society* **2011**, *in press*.
- (68) Noone, K. M.; Subramaniam, S.; Zhang, Q.; Cao, G.; Jenekhe, S. A.; Ginger, D. S. Photoinduced charge transfer and polaron dynamics in polymer and hybrid photovoltaic thin films: organic vs inorganic acceptors. *The Journal of Physical Chemistry C* **2011**, *115*, 24403-24410.
- (69) Morris-Cohen, A. J.; Vasilenko, V.; Amin, V. A.; Reuter, M. G.; Weiss, E. A. Model for desorption of ligands to colloidal quantum dots with concentration-dependent surface structure. *ACS nano* **2012**, *6*, 557-565.
- (70) Talapin, D. V.; Rogach, A. L.; Kornowski, A.; Haase, M.; Weller, H. Highly luminescent monodisperse CdSe and CdSe / ZnS nanocrystals synthesized in a hexadecylamine – trioctylphosphine oxide – trioctylphosphine mixture. *Nano Letters* **2001**, *1*, 201-211.
- (71) Wolcott, A.; Doyeux, V.; Nelson, C. A.; Gearba, R.; Lei, K. W.; Yager, K. G.; Dolocan, A. D.; Williams, K.; Nguyen, D.; Zhu, X. Anomalously large polarization effect responsible for excitonic red shifts in PbSe quantum dot solids. *Journal of Physical Chemistry Letters* **2011**, *2*, 795-800.
- (72) Luther, J. M.; Law, M.; Song, Q.; Perkins, C. L.; Beard, M. C.; Nozik, A. J. Structural, optical, and electrical properties of self-assembled films of PbSe nanocrystals treated with 1,2-ethanedithiol. *ACS NANO* **2008**, *2*, 271-280.

- (73) Mayer, C. R.; Dumas, E.; Sécheresse, F. 1,10-Phenanthroline and 1,10-phenanthroline-terminated ruthenium(II) complex as efficient capping agents to stabilize gold nanoparticles: Application for reversible aqueous–organic phase transfer processes. *Journal of Colloid and Interface Science* **2008**, 328, 452-457.



# ***Chapter 3. Orientation of P3HT by Directional epitaxial crystallization: process and process improvement***

*This chapter is dedicated to the preparation of highly oriented thin films of regio-regular poly(3-hexylthiophene) by a modified directional epitaxial crystallization(DEC) method that has been adapted from (1). DEC is a method that allows the elaboration of highly oriented and crystalline thin films of polymers and in particular of P3HT. However, the method presented by Brinkmann and Wittmann is not optimized in particular in terms of reproducibility and in-plane orientation over large areas. Herein we will present the improvements of the method that we could achieve by using a local zone melting and guiding substrates like poly(tetrafluoroethylene). The impact of the preparation conditions on the main structural properties of the P3HT thin films will be discussed and illustrated. In a first section the initial DEC method will be presented. In a second part, the main modifications and improvements of the method will be introduced. At last, a small comparative study on the properties of the films grown with the initial and the improved method will be presented.*



# 1. Description of the orientation method and the structure

## 1.1. Principle

Directional epitaxial crystallization (DEC) is a method that allows the preparation of highly oriented thin polymer films. This method was first proposed by Wittmann and Lotz in the early 90<sup>th</sup> and applied by De Rosa *et al.* to grow highly oriented domains of semicrystalline block co-polymers almost 10 years later (2, 3). In 2006, Brinkmann and Wittmann successfully applied this method to poly(3-hexylthiophene) (P3HT) and obtained highly oriented and crystalline P3HT films (1, 2). The DEC method uses crystallisable aromatic solvents that play two roles in the process depending on the temperature  $T$  with respect to the melting temperature of the solvent  $T_m$ . If  $T > T_m$ , the liquid aromatic solvent solubilizes efficiently the polymer. If  $T < T_m$ , the solvent crystallizes from the melt inducing a phase separation from the polymer. As the amount of liquid solvent decreases, the polymer concentration in the solvent increases. Upon a critical concentration  $C_c$ , the polymer starts to aggregate at the surface of the crystallized solvent and is oriented by epitaxy. In brief, the aromatic solvent plays successively the role of solvent in its liquid phase and after crystallization the role of substrate on which the polymer can grow in an oriented way by epitaxy.

To allow this epitaxial growth of the polymer on the aromatic substrate, several conditions have to be fulfilled. These conditions will be illustrated on the example of P3HT crystallized by epitaxy on a substrate of 1,3,5 trichlorobenzene (TCB) as this couple solvent-polymer allows to obtain large areas of highly oriented P3HT (1). The most evident but also important condition is that the polymer has to be soluble in the aromatic solvent in its molten state as it is the case for the solvent-polymer couple TCB-P3HT. Second, as the goal is the fabrication of relatively large areas of oriented thin films, the aromatic solvent has to allow the production of large homogenous and oriented crystalline surfaces of substrate for epitaxy. Therefore, materials crystallizing in the form of oriented platelet-like crystals are particularly suited. TCB, crystallizing from the melt has the ability to form such relatively large oriented platelet crystals. In fact, the TCB crystals have different growth kinetics in the three crystallographic directions. *Figure 1-1* shows a unit cell of a TCB crystal and the preferential growth directions on the temperature gradient of TCB crystals for illustration. The  $c_{TCB}$ -axis, which represents the fast growth direction, grows preferentially parallel to the temperature gradient. Therefore, TCB crystallizing from the melt into platelet crystals is a well suited substrate for the DEC process. The third condition that the solvent-polymer couple has to respect is the possibility of the polymer to grow by epitaxy on the surface of the crystallized solvent. Therefore a matching in the lattice parameters between the crystallizable solvent and the polymer is necessary. The epitaxial orientation of P3HT on 1,3,5 trichlorobenzene (TCB) is possible because of the relationship between the periodicity of the  $c_{TCB}$ -axis and the monomer repeat period of the P3HT backbone ( $c_{P3HT}$ -axis periodicity of P3HT). The 1D epitaxial condition is  $c_{P3HT} \sim 2c_{TCB}$  (mismatch=5%) (1, 4, 5). This accordance in lattice parameters allows a 1D epitaxial orientation of P3HT on the platelet like crystals formed by the TCB with almost no mis-match and thus no mechanical constraints or deformations. And

at last, although this condition is not a must, it is a big advantage if the aromatic substrate can be removed easily leaving behind an oriented thin polymer film on a substrate of choice. TCB having a melting temperature of 63°C is for example easily removed under primary vacuum. The couple TCB-P3HT fulfils all these conditions and is therefore very well suited for the fabrication of highly oriented thin films of P3HT by directional epitaxial crystallization on TCB as it was shown in the literature (4, 5).

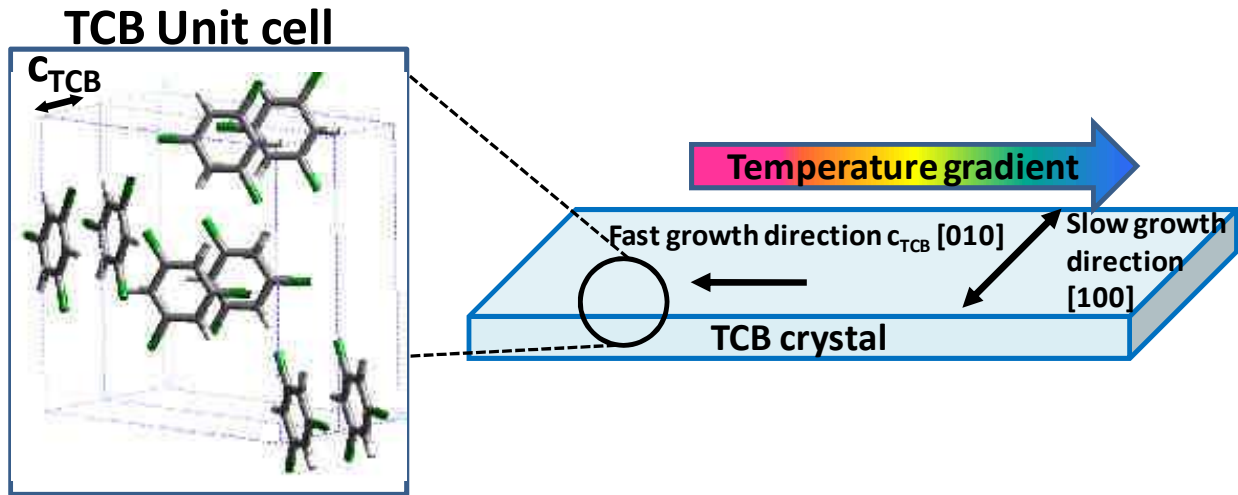


Figure 1-1 : Illustration of the directional crystallization of TCB from the melt. The  $c$ -axis of the TCB crystals grows parallel to the temperature gradient. The anisotropic growth kinetics of the three crystallographic directions allows the fabrication of oriented platelet-like TCB crystals with a specific orientation on the substrate.

## 1.2. Morphology and structure of the oriented P3HT films

Now that the principle of the DEC method is introduced, the main morphological and crystallographic aspects of this P3HT films grown by such a method have to be introduced. The work of Brinkmann *et al.* evidenced very clearly the semi-crystalline character of P3HT oriented by epitaxy on TCB. In thin films prepared by DEC, P3HT grows into a lamellar structure with a periodicity of around 28 nm for a molecular weight of  $M_w \sim 35$  kDa (1, 5). This lamellar structure is composed by an alternation of crystalline and amorphous domains. Figure 1-2 shows the lamellar structure visualized by TEM in the bright field (BF) mode and a corresponding electron diffraction (ED) pattern reproduced from (1). The formation of the lamellar structure can be explained in terms of chain folding and chain endings as it is often observed in semi-crystalline polymers (1, 6, 7). Thus, the polymer chains are well stacked and ordered on a certain length scale forming thus the crystalline part of the film. Chain ends and chain folding give rise to the amorphous inter-lamellar zone. This alternation of amorphous and crystalline phases gives rise to a highly oriented and nanostructured morphology. This nanostructuring can be used for the fabrication of self-organized nanostructured hybrid materials comprising nanoparticles and P3HT (8). It has been demonstrated that the nanoparticles are preferentially located in the amorphous inter-lamellar zones of the oriented

P3HT film. In order to master the structure of the hybrid films, it is essential to understand how to control the growth of thin P3HT films by the DEC method.

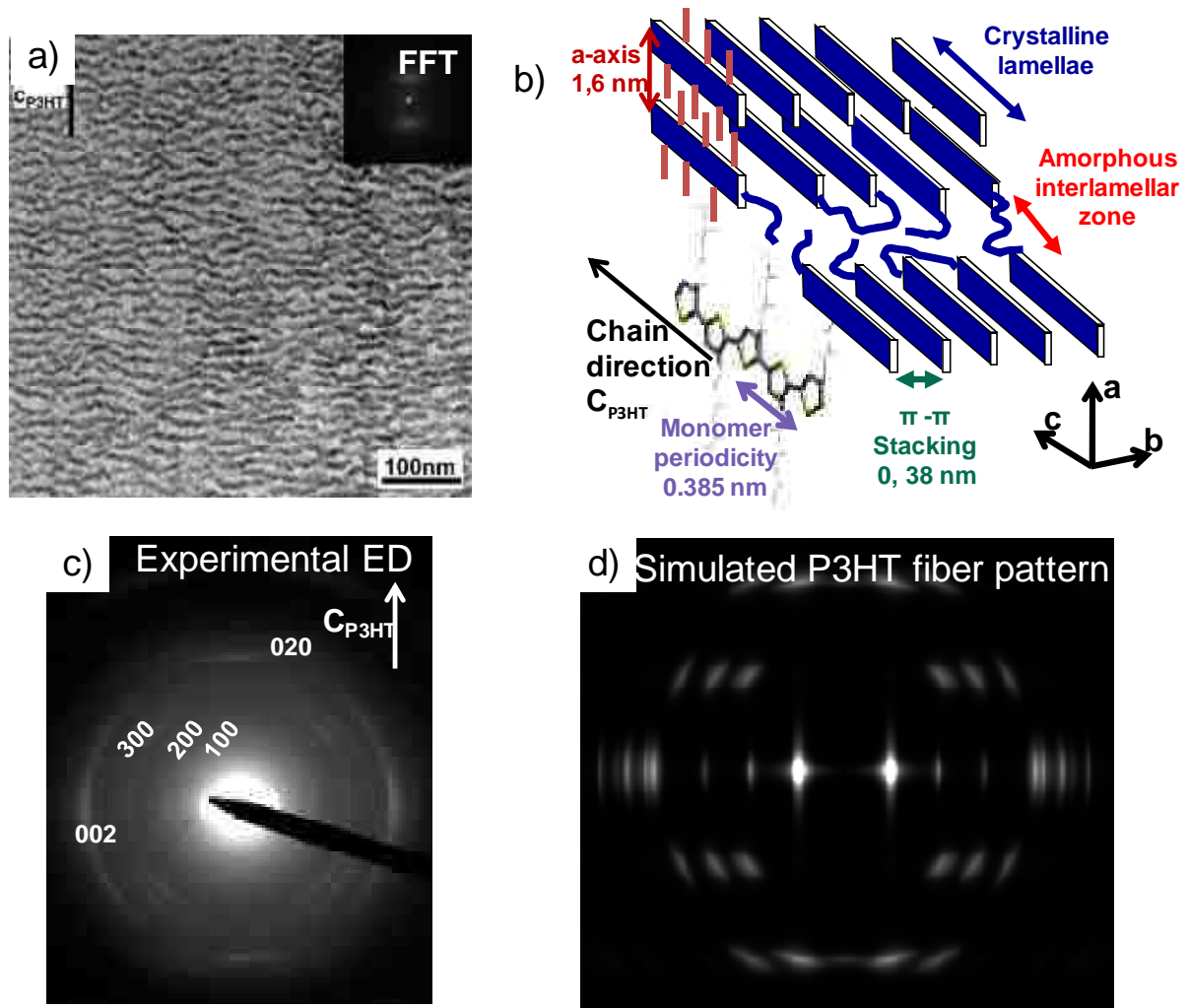


Figure 1-2: (a and c): TEM bright field (TEM-BF) image and corresponding electron (ED) diffraction pattern of a P3HT film grown by directional epitaxial crystallization on TCB. The BF image shows clearly the lamellar structure of the film with alternating crystalline domains (dark) and amorphous interlamellar zones (clear). The ED pattern is a typical fiber pattern. b) schematical representation of the lamellar structure of a semi-crystalline P3HT film and crystallographic directions of the unit cell axes. d) Simulated fiber pattern for a P3HT fiber with  $c_{P3HT}$  as fiber axis Reproduced from (1).

### 1.3. Crystalline structure of P3HT

Before starting the explanation of the electron diffraction pattern obtained by Brinkmann *et al*, the crystallographic directions in the crystalline domains of P3HT and the most typical orientations of the crystalline domains on the substrate described in the literature shall be explained. The unit cell of P3HT as determined recently by Kayunkid *et al*. (9) is monoclinic and contains two polymer chains shifted relatively to each other ( $a_{P3HT} = 1.60$  nm,

$b_{\text{P3HT}} = 0.78 \text{ nm}$ ,  $c_{\text{P3HT}} = 0.78 \text{ nm}$  and  $\gamma = 86.5 \text{ deg}$ ). This shift is enforced by the packing of the *n*-hexyl side chains crystallizing in an orthogonal sub cell. *Figure 1-3* shows the corresponding crystal structure of P3HT along the three crystallographic axes of the unit cell. The definition of the crystallographic directions in the structure of P3HT is the following: the **c-axis** refers always to the P3HT backbone direction. The **b-axis** refers to the  $\pi$ - $\pi$  stacking direction and the **a-axis** corresponds to the *n*-hexyl side-chain direction.

The electron diffraction pattern obtained by Brinkmann *et al.* on epitaxied P3HT films was interpreted as a typical fiber pattern following the work of Tashiro *et al.* (10) and by comparing the experimental ED pattern to a simulated fiber pattern of P3HT. As electron diffraction gives only information about the in-plane diffracting planes, additional proof for this fiber symmetry will be given in Chapter 4 using XRD. The ED pattern in *Figure 1-2* shows on the equator the (h00) (h=1-3) reflections corresponding to the direction along the alkyl side chains (**a<sub>P3HT</sub>-axis**). In addition, a quite intense (020) reflection corresponding to the  $\pi$ - $\pi$  stacking direction (**b<sub>P3HT</sub>-axis**) can be observed on the equator. Along the meridian, the characteristic (002) reflection coming from the monomer repeat unit along the polymer chain is observed.

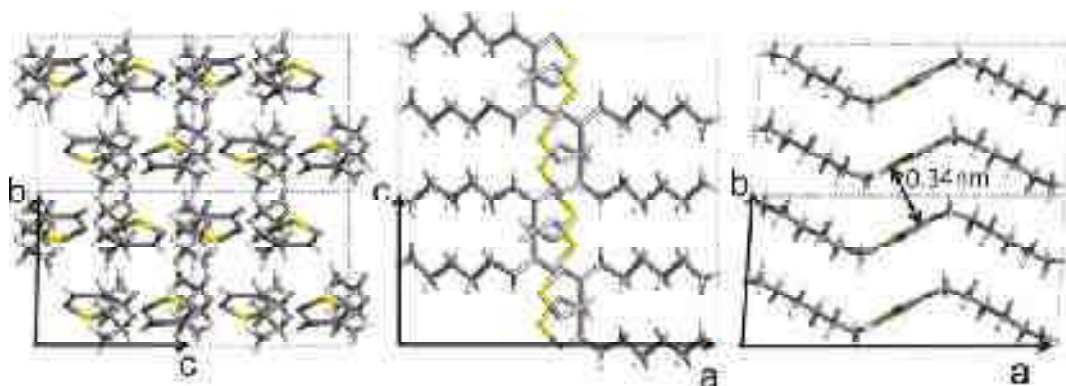


*Figure 1-3: Projections of the crystal structure of P3HT along the  $a_{\text{P3HT}}$ ,  $b_{\text{P3HT}}$  and  $c_{\text{P3HT}}$  axis of the unit cell as determined by Kayunkid *et al.* (9). Reproduced from (9).*

In the literature on P3HT, most authors report that the crystalline phase of P3HT has a preferential contact plane on the substrate (11–14). This contact plane can be either the (100) contact plane or the (010) contact plane or in some cases a coexistence of both. These orientations of the crystalline domains are referred to as “*edge-on*” for the (100) contact plane and as “*flat-on*” for the (010) contact plane. *Figure 1-4* gives a schematical representation of these orientations of the crystalline phase of P3HT on the substrate. The resulting orientation on the substrate depends strongly on the processing conditions be controlled by the processing conditions (15, 16).

In the ED pattern of DEC-oriented P3HT, the coexistence of both (100) and (020) reflections on the equator suggest either the coexistence of “*edge-on*” and “*flat-on*” domains or that the P3HT films have a fiber symmetry (only the **c-axis** is defined by epitaxy). This will be demonstrated in a later section of this chapter.

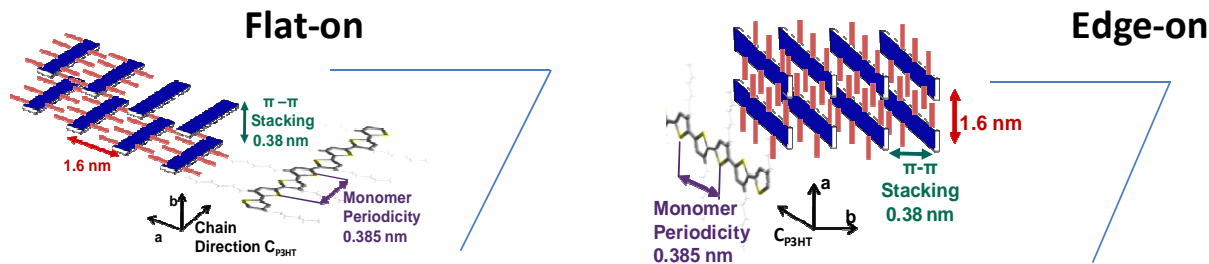


Figure 1-4: Crystallographic directions in the crystalline domains of P3HT, and schematic representation of the “flat-on” and “edge-on” orientations of the crystalline domains on the substrate.

The following paragraph is devoted to the technical description of the directional epitaxial crystallization (DEC) method applied to P3HT (1, 4). Due to its importance for the following study, the initial DEC method will again be presented here. Indeed, in order to grow samples suitable for the study of optical and electrical properties, several aspects of the original method were modified with the aim of obtaining mm<sup>2</sup> surfaces of homogenous oriented P3HT thin films. Therefore it is necessary to introduce in detail the initial method before introducing the modifications that were made.

## 2. The initial DEC process using a Koeffler bench

Figure 2-1 explains schematically the 4 main technical steps that can be distinguished in the original DEC method (4). A thin film of P3HT is prepared by drop casting, spin coating or the doctor blade method, some TCB powder is added on top of the P3HT film and the system P3HT+TCB is sandwiched between a glass slide and a cover slip and placed on the hot part of a Koeffler bench (Temperature higher than the melting temperature of TCB ( $T_m=63^\circ\text{C}$ )). Once all the P3HT is dissolved in the molten TCB, the system is moved manually towards the cold part of the Koeffler bench. Crystallization of the TCB sets in and propagates parallel to the temperature gradient through the entire film surface. As the TCB crystallizes a phase separation between the crystallized TCB and P3HT takes place. The P3HT is rejected to the surface of the crystalline TCB and can grow by epitaxy on the surface of the TCB crystals. In order to recover the highly oriented film of P3HT, the film is placed in a primary vacuum ( $10^{-2}$ mbar) for one night. Once all the TCB is evaporated, the glass slide and the cover slip can be separated easily and on both substrates, a thin film of highly oriented P3HT can be recovered.

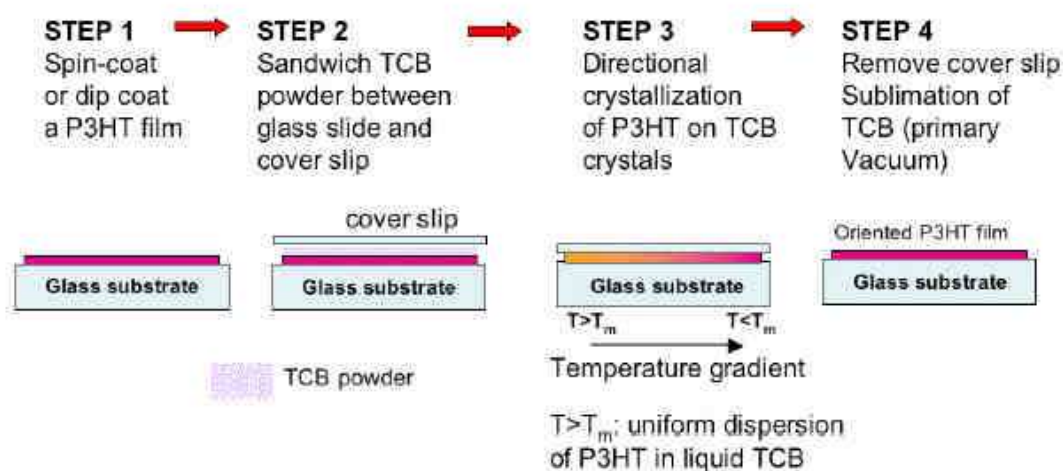


Figure 2-1: Directional epitaxial crystallization (DEC) process as described in (4).

As reported by Brinkmann *et al.* this method allows to grow highly oriented domains of P3HT (1, 4). Although a very high degree of orientation and crystallinity that can be achieved in such films, this method is still far from being useable for future applications in organic electronics. Moreover, further characterizations of the films by UV-vis absorption- and fluorescence spectroscopies and X-ray diffraction measurements remain problematic.

The main problems encountered for these complementary characterizations are:

- The inhomogeneity of the film in terms of film thickness and in-plane orientation
- The quite poor in-plane orientation on a  $\text{cm}^2$  scale, although a high degree of orientation is observed on a scale of several  $10 \mu\text{m}^2$ .
- The thickness of the films is not controlled and therefore not reproducible.
- This method uses glass substrates which are not used for device fabrication.
- Reproducibility of the quality of films due to the manual aspect of the method is lacking.
- Growth kinetics of the films is not controlled precisely as the process is operated manually. The displacement of the sample in the temperature gradient is estimated to be  $>100 \mu\text{m/s}$  and thus very fast.

DEC, applied to conducting polymers is a very powerful technique, but regarding these difficulties, the process has to be improved in order to make some further fundamental studies (optical properties, X-ray diffraction, etc) and to go one step further towards applications in devices. The complete control and reproducibility as well as the extension of highly oriented domains to the  $\text{cm}^2$  scale were a main goal of this thesis. Several attempts were made to reach this point but before modifying the method, the origin of the problems needed to be identified.

As for most techniques dealing with thin films, the quality of the finally obtained result depends very strongly on the quality of the used substrate. Thus, the basis for a high quality P3HT film grown by DEC, is a perfect TCB substrate for epitaxy. The above cited

problems are mainly due to the imperfections of the TCB substrate. *Figure 2-2* shows a polarized optical microscope (POM) image with crossed polarizers of a TCB (without P3HT) film grown by directional crystallization on a Koeffler bench.

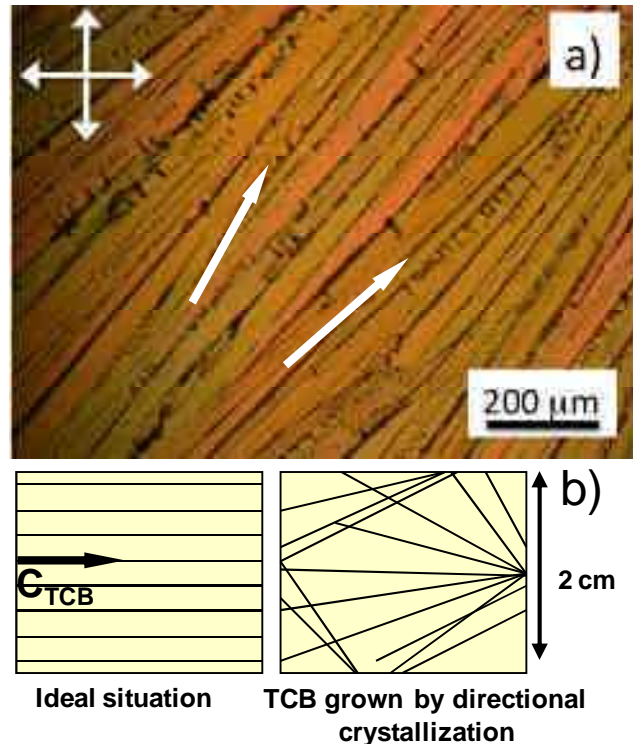


*Figure 2-2: a) POM image under crossed polarizers of a TCB film grown by directional crystallization on a Koeffler bench (9). Note the misorientation of some TCB crystals indicated by the arrows and the important amount of grain boundaries. b) Schematic illustration of the ideal situation and the TCB growth by DEC on a  $cm^2$  scale. Black lines illustrate grain boundaries.*

This image illustrates already two points that can be improved. First of all, many grain boundaries can be distinguished and second, as indicated by the arrows, adjacent crystals are not well aligned leading to a poor in-plane orientation.

The growth rate of TCB crystals is uncontrolled and quite fast due to the manual translation of the sample from the hot part of the Koeffler bench to the cooler part where crystallization sets in. Moreover, no control over the nucleation density of the TCB domains is achieved. In fact, nucleation and crystal growth are not well separated in time and take place simultaneously. The relatively reduced in-plane orientation can partially also be attributed to the absence of a well defined in-plane growth direction of TCB.

As mentioned before, the TCB crystals are preferentially oriented with the  $c_{TCB}$ -axis ( $c_{TCB}$ ) axis parallel to the thermal gradient and allow thus the growth of an oriented system. However, due to the fast translation of the sample, a quite large number of TCB crystals are growing from the edges of the glass slides and inducing a poor in-plane orientation. The in-plane orientation is often already disturbed at the very beginning of the crystallization process of the TCB by crystals growing in a “star like” way (See *Figure 2-2 b*). *Figure 2-2 b* shows schematically the situation of the in-plane orientation in the case of an ideal TCB substrate.

The ideal situation would be to have extended platelet-like crystals and a low number of grain boundaries. In addition, a perfect in-plane orientation of all platelet like TCB crystals is highly desired. To reach these objectives a combination of two approaches is proposed:

i) For an accurate control of the crystal growth kinetics, a motorized system for the controlled displacement of the growth front is essential. Such a system allows at the same time a substantial slowing down of the growth kinetics. This allows reducing the number of grain boundaries, by reducing the nucleation density. In fact, slowing down the crystal growth kinetics allows a decoupling of the nucleation and the crystal growth. Nucleation occurs at the cold end and from there crystals grow slowly at a rate equivalent to the displacement speed of the melting apparatus. A similar approach was proposed recently for the growth of single crystals of terthiophe by Schweicher *et al.* (17) and was also used by Bard *et al.* for the growth of single crystals of organic molecules (18). At the same time, this approach allows to reduce the number of TCB crystals growing from the edges.

ii) For an improved in-plane orientation, the introduction of a guiding substrate was chosen.

In the following, these two points will be discussed and the results on the improvement of the TCB substrate presented. After, the impact of these modifications on the directional epitaxial crystallization of P3HT on TCB will be studied.

### **3. Improvement of the Method: Towards a perfect TCB substrate**

#### **3.1. Reduction of the grain boundaries: Control of the growth kinetics and local melting**

As already mentioned directional crystallization is used to prepare oriented TCB films. TCB crystallizes from the melt undergoing a phase transition from its liquid to crystalline state. During this transition two processes take place: the nucleation and the crystal growth. The first step towards high quality TCB substrates is the reduction of grain boundaries and therefore the nucleation density has to be reduced. This is possible by separating the nucleation and the crystal growth. A first step in this sense was done by slowing down the growth rate and the introduction of an accurate control of the crystallization kinetics of TCB crystals. As seen in *Figure 3-1*, the translation of the sample from a hot part to a cooler part is now performed by a motorized system allowing the control of the translation speed with an accuracy of  $\pm 0.1 \mu\text{m/s}$  (see Annexe 2).

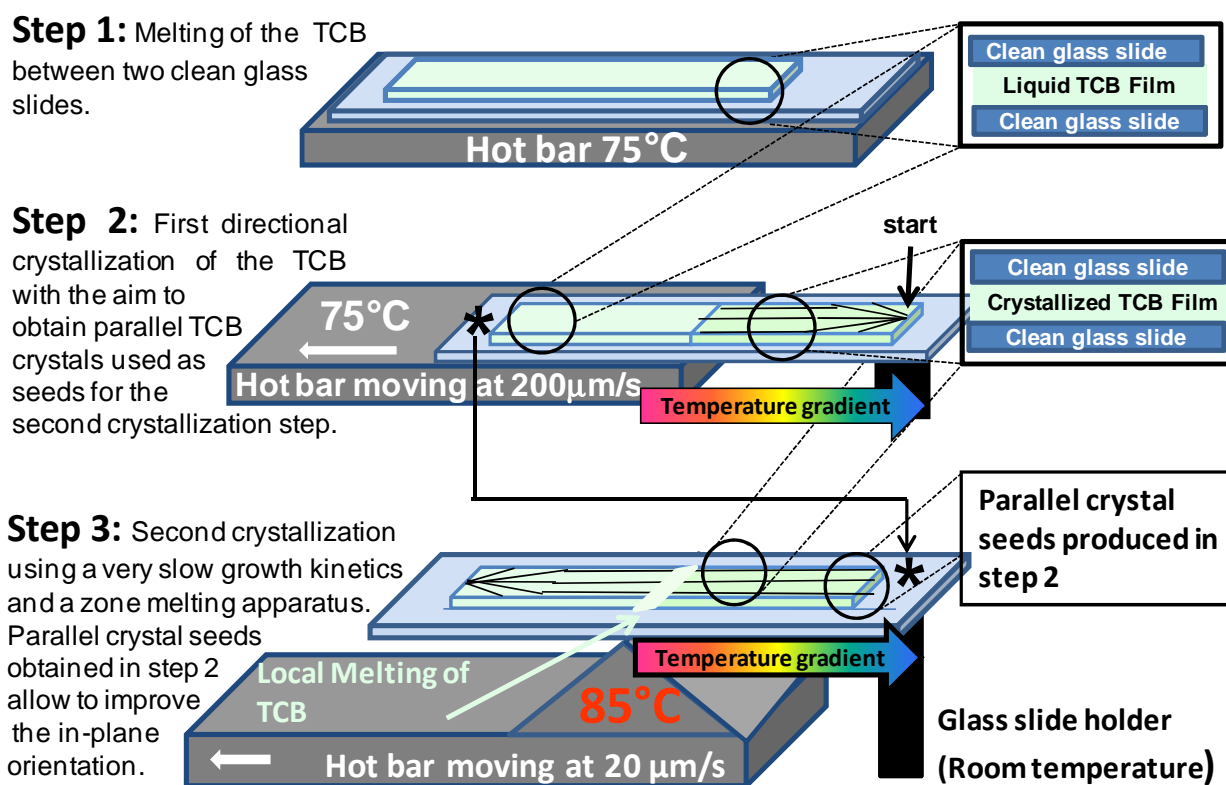


Figure 3-1 : Illustration of the setup and involved steps used for directional crystallization of TCB in a temperature gradient.

A first step in this sense was already done by Kayunkid *et al.* (9). The motorized system used here, allows the constant translation of the growth front of TCB crystals at a speed as slow as 4  $\mu\text{m/s}$ . A speed of a few  $10^{-1}\mu\text{m/s}$  up to a few  $\mu\text{m/s}$  seems to be usual for directional crystallization of organic molecules in a thermal gradient (17–19). The temperature gradient used in our setup can only be estimated very approximately to 15°–20°C/mm. Schweicher *et al.* (17) used temperature gradients in the same range of magnitude (10°C/mm and 20°C/mm). Regarding the choice of an adequate growth rate, no important differences in the TCB film quality were observed by changing the translation speed of 4  $\mu\text{m/s}$  to 20  $\mu\text{m/s}$ . This is the reason why in the following the translation speed of 20  $\mu\text{m/s}$  was chosen for reasons of time saving. In fact, it takes 40 min to grow a 5 cm long P3HT film at a rate of 20  $\mu\text{m/s}$ .

A second step to decouple the nucleation from the crystal growth is performed by a repeated passage in the temperature gradient. Indeed, the TCB is crystallized in 2 steps. The first step is performed at a speed of 200  $\mu\text{m/s}$ . This first crystallization generates well aligned TCB crystals at one end of the glass slide. These parallel TCB crystals will be used as crystal seeds for the second slow crystallization step. Thus, during the final crystallization step performed at a speed of 20  $\mu\text{m/s}$ , the TCB crystals start growing directly from the parallel seeds produced during the first rapid crystallization. Figure 3-1 illustrates the double passage of the TCB in the thermal gradient.

The second main modification is introduced as a direct consequence of the very slow translation speed. In fact, at 20  $\mu\text{m/s}$  evaporation of the TCB during the slow translation over the 5 cm long sample occurs. This gives rise to inhomogeneous films in terms of thickness in particular if the method is applied to P3HT as the concentration of P3HT will not be constant due to the evaporation of the TCB during the process. Also, it is not possible to produce large areas of films (several  $\text{cm}^2$ ) as once the TCB is evaporated; no TCB is available to form a substrate for epitaxy. To solve this problem, the hot zone (corresponding to the TCB in molten state) is limited to a 1-2 mm broad stripe. The experimental setup is illustrated in *Figure 3-1*. An exact scheme of the experimental setup is presented in the supporting information in Annexe 1. This experimental setup can be compared to a local zone melting method used to grow single crystals of conjugated molecular materials (18).

The double passage in the temperature gradient and the accurate control of the TCB crystal growth front improves the quality of the TCB substrate in 2 points. First, the nucleation and the crystal growth are decoupled resulting in a reduced number of grain boundaries. Second, as the final crystallization of the TCB crystals starts from crystal seeds that are already well in-plane aligned, the final in-plane orientation after slow growth is also improved. However, to further improve the in-plane orientation, other modifications of the growth setup are necessary. For example using rectangular substrates with higher aspect ratios ( $L/l$ ) would help further reducing the distributions of in-plane directions of the TCB crystals.

### **3.2. Improvement of the in-plane orientation: Introduction of a guiding substrate of PTFE**

To further improve the in plane orientation of the TCB crystals, two additional improvements were made. These modifications are less on the experimental setup but much more on the choice of the right coatings for the glass slides and the choice of an adequate geometry for the films. Regarding the geometry, a high aspect ratio of the upper glass cover slide turned out to improve the quality of the in-plane orientation. To improve the in-plane orientation of the TCB, we used 5mm x 5cm ( $L/l=10$ ) cover slips. The long side ( $L$ ) of the slides was aligned parallel to the growth direction. Using these high aspect ratio glass slides allow to select the TCB crystals that grow preferentially along the long edge ( $L$ ) of the slide as shown in *Figure 3-3*. The growth of the TCB crystals directed towards the lateral edges of the slides will be stopped at an early state regarding the crystallization of the entire film. This high aspect ratio is in particular very helpful for the creation of parallel crystal seeds during the first crystallization step (as explained above).

The second and crucial step towards a perfect in-plane orientation is the introduction of an orienting substrate of poly(tetrafluoroethylene) (PTFE) obtained by friction transfer following the work of Wittmann and Smith (20). *Figure 3-2* shows an AFM phase mode image of such a PTFE film. The film morphology shows a fibrillar structure with long PTFE fibers presenting a thickness of less than 50 nm. The chain axis of the PTFE polymer is oriented parallel to the friction direction. The AFM image shows that the coverage of the glass slide by the PTFE is incomplete leaving areas of the bare glass slide. The very high

orientational effect of PTFE on organic molecules has been reported by numerous authors (21).

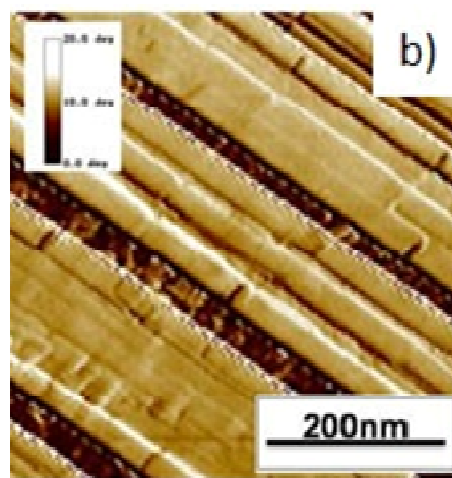


Figure 3-2 : AFM image of a PTFE film prepared by friction transfer. Reproduced from reference (20).

For example epitaxial orientation on PTFE substrates was described in the case of oligomers of phenylenevinylene (21), sexithiophenes (22), poly(p-oxybenzoate) (23). However, the role of the PTFE substrate in this work cannot be compared to the cited examples because the improved in-plane orientation of TCB crystals grown on PTFE is not ascribed to an epitaxial effect of the TCB crystals on the PTFE substrate. The important aspect of the PTFE film is much more its fibrillar morphology and in particular the topography of the PTFE that plays the role of guiding rails for the TCB crystals and so TCB grows along a preferred in-plane direction parallel to the PTFE chain direction. It is so more comparable to what was observed in the case of Zinc phthalocyanine on a Polycarbonate substrate in reference (24) or some dye molecules in reference (25), *i.e.* a grapho-epitaxial effect.

In the scope of the improvement of the in-plane orientation of the TCB crystals, a PTFE film prepared by friction transfer is a cheap and easy way to get a micro patterned substrate that could probably also be prepared by very complicated and expensive techniques such as lithography. The combination of the use of a coverslide with a high aspect ratio and the use of an orienting substrate of PTFE allow for the fabrication of a high quality TCB substrate presenting large areas of highly oriented platelet-like crystals of TCB. Figure 3-3 shows a POM image of a TCB film grown by a 2 step crystallization process with the second crystallization performed at 20  $\mu\text{m/s}$  on a PTFE guiding substrate. The improvement compared to the POM image shown in Figure 2-2 is obvious. Much less grain boundaries are observed and the in-plane orientation on a scale of several  $\text{mm}^2$  is perfect.

Now, that the TCB substrate grown by directional crystallization shows large uniformity in terms of in-plane orientation and a low number of grain boundaries, the method can be applied to the orientation of P3HT.

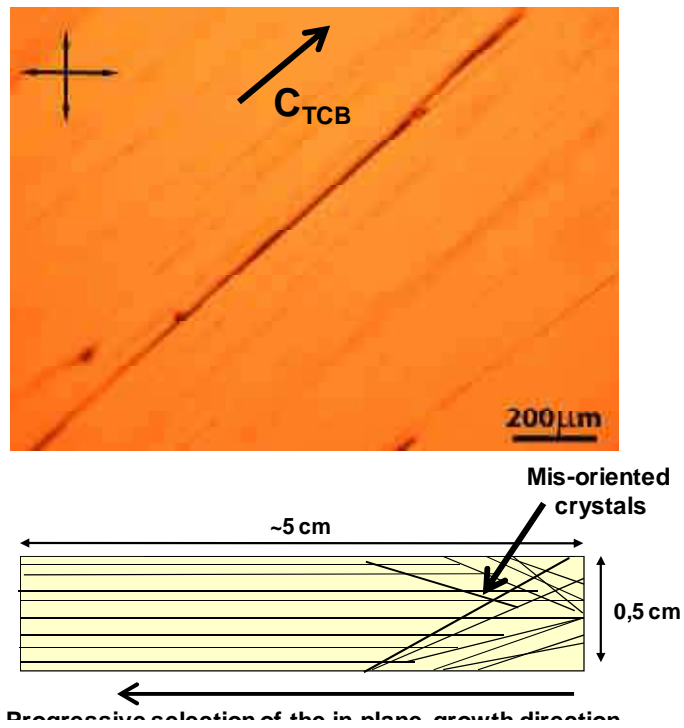


Figure 3-3: illustration of the impact of the aspect ratio on the in-plane orientation of a TCB film and POM image of highly oriented pure TCB grown by slow-DEC. As compared to the POM image of TCB grown by the initial DEC method, the large improvement of the uniformity and the grain boundaries can be clearly observed.

The influence of the improvement of the TCB substrate will now be applied to the directional epitaxial crystallization of P3HT on TCB. In particular, we will focus mainly on the impact of the translation speed of the growth front of the TCB crystals on the quality of the P3HT films.

#### 4. Application to P3HT

A study on the influence of the growing speed of the TCB crystal growth front on the quality of the finally obtained P3HT films was carried out. The process for the preparation of highly oriented P3HT thin films by epitaxy on TCB is similar to the preparation of highly oriented TCB films with the difference that the process is started with a mixture of P3HT and molten TCB. ( *Figure 6-1* shows all the steps involved in the process)

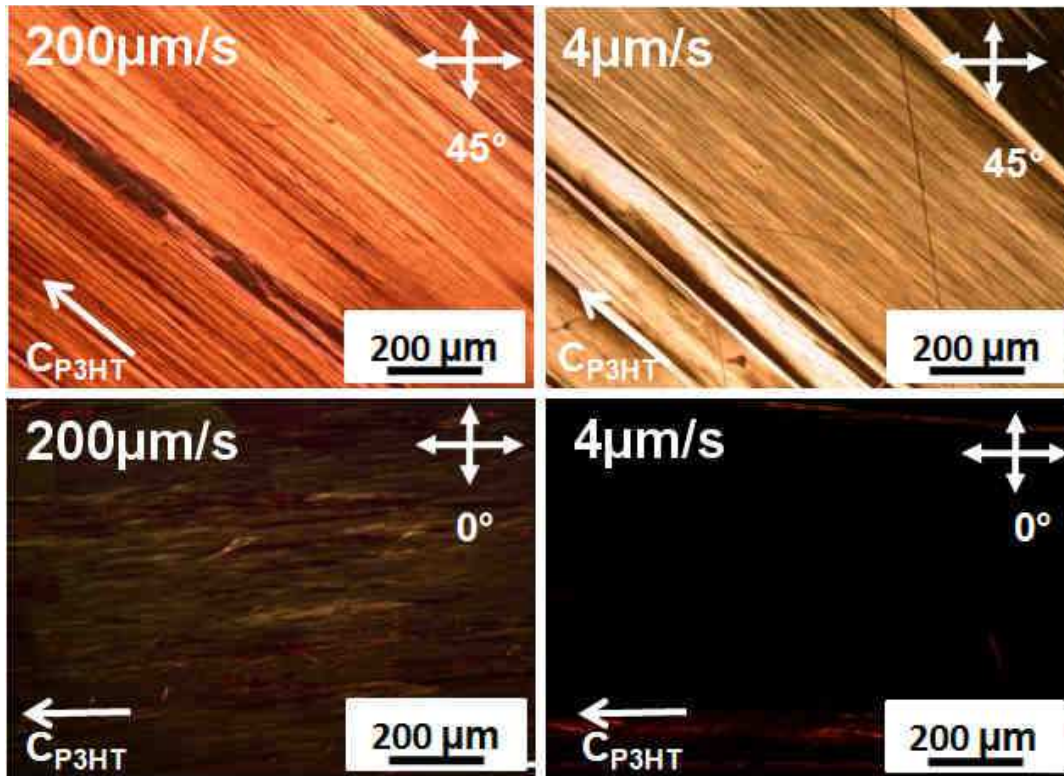


Figure 4-1 : POM image of a 50 kDa P3HT thin films grown at 200  $\mu\text{m/s}$  and 4  $\mu\text{m/s}$  respectively. The Influence of the translation speed of the TCB crystallization front on the quality of the finally recovered P3HT films is clearly evidenced.

Figure 4-1 shows the POM images of two films, the first grown at a speed of 200  $\mu\text{m/s}$  and the second at a speed of 4  $\mu\text{m/s}$ . In the case of a perfectly oriented system without any orientational defect, a POM image with one of the polarizers parallel to the polymer chain should show a complete extinction. All clear spots that can be observed in this case correspond to defects (mainly misaligned domains). For the P3HT film grown at 4  $\mu\text{m/s}$  the extinction is almost perfect when the polymer chains are parallel to one of the polarizers, except for some parts of the film that appear red and can be identified as the thicker parts. In contrast to this, the P3HT film grown at 200  $\mu\text{m/s}$  shows a multitude of orientational defects. The growth rate plays thus an important role also for the perfect orientation of the P3HT. The improvement of the orientation of the films prepared at a lower growth rate can probably be attributed to the perfect in-plane orientation of the TCB substrate. But at the same time it is possible that these improvements are also intrinsic to the crystallization of the P3HT which has much more time to grow in an oriented and well crystallized phase in the case of a slow growth rate.

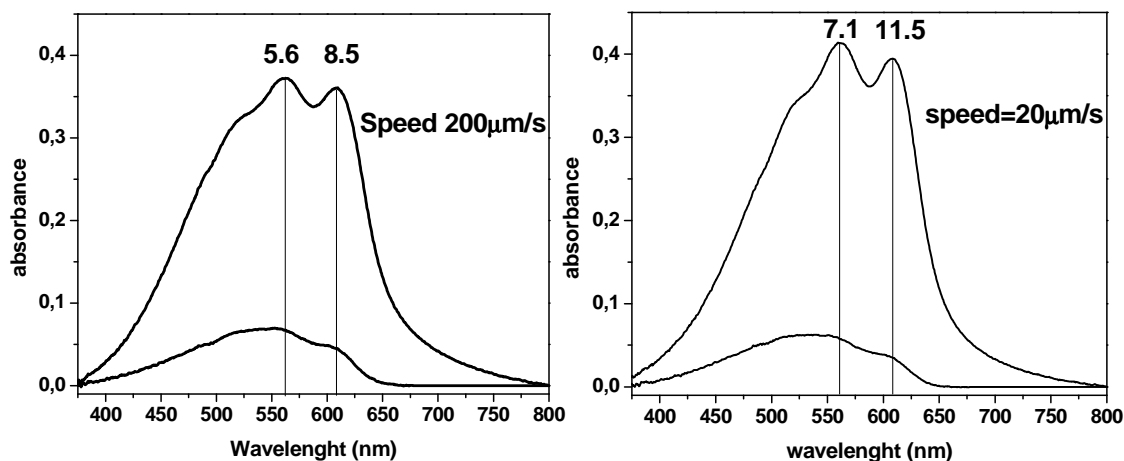


Figure 4-2 : Polarized absorption spectra of a film grown fast and slowly. The numbers above the components of the vibronic structure correspond to the dichroic ratios at those wavelengths. The vibronic structure is better defined for films grown with a low speed.

This hypothesis is further supported by the differences that can be observed in the polarized absorbance spectra of films grown at  $20 \mu\text{m/s}$  and at  $200 \mu\text{m/s}$ . Figure 4-2 shows the corresponding polarized UV-vis absorption spectra. The absorbance in the perpendicular direction of the polarization comes essentially from the amorphous and misoriented areas of the sample. Comparing the absorbance of these two films grown at different growth rates, shows differences essentially in two points. First, the maximum dichroic ratio observed in the film grown slowly is higher (11.5 at 610 nm) than that obtained for the film grown at  $200 \mu\text{m/s}$  (8.5 at 610 nm). This observation is in line with the results obtained by POM. Second, the vibronic structure is better defined in the film grown at a slow rate ( $20 \mu\text{m/s}$ ) indicating a higher degree of order and higher crystallinity. It is this improved vibronic structure that underlines the influence of the growth on both, the crystallinity and the chain packing of the P3HT. Due to the slower crystallization rate, a higher degree of crystallization can be achieved.

Below  $v=20 \mu\text{m/s}$  no significant difference in terms of the film quality could be evidenced. Thus, for reasons of time saving the speed of  $20 \mu\text{m/s}$  was chosen as standard and all films analyzed hereafter were grown at  $v=20 \mu\text{m/s}$ . Owing to the very slow translation rate, the improved DEC method will be called **Slow-DEC** in the following. A more detailed description of the motorized system used is given in Annex 3.

Although these achievements are of great importance and allow growing highly oriented films of P3HT on a  $\text{cm}^2$  scale, every modification brings in new constraints. This is especially true when the slow-DEC method has to be applied to a different substrate than glass as for example  $\text{SiO}_2$ .

In this perspective a systematic study was performed by testing various substrates such as PEDOT:PSS used in organic solar cells or PVP used as gate dielectric in organic field effect transistors. Some other substrates such as silicon wafers were tested in view of further

fundamental studies on the films for example by X-ray diffraction and the fabrication of organic field effect transistors.

## 5. Ideal substrates for uniform and extended P3HT films

When used in the previous configuration, two films of P3HT are recovered, one on the PTFE substrate and a second on the glass substrate. As a matter of fact, the uniformity of the recovered films is good on PTFE but poor on the bare glass slide. Accordingly, different attempts were made to improve the quality of the P3HT film on the glass. In fact, the PTFE substrate is not very adapted due to its high surface roughness and because there is no use of such PTFE films in terms of applications. In this matter, various attempts were made to enhance the uniformity of the P3HT film on the opposite glass slide of the PTFE by playing on the adhesion of the P3HT film on the substrate. Accordingly coating this glass slide with polymeric substrates or using flexible ITO substrates was attempted. Also transfer the method to silicon wafers with the aim of preparing OFETs and for performing XRD measurements was examined.

### 5.1.1. Attempts on silicon substrates

The initial plan of our work was to transpose the slow-DEC method to Si(100) substrates so as to fabricate OFETS with highly oriented layers of P3HT and for the preparation of highly oriented P3HT samples for X-ray diffraction measurements. This approach turned out to be impossible because of the very high thermal conductivity of the silicon wafers. In fact, local melting is impossible and even by increasing considerably the temperature gradient by cooling down the cold sample holder with liquid nitrogen, the temperature control necessary obtain local melting and a uniform propagation of the crystallization front appeared to be difficult to achieve. Not only does the thermal gradient of the substrate plays a crucial role for the successful production of homogenous highly oriented thin films of P3HT, but also the adherence of the P3HT film on the desired substrate. The direct transfer of the slow-DEC process to Si(100) substrates was not only hindered by the high thermal conductivity but also by the poor adherence of the P3HT on the silicon wafer. Thus, after evaporation of the TCB, the recovered P3HT films are homogenous on the side of the PTFE substrate but happened to be very discontinuous on the side of the silicon wafer. The unsuccessful transfer of the process to silicon wafers made it necessary to develop other solutions for the fabrication of OFETs or samples for X-ray diffraction.

Ideal substrates must fulfil two main conditions: i) a high adherence of the thin P3HT films i.e. better than that on PTFE. ii) the substrates must be suitable for future device applications and sample characterization. And at last, ease in processing of the substrate is highly desired.

### 5.1.2. Growth on polymeric substrates

Various polymeric substrates were chosen with the purpose of modifying the surface energy of the glass substrate to increase the adherence of the thin P3HT film on the polymeric substrate. A systematic study was carried out to determine substrates allowing the fabrication of homogenous films. For each type of substrate, 5 films were prepared to obtain an idea of the reproducibility. For reasons of time, it was not possible to carry out a more accurate statistics by increasing the number of films per type of substrate. However the substrates that turned out to be very useful during this study were often used hereafter for the sample preparation. The reproducibility turned out to be very satisfying although the initial study was performed on a quite low quantity of films (only 5). All the tested polymer substrates were deposited by spin coating on a clean glass slide. Details about the processing procedures are given in Annexe 4. The chemical structures of the used polymers can be found in *Figure 5-1*.

Water soluble polymers are a first choice because they allow a very easy transfer from the polymer coated glass to any other desired substrate as for example TEM grids or Silicon wafers. Highly uniform films were obtained on hydro-soluble polymers such as PEDOT:PSS, or polycyclic acid. Whereas PEDOT:PSS is also used frequently in the domain of organic photovoltaics, polyacrylic acid is interesting only for the ease of transfer of the thin P3HT film to another substrate.

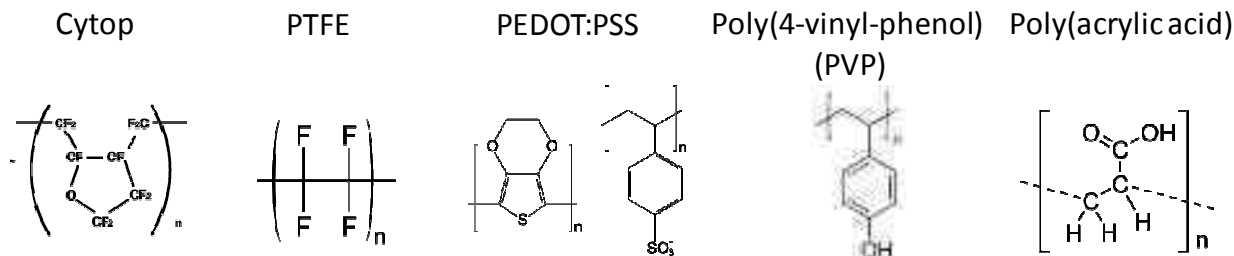


*Figure 5-1 : Chemical structure of the polymers used as substrate.*

Polymers often used as gate dielectrics in organic field effect transistors as for example poly(4-vinylphenol) (PVP) or the fluorinated polymer commercialized under the name of Cytop turned out to be very suitable to generate homogenous thin films of P3HT.

Interestingly, the films seem to have always a better adherence and show a higher homogeneity if the polymer substrate (or PTFE substrate) is in direct contact with the hot bar of the zone melting apparatus (lower slide). This study was also performed on 10 films per substrate and by varying the side of the coating (5 films with upper glass slide coated by a polymer film and the lower glass slide coated by PTFE and 5 films where the lower glass slide was coated by the polymer film and the upper glass slide coated by the PTFE substrate). This can probably be explained by the fact that the TCB starts crystallizing from the upper and colder glass slide. Therefore, the P3HT is rejected towards the lower glass slide where a better adherence of the films can be observed after the evaporation of the TCB.

In the following, all the samples were thus prepared by coating the lower glass slide (big glass slide) with a polymer and by coating the upper glass slide (small glass slide) with the PTFE substrate. As mentioned above a schematic representation of the film preparation method is given in *Figure 6-1* and a step by step description with all experimental details can be found in Annexe 1.

5.1.3. **Recapitulation:**

*Table 5-1* summarized the main results concerning the influence of the chemical nature of the substrates on the homogeneity of the obtained P3HT films. Possible applications related to the substrate are also presented. This study shows that the use of polymeric substrates is definitely the most successful as for obtaining homogenous thin P3HT films on the cm<sup>2</sup> scale. The observed trends indicate that either hydrophobic or hydrophilic substrates generate homogenous films. For both kind of polymer coatings highly homogenous films were obtained (example PEDOT:PSS and Cytos).

Substrate	Quality of the film	Uniformity	Possible application
glass	Not uniform	< mm <sup>2</sup>	OFET in inverted geometry
PTFE	No control of the film thickness because of roughness of the substrate	mm <sup>2</sup>	
Si (100)	Method not transferable to silicon wafers	< mm <sup>2</sup>	OFET, X-ray diffraction
Polyacrylic acid	Good	< mm <sup>2</sup>	Hydro-soluble: Easy transfer to other substrates
PEDOT:PSS	excellent	~ cm <sup>2</sup>	Hydro-soluble: Easy transfer to other substrates. Useful for solar cells
Cytos	excellent	~ cm <sup>2</sup>	OFETs
P-4VP	excellent	~ cm <sup>2</sup>	OFETs
OTS treated glass	Not uniform	< mm <sup>2</sup>	
ITO on PET	Not uniform	< mm <sup>2</sup>	

*Table 5-1: Influence of the chemical nature of the substrate on the oriented P3HT film uniformity.*

## 6. The final slow-DEC process

Figure 6-1 shows step by step the preparation of highly oriented P3HT thin films by the slow-DEC method by making use of the improved method for the preparation of an ideal TCB substrate and by coating the glass slides as explained above. The following study will be focused on the macroscopic and microscopic morphology of thin P3HT films grown by the slow-DEC method. Also the crystalline order and the optical properties of such films will be presented. For the TEM an XRD analysis, films were prepared on a PEDOT:PSS substrate and transferred either to TEM copper grids or to silicon wafers. For optical measurements the transparent PVP substrate was chosen.

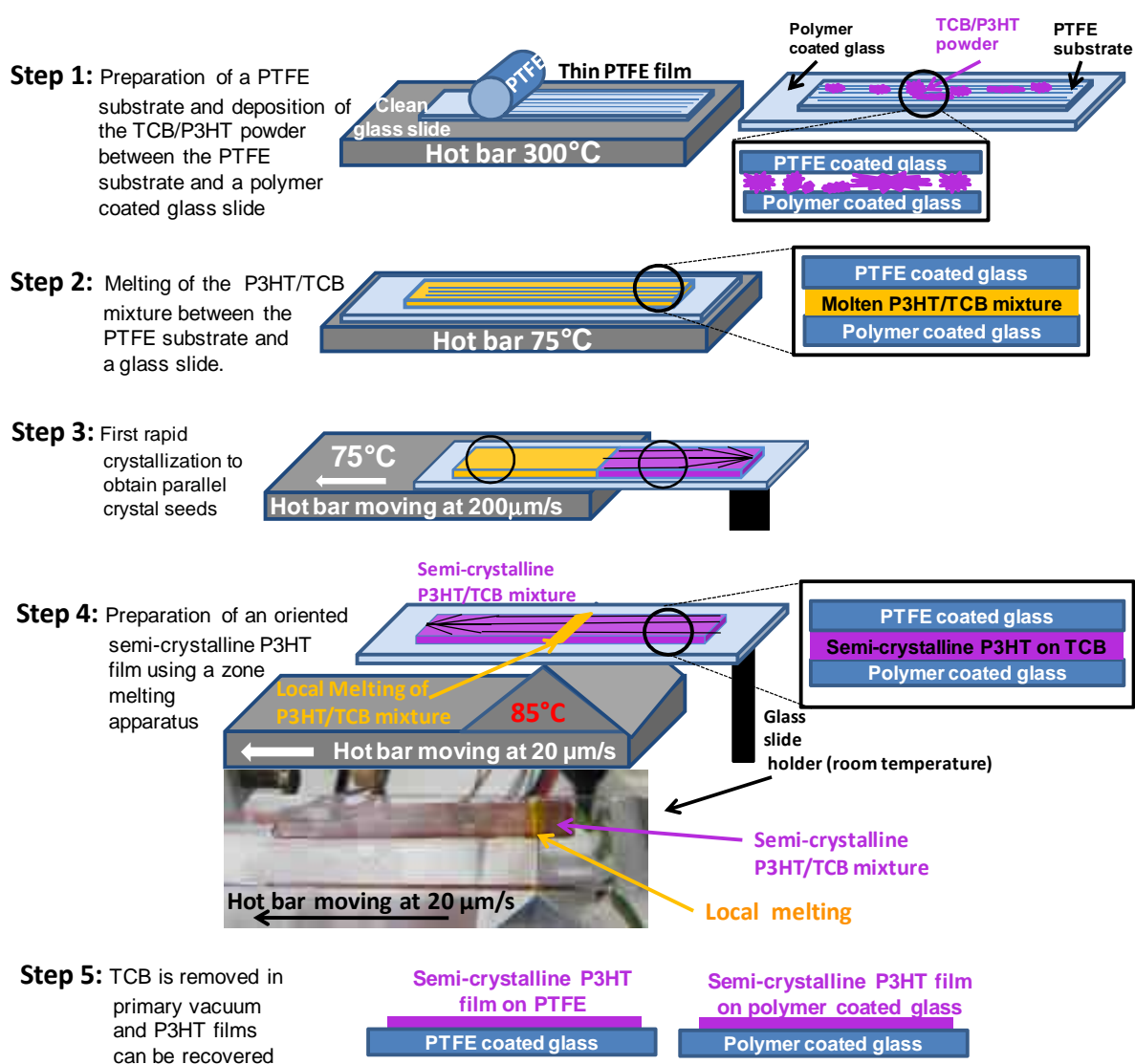


Figure 6-1 : Schematic description of the different steps involved in the slow rate directional epitaxial crystallization of P3HT (slow-DEC). The process makes use of an orienting PTFE substrate, a controlled growth rate that allows for a local zone melting over a ~2mm large stripe.

## 7. DEC versus slow-DEC: In-plane orientation and lamellar structure

The improvements achieved on a macroscopic scale by passing from the initial DEC method to slow-DEC were illustrated above. Herein, we were interested to understand if the modifications of the process and more specifically the very slow growth kinetics, affect the nanomorphology, the crystallinity and the in-plane orientation of P3HT thin films.

TEM was largely used to characterize P3HT thin films grown by the initial DEC method (1, 4, 9, 26). Therefore it is interesting to evaluate the impact of the growth kinetics and preparation conditions on the morphology and orientation as observed by TEM.

Figure 7-1 (left) shows a TEM-BF image and the corresponding electron diffraction (ED) pattern of a P3HT sample prepared by the slow-DEC method. Figure 7-1 (right) shows the TEM-BF image and the corresponding ED pattern of a sample of equivalent molecular weight grown by the initial DEC method on a Koeffler bench (1). The azimuthal angular distributions of (100) reflections of both samples were extracted from the ED patterns. This azimuthal distribution reflects the degree of in-plane orientation of the **a**-axis in the thin films.

Regarding the TEM-BF images it can be concluded that in terms of morphology, both the DEC and the slow-DEC samples show clearly the presence of an oriented lamellar morphology. The lamellar structure seems quite similar for both samples but to get a more quantitative evaluation, the lamellar periodicities were determined for both images from their respective FFTs. The slow-DEC sample yields a lamellar periodicity of 35 nm vs a lamellar periodicity of the initial DEC sample of 25-28 nm (4). Therefore it seems that the lamellar periodicity is modified to a certain extent by the important reduction of the growth rate. This observation suggests that a slower kinetics favours the growth of extended segments of P3HT by epitaxy.

Regarding the ED patterns, they both look quite similar at a first view. A more detailed look reveals however significant differences. First, the azimuthal distribution of the (100) reflection of the slow-DEC sample yields a FWHM= 21° as compared to a FWHM= 37° for the sample prepared on a Koeffler bench. This indicates a better in-plane orientation on a microscopic scale of the P3HT domains for the slow-DEC method compared to the DEC method on a Koeffler bench. This improvement of the in-plane orientation can probably be attributed to the improvement of the in-plane orientation of the TCB substrate by the introduction of a guiding PTFE layer and also by decoupling the nucleation from the TCB crystal growth.

A further difference between the ED patterns of the slow-DEC and the DEC method concerns the intensity of the meridional (002) reflection as compared to the equatorial (020) reflection. Indeed, a very intense and sharp (002) reflection is seen in the slow-DEC films pointing out increased order along the chain axis direction.

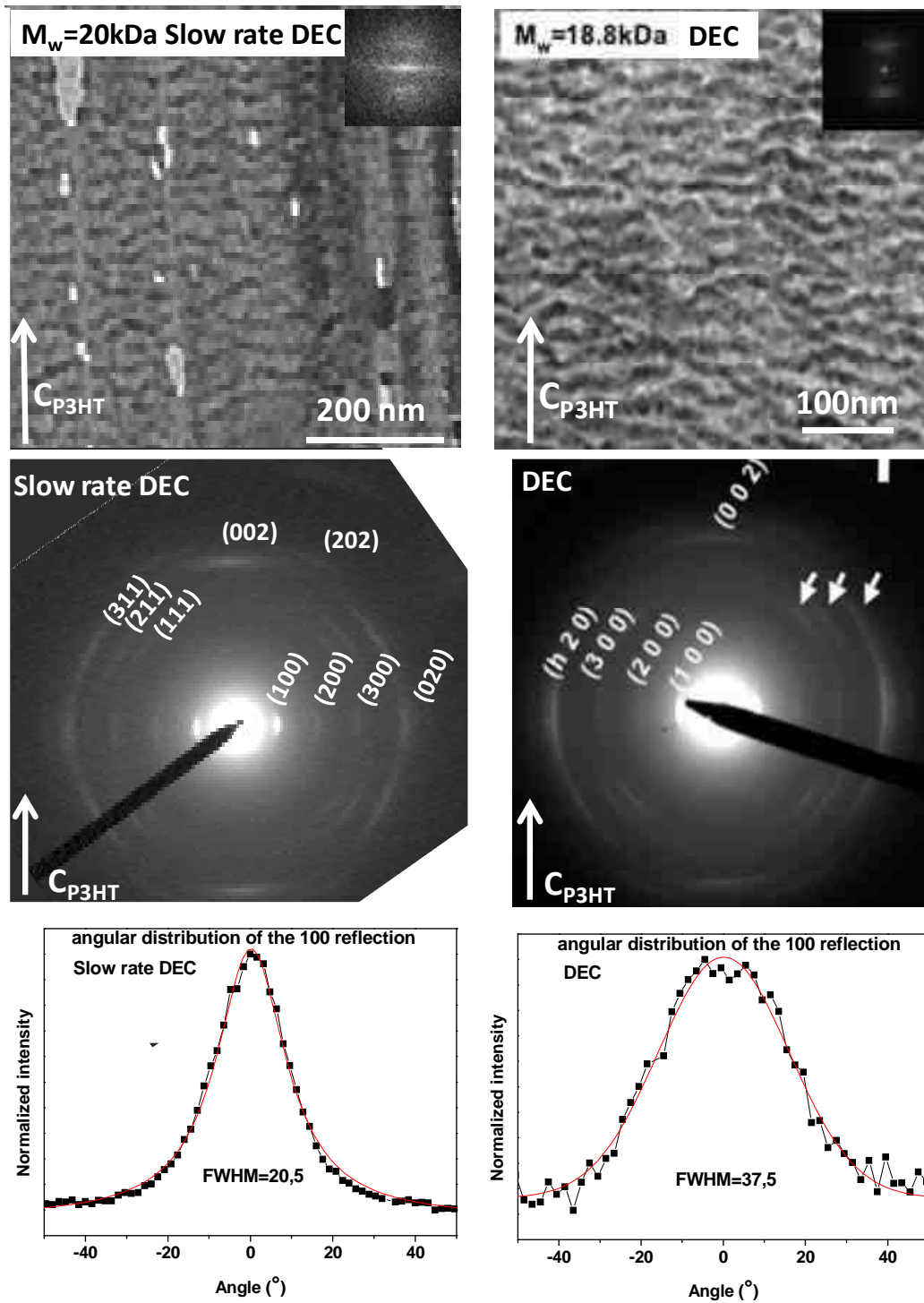


Figure 7-1 : (**up**) BF TEM images of a medium- $M_w$  (20 kDa) P3HT thin film grown by slow DEC and a equivalent P3HT sample grown by the initial DEC method (reproduced from(4)). (**middle**) Corresponding ED patterns of the slow-DEC and DEC sample. (**bottom**) azimuthal angle distributions of the (100) reflections.

## 8. Conclusion

Highly oriented P3HT films on the cm<sup>2</sup> scale were prepared by modifying in some points the initial directional epitaxial crystallization method as first presented by Brinkmann et al (1). The main modifications are:

- (i) A controlled growth rate of the TCB crystallization front achieved by the use of a motorized translation and a significant slowing down of the TCB/P3HT growth rate (20µm/s).
- (ii) The use of a zone local melting technique that limits the evaporation of the TCB during the growth.
- (iii) The use of an orienting substrate of PTFE and adequate coatings of the glass slide to enhance the surface and homogeneity of the oriented P3HT films.

With this improved method, highly oriented thin films can be grown over large areas (cm<sup>2</sup>) in a reproducible way. Such films show a very high in-plane orientation as it can be inferred from the high dichroic ratio of absorbance (>9 at 610nm) and a well developed vibronic structure.

TEM investigations indicate that the process affects also the nanoscale morphology of the films. On a microscopic scale, an improvement of the in-plane orientation is observed. Due to slower crystallization kinetics, the lamellar periodicity is higher than in films prepared with the initial method. In the following P3HT films grown by slow-DEC will be studied in more detail regarding their in-plane orientation, structure and nanomorphology. A particular attention will be given to the effect of the molecular weight of the P3HT.

- (1) Brinkmann, M.; Wittmann, J.-C. Orientation of regioregular poly(3-hexylthiophene) by directional solidification: a simple method to reveal the semicrystalline structure of a conjugated polymer. *Advanced Materials* **2006**, *18*, 860-863.
- (2) Rosa, C. D.; Park, C.; Thomas, E. L.; Lotz, B. Microdomain patterns from directional eutectic solidification and epitaxy. *Nature* **2000**, *405*, 433-437.
- (3) Wittmann, J. C.; Lotz, B. Epitaxial crystallization of polymers on organic and polymeric substrates. *Progress in Polymer Science* **1990**, *15*, 909.
- (4) Brinkmann, M.; Rannou, P. Effect of molecular weight on the structure and morphology of oriented thin films of regioregular poly(3-hexylthiophene) grown by directional epitaxial solidification. *Advanced Functional Materials* **2007**, *17*, 101-108.
- (5) Brinkmann, M.; Rannou, P. Molecular weight dependence of chain packing and semicrystalline structure in oriented films of regioregular poly(3-hexylthiophene) revealed by high-resolution transmission electron microscopy. *Macromolecules* **2009**, *42*, 1125-1130.
- (6) Li, H.; Yan, S. Surface-induced polymer crystallization and the resultant structures and morphologies. *Macromolecules* **2011**, *44*, 417-428.
- (7) Lotz, B. Structure et morphologie des polymères à l'état condensé. *Bulletin de L'union des Physiciens* **1981**, *639*, 337.
- (8) Brinkmann, M.; Aldakov, D.; Chandezon, F. Fabrication of oriented and periodic hybrid nanostructures of regioregular poly(3-hexylthiophene) and CdSe nanocrystals by directional epitaxial solidification. *Advanced Materials* **2007**, *19*, 3819-3823.
- (9) Kayunkid, N.; Uttiya, S.; Brinkmann, M. Structural model of regioregular poly(3-hexylthiophene) obtained by electron diffraction analysis. *Macromolecules* **2010**, *43*, 4961-4967.
- (10) Tashiro, K.; Kobayashi, M.; Kawai, T.; Yoshino, K. Crystal structural change in poly(3-alkyl thiophene)s induced by iodine doping as studied by an organized combination of X-ray diffraction, infrared/Raman spectroscopy and computer simulation techniques. *Polymer* **1997**, *38*, 2867-2879.
- (11) Yang, H.; Shin, T. J.; Yang, L.; Cho, K.; Ryu, C. Y.; Bao, Z. Effect of Mesoscale Crystalline Structure on the Field-Effect Mobility of Regioregular Poly(3-hexyl thiophene) in Thin-Film Transistors. *Advanced Functional Materials* **2005**, *15*, 671-676.
- (12) Zhang, R.; Li, B.; Iovu, M. C.; Jeffries-El, M.; Sauv e, G.; Cooper, J.; Jia, S.; Tristram-Nagle, S.; Smilgies, D. M.; Lambeth, D. N.; McCullough, R. D.; Kowalewski, T. Nanostructure dependence of field-effect mobility in regioregular poly(3-hexylthiophene) thin film field effect transistors. *Journal of the American Chemical Society* **2006**, *128*, 3480-1.
- (13) Zen, A.; Saphiannikova, M.; Neher, D.; Grenzer, J.; Grigorian, S.; Pietsch, U.; Asawapirom, U.; Janietz, S.; Scherf, U.; Lieberwirth, I.; Wegner, G. Effect of molecular weight on the structure and crystallinity of poly(3-hexylthiophene). *Macromolecules* **2006**, *39*, 2162-2171.
- (14) Bao, Z.; Dodabalapur, A.; Lovinger, A. J. Soluble and processable regioregular poly(3-hexylthiophene) for thin film field-effect transistor applications with high mobility. *Applied Physics Letters* **1996**, *69*, 4108.

- (15) Yang, H.; LeFevre, S. W.; Ryu, C. Y.; Bao, Z. Solubility-driven thin film structures of regioregular poly ( 3-hexyl thiophene ) using volatile solvents. *Applied Physics Letters* **2007**, *90*, 172116.
- (16) Brinkmann, M. Structure and morphology control in thin films of regioregular poly(3-hexylthiophene). *Journal of Polymer Science Part B: Polymer Physics* **2011**, *49*, 1218-1233.
- (17) Schweicher, G.; Paquay, N.; Amato, C.; Resel, R.; Koini, M.; Talvy, S.; Lemaur, V.; Cornil, J.; Geerts, Y.; Gbabode, G. Toward single crystal thin films of terthiophene by directional crystallization using a thermal gradient. *Crystal Growth and Design* **2011**, *11*, 3663-3672.
- (18) Liu, C.-Y.; Bard, A. J. In-situ regrowth and purification by zone melting of organic single-crystal thin films yielding significantly enhanced optoelectronic properties. *Chemistry of Materials* **2000**, *12*, 2353-2362.
- (19) Liu, C.-Y.; Bard, A. J. Increased photo- and electroluminescence by zone annealing of spin-coated and vacuum-sublimed amorphous films producing crystalline thin films. *Applied Physics Letters* **2003**, *83*, 5431.
- (20) Wittmann, J. C.; Smith, P. Highly oriented thin films of poly(tetrafluoroethylene) as a substrate for oriented growth of materials. *Nature* **1991**, *352*, 414-417.
- (21) Gill, R. E.; Hadziioannou, G.; Lang, P.; Garnier, F.; Wittmann, J.-C. Highly oriented thin films of a substituted oligo(para-phenylenevinylene) on friction- transferred PTFE substrates. *Advanced Materials* **1997**, *9*, 331-334.
- (22) Lang, P.; EL Ardhaoui, M.; Wittmann, J. C.; Dallas, J. P.; Horowitzl, G.; Lotz, B.; Garnier, F.; Straupe, C. Substrate dependent orientation and structure of sexithiophene thin films. *Synthetic Metals* **1997**, *84*, 605-606.
- (23) Damman, P.; Dosière, M.; Wittmann, J. C. Epitaxial polymerization of poly( p -oxybenzoate) on friction-transfer poly(tetrafluoroethylene) substrates. *Macromolecules* **1997**, *30*, 8386-8391.
- (24) Vergnat, C. Elaboration de surfaces polymers orientées et nanostructurées pour l'orientation de matériaux moléculaires conjugués, PhD dissertation, Université de Strasbourg, 2010.
- (25) Tanaka, T.; Ishitobi, M. Atomic groove effect of aligned poly(tetrafluoroethylene) surfaces upon oriented growth of linear dye molecules. *The Journal of Physical Chemistry B* **2002**, *106*, 564-569.
- (26) Brinkmann, M.; Chandezon, F.; Pansu, R. B.; Julien-Rabant, C. Epitaxial growth of highly oriented fibers of semiconducting polymers with a Shish-Kebab-like superstructure. *Advanced Functional Materials* **2009**, *19*, 2759-2766.



# ***Chapter 4. Oriented P3HT films by slow Directional Epitaxial Crystallization***

*In the previous chapter, the slow-DEC method was introduced and described in detail. Herein a complete characterisation of thin P3HT films grown by slow-DEC will be presented. The main focus of this study is the effect of the molecular weight ( $M_w$ ) on the orientation, the crystalline order, the nanomorphology and the optical properties of the films. Therefore, X-ray diffraction (XRD), Transmission Electron Microscopy in the bright field (TEM-BF), electron diffraction (ED) and high resolution (HR-TEM) mode and UV-vis absorption spectroscopy were used. Whereas medium and high- $M_w$  samples exhibit a fiber symmetry with the P3HT backbone as a fiber axis, the low- $M_w$  samples show clearly preferential contact planes of the crystalline domains on the substrate. This is directly reflected in the morphology of the thin films. Moreover a clear effect of the  $M_w$  on the lamellar structure, the size and the shape of the crystalline domains as well as the degree of in-plane orientation of the P3HT backbone was evidenced. These structural differences between the high and low- $M_w$  samples impact directly the optical properties of the thin films. In a first part of the chapter we will present the main properties of slow-DEC films on the example of medium- $M_w$  samples. In a second part the effect of the  $M_w$  on such films will be studied. Finally, the impact of the structural differences on the vibronic structure of the UV-vis absorption spectra will be analysed.*



## 1. Morphology, structure, crystallinity: Example of a medium- $M_w$ sample

The film processing conditions in general and the crystallization kinetics and  $M_w$  in particular have a strong impact on the macroscopic and microscopic properties of thin films of rr-P3HT (I-5). Here the macroscopic and microscopic morphology, the degree of orientation, the crystallinity as well as the optical properties of P3HT films prepared with a slow crystallization kinetics will be studied. Particularly, the effect of the molecular weight was investigated. But before, the main features of the films in terms of structure, morphology and microstructure will be presented on the example of P3HT of medium- $M_w$  ( $M_w=17,6$  kDa and  $M_n=13,4$  kDa) sample.

On a macroscopic scale, the main improvement made by passing from the DEC method on a Koeffler bench to the slow-DEC method is the homogeneity and the good in-plane orientation of the films on a  $\text{cm}^2$  scale. This homogeneity allows further fundamental characterisations of the films via optical measurements (UV-vis and PL) and XRD measurements. Therefore the combination of Optical Polarized Microscopy, UV-vis absorbance spectroscopy, XRD, and TEM in BF, ED and HR mode allowed for a complete characterisation of the studied system.

### 1.1. Macroscopic Morphology

*Figure 1-1* depicts the morphology of a P3HT film grown by slow-DEC using the POM. This image reveals clearly a very high birefringence indicating a high degree of orientation on a large scale of several hundreds of  $\mu\text{m}^2$ . Only a few macroscopic orientation defects are visible and are mostly located in the thicker parts of the films. The macroscopic morphology shows clearly a continuous film of P3HT with a fibrillar morphology. The fibres are oriented parallel to the growth direction *i.e.* parallel to  $\mathbf{c}_{\text{TCB}}$  and thus to the P3HT backbone  $\mathbf{c}_{\text{P3HT}}$ . This fibrillar morphology is characteristic for films grown by slow-DEC. Our observation showed that the higher the concentration of P3HT in TCB, the more this fibrillar structure is developed. This is particularly true for thick P3HT films grown by slow-DEC ( $>1$  wt% P3HT in TCB). The fibrillar aspect of the films is mainly developed in the thicker parts of the samples. Further support for this is obtained from the TEM-BF image and the corresponding section profile of the image (see *Figure 1-2*). Indeed, thickness fluctuations result in different contrast in the TEM-BF images. Darker zones are thicker. The section profile of the BF image reflects the strong fluctuations in thickness of the films. The lateral thickness of the fibres was estimated from approximately to 20-120 nm. These values depend however strongly on the sample and are sometimes difficult to evaluate due to the superposition of several fibres.

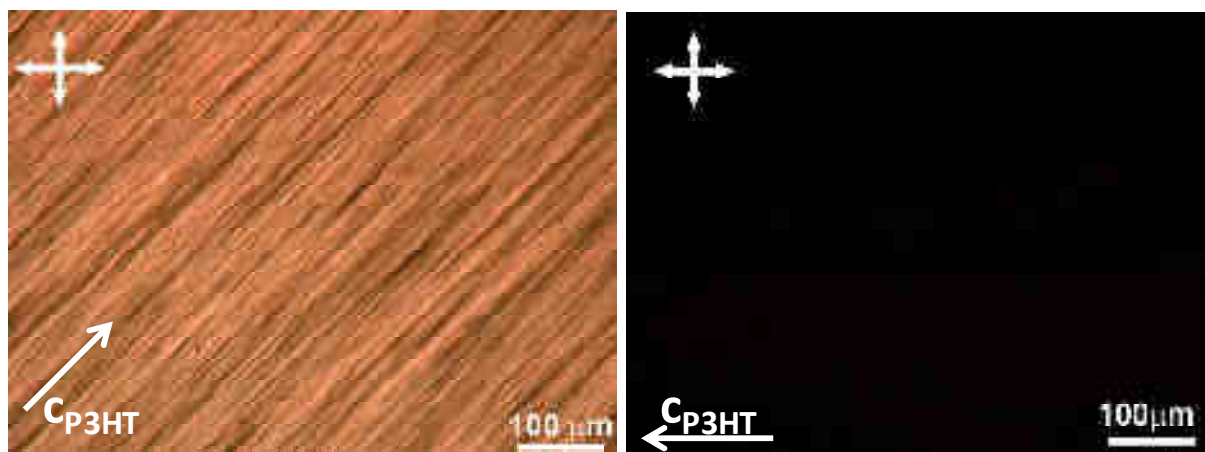


Figure 1-1: Morphology of the P3HT films oriented by slow directional epitaxial crystallization in TCB as observed by POM. The arrow indicates the direction of the  $c$  axis of P3HT macromolecules. The crossed arrows indicate the orientation of the two polarizers.

The TEM-BF image and the corresponding section profile reveal clearly that the fibrillar structure is particularly developed in the thicker part of the films, *i.e.* the parts of the films where the P3HT concentration in TCB was the highest before the crystallisation. In the thin parts of the film the sample shows a quite homogenous film-like morphology showing a clear lamellar structure. The lamellar structure is also present in the fiber-like phase of the film but in these parts the lamellar structure is more difficult to observe due the quite high thickness of the film. Therefore it is difficult to grow thick P3HT films with a low surface roughness.

The origin of this fibrillar aspect of the film can be explained by the processing method. In fact, the presence of P3HT disturbs the platelet-like crystal growth of the TCB. In the case of the growth of Shish-Kebab fibers in a solvent mixture TCB/pyridine, it has been shown that the lateral growth of the TCB crystals perpendicular to the  $c_{\text{TCB}}$  axis is impeded by the sheathing of the TCB crystal by oriented epitaxied P3HT (6). This results in needle shaped TCB crystals instead of platelet-like crystals. This effect is similar to a poisoning of the lateral growth of the TCB crystals by the layer of epitaxied P3HT. A similar effect may take place in the case of slow-DEC if the concentration of P3HT in TCB is high. The higher the concentration of P3HT, the more the needle-like crystal growth of TCB is favoured resulting in a fibrillar morphology of the final P3HT film.

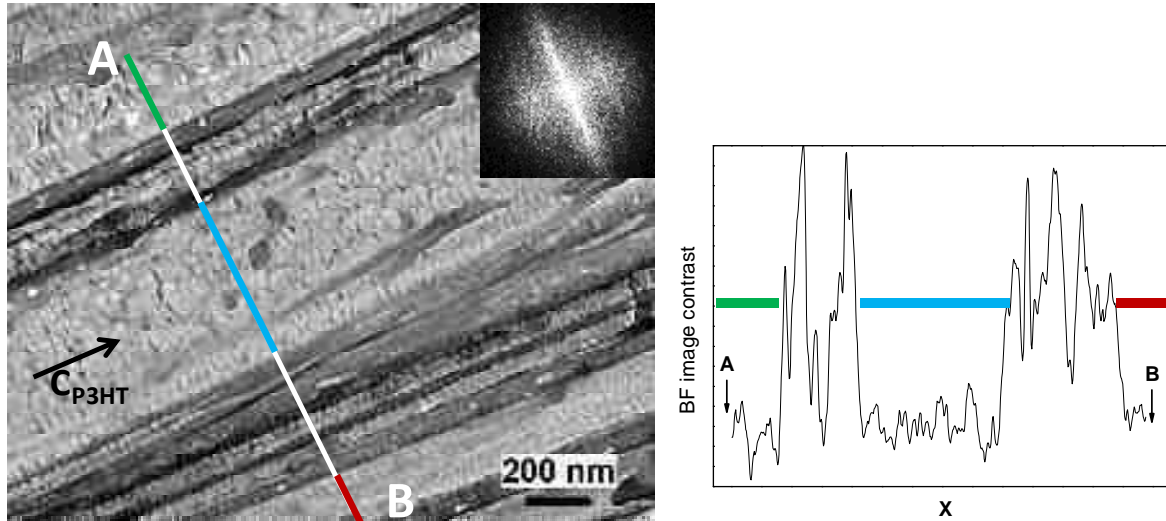


Figure 1-2: (left) TEM-BF image to illustrate the fibrillar morphology of a medium- $M_w$  sample. The fibrils have a lateral extension of approximately 20-120 nm and are separated by a thin film morphology where the lamellar structure can be clearly distinguished. The periodic character of the lamellar structure is clearly seen in the FFT of the BF image (inset). (right) Section profile along the indicated line, it appears clearly that the fibers constitute the thicker part of the film and are the main factor for the high surface roughness.

## 1.2. Structural analysis by GIXD : preferential contact plane versus fiber symmetry

The question coming up at this point is whether the macroscopically observed fiber morphology implies a fiber symmetry from the crystalline point of view. A fiber symmetry is such that only one crystallographic direction is oriented on a large scale (fiber axis  $\mathbf{c}_{\text{P3HT}}$ ) whereas the two other directions are isotropically distributed in the plane perpendicular to the fiber axis. In the particular case of P3HT grown by slow-DEC, a fiber symmetry means that all P3HT chains ( $\mathbf{c}_{\text{P3HT}}$ -axis) are oriented in the same direction whereas the  $\mathbf{a}_{\text{P3HT}}$  and the  $\mathbf{b}_{\text{P3HT}}$  axis show an isotropic distribution in the plane perpendicular to  $\mathbf{c}_{\text{P3HT}}$ . This implies that there are no preferential contact planes of the crystalline domains of P3HT on the substrate. 2D GIXD measurements can give a good insight on the orientation of the crystalline domains on the substrate. But before discussing the XRD results, the scattering configurations used for the measurements will be described.

### 1.2.1. Scattering geometries

GIXD- measurements were performed at the ESRF synchrotron in Grenoble and at the ANKA synchrotron in Karlsruhe to analyze the crystallographic orientation and structure of the epitaxied P3HT and hybrid films. The samples for XRD measurements were prepared on glass slides coated with a hydrosoluble polymer (PEDOT:PSS). The entire film was transferred to a silicon wafer by floating the sample on water and recovering the film on a silicon wafer. This operation was necessary as a direct growth of the film on Si wafers was

unsuccessful (see Chapter 3) and to avoid a large background scattering of the amorphous glass substrate. In addition, this procedure gives comparable films to those observed by TEM as these films were processed in the same way and recovered on TEM copper grids. The XRD measurements were carried out with a point detector at a wavelength of  $\lambda = 1.24 \text{ \AA}$  at ANKA and with a 2D and point detector at a wavelength of  $\lambda = 0.59 \text{ \AA}$  at the ESRF. The foot-print of the beam was around  $\sim 3 \text{ cm}$  along the beam direction allowing a statistic and macroscopic analysis of the thin film structure. Note that these scattering configurations were used for all XRD measurements presented in this thesis.

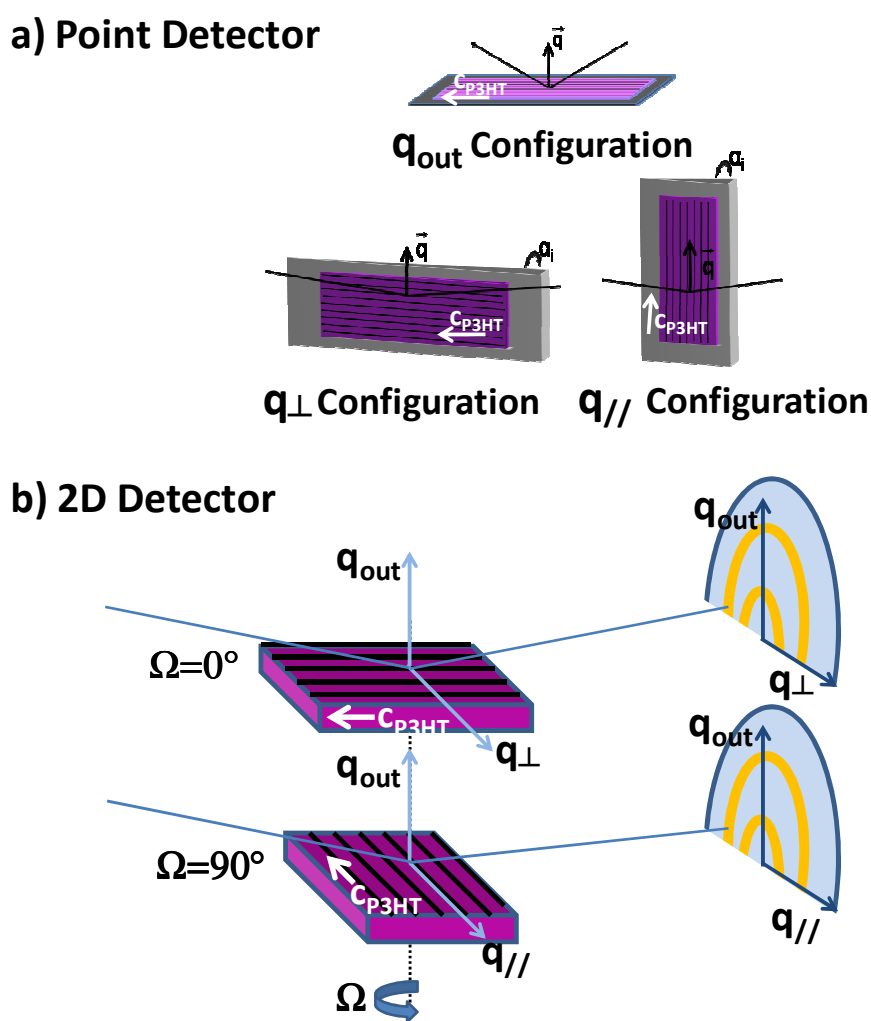


Figure 1-3: (a) Scattering configurations used for the GIXD measurements with the point detector. (b) Scattering configurations used with the 2D detector.  $q_{\perp}$  is defined as the scattering vector perpendicular to the  $c_{P3HT}$  direction and  $q_{\parallel}$  is defined as the scattering vector parallel to the  $c_{P3HT}$  direction and the  $q_{out}$  vector is along the sample's surface normal.

Both, 1D and 2D measurements give complementary information. 2D maps are well adapted to give a rapid view of the preferential orientation of the crystalline domains on the substrate (fiber symmetry, etc.). However, the larger the scattering vector  $q$ , the more the scattering geometry departs from a real  $\theta$ - $2\theta$  configuration. Therefore, 1D scans in the  $\theta$ -

**2θ** configuration are essential to provide more quantitative information on the orientation. The different scattering configurations used for the XRD measurements are depicted in *Figure 1-3 (a)* for the linear scans, and in *Figure 1-3 (b)* for the 2D maps. With the 2D detector, the out-of-plane information is recorded on the vertical axis of the detector ( $\mathbf{q}_{\text{out}}$ ) and the in-plane information on the horizontal axis (see *Figure 1-3*). We have mainly used two geometrical configurations:  $\mathbf{q} \parallel \mathbf{c}_{\text{P3HT}}$  and  $\mathbf{q} \perp \mathbf{c}_{\text{P3HT}}$ . In the following, we use the labels  $\mathbf{q}_{\parallel}$  and  $\mathbf{q}_{\perp}$  for these two configurations respectively. The scattering vector out of plane is labeled  $\mathbf{q}_{\text{out}}$ .

Beside the linear scans and the 2D maps obtained for the two configurations depicted in *Figure 1-3*, we have also performed omega ( $\Omega$ ) scans on specific reflections e.g. (100)<sub>P3HT</sub> in order to quantify the azimuthal distribution of the crystal orientations.  $\Omega = 0^\circ$  is defined as  $\mathbf{q} \perp \mathbf{c}_{\text{P3HT}}$  and  $\Omega = 90^\circ$  is defined as  $\mathbf{q} \parallel \mathbf{c}_{\text{P3HT}}$ .

### 1.2.2. 1D and 2D GIXD measurements

*Figure 1-4* shows representative 2D GIXD maps at different orientations of the sample (different  $\Omega$  angles) for a slow-DEC medium- $M_w$  sample. *Figure 1-5* shows the corresponding linear scans.

For  $\Omega = 0^\circ$ , the 2D map displays several continuous Scherrer rings corresponding to the reticular planes (h00) (h=1,2,3). An additional ring corresponding to the  $\pi$ - $\pi$  stacking (020) reflection and the (102) reflection can be clearly seen. As expected from the 2D map, the linear scans corresponding to  $\mathbf{q}_{\text{out}}$  and  $\mathbf{q}_{\perp}$  display the characteristic (100) and the (020) reflections *Figure 1-5*.

Upon turning the sample around the  $\Omega$  angle, the Scherrer rings progressively disappear at the expense of sharp reflections along the  $\mathbf{q}_{\text{out}}$  direction. The disappearance of the (h00) and the (020) Scherrer rings upon turning the sample around  $\Omega$  supports the high in-plane orientation of the  $\mathbf{c}_{\text{P3HT}}$  direction as evidenced previously by POM. This behaviour is consistent with what is expected when a fiber is tilted towards the incident X-ray beam. For  $\Omega = 90^\circ$ , only reflections along the  $\mathbf{q}_{\text{out}}$  direction are observed.<sup>4</sup> In particular, there are no reflections visible along the  $\mathbf{q}_{\parallel}$  direction.

---

<sup>4</sup> Note that the intensities for the different  $\Omega$  are not comparable due to the high aspect ratio of the sample. In fact, the footprints of the beam on the sample are different and accordingly different sample surfaces are scanned. This makes the comparison of intensities difficult.

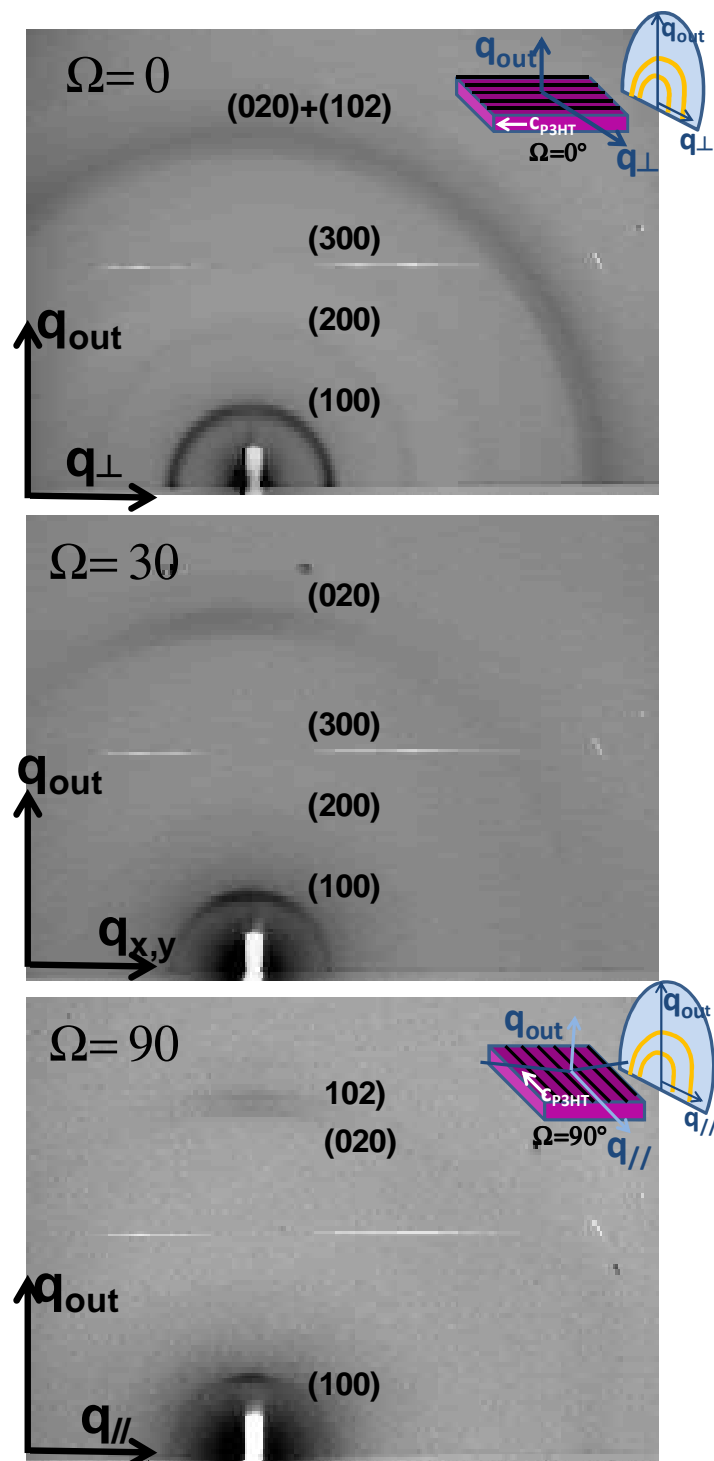


Figure 1-4: Representative 2D GIXD maps obtained for different  $\Omega$  angles. The insets show the configuration of the measurement.

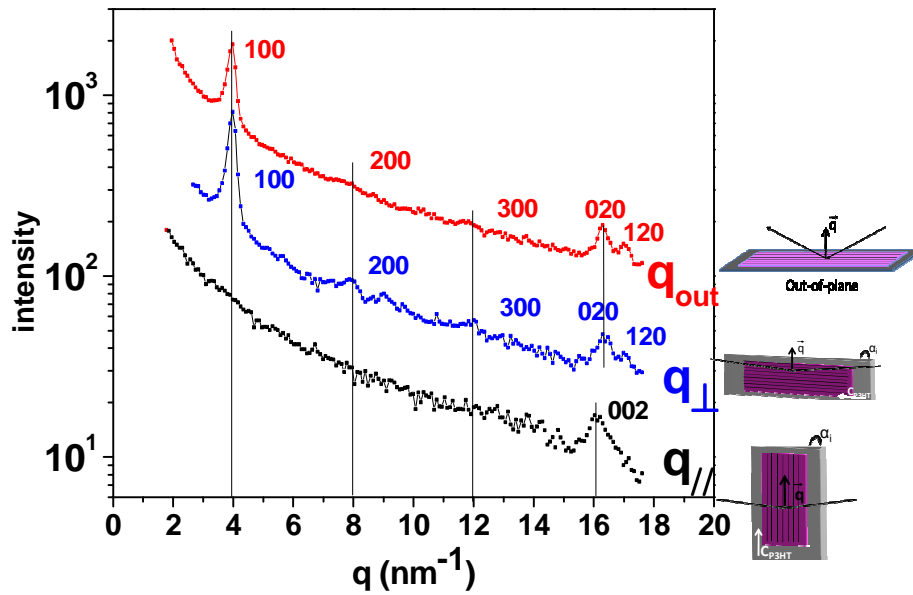


Figure 1-5 : GIXD linear scans for various scattering configurations of a 17.6 kDa P3HT sample. The insets show schematically the used configuration.

As opposed to this, the more sensitive linear scan, evidences a characteristic (002) reflection of the monomer repeat unit in the  $q_{\parallel}$  direction. The absence of this reflection in the 2D map is presumably due to the scattering geometry which is too far from the Bragg condition at the scattering angle of the (002) reflection. The observation of the (002) reflection in the linear scan is remarkable as it corresponds to the periodicity of the monomer repeat unit in the polythiophene chain which can usually not be observed in non oriented thin films. Indeed in the later films, the (002) reflection overlaps with the very intense (020) reflection *i.e.* the  $\pi$ -stacking period. Presumably, it is also the high degree of order and crystallinity that allows for the observation of the (002) reflection. In fact, statistical stacking disorder along the  $c_{P3HT}$  would induce a disappearance of this reflection. The low degree of stacking disorder in slow-DEC films can presumably be ascribed to the preparation method of epitaxied layers. For P3HT films grown by slow-DEC, the in-plane orientation of  $c_{P3HT}$  is enforced by the 1D epitaxial relation of P3HT on TCB ( $2c_{TCB} \approx c_{P3HT}$ ). Therefore the TCB substrate imposes the positions of adjacent P3HT chains allowing a perfect 3D crystallization of the P3HT with a low degree of statistical stacking disorder compared to other systems (by spin coating, *etc.*). This low degree of stacking disorder in epitaxied P3HT layers accounts for the observation of the (002) reflection.

From the linear XRD scans, the sizes of the crystalline domains were extracted by using the Scherer formula. These results will be discussed in a later section in parallel with the results obtained by HR-TEM.

Regarding again the 2D GIXD maps, the observation of a ring pattern for  $\Omega = 0$  indicates that the diffracting planes do not have a preferential orientation with respect to the substrate plane. In fact, as illustrated in *Figure 1-6* the  $a_{P3HT}$  and  $b_{P3HT}$  axes are isotropically distributed around the preferential chain axis direction in the plane ( $c_{P3HT}$ ). ED measurements

of the oriented films suggested a fiber pattern which is confirmed by the GIXD measurements: The typical fingerprint of a fiber pattern is the observation of Scherrer rings at  $\Omega = 0$  with an isotropic intensity. This ring pattern disappears progressively when the sample is rotated around the film normal ( $\Omega$ -scan).

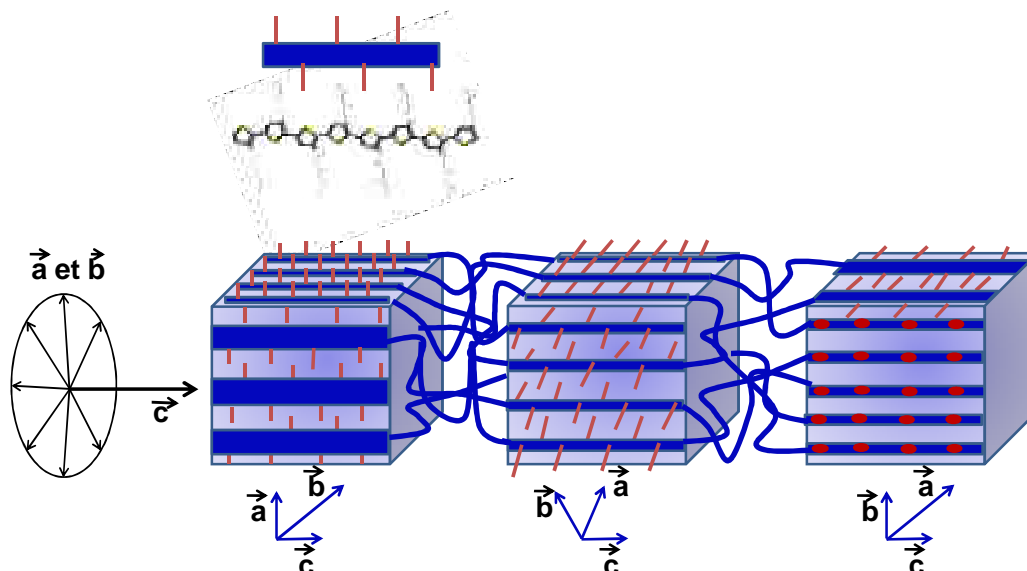


Figure 1-6: Schematical representation of a crystallographic fiber of P3HT. Only the  $c_{P3HT}$  axis is oriented whereas  $a_{P3HT}$  and  $b_{P3HT}$  have an isotropic distribution around  $c_{P3HT}$ . Note that this representation is only a schematic illustration and no information can be given about the orientation of two or more successive crystalline domains.

To the best of our knowledge, this is the first evidence of the observation of a fiber symmetry in a P3HT system. In fact, most authors report preferential contact planes: either “edge-on” or “flat-on”. The “edge-on” orientation is most widely observed (7–10). A preferential “edge-on” orientation leads to (h00) reflections mainly localized along the  $q_{out}$  direction. Even oriented P3HT ( $M_w = 64$  kDa) films prepared by epitaxy on TCB on  $SiO_2$  substrates, do not show a fiber symmetry as reported by Jimison *et al.* (11). The authors reported a coexistence of “flat-on” and “edge-on” orientation of the crystalline domains with a majority of “flat-on” contact planes but did not observe a fiber symmetry. They claimed that within a fiber, one preferential contact plane is maintained until at some point, a perturbation of the crystallization process leads to a change of the orientation of the crystallites. The preferential contact plane observed by Jimison *et al.* may possibly be induced by the use of Si (100) substrates. For the slow-DEC samples prepared on PEDOT:PSS, we could not evidence any preferential contact plane for the medium- $M_w$  sample. In contrast to the here observed fiber symmetry, in the next section, we will show that low- $M_w$  samples grows with a few preferential contact planes on the substrate. Surprisingly Shish-Kebab fibers which are grown by epitaxy on TCB in presence of a small amount of pyridine have also shown a preferential “edge-on” orientation on a glass substrate (6). The same preferential (100) contact plane was reported for thin P3HT films epitaxied on an aromatic substrate of potassium 4-bromobenzoate (K-BrBz) (12). The “edge-on” orientation is in fact the most common

orientation for thin films of P3HT processed from various solvents by classical deposition methods such as spin coating, drop casting, etc. (8–10). In a later chapter of this work the “edge-on” orientation was also obtained for thin films deposited by the Doctor blade method from a solution in chlorobenzene (see Chapter 5). Only very few authors reported a “flat-on” orientation of the crystalline domains in P3HT thin films. Recently, such a “flat-on” orientation was also reported on strain aligned P3HT by O’Connor *et al.* (13). “Flat-on” orientation was also obtained on OTS treated SiO<sub>2</sub> substrate and explained by  $\pi$ -H interactions between the thienyl backbone bearing the  $\pi$  system and the H atoms of the OTS-SAM end groups (14, 15). In a later part of this work, we will show that a preferential “flat-on” orientation of P3HT can be enforced by mechanical rubbing.

What is not clear at this point is how to reconcile the fiber symmetry evidenced in the slow-DEC sample with epitaxial growth that implies a preferential contact plane between the polymer and the TCB substrate. Our assumption is that a few P3HT domains at the P3HT/TCB interface are oriented by epitaxy and present a preferential contact plane. These domains are sufficient to induce a preferential in-plane orientation of the whole sample. But the preferential contact plane is not maintained through the entire film thickness and is lost after a few layers of well epitaxied P3HT.

The observed fiber symmetry makes the here presented system peculiar in the sense that no preferential contact plane could be evidenced and an isotropic distribution of the  $\mathbf{a}_{\text{P3HT}}$  and  $\mathbf{b}_{\text{P3HT}}$  directions can be observed whereas the  $\mathbf{c}_{\text{P3HT}}$  direction is strongly aligned as it could be evidenced by POM and by the anisotropy in the X-ray diffraction pattern probing the sample with the  $\mathbf{q}_{\perp}$  or  $\mathbf{q}_{\parallel}$  to the polymer backbone.

Although no electrical characterisations on such films will be presented here, it is interesting to have a look on how this peculiar fiber symmetry could influence the electrical properties of the slow-DEC thin films. For transport measurements in the direction perpendicular to the substrate as for example in the case of photovoltaics, a preferential “flat-on” orientation would be more suited because the  $\pi$ - $\pi$  stacking direction would be perpendicular to the substrate. For OFET measurements this system is quite adapted as the chain axis is highly oriented in the plane as it could be observed by POM and the XRD  $\Omega$ -scan. Electrical measurements on samples prepared by a similar method than DEC were performed by Jimison *et al.* and a charge transport anisotropy comparing the transport parallel and perpendicular to the chain axis of a factor of 20 was evidenced (11).

The GIXD measurements performed on a P3HT film grown by slow-DEC demonstrate that the sample has a fiber symmetry. The fiber axis is the chain axis of P3HT ( $\mathbf{c}_{\text{P3HT}}$ ). In the following the thin P3HT films grown by slow-DEC will be analyzed on a microscopic scale by means of TEM.

### 1.3. Shape and size of the crystalline domains

Polarized optical microscopy and GIXD measurements probe the sample on a macroscopic scale (mm<sup>2</sup>-cm<sup>2</sup>) yielding a statistical view on the alignment and orientation of

the samples. In the following, the slow-DEC samples shall be probed by TEM on different length scales, *i.e.* from the meso-scale (bright-field) to the molecular scale (diffraction and high resolution).

High resolution TEM (HR-TEM) measurements are particularly adapted for the visualization of the nanomorphology as they allow distinguishing crystalline and amorphous areas. HR-TEM gives directly access to the dimensions of the crystalline domains and to the chain packing in contrast to other indirect methods such as XRD. Information about the packing defects and an estimation of the crystalline domain sizes can be obtained by statistical analysis of the HR-TEM images. In addition, the dimensions can be observed along different directions (stem length ( $\mathbf{c}_{\text{P3HT}}$ ) and side-chain direction ( $\mathbf{a}_{\text{P3HT}}$ )). Such an analysis was performed on the HR-TEM images of the slow-DEC samples. The extracted numerical values were compared to their counterparts extracted from the linear XRD scans presented in section 1.2.

*Figure 1-7* shows a HR-TEM image of a medium- $M_w$  slow-DEC sample. This image confirms clearly the presence of a lamellar structure formed by alternating crystalline and amorphous domains. The crystalline domains are surrounded by yellow lines for visibility. The contrast in the HR-TEM images arises from the alternation of sulfur-riche stacks of polythiophene backbones and layers of *n*-hexyl side chains. The HR-TEM image shows thus areas of tightly packed stacks of P3HT chains separated by  $\sim 1.65$  nm ( $\mathbf{a}_{\text{P3HT}}$ ). The stack of the P3HT chains must be rigorously oriented perpendicular to the film substrate to be observed by HR-TEM. Any mis-orientation will result in a loss of contrast in the HR-TEM image. Accordingly, HR-TEM allows visualizing the semi-crystalline structure only in those areas where the crystalline domains show a “*flat-on*” orientation which represents only a fraction of the film’s surface given the fiber symmetry evidenced by XRD.

Two characteristic dimensions of the domains were estimated from the HR-TEM image. The average stem length  $L_{\text{stem}}$ , *i.e.* the extension of the domains in the  $\mathbf{c}_{\text{P3HT}}$  direction was determined by performing statistics on several images and on  $\sim 250$  stems. The extension of the domains in the  $\mathbf{a}_{\text{P3HT}}$ -axis direction  $L_a$  was performed by counting the number of stems per domain.

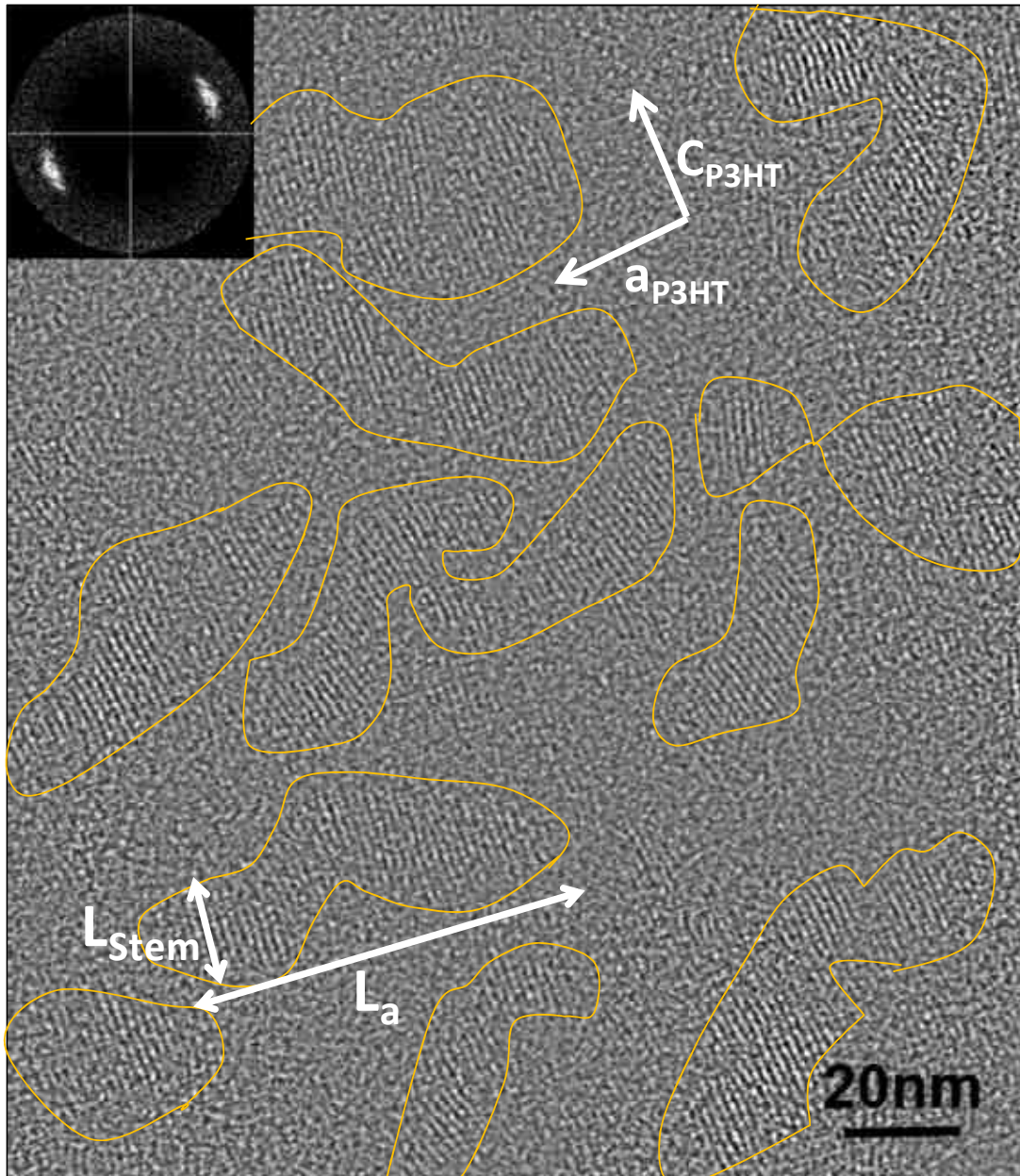


Figure 1-7: Low dose HR TEM image of the medium- $M_w$  sample prepared by slow-DEC. The alternation of crystalline and amorphous domains can be clearly observed. The yellow lines encircle the crystalline domains separated by amorphous interlamellar zones.

Due to the fiber symmetry of the films, the observed dimension  $L_a$  has to be considered with care. There are two possibilities: (i)  $L_a$  corresponds to the intrinsic lateral dimension of the crystalline domains (ii) the observed  $L_a$  is limited by a change of orientation of the crystalline lamellae with respect to the film surface (stacks are no longer oriented along the normal to the film plane). Accordingly the measured values of  $L_a$  are a lower limit to the intrinsic lateral extension of the crystalline domains.

The results of the statistical analysis performed on the HR-TEM images are displayed in Table 1-1. For means of comparison, values obtained by Brinkmann *et al.* on a P3HT film prepared by the initial DEC method on a Koeffler bench are displayed (4). The domain sizes

extracted from the linear GIXD scans presented in the previous section are also displayed. From the width of the reflections of the linear GIXD scans, an approximate size of the crystallites can be estimated using the Scherrer Formula.

	$M_w$	$M_n$	PDI	Contour Length CL (nm)	$L_{stem}$ (TEM) Or $\delta_{(002)}^{X-ray}$ (nm)	$L_a$ (TEM) Or $\delta_{(100)}^{X-ray}$	$\delta_{(020)}^{X-ray}$ (nm) (extention in $b_{P3HT}$ )
HR-TEM DEC from (4)	18.8	11	1.7	14	9	10-20 stems	—
HR- TEM Slow-DEC	17.6	13.4	1.5	15	13±4 nm Equivalent to 33 monomer units	19±7 stems Equivalent to ~ 29 nm	Not accessible by HR-TEM
X-ray Slow-DEC	17.6	13.4	1.5	15	10±2 nm equivalent 25 monomer units	19±4 nm Equivalent to ~13 stems	10±2 nm equivalent to ~26 $\pi$ -stacked chains

Table 1-1 : Size of the crystalline domains as determined from statistics of the HR-TEM images and from the linear scans of x-ray diffraction measurements by the using Scherrer formula for the  $M_w=17.6$  kDa sample. As comparison the values obtained by Brinkmann et al. from HR-TEM measurements are displayed (4).

Despite the limited statistics in the case of HR-TEM, and the approximations involved in the use of the Scherrer formula, the values of  $L_a$  and  $L_{stem}$  extracted from HR-TEM and XRD compare quite well. This shows that the sample is homogenous on large scales and the small explored area of HR-TEM measurements is representative for the entire sample surface of several  $cm^2$ .

The lower domain size obtained by the X-ray measurements can be attributed to crystallization defects as they could be evidenced on the HR-TEM images. In fact, the coherence length of the X-rays is very sensitive to defects in the crystalline structure. HR-TEM images reveal several kinds of such defects as shown in *Figure 1-8*. Orientation defects within one crystalline domain such as a curvature of the chain or splay defects were evidenced (*Figure 1-8 a and c*). Orientation defects originating from grain boundaries can be observed (*Figure 1-8 b*). In addition, stacking defects within a single crystalline domain as seen in *Figure 1-8 d* were observed. Indeed, there is a characteristic loss of contrast inside the domain which hints at a typical dislocation defect. Stacking defects such as splays and dislocations are evidence for the plasticity of the P3HT crystal. This plasticity is related to the alkyl-side chains that can accommodate the local packing constraints imposed by the  $\pi$ -stacking of the

polythiophene backbone. It was shown that such structural defects have a direct impact on the charge transport properties of the films (11).

The magnitude of the mis-alignment between neighboring nanocrystals was estimated from the HR-TEM image to  $\sim 25^\circ$ . In fact, as seen previously from the ED (see Chapter 3), the azimuthal distribution of the (100) reflection has a FWHM of  $\sim 21^\circ$  which is similar to the mis-orientation of the  $c_{P3HT}$  in the domains observed by HR-TEM.

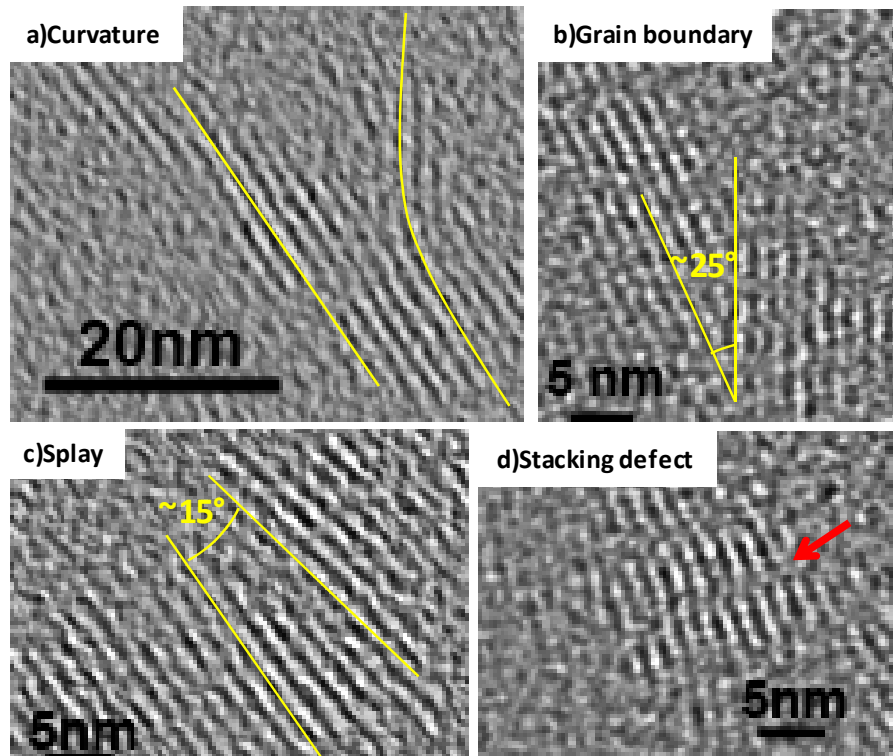


Figure 1-8 : Various defects observed in medium and high- $M_w$  samples. (a) curvature defect. (b) mis-orientation due to a grain boundary. (c) splay defect (d) Stacking defect. The yellow lines are a guide to the eye.

## 2. The effect of the molecular weight

After the full characterization of the medium- $M_w$  sample, we will now focus on the impact of the  $M_w$  on the morphology, structure and orientation of the P3HT films grown by slow-DEC. Indeed it is well known that the orientation, morphology and crystal structure of P3HT depends on the  $M_w$  which controls the occurrence of chain folding (2, 4, 16–19). Therefore it was for example important to study the influence of  $M_w$  on the formation of the lamellar structure with the aim to determine a  $M_w$  of P3HT that allows the fabrication of well nanostructured and organized hybrid materials. In particular, the amorphous interlamellar zone must be large enough to host inorganic nanocrystals. Table 2-1 collects the molecular weight data of the different samples used in this section.

	$M_w$ (kDa)	$M_n$ (kDa)	PDI	Preparation method
<b>Low <math>M_w</math></b>	6.1	5.4	1.13	Synthesized by McCullough Method
<b>Low <math>M_w</math> (1)</b>	7.9	7.2	1.08	Soxhlet extraction
<b>Medium <math>M_w</math></b>	17.6	13.4	1.3	Merck, as received
<b>high <math>M_w</math></b>	50.1	26.2	1.9	Merck, as received

Table 2-1: Macromolecular characteristics of the P3HT samples of various molecular weights used in this section.

In a first part, we will study the structure and orientation of a low- $M_w$  sample. After, we compare it to that observed for high and medium- $M_w$  samples. This study rests on TEM (BF, ED, HR-TEM) and GIXD measurements. The structural study will be followed by the investigations on the optical properties of the P3HT films vs  $M_w$ .

## 2.1. Effect of $M_w$ on the structure and orientation

### 2.1.1. Low- $M_w$ P3HT ( $M_w = 6.1$ kDa)

2D GIXD measurements were performed at the ESRF in the same configurations as explained in the previous section (see *Figure 1-3*) on a low- $M_w$  P3HT film.

*Figure-2-1 (a)* Figure 2-1 shows the 2D GIXD pattern of the low- $M_w$  sample in the  $\mathbf{q}_\perp$  configuration. At a first glance, this pattern shows a much larger number of reflections as compared to a medium- $M_w$  sample (*Figure 1-5*), suggesting a higher overall crystallinity for the low- $M_w$  sample. The XRD pattern shows following remarkable features: (i) (h00) reflections are mainly located on the equator ( $\mathbf{q}_\perp$ ), (ii) intense (h20) and (020) reflections are on the meridian ( $\mathbf{q}_{out}$ ). Besides these dominant reflections, additional ones can be identified. For instance, along the  $\mathbf{q}_{out}$  direction one can observe the (002) and the (120)/(102) reflections. These characteristics make this sample to behave differently from the medium- $M_w$  sample. It does not behave like an oriented fiber but shows rather a preferential orientation of the P3HT crystalline domains on the substrate.

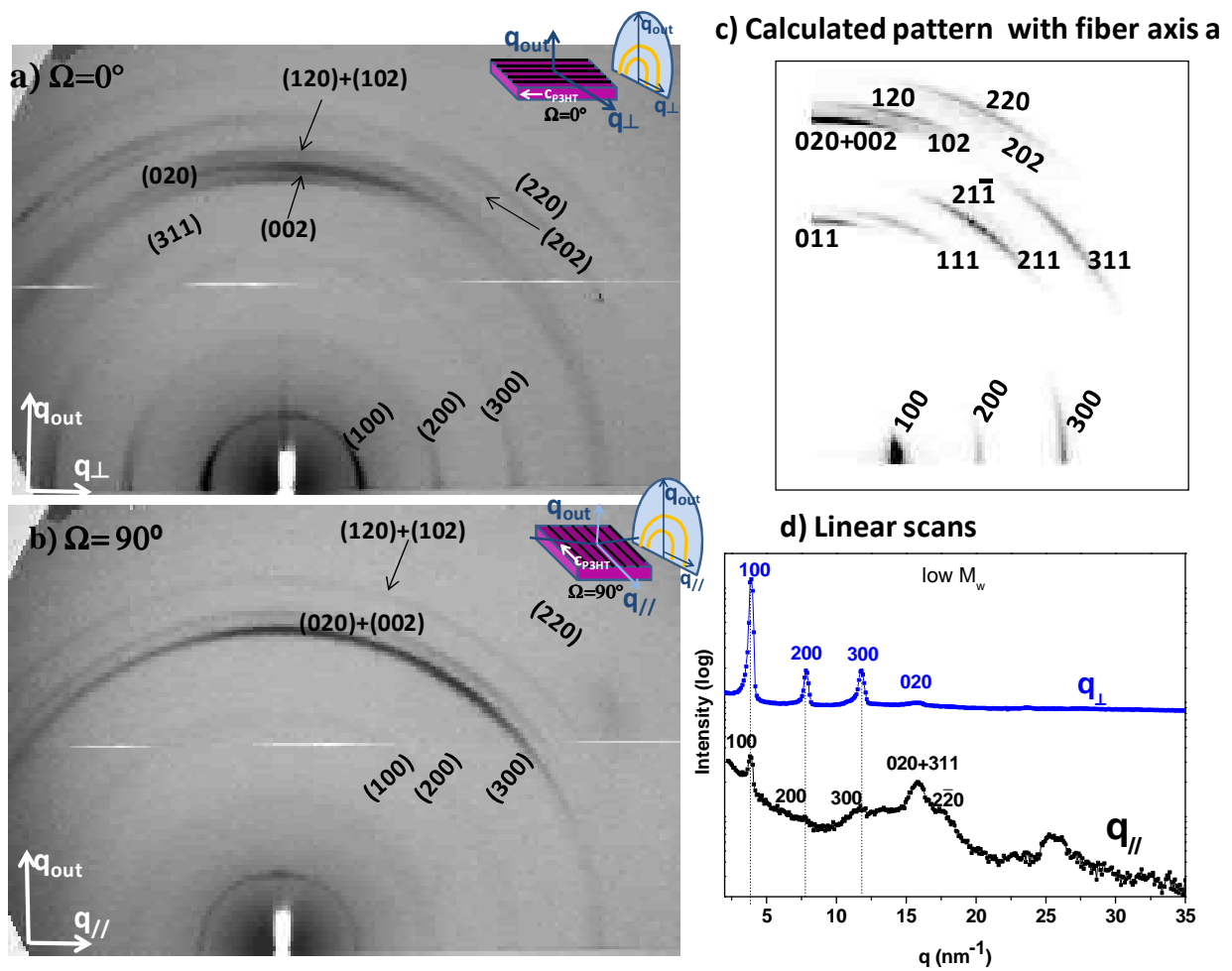


Figure 2-1: (a) 2D GIXD pattern of a low- $M_w$  sample in the  $q_{\perp}$  configuration ( $\Omega = 0^\circ$ ) (b) 2D GIXD pattern in the  $q_{\parallel}$  configuration (c) the calculated fiber pattern with fiber-axis  $a_{P3HT}$  (d) linear GIXD scans in the  $q_{\parallel}$  and  $q_{\perp}$  configuration.

In order to understand this diffraction pattern displaying a multitude of reflections, a look on what has been reported so far on the orientation of low- $M_w$  samples prepared by DEC shall be helpful. In fact, for low- $M_w$  samples, various orientations (contact planes) of the crystalline domains on the substrate were reported previously (2, 4, 20). Figure 2-2 shows a schematical illustration of these orientations.

For very thin films, Brinkmann *et al.* reported P3HT lamellae with standing P3HT chains, *i.e.* a (001) contact plane of the P3HT crystalline domains and in the same work, “flat-on” crystalline domains were also observed (*i.e.* a (010) contact plane) (4).

In a more recent work, Kayunkid *et al.* observed domains having the **c-axis** tilted by  $45^\circ$  to the substrate plane (20). Therefore, for low- $M_w$  samples, the coexistence of these three preferential orientations was reported. Thus, in low- $M_w$  samples prepared by slow-DEC, one can expect to have the coexistence of the (010), the (001) and the (011) contact planes in various proportions. Evidence for standing chains ((001) contact plane) in the sample can be obtained from the presence of the (002) reflection in the  $q_{\text{out}}$  direction on the 2D map. The

presence of the  $\pi$ -stacking (020) reflection in the  $\mathbf{q}_{\text{out}}$  and the (h00) reflection in the  $\mathbf{q}_{\perp}$  direction accounts for the presence “flat-on” domains ((010) contact plane). Both, the (010) and the (001) contact planes can be explained in terms of 1D epitaxy. Indeed, it was shown that 1 D epitaxy on TCB leads to  $\mathbf{b}_{\text{P3HT}} // \mathbf{c}_{\text{TCB}}$  or  $\mathbf{c}_{\text{P3HT}} // \mathbf{c}_{\text{TCB}}$  because the length of the  $\mathbf{b}_{\text{P3HT}}$  and  $\mathbf{c}_{\text{P3HT}}$  axes are very close to  $2 \times \mathbf{c}_{\text{TCB}}$  (4). As yet, the tilted orientation ((011) contact plane) of crystalline lamellae is not understood clearly.

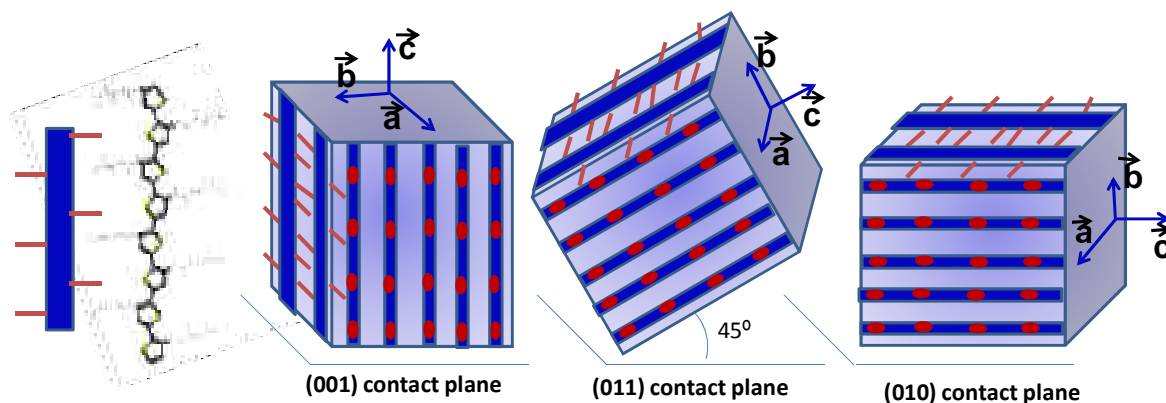


Figure 2-2 : Schematic representation of the orientations of the crystalline domains on the substrate in the case of the low- $M_w$  sample.

The common point between the three populations of oriented domains is the in-plane orientation of the  $\mathbf{a}_{\text{P3HT}} \perp \mathbf{c}_{\text{TCB}}$ . This makes the diffraction pattern of the whole sample to behave almost like a fiber pattern with the  $\mathbf{a}_{\text{P3HT}}$  as fiber axis.

Figure 2-1c depicts the calculated fiber pattern with  $\mathbf{a}_{\text{P3HT}}$  as fiber axis using the crystal structure of Kayunkid *et al.* (20). The calculated pattern accounts very well for the main features of the observed diffraction pattern, especially the “doubling” of some reflections *e.g.* (220) and (202). The fact that some of the reflections observed in the simulated pattern are not visible in the experimental pattern (for example the (011) reflection) can be ascribed to the fact that the oriented films do not exhibit a true fiber symmetry around  $\mathbf{a}_{\text{P3HT}}$  but the crystalline domains adopt mainly three preferential orientations.

The fact that P3HT domains share a common in-plane orientation of the  $\mathbf{a}_{\text{P3HT}}$ -axis is further supported by both, the linear scans displayed in Figure 2-1d and the 2D scan in the  $\mathbf{q}_{\parallel}$  direction shown in Figure 2-1b. Indeed, the equatorial (h00) reflections seen for  $\Omega = 0^\circ$  have almost disappeared in the 2D scan for  $\Omega = 90^\circ$ . Only, a continuous Scherrer ring of weak intensity can be observed for the 100 reflection. This later observation points at a small fraction of non oriented P3HT domains.

Regarding the linear scans (Figure 2-1d), the situation changes a little from what is observed in the medium- $M_w$  sample (Figure 1-5). In the  $\mathbf{q}_{\perp}$  configuration the (h00) reflections are very intense and very sharp for  $h=1,2,3$  indicating a high crystallinity. The presence of the (h00) reflection in the  $\mathbf{q}_{\parallel}$  configuration confirms the presence of a small population of

domains which is not oriented as already seen from the 2D diffraction pattern. Regarding in particular this  $\mathbf{q}_{//}$  scan compared to the medium- $M_w$  sample, many more reflections can be observed around  $\mathbf{q} = 15 \text{ nm}^{-1}$ . The presence of these reflections reflects the coexistence of various contact planes. As for the medium- $M_w$  sample, the size of the crystalline domains was extracted from the linear XRD scans. These results will be discussed in parallel with the data from the HR-TEM in section 2.3.

*Figure 2-3* shows a TEM-BF image of the low- $M_w$  sample. The “flat-on” oriented crystalline domains ((010) contact plane) appear as dark lines whereas the tilted domains ((011) contact plane) appear as light gray domains. The differences compared to the medium- $M_w$  sample are conspicuous. In fact, no fibrillar morphology can be observed in the case of the low- $M_w$  sample. This is in accordance with the absence of a fiber symmetry where  $\mathbf{c}_{\text{P3HT}}$  is the fiber axis.

To conclude, the slow-DEC P3HT films of low- $M_w$  show the following orientation features:

- (i) A high in-plane orientation of  $\mathbf{a}_{\text{P3HT}} \perp$  to  $\mathbf{c}_{\text{TCB}}$  with crystalline domains having different preferential contact planes (010), (001) and (011).
- (ii) A small fraction of non oriented domains with a powder like-pattern.

#### 2.1.2. High- $M_w$ sample ( $M_w = 50.1 \text{ kDa}$ )

From the point of view of the orientation we have evidenced clear differences between the low and the medium- $M_w$  samples. We now focus on a high- $M_w$  sample. *Figure 2-3 (right)* shows the 2D maps for  $\mathbf{q}_{//}$  ( $\Omega=90^\circ$ ) and  $\mathbf{q}_{\perp}$  ( $\Omega=0^\circ$ ). The 2D GIXD measurements of the high- $M_w$  sample show a similar evolution of the diffraction pattern as observed for the medium- $M_w$ . For  $\mathbf{q}_{\perp}$  ( $\Omega=0^\circ$ ) we see two intense rings attributed to the (100) and the (020) diffracting planes. These rings disappear and the pattern displays only reflections in the  $\mathbf{q}_{\text{out}}$  direction for ( $\Omega = 90^\circ$ ). These measurements show clearly that the high- $M_w$  sample has a similar fiber structure as the medium- $M_w$  sample where  $\mathbf{c}_{\text{P3HT}}$  is the fiber axis. The diffraction patterns of the high and medium- $M_w$  samples are very similar apart that for the high- $M_w$  samples, the reflections seem to be broader. This is in particular visible as the (020) and (102) reflections cannot be distinguished in the high- $M_w$  sample in contrast to the medium- $M_w$  sample. As proposed in earlier studies, the crystallinity of P3HT samples tends to decrease with increasing  $M_w$  which translates into a broadening of the reflections (2).

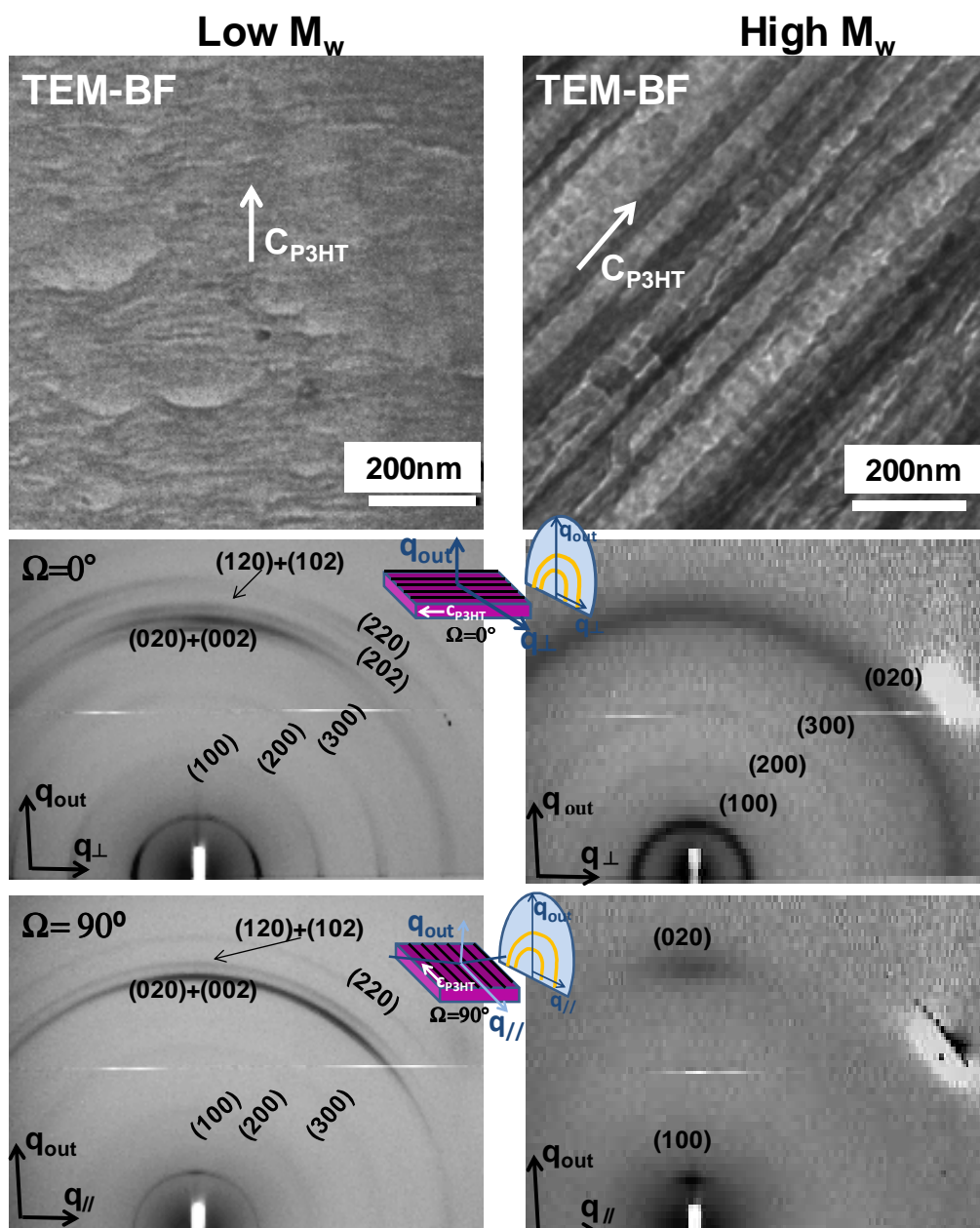
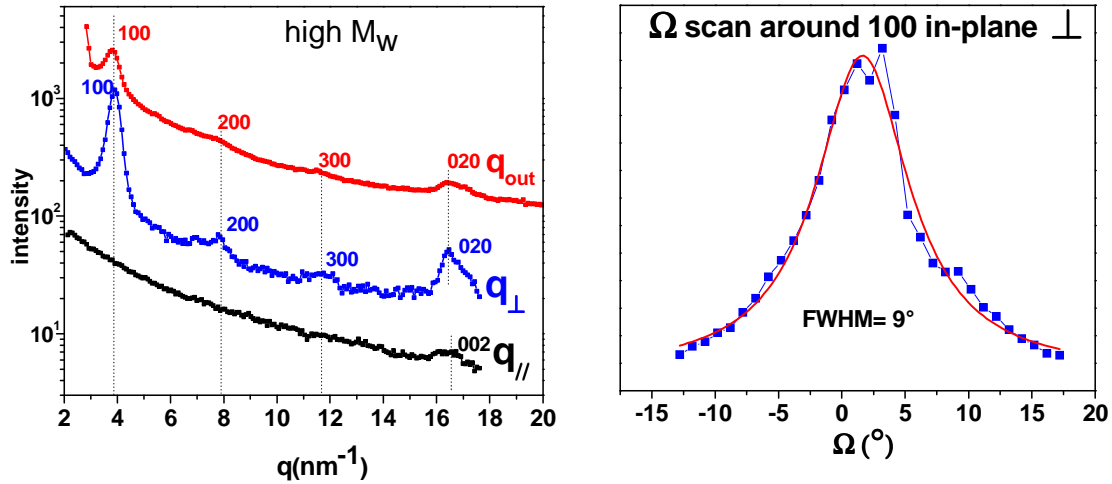


Figure 2-3: (Top) TEM- BF images of a low and high- $M_w$  sample (middle) 2D GIXD pattern of a low and high- $M_w$  sample the scattering vector  $\mathbf{q}_{\perp} \perp \mathbf{c}_{P3HT}$ . (bottom) 2D GIXD pattern of a low and high- $M_w$  sample the scattering vector  $\mathbf{q}_{\parallel} \parallel \mathbf{c}_{P3HT}$ . For means of comparison the results of the low- $M_w$  are redisplayed.

The linear XRD scans of the high- $M_w$  (Figure 2-4) are very similar to the ones observed previously for the medium- $M_w$  sample. In the  $\mathbf{q}_{\parallel}$  configuration no traces of (h00) reflections can be observed indicating a high degree of in-plane orientation of the samples. The  $\mathbf{q}_{\perp}$  and  $\mathbf{q}_{out}$  scans are quite similar due to the fiber structure observed previously. This high degree of orientation is further confirmed by the very low angular distribution observed by performing a rocking curve around the (100) reflection in the plane. For some of the best samples we managed to observe  $\text{FWHM} = 9^\circ$  for the (100) reflection. This result is similar to that obtained by Nagamatsu *et al.* for friction transferred P3HT. However, the epitaxied layers

show a much higher crystallinity as compared to friction transferred films (21). The fiber-like symmetry of the high  $M_w$ -sample evidenced by GIXD is further supported by the fibrous morphology of the samples observed in the BF (see *Figure 2-3*).



*Figure 2-4:*(left) X-ray diffractogram in various used configurations high- $M_w$  P3HT sample (right) corresponding rocking curve around the 100 in-plane reflection, a FWHM  $\sim 9^\circ$ .

To summarize the effect of the  $M_w$  on the orientation of the P3HT films grown by slow-DEC, two main points can be emphasized for films grown by slow-DEC: (i) for the high and medium- $M_w$  a fiber symmetry (with  $\mathbf{c}_{\text{P3HT}}$  as fiber axis) and a corresponding fiber-morphology was evidenced. (ii) The low- $M_w$  samples show the coexistence of specific contact planes having a common in-plane orientation of the  $\mathbf{a}_{\text{P3HT}}$  axis. These important differences are illustrated in *Figure 2-3*.

### 2.1.3. Effect of $M_w$ on the degree of in-plane orientation

As it could be seen,  $M_w$  has an important influence on the structure and the preferential contact planes of the crystalline domains on the substrate. As our aim is to obtain thin P3HT films with the best possible in-plane orientation, the effect of  $M_w$  on the latter was studied by ED measurements. *Figure 2-5* shows the ED patterns for a low, medium and high- $M_w$  sample and the corresponding azimuthal distributions of the (100) reflection. Again, the ED patterns and the FWHM of the azimuthal distributions are very similar in the case of the medium and high- $M_w$  samples. These two patterns correspond well to a fiber pattern. Indeed on the equator we observe (hk0) reflections whereas the (002) reflection is observed on the meridian. As opposed to this, for the low- $M_w$  sample, only the (h00) reflections are observed on the equator indicating a preferential orientation of the  $\mathbf{a}_{\text{P3HT}}$  axis for all crystalline domains.

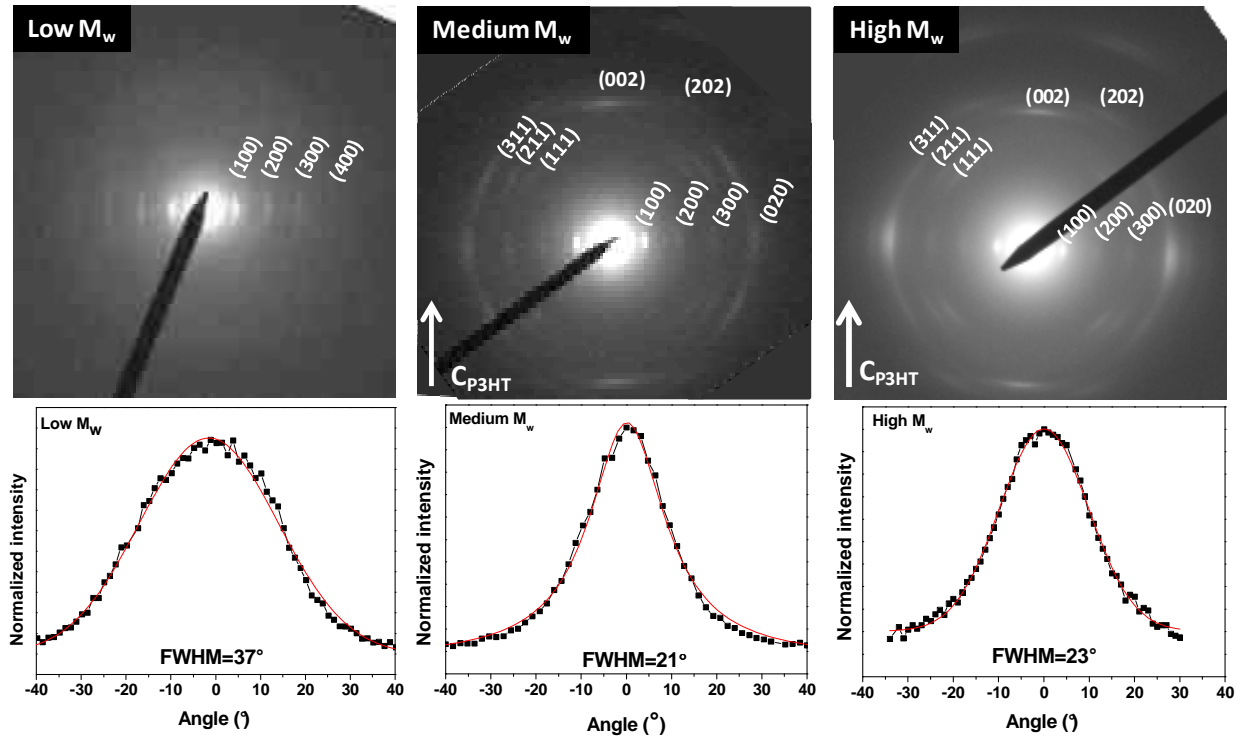


Figure 2-5 : ED patterns of respectively a low, medium and high- $M_w$  samples and the corresponding azimuthal distributions of the (100) reflection.

In order to compare the degree of in-plane orientation of the different samples, we have extracted the azimuthal intensity profile of the (100) reflection from the ED patterns (see Figure 2-5). The medium and high- $M_w$  samples exhibit similar FWHM *i.e.*  $21^\circ$  and  $23^\circ$  respectively. As opposed to this, the low- $M_w$  samples have a larger distribution of the in-plane orientation (FWHM =  $37^\circ$ ). We attribute the lower degree of in-plane orientation of the low- $M_w$  samples to the coexistence of several contact planes for the crystalline domains. An additional reason for the apparent lower degree of in-plane orientation of the low- $M_w$  P3HT films is related to the existence of P3HT domains with a (001) contact plane (standing chains). Indeed, since the unit cell of P3HT is monoclinic with  $\gamma = 86.5^\circ$ , the  $\mathbf{a}^*_{\text{P3HT}}$  axis does not lie strictly on the equator, but slightly off-axis by a few degrees.

## 2.2. Effect of $M_w$ on the lamellar structure and periodicity

### 2.2.1. TEM observations

In this work the lamellar structure is a very important issue, as the aim is to use this lamellar structure for the fabrication of highly ordered and nanostructured hybrid thin films comprising P3HT and CdSe nanocrystals. In fact, Brinkmann *et al.* showed that the nanocrystals are rejected into the amorphous interlamellar zone labelled in the following AIZ (22). Therefore, a well defined semi-crystalline structure with large AIZ that can harbour the NCs is necessary. The fabrication of such hybrid thin films will be discussed in a following chapter (Chapter 6). Here we focus essentially on the  $M_w$ -dependence of the lamellar period

(one amorphous + one crystalline) which is depicted in *Figure 2-6*. The total lamellar periodicity shown in *Figure 2-7* was determined from the BF-images by FFT.

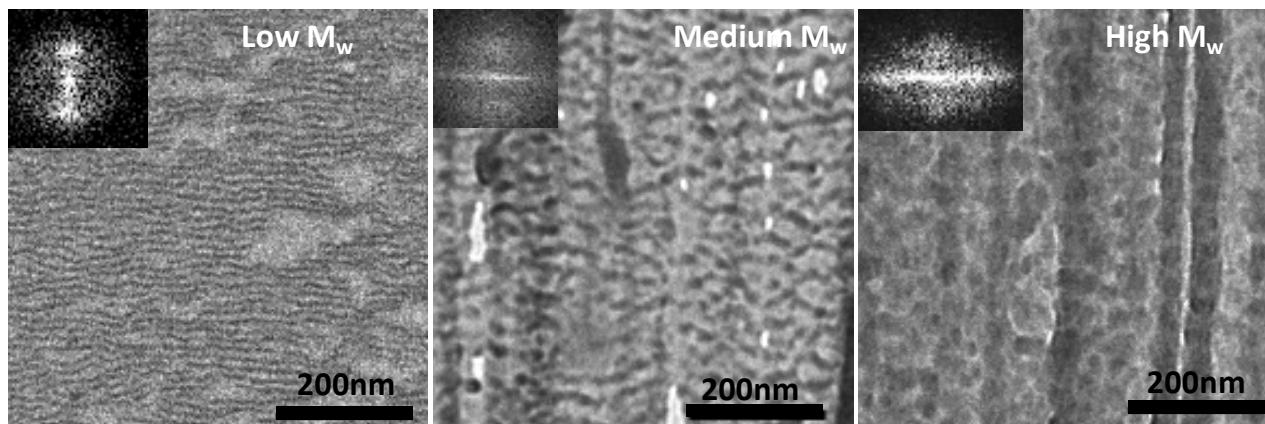
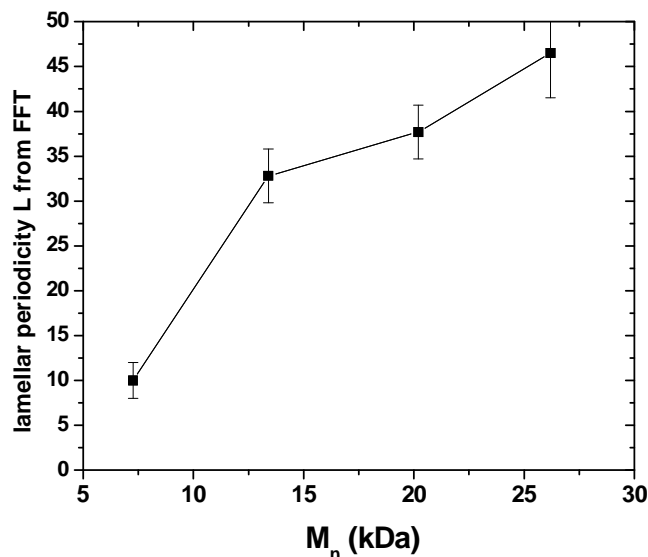


*Figure 2-6* : Lamellar structure as observed by TEM-BF imaging for slow-DEC samples with increasing molecular weight. The lamellar structure becomes fuzzier with increasing molecular weight. The insets show the corresponding FFTs.

*Figure 2-7*: Evolution of the lamellar periodicity as determined from the BF-images with increasing  $M_n$ . As comparison, the calculated contour lengths (CL) are displayed. The observed lamellar periodicities  $L$  go from 10 nm for low- $M_w$  up to 46 nm for high- $M_w$  samples.



The BF-images show the crystalline lamellae in the form of dark stripes and the AIZ appear in light gray. The evolution of the lamellar structure with increasing  $M_w$  concerns: (i) the ratio crystalline/amorphous, (ii) the total lamellar period  $L$  (one crystalline + one amorphous), and (iii) the aspect ratio of the crystalline lamellae.

For the low- $M_w$  sample, the lamellae are tightly packed underlining the absence of extended AIZ. In addition, crystalline domains are particularly extended in the direction perpendicular to the  $\mathbf{c}_{\text{P3HT}}$  direction. Moreover, for the low- $M_w$  sample, the lamellar period deduced from the FFT of the BF images matches quite well the calculated contour length (CL) of the P3HT chains ( $\text{CL}_{\text{low}} \sim 10$  nm by correcting  $M_n$  with the factor accounting for the overestimation inherent to GPC (23)). This suggests that the chains of low- $M_w$  P3HT crystallize in extended form. From the point of view of hybrid layers, this implies that low-

$M_w$  samples are not very suited for the fabrication of hybrid thin films because of the very narrow AIZ that will not be able to harbour CdSe nanoparticles. In addition, low- $M_w$  P3HT samples have poor film-forming ability and weak mechanical tenue.

For the medium- $M_w$  samples, the AIZ become predominant. Moreover, the total lamellar period  $L$  increases substantially with increasing  $M_w$  (see *Figure 2-7*). It goes typically from  $L \sim 10$  nm for low- $M_w$  up to a value of  $L \sim 46$  nm for high  $M_w$ . The extension of the lamellae perpendicular to the  $c_{P3HT}$  direction seems to be much shorter for high- $M_w$  samples than for the medium molecular weight. In the high- $M_w$  sample grown by slow-DEC the shape of the crystalline domains seems in some cases almost circular and the aspect ratio is much reduced compared to the medium and low- $M_w$  samples.

### 2.2.2. Discussion

The remarkable result obtained on the films grown by slow-DEC is the very large lamellar period of  $\sim 40$ - $47$  nm for the high- $M_w$  samples. This is specific to films grown by the slow-DEC method. In fact, Brinkmann *et al.* showed that the lamellar periodicity saturates for  $M_w > 18.8$  kDa to a value in the 25–28 nm range for films grown by DEC on a Koeffler bench (2). Most authors working on P3HT observed this saturation of the lamellar periodicity at a value of  $L \sim 30$  nm. For example, Zhang *et al.* prepared nanofibrils of rr-P3HT with various molecular weights ranging from  $M_w = 2.4$  to  $M_w = 18.4$  kDa. They observed very clearly a saturation value of the lamellar period of  $L = 30$  nm for all  $M_w > 10$  kDa (24). Müller *et al.* reported lamellar periodicities of 31 nm for a very high molecular weight ( $M_w = 344$  kDa) P3HT sample crystallized by pressure induced solidification at a pressure of 5kbar. A 60 kDa sample crystallized by the same method showed lamellar periodicities of  $L = 21$  nm (25).

Other groups, for example Wu *et al.* crystallized P3HT by heating it up to the melting temperature and subsequently cooling down the sample. In such samples they found lamellar periodicities of  $L = 27$  nm for  $M_w = 21.6$  kDa by SAXS measurements (18). Canetti *et al.* reported lamellar periodicities in the range from  $L = 11.7$  to  $L = 16.8$  nm for a  $M_w \sim 16$  kDa sample (26). All these results show that in most cases the lamellar periodicity  $L$  of P3HT shows a saturation at  $\sim 30$  nm. To our best knowledge the only paper that reports lamellar periodicities  $\sim 39$  nm is the work of Crossland *et al.* (27). In a spherulitic morphology of P3HT crystallized by exposure to  $CS_2$  vapours under controlled vapour pressure the lamellar periodicity could be extended up to 39 nm for a P3HT sample of  $M_w = 58.7$  kDa ( $M_n = 30.9$  kDa) by slowing down the crystallization kinetics. In general it is assumed that the lamellar periodicity cannot be extended to high values because of chain entanglements and chain folding in the case of high molecular weight samples which hinder a further extension of the crystalline domains in the  $c_{P3HT}$  direction.

The present results obtained in the case of slow-DEC suggest that the lamellar period of P3HT is essentially limited by the kinetics of the growth. Indeed on the Koeffler bench *i.e.* for fast growth it does not exceed  $\sim 30$  nm whereas for a slow growth ( $V = 20 \mu\text{m/s}$ ), it can increase up to  $\sim 40$ - $46$  nm. The very high lamellar periodicities observed for the high- $M_w$  sample may be surprising. However, it is known for polyethylene, that extended chain

crystallization can be obtained under high pressure (28–31). In these cases, the size of the crystalline domains is not necessarily limited by the CL, but several polyethylene chains can be added to yield large lamellar crystals. It may be suggested that for P3HT a similar behaviour is possible yielding long lamellar periodicities. Further support about this can be obtained from HR-TEM and is shown in the following section.

### **2.3. Effect of $M_w$ on the Nanomorphology and crystallite shape**

To further understand the formation of the lamellar structure and its evolution with  $M_w$  and in particular to get a better insight on the crystal packing and the shape of the crystalline domains, HR-TEM measurements were performed. Brinkmann *et al.* already studied the lamellar structure of films grown by DEC using HR-TEM for various molecular weights (2, 4). But the growth kinetics of the films was not controlled as in the present case. *Figure 2-8* shows the HR-TEM images of a low, medium and high- $M_w$  sample.

All films, independently of  $M_w$ , HR-TEM reveal nanocrystalline domains consisting of planes of  $\pi$ -stacked chains separated by the *hexyl* side chains (the contrast in the HR-TEM images arises from the alternation of sulfur-riche stacks of polythiophene backbones and layers of *n*-hexyl side chains). Statistical measurements were performed on the HR-TEM images of the three samples (low-, medium- and high- $M_w$ ) in order to get a more qualitative insight on the crystallite shapes and sizes as they appear on the HR-TEM images. The crystallite sizes were also estimated from the linear XRD measurements and calculated approximately using the Scherrer formula. *Table 2-2* collects the numerical values obtained by HR-TEM and XRD for the high, medium and low- $M_w$  samples. As seen previously for the medium- $M_w$  sample, the results obtained from the HR-TEM images and the XRD measurements match quite well for all the samples. One exception concerning the stem length of the high- $M_w$  sample has to be noted. This disagreement between the HR-TEM and XRD measurements is probably related to the difficulty to fit accurately the (002) reflection of the linear XRD. The good agreement of TEM and XRD measurements confirms the homogeneity of the films over large areas ( $\text{cm}^2$ ).

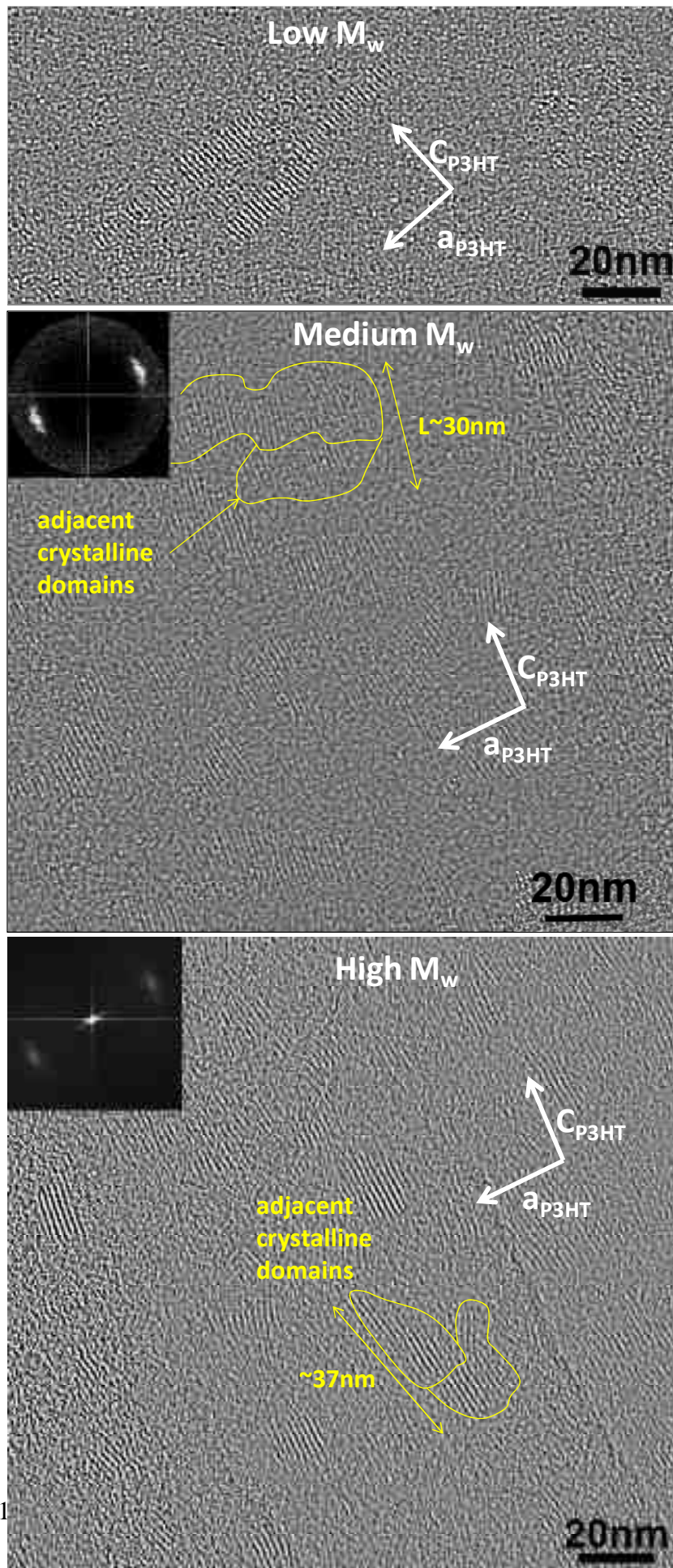


Figure 2-8: Effect of the  $M_w$  on the shape of the crystalline domains of slow-DEC P3HT samples as determined from HR-TEM.

In the HR-TEM images of the medium- $M_w$  and high- $M_w$  samples, we could evidence regions where two adjacent P3HT nanocrystals are added in the  $\mathbf{c}_{\text{P3HT}}$  direction to form one single crystalline domain (surrounded in yellow). This domain has an extension of  $\sim 30$  nm for the medium- $M_w$  and  $\sim 37$  nm for the high- $M_w$ . We believe that such a coalescence of two adjacent P3HT nanocrystals forming one crystalline domain can partially account for the large extension of the lamellar periodicity observed in the slow-DEC films (as evidenced by the TEM-BF images).

With increasing  $M_w$ , mainly two points can be noted: (i) the extension of the crystalline domains in the  $\mathbf{c}_{\text{P3HT}}$  direction (stem length  $L_{\text{stem}}$ ) increases significantly from  $\sim 6$  to  $\sim 16$  nm (ii) the extension of the crystalline domains perpendicular to the chain axis (defined as  $L_a$ ) decreases with increasing  $M_w$  from  $\sim 25$  to  $\sim 13$  stems. In other words, the anisotropy ratio  $L_a/L_{\text{stem}}$  tends towards 1 with increasing  $M_w$ . This evolution of the shape of the crystalline domains with increasing  $M_w$  could already be inferred from the TEM-BF images (Figure 2-7).

Several factors are likely to explain the different nanocrystal dimensions between low- $M_w$  and high- $M_w$  epitaxied films. Because of the fiber structure of the high- and medium- $M_w$  sample, the domain orientations are distributed around  $\mathbf{c}_{\text{P3HT}}$  which may limit the observed lateral size of the domains by HR-TEM. Considering that the observed shapes of the P3HT crystalline domains are intrinsic and not limited by the fiber symmetry of the films, other reasons can explain the shape of the crystalline domains.

First, the anisotropy of the crystal shape is certainly related to the folding ability of the chains as well as the macromolecular parameters (polydispersity). As shown previously (see Table 2-1), the low- $M_w$  P3HT is rather monodisperse and crystallizes in extended form as inferred from the matching of contour length and lamellar period. The epitaxial growth of low- $M_w$  P3HT chains is not constrained by folds. Low- $M_w$  P3HT chains crystallize like an oligomer. For medium- $M_w$  and high- $M_w$  samples, folding as well as chain entanglements tend to occur. As demonstrated by Mena Osteriz *et al.* a rather tight fold can be modeled by a sequence of about eight thiophene units in *cis* conformation leading to a radius of curvature of  $\sim 10$  Å (32). This implies that the position of the reentrant chain is about 20 Å apart from the outgoing position along the  $\mathbf{a}_{\text{P3HT}}$  direction and does therefore not occur at the expected position of the next neighbour P3HT stem (at 16.5Å). This implies that tight folding is difficult in P3HT and this is likely the reason why the lateral growth of the nanocrystals along the  $\mathbf{a}_{\text{P3HT}}$  axis is made more difficult for higher- $M_w$  P3HT.

Second, the growth of P3HT domains is certainly influenced by the diffusion kinetics of the chains on the TCB surface. Diffusion of longer chains is likely to be more difficult on the TCB substrate as compared to oligomer-like chains. This is likely to favor the growth in the  $\mathbf{a}_{\text{P3HT}}$  direction for short chains.

Third, the PDI of the low and High- $M_w$  fractions differ notably. Low- $M_w$  P3HT shows a rather low polydispersity index that explains the relative constant overall lamellar thickness (stem length). As opposed to this, high- $M_w$  P3HT is way more polydisperse (PDI=1.9). The HR-TEM images show that the distribution of stem lengths in the high- $M_w$  samples is very

high *i.e.* P3HT lamellae show a strong tapering as observed for instance in PF2/6 and PFO lamellae grown on oriented PTFE (33). In the latter systems, lamellar tapering was explained in terms of segregation between short and long chains upon crystallization. A similar effect may also occur in the case of P3HT for high- $M_w$ .

Finally, it has to be mentioned that the growth of P3HT domains is driven by the epitaxial interaction with the substrate. This interaction favors the unidirectional stretching of the chains along  $c_{TCB}$ . It can be supposed that, once a segment of a long chain is oriented by epitaxy, the remaining section will tend to align in that direction because of favorable P3HT-TCB interactions. Accordingly, for longer chains, epitaxy is certainly enhancing the growth along  $c_{P3HT}$  at the expense of the lateral growth along  $a_{P3HT}$ .

	Low $M_w$	Medium $M_w$	High $M_w$
<b>CL</b> (Calculated contour length) (nm)*	10	15	25
<b>Statistics on HR-TEM images</b>			
<b><math>L_{stem}</math></b> (nm)	$\approx 6 \pm 1$ nm	$\sim 13 \pm 4$ nm	$\sim 16 \pm 6$ nm
<b><math>L_a</math></b> (Average number of Stems per domain)	$> 25$ stems	$\sim 19 \pm 7$ stems	$\sim 13 \pm 4$ stems
<b>Statistics from X-ray diffraction</b>			
<b><math>\delta</math> of 002 <math>q_{\perp}</math></b> (nm) (counterpart to $L_{stem}$ )		$10 \pm 2$ nm	$7 \pm 2$ nm (fitting difficult)
<b><math>\delta</math> of 100 <math>q_{\parallel}</math></b> (nm) (counterpart to $L_a$ )		$19 \pm 4$ nm ( $\sim 13$ stems)	$12 \pm 3$ nm ( $\sim 8$ stems)
<b><math>\delta</math> of 020 <math>q_{\parallel}</math></b> (nm) $L_b$ (extension in $b_{P3HT}$ )		$10 \pm 2$ nm ( $\sim 26$ $\pi$ -stacked chains)	$8 \pm 2$ nm ( $\sim 21$ $\pi$ -stacked chains)

Table 2-2: Characteristics of the crystallite sized as determined from the HR-TEM images and linear X-ray diffraction measurements. Measurements were performed on 130-250 stems for the HR-TEM images. \*The contour length of the polymer chains was calculated by using the corrected  $M_n$  by using the calibration curve given in reference (23).

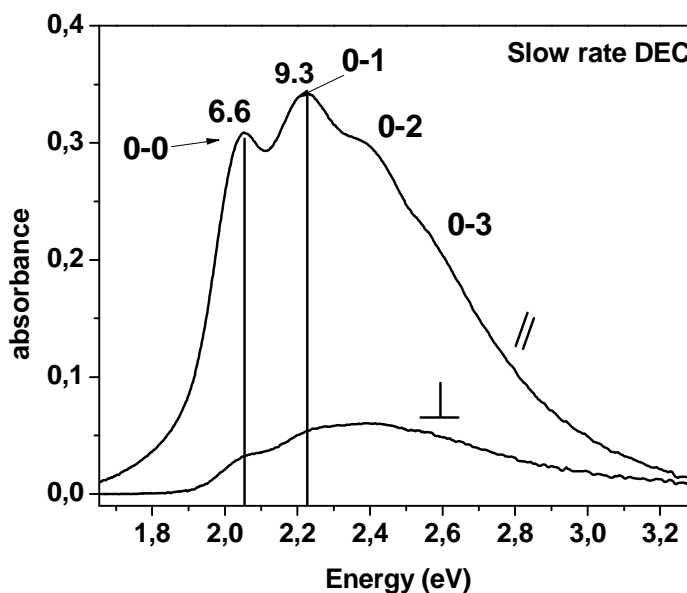
#### 2.4. Correlation between thin film structure and optical properties

It is well established that the crystalline order and orientation have a strong impact on the optical properties of thin P3HT films (3, 5, 34–38). The possibility to grow P3HT films with a high orientation and a high crystallinity was used as an opportunity to study the correlations between the structure and optical properties of the P3HT films. Herein we focused mainly on the absorption spectra of the P3HT films.

### 2.4.1. Anisotropy and vibronic structure of the absorption

Similarly to what was observed in the optical microscope under crossed polarizers (*Figure 1-1*), a high anisotropy can be observed in the polarized absorption spectrum of P3HT films grown by slow-DEC. *Figure 2-9* shows the averaged UV-vis spectrum over 5 spots of a medium- $M_w$  P3HT film for an incident light polarization parallel and perpendicular to the chain axis ( $c_{P3HT}$ ). As seen in the absorption spectrum recorded for an incident light polarized perpendicular to  $c_{P3HT}$  ( $Abs_{\perp}$ ) is almost featureless and should, in principle, correspond to the absorption from a small fraction of misaligned crystalline domains and a majority of amorphous fraction showing no polarized and no structured absorbance.

*Figure 2-9: UV-vis absorbance spectra of P3HT thin films (medium- $M_w$ ) prepared by slow-DEC in TCB for the incident light polarized parallel ( $\parallel$ ) and perpendicular ( $\perp$ ) to  $c_{TCB}$ . The numeric values in the figure correspond to the measured dichroic ratio at two wavelengths. The spectrum is an average spectrum of 5 different locations on a sample.*



The parallel contribution ( $Abs_{\parallel}$ ) comes from the well aligned crystalline part of the film. The spectra of the epitaxied films with an orientation parallel to the incident beam are similar to those observed for crystalline P3HT nanofibrils prepared from solution in *p*-xylene or anisole (39, 40). The 0-0 contribution at 610 nm (2.034eV) is particularly intense and the spectrum shows four well defined vibronic components. The dichroic ratios (DR) of epitaxied P3HT films were determined at two different wavelengths and are indicated on the spectrum. The extracted DR are of 9.3 at 610 nm and 6.6 at 560 nm. Note that in *Figure 2-9* an average spectrum of 5 different spots is displayed as the dichroic ratio varies from spot to spot. The obtained DR are quite high, in particular at a wavelength of 610 nm indicating a high level of orientation. The vibronic structure of absorbance is much better defined as compared to P3HT films prepared by spin coating, mechanical rubbing, friction transfer or strain alignment (13, 41–43) pointing at a higher degree of crystallinity of the films.

### 2.4.2. Evolution of the absorption spectrum with $M_w$

Figure 2-10 compares the UV-vis spectra of low-, medium- and high- $M_w$  samples oriented by slow-DEC for an incident light polarization parallel to the chain axis ( $C_{P3HT}$ ). Table 2-3 collects the main spectroscopic data. The spectra corresponding to an incident light polarization perpendicular to the chain axis are not displayed here as they are similar to the one shown in for the medium- $M_w$  sample. The perpendicular spectrum shows virtually no vibronic structure except a small contribution at 610 nm.

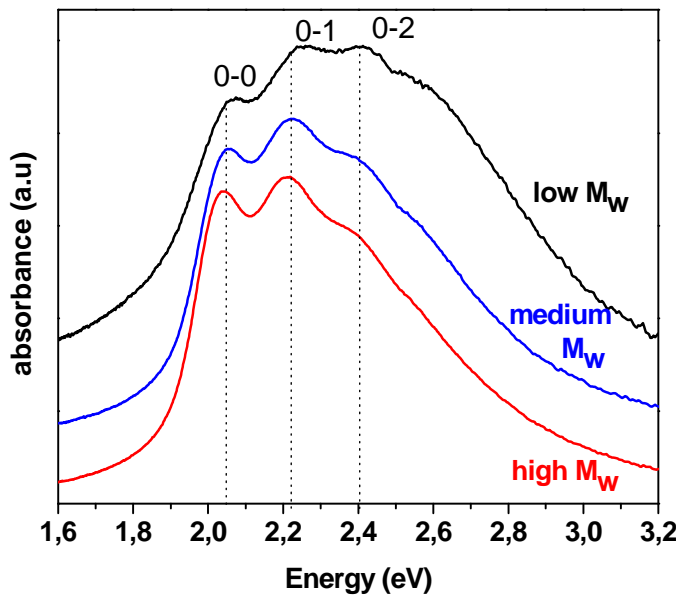


Figure 2-10 : Comparison of the UV-vis absorption spectra of P3HT films obtained by slow-DEC for different  $M_w$ . The spectra were recorded with the incident polarization // to the  $C_{P3HT}$  direction. The spectra are normalized in intensity and shifted along the ordinate axis for clarity.

There is a marked effect of  $M_w$  on the absorption spectra in terms of full width at half maximum (FWHM) and relative intensity of the different vibronic replica. Concerning the FWHM of the spectrum, it is significantly larger for low- $M_w$  (0.86 eV) as compared to medium- $M_w$  and high- $M_w$  P3HT (0.65 eV and 0.69 eV respectively). Comparing the vibronic structure of the medium and high- $M_w$  films, the 0-1 component is dominant for both, but the 0-0 component is relatively stronger in the high- $M_w$  sample compared to the low- $M_w$  sample. In the case of the low- $M_w$  sample, the 0-2 contribution is almost as intense as the 0-1 component in contrast to what is seen for high and medium- $M_w$ . A similar effect of  $M_w$  on the vibronic structure of the absorption has been reported by Zen *et al.* for spin-coated thin films (3). It has been attributed to the variation of the conjugation length with  $M_w$ : low- $M_w$  samples show shorter segments of planarized backbones than high- $M_w$  samples. Accordingly, the absorption of low- $M_w$  samples is more blue-shifted. The large FWHM observed for low- $M_w$  samples reflects a large distribution of conjugation lengths.

For all samples high DR were measured. The best obtained values and other spectroscopic data are summarized in Table 2-3. Again the high and medium- $M_w$  samples display DR in the same range whereas the low molecular weight sample shows a lower DR. This observation is consistent with the evolution of in-plane orientation with  $M_w$  presented in section 2.1.3 (Figure 2-5). As seen in Table 2-3, the observed DR are consistent with the

observed azimuthal distributions of the (100)<sub>P3HT</sub> reflection. Again, this result shows that the microscopic information on orientation obtained by TEM is representative of the whole sample on larger scales.

	CL (nm)	Best measured Dichroic ratio		FWHM (eV)	Azimuthal distribution of the (100) reflection from ED
		550 nm	610 nm		
<b>Low M<sub>w</sub> (1)</b>	10	6	11.5	0.86	37°
<b>Medium M<sub>w</sub></b>	15	10	16	0.69	21°
<b>high M<sub>w</sub></b>	25	10	14	0.65	23°

Table 2-3: Main data extracted from the UV-vis absorbance for the three different molecular weight samples.

#### 2.4.3. Discussion on the origin of the vibronic structure of the absorption spectra

As seen in the HR-TEM images, the amorphous and the crystalline domains are clearly visible in slow-DEC samples. One important advantage of highly oriented P3HT samples is the possibility to separate the absorbance arising from the amorphous fraction from that of the highly oriented and crystalline fraction. Subtracting the absorption spectrum **Abs<sub>⊥</sub>** from the **Abs<sub>//</sub>**, one should in principle yield a spectrum that is representative of the only crystalline fraction of the sample. As shown hereafter, this can be of interest for a better understanding of the origin of the vibronic structure. In non oriented thin films prepared by spin coating there is no possibility to distinguish between the absorbance of the crystalline and the amorphous phase. The high degree of orientation in slow-DEC samples makes such a distinction possible.

Figure 2-11 shows the resulting spectrum **Abs<sub>//</sub>(E) - Abs<sub>⊥</sub>(E)** for the different M<sub>w</sub>. The relative intensity of the 0-0 component becomes very strong in all cases and more particularly in the case of the high-M<sub>w</sub> sample. In order to understand this observation we will subsequently describe the main models used in previous studies to describe the structure/optical property correlations.

The origin of the vibronic structure of photoluminescence and absorbance in P3HT thin films was described and analyzed by various models (34–38, 44, 45). Brown *et al.* and Spano (34, 35, 44) claimed that the vibronic structure of P3HT cannot be described by a Frank–Condon distribution of relative intensities of the vibronic replica in particular because of the weak intensity of the 0-0 replica in emission. This motivated them to re-interpret the analysis of the vibronic structure of P3HT. Brown *et al.* considered two different emitter

states close in energy: one originating from a single molecule like state (intramolecular), and the second one from an intermolecular aggregate-like state.

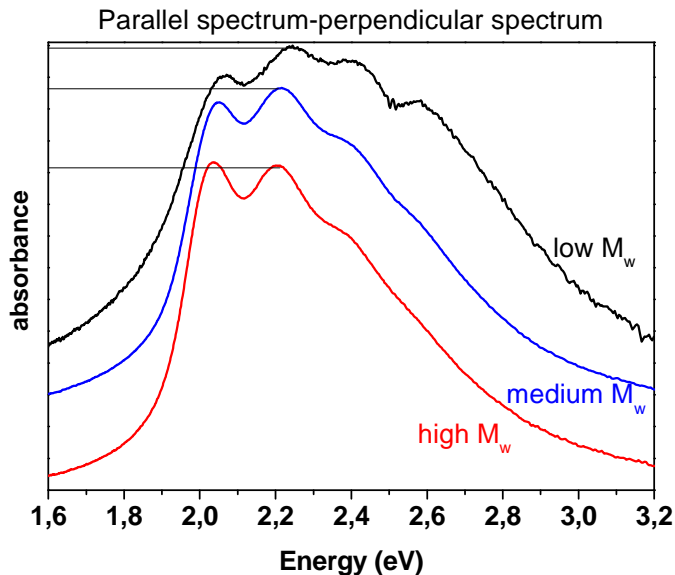


Figure 2-11: Absorbance spectra recorded with the incident polarization oriented // to the in-plane direction of the P3HT chains to which the spectra recorded with the incident polarization  $\perp$  was subtracted. The spectra are normalized in intensity and shifted along the ordinate axis for clarity.

However, a second more successful model was proposed by Spano (34–36), showing that a two emitter state model is not necessary to describe the P3HT solid state emission and absorption. Spano considered that the spectrum of P3HT is composed of two parts: one arising from weakly interacting H-aggregates (absorbing at low energies) and the second related to the amorphous fraction of the films (absorbing at higher energies). He took into account a weak excitonic coupling  $W$  in weakly interacting H aggregates of P3HT to model the lower energy component of the absorbance spectra. The higher energy part of the spectrum cannot be modeled with satisfaction by the H-aggregate model and is attributed by Spano to disordered or coiled P3HT chains in the amorphous part of the film. Spano and coworkers approximated the absorption of the amorphous part of the films with that of P3HT in solution (37, 38). To model the low energy absorbance spectrum of the H aggregates, a spectrum of the amorphous phase has thus to be subtracted.

The consideration that the spectrum of the amorphous phase is equivalent to that of a solution is a crude approximation as the environments of a polymer chain in solution and in a thin film are certainly not equivalent. This is further supported by our observations. Indeed, whereas the spectrum of P3HT in solution is peaked at approximately 2.74 eV (452 nm), the spectrum of  $\text{Abs}_{\perp}(E)$  is significantly shifted towards lower energies and peaks at  $\sim 2.4$  eV (520 nm).

The model of Spano was used by numerous groups to derive the magnitude of the excitonic coupling  $W$  in P3HT aggregates, from the careful analysis of the vibronic structure of the absorption spectra. Indeed, Spano showed that for the aggregate part of the spectrum the ratio  $A_{0-0}/A_{0-1}$  can be written in the form:

$$\frac{A_{0-0}}{A_{0-1}} = \frac{n_{0-0}}{n_{0-1}} \frac{\left(1 - \frac{W}{2E_p} e^{-S} \sum_{\nu > 0} \frac{S^\nu}{\nu! \nu}\right)^2}{S \left(1 - \frac{W}{2E_p} e^{-S} \sum_{\nu \neq 1} \frac{S^\nu}{\nu! (\nu-1)}\right)^2} \quad (\text{Eq. 4})$$

where  $E_p$  is the phonon energy of the main oscillator mode coupled to the electronic transition (assumed to be 0.18 eV corresponding to a symmetric C=C stretch) and  $W$  is the free exciton bandwidth.  $S$  is the electron-phonon coupling strength (Huang-Rhys factor) and  $n_{0-1}$  and  $n_{0-0}$  are the refractive indices at the energy of  $A_{0-1}$  and  $A_{0-0}$ . Knowing the Huang-Rhys factor  $S$ , and assuming  $n_{0-0} \approx n_{0-1}$  the free exciton bandwidth  $W$  can be directly accessed from the ratio of the intensities  $A_{0-0}/A_{0-1}$ .

For P3HT, a Huang-Rhys factor  $S=1$  is generally assumed (34–38, 46). For  $S=1$ , the ratio of intensity of the 0-0 and the 0-1 vibronic replica  $A_{0-0}/A_{0-1}$  is related to the free exciton bandwidth within the crystalline domains  $W$  and the energy of the vibration mode coupled to the electronic transition  $E_p$  following:

$$\frac{A_{0-0}}{A_{0-1}} = \left( \frac{1 - 0.24W/E_p}{1 + 0.073W/E_p} \right)^2 \quad (\text{Eq. 5})$$

Following the work by Clark *et al.*,  $W$  is related to the crystalline perfection within the P3HT aggregates: the higher the crystallinity, the lower the value of  $W$  (37, 38). Since the crystallinity of spin coated films depends strongly on the solvent that is used, a clear correlation between solvents and  $W$  was found by Clark *et al.* Typical values of  $W$  reported in the literature are:  $W \sim 120$  meV for spin coated films from chloroform,  $W \sim 30$  meV for spin coated films from isodurene and  $W \sim 57$  for spin coated films from xylene (38). Crossland *et al.* found free exciton bandwidth going from  $W \sim 90$  meV for the as coated films (from 1,2,4 trichlorobenzene) to  $W \sim 50$  meV after swelling the film in  $\text{CS}_2$  vapor followed by controlled re-crystallization (27).

As this model was developed for the part of the films formed of H-Aggregates, we applied this model on the slow-DEC samples to extract  $W$  from the crystalline only part of the films. This approach is justified as in slow-DEC samples, as the amorphous and the crystalline parts can be well distinguished as seen in HR-TEM. Applying this model to a low and medium- $M_w$  sample yields values of  $W_{\text{low}} = 28 \text{ meV}$  and  $W_{\text{medium}} = 14 \text{ meV}$ . A reduced value in  $W$  is a fingerprint of well packed, planarized and well stacked P3HT backbones and thus to a higher conjugation length. These values obtained for the slow-DEC samples are very low indicating once again the high degree of crystalline order and orientation of such films.

Although the model of Spano seems to work well for low and medium- $M_w$  samples, it does not account for the description of the high- $M_w$  sample. Indeed, from equation 1, the ratio  $A_{0-0}/A_{0-1} < 1$  for all values of  $S$ . Nevertheless,  $A_{0-0}/A_{0-1}$  is slightly larger than 1 for the high- $M_w$

(see Figure 2-11). This led us to develop an alternative qualitative interpretation of our results based on earlier reports by Hagler *et al.* on oriented MEH-PPV (47). The latter authors reported also a predominant zero-phonon 0-0 line in the absorption spectrum of highly oriented MEHPPV at 80 K. In contrast to this, for the cast MEH-PPV films the 0-0 contribution is very weak (47). Hagler *et al.* reported Huang-Rhys factors of  $S = 0.4 - S = 0.85$ . A reduced  $S$  factor is interpreted as a fingerprint of enhanced electronic delocalization. The observations of Hagler *et al.* regarding the comparison of highly oriented systems and spin coated systems, reminds our situation in the case of the high- $M_w$  sample. In fact, in comparison to spin coated P3HT films, the 0-0 component in epitaxied layers is high.

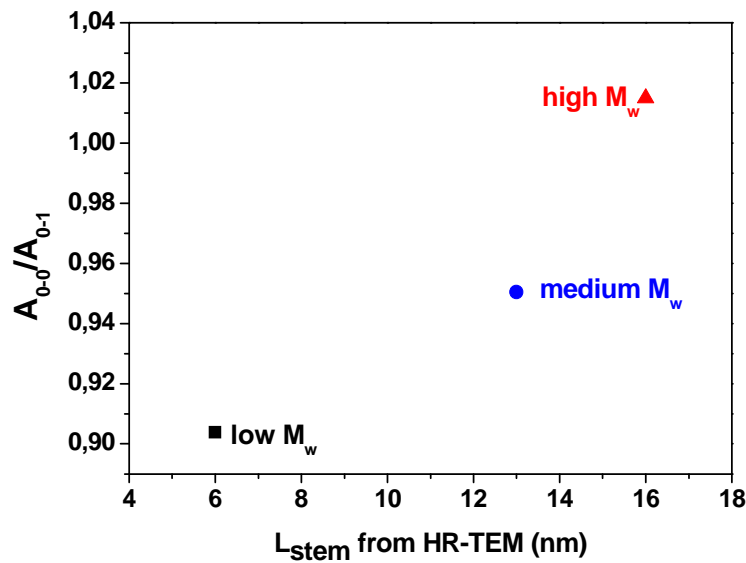


Figure 2-12 :  $A_{0-0}/A_{0-1}$  as a function of the stem length from HR-TEM.

Following the work of Hagler *et al.*, the change in the vibronic structure with increasing  $M_w$  can be interpreted in terms of a variation of the Huang-Rhys parameter  $S$  that quantifies the electron-phonon coupling (47). Our HR-TEM results have shown that the size of the crystalline ordered domains tend to increase with  $M_w$ . It can accordingly be expected that the conjugation length increases in the same way with  $M_w$ . Therefore a higher delocalization of the electronic states can be expected for higher  $M_w$ . Concomitant to the delocalization, a lowering of the electron-phonon coupling is expected when  $M_w$  increases *i.e.* a redistribution of the intensity in the 0-phonon line of the absorption spectrum. The correlation between the observations from the HR-TEM measurements and the change in the relative intensity of the 0-0 vibronic contribution is illustrated in Figure 2-12. It can be clearly seen that the relative intensity of the 0-0 contribution increases with increasing stem length suggesting an increase in the conjugation length with increasing  $M_w$ .

To further understand the correlations between the crystalline order of the thin films and their optical properties and to further elucidate the particular behavior of the vibronic structure of absorbance in the slow-DEC samples, we performed temperature dependent

polarized photoluminescence measurements. The analysis of the results of these measurements is still in progress.

### 3. Conclusion

Highly oriented P3HT films on the cm<sup>2</sup> scale were prepared by using the slow-DEC method introduced in the previous chapter. The properties of the films were studied and it could be shown that the molecular weight is a key parameter regarding several characteristics of the films.

- (i) Structure of the films: high and medium- $M_w$  samples present a crystallographic fiber structure with  $c_{P3HT}$  as fiber axis whereas low- $M_w$  samples show very clearly preferential contact planes. These differences in structure are directly reflected by the morphology of the thin films.
- (ii) Degree of in-plane orientation: The distribution of the in-plane orientation was found to be narrower in the high and medium- $M_w$  samples compared to the low- $M_w$  samples.
- (iii) Lamellar structure:  $M_w$  has a strong influence on the lamellar structure and the lamellar periodicity. Slowing down the growth kinetics by using slow-DEC allowed to increase the lamellar periodicity up to ~45 nm in the case of the high- $M_w$  sample. Such high periodicities of the lamellar structure are rarely observed for P3HT. It was shown that the lamellar structure that is the most suited for the fabrication of hybrid nanostructured materials comprising P3HT and CdSe nanocrystals is the one of medium- $M_w$  P3HT.
- (iv) Shape of the crystalline domains: The crystalline domains of low- $M_w$  are extended in the  $a_{P3HT}$  direction whereas for the high- $M_w$  the crystalline domains are preferentially extended in the  $c_{P3HT}$  direction.
- (v) Optical properties: The differences in terms of orientation and crystal domain shapes of the various  $M_w$  samples are directly reflected in the optical properties of the films. The vibronic structure of the thin films is particularly well defined. The 0-0 contribution becomes very strong with increasing  $M_w$  suggesting a higher conjugation length in these films due to the higher extension of the crystalline domains in the  $c_{P3HT}$  direction.

The high degree of crystallinity and orientation of slow-DEC films makes them particularly interesting for fundamental studies. In particular the anisotropy of these films is of interest for the study of the optical properties as it allows to study the only crystalline part of the thin films. In the following chapter, hybrid materials composed of P3HT and CdSe were characterized in terms of morphology, structure and orientation.

- (1) Brinkmann, M. Structure and morphology control in thin films of regioregular poly(3-hexylthiophene). *Journal of Polymer Science Part B: Polymer Physics* **2011**, *49*, 1218-1233.
- (2) Brinkmann, M.; Rannou, P. Effect of molecular weight on the structure and morphology of oriented thin films of regioregular poly(3-hexylthiophene) grown by directional epitaxial solidification. *Advanced Functional Materials* **2007**, *17*, 101-108.
- (3) Zen, A.; Pflaum, J.; Hirschmann, S.; Zhuang, W.; Jaiser, F.; Asawapirom, U.; Rabe, J. P.; Scherf, U.; Neher, D. Effect of molecular weight and annealing of Poly(3-hexylthiophene)s on the performance of organic field-effect transistors. *Advanced Functional Materials* **2004**, *14*, 757-764.
- (4) Brinkmann, M.; Rannou, P. Molecular weight dependence of chain packing and semicrystalline structure in oriented films of regioregular poly(3-hexylthiophene) revealed by high-resolution transmission electron microscopy. *Macromolecules* **2009**, *42*, 1125-1130.
- (5) Trznadel, M.; Pron, A.; Zagorska, M.; Chrzaszcz, R.; Pielichowski, J. Effect of molecular weight on spectroscopic and spectroelectrochemical properties of regioregular poly(3-hexylthiophene). *Macromolecules* **1998**, *31*, 5051-8.
- (6) Brinkmann, M.; Chandezon, F.; Pansu, R. B.; Julien-Rabant, C. Epitaxial growth of highly oriented fibers of semiconducting polymers with a Shish-Kebab-like superstructure. *Advanced Functional Materials* **2009**, *19*, 2759-2766.
- (7) Yang, H.; LeFevre, S. W.; Ryu, C. Y.; Bao, Z. Solubility-driven thin film structures of regioregular poly ( 3-hexyl thiophene ) using volatile solvents. *Applied Physics Letters* **2007**, *90*, 172116.
- (8) Porzio, W.; Scavia, G.; Barba, L.; Arrighetti, G.; Milita, S. Depth-resolved molecular structure and orientation of polymer thin films by synchrotron X-ray diffraction. *European Polymer Journal* **2010**, *47*, 273-283.
- (9) Joseph Kline, R.; McGehee, M. D.; Toney, M. F. Highly oriented crystals at the buried interface in polythiophene thin-film transistors. *Nature Materials* **2006**, *5*, 222-228.
- (10) Yang, H.; Shin, T. J.; Yang, L.; Cho, K.; Ryu, C. Y.; Bao, Z. Effect of Mesoscale Crystalline Structure on the Field-Effect Mobility of Regioregular Poly(3-hexyl thiophene) in Thin-Film Transistors. *Advanced Functional Materials* **2005**, *15*, 671-676.
- (11) Jimison, L. H.; Toney, M. F.; McCulloch, I.; Heeney, M.; Salleo, A. Charge-transport anisotropy due to grain boundaries in directionally crystallized thin films of regioregular poly(3-hexylthiophene). *Advanced Materials* **2009**, *21*, 1568-1572.
- (12) Brinkmann, M.; Contal, C.; Kayunkid, N.; Djuric, T.; Resel, R. Highly oriented and nanotextured films of regioregular poly(3-hexylthiophene) grown by epitaxy on the nanostructured surface of an aromatic substrate. *Macromolecules* **2010**, *43*, 7604-7610.
- (13) O'Connor, B.; Kline, R. J.; Conrad, B. R.; Richter, L. J.; Gundlach, D.; Toney, M. F.; DeLongchamp, D. M. Anisotropic structure and charge transport in highly strain-aligned regioregular poly(3-hexylthiophene). *Advanced Functional Materials* **2011**, *21*, 3697-3705.

- (14) Kim, D. H.; Jang, Y.; Park, Y. D.; Cho, K. Layered molecular ordering of self-organized poly(3-hexylthiophene) thin films on hydrophobized surfaces. *Macromolecules* **2006**, *39*, 5843-5847.
- (15) Kim, D. H.; Park, Y. D.; Jang, Y.; Yang, H.; Kim, Y. H.; Han, J. I.; Moon, D. G.; Park, S.; Chang, T.; Chang, C.; Joo, M.; Ryu, C. Y.; Cho, K. Enhancement of field-effect mobility due to surface-mediated molecular ordering in regioregular polythiophene thin film transistors. *Advanced Functional Materials* **2005**, *15*, 77-82.
- (16) Verilhac, J.-M.; LeBlevenec, G.; Djurado, D.; Rieutord, F.; Chouiki, M.; Travers, J.-P.; Pron, A. Effect of macromolecular parameters and processing conditions on supramolecular organisation, morphology and electrical transport properties in thin layers of regioregular poly(3-hexylthiophene). *Synthetic Metals* **2006**, *156*, 815-823.
- (17) Zen, A.; Saphiannikova, M.; Neher, D.; Grenzer, J.; Grigorian, S.; Pietsch, U.; Asawapirom, U.; Janietz, S.; Scherf, U.; Lieberwirth, I.; Wegner, G. Effect of molecular weight on the structure and crystallinity of poly(3-hexylthiophene). *Macromolecules* **2006**, *39*, 2162-2171.
- (18) Wu, Z.; Petzold, A.; Henze, T.; Thurn-Albrecht, T.; Lohwasser, R. H.; Sommer, M.; Thelakkat, M. Temperature and molecular weight dependent hierarchical equilibrium structures in semiconducting poly(3-hexylthiophene). *Macromolecules* **2010**, *43*, 4646-4653.
- (19) Kline, R. J.; McGehee, M. D.; Kadnikova, E. N.; Liu, J.; Fréchet, J. M. J.; Toney, M. F. Dependence of regioregular poly(3-hexylthiophene) film morphology and field-effect mobility on molecular weight. *Macromolecules* **2005**, *38*, 3312-3319.
- (20) Kayunkid, N.; Uttiya, S.; Brinkmann, M. Structural model of regioregular poly(3-hexylthiophene) obtained by electron diffraction analysis. *Macromolecules* **2010**, *43*, 4961-4967.
- (21) Nagamatsu, S.; Takashima, W.; Kaneto, K.; Yoshida, Y.; Tanigaki, N.; Yase, K.; Omote, K. Backbone arrangement in “ friction-transferred ” regioregular poly ( 3-alkylthiophene ) s. *Macromolecules* **2003**, *36*, 5252-5257.
- (22) Brinkmann, M.; Aldakov, D.; Chandezon, F. Fabrication of oriented and periodic hybrid nanostructures of regioregular poly(3-hexylthiophene) and CdSe nanocrystals by directional epitaxial solidification. *Advanced Materials* **2007**, *19*, 3819-3823.
- (23) Liu, J.; Loewe, R. S.; McCullough, R. D. Employing MALDI-MS on poly(alkylthiophenes): analysis of molecular weights, molecular weight distributions, end-group structures, and end-group modifications. *Macromolecules* **1999**, *32*, 5777-5785.
- (24) Zhang, R.; Li, B.; Iovu, M. C.; Jeffries-El, M.; Sauv e, G.; Cooper, J.; Jia, S.; Tristram-Nagle, S.; Smilgies, D. M.; Lambeth, D. N.; McCullough, R. D.; Kowalewski, T. Nanostructure dependence of field-effect mobility in regioregular poly(3-hexylthiophene) thin film field effect transistors. *Journal of the American Chemical Society* **2006**, *128*, 3480-1.
- (25) M uller, C.; Zhigadlo, N. D.; Kumar, A.; Baklar, M. A.; Karpinski, J.; Smith, P.; Kreouzis, T.; Stingelin, N. Enhanced charge-carrier mobility in high-pressure-crystallized poly (3-hexylthiophene). *Macromolecules* **2011**, *44*, 1221-1225.

- (26) Canetti, M.; Bertini, F.; Scavia, G.; Porzio, W. Structural investigation on bulk poly(3-hexylthiophene): Combined SAXS, WAXD, and AFM studies. *European Polymer Journal* **2009**, *45*, 2572-2579.
- (27) Crossland, E. J. W.; Rahimi, K.; Reiter, G.; Steiner, U.; Ludwigs, S. Systematic control of nucleation density in poly (3-hexylthiophene) thin films. *Advanced Functional Materials* **2010**, *21*, 518-524.
- (28) Wunderlich, B.; Davidson, T. Extended-chain crystals I. general crystallization conditions and review of pressure crystallization of polyethylene. *Journal of Polymer science part A-2* **1969**, *7*, 2043-2050.
- (29) Davidson, T.; Wunderlich, B. Extended-chain crystals II. crystallization of polyethylene under elevated pressure. *Journal of Polymer science part A-2* **1969**, *7*, 2051-2059.
- (30) Prime, R. B.; Wunderlich, R. Extended-chain crystals III. size distribution of polyethylene crystals grown under elevated pressure. *Journal of Polymer science part A-2* **1969**, *7*, 2061-2072.
- (31) Hikosaka, M.; Amano, K.; Ratsogi, S.; Keller, A. Lamellar thickening growth of an extended chain single crystal of polyethylene 1. pointers to a new crystallization mechanism of polymers. *Macromolecules* **1997**, *30*, 2067-2074.
- (32) Mena-Osteritz, E.; Meyer, A.; Langeveld-voss, B. M. W.; Janssen, R. A. J.; Meijer, E. W.; Bäuerle, P. Two-dimensional crystals of poly(3-alkyl-thiophen)s: direct visualization of polymer folds in submolecular resolution. *Angewandte Chemie (International ed. in English)* **2000**, *39*, 2679-2684.
- (33) Lieser, G.; Oda, M.; Miteva, T.; Meisel, A.; Nothofer, H.-G.; Scherf, U. Ordering , graphoepitaxial orientation , and conformation of a polyfluorene derivative of the “ hairy-rod ” type on an oriented substrate of polyimide. *Macromolecules* **2000**, *33*, 4490-4495.
- (34) Spano, F. C. Modeling disorder in polymer aggregates: the optical spectroscopy of regioregular poly(3-hexylthiophene) thin films. *The Journal of chemical physics* **2005**, *122*, 234701.
- (35) Spano, F. Absorption in regio-regular poly(3-hexyl)thiophene thin films: Fermi resonances, interband coupling and disorder. *Chemical Physics* **2006**, *325*, 22-35.
- (36) Spano, F. C.; Clark, J.; Silva, C.; Friend, R. H. Determining exciton coherence from the photoluminescence spectral line shape in poly(3-hexylthiophene) thin films. *The Journal of chemical physics* **2009**, *130*, 074904.
- (37) Clark, J.; Silva, C.; Friend, R.; Spano, F. Role of intermolecular coupling in the photophysics of disordered organic semiconductors: aggregate emission in regioregular polythiophene. *Physical Review Letters* **2007**, *98*, 1-4.
- (38) Clark, J.; Chang, J.-F.; Spano, F. C.; Friend, R. H.; Silva, C. Determining exciton bandwidth and film microstructure in polythiophene films using linear absorption spectroscopy. *Applied Physics Letters* **2009**, *94*, 163306.
- (39) Berson, S.; De Bettignies, R.; Bailly, S.; Guillerez, S. Poly(3-hexylthiophene) Fibers for Photovoltaic Applications. *Advanced Functional Materials* **2007**, *17*, 1377-1384.

- (40) Samitsu, S.; Shimomura, T.; Heike, S.; Hashizume, T.; Ito, K. Effective production of poly(3-alkylthiophene) nanofibers by means of whisker method using anisole solvent: structural, optical, and electrical properties. *Macromolecules* **2008**, *41*, 8000-8010.
- (41) Zhu, R.; Kumar, A.; Yang, Y. Polarizing organic photovoltaics. *Advanced Materials* **2011**, *23*, 4193-4198.
- (42) Nagamatsu, S.; Takashima, W.; Kaneto, K.; Yoshida, Y.; Tanigaki, N.; Yase, K.; Omote, K. Backbone arrangement in “friction-transferred” regioregular poly(3-alkylthiophene)s. *Macromolecules* **2003**, *36*, 5252-5257.
- (43) Hartmann, L.; Tremel, K.; Uttiya, S.; Crossland, E.; Ludwigs, S.; Kayunkid, N.; Vergnat, C.; Brinkmann, M. 2D versus 3D crystalline order in thin films of regioregular Poly(3-hexylthiophene) oriented by mechanical rubbing and epitaxy. *Advanced Functional Materials* **2011**, *21*, 4047-4057.
- (44) Brown, P.; Thomas, D.; Köhler, A.; Wilson, J.; Kim, J.-S.; Ramsdale, C.; Siringhaus, H.; Friend, R. Effect of interchain interactions on the absorption and emission of poly(3-hexylthiophene). *Physical Review B* **2003**, *67*, 1-16.
- (45) Kobayashi, T.; Hamazaki, J.-ichi; Kunugita, H.; Ema, K.; Endo, T.; Rikukawa, M.; Sanui, K. Coexistence of photoluminescence from two intrachain states in polythiophene films. *Physical Review B* **2003**, *67*, 205214.
- (46) Banerji, N.; Cowan, S.; Vauthey, E.; Heeger, A. J. Ultrafast relaxation of the poly ( 3-hexylthiophene ) emission spectrum. *Journal of Physical Chemistry C* **2011**, *115*, 9726-9739.
- (47) Hagler, T. W.; Pakbaz, K.; Voss, K. F.; Heeger, A. J. Enhanced order and electronic delocalization in conjugated polymers oriented by gel processing in polyethylene. *Physical Review B* **1991**, *44*, 8652-8665.



## **Chapter 5. Oriented thin P3HT films via mechanical rubbing**

*This chapter is dedicated to the preparation and characterization of highly oriented thin films of rr-poly(3-hexylthiophene) prepared by mechanical rubbing. The structure, the nanomorphology and the optical properties of the oriented films were investigated by GIXD, ED, HR-TEM, UV-vis absorption and PL spectroscopy and transport measurements in OFETs. In rubbed P3HT films, the chains align parallel to the rubbing direction and the orientation of the crystalline domains changes from preferential “edge-on” to “flat-on” orientation of the conjugated backbone. The maximum in-plane orientation probed by UV-vis absorption spectroscopy is a function of  $M_w$ ; the lower  $M_w$ , the higher the in-plane orientation induced by mechanical rubbing. The anisotropy of field-effect mobility measured parallel and perpendicular to the rubbing shows a similar trend. The  $M_w$ -dependence of the orientation is explained in terms of chain folding and entanglement that prevent the reorientation and reorganization of the  $\pi$ -stacked chains. Important structural differences between rubbed and epitaxied P3HT films were evidenced. These differences are directly reflected in the vibronic structure of the absorbance spectra. First we will introduce the rubbing technique. Secondly, the structural properties of a medium- $M_w$  P3HT will be presented as an example. Subsequently, the effect of the  $M_w$  on the efficiency of the rubbing process will be presented. Finally the important structural differences between rubbed films and epitaxied films prepared by slow-DEC will be highlighted.*



## 1. Introduction and Principle of the technique

Mechanical rubbing is a technique that is extensively used for the alignment and orientation of organic molecules and polymers. For example, this technique is used for the preparation of oriented substrates of polyimide on which liquid crystals can be aligned (1, 2). The rubbing method is also used to prepare oriented films of polycarbonate that can be used as orienting substrates for numerous molecules such as Zinc phthalocyanines (3–6). Orientation and improvement of the mobility upon rubbing was observed for small conjugated molecules such as  $\alpha$ -sexithiophenes (7, 8). The orientation of polymers by mechanical rubbing is possible due to the shearing forces that act on the thin films and therefore this method is similar to methods like strain alignment or orientation of polymers by friction transfer (9–12). This approach is quite different from those making use of an orienting substrate such as directional epitaxial crystallization of P3HT on 1,3,5 TCB for example. The orientation of P3HT upon mechanical rubbing is generally attributed to a combination of two effects, which are the shearing forces that allow to align the P3HT backbone parallel to the rubbing direction, and the pressure that is applied to the thin film during the rubbing that forces the molecular planes to orient parallel to the substrate (“flat-on” orientation) (13, 14). Orientation of P3AT by mechanical rubbing has however been only little described in the literature (13–17). For example, rubbing of P3HT has been demonstrated to lead to sizable anisotropic charge transport by Heil *et al.* but no clear explanation for the orientation mechanism was proposed (16). Derue *et al.* performed some rubbing and nano-rubbing on P3HT by using an AFM tip in contact mode to orient P3HT backbones (13). Recently, a very interesting work was published on the use of rubbed P3HT thin films for the fabrication of polarizing photovoltaic devices used as power converting polarizers in displays (14). But in most of these reports a clear understanding of the rubbing mechanism on the structure of P3HT films is lacking.

Herein we present a structural study on the orientation mechanism during the rubbing process. Various aspects *e.g.* the crystallinity, the in-plane orientation, the optical properties and the transport properties are investigated by using TEM (in different modes), GIXD, optical absorption spectroscopy and transport measurements in OFETs. In a first section (section 2), we will present the experimental protocol for the rubbing experiment. Secondly, the effect of rubbing on the morphology, in-plane orientation and structure on the example of a medium- $M_w$  sample ( $M_w = 17.6$  kDa,  $M_n = 13.4$  kDa) will be discussed (section 3). This study allowed proposing a tentative explanation for the orientation process. In a third part, the effect of the molecular weight on the in-plane orientation, the structure and the nanomorphology will be presented (section 4). These results could be directly correlated to the vibronic structure observed in the absorbance spectra. Finally, a comparative study highlighting the main differences and similitudes of rubbed and epitaxied thin P3HT films will be presented (section 5).

## 2. Experimental conditions

### 2.1. Mechanical Rubbing

In this work, rubbing of the P3HT films was performed with a home-made apparatus similar to the one described by Vergnat *et al.* and Brinkmann *et al.* (3, 5, 6). A cylinder (4 cm diameter) rotating at a constant speed and covered with a microfiber cloth was applied with a constant pressure of approximately 2 bar on a P3HT film that is fixed by vacuum onto a translation stage moving at a constant speed. Before being subjected to the rubbing process, P3HT thin films were deposited by the doctor-blade method from a 8 wt % solution (chlorobenzene for  $M_w \geq 17.2$  kDa or chloroform for  $M_w \leq 8$  kDa) on a clean glass slide for optical measurements and TEM characterization. For X-ray diffraction measurements, thin films were directly deposited on silicon wafers. A detailed description of the experimental setup and deposition procedure of the thin films can be found in Annexe 3. An important parameter in all rubbing experiments is the the rubbing length, defined as the length of the rubbing tissue which contacts a certain point of the polymer film at a constant pressure. For the used experimental setup one rubbing cycle is defined by a rubbing length of ~50cm. For the maximum degree of orientation 2-4 rubbing cycles are necessary (total rubbing length of 100 to 200 cm). The number of rubbing steps necessary to achieve the highest possible degree of orientation of the thin films depends however strongly on the thickness of the latter. Also, as the orientation process depends on the applied pressure, small variations in the substrate thickness can influence the number of rubbing cycles necessary to get a highest degree of orientation. For the rubbing experiments presented in the following, the number of rubbing steps is noted as **R<sub>x</sub>** (**x = 0-5**) where x designs the number of rubbing cycles. Unless specified, all samples were rubbed to achieve the highest orientation while avoiding material loss by scratching. This point of maximum orientation upon rubbing can be observed by an experienced eye of the scientist by observing the film after each rubbing step with a polarized optical microscope.

### 2.2. GIXD measurements

Using GIXD, the structure and orientation of the films was probed. GIXD measurements were performed at the ESRF and allowed to get a good insight in the structural transformations that are involved in P3HT films by the rubbing process. The scattering configurations are the same as described previously for the samples grown by slow-DEC (see Chapter 4). In addition, the XRD measurements were performed at various incidence angles  $\alpha$  of the incident X-ray beam. In fact, changing the incidence angle allows controlling the penetration depth of the X-ray beam in the films. Thus it is possible to investigate the structure of the very surface layer of the films separately from the bulk of the films. In our case we were particularly interested to understand how the orientation induced by mechanical rubbing propagates through the entire film thickness.

The relation between the incident angle  $a$  of the X-ray beam and the penetration depth  $P(a)$  can be expressed as follows:

$$P(a) = \frac{-\lambda}{4\pi B(a)}$$

With  $B(a) = \frac{-1}{\sqrt{2}} \sqrt{\sqrt{\left(a^2 - 2 \frac{\rho_e r_0 \lambda^2}{2\pi}\right)^2 + 4\beta^2} - \left(a^2 - 2 \frac{\rho_e r_0 \lambda^2}{2\pi}\right)}$  where  $\alpha$  is the incidence angle of the X-rays,  $\lambda$  is the wavelength  $\rho_e$  is the electron density of the sample,  $r_0$  is the classical electron radius, and  $\beta$  is the absorption coefficient of the X-ray beam by the sample.

In our case, the wavelength was  $\lambda = 0.59 \text{ \AA}$  and the incidence  $\alpha$  angle was varied in most cases from  $\alpha = 0.01^\circ$  allowing to probe only the very first layers at the “film-air” interface of the film to  $\alpha = 0.06^\circ$  allowing a deep penetration of the beam and thus the analysis of the entire film thickness. These measurements were performed in two configurations *i.e.* with  $\mathbf{q} // \mathbf{c}_{\text{P3HT}}$  and with  $\mathbf{q} \perp \mathbf{c}_{\text{P3HT}}$ .  $\Omega$  scans allowing to study the degree of in-plane orientation of the thin films were performed on the rubbed P3HT films. The  $\mathbf{q}$  vector in the plane of the substrate that are neither  $//$  nor  $\perp$  to  $\mathbf{c}_{\text{P3HT}}$  will be noted  $\mathbf{q}_{\text{in}}$  (for example in the case of non oriented samples).

In the following, we studied the morphology and optical properties of the thin films that were rubbed to the maximum degree of orientation for a medium  $M_w$ . After, the influence of the number of rubbing steps on the structure and the orientation of the P3HT thin films was probed by GIXD measurements performed at ESRF. GIXD was used with different incidence angles to probe the structure of the rubbed layers trough the entire thickness of the films

### **3. Effect of mechanical rubbing on the structure and orientation of medium $M_w$ (17.6 kDa) P3HT film**

The main characteristic features on the effect of mechanical rubbing on thin P3HT layers will first be introduced on the example of a medium- $M_w$  sample. Afterwards the effect of  $M_w$  on the orientation, structure and optical properties will be investigated.

#### **3.1. Morphology of the rubbed P3HT films**

Figure 3-1 shows a POM image of a medium- $M_w$  sample ( $M_w = 17.6 \text{ kDa}$ ) that was rubbed 4 times. The observation of rubbed P3HT films under POM reveals a very high birefringence *i.e.* a high degree of in-plane orientation on a large scale similar to what was observed in the case of films grown by slow-DEC. But at this point, no detailed comparison of rubbed and epitaxied P3HT films will be presented. The reader is referred to section 5. Here we focus exclusively on the properties of rubbed P3HT films.

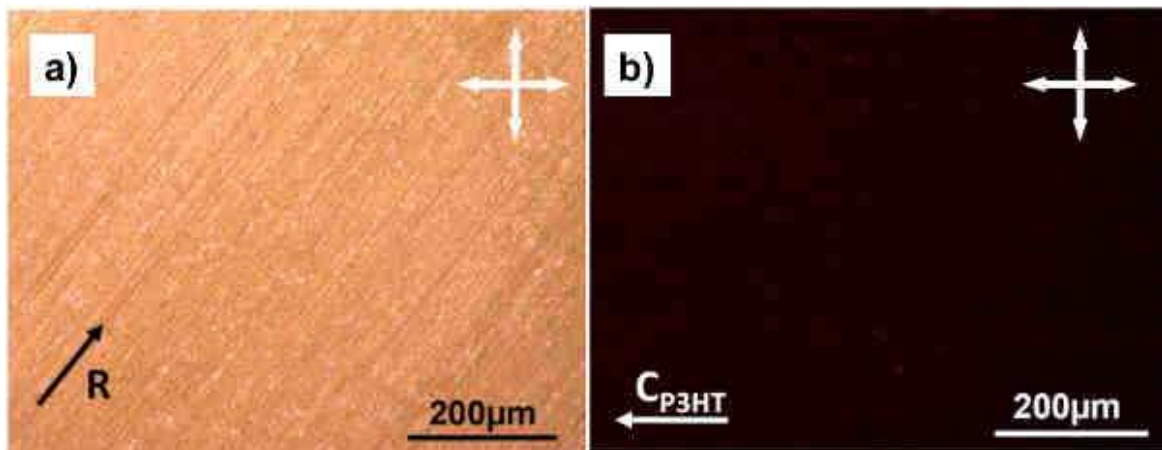


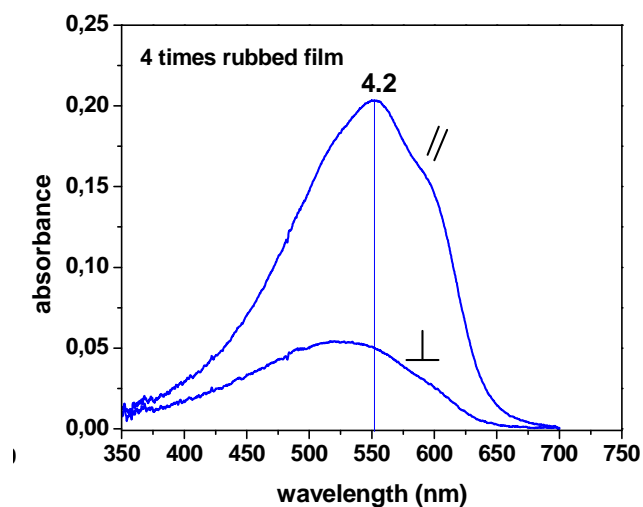
Figure 3-1: Morphology of a P3HT (17.6 kDa) film oriented by rubbing as observed under POM. The arrows indicate the direction of the rubbing and at the same time the  $c_{P3HT}$  direction of P3HT macromolecules. The crossed arrows indicate the orientation of the crossed polarizers.

The morphology of rubbed films as observed by TEM-BF measurements reveals a homogenous and featureless morphology and is therefore not displayed here. The film-thickness is rather homogenous and no big changes in the gray levels over the entire picture can be evidenced. No periodic lamellar morphology with crystalline domains that alternate with amorphous interlamellar zones in a periodic manner can be distinguished. This is a remarkable difference between rubbed and epitaxied layers that gives a first hint that the crystalline organization in the two systems presents significant differences.

### 3.2. In-plane orientation of the rubbed films

As seen from the POM image (Figure 3-1), the rubbed thin films exhibit a good degree of in-plane orientation. Further support for the good in-plane orientation can be obtained by polarized UV-vis spectroscopy and ED measurements. Figure 3-2 depicts the absorption spectrum of a R4 film with the incident light polarized parallel and perpendicular to the rubbing direction R. The // contribution stems from the well oriented and crystalline parts of the film whereas the  $\perp$  originates from the amorphous and misaligned parts of the thin films. The rubbed thin films exhibit a high anisotropy of optical absorption with a characteristic dichroic ratio (DR) of 3.6 - 4.2 (depending on the film and the spot) at 550 nm and two rather broad vibronic replica centered at 610 nm (0-0) and 555 nm (0-1) can be observed. Regarding the DR of rubbed films, Tanaka *et al.* reported very similar DR to those obtained in this work. Zhu *et al.* reported much higher DR going up to 14 in a recently published work on rubbed P3HT films (14, 18). But unfortunately these authors did not mention the molecular weight of the used P3HT. In a following section (section 4), we will show that the maximum DR that can be obtained in rubbed P3HT films depends very strongly on the molecular weight of the polymer and therefore a pertinent comparison of DR without knowing the  $M_w$  of the used polymer is impossible. Other aspects of the UV-vis absorption spectrum of rubbed films *e.g.* the vibronic structure will be discussed later.

Figure 3-2: UV-vis absorbance spectra of P3HT thin films ( $M_w = 17.6\text{kD}$ ) oriented by rubbing for the incident light polarized parallel (//) and perpendicular ( $\perp$ ) to the rubbing direction. The numerical values in the figure correspond to the measured DR.



To get a more accurate and quantitative insight on the degree of in-plane orientation of rubbed films, ED measurements were performed. Indeed, different levels of in-plane orientation lead to different azimuthal distributions of the reflections in the ED pattern. Figure 3-3 shows an ED pattern and the corresponding azimuthal distribution of the (100) reflection.

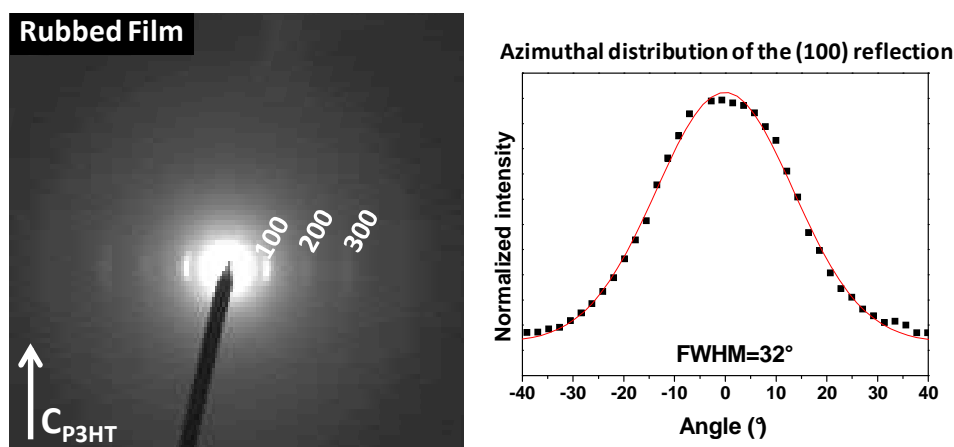


Figure 3-3 : ED and corresponding azimuthal distribution of the (100) reflection of a rubbed P3HT film.

Mainly the (h00),  $h=1,2,3$  reflections can be observed on the equator. This indicates a preferential “flat-on” orientation of the crystalline domains. The azimuthal distribution of the (100) reflection has a  $\text{FWHM} \sim 32^\circ$ . Other reports in the literature on oriented P3HT systems exhibit slightly better levels of in-plane orientation. For example, O’Connor *et al.* reported  $\text{FWHM} \sim 20^\circ$  for P3HT ( $M_n = 62\text{ kDa}$ ) films oriented by the strain alignment method (9). Toney *et al.* reported distributions of the in-plane orientation  $\sim 20^\circ$  for rubbed polyimides (19). Nagamatsu *et al.* reported a very narrow distribution characterized by a  $\text{FWHM} \sim 10^\circ$  for friction transferred P3HT (10). The observed degree of in-plane orientation of the rubbed layers lies slightly below that of P3HT oriented by epitaxy on TCB. However, the advantage

of mechanical rubbing is that the method is easy to apply to films deposited on any type of substrate.

POM, polarized UV-vis spectroscopy, and ED measurements allowed to show that the P3HT backbone ( $\mathbf{c}_{\text{P3HT}}$ ) aligns parallel to the rubbing direction. Herein we studied thin films that were rubbed to a maximum degree before damage by scratching is observed. In the following, the evolution of the orientation of the thin films with increasing rubbing length was investigated. In particular, we were interested in the structure and orientation of the crystalline P3HT domains on the substrate. In addition, the propagation of the orientation induced by the rubbing through the entire film thickness was studied by means of GIXD measurements.

### 3.3. Evolution of the structure with increasing rubbing length

This section focuses on the impact of the rubbing length on the in-plane orientation and on the orientation of the crystalline P3HT domains on the substrate. The P3HT films ( $M_w = 17.6$  kDa) were subjected to an increasing number of rubbing cycles, each of them defined by a rubbing length  $l \sim 50$  cm. The samples are labeled R0 (no rubbing), R1 (after 1 rubbing cycle), R2 (after two rubbing cycles), *etc.*

#### 3.3.1. Thin Film structure and orientation before rubbing

The analysis of the as deposited film (by the Dr. Blade method) is important as it constitutes the starting point for the following rubbing experiments. *Figure 3-4* depicts the GIXD pattern of a R0 medium- $M_w$  sample for an incidence angle of the X-ray beam of  $\alpha = 0.06^\circ$  and  $\alpha = 0.01^\circ$ , i.e. probing the bulk of the film and the top surface layers respectively. The (h00)  $h=1,2,3$  reflections appear clearly in the  $\mathbf{q}_{\text{out}}$  direction with a small arced contribution. In the  $\mathbf{q}_{\text{in}}$  direction only the  $\pi$ -stacking reflection can be observed. This is characteristic for a preferential “*edge-on*” orientation of the crystalline domains on the substrate. Only a small amount of domains is not oriented giving rise to the arced contribution of the (h00) reflections. The isotropic distribution of the in-plane orientation of the P3HT nanocrystallites was verified by checking the invariance of the 2D GIXD map when turning the sample around  $\Omega$ . As expected R0 films, do not display any preferential in-plane orientation. No significant evolution of the diffraction pattern with increasing penetration depth of the X-ray beam could be observed. This indicates that the film structure is homogenous over the entire film thickness ( $\sim 50 - 100$  nm).

In summary, the starting point before rubbing is a thin P3HT film with a clear “*edge-on*” orientation of the crystalline domains on the substrate and the complete absence of in-plane orientation of the  $\mathbf{c}_{\text{P3HT}}$  direction.

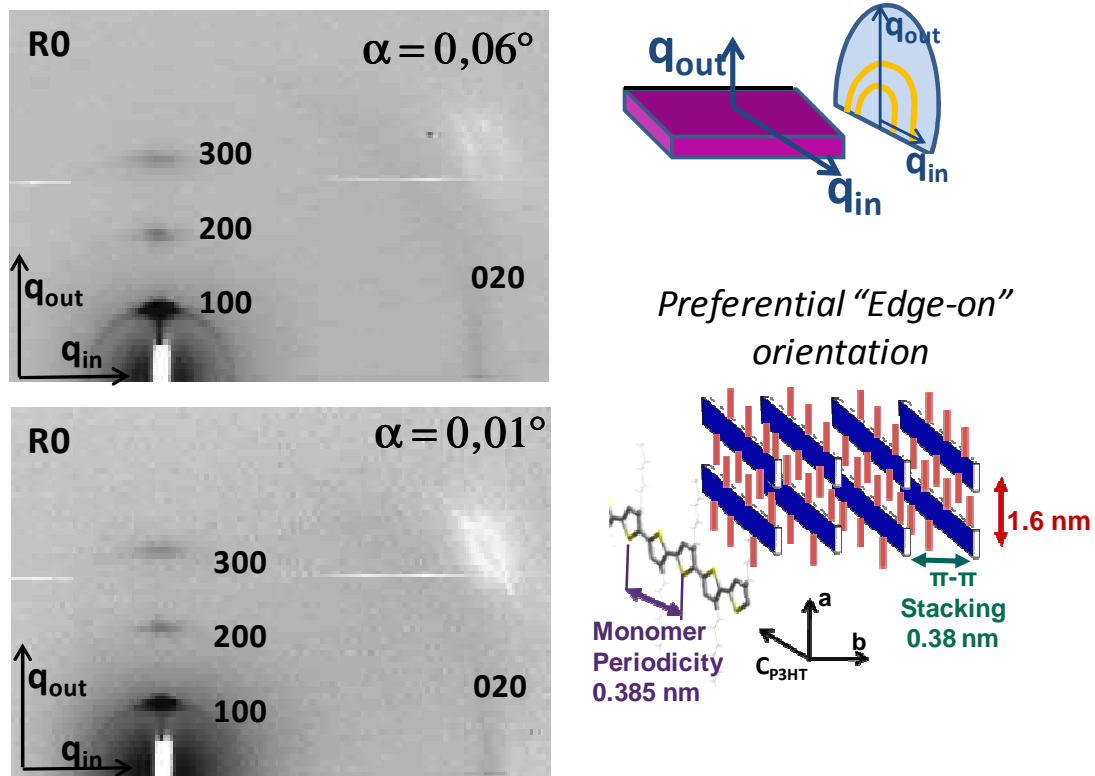


Figure 3-4 : Evolution of the 2D GIXD pattern of a non rubbed medium- $M_w$  sample with increasing penetration depth of the x-ray beam. Before rubbing, a clear “edge-on” orientation of the crystalline domains on the substrate is observed. The diffraction pattern exhibits an isotropic character in the plane as verified by a corresponding  $\Omega$ -scan around the  $q_{out}$  direction.

### 3.3.2. After one rubbing cycle R1

Figure 3-5 R1 shows the 2D GIXD patterns in the  $q_{//}$  and  $q_{\perp}$  configuration of the R1 sample. The incident angle was  $\alpha = 0.06^\circ$  allowing to probe the entire film thickness. The diffraction map of the R1 sample is at strong variance to that of the R0 sample. From the 2D GIXD map, confirmation of the good in-plane orientation of the R1 sample is obtained from the absence of in-plane reflections in the  $q_{//}$  direction for the 2D map in the  $q_{//}$  configuration.

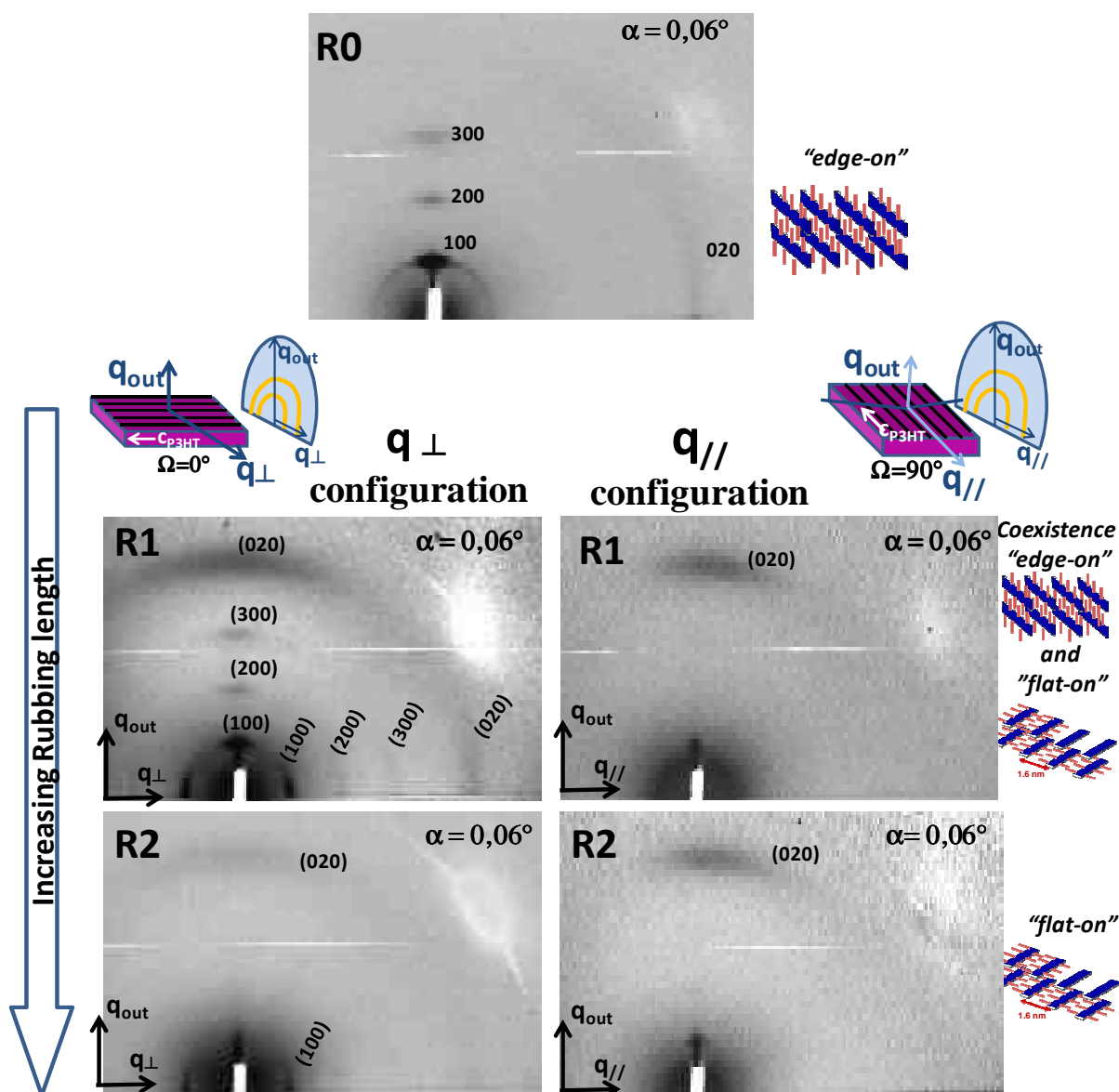


Figure 3-5 : 2D GIXD pattern of a medium- $M_w$  sample before (R0) and after one (R1) and two (R2) rubbing cycles. The two scattering configurations  $\mathbf{q} // \mathbf{R}$  and  $\mathbf{q} \perp \mathbf{R}$  were used. The incidence angle of the beam was  $\alpha=0,06^\circ$ .

The 2D map of the R1 sample in the  $\mathbf{q}_\perp$  configuration shows following main features: (i) arced reflections corresponding to the (h00) reticular planes in both, the  $\mathbf{q}_\perp$  and the  $\mathbf{q}_{out}$  directions (ii) strong reflections corresponding to the  $\pi$ -stacking direction (020) in the  $\mathbf{q}_{out}$  direction and weaker in the  $\mathbf{q}_\perp$  direction. Accordingly, the 2D GIXD maps allow to specify the orientation distribution of the P3HT crystalline domains on the substrate. Mainly two populations of P3HT nanocrystals are found: One with a preferential “edge-on” orientation and the other one with a preferential “flat-on” orientation on the substrate. For both populations the chain axis  $\mathbf{c}_{P3HT}$  is aligned parallel to the rubbing direction. In other words, no more P3HT domains with the  $\mathbf{a}_{P3HT}$  axis parallel to the rubbing direction are evidenced for the 1R sample.

Rubbing does thus not only align the P3HT backbone parallel to the rubbing direction, but induces also a re-orientation of the crystalline domains from the native preferential “*edge-on*” orientation to a preferential “*flat-on*” orientation after rubbing.

### 3.3.3. After two rubbing cycles (R2):

As seen above, after one rubbing cycle, there is a coexistence of “*flat-on*” and “*edge-on*” oriented domains in the films. Herein, the evolution of the orientation of the crystalline domains with an additional rubbing step was investigated.

*Figure 3-5 R2* shows the 2D GIXD scans in the  $\mathbf{q}_{//}$  and  $\mathbf{q}_{\perp}$  configuration of the R2 sample and *Figure 3-6* shows corresponding linear XRD scans. The 2D map of the R2 sample shows mainly that: (i) The  $\pi$ -stacking reflection (020) appears very clearly and exclusively in the  $\mathbf{q}_{\text{out}}$  direction. (ii) In the  $\mathbf{q}_{\text{out}}$  direction scattering from the beam stop and a weak (100) reflection can be seen. Higher order reflections, *i.e.* (200) and (300) have totally disappeared. (iii) The (h00) reflections appear clearly in the  $\mathbf{q}_{\perp}$  direction. This diffraction pattern as observed for the  $\mathbf{q}_{\perp}$  configuration of the R1 sample is characteristic for a majority of “*flat-on*” oriented domains with a marginal population of “*edge-on*” domains as inferred from the weak intensity of the (100) reflection in the  $\mathbf{q}_{\text{out}}$  direction. Therefore, the structure of the R2 sample differs strongly from that of the R1 sample.

The linear scans show a high anisotropy between  $\mathbf{q}_{//}$  and  $\mathbf{q}_{\perp}$ . In the  $\mathbf{q}_{\perp}$  configuration the strong (h00) and a weak (020) reflections appear very clearly whereas in the  $\mathbf{q}_{//}$  configuration no reflections are observed. The presence of the weak (020) reflection confirms a small amount of “*edge-on*” oriented domains as seen from the 2D map. The absence of (h00) reflections in the  $\mathbf{q}_{//}$  direction indicates that all crystalline domains are oriented with  $\mathbf{c}_{\text{P3HT}}$  parallel to the rubbing direction. The fact that the (002) reflection coming from the monomer repeat unit in the  $\mathbf{q}_{//}$  configuration is not observed is at variance to what was seen for epitaxied P3HT layers. This lets suggest that, although the in-plane orientation of the  $\mathbf{c}_{\text{P3HT}} // \mathbf{R}$  is clearly defined; the crystalline order within rubbed layers is not as perfect as in epitaxied layers. A more detailed comparison between rubbed and epitaxied films will be presented in section 5.

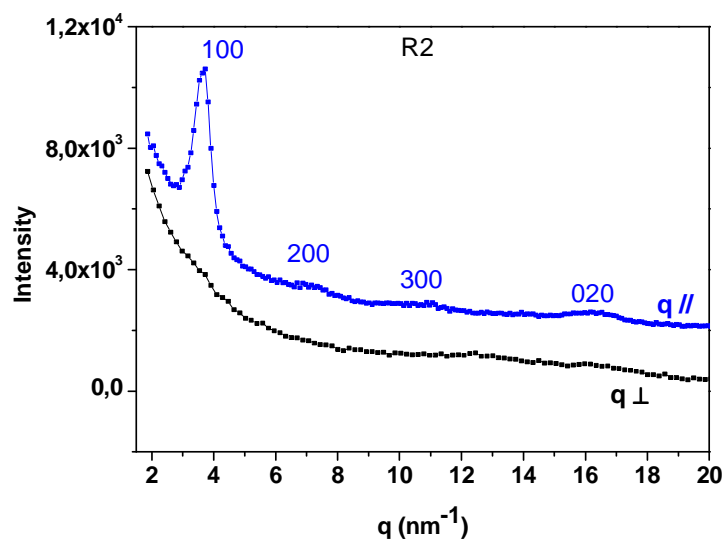


Figure 3-6: GIXD line scan of a medium- $M_w$  sample rubbed after 1 rubbing cycle. i.e. a rubbing length of 50cm. The  $c_{P3HT}$  direction is parallel to the rubbing direction  $R$ . Two scattering configurations with the  $q_{//}$  and  $q_{\perp}$   $c_{P3HT}$  were probed. The incident angle of the beam was  $\alpha=0,05^\circ$  allowing to probe the entire film thickness.

To summarize: With increasing number of rubbing cycles, the ratio “edge-on” / “flat-on” tends clearly to decrease, the “flat-on” population becoming the dominant one. However, both populations correspond to crystalline domains with the chain axis oriented parallel to the rubbing direction. In other words, already for two rubbing cycles, the majority of the P3HT domains are aligned parallel to the rubbing direction.

### 3.4. Propagation of the orientation through the Film thickness

It was shown that mechanical rubbing enforces significant structural modifications in rubbed P3HT films. Herein we study the orientation of the crystalline domains as a function of their depth in the bulk of the films. GIXD were realized while changing the incidence angle  $\alpha$  of the X-ray beam that controls the penetration depth  $P(\alpha)$  of the X-ray beam into the film.

#### 3.4.1. Case of the 1R sample

The measurements as a function of  $P(\alpha)$  were performed in the  $q_{//}$  and the  $q_{\perp}$  configuration. The diffraction patterns in the  $q_{//}$  configuration will not be shown here as most of the information can be extracted in the  $q_{\perp}$  direction. Figure 3-7 shows the evolution of the diffraction pattern with decreasing  $P(\alpha)$ , i.e. probing progressively the entire film thickness and the top surface layers of the sample.

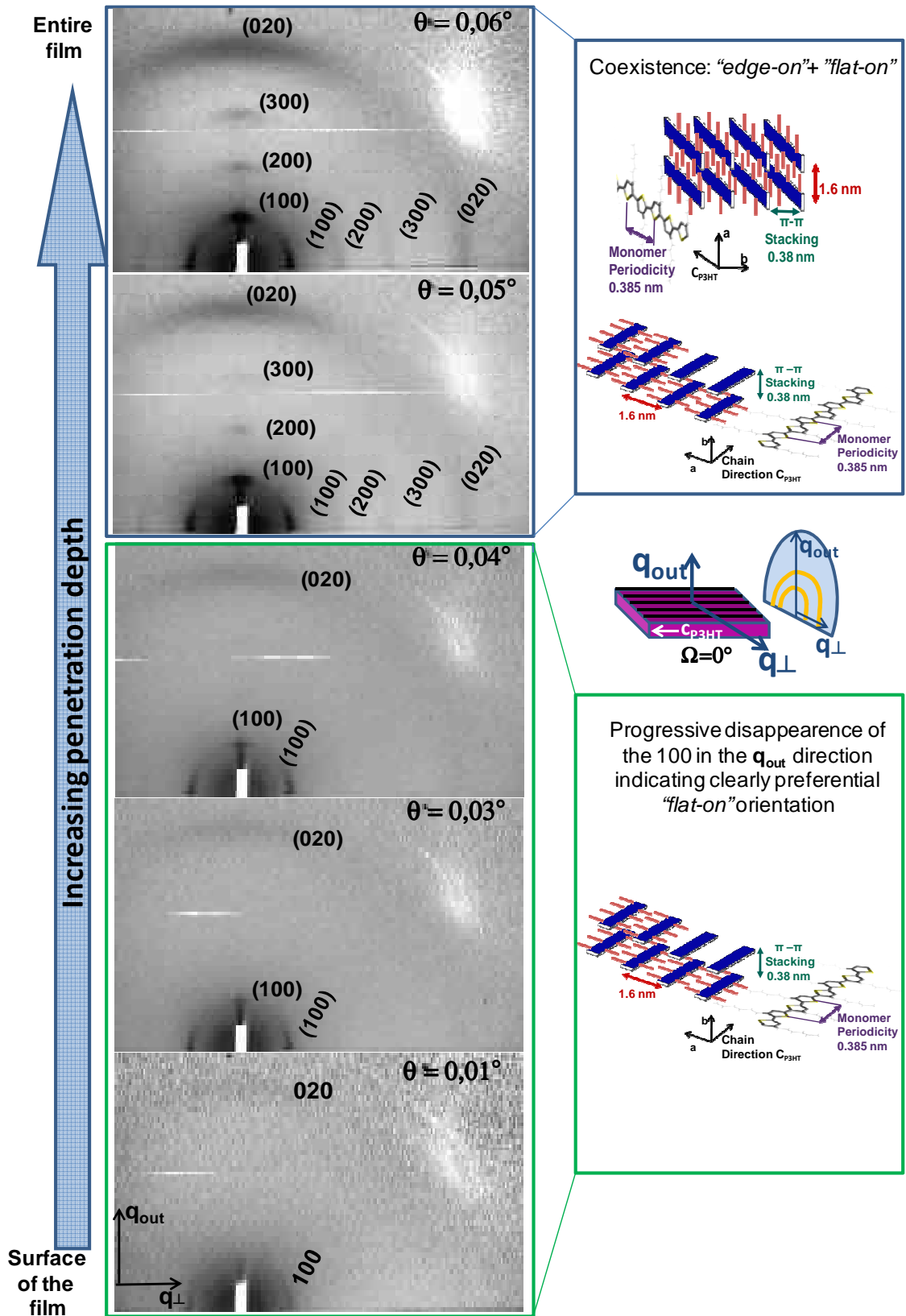


Figure 3-7: Evolution of the GIXD pattern with increasing penetration depth for a R1 medium- $M_w$  sample.

A first glance at these patterns allows to observe significant differences as a function of  $\mathbf{P}(\alpha)$ .

- (i) Probing the entire film thickness ( $\alpha = 0.06^\circ$ ): For this pattern, the (h00) and the (020) reflections appear clearly along both, the equator and the meridian. As seen previously this is a fingerprint of the coexistence of two populations presenting either a “*edge-on*” or a “*flat-on*” orientation. The rubbing process allows to re-orient a fraction of the initial “*edge-on*” oriented domains.
  
- (ii) By decreasing progressively  $\mathbf{P}(\alpha)$  ( $\alpha = 0.05^\circ - 0.03^\circ$ ) the (h00) reflections disappear progressively in the  $\mathbf{q}_{\text{out}}$  direction and the (020) reflection disappears progressively in the  $\mathbf{q}_\perp$  direction. For a better visualization of this effect, *Figure 3-8* displays the relative intensities of the (100) in the  $\mathbf{q}_{\text{out}}$  and in the  $\mathbf{q}_\perp$  direction ( $I(100)_{\text{out}}/I(100)_\perp$ ).<sup>5</sup>  
 The significant decrease of the (020) reflection on the equator indicates a reduced number of crystalline domains in the “*edge-on*” orientation at the benefit to the “*flat-on*” domains. This is consistent with the loss of intensity of the (h00) reflections on the meridian.<sup>6</sup>
  
- (iii) Probing only the sample at the film-air interface: In this case, the (h00) reflection appears exclusively in the  $\mathbf{q}_\perp$  direction indicating that the first layers of the film at the film-air interface are essentially composed of “*flat-on*” oriented domains.

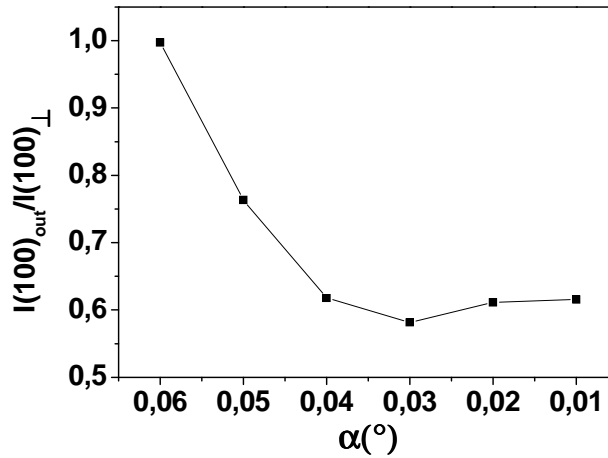
The evolution of the diffraction patterns with  $\mathbf{P}(\alpha)$ , underlines two important aspects. First, the *film-air* interface ( $\alpha = 0.01^\circ$ ) is constituted mainly by “*flat-on*” crystalline domains. Second, the middle layers and the layers at the “*film-substrate*” interface are composed of two populations showing either a preferential “*flat-on*” or “*edge-on*” orientation.

---

<sup>5</sup> It has to be noted that this evolution is very qualitative, because the beam stop which causes scattering of the direct beam in particular in the  $\mathbf{q}_{\text{out}}$  direction.

<sup>6</sup> The general loss of intensity with decreasing  $\mathbf{P}(\alpha)$  is due to the amount of sample that is probed which decreases with decreasing  $\mathbf{P}(\alpha)$ .

Figure 3-8: Evolution of the ratio of “flat-on” and “edge-on” domains as a function of the penetration depth. The continuous line is a guide to the eye. Due to the scattering of the beam stop this evolution can only account for a qualitative description.



To conclude: (i) the in-plane orientation of the  $c_{P3HT} // \mathbf{R}$  is well defined as it can be seen from the absence of (h00) reflections in the  $\mathbf{q} //$  direction for the R1 sample (Figure 3-5). (ii) The 2D diffraction patterns as a function of  $\mathbf{P}(\alpha)$  indicate that the preferred orientation of the crystallites varies from the top surface layers where a preferred “flat-on” orientation is observed, to the bulk of the films where “flat-on” and “edge-on” domains coexist.

### 3.4.2. Case of the 2R sample

A film subjected to two successive rubbing cycles shall be analysed in order to further investigate the reorientation from the “edge-on” to the “flat-on” orientation with increasing rubbing length. Figure 3-9 shows the evolution of the 2D GIXD patterns for a R2 sample as a function of the incident angle. No significant differences can be observed when changing the incidence angle  $\alpha$ . Independently of  $\mathbf{P}(\alpha)$ , the  $\pi$ -stacking reflection appears exclusively in the  $\mathbf{q}_{out}$  direction whereas the (100) reflection appears in the  $\mathbf{q}_{\perp}$  direction. This is a fingerprint of a preferential “flat-on” orientation of the crystalline domains through the entire film thickness.<sup>7</sup> The signal to noise ratio in this sample is larger than in the previous samples because of the reduced total thickness of the film. In fact, due to the rubbing, a loss of material can be observed. The overall loss of intensity of the reflections suggests also a loss of crystallinity of the rubbed films as compared to the as-deposited films. This is further substantiated by the evolution of the UV-vis absorption spectrum versus rubbing (see section 4.4).

To summarize: In the R2 film, the majority of crystalline domains has flipped from the initial “edge-on” orientation to a preferential “flat-on” orientation through the entire films thickness while the chains have been aligned parallel to the rubbing direction.

<sup>7</sup>

The signal which appears on the meridian at a similar position than the (100) reflection comes probably in majority from some scattering due to the beam stop as already mentioned previously.

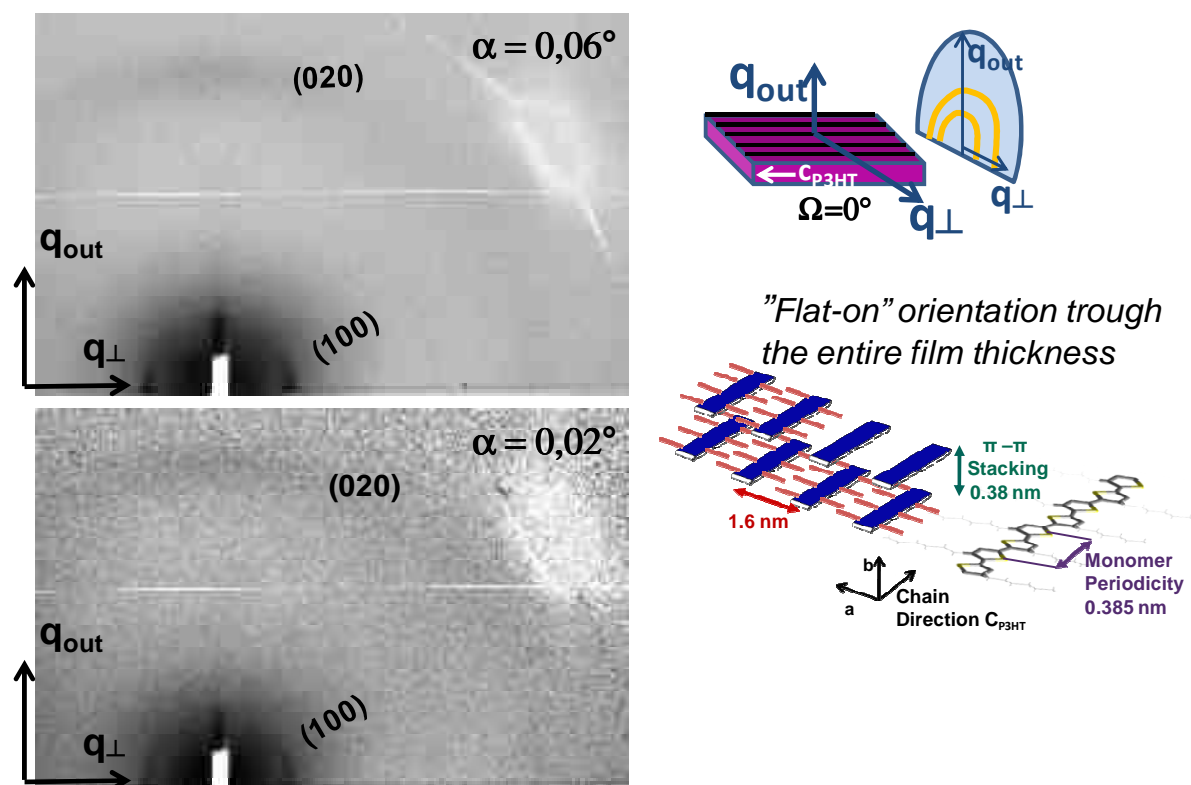


Figure 3-9: Evolution of the GIXD pattern with decreasing  $P(\alpha)$  for a R2 sample (i.e. rubbing length  $\approx 100\text{cm}$ ) in the  $q_{\perp}$  configuration.

### 3.5. Possible scenario and interpretation of the orientation of P3HT upon rubbing:

Based on the GIXD results obtained for the rubbed P3HT films, mainly three key points can be highlighted.

- (i) Upon rubbing, P3HT backbones align parallel to the rubbing direction ( $C_{P3HT} // \mathbf{R}$ ). This seems effective from the first rubbing step.
- (ii) The orientation of the crystalline domains changes from a preferential “edge-on” to a preferential “flat-on” orientation. This re-orientation of the crystallites propagates from the “film-air” interface through the bulk of the thin films.
- (iii) One rubbing cycle is not sufficient to reorient the domains through the entire film thickness. Depending on the total thickness of the film, a second or third rubbing cycle is necessary. *Figure 3-10* illustrates schematically this process. This observation is in agreement with the work of van Aerle *et al.* showing the progressive propagation of orientation in a polyimide film upon increasing rubbing length ( $l$ ). Van Aerle *et al.* showed that upon rubbing the surface layers are instantly oriented to a maximum degree of orientation. They claim

that additional rubbing steps does not allow to further improve the orientation of these top layers, but help to propagate the orientation through the bulk of the films (1).

**Discussion:** The efficient re-orientation of the P3HT domains upon mechanical rubbing is ascribed to the anisotropic mechanical properties of P3HT. Indeed, the interactions in a P3HT crystal are highly anisotropic. Whereas in the  $\mathbf{b}_{\text{P3HT}}$  direction strong  $\pi$ -stacking interactions are predominant, in the  $\mathbf{a}_{\text{P3HT}}$  direction weak Van der Waals interactions between layers of  $\pi$ -stacked polythiophene backbones separated by layers of alkyl side chains occur. Our interpretation of the total reorientation of the P3HT domains upon rubbing is based on the possibility to disrupt order along the  $\mathbf{a}_{\text{P3HT}}$  axis more easily than along the  $\mathbf{b}_{\text{P3HT}}$  axis. It is assumed that rubbing of P3HT films causes the planes of  $\pi$ -stacked chains to flip more or less collectively from an “edge-on” to a “flat-on” orientation of the conjugated backbone on the  $\text{SiO}_2$  substrate. It is proposed that rubbing of a P3HT film does not only induce a coil to “stretched chain” conformational change, as observed in the case of a “soft” polyethylene chain (20) but it allows reorientation of preexisting aggregates of  $\pi$ -stacked P3HT chains so that the  $\pi$ -stacking direction orients parallel to the substrate normal. Derue *et al* also observed a “flat-on” orientation of the P3HT macromolecules upon rubbing. P3HT films prepared by friction transfer also show similar orientation (10, 13). Very recently a similar flipping of the crystalline domains from an “edge-on” to a “flat-on” orientation was reported for strain aligned P3HT by O’Connor *et al* (9). Therefore it seems that P3HT oriented by mechanical methods exhibits frequently a preferential “flat-on” orientation in contrast to what is observed for non oriented films.

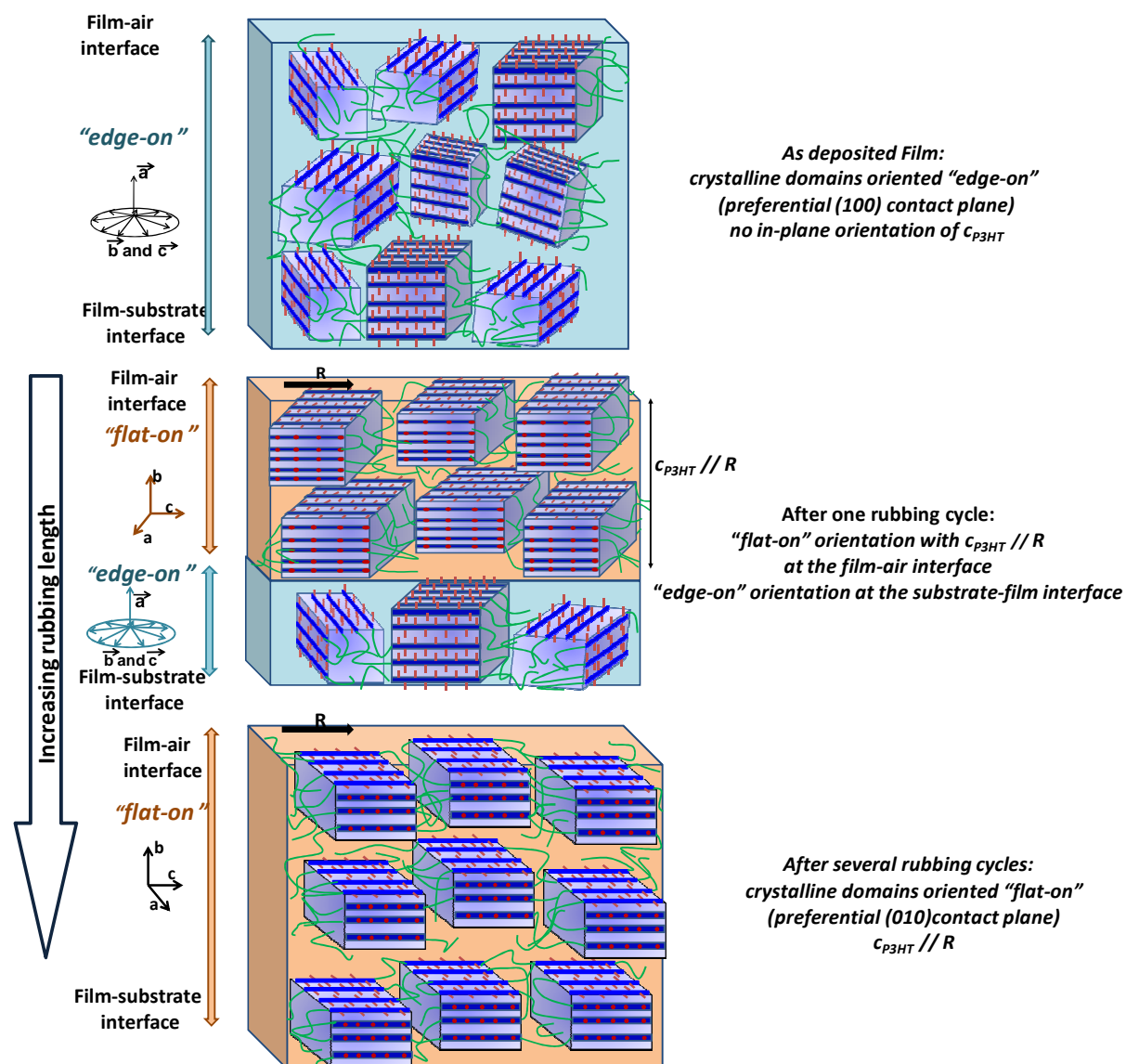


Figure 3-10 : Schematic illustration of the change of P3HT crystallite orientation in the rubbed films with increasing rubbing length. After rubbing, the in-plane orientation of  $c_{P3HT}$  is parallel to the rubbing direction and the orientation of the crystalline domains flips from a preferential "edge-on" to a preferential "flat-on" orientation. This process propagates from the "film-air" interface through the entire film thickness with increasing rubbing length. The rubbing direction is indicated by R.

#### 4. Effect of $M_w$ on P3HT film oriented by mechanical rubbing

It is well established that the molecular weight of P3HT has an impact on the crystallinity of spin-coated films (21–25) and in the case of epitaxied layers of P3HT the influence of  $M_w$  on the spectroscopic data of the thin films was evidenced in the previous chapters. These results prompted us to analyze the effect of  $M_w$  on the orientation, the structure, the crystallinity and the optical properties of rubbed P3HT films. Some of results were obtained in collaboration with S. Uttiya (post doctoral fellow at the Institut Charles Sadron). The macromolecular parameters of the used samples are displayed in *Table 4-1*. Unless specified, the low- $M_w$  P3HT corresponds to the  $M_w = 6.4$  kDa and the medium- $M_w$  corresponds to  $M_w = 17.6$  kDa

$M_w$ (kDa)	$M_n$ (kDa)	PDI	Used for	Preparation method
4.7	2.98	1.59	GIXD	Soxhlet extraction
6.4 (Low- $M_w$ )	5.8	1.1	UV-vis, TEM, OFET	Grignard metathesis
7.9	6.9	1.1	UV-vis	Soxhlet extraction
17.6 (medium- $M_w$ )	13.4	1.3	UV-vis, TEM, GIXD	Merck as received
24.7	15.1	1.6	OFET	Merck as received
35	24.4	1.4	OFET	Soxhlet extraction
50.1	26.2	1.9	UV-vis	Merck as received
70	34.3	2.0	UV-vis	

*Table 4-1: Macromolecular characteristics of the P3HT samples of various molecular weights used in this section.*

##### 4.1. In-plane orientation vs $M_w$

In a first step, we have used UV-vis spectroscopy to follow the dependence of the in-plane orientation of rubbed P3HT films as a function of  $M_w$ . The macromolecular parameters of the used samples can be found in *Table 4-1*.

*Figure 4-1* depicts the dependence of the observed dichroic ratio measured at 555 nm for rubbed P3HT films as a function of the applied rubbing cycles for  $6.4 \leq M_w \leq 70$  kDa. For all samples, the same characteristic trend is observed. The dichroic ratio increases first when the number of rubbing cycles increases. It decreases slightly when the number of rubbing cycles is beyond a certain value (three to four rubbing cycles). However, the maximum dichroic ratio observed in the films tends to increase gradually with decreasing values of  $M_w$ , as seen in the inset of *Figure 4-1*. The P3HT films made of the high  $M_w$  (70 kDa) sample

exhibit only weak in-plane orientation, whereas the highest in-plane orientation is observed for films made from the lowest  $M_w$  (6.4 kDa). Overall, these results highlight the strong impact of the  $M_w$  on the alignment of the films enforced by mechanical rubbing. The higher the  $M_w$ , the lower the in-plane orientation induced by rubbing.

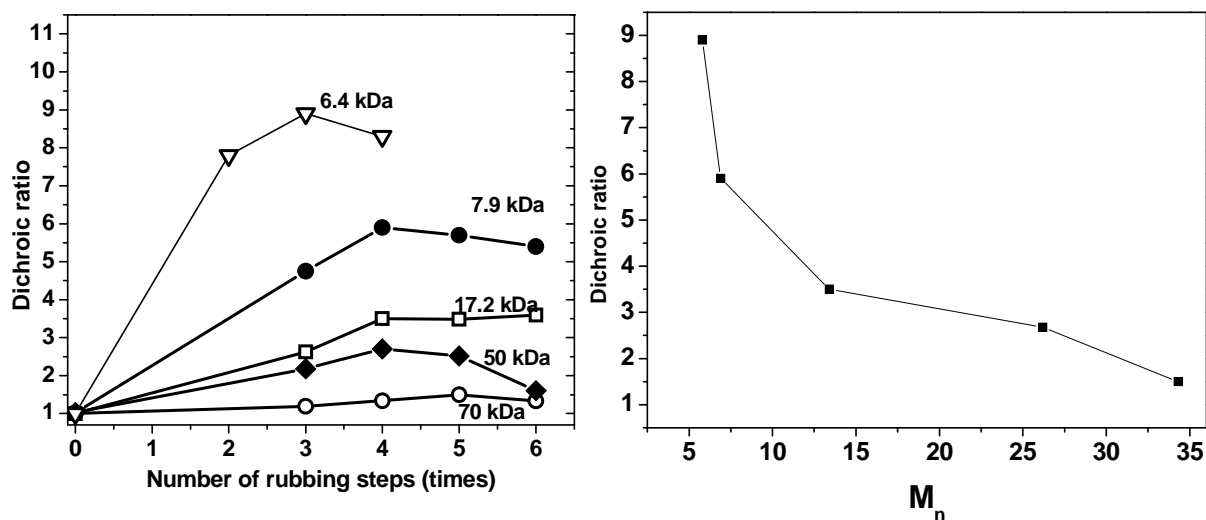


Figure 4-1: (left) Evolution of the dichroic ratio measured at 550 nm for rubbed P3HT films corresponding to different  $M_w$  in the range ( $M_w=6.4\text{--}70$  kDa) as a function of the number of rubbing cycles. (right) highest observed DR of the rubbed thin films as a function of  $M_n$ . The black lines are a guide to the eye.

In the previous chapter (Chapter 4) and in previous published works it was shown that high- $M_w$  show a lower degree of crystallinity in particular in the  $\mathbf{ap}_{3\text{HT}}$  direction (26). This effect was attributed to chain folding and chain entanglements that limit the chain mobility at the surface of the TCB. It is logical to assume that the higher the  $M_w$ , the higher the probability of entanglements and tie chains that interconnect adjacent crystalline domains. The  $M_w$  threshold for the apparition of chain folding and chain entanglements corresponds to the saturation of the lamellar periodicity. It lies close to  $M_w \sim 10$  kDa (24, 27). Based on these considerations, we propose that these entanglements hinder the chain and P3HT nanocrystal re-orientation upon mechanical rubbing of high  $M_w$  samples. This view is supported by the observation that the maximum DR of the rubbed layers (Figure 4-1 right) tends to increase sharply when  $M_w \leq 10$  kDa, *i.e.*, in the absence of chain folding. Accordingly, the present results on the chain alignment induced by mechanical rubbing of P3HT films reveal indirectly the existence of interconnecting chains (and possibly tie-crystallites) between crystalline nanodomains as well as chain entanglements for P3HT with  $M_n \geq 17.6$  kDa.

As illustrated in the schematic Figure 4-2, it is possible to distinguish two cases. For  $M_w < 10$  kDa, P3HT behaves rather like an oligomer and the absence of interconnections and chain entanglements allows P3HT domains to re-orient upon rubbing. For  $M_w > 10$  kDa, P3HT shows progressively semi-crystalline character as the value of  $M_w$  increases. The orientation induced by rubbing decreases with increasing  $M_w$ , *i.e.*, with higher concentration of chain

entanglements and interconnections between crystalline domains. P3HT films with  $M_w \geq 50$  kDa show only marginal alignment upon rubbing. This behaviour might be used as a novel and indirect method to measure the onset of chain entanglement, i.e., the so-called entanglement molecular weight  $M_e$  for a conjugated polymer like P3HT.

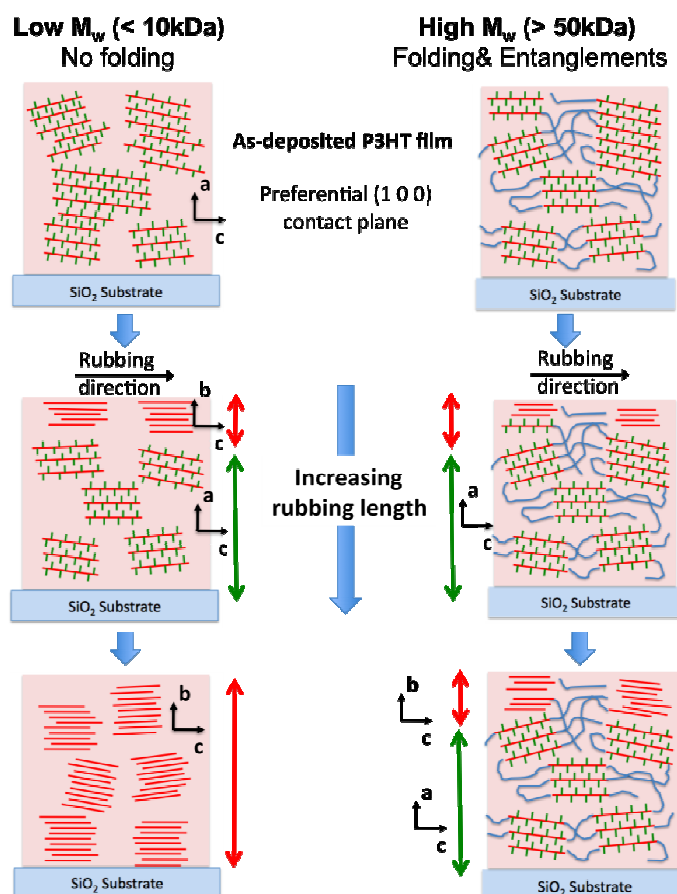


Figure 4-2: Schematic illustration of the change of P3HT crystallite orientation in the rubbed films with increasing rubbing length for the case of non folding chains ( $M_w < 10$  kDa) and strongly entangled and folded P3HT chains ( $M_w > 50$  kDa).

As the UV-vis absorbance measurements could clearly evidence, the orientation of high molecular weight sample by mechanical rubbing is rather difficult due to chain entanglements that hinder the orientation process. Therefore, in the following we focus mainly on the medium- and low- $M_w$  samples.

#### 4.2. Structure and orientation of low- $M_w$ samples

In a previous chapter (see DEC) it was observed that the structure and the orientation of the crystalline domains of low- $M_w$  samples differ strongly from those of a medium- or high- $M_w$  P3HT in the case of sample grown by slow-DEC. Indeed, a fiber structure was observed in the case of high- and medium- $M_w$  samples whereas clear preferential contact planes were evidenced for the low- $M_w$  sample. Herein GIXD measurements were performed

on a rubbed low- $M_w$  ( $M_w = 4.7$  kDa) sample in order to investigate the structure and orientation of the films. We chose to study a R1 sample (not fully oriented) to be able to analyze the evolution of the structure with increasing  $P(\alpha)$ .

#### 4.2.1. Effect of $M_w$ on the crystallinity and crystal structure of rubbed films

Figure 4-3 shows the GIXD linear scans in the  $\mathbf{q}_\perp$  and the  $\mathbf{q}_\parallel$  configuration of a low- $M_w$  sample. For means of comparison, the linear scan of a medium- $M_w$  sample in the  $\mathbf{q}_\perp$  configuration is also displayed.

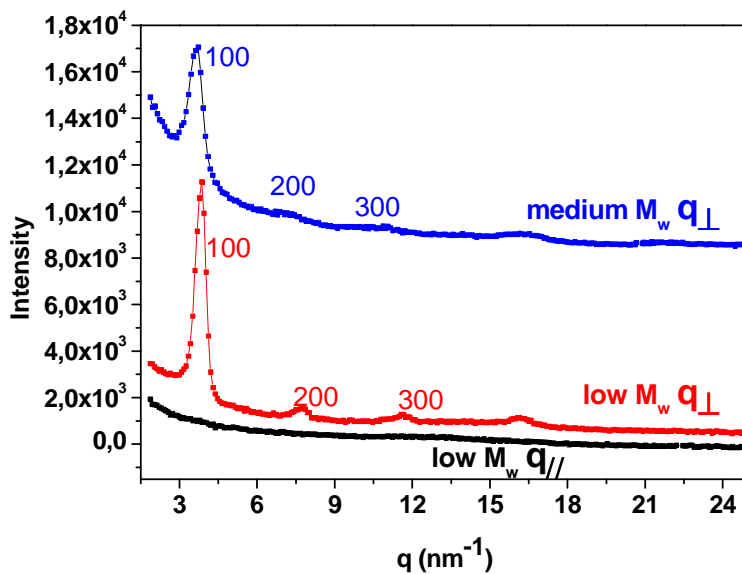


Figure 4-3 : linear in-plane GIXD scans in the  $\mathbf{q}_\perp$  and  $\mathbf{q}_\parallel$  configuration for a low- $M_w$  ( $M_w = 4.7$  kDa) sample. For means of comparison, the  $\mathbf{q}_\perp$  scan of a medium- $M_w$  ( $M_w = 17.6$  kDa) sample is displayed. The graphs were shifted along the ordinate for clarity.

In the  $\mathbf{q}_\perp$  scan strong and well defined (h00)  $h=1,2,3$  reflections can be seen, whereas in the  $\mathbf{q}_\parallel$  scan of the low- $M_w$  sample, no reflections are visible. This is characteristic for a high degree of in-plane orientation of the sample. The absence of the (002) reflection coming from the monomer repeat unit is at variance with the observations made for slow-DEC films. This point will be discussed in detail in section 5.

Comparing the  $\mathbf{q}_\perp$  scan of the low- $M_w$  to the  $\mathbf{q}_\perp$  scan of the medium- $M_w$  sample reveals mainly two significant differences. First, the (h00) reflections and in particular the (200) and the (300) are much better defined for the low- $M_w$  sample as compared to the medium- $M_w$  sample. Second, the  $a_{P3HT}$  parameter of the low- $M_w$  sample is a bit lower than for the medium- $M_w$  sample as expected from the literature (25). For the low- $M_w$   $a_{P3HT}^{low} = 1.63$  nm and for the medium- $M_w$   $a_{P3HT}^{medium} = 1.71$  nm. A similar evolution (Increase of  $a_{P3HT}$  with decreasing  $M_w$ ) was previously reported by Zen *et al.* as well as by Brinkmann *et al.* (24, 25). The higher value of the  $a_{P3HT}$  parameter in high- $M_w$  samples was attributed to the occurrence of reentering chains after folding (24, 25, 28). Such reentrant chains are absent in low- $M_w$  P3HT that does not fold. In fact, the reentrant chains into the lattice (after folding) exert some stress on the close packing of the chains and induce an increase of the lattice parameter with increasing amount of folds and reentrant chains (*e.g.* with increasing  $M_w$ ).

Therefore, this observation is in very good agreement with the results of the UV-vis measurements. Indeed, it was shown that due to the absence of chain folding in the low- $M_w$  the latter can be more easily oriented by mechanical rubbing.

The better defined (h00) reflections are a fingerprint of a better overall crystallinity of the low- $M_w$  samples. Decreasing crystallinity with increasing  $M_w$  was previously observed for the slow-DEC samples and reported in the literature (24). Further support for the better defined crystalline order in the low- $M_w$  sample was obtained from ED measurements. As seen in *Figure 4-4*, the ED pattern of the medium- $M_w$  rubbed P3HT films shows exclusively the strong (h00) reflections with  $h=1-3$ .

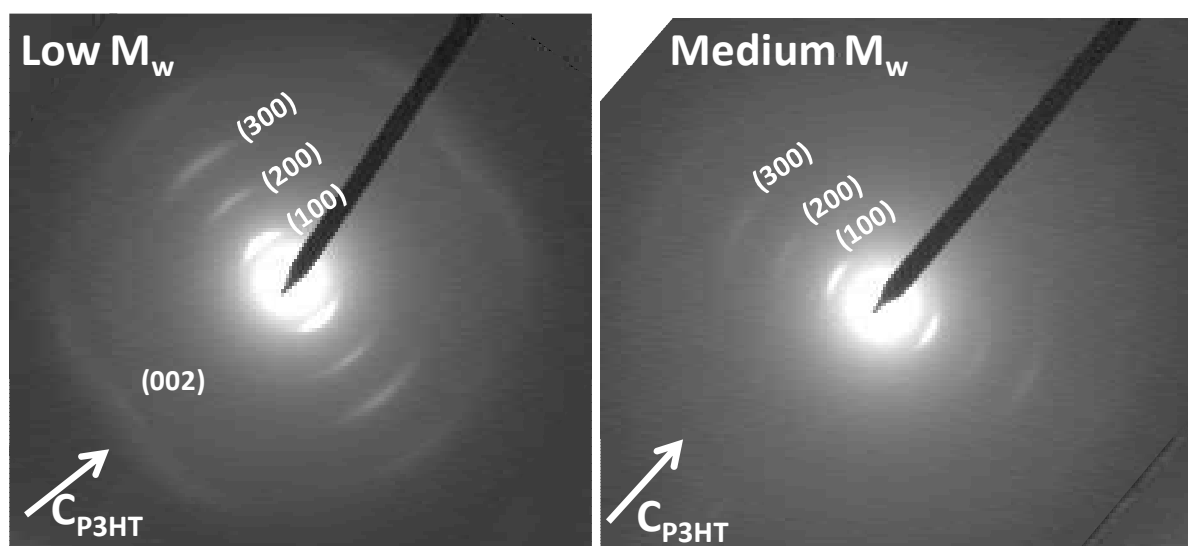


*Figure 4-4* : ED patterns of a low and a medium- $M_w$  sample ( $M_w=6.4$  and  $17.6$  kDa).

For the low- $M_w$  sample, in addition to these strong (h00) reflections, weak and broad reflections indexed as (h02) with  $h=0$  and  $2$  are observed on the first layer line. Although very broad, the presence of the (002) reflection coming from the monomer repeat unit in the ED pattern of the low- $M_w$  sample, suggests a better defined order along the P3HT backbone in these samples as compared to the medium- $M_w$  film. However, the medium as well as the low- $M_w$  display significantly different ED patterns as compared to equivalent epitaxied thin films. In fact, the ED patterns of the epitaxied films for a medium- $M_w$  sample show intense and sharp (h02) reflections indicative of well defined translational order along the chain-axis direction in the crystalline domains. A more detailed comparison of the crystalline order in rubbed and epitaxied layers will be presented in section 5.

The sizes of the crystalline domains were also estimated from these linear scans by using the Scherrer formula. The results of this analysis will be discussed in parallel with results regarding the nanomorphology as observed by HR-TEM.

In the following we were interested in other structural differences in the low- $M_w$  as compared to the medium- $M_w$  sample. GIXD measurements were performed to get a better insight on the orientation of the crystalline domains on the substrate.

#### 4.2.2. Orientation of the crystalline domains of a low- $M_w$ sample

##### a) Description of the $q_{\perp}$ and the $q_{\parallel}$ 2D GIXD pattern:

Figure 4-5 (a and b) shows the GIXD pattern for a R1 low- $M_w$  sample ( $M_w=4.7$  kDa) in the  $q_{\perp}$  and  $q_{\parallel}$  configurations. The GIXD pattern consists mainly of (i) continuous Scherrer rings from the (h00) reticular planes, (ii) (h00) reflections in the  $q_{out}$  and in the  $q_{\perp}$  direction and (iii) a (020) reflection in the  $q_{out}$  direction. The Scherrer rings progressively disappear by turning the sample around  $\Omega$ . At  $\Omega=90^\circ$ , only sharp reflections in the  $q_{out}$  direction are visible. The observed “doubling” of the (h00) reflections is not yet understood. A similar evolution of the Scherrer rings was previously observed for a medium- $M_w$  sample prepared by slow-DEC. Such a pattern hints at the existence of mainly three populations of domain orientations:

- (i) Domains with a fiber symmetry around the rubbing direction ( $\mathbf{c}_{P3HT}/\mathbf{R}$ ) giving rise to Scherrer rings.
- (ii) Domains with a preferential “edge-on” orientation (native orientation before the rubbing process) giving rise to the (h00) reflections in the  $q_{\perp}$  direction.
- (iii) Domains with a preferential “flat-on” orientation and ( $\mathbf{c}_{P3HT}/\mathbf{R}$ ) giving rise to the (020) in the  $q_{out}$  direction and the (h00) in the  $q_{\perp}$  direction. This domain orientation was most probably enforced by the rubbing as observed previously for the medium- $M_w$  sample.

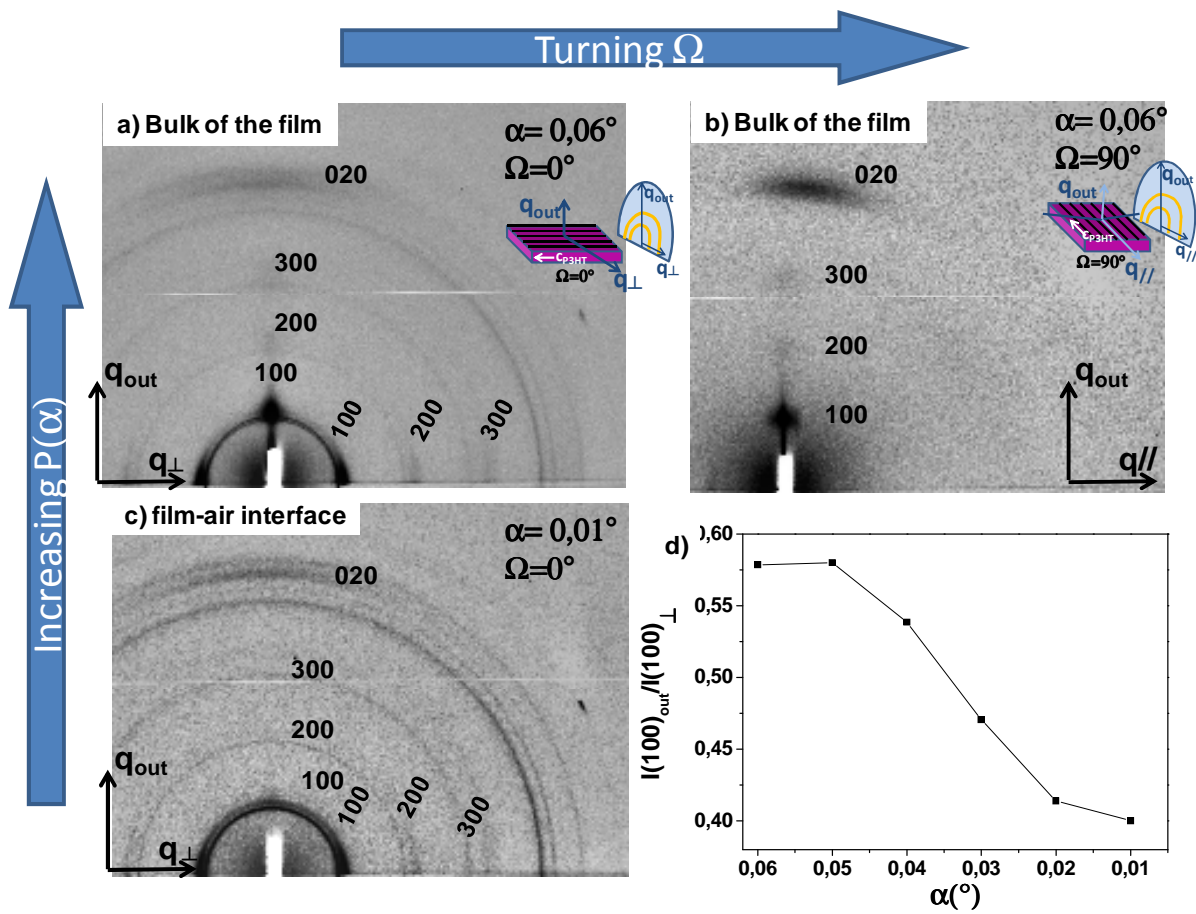


Figure 4-5: (a and b) GIXD pattern for a low- $M_w$  sample in the configurations  $q_{\perp}$  and  $q_{\parallel}$  parallel to the rubbing direction after 1 rubbing cycle (R1). (a and d) Evolution of the GIXD pattern with increasing penetration depth for a R1 low- $M_w$  sample ( $M_w=4.7$ ).

No such fiber-like symmetry was observed for the rubbed medium- $M_w$  sample. The population of domains presenting a fiber symmetry is a fingerprint of the low- $M_w$  *i.e.* of the absence of chain folding and chain entanglements. Indeed, chain entanglements and interconnections between the crystalline domains account for a more or less collective orientation of the P3HT nanocrystals upon rubbing. Therefore, the orientation on the substrate of one crystalline domain enforced by rubbing can be transmitted to a nearest neighbour nanocrystal. In low  $M_w$ , (*i.e.* no entanglements and interconnections), each nanocrystals has an individual behaviour and can thus adopt any orientation independently from the one of adjacent crystalline domains. By the rubbing process, only the orientation  $\mathbf{c}_{P3HT} // \mathbf{R}$  is enforced for all crystalline domains, whereas the change in orientation of the crystalline domains on the substrate occurs only for a part of the P3HT nanocrystals.

In the following we studied the orientation of the crystalline domains as a function of their depth within the film (bulk of the films vs “film-air” interface).

**b) Evolution of the structure with  $P(\alpha)$ :**

Figure 4-5 (a and d) shows the evolution of the GIXD pattern with increasing penetration depth  $P(\alpha)$  of the X-ray beam for a low- $M_w$  sample. When probing the entire film thickness, three populations of P3HT crystallites orientation are clearly evidenced (Figure 4-5 (a)). With decreasing  $P(\alpha)$ , the main change is a further decrease in intensity of the sharp (h00) reflections in the  $\mathbf{q}_{\text{out}}$  direction. No difference in the Scherrer rings and the (h00) reflections in the  $\mathbf{q}_{\perp}$  direction is observed between the bulk and the “film-air” interface. Figure 4-5 (d) shows the evolution of the ratio of the (100) intensities  $I_{(100)\text{out}}/I_{(100)\perp}$  for better visualization of the progressive loss in intensity of the (100) reflection in the  $\mathbf{q}_{\text{out}}$  direction. Therefore it can be said that the P3HT crystalline domains giving rise to the fiber-pattern are found in the entire film after rubbing. In the bulk of the film all three populations are present, whereas at the film-air interface a mixture of the “flat-on” and oriented fiber-like domains coexist. The complete absence of reflections in the  $\mathbf{q}_{\parallel}$  direction ( $\Omega = 90^\circ$ ) hints at the very good in-plane alignment of the P3HT chains ( $\mathbf{c}_{\text{P3HT}} // \mathbf{R}$ ) in the whole film. Accordingly, the rubbing of the low- $M_w$  sample induces (i) a global chain alignment with  $\mathbf{c}_{\text{P3HT}} // \mathbf{R}$  from the first rubbing cycle and (ii) a progressive flipping of the domains orientation to the “flat-on” orientation. In other words, upon rubbing the domains with a fiber symmetry progressively flip to the “flat-on” orientation. We believe that the reorientation of the “edge-on” orientation to a “flat-on” orientation propagates through the entire film thickness starting at the “film-air” interface with increasing rubbing length as shown for the medium- $M_w$  sample. A complete series of measurements of rubbed P3HT films with various  $M_w$  (low, medium, high) and increasing number of rubbing steps was realized at synchrotron soleil. These data were not integrated into this manuscript but validate the present results.

**4.3. Morphology and nanomorphology: medium- versus low- $M_w$** 

Figure 4-6 shows the TEM-BF images of a low- and medium- $M_w$  ( $M_w=6.4$  kDa and  $M_w=17.6$  kDa) sample and the corresponding HR-TEM micrographs. The observation of the rubbed thin films morphology by TEM in the bright field mode indicates that the periodic lamellar morphology with crystalline domains that alternate with amorphous interlamellar zones in a periodic manner (26, 29) marginally seen for rubbed films of low- $M_w$  (6.4 kDa) *i.e.* for P3HT samples crystallizing with extended chains. The lamellar periodicity (one amorphous + one crystalline phase) is very small because of the very short polymer chains. This is comparable to what is observed in low- $M_w$  samples grown by slow-DEC. However, the contrast in the BF image is not comparable to that obtained in the DF for epitaxied films. A strong defocus is necessary to catch the feeble contrast between the crystalline and the amorphous phase. This limited BF contrast suggests a rather poor overall crystallinity of the rubbed films. In contrast to the low- $M_w$  samples, the rubbed films of higher  $M_w$  ( $M_w > 10$  kDa) do not reveal any lamellar structure or nanomorphology.

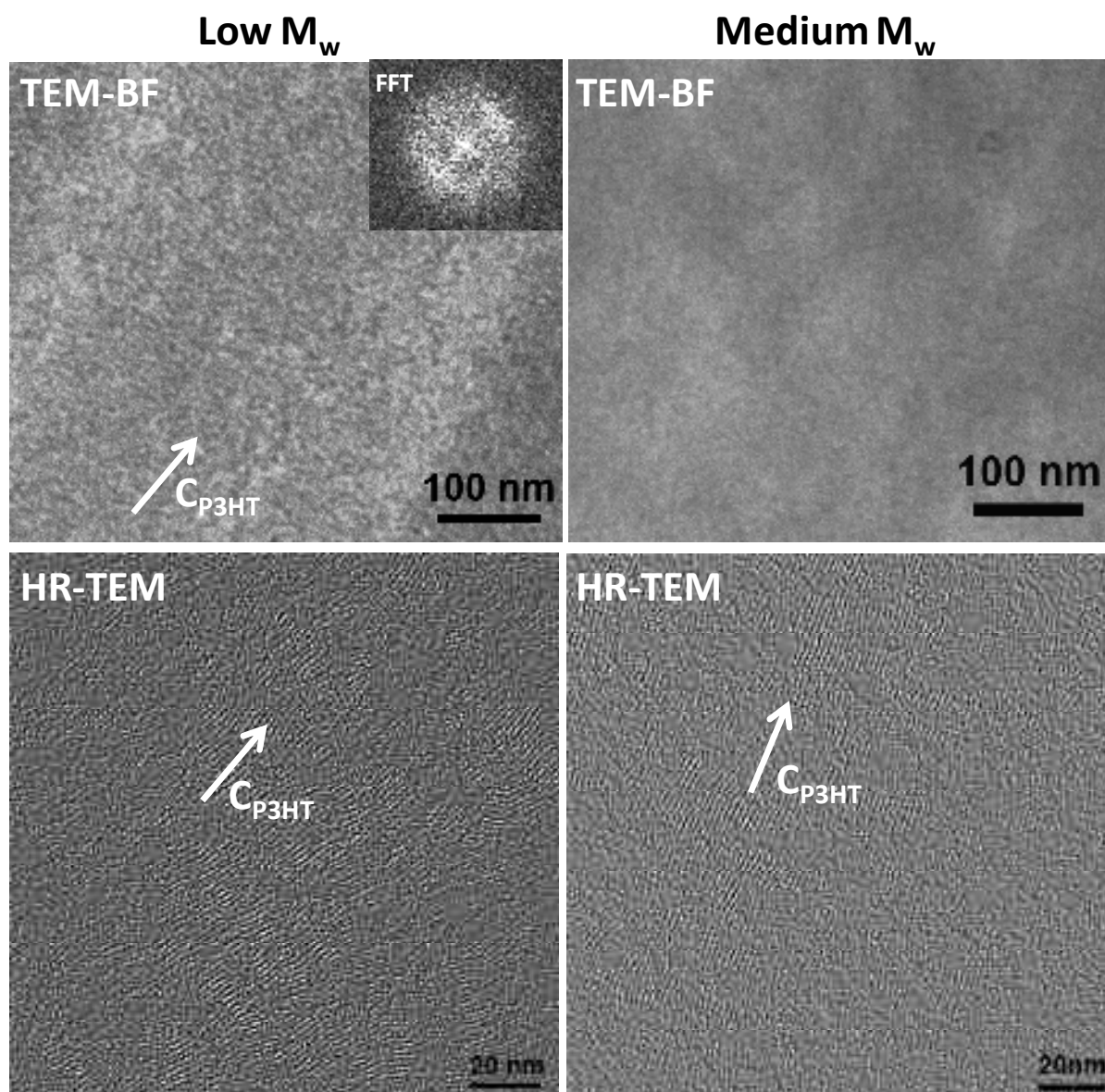


Figure 4-6: TEM-BF images of a rubbed low- and medium- $M_w$  sample and the corresponding HR-TEM images ( $M_w = 6.4$  kDa and  $M_w = 17.6$  kDa).

The HR-TEM images of Figure 4-6 allow to get a better insight on the chain packing within the thin films. The HR-TEM observations confirm the absence of a regular and periodic alternation of crystalline and amorphous domains in the rubbed P3HT films. As seen in Figure 4-6 the distinction between crystalline and disordered domains is difficult in the rubbed layers. In particular there are no sharp contours and boundaries between the crystalline lamellae and surroundings amorphous zones as seen for the slow-DEC samples. Despite the very fuzzy contours of the crystalline domains and the significant fluctuations in the domain dimensions observed in the HR-TEM images, the average stem length in the nanocrystals  $L_{\text{stem}}$  and the extension of the domains along the  $\mathbf{a}_{\text{P3HT}}$  axis  $L_a$  was estimated from a careful statistical analysis. The domain sizes in the  $\mathbf{a}_{\text{P3HT}}$  direction were in addition estimated from the XDR linear scans by using the Scherrer formula on the (100) reflection. The results of this analysis can be found in Table 4-2.

Both the rubbed films of the low and medium P3HT samples show an average stem length  $L_{\text{stem}} \approx 5\text{--}6$  nm (12–15 monomer units). Regarding the domain dimensions perpendicular to the chain axis, for the medium- $M_w$  sample  $L_a \approx 10\text{--}20$  stems. In the case of the low- $M_w$  samples the estimation of the number of stems by HR-TEM fluctuates strongly, but a similar extension along  $L_a$  than for the medium- $M_w$  samples could be evidenced. The  $L_a$  values as extracted from XRD linear scans show however a larger extension in the  $L_a$  direction in the case of the low- $M_w$  sample as compared to the medium- $M_w$  samples. A similar trend was previously observed for the slow-DEC films.<sup>8</sup>

The invariance of the stem length ( $C_{\text{P3HT}}$ ) with increasing  $M_w$  as evidenced by HR-TEM is rather surprising and in contrast to what was seen in the epitaxied layers grown by slow-DEC. Possibly, the strong mechanical forces applied to the films during the rubbing can induce the disruption of previously formed crystals. A more detailed comparison between the rubbing and the slow-DEC method will be presented in section 5. In the following, the impact of the nanomorphology and the crystalline order in rubbed films on their UV-vis spectra will be studied.

	$L_{\text{stem}}$ HR-TEM	$L_{\text{stem}}$ X-ray	$L_a$ HR-TEM	$L_a$ X-ray
low $M_w$	5–6 nm	Not accessible	10-20 stems	24±5nm (~15 stems)
High $M_w$	5–6 nm	Not accessible	10–20 stems	17±4nm (~10 stems)

Table 4-2: Sizes of the crystalline domains as evidenced from HR-TEM and linear XDR scans.<sup>8</sup>

#### 4.4. Vibronic structure of absorbance

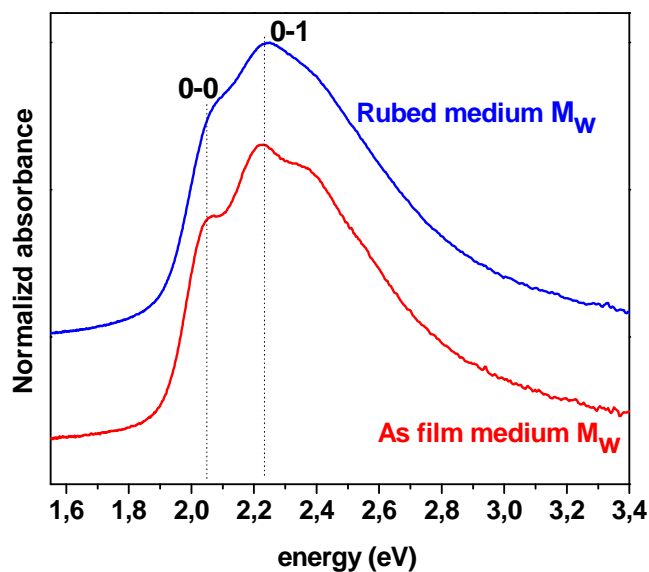
As shown in a previous chapter (see Chapter 4), the nanomorphology and the crystalline order on one hand and the  $M_w$  distribution on the other hand have a strong influence on the vibronic structure of absorbance (23, 30–35). In a first point, we were interested how the rubbing process influences the vibronic structure, and in a second point we studied the effect of  $M_w$  on the vibronic structure of absorbance.

##### 4.4.1. Effect of rubbing on the vibronic structure of absorbance

Figure 3-7 shows the absorbance spectra of the as deposited film (by the doctor blade method from chlorobenzene) and of a rubbed film of a medium- $M_w$  P3HT. For the rubbed film, the incident light was polarized parallel to the rubbing direction R.

<sup>8</sup> Note that the  $M_w$  the sample used for GIXD and the sample used for the HR-TEM is not strictly identical ( $M_w = 6.4$  kDa for HR-TEM and ED whereas  $M_w = 4.7$  kDa for GIXD measurements)

Figure 4-7: Comparison of the UV-vis absorption spectra of a rubbed and an as-deposited film of a medium- $M_w$  P3HT ( $M_w = 17.6$  kDa). For the rubbed film, the spectra were recorded with the incident polarization oriented parallel to the in-plane direction of the P3HT chains. The spectra were normalized in intensity and shifted along the ordinate axis for clarity.



The rubbed thin films exhibit two rather broad vibronic replica centered at 2.06 nm (0–0) and 2.25 eV (0–1). Compared to the as deposited film and also compared to epitaxied layers of P3HT, rubbed films exhibit only a poorly defined vibronic structure of absorbance with a predominant 0-1 component. It is interesting to note that other reports on P3HT films aligned by mechanical rubbing show a very similar vibronic structure (14, 16, 18). P3HT films oriented by other methods based on the application of shearing forces show equally a similar and poorly defined vibronic structure. This is for example the case of P3HT obtained by a friction transfer method (10) or by strain alignment (9). Therefore, it seems quite general that P3HT films oriented by mechanical shearing forces exhibit only a poorly defined vibronic structure as compared to films deposited from solution in high boiling point solvents by usual methods (spin-coating, drop-casting, etc.) or to films prepared by slow-DEC. We believe that, P3HT films spin coated from high boiling point solvents in the same manner than P3HT films prepared by slow-DEC show a higher crystalline order than rubbed films. Indeed, in films prepared from solution or by slow-DEC, the polymer chains have a given time to assemble and to form well defined crystals upon solvent evaporation. In contrast to this, in rubbed films the strong mechanical forces applied to the films can presumably disrupt this native crystalline order especially between adjacent stacks of  $\pi$ -stacked polythiophene chains separated by weak van der Waals interactions. This translates into a much less defined vibronic structure of absorbance. Although oriented, rubbed layers show a rather poor degree of crystalline order.

#### 4.4.2. Effect of $M_w$ on the vibronic structure of absorbance

Figure 4-8 Compares the UV-vis absorption spectra of oriented P3HT by mechanical rubbing for two different  $M_w$  of the polymer (17.6 kDa and 6.4 kDa). The high- $M_w$  samples exhibit a very similar vibronic structure of absorbance and are therefore not displayed. The spectra were recorded with the incident polarization oriented parallel to the in-plane direction

of the P3HT chains. Table 4-3 collects the main spectroscopic data for the different  $M_w$  samples.

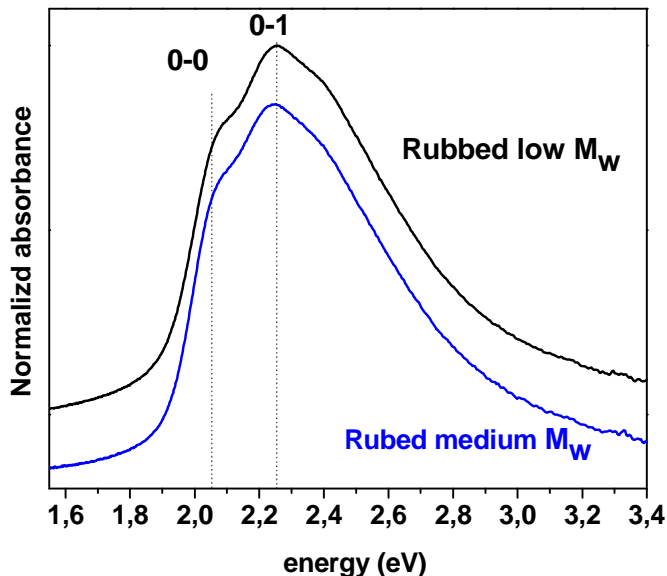


Figure 4-8: Comparison of the UV-vis absorption spectra of oriented P3HT by mechanical rubbing for two different  $M_w$  of the polymer (17.6 kDa and 5.6 kDa). The spectra were recorded with the incident polarization oriented parallel to the in-plane direction of the P3HT chains. The spectra were normalized in intensity and shifted along the ordinate axis for clarity.

There is only a marginal effect of  $M_w$  on the vibronic structure in the case of rubbed samples. No clear change in terms of vibronic structure can be observed for the low- $M_w$  sample as it was found for epitaxied P3HT films. The invariance of the FWHM of the spectra with decreasing  $M_w$  seems surprising at a first look. Indeed, a strong broadening of the UV-vis spectra for low- $M_w$  samples is reported in the literature (23). Such a broadening was also observed for the slow-DEC samples (see Chapter 4). The reason for the low influence of  $M_w$  on the UV-vis spectra of rubbed layers lays probably in the structural properties of rubbed thin P3HT films. As seen from HR-TEM, in the rubbed layers no periodic semi-crystalline structure can be evidenced. In addition, it could be clearly seen that the extension of the stems in rubbed thin is independent of  $M_w$  ( $L_{\text{stem}} \sim 6\text{nm}$ ). Therefore it seems logical to assume that in rubbed thin films the conjugation length is independent of the molecular weight.

As shown for the slow-DEC films a more quantitative analysis of the vibronic structure of absorbance can be made by modelling the aggregate part of the spectrum by the model of Spano (31, 32, 35). This allows to extract the free exciton band width  $W$  from the intensity ratio  $A_{0-0}/A_{0-1}$ . However, as seen from the HR-TEM images, in the rubbed films it is impossible to distinguish a crystalline part and an amorphous part within the film. This makes the rubbed films very peculiar as compared to spin coated or epitaxied P3HT thin films where a clear separation of the amorphous and the crystalline phases is observed. As the Spano model is based on the distinction between the absorbance of the amorphous and of the crystalline part of the films, it is not sure that this model accounts well for a system where such a distinction is much less pronounced. We thus chose to limit the discussion to a comparison of the ratio  $A_{0-0}/A_{0-1}$  rather than applying the Spano model for the extraction of

the free exciton bandwidth  $W$  to the rubbed films. The ratio of intensities  $A_{0-0}/A_{0-1}$  is independent of the  $M_w$  in the rubbed layers as it can be seen from Table 4-3.

Preparation method	$M_w$ (kDa)	Best measured Dichroic ratio		FWHM (eV)	$A_{0-0}/A_{0-1}$
		555nm	605nm		
rubbing	5.6 (low $M_w$ )	9	13	0.62	~0.76
rubbing	7.9	6	9	0.63	~0.77
rubbing	17.6 (medium $M_w$ )	4	5.5	0.62	~0.77
Doctor blade from chlorobenzene	17.6	Not oriented		0.62	~0.76
Slow-DEC	17.6	10	16	0.69	~0.90
Spin coating from xylene (ref (35))		Not oriented			~0.81
Spin coating from chloroform (ref (35))		Not oriented			~0.64

Table 4-3 : Recapitulation of the spectroscopic data of the different molecular weight samples oriented by the rubbing method.

P3HT films prepared by various methods (rubbing, epitaxy, spin coating) differ strongly in terms of crystalline order. A high degree of crystalline order results generally in a high ratio of  $A_{0-0}/A_{0-1}$ . Both, P3HT films spin coated from high boiling point solvents (xylene) and more particularly epitaxied P3HT films show a higher ratio  $A_{0-0}/A_{0-1}$  as compared to the rubbed films and as compared to spin coated films from a low boiling point solvent (chloroform). Therefore, it can be said that epitaxied layers as well as spin coated layers from high boiling point solvents have a higher degree of crystalline order as compared to the rubbed P3HT layers.

#### 4.5. Impact of rubbing and $M_w$ on the field effect charge mobility

In collaboration with the research group of Prof. Sabine Ludwigs at the University of Freiburg, the rubbed thin films were characterised in terms of charge carrier mobility in the direction perpendicular and parallel to the rubbing direction in the Field effect transistor configuration.

##### 4.5.1. Transistor fabrication and experimental protocol

For a more detailed description of the experiential protocol see Annexe 10. Here the transistor fabrication will be described only briefly.

Prefabricated transistors in a bottom gate, bottom contact configuration were purchased from the Fraunhofer Institute for Photonic Microsystems (IPMS). Highly n-doped silicon wafers with a 300 nm thick SiO<sub>2</sub> layer obtained by thermal oxidation served as gate electrode and gate insulator, respectively. Gold source and drain electrodes of 40 nm thickness constituted interdigitated transistor channels with a length (L) of 20 μm and a width (W) of 10 mm. The P3HT films were directly deposited on the pre-patterned substrates via spin coating under nitrogen atmosphere. To ensure identical rubbing conditions for all samples, three P3HT films with different M<sub>w</sub> were fixed on a microscope glass slide and rubbed during the same run. After rubbing of the films, the electronic characterization of the FETs was carried out in a nitrogen atmosphere using a Keithley 2636 Dual channel sourcemeter in a glove box. Field effect mobilities (μ<sub>FET</sub>) were determined from the transfer characteristics curve in the saturation regions using the following equation:

$$I_{SD} = \frac{W}{2L} C_i \mu_{FET} (V_g - V_0)^2$$

where I<sub>SD</sub> is the source-drain current in the saturation regime, V<sub>g</sub> is the source-gate voltage, C<sub>i</sub> is the insulator capacity, L and W are the channel length and width and V<sub>0</sub> is the turn-on voltage.

#### 4.5.2. Charge transport anisotropy

In order to evaluate the impact of chain orientation on the anisotropy of charge mobility, P3HT films with different M<sub>w</sub>'s were subjected to an increasing number of rubbing steps. *Figure 4-9* shows the evolution of the mobilities parallel (μ<sub>//</sub>) and perpendicular (μ<sub>⊥</sub>) to the rubbing direction when the number of rubbing steps increases for P3HT films with M<sub>w</sub>=35 kDa, 24.7 kDa and 5.8 kDa respectively. As expected from earlier studies, the 5.8 kDa sample exhibits the lowest initial mobility as compared to the 27 kDa and 35 kDa samples (22, 36). Regardless of M<sub>w</sub>, rubbing induces some anisotropy of charge mobility which tends to increase with the number of rubbing cycles. However the higher M<sub>w</sub>, the lower the observed anisotropy of charge mobility. The films of 5.8 kDa exhibit a very high anisotropy of charge transport after two rubbing cycles with μ<sub>//</sub> / μ<sub>⊥</sub> = 22 whereas for the 35 kDa sample μ<sub>//</sub> / μ<sub>⊥</sub> < 2.

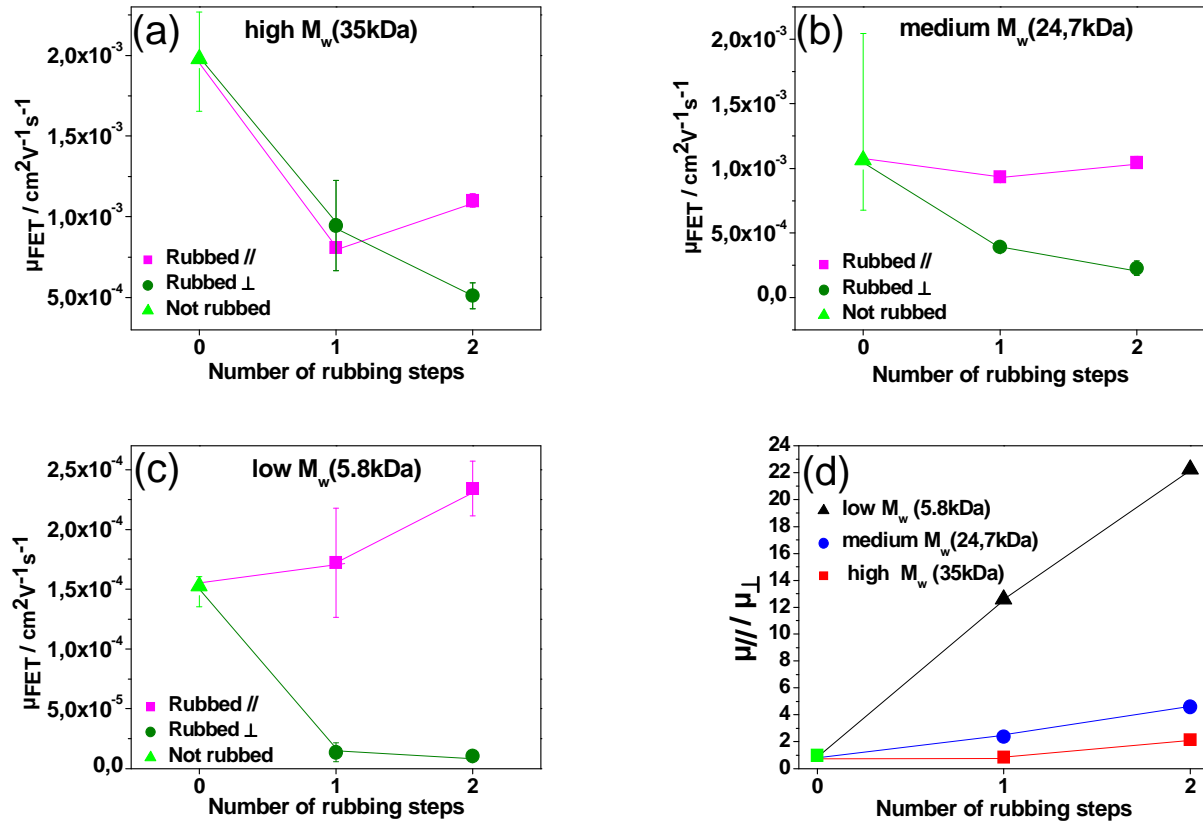


Figure 4-9: Measured field effect mobility parallel ( $\mu_{\parallel}$ ) and perpendicular ( $\mu_{\perp}$ ) to the rubbing direction as a function of rubbing steps for P3HT with different molecular weights (a) high  $M_w=35$  kDa, (b) medium  $M_w=24.7$  kDa and (c) low  $M_w=5.8$  kDa. (d) Ratio of  $\mu_{\parallel}$  and  $\mu_{\perp}$  as a function of rubbing steps for the three different molecular weights.

This observation is fully consistent with results obtained from the UV-vis absorption spectroscopy indicating that the alignment of the polymer chains and the reorientation of the crystalline domains are most efficient for low- $M_w$  P3HT i.e. in the absence of interconnections and chain entanglements. In low- $M_w$  P3HT, rubbing orients efficiently the P3HT chains parallel to the rubbing direction ( $\mathbf{c}_{\text{P3HT}}/\mathbf{R}$ ). The absence of interconnections in low- $M_w$  P3HT films allows for a complete reorientation of crystalline domains upon rubbing and it thus amplifies the intrinsic anisotropy of charge mobility in P3HT between the chain axis direction  $\mathbf{c}_{\text{P3HT}}$  and the  $\mathbf{a}_{\text{P3HT}}$  direction. Anisotropy of charge transport properties of P3HT thin films were also reported for P3HT oriented by strain alignment by O'Connor *et al.* and by epitaxy by Jimison *et al.* (9, 37). O'Connor *et al.* reported a charge transport anisotropy of a factor of 9 for a strain aligned P3HT ( $M_w = 117$  kDa, PDI = 1.9) sample. Jimison *et al.* reported anisotropy up to 20 for epitaxial P3HT ( $M_w = 64$  kDa, PDI = 2.63).

The lower anisotropy observed in the rubbed layers as compared to that reported in the literature can be easily understood taking into account the orientation within the bulk of the films as evidenced by GIXD. In fact, in OFETs, charge transport is confined at the interface between the dielectric and the P3HT layer. We have shown that the orientation in rubbed thin films propagates from the air-film interface through the entire film thickness. Therefore, the

zone where the charge transport was measured in the films is the less oriented one. This is in particular the case of high  $M_w$  samples where chain entanglements hinder the efficient reorientation of the P3HT upon rubbing. To access the charge mobility of the best oriented top surface of the films, top gate top contact would be more suited. The important finding of this study is the correspondence between the in-plane orientation probed by UV-vis and the corresponding charge mobility. The impact of  $M_w$  on the chain orientation by rubbing translates into a corresponding anisotropy of the charge mobility in OFETs.

## 5. **Rubbing versus slow-DEC: A comparative study**

We have prepared and characterized highly oriented thin films by using two different methods, namely (i) mechanical rubbing and (ii) slow directional epitaxial crystallization. Herein the differences in structure, orientation, crystalline order, morphology and UV-vis absorption spectroscopy will be highlighted. We choose to present this comparative study for a medium- $M_w$  P3HT. The differences in morphology of the P3HT thin films prepared by these two methods will influence the morphology of the resulting hybrids as it will be shown in the following chapters.

### 5.1. **Structure: Fiber symmetry versus preferential contact plane**

Figure 5-1 depicts the TEM BF-images and the 2D GIXD maps of an epitaxied and rubbed P3HT film. The TEM- BF image shows clearly that only the epitaxied layers have a structured morphology presenting (i) a fibrillar morphology in the thicker parts of the film and (ii) a well defined periodic lamellar structure with alternating amorphous and crystalline domains as described in previous chapters and in the literature (24, 26, 29). The rubbed samples do not reveal any peculiar morphological features and present a quite regular and smooth surface. These differences in morphology are directly reflected in the structure of the films. Epitaxied P3HT films exhibit clearly an oriented fiber symmetry where the fiber axis ( $C_{P3HT}$ ) is well aligned parallel to the  $C_{TCB}$  direction. In contrast to this, the rubbed films show clearly a preferential “flat-on” orientation on the substrate. Epitaxied and rubbed films do not only differ from a point of view of morphology and structure, but important differences can be observed in terms of crystalline order. These differences were clearly evidenced by HR-TEM, ED and linear GIXD measurements. These differences will be discussed in the following section.

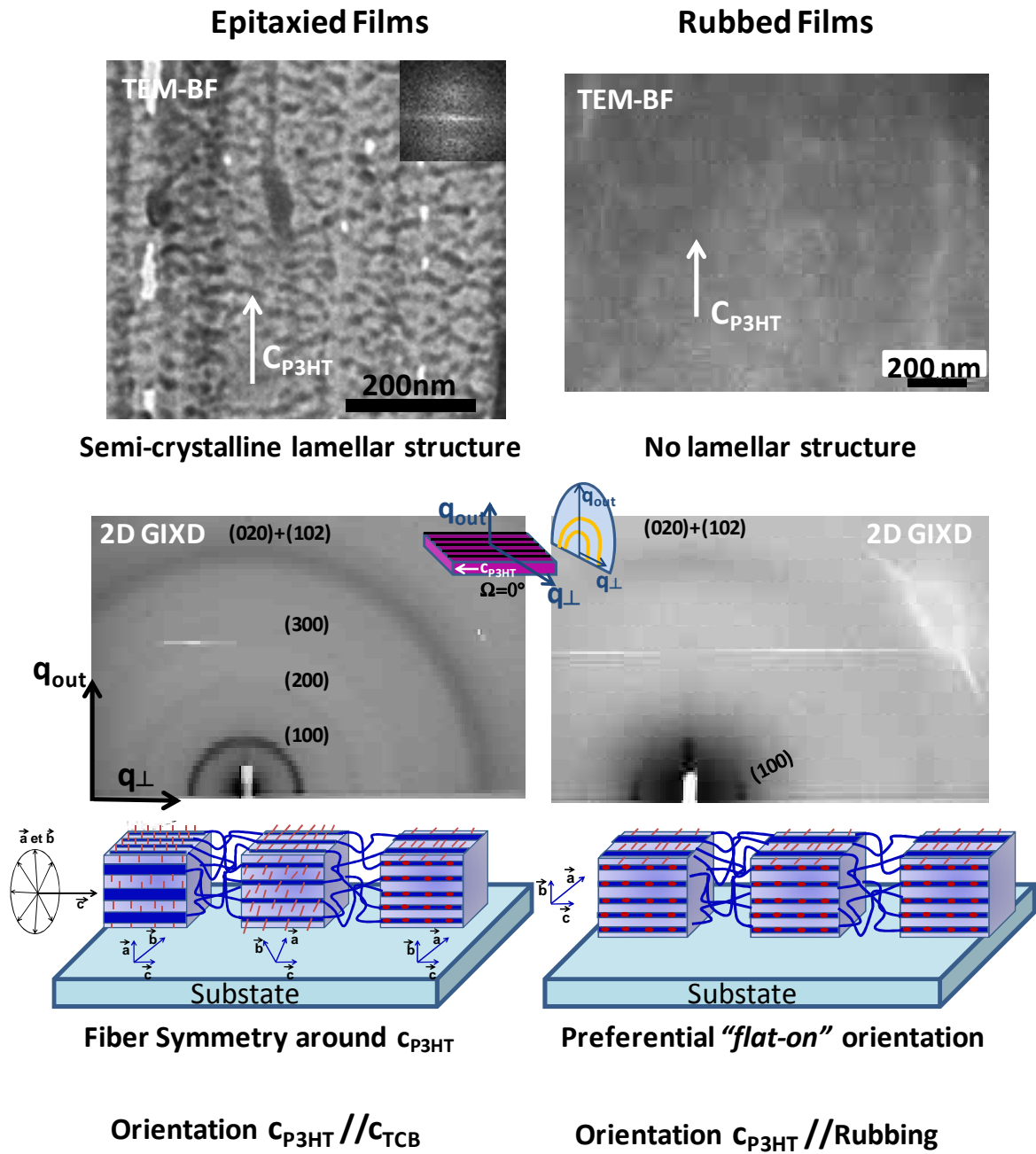


Figure 5-1 : TEM-BF image and 2D GIXD maps of a medium- $M_w$  sample prepared by slow-DEC (left) and by mechanical rubbing (right).

### 5.2. In-pane orientation nanomorphology and crystalline order

Figure 5-2 depicts the characteristic HR-TEM micrographs and the corresponding ED patterns as well as the azimuthal angular distribution of the (100) reflection an epitaxied and a rubbed thin film of medium- $M_w$  P3HT.

(i) **In-plane orientation:** As shown before, both epitaxied and rubbed P3HT films show a high level of in-plane orientation as inferred from the POM images. In epitaxied films  $\mathbf{c}_{\text{P3HT}}$  aligns parallel to the  $\mathbf{c}_{\text{TCB}}$  direction ( $\mathbf{c}_{\text{P3HT}} // \mathbf{c}_{\text{TCB}}$ ) and in rubbed layers,  $\mathbf{c}_{\text{P3HT}}$  aligns parallel to the rubbing direction ( $\mathbf{c}_{\text{P3HT}} // \mathbf{R}$ ). The comparison of the ED patterns of both, epitaxied and rubbed thin films allows for a more quantitative comparison of the degree of in-plane orientation in these films. Different levels of in-plane orientation lead to different azimuthal distributions of the (100) reflection in the ED patterns. For epitaxied films  $\text{FWHM}_{(100)} \sim 21^\circ$  and for rubbed films  $\text{FWHM}_{(100)} \sim 32^\circ$ . Thus, the degree of in-plane orientation is slightly better in the films grown by slow-DEC. Moreover, a detailed comparison of the ED patterns and HR-TEM micrographs reveals additional structural differences between the rubbed and the epitaxied samples.

(ii) **Nanomorphology:** In both epitaxied and rubbed P3HT films, HR-TEM shows nanocrystalline domains consisting of planes of  $\pi$ -stacked chains separated by the *n-hexyl* side chains. The HR-TEM observations confirm the absence of a regular and periodic alternation of crystalline and amorphous domains in the rubbed P3HT films as already observed in the TEM BF image. In rubbed films of medium  $M_w$ , the distinction between crystalline and disordered domains is not as obvious as in the epitaxied layers. In order to get a more quantitative comparison of rubbed and epitaxied P3HT films, statistics on the crystallite size for both samples are compared. Despite significant fluctuations in the domain dimensions observed in the HR-TEM images of the rubbed films, the average stem length in the nanocrystals  $L_{\text{stem}}$  and the extension of the domains along the a axis  $L_a$  were estimated from a careful statistics and compared to the values obtained previously on epitaxied layers. Rubbed films show an average stem length  $L_{\text{stem}} \sim 5\text{-}6$  nm (12-15 monomer units). In contrast to this, in the epitaxied films of the medium  $M_w$ , the average stem length is of the order of  $L_{\text{stem}} \sim 13\text{nm}$  ( $> 30$  monomer units) *i.e.* twice as long. Regarding the domain dimensions perpendicular to the chain axis, the extension of the crystalline domains along the a axis is rather similar for both epitaxied and rubbed films. For instance, in both the epitaxied and rubbed films of the medium molecular weight sample,  $L_a \sim 15\text{-}20$  stems. This similarity is further supported by the presence of three visible orders of the (h00) reflections in the ED patterns of both the epitaxied and the rubbed films. In short, for the same  $M_w$ , the chain length ( $L_{\text{stem}}$ ) in the crystalline domains is larger in the epitaxied films as compared to the rubbed layers.

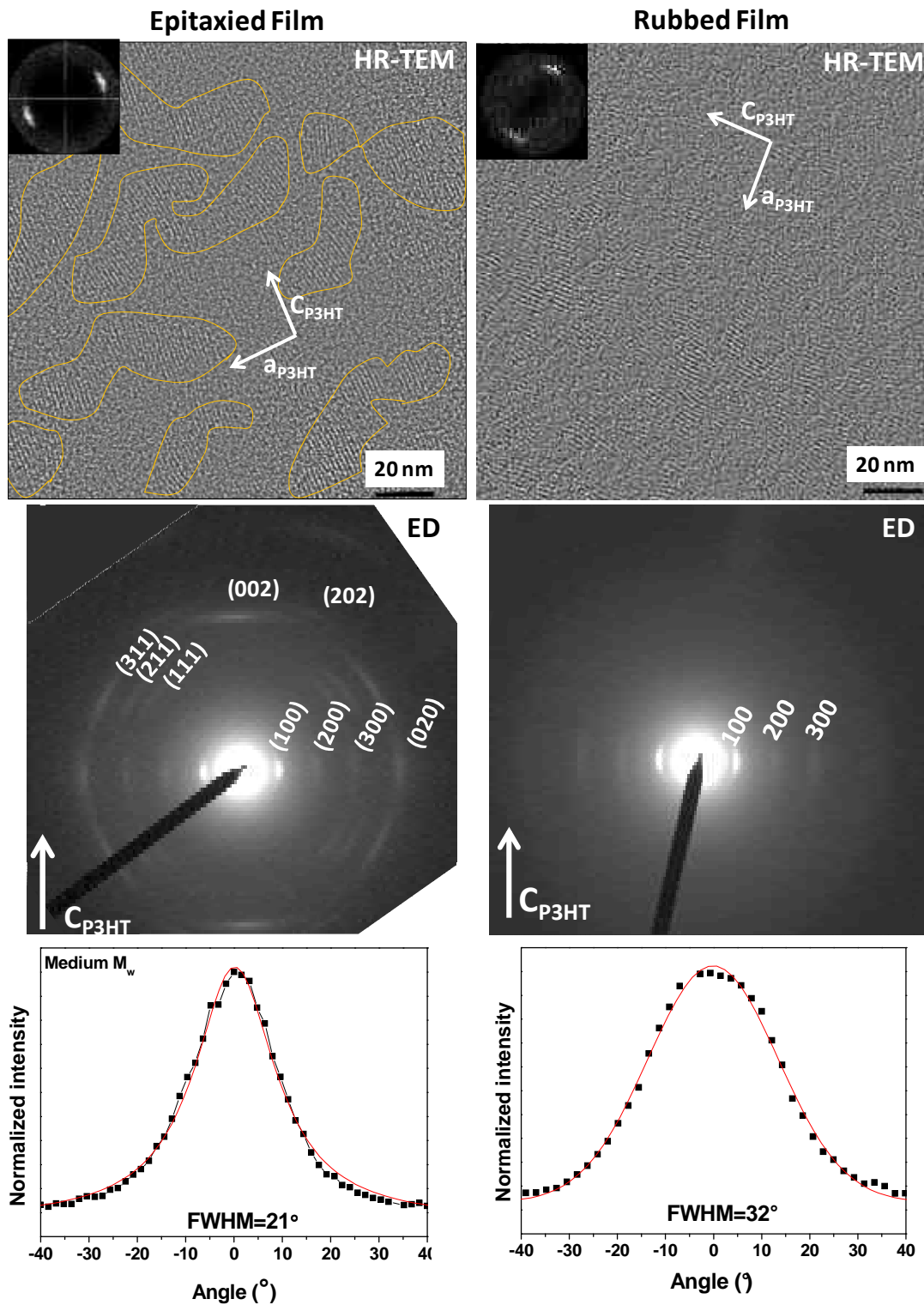
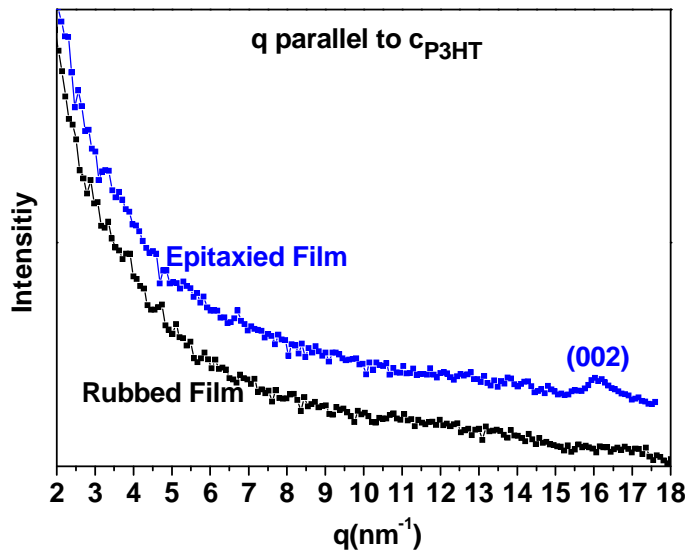


Figure 5-2: Comparison of characteristic HR-TEM images, ED patterns and corresponding azimuthal distributions of the (100) reflection of two oriented P3HT films. (Left) P3HT film oriented by slow-DEC (right) rubbed P3HT film. The insets in the upper left corner of the HR-TEM images correspond to the Fast Fourier Transforms.

(iii) **3D versus 2D crystalline order:** Rubbed and epitaxied P3HT films do not only differ in terms of average size of crystalline domains as observed by HR-TEM. A careful

comparison of the ED patterns of the rubbed and epitaxied films reveals besides the degree of in-plane orientation further important differences. As seen in *Figure 5-2* the ED pattern of the rubbed P3HT films shows essentially the strong (h00) reflections with  $h=1-3$ . In contrast to this, the ED patterns of the epitaxied films show rather intense and sharp (h02) reflections indicative of well defined translational order along the chain axis direction in the crystalline domains. A similar observation can be made regarding the results of the linear GIXD scans with the scattering vector  $\mathbf{q} \parallel \mathbf{c}_{\text{P3HT}}$  direction (see *Figure 5-1*). The (002) reflection is exclusively seen in the case of epitaxied thin films. Therefore, it can be concluded that in the case of epitaxied thin films there is a very low degree of stacking disorder along the P3HT backbone. Thus, epitaxied layers display a 3D crystalline order whereas rubbed thin films show a 2D crystalline order.



*Figure 5-3* : GIXD linear scans with the scattering vector  $\mathbf{q}$  parallel to the  $\mathbf{c}_{\text{P3HT}}$  direction of an epitaxied and a rubbed P3HT film of medium- $M_w$  P3HT.

**Discussion:** The origin of the 2D vs 3D crystalline order can be explained by using the crystal structure of P3HT as refined by Kayunkid *et al* (38). The unit cell of P3HT contains two chains per cell that are  $\pi$ -stacked along the  $\mathbf{b}_{\text{P3HT}}$  axis (38). The two chains are shifted one to another along the  $\mathbf{c}_{\text{P3HT}}$  axis to allow a regular packing of the  $n$ -hexyl side chains. The present results suggest that this translational order along the chain axis direction is poorly defined for the rubbed P3HT films resulting in the quasi absence of the (h02) reflections in the ED pattern. In other words, the lamellar structure of P3HT associated with the periodic alternation of  $\pi$ -stacked polythiophene backbones and layers of  $n$ -hexyl side chains is observed by HR-TEM for both rubbed and epitaxied layers. However, rubbed and epitaxied layers differ in terms of *intra-lamellar* order *i.e.* order within  $\pi$ -stacked layers of P3HT chains.

One can invoke two possible origins of the *intra-lamellar* disorder. In a first hypothesis, the polythiophene backbones are regularly  $\pi$ -stacked and the disorder concerns the layers of *n*-hexyl side chains. In the recent work by Wu *et al.*, evidence for side-chain disorder has been obtained by  $^{13}\text{C}$  MAS NMR and X-ray diffraction (39). Two crystal phases of P3HT, phase I and II, have been proposed with a transition from phase I to phase II around  $T = 60^\circ\text{C}$  (39–41). Phase I is described as a well organized 3D crystalline phase whereas phase II is a 2D crystalline phase in which the side chains are less ordered *i.e.* a smectic-like structure. The structural results gathered in this study, suggest that the P3HT films grown by epitaxy are formed of phase I, the 3D crystalline form, coexisting with the amorphous phase as evidenced by TEM in BF and HR-TEM modes. Instead, the rubbed films of P3HT may be compared to a liquid crystalline phase showing only a 2D order with a significantly higher level of side chain disorder that disrupts 3D translational order.

The second possible origin of *intra-lamellar* disorder could be related to stacking defects between successive  $\pi$ -stacked polythiophene backbones as illustrated in *Figure 5-4*. In the crystalline structure of P3HT, the relative position of two successive  $\pi$ -stacked chains, and in particular the shift along the  $\mathbf{c}_{\text{P3HT}}$  axis of the two chains in the unit cell, is imposed by the ordered lattice formed by the *n*-hexyl side chains (38). In a disordered system, statistical disorder along the chain axis of the  $\pi$ -stacked backbones can account for the absence of (h02) reflections in the ED patterns of the rubbed layers. It can be postulated that, both the disorder within the layers of *n*-hexyl side-chains and the stacking disorder of the polythiophene backbones do coexist and are interrelated. If the side chains are in a disordered state, there is no doubt that the  $\pi$ -stacking of the polythiophene backbones will also be affected. As shown hereafter, these different levels of disorder have some direct impact on the optical properties of the P3HT films.

The difference in crystalline order observed in the oriented P3HT films grown by epitaxy and rubbing can be explained by the use of two different orientation methods where one makes use of an orienting substrate and the other one makes use of shearing forces. In films grown by directional epitaxial crystallization, the preferential in-plane orientation of P3HT chains is enforced by the TCB substrate via 1D epitaxy ( $2\mathbf{c}_{\text{TCB}} \approx \mathbf{c}_{\text{P3HT}}$ ). The TCB substrate imposes adjacent P3HT chains to be in registry along the  $\mathbf{c}_{\text{P3HT}}$  direction so that successive layers of  $\pi$ -stacked chains generate 3D crystalline domains. As opposed to this, in the rubbed P3HT layers, the applied shear force orients the in-plane direction of the chains but does not fix the relative positions of P3HT chains. There is accordingly no external driving force to 3D crystalline order in the case of rubbing.

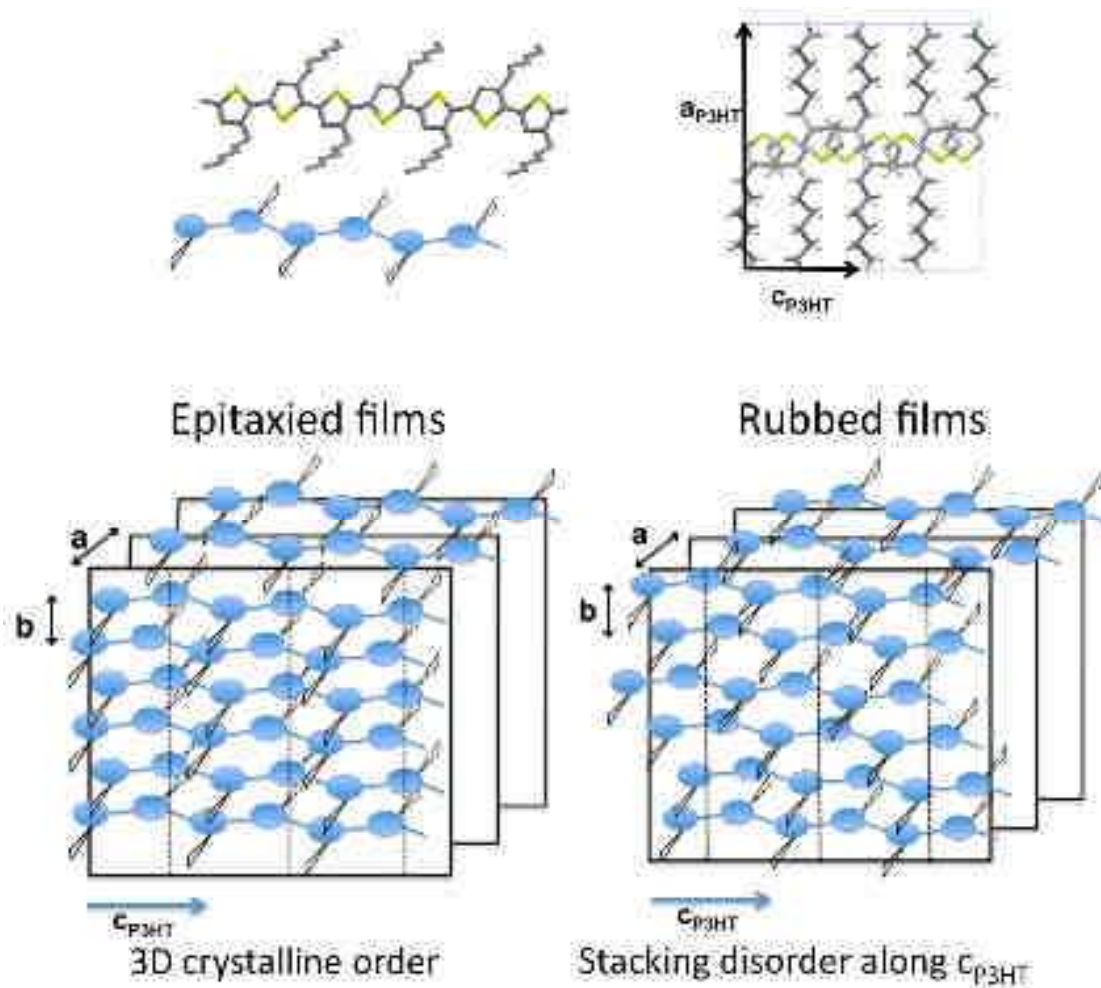


Figure 5-4: Schematic illustration of the different levels of order in P3HT thin films oriented by mechanical rubbing and slow-DEC. In epitaxied layers, translational order is present along all three unit cell directions. As seen in the upper right corner, the unit cell of P3HT contains two P3HT chains with a well defined shift along the  $b_{P3HT}$  axis. In contrast, for the rubbed P3HT films, lamellae of  $\pi$ -stacked polythiophene backbones are still separated one from another by a regular period of 1.6 – 1.65 nm but statistical stacking disorder along the chain axis direction  $c_{P3HT}$  suppresses 3D crystalline order.

### 5.3. UV-vis absorbance spectroscopy

The important structural differences between rubbed and epitaxied P3HT films highlighted by ED and HR-TEM should translate into important differences in the UV-vis absorption spectra. Figure 5-5 compares the UV-vis spectra of P3HT films oriented by slow-DEC and rubbing for an incident light polarization parallel and perpendicular to the chain axis ( $c_{P3HT}$ ). Regarding the rubbed layers the spectrum shows a poorly defined vibronic structure with a predominant 0-1 component. Epitaxied films exhibit a broader absorption spectrum as compared to the rubbed films and a better defined vibronic structure. In particular, for the

epitaxied films of the medium- $M_w$  P3HT, the 0-0 contribution at 610 nm (2.034eV) is particularly intense and the spectra show four well defined vibronic components. The dichroic ratios obtained in epitaxied films is 6.6 at 510 nm and therefore higher than in rubbed films (4.2 at 510 nm) indicating a better degree in plane orientation as it was already evidenced from the ED patterns. Regarding the ratio of intensity  $A_{0-0}/A_{0-1}$ , epitaxied films show a ratio  $A_{0-0}/A_{0-1} \sim 0.9$  versus a  $A_{0-0}/A_{0-1} \sim 0.76$  for rubbed films. A high  $A_{0-0}/A_{0-1}$  ratio is generally interpreted as a high degree of crystallinity in the films. HR-TEM images show that the extension of the P3HT stems in the crystalline domains is two times larger in epitaxied layers than in rubbed films.

To further understand the UV-vis spectra of rubbed and epitaxied thin films, polarized temperature dependent photoluminescence measurements were performed. A detailed analysis of these data is still in progression and therefore not presented in this manuscript.

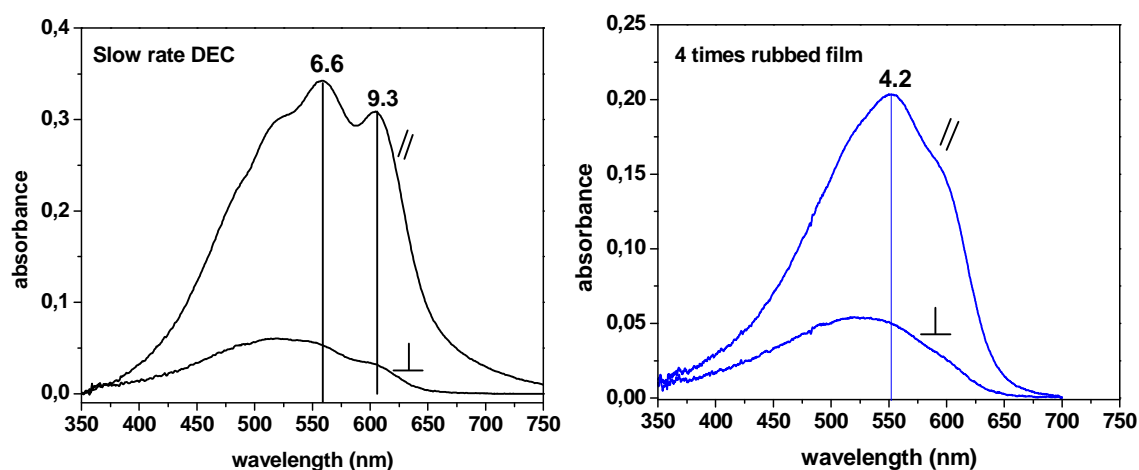


Figure 5-5: Comparison of the UV-vis absorbance spectra of P3HT thin films ( $M_w=17.2kD$  (right) prepared by slow-DEC in TCB (left) oriented by rubbing for the incident light polarized parallel (//) and perpendicular ( $\perp$ ) to the rubbing direction (respectively  $c_{TCB}$  direction for slow-DEC). The numerical values in the figure correspond to the measured dichroic ratio at two wavelengths.

## 6. Conclusion

We have prepared oriented thin P3HT films by mechanical rubbing. Rubbing of the P3HT films causes (i) orientation of the chains parallel to the rubbing direction and (ii) a flip of a preferential “edge-on” to a preferential “flat-on” orientation of the crystalline domains. We showed that the orientation of the thin films propagates from the film-air interface through the bulk of the film with increasing number of rubbing steps. The maximum degree of in-plane orientation achieved in the rubbed films is a function of  $M_w$ . High in-plane orientation is achieved for low  $M_w$  samples. Reorientation of  $\pi$ -stacked chains in high- $M_w$  films is hindered by a reduced chain mobility caused by the presence of chain entanglements

and tie-chains interconnecting crystalline P3HT domains. This  $M_w$  dependence of P3HT chain alignment and reorientation of crystalline domains is further manifested in the anisotropy of charge mobility ( $\mu_{//} / \mu_{\perp}$ ) induced by rubbing. Indeed, this anisotropy tends to increase with decreasing  $M_w$  underlining the difference between an oligomer-like system ( $M_w < 10$  kDa) and a semi-crystalline system ( $M_w > 10$  kDa) made of highly interconnected crystalline domains. Important structural and morphological differences were evidenced comparing the rubbed films to those prepared by slow-DEC. Whereas films grown by slow-DEC show a high level of crystallinity with a 3D translational order, rubbed layers show a “smectic-like” order with a periodic succession of planes of  $\pi$ -stacked polythiophene chains with marginal translational order along the chain-axis direction. It was shown that the differences in intralamellar order are directly reflected in the vibronic structure of the absorption spectra of the films. In epitaxial films with 3D crystalline order, a redistribution of the spectral weight in the zero-phonon peak is observed. Additional polarized absorption and emission spectra measurements of the epitaxied layers will be necessary to clarify further the impact of crystalline order on the optical properties of the P3HT films grown by slow-DEC and oriented by mechanical rubbing.

- (1) Van Aerle, N. A. J. M.; Barmantlo, M.; Hollering, R. W. J. Effect of rubbing on the molecular orientation within polyimide orienting layers of liquid-crystal displays. *Journal of Applied Physics* **1993**, *74*, 3111-3120.
- (2) Kim, Y. B.; Olin, H.; Park, S. Y.; Choi, J. W.; Komitov, L.; Matuszczyk, M.; Lagerwall, S. T. Rubbed polyimide films studied by scanning force microscopy. *Applied Physics Letters* **1995**, *66*, 2218.
- (3) Vergnat, C. Elaboration de surfaces polymers orientées et nanostructurées pour l'orientation de matériaux moléculaires conjugués, PhD dissertation, Université de Strasbourg, 2010.
- (4) Vergnat, C.; Landais, V.; Legrand, J.-F.; Brinkmann, M. Orienting semiconducting nanocrystals on nanostructured polycarbonate substrates: impact of substrate temperature on polymorphism and in-plane orientation. *Macromolecules* **2011**, *44*, 3817-3827.
- (5) Vergnat, C.; Uttiya, S.; Pratontep, S.; Kerdcharoen, T.; Legrand, J.-F.; Brinkmann, M. Oriented growth of zinc(II) phthalocyanines on polycarbonate alignment substrates: Effect of substrate temperature on in-plane orientation. *Synthetic Metals* **2011**, *161*, 251.
- (6) Brinkmann, M.; Pratontep, S.; Chaumont, C.; Wittmann, J.-C. Oriented and nanostructured polycarbonate substrates for the orientation of conjugated molecular materials and gold nanoparticles. *Macromolecules* **2007**, *40*, 9420-9426.
- (7) Matsushima, T.; Murata, H. Enhanced charge-carrier injection caused by molecular orientation. *Applied Physics Letters* **2011**, *98*, 253307.
- (8) Chen, X. L.; Lovinger, A. J.; Bao, Z.; Sapjeta, J. Morphological and transistor studies of organic molecular semiconductors with anisotropic electrical characteristics. *Chemistry of Materials* **2001**, *13*, 1341-1348.
- (9) O'Connor, B.; Kline, R. J.; Conrad, B. R.; Richter, L. J.; Gundlach, D.; Toney, M. F.; DeLongchamp, D. M. Anisotropic structure and charge transport in highly strain-aligned regioregular poly(3-hexylthiophene). *Advanced Functional Materials* **2011**, *21*, 3697-3705.
- (10) Nagamatsu, S.; Takashima, W.; Kaneto, K.; Yoshida, Y.; Tanigaki, N.; Yase, K.; Omote, K. Backbone arrangement in "friction-transferred" regioregular poly(3-alkylthiophene)s. *Macromolecules* **2003**, *36*, 5252-5257.
- (11) Nagamatsu, S.; Misaki, M.; Chikamatsu, M.; Kimura, T.; Yoshida, Y.; Azumi, R.; Tanigaki, N.; Yase, K. Crystal structure of friction-transferred poly(2,5-dioctyloxy-1,4-phenylenevinylene). *The journal of physical chemistry. B* **2007**, *111*, 4349-54.
- (12) Amundson, K. R.; Sapjeta, B. J.; Lovinger, A. J.; Bao, Z. An in-plane anisotropic organic semiconductor based upon poly (3-hexyl thiophene). *Thin Solid Films* **2002**, *414*, 143-149.
- (13) Derue, G.; Coppée, S.; Gabriele, S.; Surin, M.; Geskin, V.; Monteverde, F.; Leclère, P.; Lazzaroni, R.; Damman, P. Nanorubbing of polythiophene surfaces. *Journal of the American Chemical Society* **2005**, *127*, 8018-9.
- (14) Zhu, R.; Kumar, A.; Yang, Y. Polarizing organic photovoltaics. *Advanced Materials* **2011**, *23*, 4193-4198.

- (15) Bolognesi, A.; Botta, C.; Mercogliano, C.; Porzio, W.; Jukes, P. C.; Geoghegan, M.; Grell, M.; Durell, M.; Trolley, D.; Das, A.; Macdonald, J. E. Structural features in aligned poly(3-alkylthiophene) films revealed by grazing incidence X-ray diffraction. *Polymer* **2004**, *45*, 4133-4138.
- (16) Heil, H.; Finnberg, T.; von Malm, N.; Schmechel, R.; von Seggern, H. The influence of mechanical rubbing on the field-effect mobility in polyhexylthiophene. *Journal of Applied Physics* **2003**, *93*, 1636.
- (17) Abbas, M.; D'Amico, F.; Ali, M.; Mencarelli, I.; Setti, L.; Bontempi, E.; Gunnella, R. Rubbing effects on the structural and optical properties of poly(3-hexylthiophene) films. *Journal of Physics D: Applied Physics* **2010**, *43*, 035103.
- (18) Tanaka, H.; Yasuda, T.; Fujita, K.; Tsutsi, T. Highly-oriented organic thin films and application for photovoltaic device. *Molecular Crystals and Liquid Crystals* **2007**, 67-73.
- (19) Toney, M. F.; Russell, T. P.; Logan, J. A.; Kikuchi, H.; Sands, J. M.; Kumar, S. K. Near-surface alignments of polymers in rubbed films. *Nature* **1995**, *374*, 709-711.
- (20) Somani, R. H.; Yang, L.; Zhu, L.; Hsiao, B. S. Flow-induced shish-kebab precursor structures in entangled polymer melts. *Polymer* **2005**, *46*, 8587-8623.
- (21) Kline, R. J.; McGehee, M. D.; Kadnikova, E. N.; Liu, J.; Fréchet, J. M. J. Controlling the field-effect mobility of regioregular polythiophene by changing the molecular weight. *Advanced Materials* **2003**, *15*, 1519-1522.
- (22) Kline, R. J.; McGehee, M. D.; Kadnikova, E. N.; Liu, J.; Fréchet, J. M. J.; Toney, M. F. Dependence of regioregular poly(3-hexylthiophene) film morphology and field-effect mobility on molecular weight. *Macromolecules* **2005**, *38*, 3312-3319.
- (23) Zen, A.; Pflaum, J.; Hirschmann, S.; Zhuang, W.; Jaiser, F.; Asawapirom, U.; Rabe, J. P.; Scherf, U.; Neher, D. Effect of molecular weight and annealing of Poly(3-hexylthiophene)s on the performance of organic field-effect transistors. *Advanced Functional Materials* **2004**, *14*, 757-764.
- (24) Brinkmann, M.; Rannou, P. Effect of molecular weight on the structure and morphology of oriented thin films of regioregular poly(3-hexylthiophene) grown by directional epitaxial solidification. *Advanced Functional Materials* **2007**, *17*, 101-108.
- (25) Zen, A.; Saphiannikova, M.; Neher, D.; Grenzer, J.; Grigorian, S.; Pietsch, U.; Asawapirom, U.; Janietz, S.; Scherf, U.; Lieberwirth, I.; Wegner, G. Effect of molecular weight on the structure and crystallinity of poly(3-hexylthiophene). *Macromolecules* **2006**, *39*, 2162-2171.
- (26) Brinkmann, M.; Rannou, P. Molecular weight dependence of chain packing and semicrystalline structure in oriented films of regioregular poly(3-hexylthiophene) revealed by high-resolution transmission electron microscopy. *Macromolecules* **2009**, *42*, 1125-1130.
- (27) Zhang, R.; Li, B.; Iovu, M. C.; Jeffries-El, M.; Sauvé, G.; Cooper, J.; Jia, S.; Tristram-Nagle, S.; Smilgies, D. M.; Lambeth, D. N.; McCullough, R. D.; Kowalewski, T. Nanostructure dependence of field-effect mobility in regioregular poly(3-hexylthiophene) thin film field effect transistors. *Journal of the American Chemical Society* **2006**, *128*, 3480-1.

- (28) Brinkmann, M. Structure and morphology control in thin films of regioregular poly(3-hexylthiophene). *Journal of Polymer Science Part B: Polymer Physics* **2011**, *49*, 1218-1233.
- (29) Brinkmann, M.; Wittmann, J.-C. Orientation of regioregular poly(3-hexylthiophene) by directional solidification: a simple method to reveal the semicrystalline structure of a conjugated polymer. *Advanced Materials* **2006**, *18*, 860-863.
- (30) Trznadel, M.; Pron, A.; Zagorska, M.; Chrzaszcz, R.; Pielichowski, J. Effect of molecular weight on spectroscopic and spectroelectrochemical properties of regioregular poly(3-hexylthiophene). *Macromolecules* **1998**, *31*, 5051-8.
- (31) Spano, F. C. Modeling disorder in polymer aggregates: the optical spectroscopy of regioregular poly(3-hexylthiophene) thin films. *The Journal of chemical physics* **2005**, *122*, 234701.
- (32) Spano, F. Absorption in regio-regular poly(3-hexyl)thiophene thin films: Fermi resonances, interband coupling and disorder. *Chemical Physics* **2006**, *325*, 22-35.
- (33) Spano, F. C.; Clark, J.; Silva, C.; Friend, R. H. Determining exciton coherence from the photoluminescence spectral line shape in poly(3-hexylthiophene) thin films. *The Journal of chemical physics* **2009**, *130*, 074904.
- (34) Clark, J.; Silva, C.; Friend, R.; Spano, F. Role of intermolecular coupling in the photophysics of disordered organic semiconductors: aggregate emission in regioregular polythiophene. *Physical Review Letters* **2007**, *98*, 1-4.
- (35) Clark, J.; Chang, J.-F.; Spano, F. C.; Friend, R. H.; Silva, C. Determining exciton bandwidth and film microstructure in polythiophene films using linear absorption spectroscopy. *Applied Physics Letters* **2009**, *94*, 163306.
- (36) Verilhac, J.-M.; LeBlevenec, G.; Djurado, D.; Rieutord, F.; Chouiki, M.; Travers, J.-P.; Pron, A. Effect of macromolecular parameters and processing conditions on supramolecular organisation, morphology and electrical transport properties in thin layers of regioregular poly(3-hexylthiophene). *Synthetic Metals* **2006**, *156*, 815-823.
- (37) Jimison, L. H.; Toney, M. F.; McCulloch, I.; Heeney, M.; Salleo, A. Charge-transport anisotropy due to grain boundaries in directionally crystallized thin films of regioregular poly(3-hexylthiophene). *Advanced Materials* **2009**, *21*, 1568-1572.
- (38) Kayunkid, N.; Uttiya, S.; Brinkmann, M. Structural model of regioregular poly(3-hexylthiophene) obtained by electron diffraction analysis. *Macromolecules* **2010**, *43*, 4961-4967.
- (39) Wu, Z.; Petzold, A.; Henze, T.; Thurn-Albrecht, T.; Lohwasser, R. H.; Sommer, M.; Thelakkat, M. Temperature and molecular weight dependent hierarchical equilibrium structures in semiconducting poly(3-hexylthiophene). *Macromolecules* **2010**, *43*, 4646-4653.
- (40) Pascui, O. F.; Lohwasser, R.; Sommer, M.; Thelakkat, M.; Thurn-Albrecht, T.; Saalwachter, K. High Crystallinity and Nature of Crystal-Crystal Phase Transformations in Regioregular Poly(3-hexylthiophene). *Macromolecules* **2010**, *43*, 9401-9410.
- (41) Yuan, Y.; Zhang, J.; Sun, J.; Hu, J.; Zhang, T.; Duan, Y. Polymorphism and structural transition around 54 ° C in regioregular poly ( 3-hexylthiophene ) with high crystallinity as revealed by infrared spectroscopy. *Macromolecules* **2011**, *in press*



# ***Chapter 6. Oriented and nanostructured hybrid thin films prepared by slow Directional Epitaxial Crystallization***

*Highly oriented and nanostructured hybrid thin films made of regioregular poly(3-hexylthiophene) and colloidal CdSe nanocrystals were prepared by the slow rate directional epitaxial crystallization (slow-DEC) technique presented in Chapter 3. The structure of the films has been analyzed by polarized optical microscopy, UV-vis spectroscopy, X-ray diffraction, electron diffraction and 3D electron tomography to afford a multi-scale structural and morphological description of the highly oriented nanostructured hybrid films. In particular, a quantitative analysis of the reconstructed volumes based on electron tomography allowed to establish a 3D map of the distribution of the CdSe spherical or nanorod-shaped nanocrystals in the bulk of the hybrid films. The influence of the P3HT:CdSe weight ratio on the 3D structure of the hybrid layers was thus obtained. In all cases, a bilayer structure was observed. It consists of a first oriented layer of pure P3HT grown epitaxially on the TCB substrate and of a second oriented P3HT layer containing CdSe nanocrystals sequestered in the amorphous interlamellar zones of the polymer. The thickness of the P3HT layer containing CdSe nanoparticles increases gradually with increasing content of NCs in the films. A growth model is proposed to explain this original bilayer structure of the hybrid CdSe NCs and P3HT films. In addition to this study of the thin hybrid thin films prepared with as-synthesised CdSe NCs, the effect of the surface functionalization of the NCs with polypyridine ligands (hexyl-pyridine, phenanthroline and terpyridine) on the thin film morphology was also investigated by TEM.*



## 1. Introduction to nanostructured hybrid Materials

As mentioned in Chapter 1, nanocomposites made of polymers and colloidal inorganic nanocrystals (NCs) have recently raised a lot of interest because they afford the possibility to combine the unique properties of nanoparticles (*e.g.* the tunability of the band gap for semiconducting NCs such as CdSe NCs) and the ease of processability inherent to polymers (1, 2). Whereas the controlled dispersion of clay nanosheets in polymers like nylon afforded materials with improved mechanical properties (*e.g.* high tensile strength) (3), nanocomposites combining semiconducting NCs and  $\pi$ -conjugated polymers like regioregular poly(3-hexylthiophene) (P3HT) have emerged as interesting hybrid materials for the elaboration of devices for printed electronics such as solar cells (4–10). However, it has been recognized that many parameters affect the fabrication of efficient devices. Among those: (i) the control of the interface between the polymer and the nanocrystals via a controlled surface treatment of the nanocrystals; (ii) the nanoscale dispersion of nanoparticles within the layers of polymers like P3HT is an essential but yet difficult step towards the optimization of the photophysical and the charge transport properties in devices such as hybrid solar cells. Therefore, there is a stringent need for the development of simple elaboration methods that yield hierarchically structured systems as required in the case of bulk photovoltaic junctions showing: (i) a nanostructuring into donor and acceptor domains of typical sizes around 10nm; (ii) an orientation of the facile transport direction of the charge carriers perpendicular to the plane of the film in order to improve their collection at the electrodes (2, 11–14).

Many approaches are used for the controlled fabrication of hierarchical hybrid nanostructures (15–24). The use of block copolymers was shown to be a good approach for the fabrication of ordered nanostructures. For example, Zou *et al.* used phase segregated block copolymers composed of polystyrene (PS) and poly-2-vinylpyridine (P2VP). They showed that TOPO coated NCs are exclusively located in the polystyrene domains whereas polyethylene glycol (PEG) coated NCs are preferentially located in the P2VP domains. This can be explained by favourable molecular interactions between TOPO and PS and PEG and P2VP (20). Another approach for the fabrication of nanostructures is the use of template substrates (18, 19, 25). In this sense Zhang *et al.* prepared nanostructures of CdSe nanorods on a polystyrene-PMMA block copolymer with 30 nm large channels. The nanorods were floated on the patterned template and located within these channels giving rise to a 30 nm periodic assembly (18, 19). Bockstaller *et al.* showed that entropic effects can also lead to the fabrication of highly ordered nanostructures. They used a block-copolymer of (polystyrene-*b*-ethylene propylene) (PS-PEP) silica and gold NCs of different sizes. They observed that the silica particles are located within the PEP domains whereas the gold particles align exclusively at the interfaces between PS and PEP (26, 27).

Following a different approach, M. Brinkmann *et al.* have recently demonstrated the possibility to use the semi-crystalline structure of regioregular P3HT as a scaffold to prepare nanostructured and oriented hybrid films containing CdSe NCs (28). As shown in a previous chapter (see Chapter 4), directional epitaxial crystallization (DEC) of P3HT in 1,3,5-

trichlorobenzene (TCB) leads to highly oriented and crystalline P3HT layers with a regular nanostructuring made of alternating crystalline domains and amorphous interlamellar zones as seen in Chapter 4. When the DEC method is performed in the presence of CdSe NCs, there is a preferential confinement of the nanoparticles in the amorphous interlamellar zones (AIZ) of the polymer. One thus obtains highly oriented and nanostructured hybrid films with a periodic alternation of pure crystalline lamellae of P3HT separated by amorphous zones of P3HT hosting the CdSe NCs (28). In this work, the authors also showed that the period of nanostructuring is approx. 28 nm, *i.e.* matching the length scale requirements for organic and hybrid solar cells. *Figure 1-1* shows a TEM-BF image of such a film. As seen in Chapter 4, for the slow-DEC samples, the lamellar period is function of the  $M_w$ .

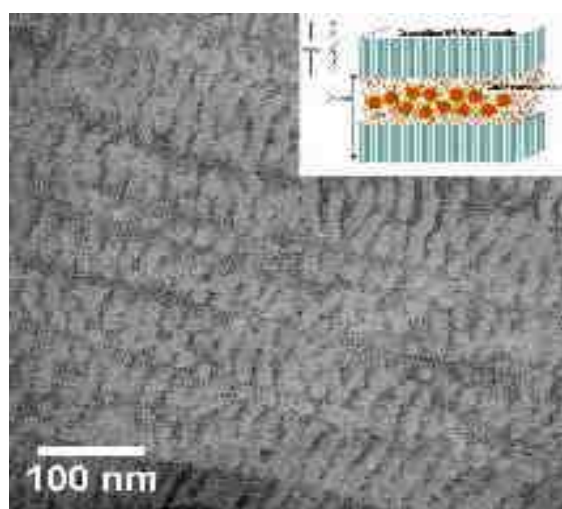


*Figure 1-1: TEM-BF image of a hybrid film composed of P3HT and CdSe NCs prepared by directional epitaxial crystallization. Reproduced from (28).*

The development of the slow-DEC method which was extensively explained in a previous chapter of this work (Chapter 3) allows for a controlled and slow growth of the crystallization front of the crystallizable solvent TCB and hence affords uniform films with  $\text{mm}^2$  to  $\text{cm}^2$  surfaces of highly oriented and nanostructured P3HT/CdSe films, as compared to a few  $\mu\text{m}^2$  for the previous method on the Koeffler Bench (28). In this work, following the first studies published by Brinkmann *et al* (28), we were interested in performing a more detailed study of the hybrid thin films grown by the novel slow-DEC growth method. Indeed, the hybrid films prepared by the slow-DEC allow the combination of two main important features in view of their application in devices such as field effect transistors or solar cells: (i) The P3HT is highly oriented. The transport properties are therefore expected to be highly anisotropic (29, 30). (ii) These hybrid films are nanostructured on length scales relevant for their use as active layer in flexible solar cells.

The principle of fabrication of such hybrid thin films is the same than in the case of pure P3HT thin films with the only difference that the thin films are grown in the presence of a defined amount of CdSe NCs. In the following, we will use the relative weight ratio of

P3HT to CdSe NCs (P3HT:CdSe) to characterize the composition of the hybrids. The obtention of large areas of hybrid thin films allowed performing their characterization by UV-vis spectroscopy and XRD measurements.

At first, we were interested in the effect of the presence of spherical NCs on the in-plane orientation of the hybrid thin films and on their crystallinity. By means of electron tomography measurements, we investigated the 3D distribution of spherical NCs within the films and the influence of the ratio P3HT/CdSe. Then, we were interested in the effect of the morphology of the NCs (spherical or rod-shaped NCs) on the nanostructuration and in-plane orientation of the hybrid thin films. Therefore rod-shaped NCs having various aspect ratios were incorporated into the thin films. The effect of the weight ratio of NRs in the films was investigated. At last, using our experience on surface functionalization of CdSe NCs with polypyridines (see Chapter 2), we studied the influence of the capping ligands on the nanostructuration of hybrid thin films prepared by slow rate DEC with spherical CdSe NCs.

## 2. Hybrid thin films prepared with as synthesized CdSe NCs

As seen in Chapter 2, colloidal NCs are formed by an inorganic core and a surface layer capped with organic molecules, the so-called ligands or surfactants. At first, we prepared hybrid thin films made of P3HT and spherical as-synthesized CdSe nanocrystals, *i.e.* NCs covered with their synthesis ligands namely oleylamine, stearic acid and TOPO (see Chapter 2 for more details). At first, we will focus on spherical NCs.

### 2.1. Case of spherical NCs

#### 2.1.1. In-plane orientation of the hybrid thin films

As we are interested in the fabrication of oriented hybrid materials, the in-plane orientation of the films is an important parameter to study. The possibility to grow large surfaces of highly oriented films of pure P3HT by slow-DEC was illustrated and emphasized in Chapter 3. In a first attempt, we studied the influence of the presence of spherical NCs on the in-plane orientation and the crystallinity of the films. *Figure 2-1* shows the polarized UV-vis spectrum of a hybrid film composed of spherical NCs and P3HT in a weight ratio P3HT:CdSe 1:1.

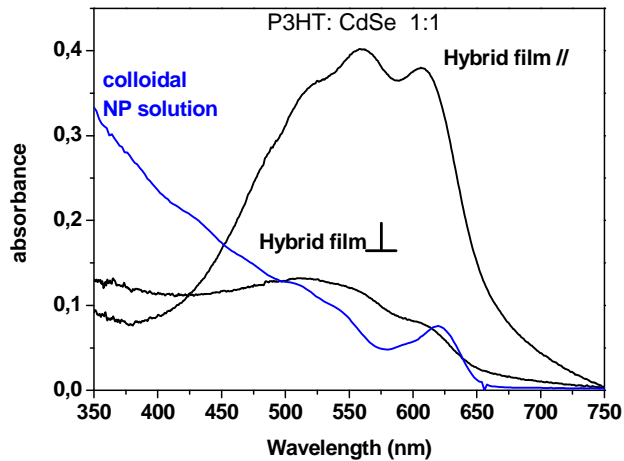


Figure 2-1: Polarized UV-vis absorption spectra of a hybrid film composed of P3HT ( $M_w=50$  kDa) and nanospheres (1:1 w/w) for the incident light polarized parallel (//) and perpendicular ( $\perp$ ) to the P3HT chain direction. For comparison, the absorption spectrum of a colloidal solution of CdSe NCs is also displayed.

Although it is not possible to extract a precise dichroic ratio of the P3HT from the absorption spectra due to the overlap of the absorption spectrum of P3HT with that of the CdSe NCs, a high anisotropy of the UV-vis in the perpendicular and the parallel orientation can be seen. This indicates that for a hybrid thin film of this composition, the overall in-plane orientation is not hampered. This is further confirmed by the POM image of a sample composed of NCs and P3HT in the ratio 1:1 (see Figure 2-2). Both, the absorption spectra and POM images of this hybrid film indicate that the orientation degree of the films is similar to that obtained for a pure P3HT films.

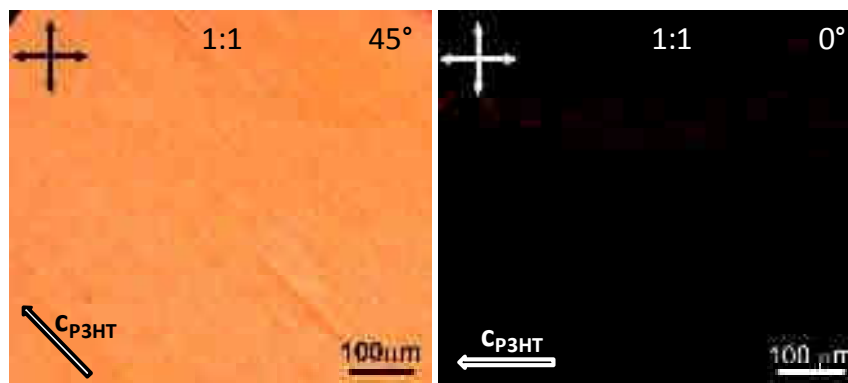


Figure 2-2: POM images of an oriented hybrid films composed of P3HT ( $M_w=50$  kDa) and spherical CdSe NCs in a weight ratios P3HT: CdSe of 1:1.

### 2.1.2. Crystallinity of the hybrid films

The in-plane orientation of the hybrid films (composition 1:1 in weight) and their crystallinity were further investigated by electron diffraction, out-of-plane and in-plane GIXD measurements. The ED patterns of the hybrid films will be discussed in more detail in a later section. At this point it can be mentioned that from the ED pattern it can be seen that the fiber

symmetry evidenced for epitaxied P3HT films (see Chapter 4) is maintained in the case of hybrids.

While ED affords a local view of crystalline order and orientation, long-range in-plane orientation on a cm scale was probed by GIXD. Typical GIXD profiles were recorded for two directions of the scattering vector  $\mathbf{q}$ :  $\mathbf{q} \perp \mathbf{c}_{\text{P3HT}}$  and  $\mathbf{q} \parallel \mathbf{c}_{\text{P3HT}}$  where  $\mathbf{c}_{\text{P3HT}}$  is the chain axis direction of P3HT. The GIXD scans of pure P3HT have already been extensively discussed in Chapter 4. Here it is displayed only for means of comparison. As seen in *Figure 2-3*, the same characteristic diffraction profiles of oriented P3HT are observed in the hybrid P3HT:CdSe NCs layers with a ratio 1:1 for the different scattering geometries. The main difference is the presence of a broad peak around  $q = 7.9 \text{ nm}^{-1}$  corresponding most presumably to the overlap of the  $(100)_{\text{CdSe}}$  and  $(002)_{\text{CdSe}}$  reflections of the wurtzite structure of CdSe (see Chapter 2). This peak is observed for all scattering configurations, as expected for a powder-like diffraction pattern of spherical wurtzite-like CdSe nanocrystals. Besides the appearance of the CdSe reflections, there is no significant difference of the diffractograms of the hybrid and that of pure P3HT. This indicates that, for this blend proportion, the crystalline structure of P3HT is not significantly affected by the presence of the NCs.

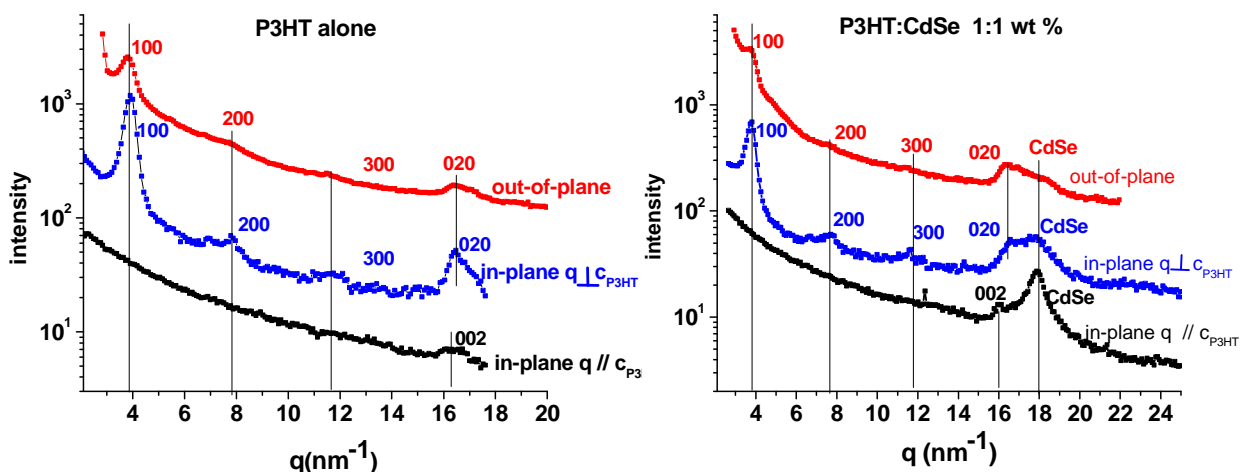


*Figure 2-3: (left) XRC scans of oriented thin films of P3HT (50 kDa) (right) and hybrid film composed of P3HT (50 kDa)/CdSe spherical NCs (1:1 in weight) Red curve: out-of-plane configuration. Blue curve: GIXD with  $\mathbf{q} \perp \mathbf{c}_{\text{P3HT}}$ . Black curve:  $\mathbf{q} \parallel \mathbf{c}_{\text{P3HT}}$ .*

### 2.1.3. 3D distribution of CdSe nanospheres within the hybrid films

The above studied results give a good insight on the orientation and the crystallinity of the hybrid thin films. TEM-BF images of the hybrid thin films grown by slow-DEC (see *Figure 2-8*) show clear nanostructuration with a periodic alternation of pure crystalline lamellae of P3HT separated by amorphous zones of P3HT hosting the CdSe NCs. This nanostructuration is similar to that observed by Brinkmann *et al.* and shown in *Figure 1-1* (28). This nanostructuration of the hybrid films is observed in the plane of the film using

standard transmission electron microscopy (TEM) but without having any information on the 3D dispersion of CdSe NCs in the bulk of the films. In that regard, characterisation methods based on TEM are particularly adapted thanks to the sub-nanometer resolution of the imaging modes in real space, as well as to the multitude of information that they can provide (structural, morphological, chemical etc.). However, when used in a standard way by acquisition of an image, a diffraction pattern or a spectrum, they remain two-dimensional techniques of investigation and are generally not able to provide 3D spatially-resolved information.

In collaboration with Ovidiu Ersen and Lucian Roiban at the “Institut de Physique et Chimie des Matériaux de Strasbourg”, we investigated the “bulk” 3D structure of the hybrid thin films grown slow-DEC by means of TEM-based tomography. The ability of TEM tomography for determining the spatial distribution of nanoparticles inside a 3D architecture has been the focus of several recently published works (31–33) especially in the field of hybrid materials for solar cells (12, 14, 34–36). Following this framework, the main objective of this section is to report a full 3-dimensional morphological description of nanostructured and oriented hybrid P3HT/CdSe NCs materials and to understand the underlying growth mechanism involved in the slow-DEC process for the growth of these films. For the present study, samples with spherical nanocrystals and blend ratios CdSe:P3HT of 1:1, 1:2 and 1:3 (w/w) were prepared. The tomography results presented here were obtained for the film recovered from the PEDOT:PSS coated glass slide. The films recovered on the PTFE side are much thinner and less uniform and therefore much more difficult to image by electron tomography (ET).

#### 2.1.3.1. Tomographic analysis of the P3HT/CdSe 1:1 sample

Herein, we will first illustrate the methodology of electron tomography as applied to the 1:1 (wt%) sample and give the main findings. Later, we will present the results obtained for hybrid thin films with different blend ratios (P3HT:CdSe 1:1, 1:2, 1:3 in wt%). For technical details on the tomographic measurements see Annexe 7. For these experiments spherical NCs of batch 1 ( $\varnothing=5.3$  nm) were used. The used P3HT is characterized by  $M_w=17.6$  kDa,  $M_n=13.4$  kDa or alternatively  $M_w=50.1$  kDa and  $M_n=26.2$ . The conclusions of the tomography analysis are similar for P3HT  $M_w$

*Figure 2-4* illustrates the steps of the tomographic analysis and summarizes the results obtained for the sample P3HT:CdSe 1:1 (w/w). It depicts different views for this sample corresponding to *a*) a 2D BF-TEM projection, *b*) typical longitudinal (top) and transversal (bottom left) slices extracted from the reconstructed volume and the summation of all transversal cross-sections (bottom right). *Figure 2-4 c*) and *d*) show the resulting 3D modelling of the NCs distribution in the film. The tomographic reconstruction reveals unambiguously a bilayer structure. The first top layer does not contain NCs in its bulk but only a thin surface layer corresponding to a surface decoration with individual NCs (not a dense layer). Below the first layer of pure P3HT, a second layer containing NCs is evidenced. For a film with a total thickness of about 120 nm, the two layers have a thickness of 70 nm (P3HT only) and 50 nm (P3HT and NCs) respectively. From the geometry of the tomography

experiment and the use of fiducial gold NCs, one can infer that the surface of the pure P3HT layer was in contact with the TCB crystal whereas the hybrid layer was on the side of the PEDOT:PSS-coated glass slide. Overall, this bilayer morphology is very peculiar and is at variance with reported results on spin-coated thin films of CdSe/P3HT or films of P3HT/TiO<sub>2</sub> as well as films composed of CdSe and poly(2-methoxy-5-(3'-7-dimethyloctyloxy)-1,4-phenylene vinylene) (4, 12, 35, 36).

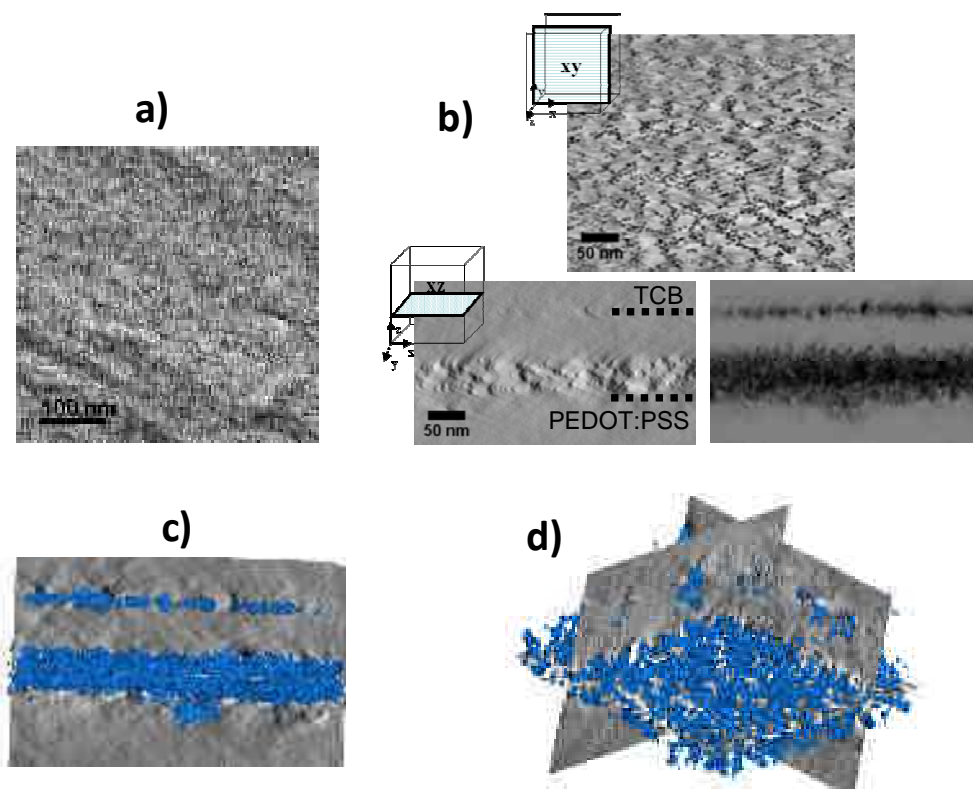


*Figure 2-4 : Tomographic analysis of the P3HT/CdSe hybrid film (1:1 in wt%). a) Typical bright field TEM image from the tilt series used to calculate the volume of the hybrid film. b) **Top**: example of a longitudinal slice extracted from the reconstructed volume. **Bottom left**: typical cross-section at a chosen location. **Bottom right**: sum of cross-sectional images along one direction in the plane of the film showing clearly the bilayer structure and the surface decoration of the top P3HT layer. c), d): 3D modelling of the CdSe nanoparticles (in blue), which provides a reliable 3D distribution of CdSe NCs in the films.*

In the latter films, high-density aggregated regions of nanoparticles are surrounded by lower-density regions but no vertical distribution of NCs in the film was observed. A vertical phase segregation with the enrichment of the PEDOT:PSS electrode with the polymer was reported in the case of thin films comprising a poly(**para**-phenylene vinylene) derivative and CdSe tetrapods and more recently in blends of CdSe nanorods with various functional polymers prepared by drop casting under controlled evaporation (37, 38). An enrichment in rod-shaped NCs at both surfaces of the film leaving a NCs-free portion in the middle of the film was reported for thiophene-based copolymers/CdSe NCs spin coated films (39). In the present case, it may be anticipated that the vertical phase separation corresponds to a

thermodynamically more stable situation which is accessible due to the slow epitaxial growth process using the zone melting process contrary to the situation observed in the case of hybrid layers prepared by spin-coating.

#### 2.1.3.2. Tomographic analysis of samples with CdSe nanospheres and other blend ratios

In order to understand the origin of this vertical phase separation, similar tomographic analyses were carried out on the hybrid films with different P3HT: NCs blend ratios (1:2 and 1:3 in w/w). *Figure 2-5* depicts typical cross-sections of the films for these additional samples. The 1:2 and 1:3 samples show a similar bilayer structures as the 1:1 sample. A pure P3HT layer and a hybrid P3HT:CdSe NCs layer can be observed. In all cases a surface decoration by CdSe NCs was observed on the top of the P3HT layer. It is assumed that this decoration layer corresponds to NCs that have been trapped at the surface of the TCB crystal at the beginning of the epitaxial crystallization of P3HT. However, the relative thickness of the hybrid versus pure P3HT layer changes with the P3HT:CdSe ratio. This is clearly visible in the cross-sectional views of the films for different P3HT:CdSe ratios. The higher the ratio of NCs in the films, the thicker the hybrid layer comparatively to the pure P3HT layer. These observations suggest a growth mechanism whereby the concentration of the CdSe NCs in liquid TCB must reach a threshold value before the nanoparticles can be incorporated in the oriented P3HT polymer matrix. To the best of our knowledge, this is the first evidence of a growth process of hybrid electro-active layers that allows such a bilayer structure with a rather sharp transition of the NP content in the direction normal to the film plane.

A statistical analysis of the NCs distribution in the reconstructed volumes yields quantitative informations on their densities in the analysed area as well as the distribution of the NCs along the z-direction (see histograms at the right of the cross sectional views in *Figure 2-5*). The results of the statistical analysis are summarized in *Table 2-1*. The histograms in *Figure 2-5* demonstrate that the 1:1 films show a rather sharp interface between the pure P3HT layer and the layer containing CdSe NCs. As opposed to this, in both the 1:2 and the 1:3 samples, the NCs are distributed in a thicker layer and the interface between the pure P3HT layer and the hybrid layer is less abrupt.

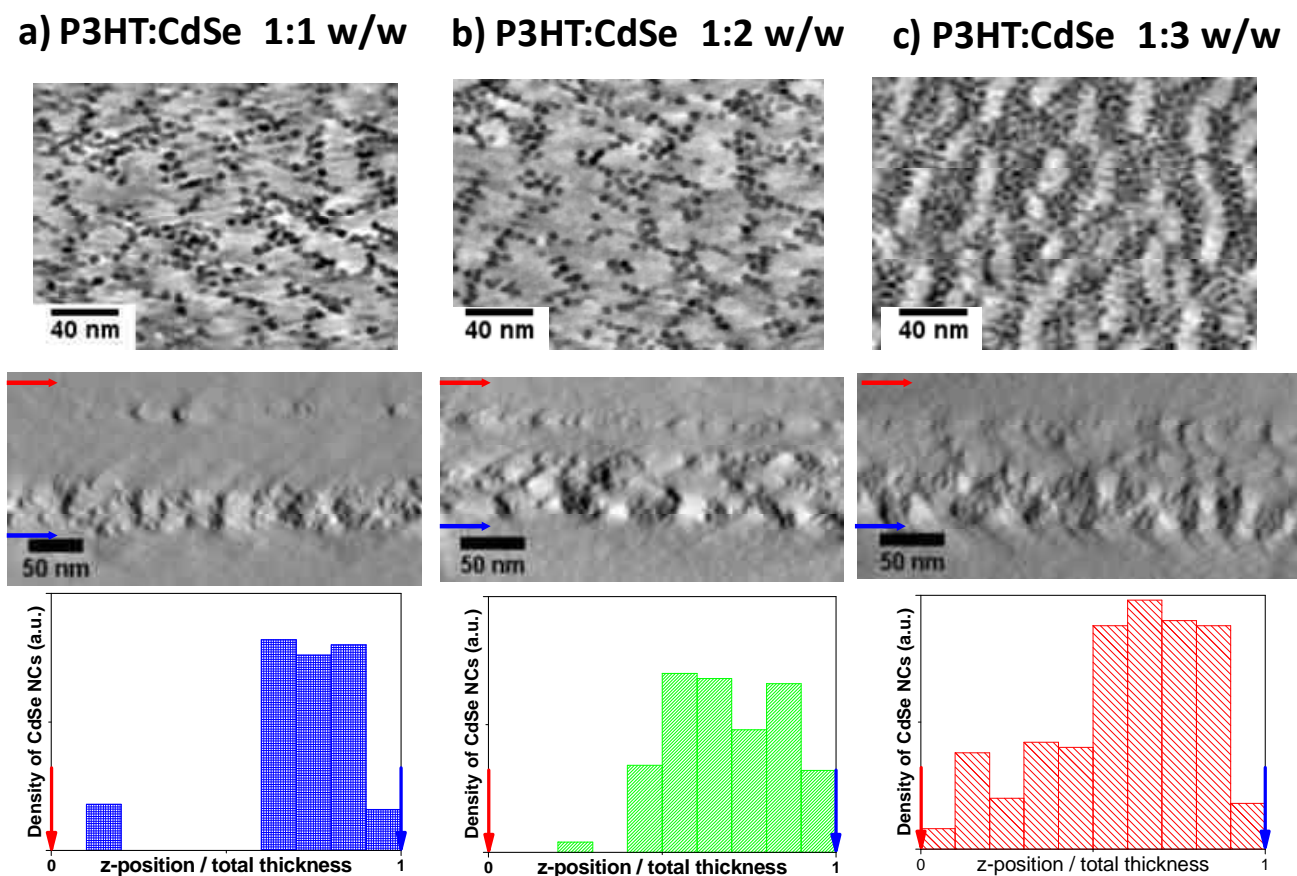


Figure 2-5: Comparative electron tomography study of hybrid oriented P3HT:CdSe NCs films with blend ratios (wt %) a) 1:1, b) 1:2 and c) 1:3. **Top:** Typical longitudinal slices extracted from the reconstructed volumes corresponding to the hybrid layers of the films. **Middle:** Typical cross-section slices extracted from the tomographic reconstructions obtained for the three analysed hybrid films. **Bottom:** Normalized histograms showing the variation of the density of NCs within the film when increasing the thickness for the analysed specimens (1:1 in blue, 1:2 in green, 1:3 in red). The same size of the area considered for the statistical analysis was considered for the three specimens. The red and blue arrows indicate the TCB and PEDOT:PSS sides, respectively.

The peculiar bilayer structure implies that apart from the surface decorated side of the film, the majority of the NCs is located in one layer whose relative thickness increases with the concentration of CdSe NCs in TCB. Accordingly, for a given relative concentration P3HT:CdSe, a higher density of NCs will be observed in the bilayer films grown by slow-DEC as compared to spin-coated films where NCs present a rather uniform distribution throughout the entire film thickness (4, 12, 35, 36). In addition, when increasing the blend ratio P3HT:CdSe from 1:1 to 1:3, the density of NCs averaged in the hybrid layer embedding the NCs increases by nearly one order of magnitude, from approx.  $1300 \times 10^6 \text{ nm}^{-3}$  to  $9900 \times 10^6 \text{ nm}^{-3}$ . Taking into account that a spherical NC of diameter 5.3 nm occupies a volume of approx.  $78 \text{ nm}^3$ , this implies that the volume fraction occupied by the NCs in the layer hosting the NCs changes from approx. 10 % (P3HT:CdSe 1:1) to 77 % (P3HT:CdSe 1:3).

Although approximative, this volumic fraction should be compared to that of the amorphous interlamellar zones in pure oriented P3HT films which is approximately 60 - 70 % (determined from the bright field TEM images where the crystalline domains appear as dark stripes and the amorphous interlamellar zones as brighter areas) (40, 41) . Accordingly, in the hybrid layers of the 1:3 sample, the volume occupied by the CdSe NCs exceeds that of the amorphous P3HT in the pure epitaxied P3HT films. This observation suggests that for the 1:3 samples, the semi-crystalline morphology of the epitaxied P3HT matrix is perturbed by the presence of CdSe nanoparticles. Furthermore, the high NC density achieved in the hybrid layers translates into a significant evolution of the average distance separating the surface of adjacent NCs from approximately 3 nm for the 1:1 sample to nearly close-contact (0 nm) for the 1:3 system. Accordingly, the 1:3 sample, shows percolating pathways, which should be of interest for interparticle charge transport via charge hopping between NCs (42, 43).

<b>P3HT:CdSe blend ratio (w/w)</b>	<b>Total thickness of the film (nm)</b>	<b>Thickness of the layer with NCs (nm / % of the total layer)</b>	<b>Average density of NCs in the layer with NCs (<math>10^{-6} \text{ nm}^{-3}</math>)</b>	<b>Volume fraction occupied by the NCs in the layer with NCs (%)</b>	<b>Average separation between adjacent NCs (nm)</b>
1:1	120	50 nm / 41 %	1300	10.3	2.8
1:2	80	46 nm / 57 %	4600	35.6	0.3
1:3	90	65 nm / 70 %	9900	76.9	0

*Table 2-1 : Results of the analysis of the tomographic 3D reconstructions of the hybrid oriented thin films P3HT:CdSe spherical NCs with different blend ratios: total thickness of the films and thickness of the layer hosting the CdSe NCs, density of NCs and volume fraction occupied by the NCs in the layer hosting NCs (assuming spherical NCs with a diameter of 5.3 nm of the inorganic core corresponding to a volume per NC of  $78 \text{ nm}^3$ ) and average separation between adjacent NCs.*

To provide more information on the growth mechanism and the microstructural characteristics of the film, a more detailed analysis was performed. By analysing the whole reconstructions in the cross-sections of the reconstructed volumes, one can observe that the presence of NCs influences the crystalline-amorphous alternation, especially when the density of NCs to be incorporated reaches a critical value. *Figure 2-6a* presents a cross-sectional slice for the 1:3 sample taken perpendicular to the growth direction of the crystal where this effect is clearly visible: the spatial extension of the amorphous interlamellar zones where the NCs are incorporated varies in the depth of the hybrid layer. Using these observations, a microstructural model can be proposed and is shown in *Figure 2-6b*, which illustrates that the amorphous interlamellar zones containing the NCs show a "trapezoidal" shape in the cross section (in blue). The trapezoidal shape is such that the volume fraction of the crystalline

lamellae (not containing CdSe nanoparticles) decreases at the expense of the amorphous interlamellar zones hosting the CdSe nanoparticles that tend to occupy a larger volume. This microstructural model supports the assumption that the epitaxial crystallization of P3HT is modified by the incorporation of high amounts of CdSe nanoparticles (for the blend ratio P3HT:CdSe NCs 1:3). It also suggests that the relative concentration of CdSe NCs with respect to P3HT increases gradually as the epitaxial growth of the film proceeds.

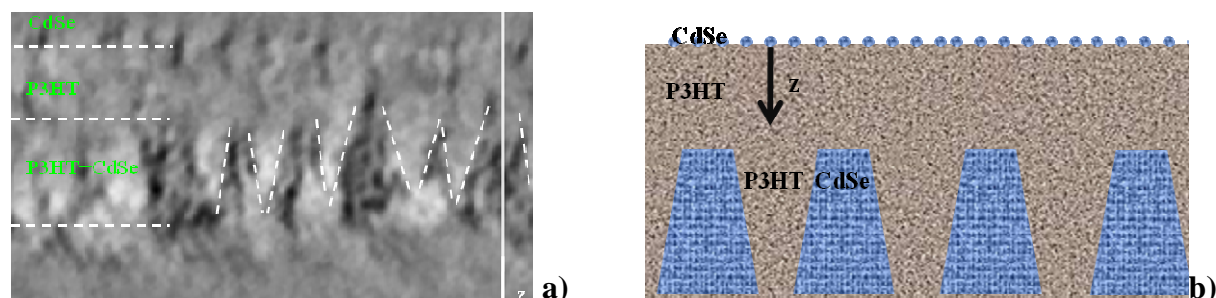


Figure 2-6: a) Example of cross-sectional slice extracted from the tomographic reconstruction calculated for the sample P3HT:CdSe with an 1:3 blend ratio (wt %), showing the increase of the lateral extension of the amorphous areas (where the NCs are sequestered) in the detriment of the crystalline lamellas. b) Schematic representation of the 3D architecture of the hybrid thin films.

#### 2.1.4. Proposal for a growth scenario of the oriented hybrid films

The bilayer structure of the films can have different origins *e.g.* interface effects, self-assembly of nanoparticles or entropic effects (44, 45). However, the peculiarity of directional epitaxial crystallization suggests specific aspects related to this mechanism of growth. Firstly, there is obviously no “macrophase” separation at play between P3HT and CdSe nanospheres under the growth conditions used herein. Instead a “microphase”-like phase separation is observed in the semi-crystalline P3HT matrix. From an energetic point of view, the preferential confinement of CdSe to the amorphous interlamellar zones (AIZs) can be explained in the following manner.

On the one side, the inclusion of NCs in the AIZs implies an entropic penalty due to the perturbation of the polymer chain conformation by the CdSe NCs which might be partly counterbalanced by favorable P3HT-CdSe interactions through the alkyl chains of both the trioctylphosphine oxide ligands of the CdSe NCs and the *n*-hexyl side groups of P3HT. On the other side, including the NCs in the crystalline parts of the polymer matrix would result in a high enthalpic penalty which is not observed. Instead of that, confining CdSe NCs in the AIZs results in a close-packed network of CdSe NCs *i.e.* a favourable enthalpic contribution. Accordingly, in the presence of CdSe NCs, the epitaxial crystallization of P3HT into a semi-crystalline matrix is the driving force for the observed “microphase” separation of CdSe NCs in the polymer matrix. Although these energetic considerations can account for the observed “microphase” separation, the generation of a bilayer structure made of a pure P3HT layer and a hybrid layer must rely on a different mechanism. The findings of the tomographic study will

be used to draw the main lines of a possible growth scenario that accounts for this specific double layer structure.

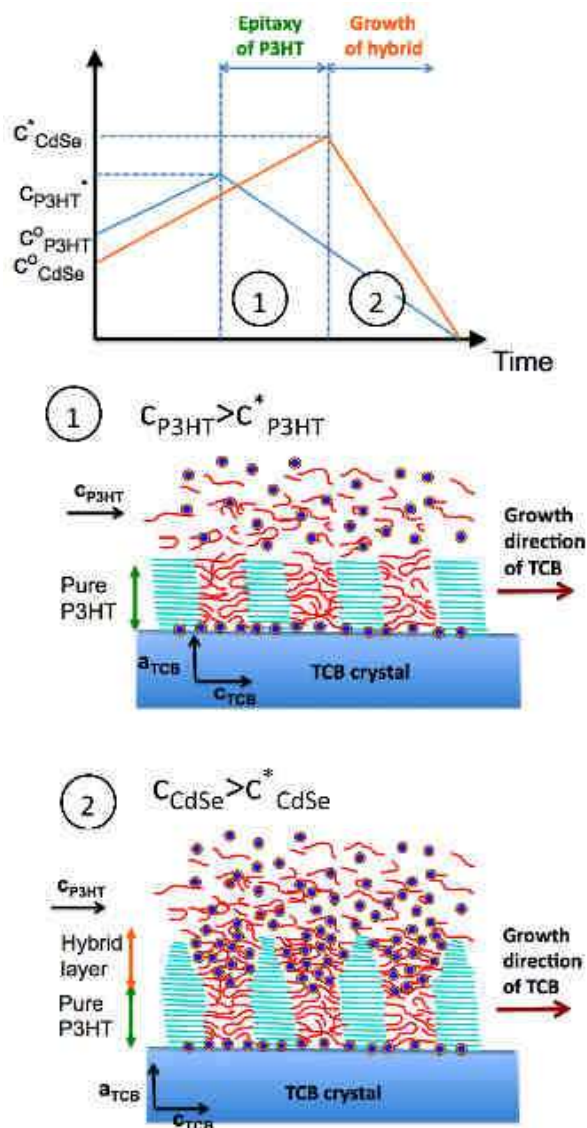


Figure 2-7 : Rationale of the growth mechanism of the oriented and nanostructured hybrid films prepared by epitaxial crystallization in TCB. The upper graph illustrates the possible time dependence of the concentration of P3HT and CdSe NCs at the growth front upon crystallization of TCB. The two lower parts represent the two stages of the growth: 1) epitaxy of the pure P3HT layer and 2) overgrowth of the hybrid layer with the incorporation of CdSe NCs in the amorphous interlamellar zones.

The general frame of the proposed growth mechanism is depicted in Figure 2-7 . As shown in Chapter 3 and in previous studies, the orientation and nanostructuring of the P3HT film is driven by a 1D epitaxial mechanism whereby P3HT polymer chains align parallel to the stacking axis of the TCB molecules *i.e.* along the  $c_{\text{TCB}}$  direction (40, 41). As a matter of fact, when grown in a confined environment between two polymer-coated slides, the TCB

crystals grow in the form of large extended platelets with extended (100) facets onto which epitaxy of P3HT occurs. Crystallization of TCB is supposed to start at the colder upper PTFE-coated glass surface (see Chapter 2). As the growth front advances horizontally, the TCB crystal fills in the gap to the lower PEDOT:PSS-coated slide, confining more and more the remaining liquid ternary mixture TCB/P3HT/CdSe. The fact that the first layer on the TCB is almost pure P3HT suggests that a certain concentration threshold must be reached before CdSe NCs become sequestered in the AIZs of the epitaxied P3HT layer. In other words, the bilayer structure can be understood as the consequence of the existence of two critical concentrations,  $c_{P3HT}^*$  and  $c_{CdSe}^*$  as illustrated in *Figure 2-7*. The progressive crystallization of TCB results in a change of the concentration at time  $t$  of the polymer and the NCs in the solution,  $c_{P3HT}(t)$  and  $c_{CdSe}(t)$  respectively. As TCB crystallizes, the overall concentration of both CdSe NCs and P3HT increase with time (see *Figure 2-7*). For  $c_{P3HT}(t) = c_{P3HT}^*$ , aggregation and crystallization of P3HT on the surface of TCB sets in. However, CdSe NCs remain in the liquid TCB solution, possibly because the solubility of CdSe NCs in TCB is higher than that of P3HT. In addition, the strong preferential epitaxial interaction between the TCB crystal surface and the P3HT chains certainly leads to an enrichment of the TCB crystal surface with P3HT. As the growth of the P3HT layer goes on, the concentration of the CdSe NCs in the remaining ternary mixture relatively to P3HT increases until it reaches a critical value  $c_{CdSe}^*$ . For  $c_{CdSe}(t) = c_{CdSe}^*$ , co-aggregation of P3HT and CdSe NCs starts. However, the enthalpic penalty associated with the inclusion of CdSe NCs in the crystalline zones of P3HT enforces the rejection of the nanoparticles into the amorphous interlamellar zones (AIZ) of P3HT. As a consequence, the second hybrid layer shows a nanostructured morphology with pure crystalline P3HT lamellae alternating with “doped” amorphous interlamellar zones. This growth scenario is further supported by the observation of an increasing thickness of the hybrid P3HT/CdSe layer comparatively to the pure P3HT layer when the relative ratio CdSe/P3HT increases. Indeed, when the relative concentration of NCs *vs.* polymer in solution increases, then the critical concentration  $c_{CdSe}^*$  is reached earlier during the growth process. This results in a larger relative thickness of the hybrid layer comparatively to the pure P3HT layer.

We have presented a complete morphological study of hybrid thin films prepared with P3HT and spherical CdSe nanocrystals. These films present a clearly defined nanostructure. In addition, TEM tomography revealed a peculiar bilayer structure in the volume of the films. In the following we were interested in the influence of the NCs shape on the nanostructuring and the orientation of the hybrid films prepared by slow-DEC as well as on the 3D distribution of the NCs within the film.

## 2.2. Case of Rod shaped NCs

### 2.2.1. Effect of the shape of the NCs on the morphology of the hybrid films

We were first interested in studying the effect of the nanocrystals shape on the nanostructuration of the hybrids films prepared by slow-DEC. Therefore, rod shaped nanocrystals with various aspect ratios were integrated into the hybrid films. *Figure 2-8* shows the TEM-BF images of hybrid P3HT: CdSe NCs prepared with spherical NCs, and rod shaped NCs of the two different sizes.

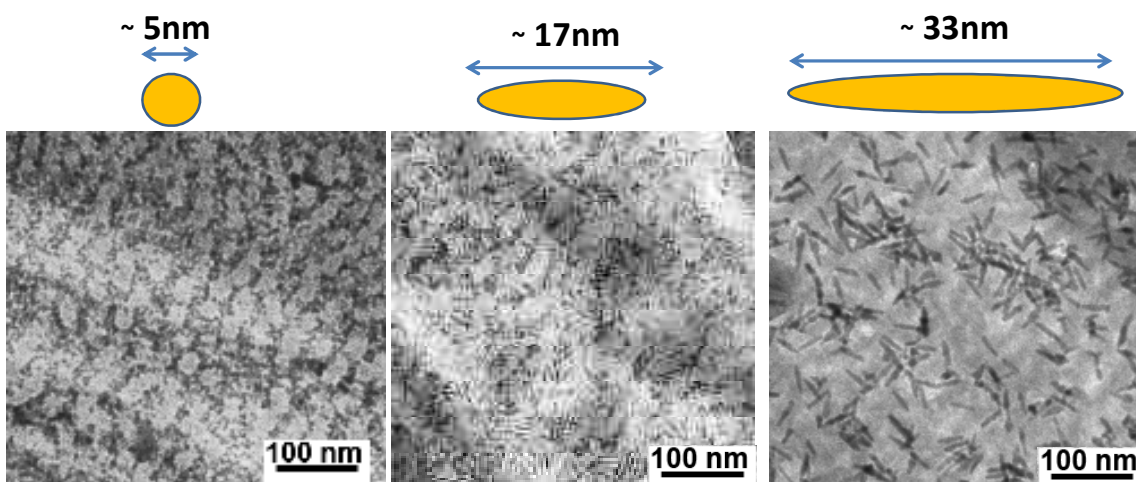


*Figure 2-8 Influence of the aspect ratio of the CdSe NCs on the morphology of the oriented and nanostructured hybrid thin films prepared by slow-DEC rate. The macromolecular parameters of the used P3HT are  $M_w = 17.6$  kDa and  $M_n = 13.4$  kDa.*

As seen in Chapter 4, the lamellar periodicity of a medium  $M_w$  P3HT ( $M_w = 17.6$  kDa) sample is of  $\sim 32$  nm (1 crystalline lamella + 1 amorphous interlamellar zone). In the crystalline lamellae, the average stem length was estimated from HR-TEM images to be  $\sim 13$  nm. This implies that in this case, the amorphous interlamellar zone (AIZ) is approximately  $\sim 19$  nm large. The choice of the size and aspect ratio of the CdSe NRs was done such that they are smaller and in a second case longer than the AIZ. Therefore short NRs (length 17 nm  $\times$  diameter 5 nm corresponding to an aspect ratio of 3.4) and long NRs (33 nm  $\times$  5 nm, aspect ratio 6.6) were incorporated in the films. A well defined nanostructuration is observed for the spherical and the short NRs, whereas the film prepared with longer NRs do not show any nanostructuration but rather suggests a surface decoration of the CdSe NRs onto the oriented P3HT thin film. A similar effect was previously observed (28). For the long rods, two points have to be mentioned: (i) The lamellar structure of the P3HT can be clearly seen in the TEM-BF image. Therefore, the lack of nanostructuration cannot be attributed to the absence of lamellar structure of the P3HT. (ii) There is no macrophase separation between the NRs and the P3HT, the absence of nanostructuration can thus not be ascribed to a lower solubility in TCB of the long NRs as compared to the nanospheres. These results show that the critical

parameter to consider is the length of the NRs compared to the thickness of the AIZ. The NRs with lengths longer than the latter cannot be embedded in the films.

In the following we were interested in the in-plane orientation of the hybrid films composed of P3HT and CdSe nanorods in various weight ratios.

### 2.2.2. *In-plane of the hybrids: effect of the weight ratio of the nanorods*

Whereas in the case of oriented films of pure P3HT, the question of the in-plane orientation only involves the in-plane orientation of the  $\mathbf{c}_{\text{P3HT}}$  axis (*i.e.* corresponding to the polymer chain axis), in the case of hybrids with rod shaped NCs, two different types of in-plane orientations can be considered: (i) The first one concerns the in-plane orientation of the P3HT polymer chains within the hybrid film and how it is affected by the presence of NCs. (ii) The second one concerns the orientation of rod shaped NCs compared to the average orientation of the polymer chains. However, with experimental techniques such as POM and UV-vis absorption, it is not possible to distinguish between the orientation of the entire film and the orientation of its components.

*Figure 2-9* shows the POM images of two hybrid thin films composed of P3HT and CdSe NR (17 nm x 5 nm) in a weight ratio 1:1 and 1:3 respectively. As already seen for the spherical particles, the POM images of the 1:1 sample indicate that the orientation degree should be similar to that obtained for a pure P3HT film. As seen in *Figure 2-9* the in-plane orientation of the hybrid thin films is significantly affected for blends with higher contents of CdSe NRs. In fact, whereas for a 1:1 wt% sample the extinction is almost perfect when the orientation axis  $\mathbf{c}_{\text{P3HT}}$  is parallel to one of the polarizers, many clear spots corresponding to non oriented or mis-oriented areas of the film can be seen for the 1:3 wt%, sample. At this point it is difficult to conclude about the origin of the degradation of the overall in-plane orientation of the film with increasing amount of NRs. There are essentially two possible reasons: (i) the orientation of the P3HT is affected by the presence of the CdSe NRs; (ii) the non oriented areas correspond to clusters of randomly oriented NRs. Most probably, the multitude of non oriented parts of the film can be explained by a combination of these two effects.

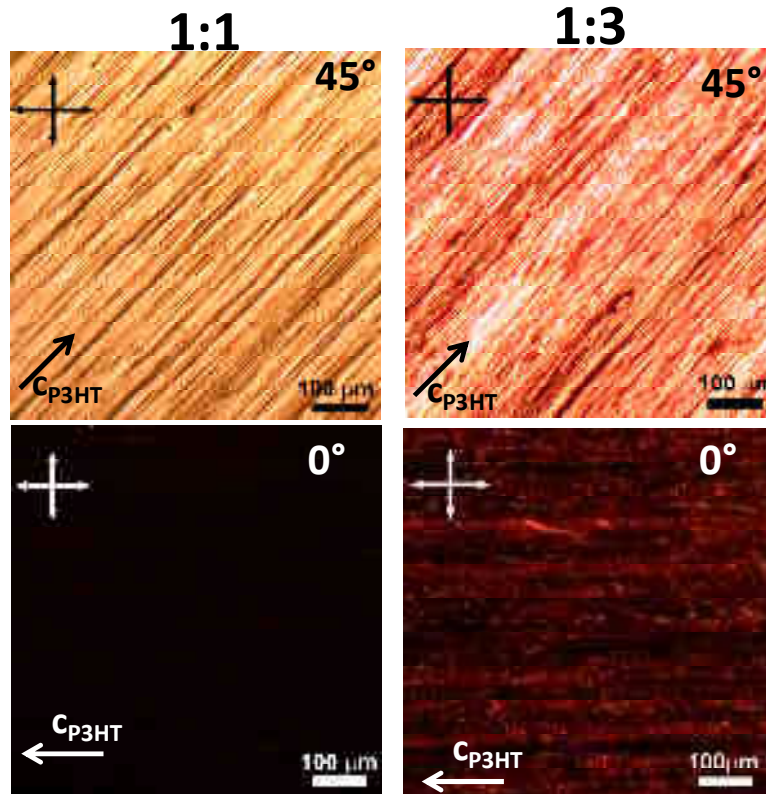


Figure 2-9 : POM images of oriented hybrid films composed of P3HT ( $M_w=17.6$  kDa) and CdSe NRs ( $17 \times 3$  nm) for weight ratios P3HT:CdSe of 1:1 (left images) and 1:3 (right).

To get further information about the degree of in-plane orientation of the P3HT and the CdSe NRs separately, and on the morphology of the hybrids, TEM-BF and ED measurement were performed.

### 2.2.3. Orientation of CdSe nanorods

Figure 2-10 shows typical TEM-BF images and the corresponding ED patterns of hybrid films composed of a medium  $M_w$  P3HT ( $M_w = 17.6$  kDa) and short CdSe NRs ( $17 \text{ nm} \times 5 \text{ nm}$ ) with compositions of 1:1, 1:2 and 1:3. From the TEM-BF images it can be seen that a good nanostructuration was obtained for all samples although for the 1:3 sample this is less obvious. A careful look on the TEM-BF images of the films shows that: (i) For the 1:1 sample, the majority of NRs are lying with their long axis flat-on the substrate. (ii) For the 1:2 sample, a population of “standing” NRs (with the long axis perpendicular to the substrate) can be clearly seen as dark round spots. (iii) For the 1:3 sample, it is difficult to identify lying rods partly because of the too high density of NRs. Another possibility is that for high ratios of NRs the latter tend to align more and more with their long axis perpendicular to the substrate (in the ideal case in a compact hexagonal structure) in order to fit into the space available in the AIZ of the polymer. However, this effect is not clear. Additional Tomographic analyses would be necessary to verify this point.

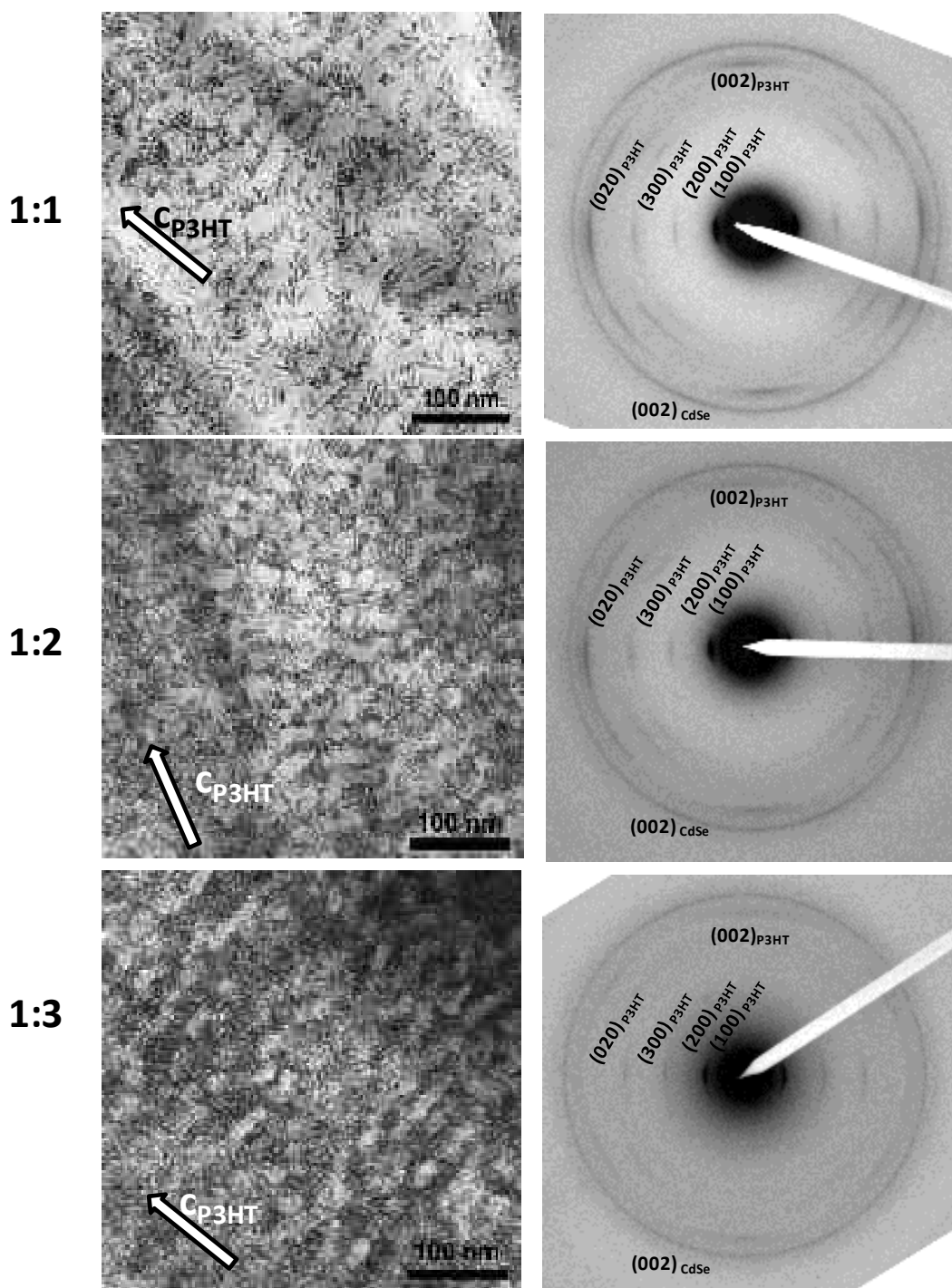


Figure 2-10 : Typical ED pattern and corresponding TEM BF-image of a oriented hybrid film composed of P3HT ( $M_w = 17.6\text{kDa}$ ) and CdSe NRs ( $17 \times 3\text{nm}$ ) with a ratio P3HT:CdSe 1:1 in wt %..

Regarding the ED patterns of the samples the reflections  $(100)_{\text{CdSe}}$  and  $(002)_{\text{CdSe}}$  from the CdSe NRs, show a continuous ring. This indicates that there is no preferential orientation of the CdSe NRs in the plane of the film. For samples with different ratios P3HT:CdSe (1:2 and 1:3 blends) the observations are the same *e.g.* a nanostructuration with an alternation of crystalline and amorphous lamellae of P3HT but a poor in-plane orientation of the NRs. This

is in contrast to the in-plane orientation of CdSe NRs reported by Brinkmann *et al.* for hybrids prepared by the initial DEC method on a Koeffler bench (28). This difference may be due to the fact that in the present case, the hybrids were prepared using a much slower growth rate as compared to the work of Brinkmann *et al.* Thus, the NRs have more time to reorient in all directions whereas in the original method, the orientation of the NRs parallel to the  $c_{P3HT}$  direction is possibly frozen-in during the fast crystallization of the P3HT. In addition, for the slow-DEC method, the extension of the crystalline lamellae is larger than for the DEC method on the Koeffler bench. Accordingly, the volume of the AIZ is reduced in the case of slow-DEC films, forcing the NRs to orient with their long axis normal to the substrate.

#### 2.2.4. **In-plane orientation of the P3HT**

In the ED patterns of all samples, the reflections coming from the P3HT are clearly defined. The ED patterns seen in *Figure 2-10* show on the equator both, the intense (h00) P3HT (h=1-3) and the strong (020) P3HT reflections. Along the meridian, the (002) P3HT reflection corresponding to the monomer repeat period long the chain direction is observed. The observation of the latter reflection is a fingerprint of the high crystalline order in the epitaxied layers. As already seen previously (see Chapter 4), epitaxied P3HT films have a fiber-like structure with  $c_{P3HT}$  as the fiber axis. The ED pattern confirms that in the case of hybrids, this fiber structure is maintained. In order to get a more quantitative insight on the degree of in-plane orientation of the films, the azimuthal angular distribution of the (100)<sub>P3HT</sub> reflection was extracted from the ED patterns. The evolution of the FWHM characterizing the distribution of the (100)<sub>P3HT</sub> reflection with increasing weight ratio of CdSe NRs is displayed in *Table 2-2*.

	<b>P3HT</b>	<b>1:1</b>	<b>1:2</b>	<b>1:3</b>
FWHM of azimuthal distribution of (100) <sub>P3HT</sub>	21°	22°	25°	25°

*Table 2-2: FWHMs of the azimuthal angular distribution of the (100) P3HT reflection as extracted from the ED patterns of samples with increasing ratio of NRs.*

As it could be inferred from the POM image, the in-plane orientation of the P3HT in the 1:1 sample is not affected by the presence of the NRs. With an increasing amount of NRs, the degree of in-plane orientation of the P3HT is slightly degraded although this effect is not significant. These results let suggest that the high amount of clear spots seen on the POM image are most presumably due to the clusters of non-oriented NRs. Such clusters can be seen in the TEM-BF image of the 1:3 sample.

In the following we were interested to investigate the 3D distribution of the rod shaped NCs in the bulk of the films by means of TEM tomography.

### 2.2.5. Tomographic analysis of samples with CdSe nanorods

The electron tomography analysis and the derived 3D volume reconstruction were also performed for hybrids prepared with as-synthesized CdSe nanorods of various aspect ratios and for different weight proportions. CdSe NRs with sizes that allow their good incorporation into the bulk of the oriented and nanostructured P3HT host matrix as discussed above were selected for those studies. In *Figure 2-11* we present one example of a hybrid material obtained with CdSe nanorods ( $11 \times 5$  nm corresponding to an aspect ratio of 2.2) for a P3HT/CdSe blend ratio of 1:1 (wt%). As seen for the spherical NCs (see *Figure 2-5*), the hybrid film presents a bilayer structure with a NRs-free layer of oriented P3HT and a hybrid nanostructured layer. A surface decoration CdSe NRs is also observed on the side of the film that was in contact with the TCB crystal during growth.

These results show that the growth mechanism of these hybrids is independent to a certain extent to the shape of the nanocrystals. For the rod shaped NCs, the growth mechanism seems to be the same than the one presented here above for the spherical NCs.

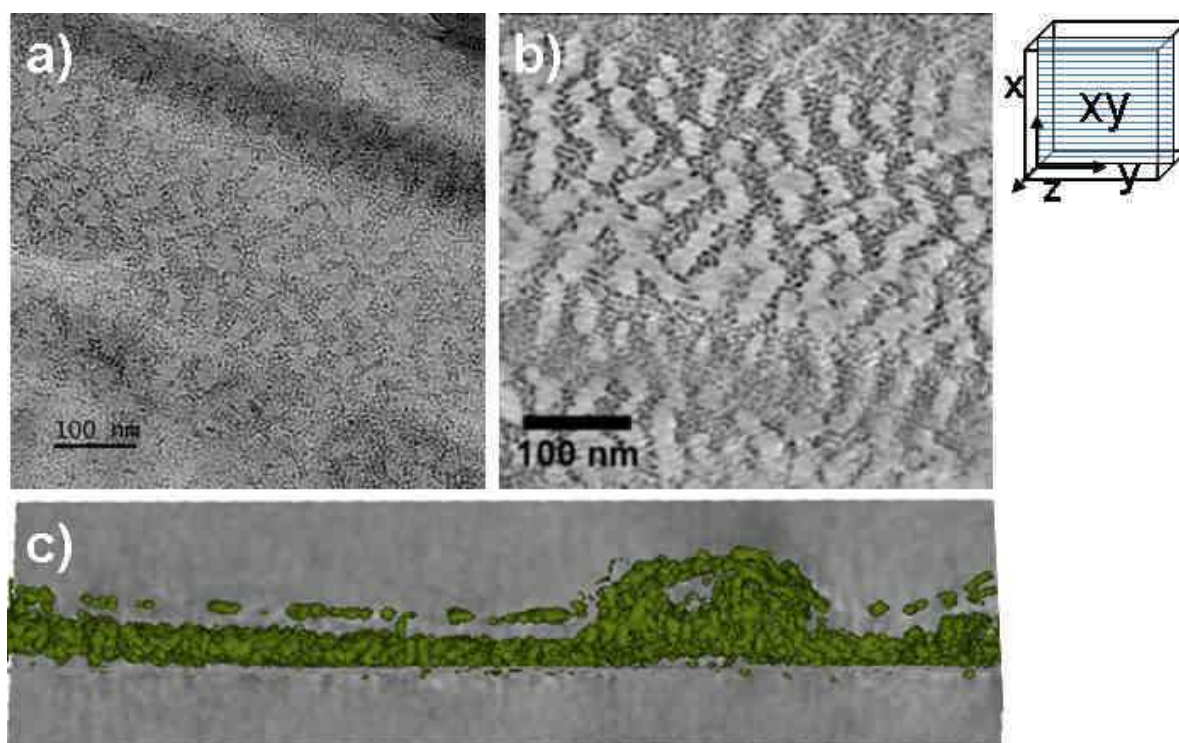


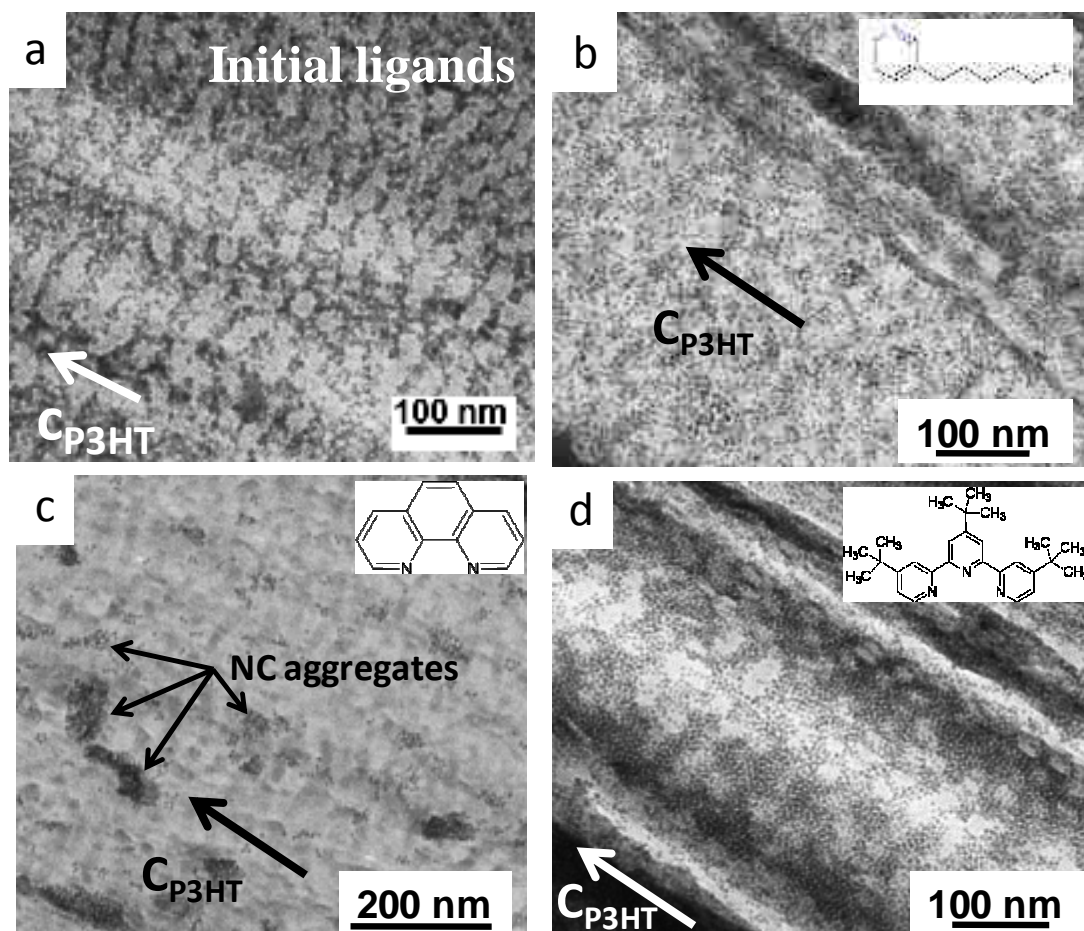
*Figure 2-11 : Tomographic analysis of a P3HT/CdSe hybrid film (1:1) prepared with as synthesized CdSe nanorods (11 nm  $\times$  5 nm). **a**) Typical TEM-BF image from the tilt series used to calculate the volume of the hybrid film. **b**) Example of a longitudinal slice extracted from the reconstructed volume. **c**) Transversal slice extracted from the 3D modelling of the hybrid with the CdSe nanorods (in green) which provides the distribution of CdSe NRs in the bulk of the film. As with the spherical NCs, the hybrid clearly presents a bilayer structure with a top layer corresponding to surface decoration with CdSe NRs (side of the film which was in contact with the TCB crystal).*

We have presented a structural and morphological study of hybrid thin films made of P3HT and CdSe NCs capped with their synthesis ligands. In the following we were interested in the study of hybrids made of P3HT and surface functionalized CdSe nanocrystals. In this study we focussed on spherical NCs only.

### **3. Effect of the surface functionalization of the CdSe NCs on the morphology of the oriented hybrid films**

As mentioned previously in Chapter 2, CdSe NCs are composed by an inorganic core which is surrounded by a layer of organic molecules called ligands or surfactants. These ligands ensure the colloidal stability of the CdSe NCs and avoid their aggregation. However, the ligands used for the synthesis of the NCs, form an insulating barrier which is very defavourable for electronic applications. Following this, we studied the functionalization of CdSe NCs with various polypyridines as capping ligands (see Chapter 2) and subsequently prepared hybrid oriented thin films by slow-DEC. To study the influence of the capping ligands on the thin films morphology, spherical NCs of batch 1 were used.

The NCs surface functionalization with polypyridine ligands and the characterization of the functionalization experiments have already been described in Chapter 2. In this section, we present the influence of the chemical nature of the capping polypyridine ligands on the nanomorphology of the hybrid films. More precisely, the aim of this study was twofold. First, we wished to understand if the presence of the polypyridine ligands in the P3HT/TCB mixture does disturb the directional epitaxial crystallization of P3HT into a lamellar structure. In fact, Brinkmann *et al.* have previously observed that the presence of pyridine changes significantly the morphology of P3HT when processed using the DEC method and gives rise to the formation of so-called shish-kebab fibers and not to thin films as expected (46). Therefore pyridine is not appropriate as a capping ligand of NCs to obtain oriented hybrid thin films by DEC. The second goal of this study was to understand which conditions the “new” ligands have to fulfill in order to generate nicely nanostructured and oriented hybrid films.



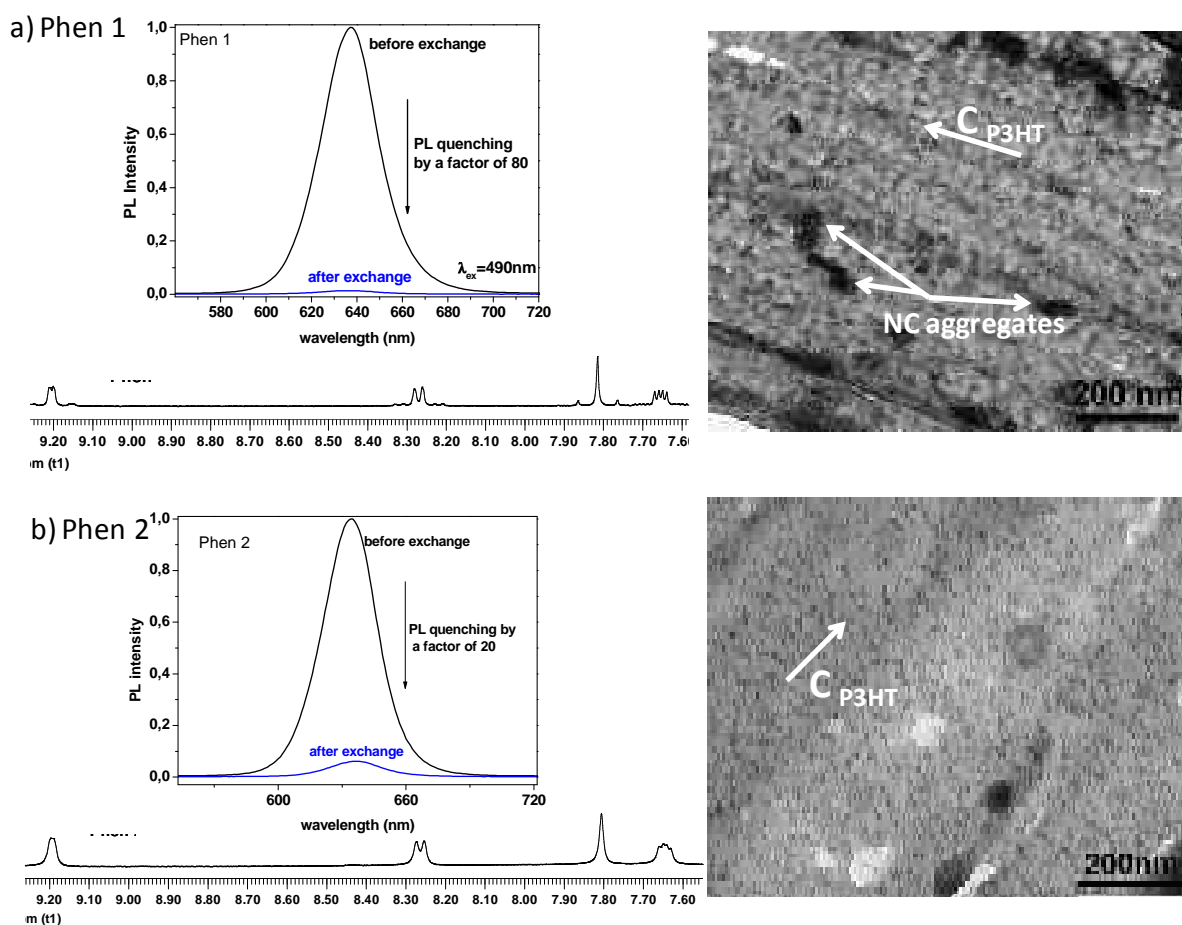
*Figure 3-1 : Influence of the capping ligands of the CdSe nanocrystals on the morphology of hybrid thin films grown by slow-DEC. (a): hybrid thin film prepared with as-synthesized CdSe NCs ; (b): hybrid thin film prepared with CdSe NCs capped with 3-n-hexylpyridine (HexPy); (c):1-10 phenanthroline (Phen); (d): 4,4',4''-Tri-tert-Butyl-2,2':6',2''-terpyridine (TerPy). For more details about the surface functionalization of CdSe NCs with polypyridines, refer to Chapter 2.*

Figure 3-1 shows TEM-BF images of hybrid thin films where the NCs were functionalized with 3-n-hexylpyridine (HexPy), 1,10-phenanthroline (Phen) and 4,4',4''-tri-tert-butyl-2,2':6',2''-terpyridine (TerPy). None of these ligands disturbs the epitaxial crystallization of P3HT into a semi-crystalline film as was observed in the case of pyridine (46). As seen in Figure 3-1 it seems that NCs functionalized with fully conjugated ligands such as Phen tend to aggregate and produce a macrophase separation within the thin films. This aggregation can be probably attributed to strong  $\pi$ - $\pi$  stacking interactions of the Phen ligands capped on two adjacent nanocrystals. In contrast to this, NCs capped with ligands having solubilizing alkyl groups such as the HexPy and TerPy give hybrids with nanostructuring similar to the one observed as-synthesized NCs. However these results must be analyzed with care as the ligand exchange rate is very difficult to estimate and we cannot be sure that in all cases this rate of exchange was the same. A more extensive study would require that not only the chemical structure of the capping ligands but also the rate of exchange should be varied and the influence of both parameters on the morphology of the

obtained hybrids studied. The issues raised by the surface functionalization of NCs were discussed in details in Chapter 2.

An illustration of the importance of the exchange ratio of the NCs will be illustrated with 1-10 phenanthroline (Phen) as the capping ligand of the NCs. As seen in Chapter 2, a quantification and thus an exact determination of the ligand exchange ratio was not possible in this due to the fast exchange dynamics on the NMR time scale that did not allow to separate the NMR peaks corresponding to Phen molecules bound and unbound to the surface of the NCs. In order to get an idea about the reproducibility of the results regarding the aggregation of the NCs within the oriented films the same experiment was repeated twice in the case of Phen ligands.

Two different ligand exchange reactions with Phen were thus performed with CdSe NCs from batch 1, using each time the same protocol for the ligand exchange. They will hereafter be referred to as **Phen1** and **Phen2**. Both samples of exchanged NCs showed a PL quenching and a broadening of the NMR peaks in the aromatic region of chemical shifts (see *Figure 3-2*). The quenching of the PL was much stronger in the case of Phen1 (with a factor of 80) than for Phen 2 (quenching factor of 20). However, as discussed in Chapter 2, it is not possible to derive the ligand exchange ratio from PL quenching measurements. In addition these data were recorded after the washing procedure. As mentioned previously the washing procedure is necessary, but disturbs strongly the equilibrium and creates trap states by loss of ligands. What exactly happens on a NCs surface during the washing procedure is not controllable. This makes it very difficult to conclude from the PL quenching experiments on the exchange ratio after a washing procedure. Regarding the NMR spectra of Phen 1 and Phen 2, the broadening of the NMR peaks seems to be stronger in the case of Phen 2. This effect can originate either from a higher exchange ratio of Phen 2 compared to Phen 1, or alternatively from a more efficient washing for Phen 2 where a higher amount of unbound free Phen ligands was removed. Based on these combined informations, it is not possible to conclude about the rate of ligand exchange for Phen 1 and Phen 2. Both Phen 1 and Phen 2 samples were integrated into oriented nanostructured P3HT thin films grown by slow rate DEC. The morphology of these films was studied by TEM in bright field mode. Whereas the oriented hybrid film prepared with Phen1 NCs shows strong aggregation, Phen 2 NCs were perfectly integrated into the oriented nanostructured P3HT matrix. Contrarily to TOP, OA and SA, 1-10,phenanthroline does not have long alkyl chains. It is therefore expected to show less favourable interactions with P3HT. Thus, the aggregation of NCs in the hybrid films grown by slow-DEC using the Phen1 NCs could be explained by the higher ligand exchange rate compared to Phen2: there remain not enough of the original ligands (TOP, OA, SA) to allow an efficient incorporation of the NCs in the oriented P3HT matrix. In contrast to this, for Phen 2 the lower exchange rate allows a good dispersion of the NCs in the film.



*Figure 3-2: Illustration of the importance of the exchange rate for reproducible and comparative studies. Two different ligand exchanges using 1-10 phenanthroline (Phen) were performed with spherical CdSe NCs from batch 1 and hybrid P3HT:Phen-NCs oriented hybrid thin films were thereafter prepared in the same operating conditions. The PL quenching after exchange was measured as well as the NMR spectrum. In one case, the CdSe NCs aggregate whereas in the other case, a nice nanostructuration is observed.*

To summarize, the results presented in *Figure 3-2* point out that a quantitative characterization of the NCs surface chemistry after ligand exchange is the key point for the development of hybrid materials for flexible and large photovoltaics and electronics.

#### 4. Conclusion

The combination of different experimental characterization techniques allowed to fully characterize hybrid films prepared by slow-DEC with P3HT and CdSe spherical and rod-shaped nanoparticles. In a first attempt, NCs having their synthesis capping ligands were used. It was shown that the presence of NCs up to a ratio of 1:1 does not affect the crystallinity and the in-plane orientation of the P3HT as probed by XRD. Nevertheless, if the films are loaded with NCs with a P3HT:CdSe weight ratio of 1:3, both the in-plane orientation of the hybrid films and the lamellar structure are affected by the NCs.

TEM tomography measurements allowed to unravel the complex and unique 3D structure of the oriented thin films of P3HT/CdSe spherical nanocrystals grown by epitaxy using a zone melting geometry. Most importantly, the analysis of the three dimensional morphology of the films using electron tomography reveals that the thin films have a bilayer structure with a pure P3HT layer and an overcoating hybrid P3HT/CdSe layer. Both layers show a high degree of in-plane orientation of the P3HT chains as revealed by GIXD as well as an intrinsic nanostructuration related to the semi-crystalline structure of P3HT with alternation of crystalline lamellae and amorphous interlamellar zones harbouring the CdSe NCs. As a matter of fact, by changing the CdSe/P3HT ratio, it is further possible to tune the relative thickness of the pure P3HT and the P3HT/CdSe hybrid layer: the larger the ratio of CdSe in the films, the thicker the hybrid layer gets. Using the reconstructed volumes derived from the tomography analysis, a quantitative analysis was performed which allowed to derive parameters such as the density of NCs as a function of the z transversal position. This analysis shows that when increasing proportion of NCs, in addition to a thickening of the layer loaded with NCs, there is a “densification” of this layer with more CdSe NCs in the amorphous zones of the polymer. This is at variance with what is obtained for spin-coated layers of similar hybrids where NCs are rather uniformly distributed throughout the whole film thickness. Similar bilayer structures were also observed for hybrids prepared by slow-DEC with short CdSe nanorods. Based on all these results, a scenario for the epitaxial growth of the films was proposed to account for this peculiar bilayer structure of the P3HT/CdSe films. It is suggested that the bilayer structure of the films is a consequence of the different solubilities of the polymer and the nanoparticles in the crystallizable solvent.

Finally, the study of the morphology of hybrid thin films prepared with spherical NCs where the surface is functionalized with various polypyridine capping ligands revealed two points. First, the ligands studied did not affect the epitaxial crystallization of the P3HT at variance with what was previously observed with pyridine which led to the formation of shish-kebab P3HT fibers (46). Second, the chemical nature of the ligands plays an important role on the nanostructuration of the hybrid films. But even more important than the chemical nature of the ligands, is the rate of the ligand exchange, a parameter which for some ligands is difficult to derive quantitatively, as explained in Chapter 2.

- (1) Gomez-Romero, P. Hybrid organic-inorganic materials-in Search of synergic activity. *Advanced Materials* **2001**, *13*, 163-174.
- (2) Saunders, B. R.; Turner, M. L. Nanoparticle-polymer photovoltaic cells. *Advances in colloid and interface science* **2008**, *138*, 1-23.
- (3) Podsiadlo, P.; Kaushik, A. K.; Arruda, E. M.; Waas, A. M.; Shim, B. S.; Xu, J.; Nandivada, H.; Pumplin, B. G.; Lahann, J.; Ramamoorthy, A.; Kotov, N. a Ultrastrong and stiff layered polymer nanocomposites. *Science* **2007**, *318*, 80-3.
- (4) Huynh, W. U.; Dittmer, J. J.; Alivisatos, A. P. Hybrid nanorod-polymer solar cells. *Science* **2002**, *295*, 2425-7.
- (5) Huynh, W. U.; Dittmer, J. J.; Libby, W. C.; Whiting, G. L.; Alivisatos, A. P. Controlling the morphology of nanocrystal-polymer composites for solar cells. *Advanced Functional Materials* **2003**, *13*, 73-79.
- (6) Dayal, S.; Kopidakis, N.; Olson, D. C.; Ginley, D. S.; Rumbles, G. Photovoltaic devices with a low band gap polymer and CdSe nanostructures exceeding 3% efficiency. *Nano letters* **2010**, *10*, 239-42.
- (7) Borchert, H. Elementary processes and limiting factors in hybrid polymer/nanoparticle solar cells. *Energy & Environmental Science* **2010**, *3*, 1682.
- (8) Zhou, Y.; Eck, M.; Krüger, M. Bulk-heterojunction hybrid solar cells based on colloidal nanocrystals and conjugated polymers. *Energy & Environmental Science* **2010**, *3*, 1851.
- (9) Beek, W. J. E.; Wienk, M. M.; Janssen, R. a. J. Hybrid solar cells from regioregular polythiophene and ZnO nanoparticles. *Advanced Functional Materials* **2006**, *16*, 1112-1116.
- (10) Xu, T.; Qiao, Q. Conjugated polymer-inorganic semiconductor hybrid solar cells. *Energy & Environmental Science* **2011**, *4*, 2700.
- (11) Günes, S.; Neugebauer, H.; Sariciftci, N. S. Conjugated polymer-based organic solar cells. *Chemical reviews* **2007**, *107*, 1324-38.
- (12) Hindson, J. C.; Saghi, Z.; Hernandez-Garrido, J.-C.; Midgley, P. a; Greenham, N. C. Morphological study of nanoparticle-polymer solar cells using high-angle annular dark-field electron tomography. *Nano letters* **2011**, *11*, 904-9.
- (13) Martínez-Ferrero, E.; Albero, J.; Palomares, E. Materials, Nanomorphology, and Interfacial Charge Transfer Reactions in Quantum Dot/Polymer Solar Cell Devices. *The Journal of Physical Chemistry Letters* **2010**, *1*, 3039-3045.
- (14) Yang, X.; Loos, J. Toward high-performance polymer solar cells: the importance of morphology control. *Macromolecules* **2007**, *40*, 1353-1362.
- (15) Tomczak, N.; Janczewski, D.; Han, M.; Vancso, G. J. Designer polymer – quantum dot architectures. *Progress in Polymer Science* **2009**, *34*, 393-430.
- (16) Li, L.; Miesch, C.; Sudeep, P. K.; Balazs, A. C.; Emrick, T.; Russell, T. P.; Hayward, R. C. Kinetically trapped co-continuous polymer morphologies through intraphase gelation of nanoparticles. *Nano letters* **2011**, *11*, 1997-2003.
- (17) Gupta, S.; Zhang, Q.; Emrick, T.; Balazs, A. C.; Russell, T. P. Entropy-driven segregation of nanoparticles to cracks in multilayered composite polymer structures. *Nature Materials* **2006**, *5*, 229-233.

- (18) Zhang, Q.; Xu, T.; Butterfield, D.; Misner, M. J.; Ryu, D. Y.; Emrick, T.; Russell, T. P. Controlled placement of CdSe nanoparticles in diblock copolymer templates by electrophoretic deposition. *Nano letters* **2005**, *5*, 357-61.
- (19) Zhang, Q.; Gupta, S.; Emrick, T.; Russell, T. P. Surface-functionalized CdSe nanorods for assembly in diblock copolymer templates. *Journal of the American Chemical Society* **2006**, *128*, 3898-9.
- (20) Zou, S.; Hong, R.; Emrick, T.; Walker, G. C. Ordered CdSe nanoparticles within self-assembled block copolymer domains on surfaces. *Langmuir* **2007**, *23*, 1612-4.
- (21) Bokel, F. A.; Sudeep, P. K.; Pentzer, E.; Emrick, T.; Hayward, R. C. Assembly of poly(3-hexylthiophene)/CdSe hybrid nanowires by cocrystallization. *Macromolecules* **2011**, *44*, 1768-1770.
- (22) Fogg, D. E.; Radzilowski, L. H.; Dabbousi, B. O.; Schrock, R. R.; Thomas, E. L.; Bawendi, M. G. Fabrication of quantum dot-polymer composites□: semiconductor nanoclusters in dual-function polymer matrices with electron-transporting and cluster-passivating properties. *Macromolecules* **1997**, *30*, 8433-8439.
- (23) Fogg, D. E.; Radzilowski, L. H.; Blanski, R.; Schrock, R. R.; Thomas, E. L. Fabrication of quantum dot / polymer composites□: phosphine-functionalized block copolymers as passivating hosts for cadmium selenide nanoclusters. *Macromolecules* **1997**, *30*, 417-426.
- (24) Hashimoto, T.; Harada, M.; Sakamoto, N. Incorporation of metal nanoparticles into block copolymer nanodomains via in-situ reduction of metal ions in microdomain ppace. *Macromolecules* **1999**, *32*, 6867-6870.
- (25) Schweikart, A.; Pazos-Pérez, N.; Alvarez-Puebla, R. a.; Fery, A. Controlling inter-nanoparticle coupling by wrinkle-assisted assembly. *Soft Matter* **2011**, *7*, 4093.
- (26) Bockstaller, M. R.; Lapetnikov, Y.; Margel, S.; Thomas, E. L. Size-selective organization of enthalpic compatibilized nanocrystals in ternary block copolymer/particle mixtures. *Journal of the American Chemical Society* **2003**, *125*, 5276-7.
- (27) Bockstaller, M. R.; Mickiewicz, R. a.; Thomas, E. L. Block copolymer nanocomposites: perspectives for tailored functional materials. *Advanced Materials* **2005**, *17*, 1331-1349.
- (28) Brinkmann, M.; Aldakov, D.; Chandezon, F. Fabrication of oriented and periodic hybrid nanostructures of regioregular poly(3-hexylthiophene) and CdSe nanocrystals by directional epitaxial solidification. *Advanced Materials* **2007**, *19*, 3819-3823.
- (29) Jimison, L. H.; Toney, M. F.; McCulloch, I.; Heeney, M.; Salleo, A. Charge-transport anisotropy due to grain boundaries in directionally crystallized thin films of regioregular poly(3-hexylthiophene). *Advanced Materials* **2009**, *21*, 1568-1572.
- (30) O'Connor, B.; Kline, R. J.; Conrad, B. R.; Richter, L. J.; Gundlach, D.; Toney, M. F.; DeLongchamp, D. M. Anisotropic structure and charge transport in highly strain-aligned regioregular poly(3-hexylthiophene). *Advanced Functional Materials* **2011**, *21*, 3697-3705.
- (31) Ersen, O.; Werckmann, J.; Houllé, M.; Ledoux, M.-J.; Pham-Huu, C. 3D electron microscopy study of metal particles inside multiwalled carbon nanotubes. *Nano letters* **2007**, *7*, 1898-907.

- (32) Ersen, O.; Bégin, S.; Houllé, M.; Amadou, J.; Janowska, I.; Grenèche, J.-M.; Crucifix, C.; Pham-Huu, C. Microstructural investigation of magnetic CoFe<sub>2</sub>O<sub>4</sub> nanowires inside carbon nanotubes by electron tomography. *Nano letters* **2008**, *8*, 1033-40.
- (33) Friedrich, H.; Sietsma, J. R. a; de Jongh, P. E.; Verkleij, A. J.; de Jong, K. P. Measuring location, size, distribution, and loading of NiO crystallites in individual SBA-15 pores by electron tomography. *Journal of the American Chemical Society* **2007**, *129*, 10249-54.
- (34) Van-Bavel, S. S.; Sourty, E.; de With, G.; Loos, J. Three-dimensional nanoscale organization of bulk heterojunction polymer solar cells. *Nano letters* **2009**, *9*, 507-13.
- (35) Oosterhout, S. D.; Wienk, M. M.; van Bavel, S. S.; Thiedmann, R.; Koster, L. J. A.; Gilot, J.; Loos, J.; Schmidt, V.; Janssen, R. a J. The effect of three-dimensional morphology on the efficiency of hybrid polymer solar cells. *Nature materials* **2009**, *8*, 818-24.
- (36) Li, S.-S.; Chang, C.-P.; Lin, C.-C.; Lin, Y.-Y.; Chang, C.-H.; Yang, J.-R.; Chu, M.-W.; Chen, C.-W. Interplay of three-dimensional morphologies and photocarrier dynamics of polymer/TiO<sub>2</sub> bulk heterojunction solar cells. *Journal of the American Chemical Society* **2011**, *133*, 11614-20.
- (37) Sun, B.; Snaith, H. J.; Dhoot, A. S.; Westenhoff, S.; Greenham, N. C. Vertically segregated hybrid blends for photovoltaic devices with improved efficiency. *Journal of Applied Physics* **2005**, *97*, 014914.
- (38) Modestino, M. A.; Chan, E. R.; Hexemer, A.; Urban, J. J.; Segalman, R. A. Controlling nanorod self-assembly in polymer thin films. *Macromolecules* **2011**, *44*, 7364-7371.
- (39) Aldakov, D.; Jiu, T.; Zagorska, M.; de Bettignies, R.; Jouneau, P.-H.; Pron, A.; Chandezon, F. Hybrid nanocomposites of CdSe nanocrystals distributed in complexing thiophene-based copolymers. *Physical chemistry chemical physics* **2010**, *12*, 7497-505.
- (40) Brinkmann, M.; Wittmann, J.-C. Orientation of regioregular poly(3-hexylthiophene) by directional solidification: a simple method to reveal the semicrystalline structure of a conjugated polymer. *Advanced Materials* **2006**, *18*, 860-863.
- (41) Brinkmann, M.; Rannou, P. Effect of molecular weight on the structure and morphology of oriented thin films of regioregular poly(3-hexylthiophene) grown by directional epitaxial solidification. *Advanced Functional Materials* **2007**, *17*, 101-108.
- (42) Yu, D.; Wehrenberg, B. L.; Jha, P.; Ma, J.; Guyot-Sionnest, P. Electronic transport of n-type CdSe quantum dot films: Effect of film treatment. *Journal of Applied Physics* **2006**, *99*, 104315.
- (43) Vanmaekelbergh, D.; Liljeroth, P. Electron-conducting quantum dot solids: novel materials based on colloidal semiconductor nanocrystals. *Chemical Society reviews* **2005**, *34*, 299-312.
- (44) Krishnan, R. S.; Mackay, M. E.; Duxbury, P. M.; Pastor, A.; Hawker, C. J.; Van Horn, B.; Asokan, S.; Wong, M. S. Self-assembled multilayers of nanocomponents. *Nano letters* **2007**, *7*, 484-9.
- (45) Mackay, M. E.; Tuteja, A.; Duxbury, P. M.; Hawker, C. J.; Van Horn, B.; Guan, Z.; Chen, G.; Krishnan, R. S. General strategies for nanoparticle dispersion. *Science* **2006**, *311*, 1740-3.

- (46) Brinkmann, M.; Chandezon, F.; Pansu, R. B.; Julien-Rabant, C. Epitaxial growth of highly oriented fibers of semiconducting polymers with a Shish-Kebab-like superstructure. *Advanced Functional Materials* **2009**, *19*, 2759-2766.





## ***Chapter 7. Oriented hybrid thin films by mechanical rubbing***

*The controlled fabrication of oriented hybrid materials composed of P3HT and colloidal nanocrystals of CdSe where both the polymers as well as the NRs are aligned are of interest for ambipolar field transistors for example. The controlled orientation of the NRs is to date still difficult although in the last years many progress was made in this sense. Herein we applied mechanical rubbing to hybrid thin films. Upon rubbing, the NRs long axis as well as the P3HT backbone tend to align parallel to the rubbing direction. The thin films were characterized by the combination of TEM (BF, HR, ED), GIXD, and UV-vis spectroscopy. This allowed to draw a quite complete picture of the hybrid rubbed films in terms of morphology, in-plane orientation, and structure. The effect of the ratio of CdSe NRs in the polymer matrix on the orientation of the films was studied. It was found that with increasing amount of NRs the degree of in-plane orientation is degraded tending toward that of pure NR films. We could furthermore show using electron diffraction and HR-TEM that the orientation of the NRs is induced by the P3HT matrix.*



## 1. Orientation of Nanorods and hybrids: State of the art

As compared to nanospheres, rod-shaped nanoparticles are frequently reported to be more suited for device applications either for their better charge transport properties or for their polarized optical properties (1–3). For the efficient fabrication of working devices, the control of the orientation of the nanorods is essential. Therefore, the control of the orientation of the NRs in quantum dot solids either by self-assembly or by the application of external forces (electric, magnetic field) has recently gained a lot of interest (4–10). The final aim is to control perfectly the alignment of rod-shaped nanoparticles either with their long axis parallel to the substrate or perpendicular to the latter in devices. Perpendicular alignment of nanorods is of course quite appealing for photovoltaic devices and was realized by different methods such as controlled evaporation of the solvent or by means of an external electric field (11–15). Thin films of NRs with their long axis parallel to the substrate presenting a preferential in-plane orientation were obtained by mechanical rubbing of a thin film of NRs with a velvet cloth (16–19). Stretching of polymers such as polyethylene or poly(vinyl alcohol) containing rod shaped colloidal nanocrystals was reported to yield uniaxially aligned NRs within the stretched polymer matrix (18, 20–23). In this sense, rods of CdSe were used for polarizing diodes by aligning the rods in stretched ultrahigh molecular weight polyethylene (18). A method that is also frequently used for the orientation of nanorods and the fabrication of devices is the use of template patterns such as for example PDMS (24, 25). All these studies show that the control of the alignment of nanorods initially difficult, has steadily progressed during the last decade. As seen in the previous chapters and as reported in many studies, the orientation and the control of the morphology of conjugated polymers in particular P3HT starts also to be well mastered (26). Very frequently, in the case of hybrid materials made of conjugated polymers and NCs, either the organic or the inorganic phase is well oriented. Schierhorn *et al.* realized for example hybrid materials composed of vertically aligned NR between which P3HT was dispersed (27). Gupta *et al.* realized vertically aligned NR within a P3HT matrix by applying an electric field but the P3HT was not oriented (15). Snaith *et al.* reported hybrid films composed of oriented polyacrylate and non-oriented nanocrystals (28). However, to the best of our knowledge, much less is reported about hybrid systems composed of conjugated polymers and colloidal quantum dots where both the organic as well as the inorganic phase present a preferential orientation. In this sense, Brinkmann *et al.* reported the orientation of the long axis of CdSe NRs parallel to the  $\mathbf{c}_{\text{P3HT}}$  direction in thin films grown by DEC (29).

Herein we were interested in the fabrication of oriented hybrids composed of CdSe NRs and P3HT, where both the NRs as well as the P3HT possess a high degree of in-plane orientation. It will be shown that mechanical rubbing of hybrid thin films is an easy way for the fabrication of such hybrid thin films. Materials having these characteristics could be of interest for ambipolar transistors for example. However, our study was restricted on the morphological and structural aspects of such films and the used NRs were capped with their synthesis ligands, *i.e.* not optimized for charge transport.

In the following, a P3HT of medium-Mw ( $M_w=17.6$ ,  $M_n=13.4$ ,  $PDI=1.3$ ), and NRs of the dimensions  $20\text{ nm} \times 5\text{ nm}$  (aspect ratio of 4) were used. The procedure for the fabrication of hybrid oriented thin films by mechanical rubbing is analogous to the rubbing procedure of pure P3HT. The only difference is that instead of depositing a thin film of pure P3HT, a mixture of P3HT and CdSe NRs is deposited by the doctor blade method. For the experimental details (solvent mixture, concentration, etc.) as well as for the rubbing procedure see Chapter 5 and Annexe 3. For optical measurements, the thin films were deposited on clean glass slides whereas for the X-ray diffraction measurements the films were deposited on Si(100) wafers. Our study focuses on the study of hybrid thin films with various blend ratios P3HT:CdSe and rubbed with a maximum of rubbing steps before scratching of the film occurs. Note that in the case of hybrids scratching occurs more easily than in the case of pure P3HT films due to the mechanical inhomogeneity of the films. In the following, the relative composition of the films will be given in wt % as follows P3HT:CdSe X:Y.

In a first attempt, we were interested in the study of a thin film of pure CdSe NRs by mechanical rubbing with particular interest on the in-plane orientation and morphology of such films. In a second step of the study, a hybrid thin film composed of P3HT and CdSe NRs with a ratio of P3HT:CdSe 1:1 in wt% was studied before and after the rubbing process. Finally we were interested in hybrid thin films with increasing ratio of CdSe NRs. Samples of different ratios of P3HT: CdSe in wt% (2:1, 1:1, 1:2, 1:3) were prepared. Our main interest was to understand the influence of the amount of CdSe NRs in the polymer matrix on the in-plane orientation that can be achieved in such films. We were also interested in the UV-vis absorption of hybrid rubbed thin films oriented by rubbing. And at last, we present a comparative study of hybrid materials fabricated by the slow-DEC method and those prepared by mechanical rubbing.

## **2. Effect of rubbing on thin films of NRs**

First of all, we studied the effect of rubbing on a thin film of pure NRs. Besides studying the effect of rubbing on the orientation of the NRs, this allowed us to identify the reflections of the CdSe NRs in the electron diffraction patterns and to ensure that in the initial thin films, the NRs are well dispersed. Although it has been previously reported that mechanical rubbing with a velvet cloth induces uniaxial alignment of the nanorods with their long axis parallel to the rubbing direction  $\mathbf{R}$  (16–19), in our case this alignment was observed only locally and not over the entire surface of the thin film. *Figure 2-1* shows the TEM-BF images, the corresponding ED patterns as well as line sections of the ED patterns of two representative areas of a rubbed thin film of NRs. The orientation is far from being isotropic over the entire sample surface. Two types of areas can be distinguished. In a first type, the NRs are oriented by the rubbing process as it can be directly seen from the TEM-BF image. This is further confirmed by the ED pattern where the  $(002)_{\text{CdSe}}$  reflection (corresponding to the direction parallel to the long axis of the NRs) as well as the  $(100)_{\text{CdSe}}$  and  $(101)_{\text{CdSe}}$

reflections are clearly arced. A second type of area shows a poor degree of in-plane orientation of the NRs.

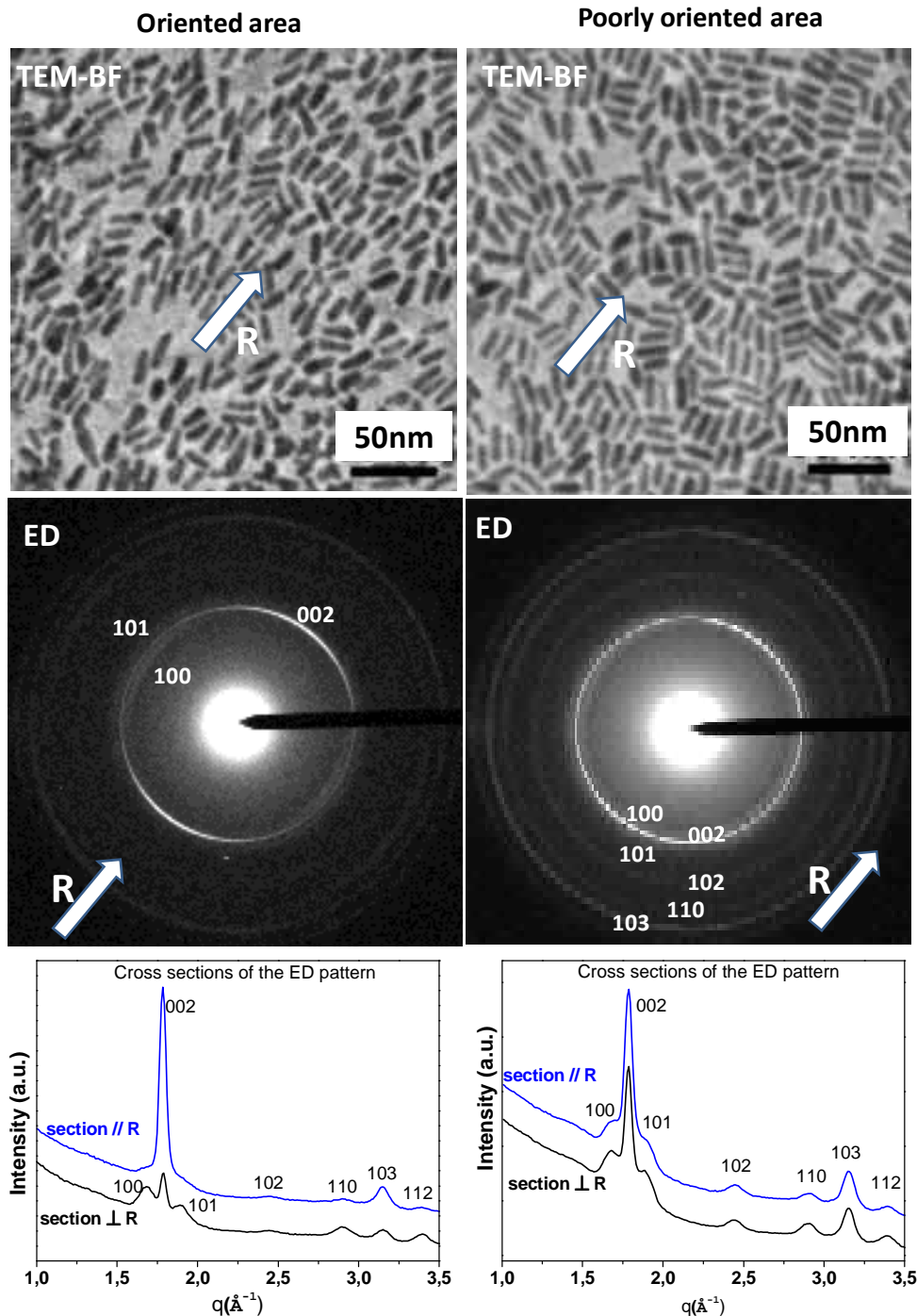


Figure 2-1: (*top*) TEM-BF images and (*middle*) corresponding ED patterns of two representative areas of the sample (one oriented and one poorly oriented area). (*bottom*) section profiles of the ED patterns in the direction // and  $\perp$  to the direction of rubbing indicated by the arrow indexed with R.

This can be seen from the TEM-BF and from the ED pattern where the  $(002)_{\text{CdSe}}$ , the  $(100)_{\text{CdSe}}$  and  $(101)_{\text{CdSe}}$  appear as a continuous rings with only slight intensity reinforcements. We found a FWHM=  $46^\circ$  for the azimuthal distribution of the  $(002)_{\text{CdSe}}$  reflection in the

oriented areas of the sample. Breiby *et al.* reported distributions of the in-plane orientation in rubbed films of CdSe NRS of FWHM=52° over an area in the range of ≈ mm<sup>2</sup>.

However, our aim was not the elaboration of highly oriented thin films of NRs, but we are seeking for highly oriented hybrid thin films composed of P3HT and CdSe NRs. Therefore the rubbing of the NRs films served mainly for the identification of the reflections in the ED patterns of the NR. *Table 2-1* summarizes the  $d_{hkl}$  values that were extracted from the ED patterns and for means of comparison, the values calculated for the wurtzite structure of CdSe are displayed.

Crystal planes	$d_{hkl}$ (Å) from ED	$d_{hkl}$ (Å) from Cerius
100	3.74	3.72
002	3.51	3.51
101	3.34	3.29
102	2.56	2.55
110	2.17	2.15
103	2.00	1.98
112	1.85	1.86

*Table 2-1 :  $d_{hkl}$  values of the CdSe NRs as determined from the ED pattern and calculated  $d_{hkl}$  values for the wurtzite structure of CdSe*

Further improvement of the method regarding thin films of NRs alone may result in thin films that are homogeneously aligned over the entire film surface (several cm<sup>2</sup>). In fact, herein we did not adapt the process to the NRs system and we simply applied the same experimental protocol as for P3HT films. The treatment of the glass slide for a better adherence of the NR could bring improvements. Breiby *et al.* and Chin *et al.* used for example PEDOT:PSS coated glass (16, 17).

In the following sections we focused on the effect of the blend composition on the morphology and structure of hybrid rubbed films.

### **3. Rubbed hybrid thin films: morphology, structure, orientation**

#### **3.1. Case of the as deposited film (not rubbed R0)**

Being the starting point of all further experiments, the characterisation of the hybrid thin films in terms of morphology and structure before the rubbing process is essential. Therefore, TEM and GIXD measurements were performed on an as deposited thin film of P3HT:CdSe 1:1 in wt%. In *Figure 3-1* the TEM-BF image, the corresponding ED pattern as well as a 2D GIXD map are displayed. The scattering configurations for the 2D GIXD measurements are the same as described in the previous chapters.

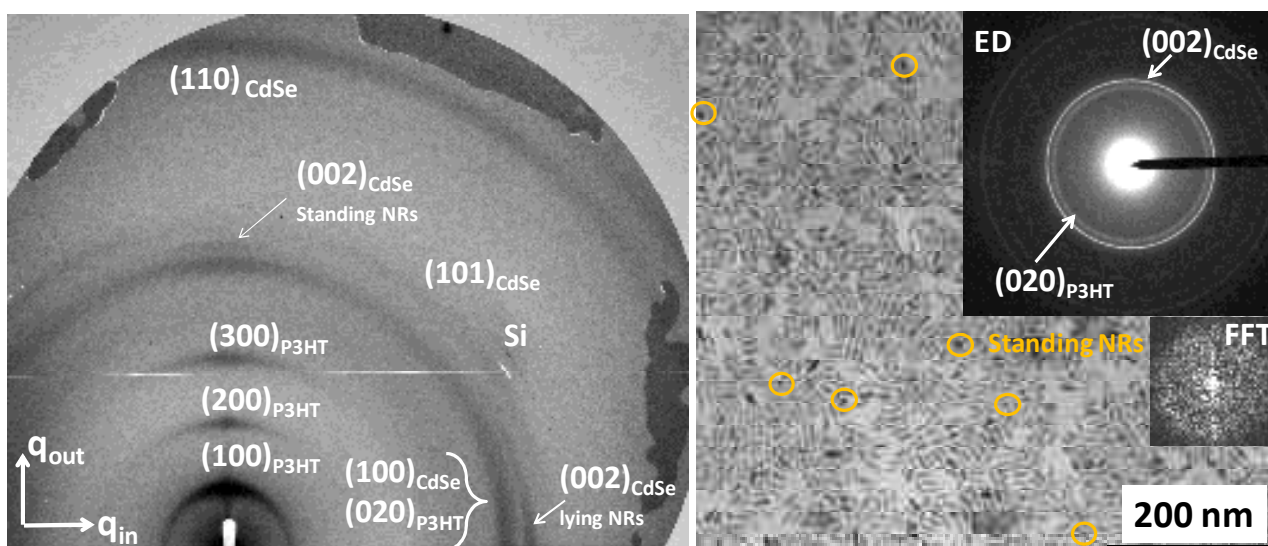


Figure 3-1: (left) 2D GIXD map (right) TEM-BF and corresponding ED pattern of an as deposited hybrid thin film with a composition of P3HT:CdSe 1:1 in wt%. The inset shows the FFT of the TEM-BF image. The yellow circles evidence some standing rods (with their long axis perpendicular to the plane of underlying substrate).

**Orientation of the NRs:** From the TEM-BF image, it can be clearly seen that the NRs are well dispersed and not aggregated. As expected, it appears clearly that the NRs are oriented in majority with their long axis parallel to the substrate although some standing rods can be distinguished. In most reported works on hybrid materials, the NRs are lying flat on the substrate (2, 29). For a majority of standing NRs, generally special processing conditions are necessary (11, 14). As seen from the TEM-BF image, before rubbing no preferential in-plane orientation of the long axis of these NRs can be identified. This is further supported by the ED pattern where the  $(002)_{\text{CdSe}}$  reflection of the NRs is clearly observed as a continuous arc. The 2D GIXD map gives further support about the orientation of the rods parallel to the substrate as the  $(002)_{\text{CdSe}}$  appears essentially in the in-plane ( $\mathbf{q}_{\text{in}}$ ) direction.

**Orientation of the P3HT:** the 2D GIXD map shows the  $(h00)_{\text{P3HT}}$  reflections of the P3HT mainly in the  $\mathbf{q}_{\text{out}}$  direction although some much weaker in-plane contribution can be distinguished. This is the fingerprint of a preferential “edge-on” orientation of the P3HT with a small amount of powder-like distributed domains. This is identical to what was seen in **R0** films of pure P3HT (see Chapter 5). The ED pattern showing the  $\pi$ -stacking  $(020)$  reflection of the P3HT as a continuous ring indicates that there is no preferential in-plane orientation of the crystalline P3HT domains.

To summarize, before the rubbing process, the hybrid films present a preferential “edge-on” orientation of the P3HT crystalline domains whereas NRs lie preferentially with  $\mathbf{c}_{\text{CdSe}}$  in the plane of the substrate (see schematic in Figure 3-2). Neither the P3HT nor the NRs have any preferential in-plane orientation. In the following, we will study the influence of mechanical rubbing on the morphology and the orientation of such a hybrid thin film.

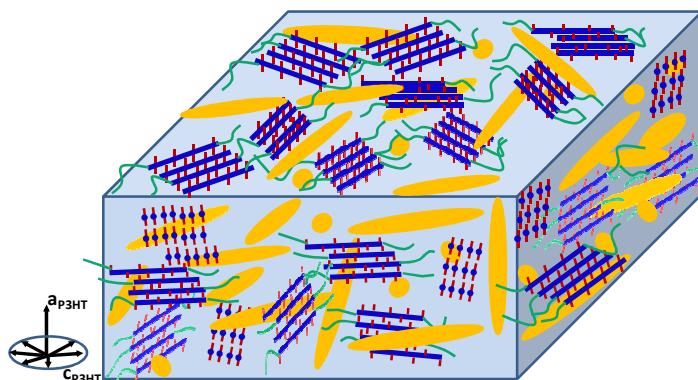


Figure 3-2 : Schematic illustration of the hybrid film before rubbing. The P3HT has a preferential “edge-on” orientation. The CdSe NRs are preferentially oriented flat-on but some standing NRs can be observed.

### 3.2. Structure and morphology of hybrid thin films after rubbing

In contrast to most reported works on the alignment of nanorods by mechanical rubbing (16–18), we were mainly interested in the fabrication of hybrid thin films where the NR as well as the polymer (P3HT) show a high degree of in-plane orientation. Such oriented hybrid materials are of interest for ambipolar field effect transistors for example. The effect of an increasing number of rubbing cycles on the alignment of pure P3HT thin films was discussed in detail in a previous chapter (see chapter 5). It was shown that rubbing of P3HT results in (i) an alignment of the  $c_{P3HT}$  direction parallel to the rubbing direction. (ii) the orientation of the crystalline domains changes from a preferential “edge-on” orientation before rubbing, to a preferential “flat-on” orientation after rubbing. Herein we will show, that mechanical rubbing is not only suited for the preparation of highly oriented pure P3HT thin films as shown in Chapter 5 or for the fabrication of oriented thin films of nanorods as reported in the literature rubbing (16–18). In fact, rubbing allows for the fabrication of highly oriented hybrid thin films composed of P3HT and CdSe nanorods where both components are aligned parallel to the rubbing direction, and this on large areas in a quite simple and fast process.

In a first attempt, we investigate the effect of rubbing on the orientation, morphology and the structure of a hybrid sample having the composition 1:1. In a second step, the effect of an increasing amount of NRs in the films will be studied. Therefore samples of following compositions will be studied: 1:1 1:2 and 1:3

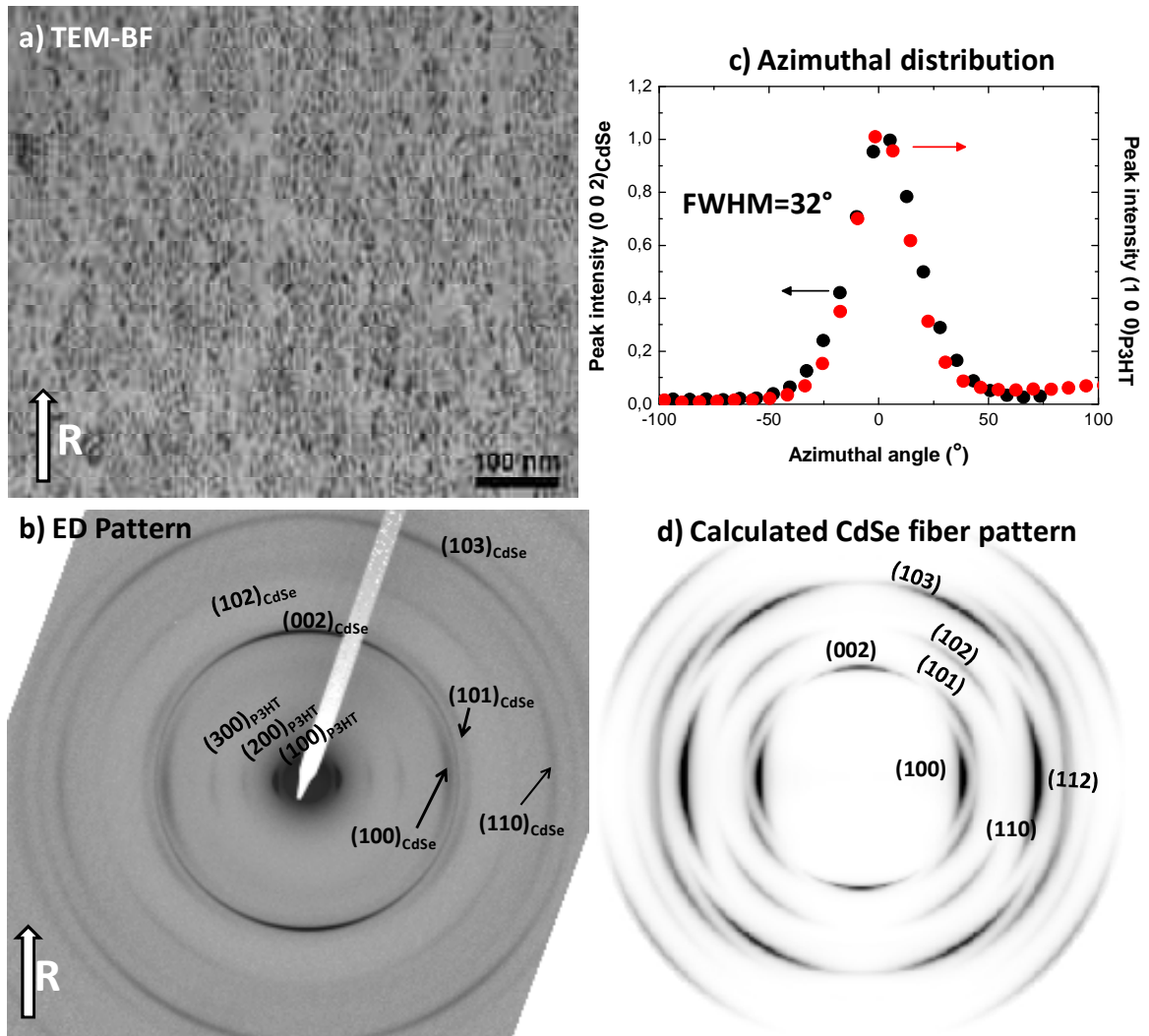


Figure 3-3: (a) TEM-BF image of a rubbed sample with a composition 1:1 and (b) corresponding ED pattern. (c) azimuthal angle distribution as determined from the ED pattern of the  $(100)_{P3HT}$  and the  $(002)_{CdSe}$  reflections. (d) Calculated fiber pattern of CdSe for an azimuthal in-plane distribution characterized by a FWHM~15°.

Figure 3-3 a and b, shows the TEM-BF image of a rubbed 1:1 hybrid thin film and the corresponding ED pattern. A simulated diffraction pattern of a CdSe fiber is also displayed. It was obtained by taking into account the dimensions of the CdSe NRs and an in-plane distribution of the fiber axis characterised by a FWHM=15°. In contrast to the pure rubbed NRs, in the case of hybrids the orientation of the NRs with the long axis parallel to the rubbing direction is much more pronounced. This orientation is uniform and could be observed over the entire sample surface. Although from the TEM-BF it can be unambiguously concluded that the rubbing induced an orientation of the NRs, no conclusions can be made about the orientation of the level of orientation of the P3HT as it cannot be clearly seen in the TEM image. It is also difficult to quantify the degree of in-plane orientation of the rods from such a BF-image. Therefore diffraction measurements were performed.

The ED pattern shows clearly the reflections of the P3HT and the NRs indicating that there is no macrophase separation between the two after the rubbing process. On the meridian

of the ED pattern, an arced reflection corresponding to the  $(002)_{\text{CdSe}}$  reflection can be observed. On the equator, a multitude of reflections is present coming from both, P3HT and from the NRs. The  $(h00)_{\text{P3HT}}$  reflections are clearly seen, as well as the broad  $(100)_{\text{CdSe}}$  and  $(101)_{\text{CdSe}}$  reflections. From this ED pattern, it can thus be concluded that both, the CdSe NRs as well as the P3HT show a preferential in-plane orientation with the  $\mathbf{c}_{\text{P3HT}}$  and  $\mathbf{c}_{\text{CdSe}}$  axis parallel to the direction of rubbing  $\mathbf{R}$ . The presence of the  $(h00)_{\text{P3HT}}$  reflections and the absence of the  $\pi$ -stacking reflection of the P3HT, indicates that the crystalline domains of the P3HT flipped from the “edge-on” to the “flat-on” orientation as upon rubbing of pure P3HT layers.

Comparing the ED pattern of the NRs to a simulated fiber pattern of CdSe with as fiber axis the long axis of the NRs ( $[001]$  direction), shows significant differences in terms of relative intensities of the reflections. In the case of the simulated fiber of CdSe, the  $(100)$  and the  $(103)$  reflections are unambiguously the most intense reflections. In contrast to this, on the experimental ED patterns it is clearly the  $(002)$  reflection which is the most intense. A possible explanation for these differences can be that the CdSe NRs have preferential contact planes and do not show a pure fiber symmetry. This could be further supported by the TEM BF image. In fact, the differences in contrast of different NRs are due in part to different orientations of the rods long axis ( $\mathbf{c}_{\text{CdSe}}$ ). The majority of the rods appear with low contrast and have probably the same or an equivalent contact plane. Breiby *et al.* also reported preferential contact planes of the NRs on a PEDOT:PSS coated glass slide after rubbing (16). Indeed, Breiby *et al.* reported a preferential alignment of  $\mathbf{c}_{\text{CdSe}}//\mathbf{R}$  and the a-c (or, equivalently, b-c) plane parallel to the sample surface plane.

In order to get a more accurate view on the degree of the in-plane orientation of the P3HT as well as of the CdSe NRs, the azimuthal distribution of the crystalline P3HT domains and the CdSe NRs was deduced from the intensity distributions of the  $(100)_{\text{P3HT}}$  as well as of the  $(002)_{\text{CdSe}}$  diffraction peaks in the ED patterns.

The corresponding azimuthal intensity profiles are shown in Figure 3-3c. interestingly, there is an almost perfect matching between both azimuthal distributions; both display a FWHM $\sim 32^\circ$ . The point that both, the organic and the inorganic phase have a so closely related in-plane distribution is noticeable and suggests that the polymer matrix enforces the orientation of the CdSe NRs. Further support for this idea will be given later. In order to get a view on the degree of the out-of plane orientation of the rods as well as on the degree of orientation of the sample on the  $\text{cm}^2$  scale, GIXD measurements were performed.

### 3.2.1. Comparison of the in-plane and out-of plane distribution of the NRs

Figure 3-4 shows the GIXD map of the hybrid thin film for different angles of  $\Omega$ .  $\Omega=0^\circ$  corresponds to the position where the scattering vector  $\mathbf{q}\perp\mathbf{R}$ .  $\Omega=90^\circ$  corresponds to the position where the scattering vector  $\mathbf{q}//\mathbf{R}$ . Figure 3-5 shows the linear GIXD scans in the

in-plane configuration of two hybrid thin films with different contents in NRs and corresponding  $\Omega$  rocking curves around the  $(002)_{\text{CdSe}}$  reflection. For the sake of clarity, in the following we will describe the structure of the P3HT and the NRs separately.

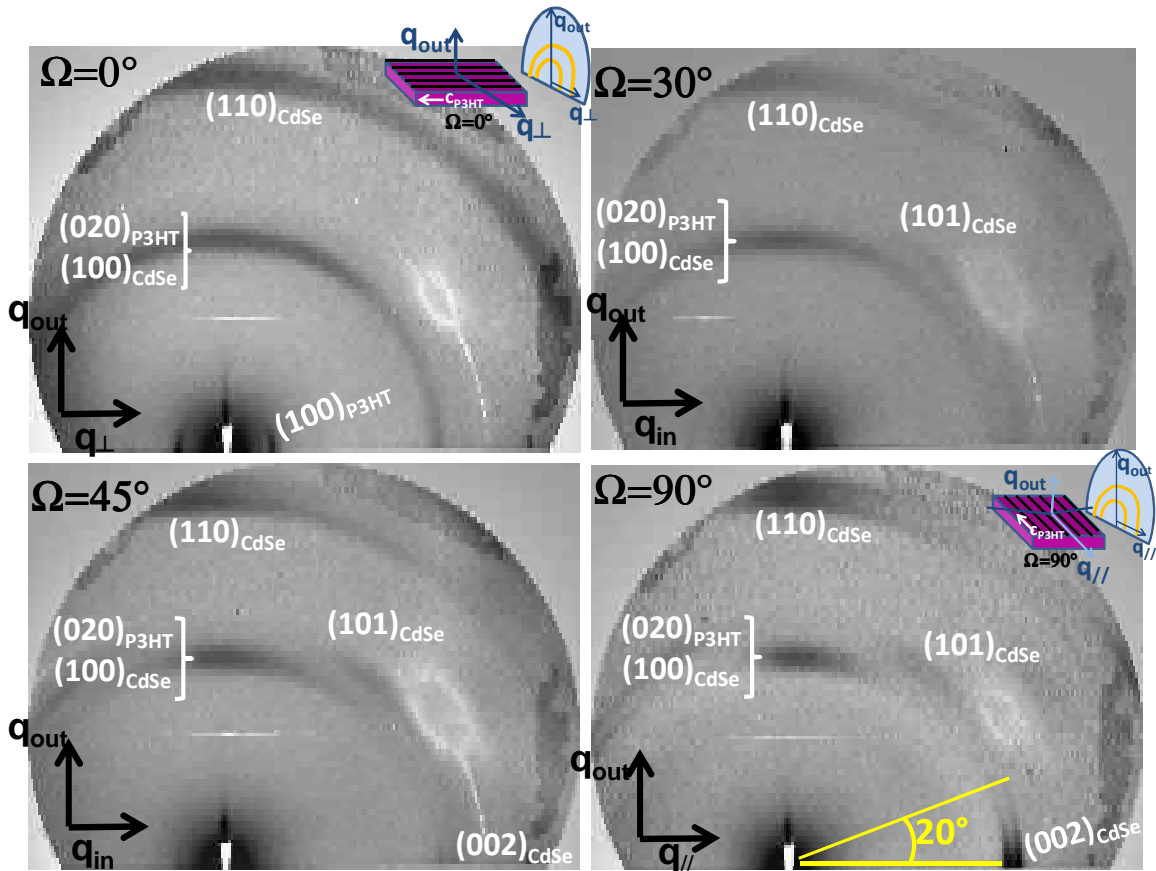


Figure 3-4 : 2D GIXD of a rubbed hybrid sample with a composition of 1:1. The pattern was recorded for different positions of the sample.  $\Omega=0$  corresponds to the configuration where the scattering vector  $\mathbf{q} \perp \mathbf{R}$  and  $\Omega=90$  corresponds to  $\mathbf{q} // \mathbf{R}$ .

**P3HT:** The behaviour of the P3HT in the hybrid thin films upon rubbing is very similar to the behaviour of pure P3HT rubbed layers. Regarding the 2D GIXD maps (Figure 3-4) for  $\Omega=0^\circ$ , the  $(h00)_{\text{P3HT}}$  reflections can be clearly seen in the  $\mathbf{q}_\perp$  direction and the  $(020)_{\text{P3HT}}$  reflection which is overlapping with reflections coming from the CdSe can be seen in the  $\mathbf{q}_{\text{out}}$  direction. For  $\Omega=90^\circ$ , only the  $\pi$ -stacking reflection which is overlapping with the  $(100)_{\text{CdSe}}$  can be seen in the  $\mathbf{q}_{\text{out}}$  direction. This indicates clearly that in the case of hybrids, as for pure P3HT the orientation of the crystalline domains flips from a preferential “edge-on” to a preferential “flat-on” orientation. Regarding the linear scans (Figure 3-5), for the configuration  $\mathbf{q}_\perp \mathbf{R}$ , the  $(h00)_{\text{P3HT}}$  reflections as well as the  $(020)_{\text{P3HT}}$  reflection are well defined whereas in the configuration  $\mathbf{q} // \mathbf{R}$ , no reflection coming from the P3HT can be distinguished. This confirms once again the very good orientation of the  $\mathbf{c}_{\text{P3HT}}$  direction parallel to the rubbing direction  $\mathbf{R}$ .

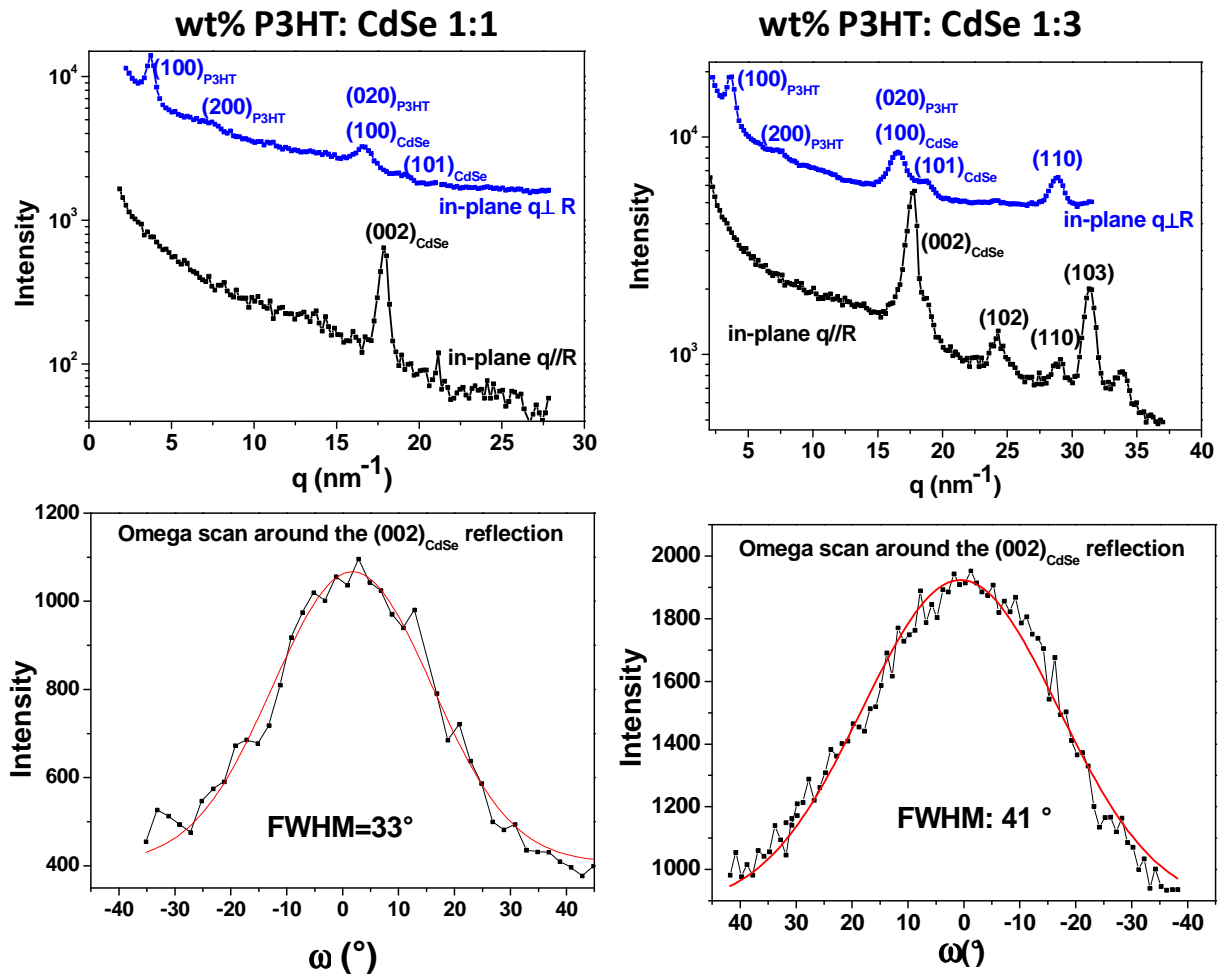


Figure 3-5 : (top) GIXD linear scans of two rubbed hybrid films with different amounts of NRs (wt% P3HT: CdSe 1:1 and 1:3). (bottom) corresponding  $\Omega$ -scans around the  $(002)_{\text{CdSe}}$  reflection.

**CdSe NRs:** The 2D GIXD map (Figure 3-4) for  $\Omega=0^\circ$  a relatively large and fuzzy arced reflection that can be attributed to an overlap of the  $(100)_{\text{CdSe}}$  and the  $(020)_{\text{P3HT}}$  reflections. The reinforcement of this reflection in the  $\mathbf{q}_{\text{out}}$  direction can be probably explained by the overlap of the  $(020)_{\text{P3HT}}$  line showing preferential orientation. Alternatively, it may suggest the preferential orientation of the  $(100)_{\text{CdSe}}$  along  $\mathbf{q}_{\text{out}}$ . At higher  $q$  values, a broad arc that corresponds to the  $(110)_{\text{CdSe}}$  reflection can be seen. A closer look on this reflection shows that there are reinforcements of the intensity along two different directions. By turning the sample by an angle of  $\Omega=30^\circ$ , significant changes occur. The angular intensity distribution of the  $(100)_{\text{CdSe}}$  gets narrower and the  $(101)_{\text{CdSe}}$  reflection becomes apparent. In a similar way, the  $(110)_{\text{CdSe}}$  starts losing its arced shape and is clearly reinforced in the  $\mathbf{q}_{\text{out}}$  direction. Continuing turning the sample to  $\Omega=45^\circ$ , this effect becomes more pronounced and the  $(100)_{\text{CdSe}}$  as well as the  $(110)_{\text{CdSe}}$  reflections are visible only in the  $\mathbf{q}_{\text{out}}$  direction. Additionally, a very weak but sharp reflection starts to appear in the  $\mathbf{q}_{\text{in}}$  direction. This weak reflection is indexed  $(002)_{\text{CdSe}}$  and stems from some misaligned NRs. For  $\Omega=90^\circ$ , the

$(100)_{\text{CdSe}}$  and  $(110)_{\text{CdSe}}$  reflections along  $\mathbf{q}_{\text{out}}$  are strongly narrowed with respect to their angular spread in the  $\mathbf{q}_{\text{out}}$  direction. On the equator, the sharp  $(002)_{\text{CdSe}}$  is observed.

Regarding the linear scans (*Figure 3-5*), for  $\mathbf{q} // \mathbf{R}$ , the  $(100)_{\text{CdSe}}$ ,  $(110)_{\text{CdSe}}$  and the  $(101)_{\text{CdSe}}$  as well as reflections from the P3HT can be clearly seen. For  $\mathbf{q} \perp \mathbf{R}$ , no reflection of the P3HT can be observed; the scan is dominated by the  $(002)_{\text{CdSe}}$  reflections in the case of the 1:1 blend. At higher  $\mathbf{q}$  values, a multitude of reflections coming from the CdSe NRs can be observed as seen in the scan of the 1:3 blend.

The weak reflection in the  $\mathbf{q}_{\text{out}}$  attributed to the  $(002)_{\text{CdSe}}$  of standing NRs that has been observed before the rubbing process (*Figure 3-1*) has completely vanished after rubbing. This indicates that the rubbing process induced the orientation of these rods with their long axis parallel to the substrate. This is in some sense similar to the reorientation from “edge-on” to “flat-on” of the P3HT after rubbing.

The reinforcement of the  $(110)_{\text{CdSe}}$  and also of the  $(100)_{\text{CdSe}}$  indicate the possible presence of preferential contact planes of the NRs on the substrate as it was anticipated from the comparison of the experimental and the simulated ED pattern. Preferential contact planes of the NRs upon rubbing were also observed by Breiby *et al.* (16).

Taking together the 2D GIXD map and the linear  $\Omega$  scans allow to extract the angular distribution of the NRs both along the rubbing direction  $\mathbf{R}$  and in the out-of-plane direction. The out-of plane distribution of the nanorods is characterized by a FWHM  $\sim 20^\circ$  as inferred from the 2D GIXD map at  $\Omega=90^\circ$  (*Figure 3-5*). From TEM as well as from the linear  $\Omega$ -scan, the in-plane distribution in the case of a 1:1 shows a FWHM  $\sim 32^\circ$ . The good agreement of the results from ED and GIXD measurements shows that the orientation of the NRs in the case of hybrid films is homogeneous over the entire film surface probed by GIXD (in the range of  $\text{cm}^2$ ).

Breiby *et al.* reported for rubbed thin films composed of NRs alone ( $8 \text{ nm} \times 22 \text{ nm}$ ) a FWHM  $= 52^\circ$  for the in-plane orientation and a FWHM  $= 18^\circ$  for the out-of plane orientation (16). Therefore, the in-plane orientation obtained in the case of our hybrid films composed of P3HT and CdSe NRs surpasses that observed for rubbed NRs.

In the following, the effect of increasing relative amount of NRs in the hybrid thin films will be studied. Particular interest will be paid to the effect of the increasing amount of NRs on the in-plane orientation of the hybrid thin films.

### 3.2.2. Effect of the wt% of NR on the in-plane orientation

To get a more precise view on the influence of the relative amount of NRs in the hybrid thin films, we analyzed rubbed thin films with an increasing ratio of NRs by both ED and GIXD measurements. Thin hybrid P3HT:CdSe NRs films with the following compositions were analysed and compared: **pure P3HT, 2:1, 1:1, 1:2, 1:3 and pure NRs.**

Figure 3-6 shows the TEM-BF and the corresponding ED patterns of hybrid samples of various compositions. From the TEM-BF it can be seen that there is no aggregation of the NRs in the samples studied, *i.e.* a good dispersion of the NRs is achieved. The NRs tend to align parallel to the rubbing direction ( $c_{CdSe}/R$ ) in all cases. However, it seems that the samples get less ordered with increasing amount of NRs. A closer look on the  $(002)_{CdSe}$  in the ED patterns of the different samples confirms this trend. In fact, the angular spread of this reflection increases with increasing amount of NRs in the sample. To get a more quantitative view of this effect, the FWHM of the azimuthal distributions of the  $(100)_{P3HT}$  and the  $(002)_{CdSe}$  reflections were extracted from the ED patterns. As observed for the 1:1 sample (see Figure 3-3), for a given composition, the azimuthal distributions of the  $(100)_{P3HT}$  and the  $(002)_{CdSe}$  reflections of the same sample match closely. This observation confirms that the degree of in-plane orientation of the NRs is imposed by the in-plane orientation of the P3HT matrix.

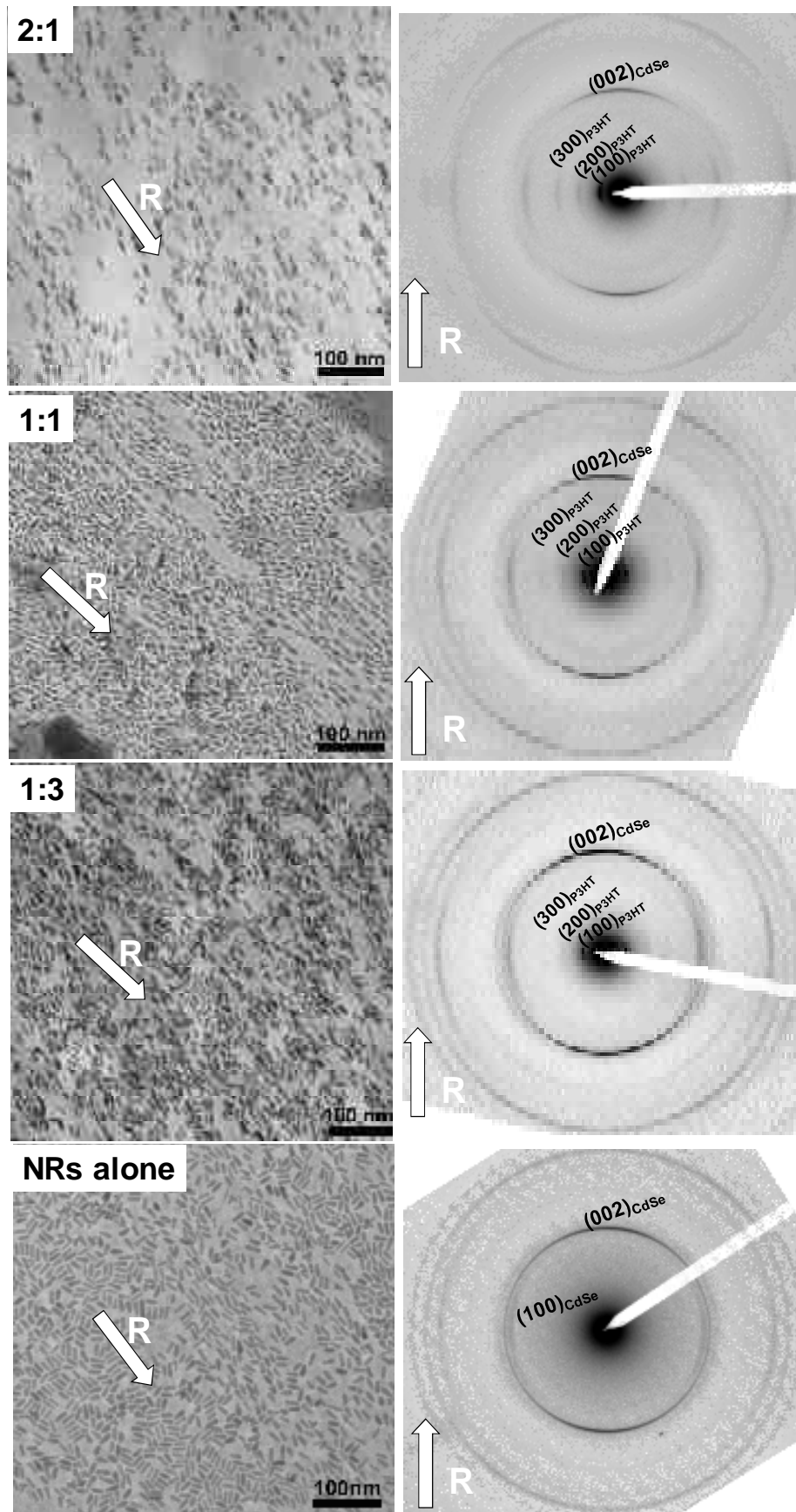


Figure 3-6: TEM-BF and corresponding ED patterns of hybrid thin films with increasing relative amount of NRs. Samples with ratios P3HT:CdSe 2:1, 1:1, 1:3 and NRs alone are presented

Figure 3-7 shows the evolution of the FWHM of the azimuthal distribution of the  $(002)_{\text{CdSe}}$  as a function of the composition of the sample. The values were extracted from the ED patterns or obtained by linear GIXD  $\Omega$ -scans around the  $(002)_{\text{CdSe}}$  reflection. The results obtained by ED on a relatively small scale match well the results obtained by GIXD on the  $\text{cm}^2$  scale. This confirms that the information obtained by TEM is representative of the entire sample. Samples characterized by a ratio P3HT:CdSe up to 1:2 show similar in-plane distributions  $c_{\text{P3HT}}/\text{NR}$  long axis. For the 1:3 sample, the in-plane orientation of the NRs is characterized by a FWHM =  $42^\circ$  for the  $(002)_{\text{CdSe}}$  reflection. This value approaches that obtained for rubbed NRs thin films.

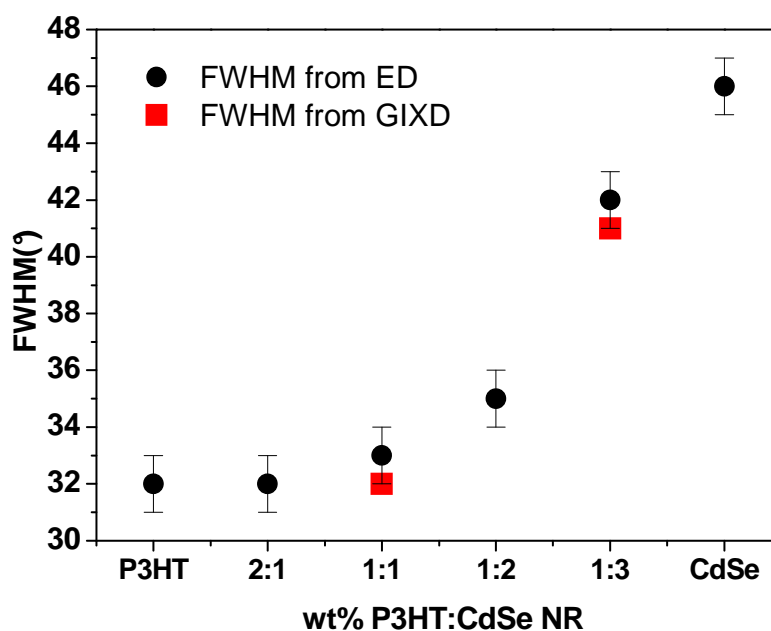


Figure 3-7 : **Black dots:** FWHM of the azimuthal distribution extracted from the ED patterns of the  $(100)_{\text{P3HT}}$  and  $(002)_{\text{CdSe}}$ . **Red dots** FWHM extracted from GIXD  $\Omega$ -scans around the  $(002)_{\text{CdSe}}$  reflection.

Two important points can be concluded from this analysis:

(i) The in-plane orientation of the thin films is significantly improved in the case of hybrid thin films compared to films composed of NRs alone. Indeed, Figure 3-7 shows clearly that the level of in-plane alignment of the NRs tends towards the level of in-plane alignment of the pure P3HT as the ratio of P3HT in the films increases. In the case of hybrids, the observed orientation is uniform over the entire film in contrast rubbed films of pure NRs.

(ii) For all compositions of the hybrids, the degree of in-plane orientation of both the P3HT as well as the NRs tend to match very closely.

For these reasons, we believe that the alignment of the soft polymer matrix upon rubbing draws the orientation of the NRs while giving the necessary mechanical toughness to

the films which ensures a uniform orientation of the NRs over the entire film surface. *Figure 3-8* schematically illustrates the orientation of a thin film of pure NRs and of a hybrid thin film with a 1:1 composition. Stretching of polymers such as polyethylene or poly(vinyl alcohol) containing rod shaped colloidal nanocrystals was reported to yield uniaxially aligned NRs within the polymer matrix (18, 20–23). We believe that the reorientation of the NRs in the rubbed P3HT matrix undergoes a similar process.

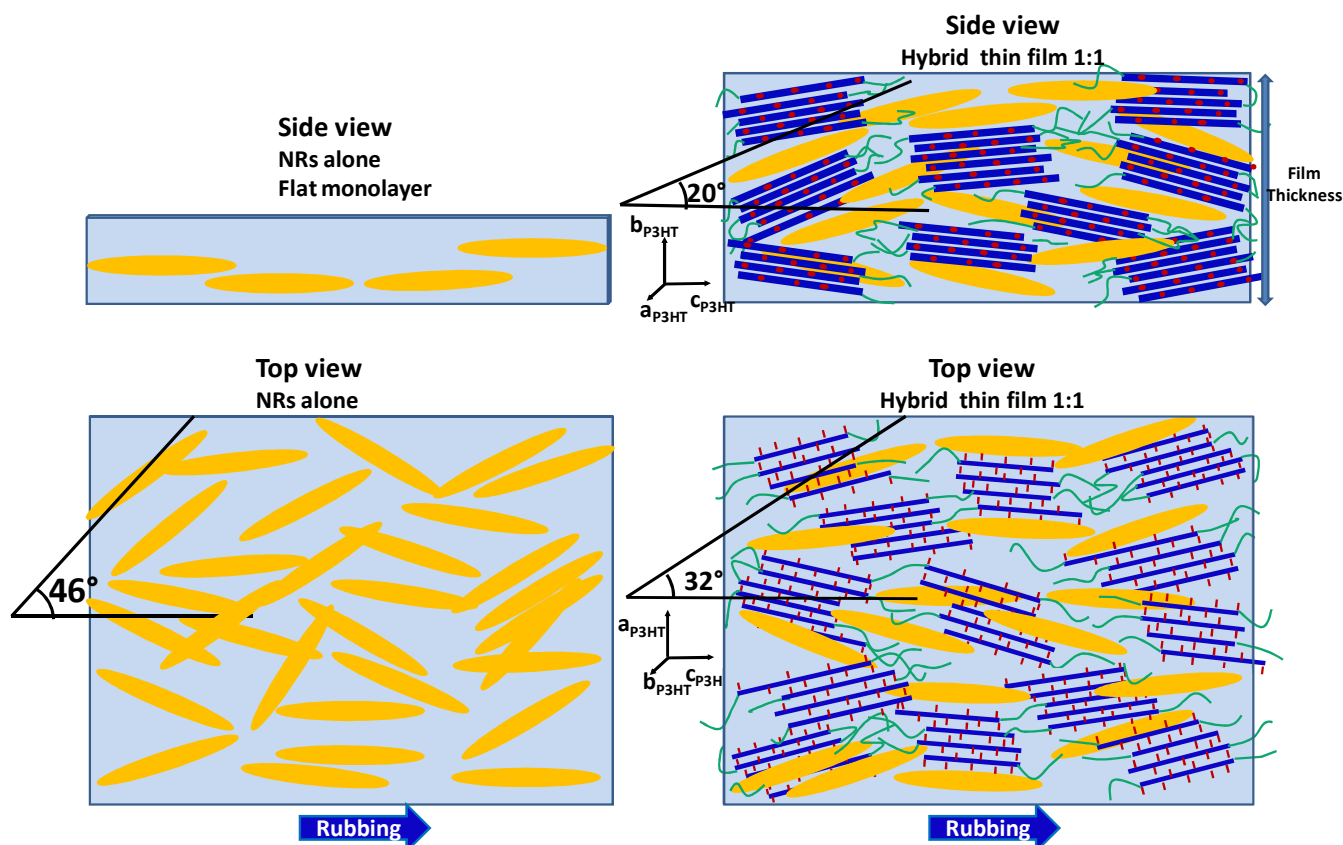


*Figure 3-8* : Schematic representation of the orientation of the NRs in rubbed thin films. (**left**) Case of NRs alone. (**right**) case of a hybrid with a composition 1:1.

To further visualize the correlation between the orientation of the NRs and the P3HT chain orientation, we performed HR-TEM observations of the hybrid layers. In fact, HR-TEM gives directly access to the crystalline domains and to the chain packing of the latter in a 2D projection in contrast to other indirect methods such as X-ray diffraction. *Figure 3-9* shows a representative HR-TEM image obtained for a hybrid film with a composition 2:1. HR-TEM reveals domains consisting of planes of  $\pi$ -stacked chains separated by the *hexyl* side chains ( $a_{\text{P3HT}}=1.65$  nm periodicity). In HR-TEM, the “flat-on” oriented crystalline domains can be clearly seen as the contrast in such images arises from the alternation of sulfur-rich stacks of polythiophene backbones and layers of *n*-hexyl side chains.

*Figure 3-9* shows that the local orientation of the NRs follows the one of the adjacent P3HT polymer stacks. This effect is illustrated by red arrows on the HR-TEM image. This

observation gives further support for the assumption that the soft P3HT induces the efficient alignment of the CdSe NRs upon rubbing.

The fact that it is possible to image on a molecular scale the exact orientation of the P3HT and the CdSe NRs opens possibilities for fundamental studies. The NRs could for example be used as local probes to get information about changes of the polymer on the molecular scale for example in solvent annealing experiments.

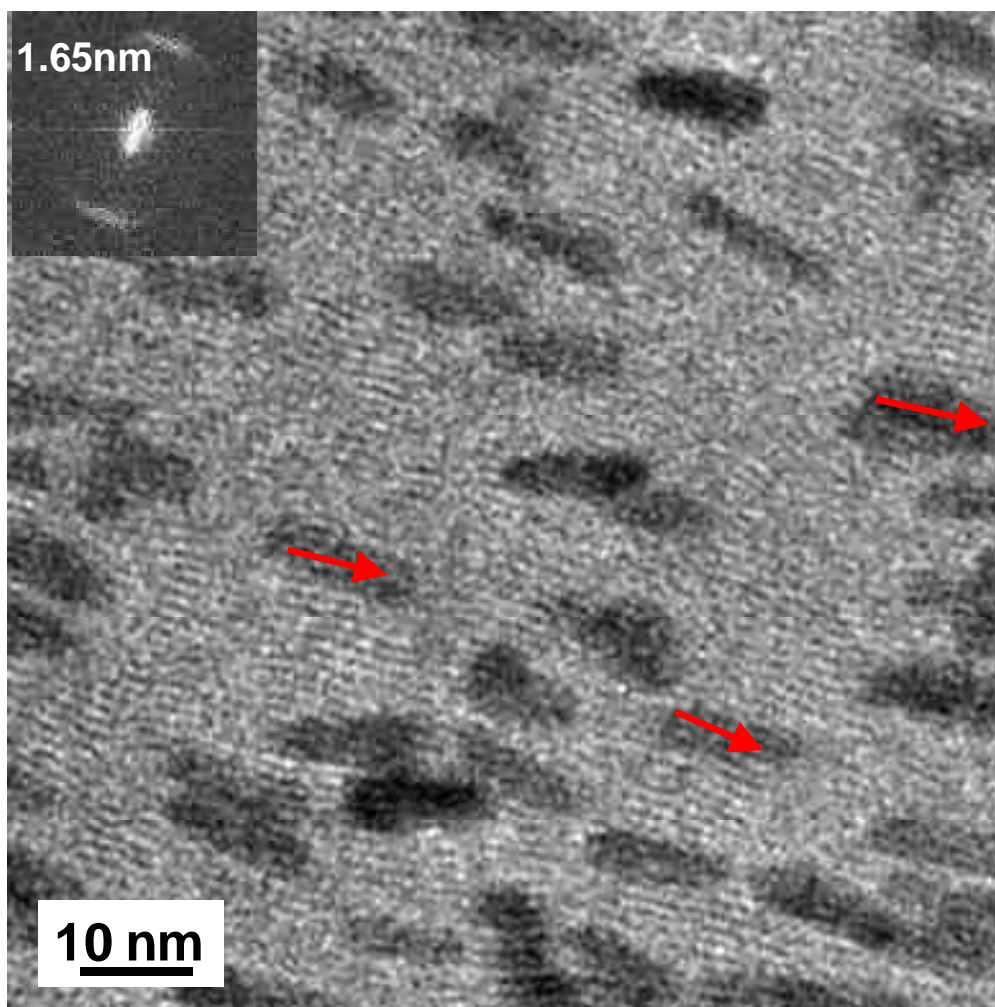


Figure 3-9: HR-TEM image of a rubbed hybrid thin film with a composition 2:1. The inset shows the FFT with the periodicity along the  $a_{P3HT}$ -axis of the P3HT.

#### 4. Anisotropy of the UV-vis absorbance

In the following, we are interested in the optical properties of rubbed thin films. In particular, we wish to study in how the structure of the films affects their UV-vis spectrum. Anisotropy of the optical properties of rod-shaped NCs has frequently been reported in previous published work (3, 17, 18, 24, 25, 30, 31). For example, Hore *et al.* studied the

optical absorption properties gold NRs dispersed in a PMMA matrix (32). Quantum rods of CdSe with an aspect ratio of 2.3 were used for polarizing diodes by aligning the rods in stretched ultrahigh molecular weight polyethylene (18). The same authors performed also rubbing experiments on a thin film of CdSe NRs by using a velvet cloth and reported anisotropy of the optical properties of the thin films. Dichroic ratios (DR) of the PL emission of around 2.3 were reported for such thin films (18). For nanowires with high aspect ratio of indium phosphide, dichroic ratios of 20-50 were reported (33).

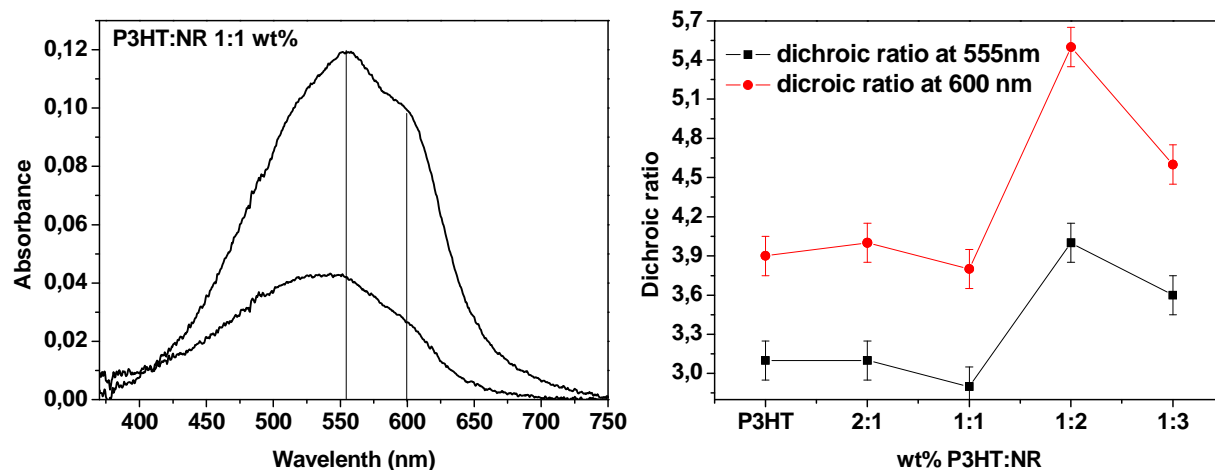


Figure 4-1: (left) example of an UV-vis spectrum of a hybrid thin film with a composition P3HT:CdSe 1:1 with the incident polarization parallel and perpendicular to the rubbing direction. (right) dichroic ratio of the thin films as a function of the relative amount of NRs in the film.

Our case is different from most reports of the literature in the sense that we have hybrid thin films where the NRs as well as the polymer (P3HT) are highly oriented and have both anisotropic optical properties. Therefore the anisotropy that is observed in the UV-vis spectrum cannot be attributed to the polymer or the NRs but it concerns the entire hybrid system. The hybrid thin films were rubbed only 1 time as for a higher amount of rubbing cycles scratching of the thin films was observed. Further investigations are necessary to limit this damage, for instance by achieving a better control of the pressure during the rubbing process or by using a functionalized substrate for better adherence of the hybrid thin film. Figure 4-1 (left) displays the UV-vis absorption spectrum of a rubbed hybrid 1:1 thin film and Figure 4-1 (right) shows the evolution of the extracted dichroic ratios (DR) as a function of the blend composition. For means of comparison the dichroic ratio of a pure rubbed P3HT sample was measured.

The UV-vis spectrum of the rubbed hybrid thin films is very similar to that of pure P3HT layers. It shows two vibronic components centered at 600 nm and 555 nm. For high amounts of NRs, an increase of the absorption at low wavelengths is observed. It can be attributed to the absorbance of the NRs. The DR stays constant and close to the DR of pure P3HT up to a sample composition of 1:1. For the compositions of 1:2 and 1:3 an increase of the DR can be observed.

This constant DR for the blend compositions up to 1:1 is in accordance with the observations regarding the in-plane orientation of the samples. In fact, it was shown previously by ED and GIXD that the in-plane orientation of hybrid thin films is not affected up to a sample composition of 1:1. The observed increase of the DR for the 1:2 and 1:3 samples is however surprising. In fact, a degradation of the in-plane orientation was observed for these samples whereas the DR is increasing. A possible explanation for such an evolution could be that for samples with a low ratio of NRs, the UV-vis spectrum is dominated by the oriented P3HT matrix and that there is no significant contribution of the NRs. For samples with a higher amount of NRs, the latter contribute increasingly to the absorption spectrum of the hybrid film. As the NRs are oriented and show anisotropic optical absorbance, the anisotropy of the total absorption of the blend increases despite a degraded in-plane orientation. At a blend ratio of 1:3, the in-plane orientation starts to be degraded and the entire film is less oriented as mentioned before. In addition, at this composition the film presents a fragile mechanical stability due to the high amount of NRs. Indeed, the higher the relative amount of NRs in the films, the lower the rate of chain entanglements in the P3HT matrix and thus, the film is mechanically less stable. This leads to scratching damage during the rubbing procedure. Therefore the dichroic ratio of the 1:3 sample is lower compared to the 1:2 sample.

## 5. Rubbing vs epitaxy: A comparative study

We have presented two different methods for the fabrication of highly oriented hybrids composed of P3HT and CdSe nanorods: (i) mechanical rubbing, (ii) slow-DEC. Herein we will compare hybrids oriented by these two methods and present the main differences in terms of morphology and structure. *Figure 5-1* shows the BF-images and the corresponding ED patterns of an epitaxied and a rubbed hybrid film.

The main differences in terms of morphology and structure of the films concern: (i) the nanostructuration and (ii) the alignment of the NRs in the polymer matrix.

The well defined nanostructuration of the epitaxied hybrids is absent in rubbed thin films. Indeed, in epitaxied films, the lamellar structure of the P3HT matrix enforces the confinement of the nanoparticles are rejected into the amorphous interlamellar zones (29). Except for low  $M_w$  P3HT, no lamellar structure could be evidenced in rubbed films of pure P3HT. This absence of a lamellar structure goes along with the absence of a nanostructuration in the case of rubbed hybrid thin films.

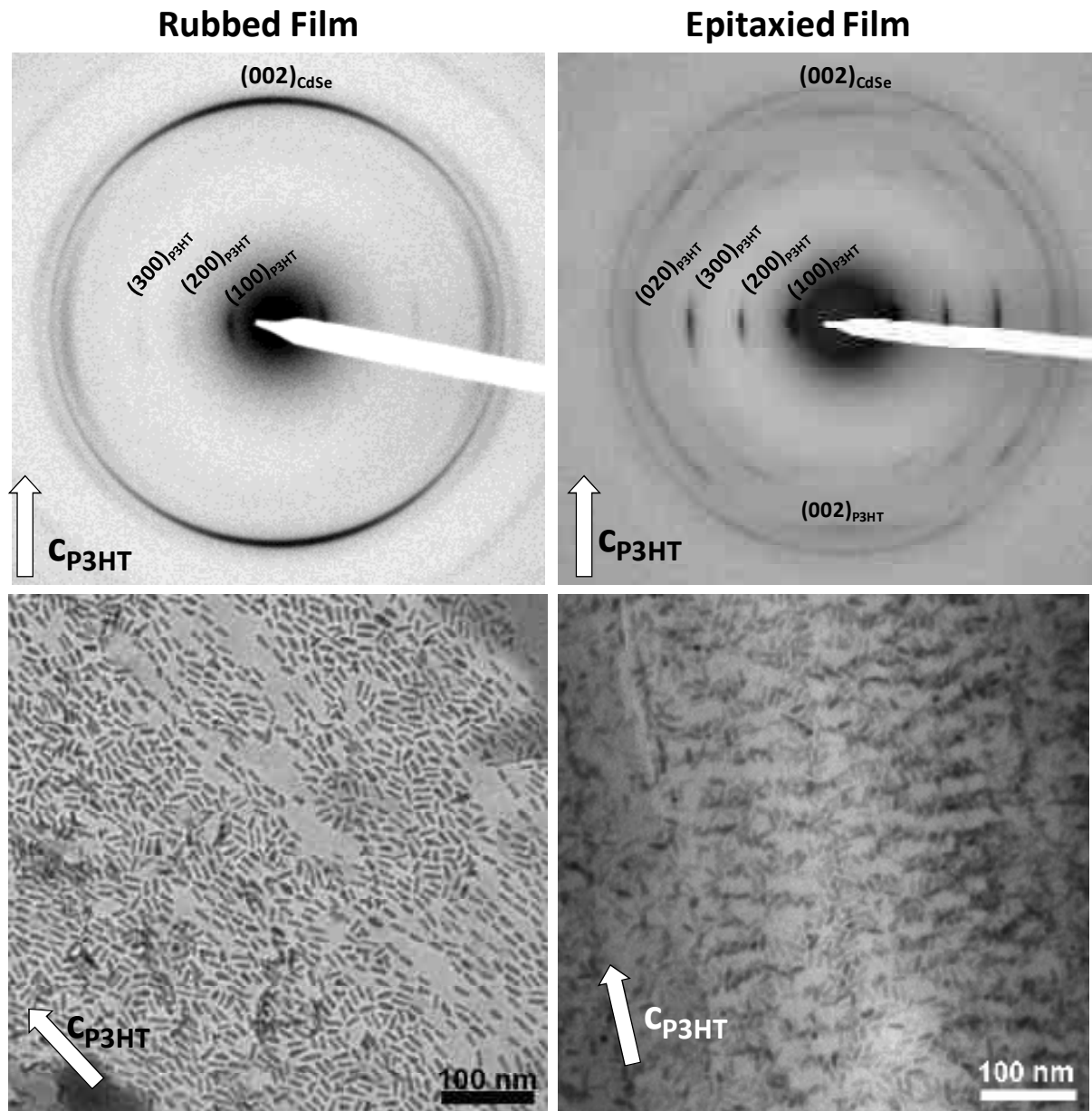


Figure 5-1 : Electron diffraction and bright field TEM images of hybrid thin films composed of a medium-Mw ( $M_w=17.6$  kDa) and CdSe nanorods ( $5\text{nm} \times 20\text{nm}$ ) prepared by rubbing (left) and slow rate DEC (right).

Another major difference that can be noted from the careful comparison of the ED patterns concerns the intensity of the  $(002)_{\text{CdSe}}$  reflection. Indeed, this reflection appears very intense for the rubbed films as compared to a rather weak reflection in the epitaxied layers. The alignment of the NRs parallel to  $\mathbf{R}$  ( $c_{P3HT}$ ) is well defined in rubbed layers, whereas it is poor in the epitaxied thin films. In rubbed hybrids, NRs are mostly lying flat on ( $c_{\text{CdSe}}$  in the plane) in the polymer matrix with  $c_{\text{CdSe}}//\mathbf{R}$ . In epitaxied layers, the orientation of the rods is mainly determined by the available space in the amorphous interlamellar zones (AIZ). Figure 5-1 suggests that only a part of the NRs are strictly lying flat on the substrate presumably because the length of the NRs exceeds in some parts the average width of the AIZ. Indeed, from HR-TEM and TEM-BF of pure epitaxied P3HT films of medium-Mw we observed a

total lamellar periodicity of  $L \sim 32\text{nm}$  and an average stem length of  $L_{\text{stem}} \sim 13\text{nm}$  (see chapter 4). Therefore the average size of the AIZs can be estimated to  $L_{\text{AIZ}} \sim 19\text{nm}$ . As the used NRs have an average length of  $\sim 20\text{nm}$ , their dimensions exceed the average size of the AIZs in some zones of the films leading to an inclination of the rods. A population of such inclined NRs was indeed observed by in electron tomography experiments (these results are not discussed).

The main morphological and structural differences observed for rubbed and epitaxied layers of pure P3HT have a direct influence on the resulting hybrid. The semicrystalline P3HT matrix observed for the epitaxied layers serves as a scaffold for the fabrication of nanostructured hybrids. In the rubbed layers, the orientation of the soft P3HT matrix with  $\mathbf{c}_{\text{P3HT}} // \mathbf{R}$  draws the orientation of the NRs.

## 6. Conclusion

Mechanical rubbing is a new method for the fabrication of hybrid materials where the organic as well as the inorganic component display a high degree of in-plane orientation. Mechanical rubbing allows for the fabrication of hybrid films where the  $\mathbf{c}_{\text{P3HT}}$  and the long axis of the NRs align parallel to the rubbing direction. The NRs are preferentially aligned with the long axis lying flat-on the surface and the P3HT shows a preferential “flat-on” orientation.

We studied the effect of the ratio of NRs in the polymer matrix on the degree of in-plane orientation of the thin films. One of the main results is that the NRs are oriented by the polymer matrix. With increasing ratio of NRs in the thin films, the degree of in-plane orientation is degraded. In all cases, the rubbed hybrids show a high level of in-plane orientation of the NRs as compared to rubbed NRs layers.

Hybrid thin films prepared by mechanical rubbing show no nanostructuration but a clear alignment of the NRs along the  $\pi$ -stacked polythiophene backbones, whereas in hybrid thin films prepared by slow-DEC, a clear nanostructuration can be observed but the rods are only poorly oriented.

Due to mechanical fragility of the hybrid thin films, scratching of the thin films during the rubbing occurs quite easily. Further investigations are necessary in this sense to improve the mechanical quality of the layers. The improvement of the mechanical stability of the layers is possible via (i) increasing the anchoring of the NRs in the polymer matrix by adequate surface functionalization of the rods. (ii) by improving the adherence of the hybrid layer on the substrate, *e.g.* via surface functionalization of the glass substrate. (iii) using a higher  $M_w$  P3HT to increase the number of entanglements and therefore increase the mechanical stability of the film. For this last possibility the right equilibrium has to be found since entanglements hinder the orientation by mechanical rubbing.

However, mechanical rubbing is a technique that allows to obtain large areas ( $\sim\text{cm}^2$ ) of highly oriented hybrid thin films where both the organic and the inorganic phase present a high degree of in-plane orientation. The two main advantages of the rubbing process are its rapidity and the possibility to scale-up the method so as to fabricate large areas of oriented hybrids.

- (1) Huynh, W. U.; Dittmer, J. J.; Alivisatos, A. P. Hybrid nanorod-polymer solar cells. *Science* **2002**, *295*, 2425-7.
- (2) Dayal, S.; Reese, M. O.; Ferguson, A. J.; Ginley, D. S.; Rumbles, G.; Kopidakis, N. The effect of nanoparticle shape on the photocarrier dynamics and photovoltaic device performance of poly(3-hexylthiophene):CdSe nanoparticle bulk heterojunction solar cells. *Advanced Functional Materials* **2010**, *20*, 2629-2635.
- (3) Hu, J.; Li, L. S.; Yang, W.; Manna, L.; Wang, L. W.; Alivisatos, A. P. Linearly polarized emission from colloidal semiconductor quantum rods. *Science* **2001**, *292*, 2060-3.
- (4) Persano, A.; De Giorgi, M.; Fiore, A.; Cingolani, R.; Manna, L.; Cola, A.; Krahne, R. Photoconduction properties in aligned assemblies of colloidal CdSe/CdS nanorods. *ACS nano* **2010**, *4*, 1646-52.
- (5) Evans, B. A.; Shields, A. R.; Carroll, R. L.; Washburn, S.; Falvo, M. R.; Superfine, R. Magnetically actuated nanorod arrays as biomimetic cilia. *Nano letters* **2007**, *7*, 1428-34.
- (6) Ryan, K. M.; Mastroianni, A.; Stancil, K. a; Liu, H.; Alivisatos, A. P. Electric-field-assisted assembly of perpendicularly oriented nanorod superlattices. *Nano letters* **2006**, *6*, 1479-82.
- (7) Li, L.-shi; Walda, J.; Manna, L.; Alivisatos, A. P. Semiconductor nanorod liquid crystals. *Nano letters* **2002**, *2*, 557-560.
- (8) Talapin, D. V.; Lee, J.-S.; Kovalenko, M. V.; Shevchenko, E. V. Prospects of colloidal nanocrystals for electronic and optoelectronic applications. *Chemical reviews* **2010**, *110*, 389-458.
- (9) Ghezelbash, A.; Koo, B.; Korgel, B. a Self-assembled stripe patterns of CdS nanorods. *Nano letters* **2006**, *6*, 1832-6.
- (10) Sun, B.; Siringhaus, H. Surface tension and fluid flow driven self-assembly of ordered ZnO nanorod films for high-performance field effect transistors. *Journal of the American Chemical Society* **2006**, *128*, 16231-7.
- (11) Baker, J. L.; Widmer-Cooper, A.; Toney, M. F.; Geissler, P. L.; Alivisatos, a P. Device-scale perpendicular alignment of colloidal nanorods. *Nano letters* **2010**, *10*, 195-201.
- (12) Hung, A. M.; Konopliv, N. A.; Cha, J. N. Solvent-based assembly of CdSe nanorods in solution. *Langmuir* **2011**, *27*, 12322-8.
- (13) Rivest, J. B.; Swisher, S. L.; Fong, L.-K.; Zheng, H.; Alivisatos, A. P. Assembled monolayer nanorod heterojunctions. *ACS nano* **2011**, *5*, 3811-6.
- (14) Modestino, M. A.; Chan, E. R.; Hexemer, A.; Urban, J. J.; Segalman, R. A. Controlling nanorod self-assembly in polymer thin films. *Macromolecules* **2011**, *44*, 7364-7371.
- (15) Gupta, S.; Zhang, Q.; Emrick, T.; Russell, T. P. "Self-corralling" nanorods under an applied electric field. *Nano letters* **2006**, *6*, 2066-9.
- (16) Breiby, D. W.; Chin, P. T. K.; Andreasen, J. W.; Grimsrud, K. a; Di, Z.; Janssen, R. a J. Biaxially oriented CdSe nanorods. *Langmuir* **2009**, *25*, 10970-4.

- (17) Chin, P. T. K.; Hikmet, R. A. M.; Meskers, S. C. J.; Janssen, R. A. J. Energy transfer and polarized emission in cadmium selenide nanocrystal solids with mixed dimensionality. *Advanced Functional Materials* **2007**, *17*, 3829-3835.
- (18) Hikmet, R. A. M.; Chin, P. T. K.; Talapin, D. V.; Weller, H. Polarized-light-emitting quantum-rod diodes. *Advanced Materials* **2005**, *17*, 1436-1439.
- (19) Amit, Y.; Faust, A.; Lieberman, I.; Yedidya, L.; Banin, U. Semiconductor nanorod layers aligned through mechanical rubbing. *Physica Status Solidi (a)* **2011**, *8*, n/a-n/a.
- (20) Van der Zande, B. M. I.; Pagès, L.; Hikmet, R. A. M.; Van Blaaderen, A. Optical properties of aligned rod-shaped gold particles dispersed in poly ( vinyl alcohol ) films. *Journal of Physical Chemistry B* **1999**, *103*, 5761-5767.
- (21) Al-Rawashdeh, N. A. F.; Sandrock, M. L.; Seugling, C. J.; Foss, C. A. Visible region polarization spectroscopic studies of template-synthesized gold nanoparticles oriented in polyethylene. *Journal of Physical Chemistry B* **1998**, *102*, 361-371.
- (22) Murphy, C. J.; Orendorff, C. J. Alignment of gold nanorods in polymer composites and on polymer surfaces. *Advanced Materials* **2005**, *17*, 2173-2177.
- (23) Murphy, C. J.; Sau, T. K.; Gole, A. M.; Orendorff, C. J.; Gao, J.; Gou, L.; Hunyadi, S. E.; Li, T. Anisotropic metal nanoparticles: Synthesis, assembly, and optical applications. *The journal of physical chemistry. B* **2005**, *109*, 13857-70.
- (24) Rizzo, A.; Mazzeo, M.; Palumbo, M.; Lerario, G.; D'Amone, S.; Cingolani, R.; Gigli, G. Hybrid light-emitting diodes from microcontact-printing double-transfer of colloidal semiconductor CdSe/ZnS quantum dots onto organic layers. *Advanced Materials* **2008**, *20*, 1886-1891.
- (25) Rizzo, A.; Nobile, C.; Mazzeo, M.; De Giorgi, M.; Fiore, A.; Carbone, L.; Cingolani, R.; Manna, L.; Gigli, G. Polarized light emitting diode by long-range nanorod self-assembling on a water surface. *ACS nano* **2009**, *3*, 1506-12.
- (26) Brinkmann, M. Structure and morphology control in thin films of regioregular poly(3-hexylthiophene). *Journal of Polymer Science Part B: Polymer Physics* **2011**, *49*, 1218-1233.
- (27) Schierhorn, M.; Boettcher, S. W.; Peet, J. H.; Matioli, E.; Bazan, G. C.; Stucky, G. D.; Moskovits, M. CdSe nanorods dominate photocurrent of hybrid CdSe- P3HT photovoltaic cell. *ACS nano* **2010**, *4*, 6132-6136.
- (28) Snaith, H. J.; Whiting, G. L.; Sun, B.; Greenham, N. C.; Huck, W. T. S.; Friend, R. H. Self-organization of nanocrystals in polymer brushes. Application in heterojunction photovoltaic diodes. *Nano letters* **2005**, *5*, 1653-7.
- (29) Brinkmann, M.; Aldakov, D.; Chandezon, F. Fabrication of oriented and periodic hybrid nanostructures of regioregular poly(3-hexylthiophene) and CdSe nanocrystals by directional epitaxial solidification. *Advanced Materials* **2007**, *19*, 3819-3823.
- (30) Artemyev, M.; Möller, B.; Woggon, U. Unidirectional alignment of CdSe. *Nano letters* **2003**, *3*, 12-15.
- (31) Talapin, D. V.; Koeppe, R.; Götzinger, S.; Kornowski, A.; Lupton, J. M.; Rogach, A. L.; Benson, O.; Feldmann, J.; Weller, H. Highly emissive colloidal CdSe / CdS heterostructures of mixed dimensionality. *Nano letters* **2003**, *3*, 1677.
- (32) Hore, M. J. A.; Composto, R. J. Nanorod self-assembly for tuning optical absorption. *ACS nano* **2010**, *4*, 6941-9.

- (33) Wang, J.; Gudixsen, M. S.; Duan, X.; Cui, Y.; Lieber, C. M. Highly polarized photoluminescence and photodetection from single indium phosphide nanowires. *Science* **2001**, *293*, 1455-7.





## *Conclusions and perspectives*

The aims of this thesis were multiple. One main part concerned the understanding and the improvement of the orientation processes and the full structural and morphological characterization of thin films made of pure P3HT oriented by two different methods, namely (i) slow directional epitaxial crystallization (slow-DEC) and (ii) mechanical rubbing. Another part concerned the elaboration and full characterization of oriented/nanostructured hybrid materials composed of P3HT and CdSe nanocrystals prepared by these two methods. In addition, we were interested in the surface functionalization of CdSe NCs with various polypyridine ligands and the integration of the functionalized NCs into the P3HT matrix.

The initial DEC method on the Koeffler bench as proposed by Brinkmann and Wittmann (1) was substantially improved by:

- (i) controlling the growth rate of the TCB crystallization front by the use of a motorized translation bench and a significant slowing down of the TCB/P3HT growth rate ( $20\mu\text{m/s}$ );
- (ii) using a local zone melting technique that limits the evaporation of the TCB during growth;
- (iii) using an orienting substrate of PTFE and enhancing the homogeneity of the oriented P3HT films via adequate coatings of the glass substrates.

This allowed the reproducible preparation of oriented thin films with areas of several  $\text{cm}^2$ . In thin films prepared by DEC, the  $\mathbf{c}_{\text{P3HT}}$  direction orients parallel to the  $\mathbf{c}_{\text{TCB}}$  direction due to a 1D epitaxial relation ( $\mathbf{c}_{\text{P3HT}} \sim 2\mathbf{c}_{\text{TCB}}$ ). The possibility to grow highly oriented P3HT films on larger scales enabled the characterization of the films by techniques such as GIXD, UV-vis absorption and PL spectroscopy. The GIXD measurements revealed that the structure of the films depends on the molecular weight of the P3HT. Indeed, for  $M_w > 10$  kDa, the samples present a fiber structure with  $\mathbf{c}_{\text{P3HT}}$  as fiber axis whereas low- $M_w$  samples show the existence of mainly three preferential contact planes, *i.e.* the (010), the (001) and the (011) contact planes. These differences in structure are directly reflected by the morphology of the thin films. The slowing-down of the growth kinetics of the TCB crystallization front results in an increase of the lamellar periodicity to values of  $L \sim 40 - 45$  nm. These values are larger to

those generally reported in the literature (2, 3). The differences in terms of orientation and nanomorphology of the various  $M_w$  samples are directly reflected in the optical properties of the films. The vibronic structure of absorbance is particularly well defined. The 0-0 contribution becomes very strong with increasing  $M_w$  suggesting a higher conjugation length in these films due to the higher extension of the crystalline domains in the  $\mathbf{c}_{P3HT}$  direction.

In parallel to the slow-DEC method, highly oriented P3HT films were prepared by mechanical rubbing. Mechanical rubbing allows for the fabrication of large areas of oriented P3HT films without requiring orienting substrates. Rubbing of the P3HT films causes (i) the orientation of the chains parallel to the rubbing direction ( $\mathbf{c}_{P3HT}/\mathbf{R}$ ) and (ii) a flip of the native preferential “*edge-on*” orientation to a preferential “*flat-on*” orientation of the crystalline domains on the substrate. It was shown that the orientation of the thin films propagates from the film-air interface through the bulk of the film with an increasing number of rubbing steps. The maximum degree of in-plane orientation achieved in the rubbed films is a function of  $M_w$ . High in-plane orientation is achieved for low- $M_w$  samples. Reorientation of  $\pi$ -stacked chains in high- $M_w$  films is hindered by a reduced chain mobility caused by the presence of chain entanglements and tie-chains interconnecting crystalline P3HT domains. UV-vis absorption spectroscopy allows to measure  $M_e$ , the molecular weight corresponding to the onset of chain folding and entanglements.

The orientation process differs strongly for the slow-DEC and the rubbing method. Whereas slow-DEC is based on the use of an orienting substrate (oriented TCB), mechanical rubbing induces the orientation of the polymer chains via shearing forces. These differences influence directly the morphology and the structure of the resulting films. The main observed differences are summarized in *Figure 2*. Whereas films grown by slow-DEC show a characteristic semi-crystalline lamellar structure, such a nanostructuration was not evidenced for the rubbed thin films. Besides these morphological differences, the degree of crystallinity of the rubbed and epitaxied films differs. Indeed, films grown by slow-DEC show a high level of crystallinity with 3D translational order whereas rubbed layers show “smectic-like” order with a periodic succession of  $\pi$ -stacked polythiophene chains with marginal translational order along the chain-axis ( $\mathbf{c}_{P3HT}$ ) direction. It was shown that the differences in intralamellar order are directly reflected in the vibronic structure of the absorption spectra of the films. In epitaxial films with 3D crystalline order, the vibronic structure is much better defined and a redistribution of the spectral weight in the zero-phonon peak is observed.

Once the method of orientation was well mastered, we applied it for the preparation of highly oriented hybrid thin films composed of P3HT and CdSe NCs. We focused on the effect of the chemical nature of the capping ligands of the CdSe NCs on the morphology of the hybrid films. In particular, we studied the effect of surface functionalization on the dispersion of the NCs in the polymer matrix. Therefore, two batches of spherical CdSe nanocrystals were synthesized by an hot-injection organometallic route (4). In addition, rod shaped NCs of various aspect ratios were synthesized. The surface ligands of the obtained CdSe nanocrystals were exchanged in the liquid phase using various polypyridine molecules. It was shown using

advanced  $^1\text{H}$  Nuclear Magnetic Resonance techniques that the polypyridine ligands are adsorbed on the NCs surface. The adsorption-desorption kinetics (on the NMR timescale) is a function of the chemical nature of the ligand. Whereas the TerPy ligand having three anchoring sites shows a slow adsorption-desorption kinetics, the bi-dentate and mono-dentate ligands Phen and HexPy show faster exchange kinetics as compared to the NMR time scale. A quantification of the number of ligands on a NCs surface could be extracted from the NMR measurements for the TerPy ligand-exchanged nanocrystals. We found that after exchange the capping layer of one NC is composed on average of 27 TerPy ligands, 11 TOP ligands, 58 OA ligands and 52 SA ligands.

The as-synthesized NCs were integrated into hybrid thin films grown by slow-DEC. TEM tomography was used to visualize the 3D structure of the oriented thin films composed of P3HT and CdSe nanocrystals. Most importantly, electron tomography revealed that the thin films have a bi-layer structure showing a pure P3HT layer and a hybrid P3HT/CdSe overlayer. Both layers show a high level of in-plane orientation of the P3HT chains as revealed by GIXD (using synchrotron radiation), as well as an intrinsic nanostructuration related to the semi-crystalline structure of P3HT with alternation of crystalline lamellae and amorphous interlamellar zones harbouring the CdSe NCs. We showed that the relative thickness of the two layers is a function of the P3HT:CdSe ratio: the higher the relative ratio of CdSe is, the thicker the hybrid layer and the thinner the layer of pure P3HT get. The study of the morphology of the hybrid thin films prepared with polypyridine functionalized spherical NCs revealed differences as a function of the chemical structure of the ligands. Whereas the fully conjugated ligands lead to the aggregation of the NCs, ligands having solubilizing groups allow for a good dispersion of the NCs into the P3HT matrix.

Hybrid oriented thin films were also prepared by using the rubbing method. Mechanical rubbing allows for the fabrication of large areas ( $\sim\text{cm}^2$ ) of hybrid materials where both, the P3HT chains and the CdSe NRs show a well defined in-plane orientation. In rubbed hybrid films, the  $\mathbf{c}_{\text{P3HT}}$  and the long axis of the NRs align parallel to the rubbing direction ( $\mathbf{c}_{\text{P3HT}} // \mathbf{R}$  and  $\mathbf{c}_{\text{TCB}} // \mathbf{R}$ ). The NRs are preferentially aligned with the long axis lying flat on the substrate and the P3HT shows a preferential “flat-on” orientation of the crystalline domains. The orientation of the NRs is dictated by the orientation of the P3HT matrix. In all cases, the rubbed hybrids showing a higher level of in-plane orientation of the NRs as compared to rubbed NRs layers. The two main advantages of the rubbing process are its rapidity and the possibility to scale-up the method so as to fabricate large areas of oriented hybrids.

Comparing hybrid thin films prepared by mechanical rubbing and by slow-DEC reveals important differences which are summarized in *Figure 2*. Rubbed thin films show no nanostructuration but a clear alignment of the NRs along the  $\pi$ -stacked polythiophene backbones, whereas in hybrid thin films prepared by slow-DEC, a clear nanostructuration can be observed but the rods are only very poorly oriented, presumably for reasons of space filling in the amorphous interlamellar zones of P3HT.

Both, mechanical rubbing and slow-DEC were used for the elaboration of highly oriented P3HT and hybrid thin films. These two methods are potentially very interesting for various topics. On one hand, the methods and the procedures developed in this work can be applied to other polymers, such as other semiconducting NCs (*e.g.* heavy-metal free) and other types of capping ligands. On the other hand, many aspects need to be further explored *e.g.* the electrical characterization or the photoluminescence properties of the oriented films. In particular, the ambipolar charge transport in the rubbed hybrid thin films as well as the charge transport properties of the pure P3HT slow-DEC films need to be investigated. Indeed, both systems are interesting for applications in plastic electronics. The integration of hybrid slow-DEC films with their peculiar bi-layer structure and the nanostructuration in photovoltaic devices would be of great interest. The rubbed hybrids with their high degree of in-plane orientation of the P3HT as well as the NRs are of interest as active layers for ambipolar transistors. However, the electrical characterization of the hybrids needs first a better mastering of the interface between the NCs and the polymer. In other words, the control of the ligand exchange step should be improved and ligands allowing for good charge transport properties should be used. A complete study of the influence of the ligands on the morphology of rubbed hybrids would also be of interest. A deeper understanding of the influence of the ligands on the nanocrystals energy levels and wave functions is also of great importance for hybrid heterojunctions in general. However, few is known on the influence of the capping ligands on the nanocrystals energy levels upon surface functionalization.

Another challenge is the elaboration of rubbed hybrids whilst avoiding to scratch the films. This is essential for electrical transport measurements. The improvement of the mechanical stability of the layers is possible via: (i) a better “anchoring” of the NRs in the polymer matrix using an adequate surface functionalization of the rods; (ii) by improving the adherence of the hybrid layer on the substrate, *e.g.* via surface functionalization of the substrate; (iii) by using a higher  $M_w$  P3HT to increase the number of entanglements and therefore increase the mechanical stability of the film. In the latter case, the right  $M_w$  has to be found since entanglements hinder the chain orientation by mechanical rubbing.

Regarding the rubbing of pure polymer films, the application of the method to other polymers would be of interest. In particular, a fundamental study of the orientation process by mechanical rubbing as a function of the rigidity of the polymer backbone is appealing. First results on rubbing of rigid polyfluorenes underline a very different behaviour as compared to P3HT.

The further understanding of the optical properties of the epitaxied and rubbed films is in progress. Indeed, although not presented in this manuscript, temperature dependent polarized photoluminescence measurements were performed on these films. The results are promising and will reveal interesting correlations between crystalline order and emission properties of the P3HT films. Notable differences between rubbed and slow-DEC films are evidenced.

Also to be mentioned, numerous research groups are presently focusing on low band gap conjugated polymers for their application in solar cells (5, 6). The main motivation is to extend the absorption spectrum to provide a better coverage of the solar spectrum. Another point of care is to improve the charge carrier mobility. These novel materials need fundamental characterizations and it would be of great interest to elaborate highly oriented and crystalline thin films of these novel systems. This could be for example be important for the determination of their crystal structure as it was done in the case of P3HT (7). Preliminary studies applying the slow-DEC method as developed in the scope of this to low band gap polymers yielded interesting results. Indeed, highly crystalline and oriented films of low band gap polymers were obtained which can be used in the future for their structural and morphological characterization.

In conclusion, the research on conjugated polymers and hybrid materials composed of semi-conducting nanocrystals and polymers is mainly motivated by their application in the field of low-cost materials for organic and large area electronics. However, as emphasized in this work, these materials raise numerous fundamental questions. These concern their chemistry, their structure as well as their physical properties. The future understanding of these fundamental aspects is a key point in view of their successful integration in devices.

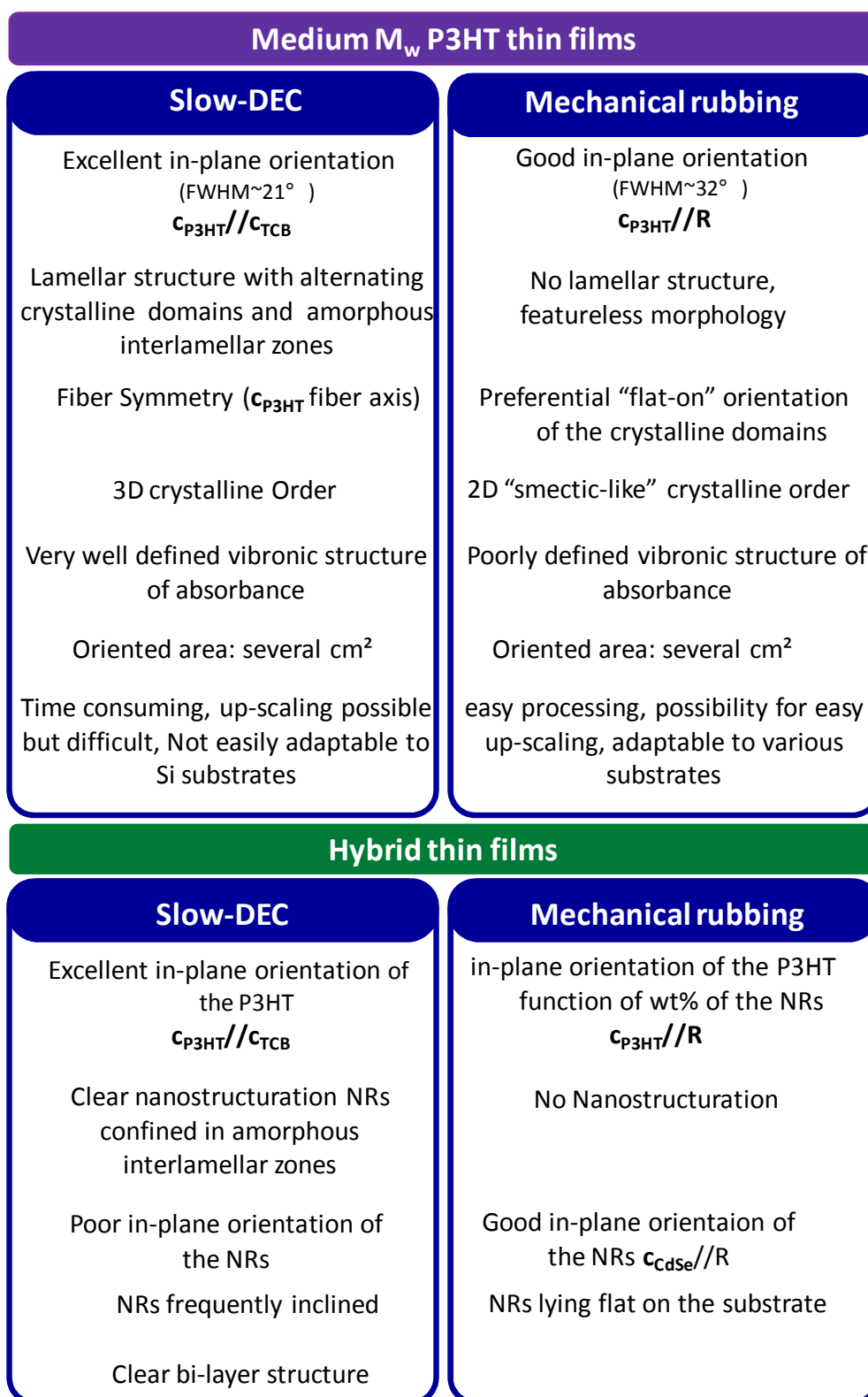


Figure 2 : Summary of the main characteristics of rubbed and epitaxied P3HT and hybrid thin films.

- (1) Brinkmann, M.; Wittmann, J.-C. Orientation of regioregular poly(3-hexylthiophene) by directional solidification: a simple method to reveal the semicrystalline structure of a conjugated polymer. *Advanced Materials* **2006**, *18*, 860-863.
- (2) Zhang, R.; Li, B.; Iovu, M. C.; Jeffries-El, M.; Sauv e, G.; Cooper, J.; Jia, S.; Tristram-Nagle, S.; Smilgies, D. M.; Lambeth, D. N.; McCullough, R. D.; Kowalewski, T. Nanostructure dependence of field-effect mobility in regioregular poly(3-hexylthiophene) thin film field effect transistors. *Journal of the American Chemical Society* **2006**, *128*, 3480-1.
- (3) Brinkmann, M.; Rannou, P. Effect of molecular weight on the structure and morphology of oriented thin films of regioregular poly(3-hexylthiophene) grown by directional epitaxial solidification. *Advanced Functional Materials* **2007**, *17*, 101-108.
- (4) Protiere, M.; Nerambourg, N.; Renard, O.; Reiss, P. Rational design of the gram-scale synthesis of nearly monodisperse semiconductor nanocrystals. *Nanoscale research letters* **2011**, *6*, 472.
- (5) Jeltsch, K. F.; Sch adel, M.; Bonekamp, J.-B.; Niyamakom, P.; Rauscher, F.; Lademann, H. W. a.; Dumsch, I.; Allard, S.; Scherf, U.; Meerholz, K. Efficiency enhanced hybrid solar cells using a blend of quantum dots and nanorods. *Advanced Functional Materials* **2012**, *in press*.
- (6) Lee, M. J.; Gupta, D.; Zhao, N.; Heeney, M.; McCulloch, I.; Sirringhaus, H. Anisotropy of charge transport in a uniaxially aligned and chain-extended, high-mobility, conjugated polymer semiconductor. *Advanced Functional Materials* **2011**, *21*, 932-940.
- (7) Kayunkid, N.; Uttiya, S.; Brinkmann, M. Structural model of regioregular poly(3-hexylthiophene) obtained by electron diffraction analysis. *Macromolecules* **2010**, *43*, 4961-4967.



## *Annexes and experimental protocols*



## 1. Step by step instruction for slow rate DEC

For the preparation of thin films by the slow-DEC method, several steps are involved which will be detailed here.

### 1.1. The powder preparation

The first step consists in preparing the powder mixture of TCB and P3HT (TCB/P3HT/CdSe). For the powder preparation, the used TCB must first be purified by successive evaporation and re-crystallization. Thereafter, the desired amount of TCB is placed in a suited glassware and heated up to around 70°C. The glassware is covered with a lid onto which TCB re-crystallizes and from which it can be recovered.

Generally a powder mixture contains 1 mg of P3HT and 400 mg of TCB. For the preparation of thicker films, the relative concentration of P3HT can be increased. The 400 mg TCB and 1 mg P3HT are dissolved in an arbitrary amount of chloroform. In order to obtain a perfectly homogenous solution, the flask is placed onto a slightly heated hot plate for more than 10 minutes. Once the solution is homogenous, the flask is opened and left at **room temperature** until all the chloroform is evaporated. This generally takes one night. A violet P3HT/TCB powder is then obtained.

For the preparation of hybrid thin films, the desired amount of NCs is added to the solution before evaporation of the TCB, the ratio P3HT/TCB being unchanged.

### 1.2. The film preparation

The second step consists in the film preparation. The glass slides have first to be prepared (cleaning and adequate coating) as described hereafter. The hotplate of the « PTFE machine » is heated to a temperature of  $T \approx 75^{\circ}\text{C}$  (allowing the melting of the TCB)

**Step 1:** ~25 mg of the P3HT/TCB powder are deposited on the “small” PTFE-coated glass slide (*Figure 1-1*). The whole (glass slide + powder) is placed for a short moment onto the hot plate, just the time necessary for the powder to melt. Afterwards, the molten solution must be spread over the entire glass slide before re-solidification. The “powder “sticks now to the small glass slide and the latter can be deposited on a polymer (PVP, PEDOT:PSS, etc.) coated larger glass slide in order to sandwich the P3HT/TCB powder between the two coated glass slides. Afterwards, the system undergoes two crystallization steps as described hereafter.



Figure 1-1 : approx. 25mg of the P3HT/TCB powder deposited on a PTFE coated small glass slide

**Step 2 First rapid crystallization :** The system is placed onto the hot plate (the polymer coated slide at the bottom and the PTFE coated slide on the top). The powder is left to melt until the obtention of a homogenous liquid film (air bubbles must be avoided). This is illustrated in *Figure 1-2 a*. Once a homogenous liquid film is formed, the end of the bottom glass slide is fixed on the fixation (with adhesive tape) and the hot plate is moved at a constant velocity of  $200\mu\text{m/s}$ . Crystallization sets on at the side of the film that is fixed to the cold holder. *Figure 1-2 b* illustrates this step. The crystallization propagates to the entire film surface. The challenge is to obtain perfectly parallel TCB crystals at the ending of the film. These parallel crystals are of major importance as they will serve as the nucleation seeds in the second crystallization step. The more parallel these seeds are, the better the in-plane orientation of the final film will be.

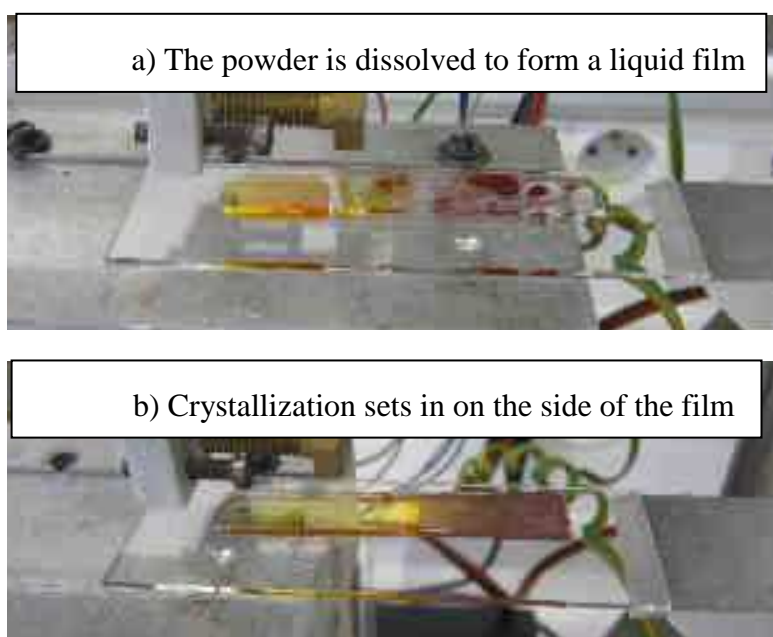


Figure 1-2: Illustration of Step 2 of the slow rate DEC process. a) the powder is molten between the two coated glass slides to form an homogenous P3HT/TCB liquid film. b) First crystallization at  $200\mu\text{m/s}$ . The film starts to crystallize on the cold side of the sample holder and propagates through the entire film in order to obtain parallel TCB crystals at the end that can be used as seeds for the second crystallization step.

**Step 3 Final crystallization** (see Figure 1-3): For the second and final crystallization, as mentioned before the obtained TCB crystals produced during the first crystallization step are used as nucleation seeds for the P3HT. The second crystallization is performed by using the « local melting triangle » temperature of the hot-plate heated at  $T \sim 83-85^{\circ}\text{C}$ . The height of the apex of the triangle is adjusted in order to have the glass slide in horizontal position. The side of the slides showing the parallel crystal seed is kept fixed on the holder. Once the local melting sets in the translation of the “hot triangle” at a speed of  $20\mu\text{m/s}$  allows for the complete recrystallization of the film.



Figure 1-3 : Second crystallization with the local melting apparatus.

**Step 4 Elimination of the TCB:** Once the crystallization of P3HT is finished, the TCB must be removed in order to recover the P3HT films. Therefore, the film is placed for one night into primary vacuum which allows eliminating TCB by sublimation. Once all the TCB has evaporated, it is easily to separate the upper (small) and the lower (large) glass slides and to recover a thin oriented and nanostructured P3HT film on both surfaces.

## 2. PTFE machines improvement and users' guide

The PTFE machine is a homemade machine initially designed for the preparation of PTFE films by friction transfer (1). It is composed of a motorized translating hot plate and of an apparatus allowing to apply a controlled pressure (5bar) necessary for the PTFE film preparation. For the use of the “PTFE machine” for the directional epitaxial crystallization (DEC) some modifications have been to made:

The initial temperature controller was replaced by a more modern one allowing to control the temperature with a precision of  $\sim \pm 2^{\circ}\text{C}$ .

The zone melting apparatus was elaborated during this PhD work. It consists of a triangle fitting exactly to the hot plate made of aluminium to allow a good temperature transfer from the hot plate to the apex of the triangle. A schematic representation of this triangle is represented in *Figure 2-1*

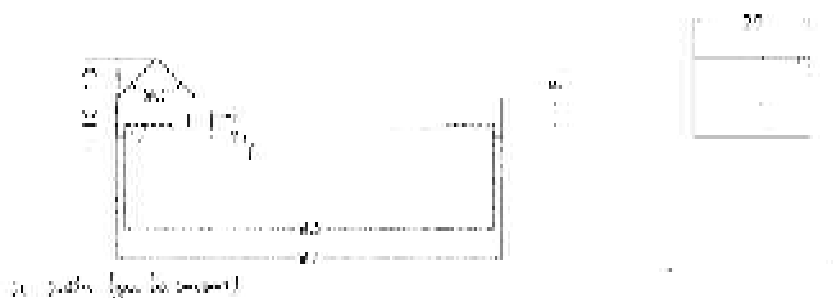


Figure 2-1: Scheme of the zone-melting triangle with exact dimensions.

Another important point is the control of the translation speed of the hotplate. As for the preparation of the PTFE films only a single speed of  $200 \mu\text{m/s}$  is used. The PTFE machine has different available translation speeds which can be adjusted by the 3 ‘screws’ that are also used to pass from the automatic mode to the manual mode. As these speeds were never used, their adjustment and also their values were unknown. The speeds were measured by marking a distance of 5 cm on a glass slide and by measuring the time necessary to run through these 5 cm. Three measurements per speed were made in order to get an idea of the errors. The available speeds are:  $V_1 = 200 \pm 0.1 \mu\text{m/s}$ ,  $V_2 = 41.15 \pm 0.1 \mu\text{m/s}$ ,  $V_3 = 20.62 \pm 0.1 \mu\text{m/s}$ ,  $V_4 = 4.1 \pm 0.1 \mu\text{m/s}$ . The adjustment of these speeds via the screw position is illustrated in Figure 2-2.

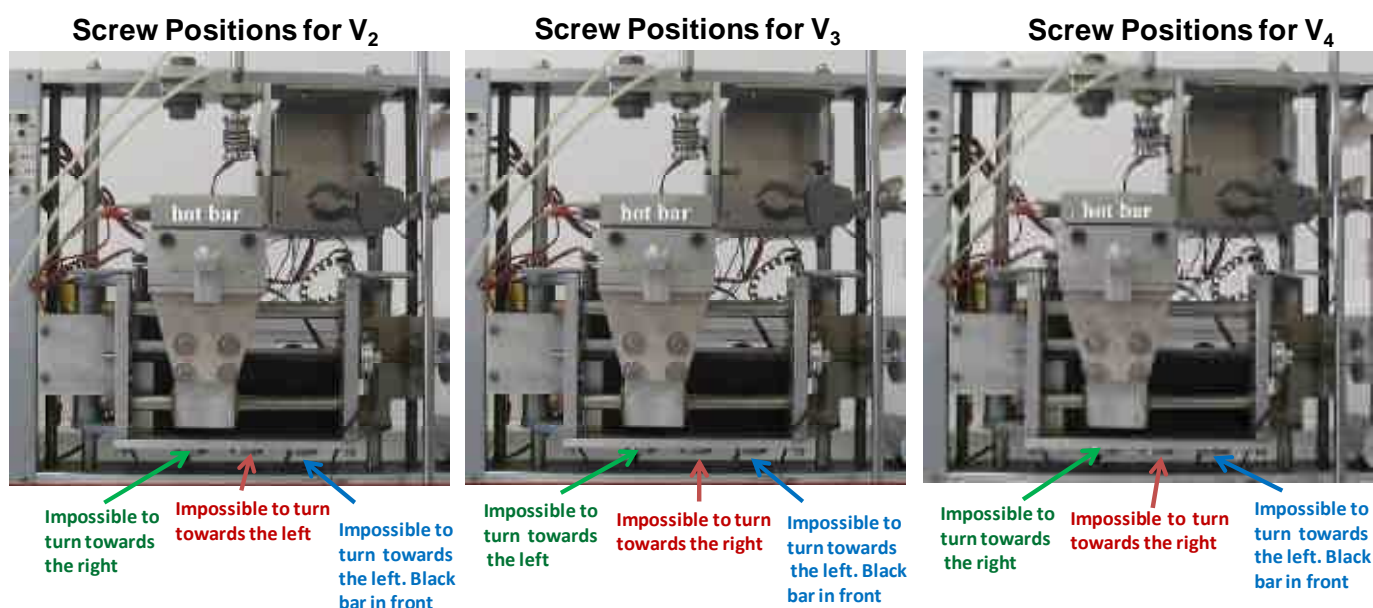
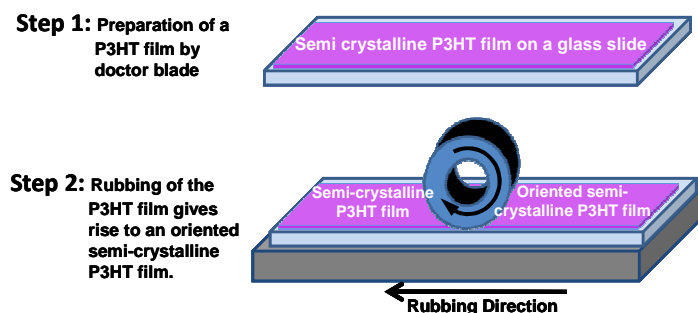


Figure 2-2: Screw positions for the adjustments of the speeds of the PTFE machine.

### 3. Detailed experimental description of mechanical rubbing

The initial rubbing process was developed by Brinkmann *et al.* and described in detail by C. Vergnat for the orientation and nanostructuring of bisphenol polycarbonate (2–5). The

orientation of P3HT by mechanical rubbing involves essentially 2 steps: (i) the preparation of an un-oriented P3HT film by the doctor blade method and (ii) followed by a rubbing step of the as-deposited films using a microfiber tissue. The preparation of the thin films by the doctor blade method is explained hereafter.



*Figure 3-1 : Schematic description of the rubbing process of a P3HT film. In a first step an un-oriented P3HT film is deposited onto a clean substrate. In a second step the film in its un-oriented state is rubbed with a microfiber cloth to induce orientation.*

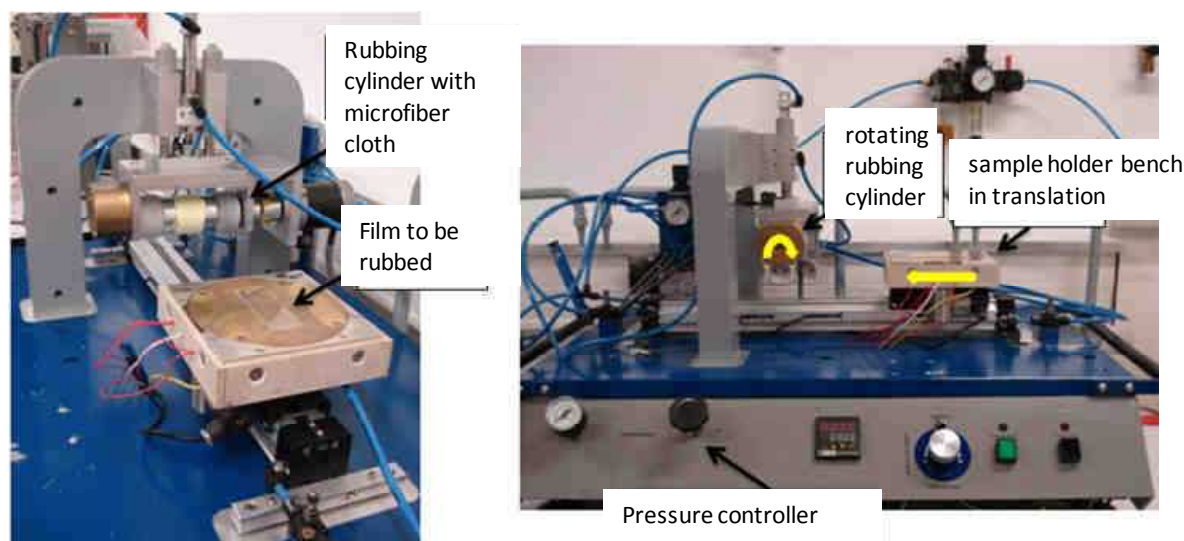


*Figure 3-2 : Photography of the home made apparatus. The P3HT film deposited onto the glass slide is translated at a constant speed below the rotating cylinder which is applied onto the film with a pressure of around 2 bar.*

*Figure 3-1* shows a schematic representation of the process and a photography of the apparatus is presented in *Figure 3-2*. The rubbing machine is composed of a cylinder (diameter 4 cm) covered by a microfiber tissue. During the rubbing process, the cylinder is rotating at a speed of approximately 100-300 turns per minute. The non-oriented P3HT film deposited on the glass slide is moving at a constant speed below the rotating cylinder which is pressed onto the P3HT film in order to have a pressure approx. 2 bar.

### 3.1. Preparation of the thin films by the doctor blade method

Before the rubbing process, the thin film is deposited on a clean glass slide (or silicon wafer) by the doctor blade method. The doctor blade used during this work is a homemade apparatus composed of a blade of Teflon a translation bench that can be heated at a controlled temperatures and moved at a constant speed forwards and backwards. To fix the distance between the Teflon blade and the substrate, we use 2 cover slits. This should approximately correspond to a distance of approx. 0.2 mm. The deposition protocol varies if pure P3HT films are deposited or if hybrid thin films are deposited



Figure 3-3: Photography of the homemade doctor blade machine. The substrate is placed on the translation bench which can be heated at a desired temperature and moved forwards and backwards.

#### 3.1.1. Pure P3HT films

For the deposition of P3HT films, solutions of 8 wt% were used. The solvent was adapted depending on the P3HT molecular weight. For  $M_w > 10$  kDa, chlorobenzene was used and for the hexane fractions ( $M_w < 10$  kDa) chloroform was preferred. The choice of solvent was done in this way as for low- $M_w$  samples processed from chlorobenzene, the films were not homogenous. The solutions were placed for approximately 1 hour at approx. 40°C to allow a complete melting of the P3HT. After, the solutions were filtered with a Teflon filter. Once the solutions are ready for processing, approximately 35-50  $\mu$ L of the solution were placed on the substrate and the translation bench was activated. For most of the films, one translation cycle was performed (one way forwards and one backwards). The translation bench was kept at room temperature.

### 3.2. Hybrid Films (P3HT + nanorods)

The preparation of hybrid films by the doctor blade method is similar to that of P3HT films. After their synthesis, the nanorods are kept in toluene, as every solvent transfer of the nanorods goes along with a loss in solubility. Hybrid solutions were thus prepared in a solvent

mixture. Hybrid films were thus solution processed from a solvent mixture chlorobenzene/toluene for P3HT with  $M_w > 10$  kDa or chloroform/toluene for P3HT  $M_w < 10$  kDa. The temperature of the hot plate was at  $\sim 35^\circ\text{C}$ .

#### 4. Preparation of the substrates

- **Cleaning procedure of the glass slides and silicon wafers:**

Glass slides: Before use, the glass slides are cleaned using the following procedure: Successive sonication for respectively 15 minutes in acetone and ethanol. After this, the glass slides are brushed with a nylon brush and sonicated for 15 min in the hellmanex solution. In order to rinse the slides, these are sonicated in milli-Q respectively three times for 15 min. After cleaning, the glass slides are dried under a nitrogen flow.

Silicon wafers: Silicon wafers were placed in a glassware covered with aluminum foil for  $\sim 30$  under a UV lamp.

- **Deposition procedure of PEDOT-PSS:** The PEDOT:PSS is diluted by 50% in MeOH and filtered with  $0,45\mu\text{m}$  TF filters (hydrophilic). Spin coating was performed in two steps:
  - 40 s at 1500 rpm after an acceleration of 375 rpm/s;
  - 40 s at 2000 rpm after an acceleration of 375 rpm/s.

- **Deposition procedure of PVP:** PVP was spin coated from a 5 mg/mL solution in isopropanol. The solution was kept under stirring until all PVP is dissolved (around 2 h). Before spin coating the solution is filtered with a PTFE filter.

- **Deposition procedure for polyacrylic acid:** Polyacrylic acid was spin coated from a 5 wt % solution in water. The spin coating procedure is the same as that used for PEDOT: PSS.

- **Deposition of Cytop:** Cytop was spin coated during 30s at 400 rpm with an acceleration of 100 rpm/s. After spin coating, the substrate with the film still liquid is deposited onto a hot plate for annealing. The complete annealing procedure involves two steps: 6 min at  $60^\circ\text{C}$  just after the spin coating and afterwards 10 min at  $100^\circ\text{C}$  for cross-linking the Cytop. This procedure gives films having a thickness of around 800-1000 nm (measured with a stylus profilometer).

- **Deposition procedure of PTFE:** PTFE films are deposited by friction transfer with the PTFE machine at  $300^\circ\text{C}$ . The method was first proposed by Wittmann and Smith. The principle is simple. A PTFE bar is applied at a constant pressure (5 bar) onto a

clean glass slide which is fixed to a hotbar maintained at 300°C and translated at a velocity of 200 μm/s. This procedure allows to get highly oriented surfaces of PTFE over the whole glass slide surface. Films prepared by this method are in general 2-100 nm thick.

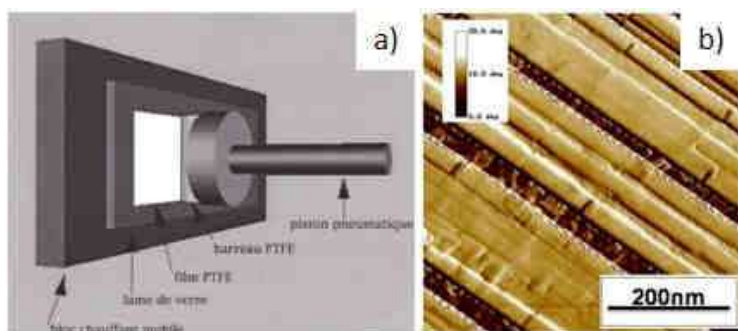


Figure 4-1 : Procedure and AFM characterization of a PTFE film deposited by friction transfer. The images are reproduced from (1)

- **OTS treatment of the glass slides:** The OTS treatment of the glass slides was performed in the vapour phase. Therefore, 10 clean glass slides were placed into a sealed jar at which was placed a glass vessel containing OTS. The sealed jar was pumped by a rotary pump in order to have a primary vacuum. Afterwards the entire jar was placed over 24 hours in an oven at 100°C. Contact angles >90° were obtained.

## 5. Optical characterizations

### 5.1. UV-visible absorption spectroscopy

#### 5.1.1. UV-vis spectroscopy of colloidal solutions of CdSe

The UV-vis spectra of a colloidal dispersion of CdSe nanocrystals placed in a quartz cuvette were recorded either on a Varian spectrometer in Strasbourg or an HP8452A Diode Array Spectrophotometer in Grenoble.

#### 5.1.2. Polarized UV-vis of P3HT or hybrid thin films

The dichroic ratio and the degree of orientation of epitaxied and rubbed P3HT/ hybrid thin films was determined by UV-visible spectroscopy measurements in the spectral range of 300 to 900 nm. A Shimadzu UV-2101PC spectrometer with a spectral resolution of 1 nm and polarized incident light was used. The orientation of the film with respect to the polarization of the incident beam is controlled by a goniometer. The parallel configuration is defined as the position where the  $c_{P3HT}$  axis is parallel to the optical polarization. For each sample, a spectrum in the parallel and perpendicular configuration were measured.

## 5.2. Photoluminescence

### 5.2.1. PL spectroscopy of colloidal solutions of CdSe

Photoluminescence spectra of colloidal dispersions of CdSe nanocrystals were measured under dilute conditions (absorbance at the excitonic peak  $\sim 0,1$  OD) in transparent quartz cuvettes. The spectra were recorded with a Hitachi F-4500 Fluorescence Spectrophotometer in Grenoble and a Jobin-Ivon Spectrometer in Strasbourg. The excitation wavelength was usually set at 490 nm. The spectra were normalized by the absorbance of the exciton peak of the same solution as the concentration is difficult to control and spectra were normalized by the integration time.

### 5.3. Optical polarized Microscopy

The polarized optical microscope images were recorded on a Leica DMR-X microscope with crossed polarizer and analyzer. The images were recorded with a CCD camera (Nikon, Coolpix995).

## 6. X-ray diffraction

### 6.1. XRD on P3HT and hybrid thin films

GIXD measurements were performed on P3HT and hybrid thin films. These measurements were performed at the ANKA synchrotron on the beamline PDIFF at a wavelength  $\lambda=1,24$  Å and at the ESRF on the beamline ID10b at a wavelength  $\lambda=0,59$  Å. The scattering configurations are described in Chapter 4.

### 6.2. XRD on CdSe NCs after Synthesis

XRD spectra of the as-synthesised nanocrystals were measured with a Philips X'pert diffractometer with a Co source ( $\lambda= 1.78$ Å). To perform the measurements, a concentrated solution of CdSe after synthesis was drop casted onto a silicon substrate.

## **7. Transmission Electron Microscopy (TEM) measurements**

### **7.1. TEM on as-synthesized CdSe Nanocrystals**

TEM imaging of the as-synthesised nanocrystals was performed on a Jeol 4000EX Transmission Electron Microscope in Grenoble. For the TEM grid preparation, a very dilute solution of CdSe NCs is drop casted onto a TEM holey carbon grid (Ted Pella). The excess of solution was removed using a filter paper and the grid was dried in a sealed jar under primary vacuum.

### **7.2. Standard TEM and TEM tomography on P3HT and hybrid thin films**

#### **7.2.1. TEM sample preparation**

The thin P3HT/hybrid films are coated by a film of amorphous carbon which is evaporated on top of the P3HT/hybrid films. After coating with amorphous carbon, regions of interest are selected using an optical microscope. To recover the thin film on the TEM grid, the procedure depends on the substrate onto which the film is deposited:

- **Thin films prepared on glass:** The thin films covered by the amorphous carbon are removed from the glass substrate by dissolving the glass in a diluted solution fluoric acid in distilled water (5%). The film is floated at the surface and can be recovered onto a TEM grid.
- **Thin films prepared on hydro-soluble substrates:** The TEM grid preparation method is the same than above but instead of fluoric acid, the films are recovered by floating them in distilled water.
- **Thin films prepared on PVP, Cytop, etc.:** After coating the films with the amorphous carbon film, polyacrylic acid is dropped onto the region of interest. Polyacrylic acid is left to dry for 3-4 hours. Afterwards the areas of the films covered by polyacrylic acid is removed from the substrate by using tweezers and placed onto the surface of distilled water with the polyacrylic acid coated side into the water. Polyacrylic acid is left to dissolve for 10-20 min, and the thin P3HT/hybrid film can be recovered on a TEM grid.

#### **7.2.2. Standard TEM**

The morphological and structural analysis of thin P3HT and hybrid films were realized with a CM 12 Philips 120kV TEM equipped with a MVIII CCD camera (Soft Imaging System; CCD = charge-coupled device). Thin films were observed in the bright field (BF), dark field (DF), diffraction (ED) and high resolution (HR) modes. The high resolution TEM images were

acquired in a modified low-dose mode to avoid beam damaging of the P3HT thin films. First, focusing and astigmatism corrections were performed on a test area, then the electron beam was blanked and the sample position was shifted to an unexposed nearby area. Stabilization of the mechanical drifts of the sample was observed after *ca.* 30-40s (6). For the acquisition and some treatments of the images the Analysis software was used.

### 7.2.3. Electron tomography experiments

The tomographic tilt series were acquired on a JEOL 2100F transmission electron microscope equipped with a field emission gun operating at 200 kV, a spherical aberration probe corrector and a GATAN Tridiem energy filter. Digital Micrograph was used as the acquisition software: it allows an automated acquisition of the tilt series by varying the tilt angle step by step and by controlling the defocusing and the specimen drift at each tilt angle. Using a high tilt sample holder from the GATAN Company, several bright field TEM tilt series were acquired for each specimen for angles between  $70^\circ$  and  $-70^\circ$  and with a tilt increment given by a  $2^\circ$  Saxton scheme. As a result, for each sample a number of about 100 TEM images were recorded and the acquisition of a tilt series represented a recording time of about 45 minutes. Irradiation damage during the acquisition of the tomographic sequences was minimized by lowering the electron doses. A  $2048 \times 2048$  pixels cooled CCD detector having a pixel size of 0.2 nm and a 1 s exposure time was employed for each record. Once the acquisition was completed, the images of the tilt series were first roughly aligned using a common cross correlation algorithm. A refinement of this initial alignment was performed using the IMOD software where some of the CdSe nanoparticles have been used as fiducial markers (7). The volume reconstructions were then computed using algebraic reconstruction techniques (ART) (8) implemented in the TomoJ software (9) for 15 iterations. Visualization and quantitative analysis of the final reconstruction were carried out using the ImageJ and 3D Slicer softwares. The characterization of the parameters of interest (density of NCS averaged in the whole film as well as its variation in the depth) was performed by using a statistical approach. This consists in the analysis of the geometrical positions of all the NCs hosted in the chosen area, taking as reference the two surfaces of the film deduced by a data segmentation procedure.

## 8. NMR

- Standard  $^1\text{H}$  NMR spectra were recorded on a Bruker 400MHz using deuterated chloroform ( $\text{CDCl}_3$ ) as the solvent for the NCs. The NMR signal of residual  $\text{CHCl}_3$  at 7,26 ppm was used as reference for the spectra. Concentrations of the solutions of NCs were approx. 5-10mg/mL to provide sufficient signal to noise ratios..
- Pulsed field gradient (PFG)  $^1\text{H}$ -NMR measurements were performed with colloidal dispersions of NCs in deuterated toluene. Deuterated chloroform is not suitable for such measurements due to undesired convection artefacts which affect the measured values of the coefficient diffusion of the species. The measurements were realized on a

Bruker 500 MHz spectrometer at a constant temperature  $T=25$  °C. For the bipolar LED (BPP-LED) sequence, we used the same as in the work of Hens *et.al* (10). In our case, a diffusion delay of  $\Delta= 200$  ms and a gradient pulse duration of  $\delta = 1$  ms were chosen.

## 9. Thermogravimetric analysis on NCs

Thermogravimetric measurements were realized under nitrogen atmosphere on a SETARAM 92-12. Approximately 10 mg of NCs were dried and placed into a platinum pan. The temperature was raised at a constant rate of 10°C/min.

## 10. Transistor fabrication

In order to measure hole mobilities in rubbed P3HT films, prefabricated transistors in a bottom gate/bottom contacts configuration were provided by the Fraunhofer Institute for Photonic Microsystems (IPMS), Dresden. Highly n-doped silicon wafers with a 300 nm thick SiO<sub>2</sub> layer obtained by thermal oxidation served as gate electrode and gate insulator respectively. Gold source and drain electrodes (40 nm thick) constituted interdigitated transistor channels with a length (L) of 20 μm and a width (W) of 10 mm. Prior to use, the transistor substrates were cleaned by ultrasonication in acetone (600 s) and subsequent exposure to an oxygen plasma (Diener Femto 100W) for 300 s.

Polymer films about 80 nm thick were spin coated from 10 mg ml<sup>-1</sup> solutions of the respective polymer in CHCl<sub>3</sub> at 2000 rpm. The polymer solutions were prepared by dissolution at 50°C for 2 h under continuous stirring followed by the immediate filtration through 200 nm PTFE filters (VWR) at room temperature. All polymer solutions and films were prepared in an inert nitrogen atmosphere. To ensure identical rubbing conditions, three P3HT films with different  $M_w$  were fixed on a microscope glass slide and rubbed during the same experimental run. After rubbing the films, the electronic characterization of the FETs was carried out in a nitrogen atmosphere using a Keithley 2636 Dual channel sourcemeter. Field effect mobilities ( $\mu_{FET}$ ) were determined from the transfer characteristics curve in the saturation regions using the following equation:

$$I_{SD} = \frac{W}{2L} C_i \mu_{FET} (V_g - V_0)^2 \quad (\text{Eq. 1})$$

where  $I_{SD}$  is the source-drain current in the saturation regime,  $V_g$  is the source-gate voltage,  $C_i$  is the insulator capacity, L and W are the channel length and width and  $V_0$  is the turn-on voltage.

- (1) Wittmann, J. C.; Smith, P. Highly oriented thin films of poly(tetrafluoroethylene) as a substrate for oriented growth of materials. *Nature* **1991**, *352*, 414-417.
- (2) Brinkmann, M.; Pratontep, S.; Chaumont, C.; Wittmann, J.-C. Oriented and nanostructured polycarbonate substrates for the orientation of conjugated molecular materials and gold nanoparticles. *Macromolecules* **2007**, *40*, 9420-9426.
- (3) Vergnat, C. Elaboration de surfaces polymers orientées et nanostructurées pour l'orientation de matériaux moléculaires conjugués, PhD dissertation, Université de Strasbourg, 2010.
- (4) Vergnat, C.; Uttiya, S.; Pratontep, S.; Kerdcharoen, T.; Legrand, J.-F.; Brinkmann, M. Oriented growth of zinc(II) phthalocyanines on polycarbonate alignment substrates: Effect of substrate temperature on in-plane orientation. *Synthetic Metals* **2011**, *161*, 251.
- (5) Vergnat, C.; Landais, V.; Legrand, J.-F.; Brinkmann, M. Orienting semiconducting nanocrystals on nanostructured polycarbonate substrates: impact of substrate temperature on polymorphism and in-plane orientation. *Macromolecules* **2011**, *44*, 3817-3827.
- (6) Brinkmann, M.; Rannou, P. Molecular weight dependence of chain packing and semicrystalline structure in oriented films of regioregular poly(3-hexylthiophene) revealed by high-resolution transmission electron microscopy. *Macromolecules* **2009**, *42*, 1125-1130.
- (7) Kremer, J. R.; Mastronarde, D. N.; McIntosh, J. R. Computer visualization of three-dimensional image data using IMOD. *Journal of structural biology* **1996**, *116*, 71-6.
- (8) Gordon, R.; Bender, R.; Herman, G. T. Algebraic reconstruction techniques (ART) for three-dimensional microscopy and X-ray photography. *Journal of theoretical biology* **1970**, *29*, 471.
- (9) Messaoudi, C.; Boudier, T.; Sorzano, C.; Marco, S. TomoJ: tomography software for three-dimensional reconstruction in transmission electron microscopy. *BMC bioinformatics* **2007**, *8*, 288.
- (10) Hens, Z.; Moreels, I.; Martins, J. C. In situ <sup>1</sup>H NMR study of the trioctylphosphine oxide capping of colloidal InP nanocrystals. *Chemical Physics and Physical Chemistry* **2005**, *6*, 2578.





# Elaboration et étude de matériaux hybrides orientés et nanostructurés d'intérêt pour l'électronique organique

## Résumé

Le but de cette thèse était d'élaborer et d'étudier des films minces hybrides orientés et nanostructurés composés d'un polymère semi-conducteur, le poly(3-hexylthiophène) regiorégulier (P3HT) et de nanocristaux semiconducteurs de CdSe (sphères, bâtonnets). Pour cela, deux méthodes ont été mises en œuvre: la croissance épitaxiale directionnelle et le brossage mécanique. Les films de P3HT purs épitaxiés et brossés se différencient en termes de nanomorphologie, d'ordre cristallin et de structure. Les premiers présentent une morphologie lamellaire et une structure de fibre où les chaînes conjuguées sont alignées suivant l'axe de fibre. Les films brossés ne présentent pas de structure lamellaire et les domaines cristallins sont orientés préférentiellement «flat-on». Ces différences se reflètent dans les propriétés optiques des films épitaxiés et brossés. Le degré d'orientation des films brossés dépend fortement du poids moléculaire et une forte anisotropie du transport de charges a été observée. Les films hybrides épitaxiés sont nanostructurés avec localisation des nanocristaux dans les zones amorphes du P3HT. Par ailleurs, l'analyse par tomographie électronique de ces films montre une structure en bicouche avec une couche hybride surmontée d'une couche de P3HT pur. Les films hybrides brossés montrent clairement un alignement des nanobâtonnets de CdSe et des chaînes du P3HT parallèlement à l'axe du brossage. Les degrés d'orientation du P3HT et des nanobâtonnets sont corrélés et dépendent de la proportion en nanoparticules indiquant que c'est la matrice polymère qui induit l'orientation des nanobâtonnets.

**Mots clés:** électronique organique, polymers semi-conducteur, Poly(3-hexylthiophene), orientation de polymères, brossage mécanique, épitaxie, nanocristaux, échange de ligands

## Résumé en anglais

The aim of this thesis was to elaborate and characterize hybrid oriented and nanostructured thin films composed of a semiconducting polymer, regioregular poly(3-hexylthiophène) (P3HT) and semiconducting CdSe nanocrystals (spheres, rods). Two orientation methods were used: directional epitaxial crystallization and mechanical rubbing. Epitaxied and rubbed films of pure P3HT show strong differences in terms of nanomorphology, crystalline order and structure. Epitaxied films possess a lamellar morphology, a 3D crystalline order and fiber symmetry where the P3HT backbones ( $\mathbf{c}_{\text{P3HT}}$ ) are aligned along the fiber axis. Rubbed films do not show a lamellar morphology and have a 2D crystalline order with crystalline domains preferentially oriented "flat-on" relative to the substrate. These differences are reflected in the optical properties of the films. The orientation degree achieved in rubbed films strongly depends on the molecular weight of the polymer. There is also a strong anisotropy of the charge transport properties. Regarding hybrid epitaxied layers, we observed a nanostructuration with a localization of the CdSe nanocrystals into the amorphous zones of the P3HT. Moreover, electron tomography analysis shows that such films have a bilayer structure with a hybrid layer covered by pure P3HT. In rubbed hybrid films prepared with nanorods, the long axis of the nanorods as well as the P3HT backbone are oriented parallel to the rubbing direction. The degree of in-plane orientation of the rods and of the P3HT matrix match closely and depend on the proportion of CdSe nanorods in the films. These results suggest that the P3HT matrix enforces the orientation of the rods.

**Keywords:** Organic electronics, Semi-conducting polymers, Poly(3-hexylthiophene), Orientation of polymers, mechanical rubbing, epitaxy, nanocrystals, ligand exchange